Characterisation of a PERCA instrument and measurements of peroxy radicals during the West African Monsoon 2006

Thesis submitted for the degree
of Doctor of Philosophy
at the University of Leicester

By

Daniel M Brookes M.Phys.
Department of Chemistry
University of Leicester

November 15, 2009

The work in this thesis was conducted at the Department of Chemistry of the University of Leicester in the Atmospheric Chemistry group between September 2005 and November 2009. The work is that of the author unless acknowledged in the thesis.

The thesis may be made available for consultation within the library of the University of Leicester.

Daniel Michael Brookes

Leicester

November 15, 2009

Abstract

Characterisation of a PERCA instrument and measurements of peroxy radicals during the West African Monsoon 2006

Daniel Michael Brookes

This thesis investigates measurements of peroxy radicals using PERCA, photolysis frequencies of ozone (j_{O^1D}) and NO_2 (j_{NO_2}) using filter radiometers (FR's) and processes controlling atmospheric chemistry within the West African Monsoon (WAM).

The chain length (CL) of the University of Leicester (UoL) ground and aircraft PERCA inlets are shown to decay exponentially with relative humidity, and a humidity interference is observed with the luminol chemiluminescence NO_2 detection technique. The altitude dependence of the CL is derived using a chain chemistry model. The aircraft PERCA NO_2 sensitivity is derived by calculating the background NO_2 concentration from reaction of ambient ozone with reagent NO.

Calibration of the UoL aircraft FR's is described; temperature, solar zenith angle and ozone column bias in the j_{O^1D} measurement is estimated. A method is proposed for cross-calibration of FR's spectral response using spectrally resolved measurements of actinic flux. An estimate for upwelling j_{O^1D} is assessed where the instrument failed during fieldwork.

Atmospheric composition is dominated by surface emissions and transport within the WAM. A nocturnal flow transports reactive VOC's and oxidation products north, anthropogenics from coastal cities and biogenics from forested regions. Significant night-time concentrations of RO_2, HO_2, and potentially OH are observed. The most photochemically active air masses observed are biomass burning (BB) plumes of Central African origin. Variations in radical composition, inferred from VOC reactivity to OH, follow the trends of the University of Leeds DSMACC box model. The ozone balance is NO_x limited within air masses where biogenic soil NO_x emissions are suggested. PERCA and FR measurements are assessed through comparison to model results. Daytime PERCA measurements compare well with DSMACC RO_2 with differences explained through measurement bias – ambient aircraft measurements appear responsive to RO_2 only, with no humidity dependence and complete HO_2 loss. Median noontime concentrations of RO_2 of 35 pptV are observed.

Acknowledgements

I have received a great deal of support from many people during the course of my PhD and feel a huge amount of gratitude toward those who have helped, personally and professionally. This thesis would not have been possible without you and I would not have made it through otherwise. I would particularly like to thank my supervisor Paul Monks for the many opportunities I have had throughout the past four years, and for encouragement when work has been frustrating, you have a knack for saying the right thing at the right time. Thanks must go to NERC for providing the financial backing for the work undertaken on this project, and for the extended funding that has allowed me the time to bring the work together in this thesis. Through the many trials and tribulations of the AMMA, OOMPH, OP3 and other field campaigns I have enjoyed the company and support of my co-workers, it has been great to have such friendship and support wherever this work has taken me across the world.

Thanks must go to the past and present members of the Atmospheric Chemistry Group. I especially want to thank Alex Parker whose expert knowledge of the PERCA instruments I hope to have built upon; I appreciate the time you spent to help me during the AMMA campaign, *probably* the most logistically difficult field campaign the group has undertaken in recent times. Particular mention must also go to the more recent PERCA people Karun, Virginia (sort of) and now Karen. Chris, Kerry, Kev, Rebecca, Bob, Karun, Timo, Zoe and others, thankyou for your friendship and listening to my ranting, I often had something to get off my chest. I must also thank the administrative and technical staff in the University of Leicester, Department of Chemistry, you are the people who facilitate much of the research we undertake. I appreciate especially your willingness to meet my requests (often at short notice) which made this work possible. Special mention must go to Phil Acton, Julie Spence, Justin Shepard, Keith Wilkinson, John Wheald, Carl Schieferstein, Roy Batchen, Sai Choudhury, Ann Crane, and Chris Goddard.

My housemates at Southernhay Avenue, Steve, Adi and Charlotte, you have all been great friends and tried your best to help me strike a decent work life balance. Cheers for putting up with my constant travelling, it was good to always have somewhere to call home in Leicester.

To my family especially my mum and dad, thankyou for the unconditional support you have given me, you have been a constant during the many challenges and have listened even if you have not always fully understood my work. Simon and Rubina, many thanks for so often welcoming me into your family home, for feeding me so well and supporting Martha whenever I have not been there.

Finally and most importantly, I must thank Martha, you understand the ups and downs of the past four years most well. Thankyou for caring for me and sticking with me, you have been the ultimate personal motivation behind this work.

Abbreviations

AEJ African Easterly Jet

AMMA African Monsoon Multidisciplinary Analysis

AOT Aerosol Optical Thickness

CBL Convective Boundary Layer

CFC Chlorofluorocarbon

CIMS Chemical Ionisation Mass Spectrometry

CRDS Cavity Ringdown Spectroscopy

DSMACC Dynamically Simple Model of Atmospheric Chemical Complexity

EOP Enhanced Observing Period

FAAM Facility for Airborne Atmospheric Measurements

FAGE Fluorescent Assay by Gas Expansion

IPCC Intergovernmental Panel on Climate Change

IR Infrared

ITCZ Intertropical Convergence Zone

ITD Intertropical Discontinuity

LAI Leaf Area Index

LIF Laser Induced Fluorescence

LOP Long term Observing Period

MACR Methacrolein

MCM Master Chemical Mechanism

MCS Mesoscale Convective System

MFC Mass Flow Controller

MFM Mass Flow Meter

MIESR Matrix Isolation Electron Spin Resonance

MVK Methyl Vinyl Ketone

NERC Natural Environment Research Council

NMHC Non Methane Hydrocarbon Compound

ppmV, ppm Parts per million by volume, parts per million

PERCA PEroxy Radical Chemical Amplifier

PerCIMS Peroxy radical Chemical Ionization Mass Spectrometry

PMT Photo Multiplier Tube

PTR-MS Proton Transfer Reaction Mass Spectrometry

ROxMas ROx Chemical Conversion/Chemical ionisation Mass spectrometry

RH Relative Humidity

RTD Resistance Temperature Detector

SAL Saharan Air Layer

sccm Standard Cubic Centimetres per Minute

SH Specific Humidity

slpm Standard Litres Per Minute

SOA Secondary Organic Aerosol

SOP Special Observing Period

STE Stratosphere Troposphere Exchange

SZA Solar Zenith Angle

TSSE Technical Specification of Scientific Equipment

TUV Tropospheric Ultraviolet and Visible Radiation Model

UV Ultraviolet

USSA US Standard Atmosphere

VOC Volatile Organic Compound

WAM West African Monsoon

WAS Whole Air Sample

Contents

1 Introduction **1**

1.1 Atmospheric Structure, Composition and Dynamical Processes 1

1.1.1 Atmospheric structure 2

1.1.2 The lower atmosphere 3

1.2 Background chemistry 8

1.2.1 Stratospheric ozone 8

1.2.2 Tropospheric chemistry of peroxy radicals 10

1.2.3 Production and destruction of tropospheric ozone 14

1.3 Chapter 1 Summary 16

2 Measurement of atmospheric peroxy radicals **17**

2.1 Measurement techniques 17

2.1.1 Chemical amplification techniques 18

2.1.2 LIF techniques 36

2.1.3 MIESR (Matrix Isolation Electron Spin Resonance spectroscopy) - Speciated measurement of HO_2, alkyl RO_2, $CH_3C(O)O_2$, NO_3 and NO_2 41

2.1.4 Developmental techniques 42

2.1.5 Summary of overview of peroxy radical measurement techniques 43

2.2 Previous campaigns involving measurements of radicals 45

2.3 Chapter 2 Summary 45

3 Characterisation and calibration of a PERCA instrument 48

3.1 The University of Leicester PERCA instruments 48

3.1.1 PERCA 4 – Aircraft PERCA instrument 49

3.1.2 PERCA 3.5 – Ground PERCA instrument 50

3.2 Inlet design, implementation and characterisation 52

3.2.1 CH_3O_2 chain length calibration 59

3.2.2 Chain length altitude dependence 64

3.2.3 Chain length humidity interference 81

3.3 NO_2 detection and calibration 102

3.3.1 LMA-3 Scintrex detector 103

3.3.2 NO_2 sensitivity calibration 105

3.3.3 NO_2 sensitivity altitude dependence 108

3.3.4 NO_2 sensitivity humidity interference 115

3.4 Calibration and characterisation of radical and NO_2 calibration sources 115

3.4.1 Permeation rate calibrations (NO_2 and CH_3I) 115

3.4.2 Determination of j_{CH_3I} 117

3.5 Data workup and error analysis 124

3.5.1 Data workup 126

3.5.2 Components of uncertainty 128

3.6 Chapter 3 Summary 131

4 Airborne Measurement of photolysis frequencies through radiometry 133

4.1 Measurements of photolysis frequencies in the atmosphere 134

4.1.1 Background theory 134

4.1.2 Chemical actinometry 140

4.1.3 Filter radiometry 141

4.1.4 Spectral radiometry 144

4.2 Calibration of the aircraft filter radiometers 145

4.2.1 Intercomparison with ground based filter radiometers prior to AMMA 148

4.2.2 Absolute calibration through cross calibration with a spectral radiometer and TUV pre/post AMMA 152

4.2.3 SpecRad-SpecRad-TUV intercomparison 160

4.2.4 Temperature, ozone column and solar zenith angle corrections for j_{O^1D} filter radiometers 165

4.3 Instrumental performance during the AMMA campaign 171

4.3.1 Assessment of correction for issues with lower position radiometers 172

4.4 Chapter 4 Summary 179

5 The African Monsoon Multidisciplinary Analysis (AMMA) 181

5.1 Overview of the AMMA project 181

5.1.1 Instrumentation fit 183

5.1.2 Background and motivations 183

5.1.3 West African Monsoon (WAM) system and dynamics 193

5.2 Overview of data from the aircraft SOP 197

5.2.1 Data coverage . . . 197
5.2.2 Measurements of radicals and photolysis rates . . . 205
5.2.3 Tracers of dynamics . . . 220
5.2.4 Distribution of biogenic VOC's . . . 224
5.2.5 Chemical tracers . . . 235
5.3 Chapter 5 Summary . . . 247

6 Analysis of results from AMMA **249**

6.1 Comparison of photolysis rate measurements to the TUV model . . . 249
6.2 Comparison of peroxy radical measurements to a photochemical box model . . . 259
6.3 Radicals and composition . . . 275
6.3.1 VOC reactivity . . . 278
6.3.2 Measured radicals . . . 287
6.3.3 Modelled radical composition . . . 294
6.4 Ozone production and loss . . . 303
6.5 Chapter 6 Summary . . . 315

7 Summary and Conclusions **321**

7.1 Summary of chapters . . . 321
7.2 General conclusions and recommendations for further research . . . 328

A Research Training Record **334**

A.1 Induction Sessions . . . 334
A.2 Training Sessions . . . 334

A.3 Level 3 and 4 Courses 335

A.4 Departmental Seminars 335

A.5 Conferences/Meetings attended 336

A.6 Conference Presentations 337

A.7 Departmental Presentations 338

A.8 Papers 339

A.9 Other 339

B Flow Control Methodology **341**

B.1 Mass Flow Control 341

Bibliography **346**

List of Figures

1.1 Altitude Temperature and Pressure Structure of the Earth's Atmosphere 3

2.1 Idealised fractional yield of HO_2 as a function of the reagent NO concentration 26

3.1 PERCA 4 inlet systems layout 50

3.2 PERCA 4 instrument layout 51

3.3 Ground PERCA system (PERCA 3.5) 54

3.4 University of Leicester Dual Inlet Scheme 55

3.5 PERCA 4 aircraft inlet 57

3.6 PERCA 4 aircraft inlet plumbing 59

3.7 CH_3O_2 radical source units 60

3.8 Chain length calibration setup 63

3.9 Chain length calibration timeseries 64

3.10 PERCA III chain length altitude dependence 65

3.11 Inlet chain length model output for 298 K, 101325 Pa 71

3.12 Modelled CH_3O_2 chain length relative to modelled HO_2 chain length 73

3.13 Time evolution of chain length at 0 km and 8 km as f(NO) 75

3.14 Time evolution of chain length at 0 km and 8 km as f(CO) 77

3.15 HO_2 chain length as a function of reagent NO and CO concentration relative to ground level . . . 79

3.16 CH_3O_2 chain length as a function of reagent NO and CO concentration relative to ground level . . . 80

3.17 Comparison of modelled CL altitude dependence to PERCA III CL altitude dependence 82

3.18 AMMA humidity altitude profile . . . 84

3.19 Salisbury (2001) chain length humidity correction factor at $T = 30^o$C . . . 85

3.20 Chain length humidity calibration setup . . . 89

3.21 NO_2 sensitivity humidity calibration setup . . . 92

3.22 PERCA 4 LMA-3 Scintrex NO_2 sensitivity humidity dependence . . . 96

3.23 University of Leicester PERCA chain length humidity dependence as f(Q) . . . 98

3.24 University of Leicester PERCA chain length humidity dependence as f(RH) . . . 99

3.25 Schematic of LMA-3 Scintrex detector . . . 104

3.26 Timeseries from NO_2 sensitivity calibration . . . 106

3.27 NO_2 sensitivity calibration plot . . . 107

3.28 Time dependence of ozone NO titration from 0-10 km altitude . . . 110

3.29 Ratio of ambient ozone to NO_2 from 0-10 km altitude . . . 113

3.30 Timeseries comparing raw signal to calculated NO_2 background . . . 114

3.31 CH_3I permeation tube calibration . . . 117

3.32 j_{CH_3I} calibration fit . . . 119

3.33 Schematic diagram of experimental setup for determination of j_{CH_3I} . . . 120

3.34 Plan photograph of experimental setup for determination of j_{CH_3I} . . . 120

3.35 Photograph of experimental setup for determination of j_{CH_3I} . . . 121

3.36 Measured spectrum of Hg Pen-ray on calibrated monochromator wavelength scale (monochromator resolution ≤ 0.5 nm) 122

4.1 Wavelength dependence of selected photolysis rate coefficients 137

4.2 Design of the j_{O^1D} aircraft filter radiometer 143

4.3 Timeseries from intercomparison of filter radiometers prior to AMMA 150

4.4 Comparison of the 20518 Spectral radiometer to TUV post AMMA 154

4.5 Comparison of j_{O^1D} filter radiometers to TUV prior to/post AMMA 155

4.6 Comparison of j_{NO_2} filter radiometers to TUV prior to/post AMMA 156

4.7 Diurnal comparison of SpecRad derived photolysis rates with TUV 161

4.8 Correlation of TUV with SpecRad derived j_{O^1D} and j_{NO_2} photolysis rates 162

4.9 Correlation of SpecRad derived integrated actinic flux 164

4.10 Temperature dependence for the quantum yield of O(^{1}D) from ozone photolysis 167

4.11 Bohn *et al.* (2004) j_{O^1D} temperature correction as a function of temperature and solar zenith angle 168

4.12 Signatures of obscuration and measurement signal saturation in the lower position radiometer signals 172

4.13 Fractional contribution of upwelling j_{O^1D} as a function of altitude 173

4.14 Ratio of downwelling j-values as a function of SZA 175

4.15 Ratio of upwelling j-values as a function of SZA 175

4.16 Correlation of upwelling to downwelling j-values 176

4.17 Histogram of ratio upwelling to downwelling j-values 177

4.18 Timeseries comparing measured and estimated upwelling j_{O^1D} 178

4.19 Frequency distribution of difference between estimated and measured upwelling j_{O^1D} . 178

5.1 MODIS 10-day composite firemap for Africa during SOP2 187

5.2 Schematic diagram of the West African Monsoon 195

5.3 Spatial distribution of BAe-146 measurements 200

5.4 Temporal distribution of BAe-146 measurements 200

5.5 Spatial distribution of PERCA and filter radiometer measurements 203

5.6 Temporal distribution of PERCA and filter radiometer measurements 204

5.7 Times series of measured RO_x, OH, HO_2, j_{O^1D} and j_{NO_2} and altitude for flights B216-B217 206

5.8 Times series of measured RO_x, OH, HO_2, j_{O^1D} and j_{NO_2} and altitude for flights B218-B219A 207

5.9 Times series of measured RO_x, OH, HO_2, j_{O^1D} and j_{NO_2} and altitude for flights B219B-B220 208

5.10 Times series of measured RO_x, OH, HO_2, j_{O^1D} and j_{NO_2} and altitude for flights B223-B224A 209

5.11 Times series of measured RO_x, OH, HO_2, j_{O^1D} and j_{NO_2} and altitude for flights B224B-B225 210

5.12 Times series of measured RO_x, OH, HO_2, j_{O^1D} and j_{NO_2} and altitude for flights B226-B227 211

5.13 Times series of measured RO_x, OH, HO_2, j_{O^1D} and j_{NO_2} and altitude for flights B228-B229 212

5.14 Times series of measured RO_x, OH, HO_2, j_{O^1D} and j_{NO_2} and altitude for flights B230A-B230B 213

5.15 Times series of measured RO_x, OH, HO_2, j_{O^1D} and j_{NO_2} and altitude for flights B231-B232 214

5.16 Times series of measured RO_x, OH, HO_2, j_{O^1D} and j_{NO_2} and altitude for flights B233-B234 215

5.17 Times series of measured RO_x, OH, HO_2, j_{O^1D} and j_{NO_2} and altitude for flights B235A-B235B 216

5.18 Measured HO_2/RO_x ratio 218

5.19 Diurnal changes in meridional distribution of potential temperature 221

5.20 Diurnal changes in meridional distribution of equivalent potential temperature 222

5.21 SEVIRI/MSG NDVI and NDVI anomaly 225

5.22 Meridional and vertical distribution of isoprene and MVK+MACR 227

5.23 Matching of biogenics distribution with NDVI 228

5.24 Meridional profile of the ratio of MVK+MACR to isoprene concentrations throughout the diurnal 231

5.25 Latitude and altitude profiles of the ratio of MVK+MACR to isoprene concentrations throughout the diurnal 234

5.26 Meridional distributions of ozone and CO concentration 237

5.27 Meridional distribution of NO concentration 238

5.28 Meridional distribution of NO_2 concentration 239

5.29 Meridional distribution of NO_y concentration 240

5.30 Meridional distribution of benzene and acetonitrile concentrations 241

5.31 Correlation of ozone with CO by air mass 243

5.32 Correlation of benzene with CO within the boundary layer 246

6.1 Ratio of modelled to measured photolysis rates by altitude 253

6.2 Comparison of modelled to measured j_{O^1D} by altitude after temperature correction . . 254

6.3 Comparison of modelled and measured photolysis rates by time 256

6.4 Meridional profile of the ratio of modelled to measured photolysis rates 258

6.5 Modelled versus measured RO_x 265

6.6 Measured to modelled total RO_x ratio as a function of RH 267

6.7 Modelled RO_2 versus measured RO_x 272

6.8 $\frac{[RO_{2,DSMACC}]}{[RO_{x,PERCA}]}$ versus altitude 274

6.9 Meridional distribution of number of VOCs used to calculate OH reactivity 282

6.10 Meridional distribution of VOC OH reactivity 283

6.11 Meridional distribution of relative contribution of CO to OH reactivity 284

6.12 Meridional distribution of relative contribution of methane to OH reactivity 284

6.13 Meridional distribution of relative contribution of isoprene to OH reactivity 285

6.14 Meridional distribution of relative contribution of formaldehyde to OH reactivity . . . 285

6.15 Meridional distribution of relative contribution of acetaldehyde to OH reactivity . . . 286

6.16 Diurnal cycle in RO_x measured during AMMA SOP2 289

6.17 Diurnal cycle in HO_2 measured during AMMA SOP2 289

6.18 Diurnal cycle in OH measured during AMMA SOP2 290

6.19 Meridional distribution of RO_x measured during AMMA SOP2 290

6.20 Meridional distribution of HO_2 measured during AMMA SOP2 291

6.21 Meridional distribution of OH measured during AMMA SOP2 291

6.22 Frequency distribution of observed radical concentrations 292

6.23 Radical composition by air mass 297

6.24 Modelled RO_x, RO_2 versus measured RO_x by air mass 298

6.25 Histograms of model to measurement ratio by air mass 299

6.26 Diurnal partitioning of HO_2 and RO_2 302

6.27 Meridional distribution of ozone loss through alkene ozonolysis 305

6.28 Diurnal variation of ozone tendency 307

6.29 Meridional variation of ozone tendency 308

6.30 HYSPLIT back trajectories linked to biomass burning regions of Central Africa 310

6.31 Timeseries from flight B231 showing biomass burning plume interception 311

6.32 Net ozone tendency versus NO 316

7.1 Diurnal composite of the ratio of measured to modelled peroxy radicals 327

B.1 Ratio of pressure to temperature as a function of altitude measured during the AMMA field campaign 344

List of Tables

1.1 Composition of the Earth's atmosphere 2

2.1 Relative yield of HO_2 by radical species 25

2.2 Summary of established radical measurement techniques 44

2.3 Recent field campaigns involving the measurements of peroxy radicals 46

3.1 PERCA 4 inlet systems sub-components 52

3.2 PERCA 4 main rack sub-components 53

3.3 PERCA inlet chemistry basic chain mechanism 66

3.4 PERCA inlet chemistry reaction mechanism 67

3.5 PERCA inlet chemistry model conditions 69

3.6 Measured and nominal permeation rates of calibration perm. tubes 118

3.7 Results of j_{CH_3I} calibration of radical source unit PHOSTO-1 124

3.8 Sources of measurement uncertainty in PERCA 129

3.9 Measurement uncertainty in PERCA 130

4.1 Intercomparison schedule for filter radiometers prior to AMMA 149

4.2 "Clear sky" comparison opportunities for filter radiometers prior to/post AMMA . . . 153

5.1 AMMA chemistry instrument fit 184

5.2 AMMA aerosol and physical parameter instruments 185

5.3 Summary of flights from SOP2 198

5.4 Overall statistics for selected tracers 236

5.5 Statistics for selected tracers below 1 km altitude 238

6.1 MCM model specification 261

6.2 AMMA DSMACC model run constraints 261

6.3 WAS VOC measurements used for calculation of reactivity 280

6.4 Other VOC measurements used for calculation of reactivity 281

Chapter 1

Introduction

The work in this thesis concerns development of the understanding of measurements of peroxy radicals and photolysis rates, and the use of these measurements to investigate the processes controlling the composition of the atmosphere during the West African Monsoon 2006. This chapter provides context to these measurements through an introduction to the structure, composition and chemistry of the atmosphere.

1.1 Atmospheric Structure, Composition and Dynamical Processes

The chemical composition of the Earth's atmosphere today is in equilibrium in terms of the bulk constituents, N_2 and O_2 (see Table 1.1). At the trace level the influence of anthropogenic (i.e. resulting from the activity of humans), biogenic (summed influence of the Earth's biota), geological (e.g. volcanism) and astrophysical (e.g. solar and cosmic ray influence) perturbations are observed. Trace gases are key to many atmospheric processes so the effect of perturbations on their concentrations can be significant, e.g. ozone destruction in polar stratospheric clouds, photochemical smog formation, acid rain and aerosol formation. Understanding the mechanisms that control atmospheric composition

at the trace level is therefore key to understanding and predicting the influence on climate and air quality.

The bulk composition of the atmosphere is summarised in Table 1.1, a presentation which reflects the time average composition of the modern lower atmosphere, because the bulk by mass resides closest to the Earth's surface, owing to the pressure/density structure of the atmosphere (more or less decreasing exponentially with increasing altitude). The field measurements in this thesis were all taken within the troposphere (to be defined below), hence the bulk composition of the atmosphere is representative of the chemical environment in which the measurements were made.

Component	Value (ppmV)
N_2	780840
O_2	209460
Ar	9340
CO_2	350
Ne	18
He	5.2
CH_4	1.7
H_2	0.53
N_2O	0.3
CO	0.04–0.2
NH_3	< 0.01
H_2S	10^{-4}
SO_2	10^{-4}
H_2O	0-40000

Table 1.1: Composition of the Earth's atmosphere – Adapted from Wayne (2000)

1.1.1 Atmospheric structure

The structure of the atmosphere can be defined in terms of temperature and pressure as a function of altitude. A series of temperature inversions leads to stratification of the atmosphere into well defined layers (see Figure 1.1). These temperature inversions result from changes in composition with altitude

and the physical and chemical processes the dominant species undergo at these altitudes. From the surface with increasing altitude the layers are termed the troposphere, stratosphere, mesosphere, thermosphere and the exosphere.

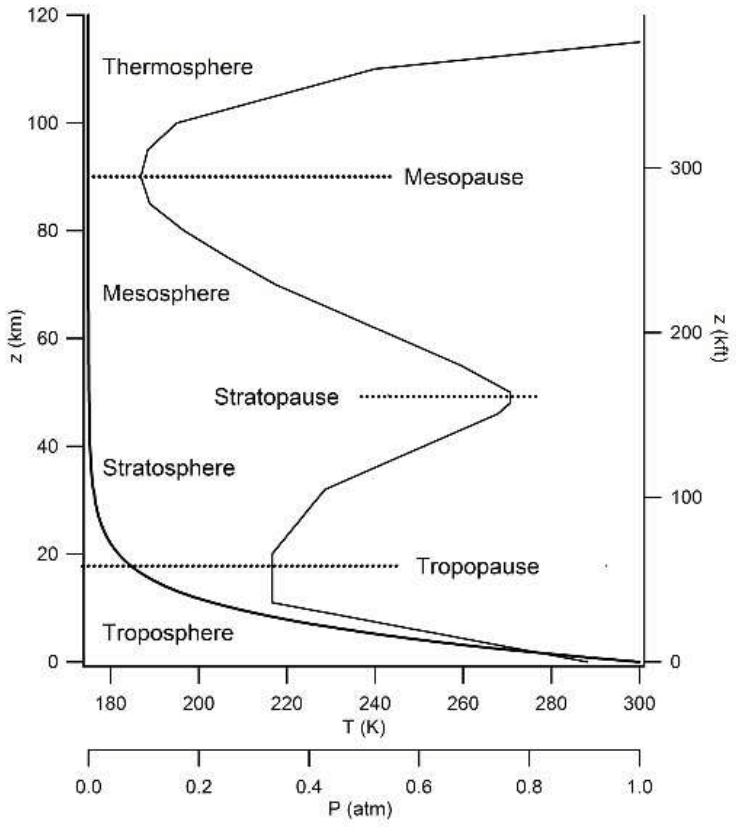

Figure 1.1: Altitude Temperature and Pressure Structure of the Earth's Atmosphere – Adapted from the US Standard Atmosphere (NOAA, NASA, & USAF (1976))

1.1.2 The lower atmosphere

In terms of this thesis and the measurements presented herein, the lower atmosphere i.e. the troposphere (from *tropos*, Greek for turning) and stratosphere (from *stratus*, Latin for layered) are of the most significance, in particular the tropical troposphere is most relevant. As suggested from the origin of the term troposphere, the lowest part of the atmosphere is characterised by dynamic movement, circulation and turbulent mixing. Furthermore the temperature gradient in the troposphere as illus-

trated in Figure 1.1 is generally negative until the tropopause (i.e. the lapse rate $\Gamma = -\frac{dT}{dz}$ is generally positive).

The surface temperature of the Earth and the lapse rate are largely explained by radiative transfer in combination with the movement of air. Incoming shortwave (ultraviolet (UV) and visible) solar radiation ($\sim$ 342 Wm^{-2}) is partially reflected in the atmosphere ($\sim$ 77 Wm^{-2}) and by the surface ($\sim$ 30 Wm^{-2}), partially absorbed in the atmosphere ($\sim$ 67 Wm^{-2}) and partially absorbed by the surface ($\sim$ 168 Wm^{-2}) (Finlayson-Pitts & Pitts, 2000). The surface re-emits the absorbed radiation in the thermal infrared (IR) dependent on the surface temperature[1]; energy is also transferred back to the atmosphere from the surface via sensible heat (conduction, convection) and latent heat (via evapotranspiration) released on condensation. The IR emission from the surface is absorbed in the atmosphere by the "greenhouse" gases (primarily water vapour, CO_2, O_3, CH_4, N_2O), clouds and aerosol. The greenhouse gases effectively trap the radiation closer to the surface as a result of their altitude profiles in density and therefore the transmission of radiation as a function of altitude.

The distribution of greenhouse gases in combination with variation in the solar intensity by latitude, time and season leads to significant variation in the radiation budget which modifies the surface temperature and lapse rate. Broadly speaking, for a diurnal cycle the heat capacity of the atmosphere maintains the temperature such that overall variations are less than 1% (Wayne, 2000); at the surface more significant variations are found dependent on the surface type which can lead to night-time temperature inversions (a negative lapse rate) and a stable nocturnal boundary layer (see below). By latitude the mean situation is for net absorption of radiation in the tropics and net loss at higher latitudes (Finlayson-Pitts & Pitts, 2000), which can be explained by a combination of factors. Lower intensity of sunlight is incident at the surface at higher latitudes, higher solar zenith angles mean sunlight is incident at the surface spread over a greater area; also the path length of sunlight through

[1] according to Wien's displacement law and assuming approximately blackbody emission i.e. $\lambda_{max} = \frac{2.898 \times 10^{-3}}{T}$ where λ is in metres and T is in Kelvin.

the atmosphere is longer meaning less light reaches the surface to be re-emitted in the IR; snow, ice and cloudiness contribute to a higher albedo at higher latitudes. The meridional variation in heating drives the transport of heat from the tropics to the poles and generates the general patterns of circulation in the atmosphere and oceans.

The lapse rate resulting from the distribution of radiative energy is modified by the transport of sensible and latent heat. Owing to the generally positive lapse rate in the troposphere an air parcel heated at the surface may be expected to rise naturally (i.e. through convection) due to buoyancy, resulting from the lower density of the warm air parcel compared to cooler air aloft. Under adiabatic conditions a rising air parcel expands and cools as the pressure decreases with altitude. If its temperature drops below the surrounding air temperature further convection is suppressed since the air parcel is then denser than its surroundings, and the atmosphere is stable. The rate of temperature change with altitude for dry air is defined as the dry adiabatic lapse rate $\Gamma_d = \frac{g}{c_p}$ (where g is the acceleration due to gravity and c_p is the specific heat capacity of air at constant pressure). In the presence of water vapour an air parcel rising adiabatically will cool until the air temperature reaches dewpoint, at this temperature the air is saturated and water may condense releasing latent heat. The rate of temperature change with altitude of a saturated air mass rising adiabatically defines the saturated adiabatic lapse rate, Γ_s. The saturated adiabatic lapse rate is less than the dry adiabatic lapse rate because of the release of latent heat. Whether the environmental lapse rate (Γ_e) is less than or greater than the dry or saturated adiabatic lapse rate determines whether an air mass is respectively stable or unstable in relation to convection. The saturated adiabatic lapse rate applies only once an air parcel reaches the dewpoint temperature.

Related thermodynamic quantities which provide indicators of atmospheric mixing and stability are the potential temperature, θ, and equivalent potential temperature, θ_e. The potential temperature is defined as the temperature that an air parcel would have if brought dry adiabatically to a pressure

of 1000 hPa. As such air parcels maintain the same potential temperature while rising or sinking dry adiabatically, hence the potential temperature is useful as a tracer for mixing. Furthermore if potential temperature is conserved and air parcels move along surfaces of constant θ, the potential temperature can provide a tracer of the history of an air parcel. The equivalent potential temperature is defined as the temperature that an air parcel would have after rising and expanding dry adiabatically until saturated, then rising while undergoing pseudo-adiabatic expansion (i.e. if the moisture content condenses out instantaneously as the air parcel rises and the latent heat of condensation is used to heat the air parcel) until all moisture is condensed out, and then brought dry adiabatically to a pressure of 1000 hPa. Equivalent potential temperature therefore considers the potential warming of an air parcel due to condensation along with the cooling due to adiabatic expansion. For saturated air or air near saturation the condition for stability with respect to convection is that the equivalent potential temperature has to rise with altitude ($\frac{d\theta_e}{dz} > 0$). If this is not true then an air parcel displaced upward can be warmer than the surrounding air owing to the release of latent heat of condensation, and would therefore continue to rise.

The temperature inversion defined as the tropopause marks the boundary between the troposphere and the stratosphere. The reason the temperature inversion occurs is a good example of the influence of photochemistry in the structure and dynamics of the atmosphere. Here the *in situ* absorption of intense shortwave solar radiation by O_2 and O_3 (see Section 1.2.1) generates heat and means the temperature begins to rise with altitude, and continues to rise throughout the stratosphere (i.e. the lapse rate is negative throughout). This means the stratosphere is stable with respect to convection since the environmental lapse rate is less than the adiabatic lapse rate; it also means the timescale for mixing in the stratosphere is months to years (Finlayson-Pitts & Pitts, 2000). The temperature inversion owes its existence to a persistent stratospheric ozone layer which results from a balance between stratospheric ozone production and loss (see Section 1.2.1).

The troposphere itself may also be subdivided generally in terms of distinct (though transient) regions by altitude. At the base of the troposphere is what is called the "boundary layer", a region of highly turbulent mixing next to the ground (Wayne, 2000) where the atmosphere directly interacts with the surface. Here the atmosphere is dynamically under the influence of the surface through friction dependent on the surface type and topography, and direct exchange of energy and chemical constituents occurs. The timescale of these interactions is an hour or less following the definition of Stull (1988) given in Finlayson-Pitts & Pitts (2000). The extent of the boundary layer is variable with typical heights ranging from ∼100-3000 m in altitude. A diurnal cycle in boundary layer height results from variation in radiative heating of the surface, a simplified description of this is given by Finlayson-Pitts & Pitts (2000) and summarised here. Generally, the boundary layer height is greatest around midday when a well mixed convective boundary layer exists due to radiative heating of the surface, this lies above a shallow surface layer into which surface emissions are released; the surface emissions mix throughout the boundary layer and they or their oxidation products may potentially undergo deposition back at the surface. With the sun setting, radiative cooling of the surface and the atmosphere above means the boundary layer height is reduced. Owing to the greater heat capacity of the atmosphere, the air in the boundary layer can be warmer than the surface such that a temperature inversion is established (the lapse rate is negative) and the nocturnal boundary layer becomes stable with respect to convection. Beyond the nocturnal boundary layer exists a residual layer containing species that were well mixed in the boundary layer, but do not mix either into the nocturnal boundary layer or free troposphere above. With sunrise the surface is heated and the air that was confined to the nocturnal boundary mixes out into the residual layer. The top of the boundary layer is typically capped by a stable inversion layer and clouds can form here where the boundary layer is humid. The presence of an inversion layer, related transitions in other thermodynamic/meteorological variables and gradients in chemical composition due to a change in air mass provide a signature for the height of the boundary layer. Above the boundary layer the troposphere is free of direct surface

influence and hence is described as the "free troposphere". Since the majority of trace gas emissions into the atmosphere are from the surface, the chemistry that occurs within the boundary layer, and the transport of boundary layer air into the free troposphere and beyond has a significant role in atmospheric composition. Days may be required for mixing from the boundary layer into the free troposphere, but once there atmospheric circulation can transport surface emissions and products over considerable distances. Transport within the boundary layer is limited due to mixing and in combination with enhanced surface deposition, this means highly reactive species tend to be confined in close proximity to surface emission sources (Wayne, 2000).

1.2 Background chemistry

1.2.1 Stratospheric ozone

As mentioned in Section 1.1.2 the stratosphere is defined by rising temperature with altitude and the presence of a persistent ozone layer. Both the altitude profile of number concentration and mixing ratio (relative concentration) of ozone are peaked in the stratosphere; the natural generation of the steady state ozone concentration that is the stratospheric ozone layer is basically described by the Chapman mechanism:

$$O_2 + h\nu(\lambda < 243 \text{ nm}) \rightarrow O + O \tag{1.1}$$

$$O + O_2 + M \rightarrow O_3 + M \tag{1.2}$$

$$O_3 + h\nu(\lambda < 340 \text{ nm}) \rightarrow O(^1D) + O_2 \tag{1.3}$$

$$O_3 + h\nu(\lambda < 1180 \text{ nm}) \rightarrow O + O_2 \tag{1.4}$$

$$O + O_3 \rightarrow O_2 + O_2 \tag{1.5}$$

The layered structure of the ozone altitude profile can be understood qualitatively from the processes that dictate its photochemical production rate. Ozone is formed by photolysis of O_2 followed by

reaction of the O atoms yielded with O_2; this requires both a sufficient flux of shortwave solar radiation ($\lambda < 243$ nm) and sufficient concentrations of O_2. In the lower atmosphere the production of ozone is limited owing to the absorption of shortwave solar radiation ($\lambda < 243$ nm) above. At higher altitudes the concentration of O_2 reduces with increasing altitude and therefore the production rate falls; a maximum in production occurs between these limits.

The stability of the stratosphere with respect to convection highlighted in Section 1.1.2 means trace components introduced from the troposphere may build up to significant levels if no chemical sinks exist. In turn this means the chemistry of the stratosphere is vulnerable to the introduction of trace species that perturb the photochemical balance dictating the ozone concentration. Around the 1970's it was discovered that the reaction between atomic oxygen and ozone (Reaction 1.5) was insufficiently fast to balance the photochemical production steps and additional loss mechanisms involving other trace constituents were required. Crutzen (1970) suggested a chain reaction to destroy ozone involving NO and NO_2 may control the stratospheric ozone distribution; these can be generated from N_2O produced at the Earth surface and transported through the troposphere (where it is long lived). Johnston (1971) recognised a potential risk in reduction of stratospheric ozone through this route owing to increased NO_x emission direct into the stratosphere from increased use of supersonic aircraft. Stolarski & Cicerone (1974) proposed the potential for even greater catalytic ozone destruction through a chain reaction involving Cl and ClO. Following this Molina & Rowland (1974) recognised a significant and increasing source of Cl in the stratosphere through industrial emissions of chlorofluorocarbons (CFC's) which reach the stratosphere owing to the lack of a tropospheric sink.

Long term monitoring of the total ozone column[2] at the British Antarctic research station at Halley Bay led to the discovery of a progressive drop in total ozone column at the pole (Farman *et al.*, 1985).

[2]Total O_3 column is the integrated ozone concentration over a vertical column through the atmosphere, usually expressed in Dobson Units (DU) where 1 DU is equivalent to a 10^{-5} m layer of O_3 at STP (Finlayson-Pitts & Pitts, 2000)

This event occurred annually at the end of the polar winter with sunrise in polar spring. Key to the formation of the polar ozone hole are the extremely low temperatures that occur during polar winter in the absence of sunlight, and the confinement of the cold air within the polar vortex, a strong circumpolar cyclonic circulation, which leads to the formation of polar stratospheric clouds (PSC's) (see Wayne (2000) and references therein). Catalytically active chlorine (generated from photolysis of CFC's) is typically converted to reservoir species hydrogen chloride (HCl) and chlorine nitrate ($ClONO_2$) in the atmosphere. In contrast, anomalous chemistry occurs within the polar vortex where these reservoir species react rapidly on the surface of PSC particles releasing Cl_2. The photolysis of Cl_2 in the polar spring yields the chlorine atoms which then destroy ozone; Cl is reproduced in catalytic chain reactions the most important of which involving ClO dimers and this leads to the efficient destruction of ozone (Wayne, 2000).

The combination of the Farman *et al.* (1985) observations, along with those from satellites and the confirmation that the chlorine radicals derived from photolysis of CFC's were the primary cause of ozone loss (Jones & Shanklin, 1995), led eventually to legislation requiring the progressive reduction in industrial emissions of CFC's.

The photochemistry that can occur in the troposphere is limited to particular wavelength bands by atmospheric absorption at higher altitudes. Of relevance to tropospheric photochemistry is the strong absorption of radiation by O_3 ($210 \leq \lambda \leq 290$ nm) and O_2 ($\lambda < 230$ nm). The atmospheric cut-off for tropospheric photochemistry is therefore $\lambda \geq 290$ nm. Changes in stratospheric ozone abundances clearly have considerable implications for photochemistry in the troposphere.

1.2.2 Tropospheric chemistry of peroxy radicals

The trace composition of the troposphere is dominated by oxidation cycles involving radical species (Monks, 2005). Dependent on the relative concentrations of the main anthropogenic photochemical

pollutants, NO_x (defined as the sum of NO and NO_2) and volatile organic compounds (otherwise known as VOC's), radical oxidation cycles can lead to either the production or destruction of O_3, and a variety of secondary photochemical pollutants. Since tropospheric O_3 is both toxic to plants and animals and a highly significant greenhouse gas, understanding the processes that lead to both its production and loss is essential. The OH radical is the dominant atmospheric oxidant by reactivity, however its primary source is from photolysis of ozone limiting its influence outside of daylight. The nitrate radical (NO_3) is also a significant oxidant but has a complementary role to OH, owing to its rapid photolysis during daytime it can only exist in significant concentrations when sunlight is limited. Ozonolysis of alkenes also contributes to the oxidation of VOC's and owing to the extended lifetime of ozone compared to OH and NO_3 can be significant at any time of day. Peroxy radicals (HO_2 and RO_2, where R is an organic substituent) are formed as intermediates in the catalytic degradation of VOC's, while they have a significant role through perturbation of the photostationary state between ozone, NO and NO_2.

The primary route for the formation of the hydroxyl radical (OH) is the photolysis of tropospheric ozone in the presence of water vapour:

$$O_3 + h\nu(\lambda < 340 \text{ nm}) \rightarrow O(^1D) + O_2 \tag{1.6}$$

$$O(^1D) + H_2O \rightarrow 2OH \tag{1.7}$$

The majority of excited $O(^1D)$ atoms produced in this way are collisionally quenched back to the ground state, and reform ozone through Reaction 1.2, so the yield of OH depends on the concentration of water vapour. In relatively unpolluted (low NO_x) conditions, OH reacts mainly with CO and methane generating the hydroperoxyl (HO_2) and methylperoxy (CH_3O_2) radicals:

$$OH + CO \rightarrow H + CO_2 \tag{1.8}$$

$$H + O_2 + M \rightarrow HO_2 + M \tag{1.9}$$

$$OH + CH_4 \rightarrow CH_3 + H_2O \tag{1.10}$$

$$CH_3 + O_2 + M \rightarrow CH_3O_2 + M \tag{1.11}$$

Other non-methane VOC's are oxidised similarly leading to the formation of organic peroxy radicals, RO_2. Under low NO_x conditions radical loss occurs predominantly through the self- and cross-reaction of these radicals to form peroxides, e.g.:

$$HO_2 + HO_2 + M \rightarrow H_2O_2 + O_2 + M \tag{1.12}$$

$$CH_3O_2 + HO_2 \rightarrow CH_3O_2H + O_2 \tag{1.13}$$

The formation of peroxides can be an effective sink for peroxy radicals since H_2O_2 and CH_3O_2H readily dissolve in cloud droplets and may then be deposited at the surface by rainfall (Wayne, 2000). Alternatively, the photolysis of peroxides (products of the above self-/cross-reactions) and carbonyls (products of the partial oxidation of hydrocarbons) may reproduce peroxy radicals.

In the remote natural environment the biogenic emission of VOC's offers an additional peroxy radical production route through, in particular, oxidation of alkenes such as isoprene. To illustrate the potential significance of this source, isoprene is thought to contribute a third of total annual global VOC emissions, and more than 90% of isoprene emissions are from terrestrial plants (Guenther *et al.*, 2006). Oxidation of alkenes occurs mainly (OH and NO_3) or totally (ozone) by addition to the C=C bond(s) (Atkinson & Arey, 2003). Following the description of Atkinson & Arey (2003), the reaction of alkenes with OH yields a 1,2-hydroxyalkyl radical which then reacts with O_2 (analogously to alkyl radicals) to form the corresponding 1,2-hydroxyalkyl peroxy radical; in the presence of NO the peroxy radical reacts to form hydroxynitrates or hydroxyalkoxy radicals plus NO_2. For isoprene, the dominant products of OH initiated oxidation in the presence of NO are methacrolein plus HCHO and methyl vinyl ketone plus HCHO, from the decomposition of the 1,2-hydroxyalkoxy radical (Atkinson & Arey, 2003).

At night when OH is limited the nitrate radical may be formed through:

$$NO_2 + O_3 \rightarrow NO_3 + O_2 \tag{1.14}$$

$$N_2O_5 + M \rightleftharpoons NO_3 + NO_2 + M \tag{1.15}$$

The oxidation of NO_2 by ozone is a slow process while the decomposition of N_2O_5 is reversible, so ultimately Reaction 1.14 determines the production of NO_3. For nitrate radicals the reaction with alkenes proceeds similarly to OH with addition to the double bond to form a nitrooxyalkyl radical, followed by reaction with O_2 to form a nitrooxyalkyl peroxy radical dominating at atmospheric pressure. The peroxy radical may then react as per alkyl radicals with NO, NO_2, HO_2, RO_2 and NO_3; observed products are dominated by organic nitrates from the reaction of the peroxy radical with NO_2 (Atkinson & Arey (2003) and references therein). Product channels of particular interest lead to the production of HO_2, which in turn leads to potential production of OH at night. For example following Wayne (2000), for a generic nitrooxyalkyl peroxy radical RO_2 reacting with NO_3:

$$RO_2 + NO_3 \rightarrow RO + NO_2 + O_2 \tag{1.16}$$

$$RO + O_2 \rightarrow R'R''CO + HO_2 \tag{1.17}$$

Alternatively NO_3 can react by hydrogen abstraction:

$$NO_3 + RH \rightarrow HNO_3 + R \tag{1.18}$$

The alkyl radical product R reacting with oxygen to yield a peroxy radical, this route is relatively slow (Monks, 2005). As noted by Atkinson & Arey (2003), owing to the rapid reaction between NO and NO_3, both will not be present simultaneously at high concentration. Equally, where ozone and/or NO_2 concentrations are low, formation of the nitrate radical will be suppressed.

The reaction of alkenes with ozone proceeds by addition to form a primary ozonide, which rapidly decomposes to two sets of a carbonyl plus "Criegee" intermediate (energy rich biradical), see e.g. Rickard *et al.* (1999), Atkinson & Arey (2003). The Criegee intermediate may then either be colli-

sionally stabilised or undergo unimolecular decomposition to produce OH and an organic free radical co-product that may form RO_2 by addition of O_2.

1.2.3 Production and destruction of tropospheric ozone

Ozone is mainly produced and destroyed in the photostationary state between ozone, NO and NO_2:

$$NO + O_3 \rightarrow NO_2 + O_2 \tag{1.19}$$

$$NO_2 + h\nu(\lambda < 420 \text{ nm}) \rightarrow NO + O(^3P) \tag{1.20}$$

$$O(^3P) + O_2 + M \rightarrow O_3 + M \tag{1.21}$$

This represents a null cycle so net perturbations to the concentration of ozone occur by another means. The only known route to produce ozone in the troposphere is from the photolysis of NO_2, which may be emitted directly but most anthropogenic and natural emissions of NO_x are in the form of NO (Finlayson-Pitts & Pitts, 2000), so ozone production requires additional routes to convert NO to NO_2. In polluted regimes where NO_x is relatively high in concentration a cycle involving peroxy radicals can promote the catalytic production of O_3:

$$OH + CO \rightarrow H + CO_2 \tag{1.22}$$

$$H + O_2 + M \rightarrow HO_2 + M \tag{1.23}$$

$$HO_2 + NO \rightarrow NO_2 + OH \tag{1.24}$$

$$NO_2 + h\nu \rightarrow NO + O(^3P) \tag{1.25}$$

$$O(^3P) + O_2 + M \rightarrow O_3 + M \tag{1.26}$$

Organic peroxy radicals react similarly in the presence of NO, leading to the formation of alkoxy radicals. In turn these react rapidly in the presence of oxygen to yield HO_2 and a carbonyl product:

$$OH + RH \rightarrow R + H_2O \tag{1.27}$$

$$R + O_2 + M \rightarrow RO_2 + M \tag{1.28}$$

$$RO_2 + NO \rightarrow NO_2 + RO \tag{1.29}$$

$$RO + O_2 \rightarrow R'CHO + HO_2 \tag{1.30}$$

$$HO_2 + NO \rightarrow NO_2 + OH \tag{1.31}$$

In relatively unpolluted conditions where there are low concentrations of NO_x, catalytic destruction of O_3 occurs through the following reaction cycle which reproduces the hydroxyl radical chain initiator:

$$OH + O_3 \rightarrow HO_2 + O_2 \tag{1.32}$$

$$HO_2 + O_3 \rightarrow OH + 2O_2 \tag{1.33}$$

The recycling of OH emphasises the catalytic chain reactions for the production of ozone involve both organic and inorganic peroxy radicals, while only HO_x is involved in the catalytic destruction of ozone. Other potentially important ozone loss processes do exist e.g. reaction with alkenes, halogens, NO_3 chemistry, cloud chemistry and dry deposition (Monks, 2005). These processes may represent a minor component of the loss in the free troposphere, but can be particularly significant within the boundary layer. For example, Read *et al.* (2008) observed that up to 50% of ozone loss in the tropical Atlantic marine boundary layer can be associated with halogen chemistry.

The balance between photochemical ozone production and loss depends not only on the presence of NO_x but is also limited by the presence of radicals and their precursors. In general two regimes may be distinguished, either NO_x limited or VOC limited. At relatively high $[NO_x]/[VOC]$ (VOC limited) the reactions yielding NO_2 from NO (Reactions 1.22-1.24 and 1.27-1.29) compete with reactions such as:

$$OH + NO_2 + M \rightarrow HNO_3 + M \tag{1.34}$$

which represents a loss of both HO_x and NO_x. Alternatively under high $[VOC]/[NO_x]$ (NO_x limited) the self- and cross-reactions of peroxy radicals limit the chain propagation. This balance is non-linear and dictated by the relative rates of the dominant propagation and termination channels in the radical

chain chemistry, which complicates strategies for the control and regulation of pollution. For example under a NO_x limited regime reductions in NO_x reduce ozone production, while in a VOC limited regime reduction in NO_x may increase ozone production. A further complication as illustrated by Read *et al.* (2008) is that without consideration of additional mechanisms of ozone loss significant errors can occur in the calculation of ozone budgets.

1.3 Chapter 1 Summary

This chapter has introduced in brief a variety of key topics to provide context and illustrate the relevance of the measurements presented in this work. The background to the experimental techniques to measure peroxy radicals and photolysis rates is provided within the relevant chapters (Chapters 2 and 3, and Chapter 4 respectively), while detailed background to the field work is provided in an overview chapter (Chapter 5), and an analysis chapter (Chapter 6) places emphasis on the interpretation of the measurements.

Chapter 2

Measurement of atmospheric peroxy radicals

This chapter introduces the range of techniques currently in use for measurement of free radicals in the atmosphere, the status of these techniques and their feasibility in terms of measurements in the field. It describes in greatest detail the background to the technique of chemical amplification for the measurement of peroxy radicals as this technique has been used in this work.

2.1 Measurement techniques

There are a number of techniques actively in use for the measurement of peroxy radicals in the atmosphere and several in development which have currently not been used outside laboratory studies. A number of these techniques follow similar methodologies having developed out of the original PERCA concept (discussed below) in an attempt to overcome various deficiencies of the 'basic' technique. However, all techniques suffer their own weaknesses and with these in mind are better employed where the application suits their strengths. This section provides a short summary of the concepts of these techniques and attempts to highlight where and how these techniques may best be employed through

a critical assessment of their strengths and weaknesses.

2.1.1 Chemical amplification techniques

PERCA (PEroxy Radical Chemical Amplifier) measurement of RO_x

The PERCA (PEroxy Radical Chemical Amplifier) technique was conceived by Cantrell and Stedman (Cantrell & Stedman, 1982, Cantrell *et al.*, 1984) in the early 1980's to fill a gap in measurement capability at the time i.e. the ability to measure tropospheric concentrations of the peroxy radicals (HO_2 and RO_2). It has since been employed with success on a large number of field experiments (see section 2.2, page 45). The principle of the technique is the indirect detection of hydroperoxyl (HO_2) and hydroxyl (OH) radicals through the chemical conversion of CO to CO_2 through reaction with OH and NO to NO_2 through reaction with HO_2, followed by measurement of the reaction product NO_2. The basic scheme is as follows:

With HO_2 as the initiator and OH carrying the chain,

$$HO_2 + NO \rightarrow OH + NO_2 \tag{2.1}$$

$$OH + CO \rightarrow H + CO_2 \tag{2.2}$$

$$H + O_2 + M \rightarrow HO_2 + M \tag{2.3}$$

Or equivalently, with OH as the initiator and HO_2 carrying the chain,

$$OH + CO \rightarrow H + CO_2 \tag{2.4}$$

$$H + O_2 + M \rightarrow HO_2 + M \tag{2.5}$$

$$HO_2 + NO \rightarrow OH + NO_2 \tag{2.6}$$

Since both OH and HO_2 are reproduced this constitutes a chain reaction for both and is indistinguishable whichever initiates the chain.

The chain reaction is promoted through the controlled addition of the reagent gases (NO and CO) to the sampled airflow. Reagent flows are controlled to provide concentrations which optimise the chain reaction, typically the concentrations are of the order ∼3-10 ppmV of NO and ∼6-10% of CO dependent on the amplifier in question. The chain reaction is primarily limited through wall losses and the reaction of OH with NO to form HONO owing to the high reagent NO concentration (Cantrell, 1993); reaction of HO_2 with NO_2 to form pernitric acid (PNA) is only of significance with a high ambient NO_2 concentration (Cantrell, 1993):

$$OH + NO + M \rightarrow HONO + M \tag{2.7}$$

$$HO_2 \rightarrow \text{walls} \tag{2.8}$$

$$HO_2 + NO_2 + M \rightarrow HO_2NO_2 + M \tag{2.9}$$

Wall loss of OH however is of minimal significance since its chemical lifetime is so short (Cantrell, 1993). The optimum reagent concentration is obtained dependent on the relative importance of reactions 2.7 and 2.8, where wall loss depends on inlet geometry and material construction.

The detection of certain organic peroxy radicals (R_iO_2, where R_i is an organic substituent) is also possible where they can be efficiently converted to HO_2:

$$R_iO_2 + NO \rightarrow R_iO + NO_2 \tag{2.10}$$

$$R_iO + O_2 \rightarrow R'_iO + HO_2 \tag{2.11}$$

For example, for the methyl peroxy radical:

$$CH_3O_2 + NO \rightarrow CH_3O + NO_2 \tag{2.12}$$

$$CH_3O + O_2 \rightarrow HCHO + HO_2 \tag{2.13}$$

Tropospheric levels of OH are typically 1 to 2 orders of magnitude less than HO_2 and the concentrations of RO_2 ($=\sum_i R_iO_2$) are typically of the same order as HO_2 (Stevens *et al.* (1997), Jaegle *et al.* (2001),

Monks (2005)), hence the contribution of OH to the overall signal is typically minor. The NO_2 product of the chain reaction is a summed response to all the radicals sampled, so it can be said that the technique measures $[RO_x]$, where $[RO_x]$ is defined as:

$$[RO_x] = [OH] + [HO_2] + \sum_i [R_iO_2] \tag{2.14}$$

The sensitivity of an instrument to radicals is defined in terms of the chain length, *CL*, the number of NO_2 molecules produced per sampled radical. Defined with respect to HO_2:

$$CL_{HO_2} = \frac{\Delta[NO_2]}{[HO_2]} \tag{2.15}$$

where $\Delta[NO_2]$ is the difference between the NO_2 concentration produced by the amplification chemistry and the ambient background:

$$\Delta[NO_2] = [NO_2]_{amp} - [NO_2]_{back} \tag{2.16}$$

Knowing the chain length for HO_2 and measuring the NO_2 response $\Delta[NO_2]$, the radical concentration can be determined by rearranging Equation 2.15. The chain length defined like this is an idealisation, since in reality a number of processes lead to radical loss prior to and within the instrument reaction zone, e.g. reactions (2.7), (2.8) and (2.9). The effective chain length derived from a calibration includes any losses so the radical concentration reaching the reaction zone need not be known only the response to a given amount sampled to determine the chain length.

Since the technique is non-specific the choice of radical source used in calibration is important since this is effectively the choice of radical against which the instrument sensitivity (i.e. the calibrated chain length) is weighted whatever the radical population sampled. Ideally, the reference radical is chosen such that it is representative of the dominant radical species in the environment sampled; since HO_2 and CH_3O_2 are typically the dominant species, it makes sense to reference the sensitivity to these radicals. If the composition is relatively simple (primarily OH, HO_2 and CH_3O_2) the calibrated

signal will be a better measure of the true RO_x concentration dependent on the relative sensitivity to HO_2 and CH_3O_2. If the composition is more complicated then the question becomes what the relative response of the instrument is to the individual species that make up the population being measured, and what proportion each comprises of the total. Unless some idea of the composition is known (and given that the instruments relative sensitivity to the components) the interpretation of the signal measured becomes more qualitative than quantitative. With that in mind the measured NO_2 response in ambient air is given by:

$$\Delta[\mathrm{NO_2}] = CL_{OH}[\mathrm{OH}] + CL_{HO_2}[\mathrm{HO_2}] + \sum_i CL_{R_iO_2}[\mathrm{R_iO_2}] \tag{2.17}$$

where CL_m is the effective chain length for the individual radical species m. In practice the total RO_x concentration is calculated from the measured NO_2 response and a reference chain length $CL_{ref.}$ derived from a chain length calibration with the reference radical species:

$$[\mathrm{RO}_x]_{calc.} = \frac{\Delta[\mathrm{NO_2}]}{CL_{ref.}} \tag{2.18}$$

Rearranging Equation 2.18 in terms of $\Delta[NO_2]$ and equating this with Equation 2.17 one obtains:

$$CL_{ref.}[\mathrm{RO}_x]_{calc.} = CL_{OH}[\mathrm{OH}] + CL_{HO_2}[\mathrm{HO_2}] + \sum_i CL_{R_iO_2}[\mathrm{R_iO_2}] \tag{2.19}$$

The calculated radical concentration therefore depends on the relative sensitivity (relative chain length) for the various radical species:

$$[\mathrm{RO}_x]_{calc.} = \frac{CL_{OH}}{CL_{ref.}}[\mathrm{OH}] + \frac{CL_{HO_2}}{CL_{ref.}}[\mathrm{HO_2}] + \sum_i \frac{CL_{R_iO_2}}{CL_{ref.}}[\mathrm{R_iO_2}] \tag{2.20}$$

Dependent on whether the chain length is greater or lesser for a particular radical compared to the reference species and whether that species is a greater or lesser part of the total composition, the calculated radical concentration will be over or underestimated respectively. Hence, the accuracy depends on the relative chain length and the fractional concentration of the composition.

OH and HO_2 can initiate the chain chemistry but since typically $[OH] \ll [HO_2]$ and conversion of RO_2 yields HO_2, consideration must only be given to the efficiency of conversion of individual radical species

to HO_2, and heterogeneous inlet losses that may occur before the sample air reaches the reaction zone, i.e. the yield of HO_2, Y_{HO_2}, available for the chain reaction. The yield dictates the relative sensitivity for a given radical. These issues were considered quantitatively by Cantrell (1993) who calculated the yield for a number of radicals species through knowledge of the gas phase kinetics. Ashbourn *et al.* (1998) took an experimental approach to determine the response of the UEA-PERCA to a number of radicals relative to the response to HO_2, and showed that the gas phase kinetics cannot be considered alone. Their results have been incorporated here such that the measurements within this work may also be considered more quantitatively.

In terms of the detection of HO_x (HO_2 plus OH), losses prior to and within the reaction zone are only important since both OH and HO_2 are the initiators of the chain reaction. If one calibrates an inlet system using a well characterised source of HO_2 then these losses are included in the calibration and the HO_2 chain length derived. For the detection of organic peroxy radicals it has been found that the response of a PERCA instrument is dependent on the size and structure of the organic group, R_i, both in terms of how that determines the gas phase chemistry leading to the formation of HO_2 e.g. Cantrell (1993), and also the inlet wall losses prior to amplification e.g. Ashbourn *et al.* (1998). Hence there are two factors dictating the eventual yield of HO_2 (Y_{HO_2}) that initiates the chain reaction. At concentrations of NO typical of PERCA operating levels (3-10 ppmV) Y_{HO_2} is limited due to competing reactions to form organic nitrates and nitrites:

$$R_iO_2 + NO + M \rightarrow R_iONO_2 + M \tag{2.21}$$

$$R_iO + NO + M \rightarrow R_iONO + M \tag{2.22}$$

As pointed out by Cantrell (1993) the alkoxy radicals that are yielded in reaction (2.10) can alternatively undergo unimolecular decomposition or isomerization to form further radicals which dependent on their type may also yield HO_2:

$$R_iO + M \rightarrow R' \cdot + R''CHO \text{ (or } R'R''CO) + M \tag{2.23}$$

$$R_iO + M \rightarrow R'(OH)CH_2 \cdot + M \tag{2.24}$$

For the radical species where such routes are favoured the yield of HO_2 can be further limited through the cumulative influence of the competing reactions to form organic nitrates and nitrites (e.g. see Ashbourn *et al.* (1998)).

The structural dependency of the HO_2 yield (and therefore measurement efficiency) can be estimated from knowledge of the reaction rates and mechanism of the gas phase reactions; though to fully characterise an instrument, calibration is required to determine the heterogeneous wall loss component. Concerning the gas phase chemistry alone Cantrell (1993) calculated conversion efficiencies to HO_2 (i.e. relative yields) for a number of representative surrogate radical species using the following equation:

$$Y_{HO_2,gasphase} = \Gamma_1 \left\{\Gamma_2 + \Gamma_3(\Gamma_1\Gamma_2)_{2.23} + \Gamma_4(\Gamma_1\Gamma_2)_{2.24}\right\} \tag{2.25}$$

The Γ coefficients are the branching ratios describing various stages in the conversion to HO_2. They are defined as follows:

$$\Gamma_1 = \frac{k_{2.10}}{k_{2.10} + k_{2.21}} \tag{2.26}$$

Γ_1 describes the fraction of peroxy radicals that go on to form alkoxy radicals from Reaction 2.10 and that are not lost by formation of organic nitrates through Reaction 2.21. Γ_2 describes the fraction of alkoxy radicals that yield HO_2 directly:

$$\Gamma_2 = \frac{k_{2.11}[O_2]}{k_{2.11}[O_2] + k_{2.22}[NO] + k_{2.23} + k_{2.24}} \tag{2.27}$$

Of those alkoxy radicals that do not yield HO_2 directly but undergo decomposition, a fraction of the radicals produced may then yield HO_2 through Reactions 2.10 and 2.11 again dependent on the branching ratios Γ_1 and Γ_2 for these radicals. The yield of HO_2 from alkoxy radical decomposition therefore is:

$$Y_{HO_2,decomp} = \Gamma_1\Gamma_3(\Gamma_1\Gamma_2)_{2.23} \tag{2.28}$$

Γ_3 then describes the fraction yielding new radicals through decomposition and is defined as,

$$\Gamma_3 = \frac{k_{2.23}}{k_{2.11}[\mathrm{O_2}] + k_{2.22}[\mathrm{NO}] + k_{2.23} + k_{2.24}} \tag{2.29}$$

Likewise the yield of HO_2 from alkoxy radical isomerization:

$$Y_{HO_2,iso} = \Gamma_1\Gamma_4(\Gamma_1\Gamma_2)_{2.24} \tag{2.30}$$

Finally Γ_4 describes the fraction yielding new radicals through isomerization:

$$\Gamma_4 = \frac{k_{2.24}}{k_{2.11}[\mathrm{O_2}] + k_{2.22}[\mathrm{NO}] + k_{2.23} + k_{2.24}} \tag{2.31}$$

The total yield is therefore a sum of the yields through all applicable routes, and heterogeneous wall loss will have a cumulative reduction on the yield for each additional stage in the route to HO_2 production, dependent on the wall loss rates for the various radical products en route. The branching ratio Γ_1 is very dependent on the size and structure of the organic group; where Reaction 2.21 is minor for small peroxy radicals (CH_3O_2 and $C_2H_5O_2$) it becomes progressively favoured for larger radicals containing primary and secondary alkyl groups (Ashbourn *et al.*, 1998). The conversion of R_iO to HO_2 is very dependent on the structure of the organic group (Ashbourn *et al.*, 1998); for simple oxy radicals the conversion may involve a single step through reaction with O_2 (e.g. Reaction 2.13) the yield depending on the NO concentration through the branching ratio Γ_2. For larger, more complicated oxy radicals thermal decomposition or isomerization routes are available which may be comparatively quicker than the reaction with O_2.

Table 2.1 summarises the expected yields from gas phase conversion to HO_2 calculated by Cantrell (1993) ($Y_{HO_2,a}$), the relative response measured by Ashbourn *et al.* (1998) (equivalent to the relative yield) and here corrected for the wall loss measured ($Y_{HO_2,b}$), and the relative response measured by Ashbourn *et al.* (1998) including both wall loss and conversion losses ($Y_{HO_2,c}$).

Ashbourn *et al.* (1998) decoupled the gas phase processes from the heterogeneous processes that limit the response by measuring the relative response as a function of the reagent NO concentration. The

Radical species	$Y_{HO_2,a}$	$Y_{HO_2,b}$	$Y_{HO_2,c}$
HO_2	1.00	1.01 ± 0.10	0.69 ± 0.05
CH_3O_2	0.85	1.01 ± 0.10	0.78 ± 0.05
$C_2H_5O_2$	0.93	0.99 ± 0.10	0.95 ± 0.07
$CH_3C(O)O_2$	0.85	1.01 ± 0.10	0.76 ± 0.05
$(CH_3)_2CHO_2$	0.89	-	-
$(CH_3)_3CO_2$	0.47	-	-
$C_6H_4(OH)O_2$	≈0.95	-	-
neo-$C_5H_{11}O_2$	-	0.77 ± 0.08	0.74 ± 0.05
$HOCH_2CH_2O_2$	-	1.00 ± 0.10	0.73 ± 0.05
$CH_3CH(OH)CH(O_2)CH_3$	-	0.95 ± 0.10	0.77 ± 0.06
$(CH_3)_2C(OH)C(O_2)(CH_3)_2$	-	0.97 ± 0.10	0.81 ± 0.06

Table 2.1: Relative yield of HO_2 by radical species. Yields calculated by Cantrell (1993) ($Y_{HO_2,a}$) are for operating conditions of 10.0% v/v CO and 3.0 ppmV NO. Yields measured by Ashbourn *et al.* (1998) ($Y_{HO_2,b}$ - wall loss corrected, $Y_{HO_2,c}$ - including wall loss and conversion loss) are for operating conditions of 7.0% v/v CO and 3.0 ppmV NO.

response of the UEA-PERCA to organic peroxy radicals was found to be greater than the response to HO_2 when gas phase losses and heterogeneous loss were not separated ($Y_{HO_2,c}$). Since HO_2 only undergoes wall loss prior to entering the chain reaction it is clear that the wall loss of HO_2 exceeded the combined effects of wall loss and gas phase losses for all the organic peroxy radicals in this case.

The yields from gas phase conversion to HO_2 calculated by Cantrell (1993), $Y_{HO_2,a}$, should be similar to $Y_{HO_2,b}$ since this is effectively the measured gas phase yield, calculated by correcting for the wall loss measured by Ashbourn *et al.* (1998). This is not the case, suggesting the gas phase chemistry in the UEA-PERCA measurement situation is not well represented by the idealised calculations and that the gas phase HO_2 yield is better than expected for this instrument. Γ_1 is defined above as the branching ratio for peroxy radicals that go on to form oxy radicals and that are not lost by formation of organic nitrates; Γ_1 is independent of the reagent NO concentration (see Equation 2.26) so does not factor into the discrepancy between the calculated and measured response. However, the route to the formation of organic nitrites from the oxy radicals produced in Reaction 2.22 was expected

to lead to a considerable dependency of $Y_{HO_2,b}$ on the NO concentration dependent on the precursor peroxy radical (Ashbourn *et al.*, 1998). This was illustrated by idealised calculations for the yield (reproduced here in Figure 2.1) which ignored the wall loss component.

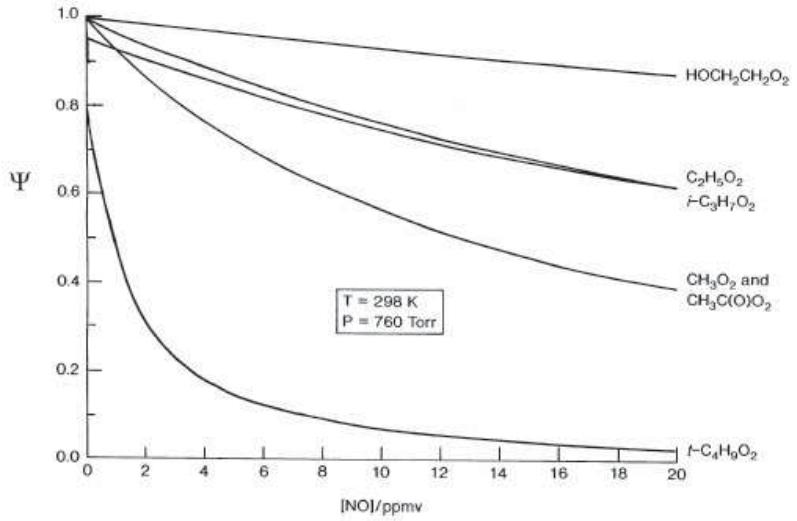

Figure 2.1: Idealised fractional yield of HO_2 (Ψ) as a function of the reagent NO concentration for a series of organic peroxy radicals ignoring wall losses; taken from Ashbourn *et al.* (1998) who in turn took the data from Jenkin *et al.* (1997), except for t-$C_4H_9O_2$ which was recalculated

Ashbourn *et al.* (1998) found this dependency was considerably weaker than calculated, being statistically insignificant for all but 2 of the peroxy radicals investigated. The radical *neo*-$C_5H_{11}O_2$ was predicted to exhibit the greatest NO concentration dependency in the HO_2 yield due to the fact that it forms HO_2 after a multi-step process via *t*-$C_4H_9O_2$ (i.e. $(CH_3)_3CO_2$ in Table 2.1 and *t*-$C_4H_9O_2$ in Figure 2.1) and CH_3O_2. The step yielding CH_3O_2 involves the slow thermal decomposition of intermediate oxy radical *t*-C_4H_9O (i.e. $(CH_3)_3CO$) which has to compete with the relatively fast reaction with NO:

$$(CH_3)_3CO \rightarrow CH_3 + CH_3C(=O)CH_3 \tag{2.32}$$

$$(CH_3)_3CO + NO \rightarrow (CH_3)_3CONO \tag{2.33}$$

The reason for this is that t-C_4H_9O does not react with O_2 to form HO_2 (as per Reaction 2.11) owing to the absence of an H atom α to the radical centre (Ashbourn *et al.*, 1998). Still, Ashbourn *et al.* (1998) observed that *neo*-$C_5H_{11}O_2$ did exhibit the greatest dependency on the NO concentration, but a factor of 30 less than expected. To explain the weak dependence it was suggested that the assumption of instantaneous mixing of the reagent NO is inaccurate. Conversion of the R_iO_2 radical to HO_2 may occur faster than the mixing of reagent NO into the flow, meaning that the conversion occurs at effectively much lower NO concentrations (30 times lower) and the loss route to form organic nitrites cannot compete as effectively. The conclusion of Ashbourn *et al.* (1998) seems reasonable, though the rate of mixing will depend on the system in question.

The yield measured by Ashbourn *et al.* (1998) is corrected for wall loss to leave only gas phase losses in the way derived here. The observed response Ψ_{obs} can be defined as the measured response to a given radical S_{RO_2} relative to the response to HO_2, S_{HO_2}:

$$\Psi_{obs} = \frac{S_{RO_2}}{S_{HO_2}} \tag{2.34}$$

The response to a given radical is due to the sampled concentration, the fractional yield of HO_2 from gas phase chemistry, Γ_G, and the fractional yield of HO_2 after heterogeneous wall losses, Γ_H. Defining the fractional yield of HO_2 from HO_2 from gas phase chemistry as Γ_{G1} ($\Gamma_{G1} = 1$); the fractional yield of HO_2 from RO_2 from gas phase chemistry as Γ_{G2}; the fractional yield of HO_2 from HO_2 after heterogeneous losses as Γ_{H1}; the fractional yield of HO_2 from RO_2 after heterogeneous losses as Γ_{H2}.

$$S_{HO_2} = \Gamma_{G1}\Gamma_{H1}[HO_2] \tag{2.35}$$

$$\Gamma_{G1} = 1 \tag{2.36}$$

$$S_{RO_2} = \Gamma_{G2}\Gamma_{H2}[RO_2] \tag{2.37}$$

$$[HO_2] = [RO_2] \tag{2.38}$$

Hence Equation 2.34 becomes:

$$\Psi_{obs} = \frac{\Gamma_{G2}\Gamma_{H2}}{\Gamma_{H1}} \tag{2.39}$$

Ashbourn *et al.* (1998) corrects the observed response for gas phase losses according to known yields from Reaction 2.10:

$$\Psi_{corr,G} = \frac{\Psi_{obs}}{\Gamma_{G2}} \tag{2.40}$$

Substituting in for Ψ_{obs} from Equation 2.39:

$$\Psi_{corr,G} = \frac{\Gamma_{H2}}{\Gamma_{H1}} \tag{2.41}$$

Ashbourn *et al.* (1998) assume *neo*-$C_5H_{11}O_2$ is not subject to significant wall losses, hence:

$$\Gamma_{H2}(neo\text{-}C_5H_{11}O_2) = 1 \tag{2.42}$$

$$\Psi_{corr,G}(neo\text{-}C_5H_{11}O_2) = \frac{1}{\Gamma_{H1}} \tag{2.43}$$

Ashbourn *et al.* (1998) then correct the observed response for heterogeneous losses by weighting relative to *neo*-$C_5H_{11}O_2$:

$$\Psi_{corr,G+H}(RO_2) = \frac{\Psi_{corr,G}(RO_2)}{\Psi_{corr,G}(neo\text{-}C_5H_{11}O_2)} \tag{2.44}$$

$$\Psi_{corr,G+H}(RO_2) = \Psi_{corr,G}(RO_2)\Gamma_{H1} \tag{2.45}$$

$$\Psi_{corr,G+H}(RO_2) = \Gamma_{H2} \tag{2.46}$$

Hence Γ_{G2} ($= Y_{HO_2,b}$ in Table 2.1) was determined by rearranging Equation 2.39 and substitution from Equations 2.43 and 2.46:

$$\Gamma_{G2} = \frac{\Psi_{obs}}{\Psi_{corr,G}(neo\text{-}C_5H_{11}O_2)\Gamma_{H2}} \tag{2.47}$$

$$\Gamma_{G2} = \frac{\Psi_{obs}}{\Psi_{corr,G}(neo\text{-}C_5H_{11}O_2)\Psi_{corr,G+H}(RO_2)} \tag{2.48}$$

Having determined the weak dependency of the UEA PERCA relative response as a function of the NO reagent concentration, Ashbourn *et al.* (1998) removed this trend to examine the wall loss

dependency on the radical type alone. The NO reagent concentration independent influence of organic nitrate formation was removed using the branching ratio Γ_1. Ashbourn *et al.* (1998) found that the rate of heterogeneous loss primarily became less important as the organic group became larger, but that it was enhanced if a polar group (such as OH or =O) was present. Hence, the gas phase loss corrected yield increased with carbon number along the series of alkyl radicals and also the β-hydroxy peroxy radicals with the β-hydroxy peroxy radical yield typically being significantly worse due to the polar group. The yield from the C_2 acyl peroxy radical $CH_3C(=O)O_2$ was also lower than the C_2 alkyl peroxy radical $C_2H_5O_2$ but not lower than the C_2 β-hydroxy peroxy radical $HOCH_2CH_2O_2$, which exhibited the lowest yield after wall loss except compared to HO_2. Mihele *et al.* (1999) found approximately equal wall loss rates for CH_3O_2 and $C_2H_5O_2$ while the loss rate for HO_2 was three times greater and attributed this to the lower polarity of the organic peroxy radicals tested. In comparison Ashbourn *et al.* (1998) found the wall loss rate for CH_3O_2 was significantly greater than that for $C_2H_5O_2$. Broadly, the conclusions are similar but clearly the exact wall loss characteristics are dependent on the inlet design and material.

The significant influence of HO_2 wall loss prior to the reaction zone has led to the idea of the development of a denuding inlet, whereby preferential loss of HO_2 before chain amplification allows discrimination between HO_x and RO_2 (Jacob, 2006). The idea is that one instrument channel is coupled to a denuding inlet to remove HO_x and measure RO_2, while a second (well matched) channel is used to measure total RO_x and the difference between the measurements would in principle separate the HO_x and RO_2 signals. In practice the use of this technique in the field was inconclusive likely owing to variation in the wall loss characteristics and other complicating factors associated with ambient composition and speciating RO_2 (Jacob, 2006).

One of the key limiting factors for the measurement of peroxy radicals through chain amplification in ambient air was the identification of a major loss in instrument response associated with the

reduction in chain length with increasing ambient humidity (Mihele & Hastie, 1998, Mihele *et al.*, 1999). Following this all groups employing chain amplification techniques and similar technologies have had to characterise and correct for the impact of [H_2O] on their measurements e.g. (Salisbury *et al.*, 2002, Sadanaga *et al.*, 2004) while some also attempt to explain the mechanism leading to the effect e.g. (Mihele *et al.*, 1999, Reichert *et al.*, 2003). Mihele & Hastie (1998) report a reduction in chain length (for HO_2) of ∼50% for a relative humidity of 40%, Salisbury *et al.* (2002) report a reduction in chain length (for CH_3O_2, though not specified) of ∼50% for a specific humidity of 8 gkg^{-1} at an inlet temperature of 28^{o}C (which corresponds to a relative humidity of ∼34%), Reichert *et al.* (2003) report a reduction in chain length (for HO_2) of ∼50% for a relative humidity of 20% and Sadanaga *et al.* (2004) report a reduction in chain length (for HO_2) of ∼50% for a relative humidity of 40%. Mihele *et al.* (1999) investigated whether the reduction in chain length with increased humidity is associated with variation in the wall loss rate for HO_2, CH_3O_2 and $C_2H_5O_2$. The HO_2 wall loss rate was found to exhibit a marked increase with relative humidity (for Teflon tubing). No significant change was observed for CH_3O_2 and $C_2H_5O_2$, suggesting the reduction in chain length is associated with the chain chemistry and not the conversion of RO_2 to HO_2. Owing to the potential high level and variable nature of atmospheric water vapour concentration it is essential to characterise the impact on a measurement and use this in combination with concomitant ambient humidity measurements to correct derived radical concentrations. The characterisation of the effect on measurements made in this work and in general using the University of Leicester PERCA instruments are discussed later, along with discussion of a rationalisation (see Section 3.2.3, Chapter 3).

The method commonly employed for NO_2 detection in PERCA is to use the chemiluminescence of an aqueous luminol (5-amino-2,3-dihydro-1,4-phthalazinedione, $C_8H_7N_3O_2$) solution when exposed to NO_2 in the presence of O_2. The emission is known to peak in the region of 424 nm (Maeda *et al.*, 1980), and measurement follows by detection of the emitted light signal. The method of luminol

chemiluminescence for the detection of NO_2 was proposed by Maeda *et al.* (1980) and has since been commercialised for the direct detection of NO_2 e.g. Drummond *et al.* (1991). The detailed chemical mechanism for luminol chemiluminescence in the presence of NO_2 is not well understood but is believed to involve two NO_2 molecules per photon leading to a quadratic dependence of the emission intensity on the NO_2 concentration (Cantrell, 1993). However, owing to the relatively low solubility of NO_2, the solvation of the second NO_2 molecule becomes the rate limiting step for photon emission and means the emission intensity is nominally linear in NO_2 concentration above 2-3 ppbV (Kelly *et al.*, 1990). The sensitivity of this method of NO_2 detection in application to PERCA measurements has been evaluated (Cantrell *et al.*, 1984, Cantrell, 1993) dependent on the reagent NO and CO concentrations. Cantrell *et al.* (1984) reported that the detection sensitivity was inversely proportional to the reagent NO concentration, though this was subsequently mitigated by optimisation of the luminol solution composition. The sensitivity can also be reduced owing to the presence of metal carbonyl compounds present in compressed CO gas cylinders (Cantrell, 1993), but this can be mitigated by passing the reagent CO through an appropriate trap prior to addition to the reaction zone of the inlet in application. Clemitshaw *et al.* (1997) report that with use of the proprietary luminol II solution (as used in this work) good linearity was observed in the range 5-150 ppbV. Clearly accurate calibration of the NO_2 sensitivity over the likely range of NO_2 encountered in ambient measurements is essential to the overall accuracy of the technique.

Another consideration has to be the potential for other radicals besides OH, HO_2 and RO_2 to produce a response if other mechanisms exist in which these species initiate chain reactions under the conditions of the inlet reaction zone. During measurements in the Antarctic (ARCTOC, Spring 1995, 1996) signals were observed from a PERCA instrument (the instrument described by Hastie *et al.* (1991)) under conditions where RO_x radicals were not expected (low ozone, at night, BrO elevated) and so an alternative radical signal was considered (Perner *et al.*, 1999). Bromine and chlorine radicals were

considered the most likely candidates as the signals occurred at low ozone concentration in the presence of these active halogens; however in laboratory experiments only chlorine was found to support chain amplification (Perner *et al.*, 1999). The chain reaction mechanism proposed:

$$OClO + NO \rightarrow ClO + NO_2 \tag{2.49}$$

$$ClO + NO \rightarrow Cl + NO_2 \tag{2.50}$$

$$Cl + CO + M \leftrightarrow ClCO + M \tag{2.51}$$

$$ClCO + O_2 + M \rightarrow ClCO_3 + M \tag{2.52}$$

$$ClCO_3 + NO \rightarrow Cl + CO_2 + NO_2 \tag{2.53}$$

With $ClCO_x$ (Cl, ClO and OClO) initiating the chain reaction and suggested loss routes being radical wall loss and combination reactions such as between Cl and NO to form nitrosylchloride, ClNO:

$$Cl + NO + M \rightarrow ClNO + M \tag{2.54}$$

In laboratory calibration of the response a chain length of the order 300 was obtained for OClO while for HO_2 a chain length of the order 160 had been determined (Perner *et al.*, 1999). This means OClO, ClO and Cl may be detected with high precision and form a significant contribution to the total signal dependent on the total radical composition. This can be viewed positively illustrating the potential of the technique for extension to detection of further radical species. However, under ambient conditions it further complicates the interpretation of the measured PERCA response if ClO_x is an important component of the radical population. Supplementary measurements and modelling of the chemistry which can elucidate the radical composition are necessary for the successful interpretation of the measured signals.

PerCIMS/ROxMas - Separate measurement of RO_x and HO_x

This technique was introduced by Reiner *et al.* (1997) as an alternative to the original PERCA methodology and takes advantage of a very similar chain reaction where the reagents used are NO and sulphur dioxide (SO_2) contrasting with NO and CO in PERCA. The product of the chain reaction is gaseous sulphuric acid (H_2SO_4) which is then measured by CIMS (Chemical Ionisation Mass Spectrometry). The technique is termed either ROxMas (ROx Chemical Conversion/Chemical ionisation Mass spectrometry) (Hanke *et al.*, 2002) or PerCIMS (Peroxy radical Chemical Ionization Mass Spectrometry) (Cantrell *et al.*, 2003) dependent on the group implementing the technique, though the measurement principles are identical. The chain reaction mechanism follows:

$$HO_2 + NO \rightarrow OH + NO_2 \tag{2.55}$$

$$OH + SO_2 + M \rightarrow HSO_3 + M \tag{2.56}$$

$$HSO_3 + O_2 \rightarrow SO_3 + HO_2 \tag{2.57}$$

$$SO_3 + 2H_2O \rightarrow H_2SO_4 + H_2O \tag{2.58}$$

Both OH and HO_2 are recycled, HO_2 in Reaction 2.57 and OH through Reaction 2.55 as in PERCA, so either can initiate a chain reaction.

Organic peroxy radicals are also detectable through the same mechanism as that of traditional PERCA where they can be efficiently converted to HO_2 through reaction with the reagent NO. Similar limitations to the sensitivity (potential interference and heterogeneous losses) must therefore be expected to exist due to varying efficiency of the conversion of different RO_2 to HO_2 as per PERCA (see Section 2.1.1). These issues are reduced by employing a low chain length and short reaction time for both the conversion and amplification processes (e.g. chain length of ≈10-15 and reaction time of the order 0.1 s (Hanke *et al.*, 2002)). The technique maintains high sensitivity (e.g. detection limit of 0.4 pptV with a 15 s averaging time (Edwards *et al.*, 2003)) due to the underlying sensitivity of the CIMS detection

technique and the low ambient gaseous H_2SO_4 background (Hanke *et al.*, 2002).

The dependence of the yield of HO_2 from RO_2 depends on the competition between the conversion route and addition reactions between RO_2 and NO and RO with NO or SO_2; so the yield depends on the concentrations of O_2, NO and SO_2. This detail has been exploited to allow the discrimination of HO_2 and RO_x. Hanke *et al.* (2002) promote the addition reactions by addition of N_2 buffer gas to dilute the O_2 content such that essentially only ambient HO_2 is measured ("HO_2-only mode"). Alternatively O_2 buffer gas is added to enhance the RO_2 to HO_2 conversion route ("HO_2+RO_2 mode"). Cantrell *et al.* (2003) instead vary the reagent NO and SO_2 concentrations, suppressing conversion with high reagent concentrations (2500 ppmV NO and 72500 ppmV SO_2) and promoting conversion with low reagent concentrations (6 ppmV NO and 300 ppmV SO_2). Owing to the varying conversion efficiency of organic peroxy radicals, suppression of RO_2 conversion is not complete in the "HO_2-only mode". Without knowing the radical composition a surrogate organic peroxy radical is used to estimate the conversion efficiency, this means only an upper limit of $[HO_2]$ and lower limit of $\Sigma_i[R_iO_2]$ are truly defined.

PERCA-LIF (PERCA-Laser Induced Fluorescence) measurement of RO_x

The PERCA-LIF technique has been recently developed and takes advantage of the PERCA chain chemistry to convert RO_2, OH and HO_2 to NO_2 while using the high sensitivity method of LIF (Laser Induced Fluorescence) for the detection of NO_2 (Sadanaga *et al.*, 2004). As currently employed the technique suffers the same complexities as PERCA owing to the identical chain mechanism being employed; these have been detailed in Subsection 2.1.1 so will not be discussed further here. The advantage of this application of the chemical amplification method is the potential for greater sensitivity in the detection of NO_2 by LIF over luminol chemiluminescence.

The system employs a reaction tube and reference tube prior to the fluorescence detection cell. In

the reaction tube the reagents CO and NO are continually added to the ambient airflow to promote the chain reaction to produce NO_2 (the mechanism described in detail in Subsection 2.1.1). By experimentation the optimum reagent concentrations have been determined as 10% CO and 3-6 ppmV NO (dependending on the length of the reaction tube). In making ambient background measurements a reference tube is employed where the reagent NO is continually added (with the same flow) and CO is replaced by an identical flow of N_2. To switch between background and chain amplified NO_2 measurement regimes either the reference tube or reaction tube respectively are directed toward the detection cell by use of a 3-way valve. This allows rapid switching between measurement modes and avoids disturbing the conditions in either tube through changing of the reagent mixture. To validate that no error was introduced by using a separate tube for the background measurement Sadanaga *et al.* (2004) report that N_2 can be directed to the reaction tube in place of CO for cross checking of the background derived. For chain length calibrations the single reaction tube is used with CO replaced by N_2 in the same way for measurement of the background signal. The chain reaction to produce NO_2 is terminated at the end of the reaction tube using a teflon filter to remove any residual RO_x, in this way the reaction time is limited to a constant known value; presumably the filter is known to not remove NO_2.

The detection of NO_2 follows by sampling a proportion of the ambient flow through an orifice into a fluorescence cell maintained at reduced pressure. The principle of NO_2 LIF (as described in Matsumoto *et al.* (2001)) involves the NO_2 molecules absorbing photons in the visible region for transition between $^2A_1$ and $^2B_2$ states. The excited NO_2 molecules then emit red-shifted fluorescence photons or are collisionally quenched back to the ground state. In the system described by Matsumoto & Kajii (2003), Sadanaga *et al.* (2004) a Nd:YAG laser is used for excitation at 532 nm and the fluorescence signal is detected using time-gated photon counting using a PMT (photomultiplier tube). In this technique the fluorescence signal is proportional to the NO_2 concentration sampled, hence the

concentration can be determined from the fluorescence signal, though this is not absolute and requires calibration.

An interference to the technique is reported by Sadanaga *et al.* (2004) related to the LIF detection of NO_2, i.e. a systematic difference in the detection of NO_2 between the reaction tube and reference tube. The difference is not related to the tubing as demonstrated by the cross check of the background derived from the reaction tube by switching from CO to N_2 addition. Instead, it is related to the different rate of collisional quenching of the laser excited NO_2 by CO when sampling the reaction tube, compared to by N_2 when sampling the reference tube. A systematic decrease in sensitivity was observed with increasing CO concentration, with a reduction in the total signal of 2% at the reagent CO concentration employed. Though the interference is minimal and easily quantified it illustrates a potential weakness in the application of the technique to ambient measurements where the sampling of other quenching species is not controlled.

The PERCA-LIF technique could offer separation of RO_2 and HO_x through modulation of the chain length by modulation of the reagent concentrations to shift the conversion efficiency of RO_2 to HO_2 as employed in the PerCIMS technique, taking advantage of the higher sensitivity of LIF NO_2 detection. The advantage of LIF NO_2 over luminol chemiluminescence may be outweighed by the simplicity of luminol chemiluminescence in application to field measurements.

2.1.2 LIF techniques

The techniques termed interchangeably as LIF (Laser Induced Fluorescence) and FAGE (Fluorescence Assay by Gas Expansion) are essentially the same technique (Clemitshaw, 2004) and can be used to measured OH and HO_2. LIF is a general term to describe this type of spectroscopic technique, using laser excitation at a particular wavelength to choose a particular transition of a target molecule and monitoring the fluorescence signal. An application of LIF has been the detection of OH and HO_2,

while FAGE refers specifically to detection by LIF at low pressure (Heard & Pilling, 2003). Recently an extension of the technique has shown promise in the detection of organic peroxy radicals by taking advantage of a similar methodology for the conversion of RO_2 to HO_2 and HO_2 to OH as the chemical amplification techniques (Fuchs, 2006, Fuchs *et al.*, 2008, 2009).

FAGE (Fluorescence Assay by Gas Expansion) measurement of HO_x

The technique was introduced for detection of HO_x by Hard and O'Brien in the 1980's (Hard *et al.*, 1984) and has been used extensively for measurements both from the ground and on board aircraft (see Section 2.2, page 45). The sampling process involves the supersonic expansion of the ambient air through a specially designed inlet nozzle into a fluorescence cell held at reduced pressure (e.g. 5.3 hPa (Dusanter *et al.*, 2008)). HO_2 cannot be detected directly through LIF, so again this is an indirect technique for HO_2; the addition of an excess of NO within the fluorescence cell efficiently converts HO_2 radicals to OH taking advantage of the same reaction employed by the chemical amplification techniques:

$$HO_2 + NO \rightarrow OH + NO_2 \tag{2.59}$$

The resulting OH is detected through LIF. An excitation laser produces 308 nm light, making use of the OH (0,0) band to promote OH from the ground state ($X^2\Pi$) to the first electronic excited state ($A^2\Sigma^+$). The fluorescence emission is extremely weak in intensity compared to scattered light from the excitation laser and is of the same wavelength, meaning it is not possible to filter for the fluorescence emission alone. Scattered light would potentially mask the fluorescence signal, however the low pressures employed extend the natural lifetime of the excited state (which is largely dependent on collisional quenching); the time difference is sufficient to separate the excitation signal from the fluorescence emission by a process of "delayed-gated" photon counting. The signal results from the sum of sampled OH and converted HO_2, to detect OH or HO_2 alone requires either a separate fluorescence cell where reagent NO is not added, or by switching on and off the NO addition, periodic measurement

in each mode could be performed using a single fluorescence cell.

Two potential interferences to the technique are also made insignificant at the low pressures employed. The loss of OH through HONO formation is pressure dependent, and therefore reduced at low pressure due to the low concentration of the third body M:

$$OH + NO + M \rightarrow HONO + M \tag{2.60}$$

The formation of additional OH from photolysis of O_3 to form $O(^1D)$ followed by subsequent reaction with water vapour is insignificant due to the reduced concentration of the reactants at low pressure.

The technique is highly sensitive particularly to HO_2 owing to the higher concentration relative to OH (e.g. HO_2:OH$\sim$10-100 in the lower and upper troposphere (Stevens *et al.* (1997) and Jaegle *et al.* (2001) respectively)) and provides data on a short time resolution. LIF/FAGE still suffers a number of limitations. The conversion of HO_2 to OH is limited by the time from sampling and addition of the reagent NO to the time at which the sampled mixture reaches the excitation laser; the yield must be known for accurate determination of the HO_2 concentration. Since the technique detects both OH and HO_2, calibrated sources of both radical species must be used for calibration of the instrument sensitivity. A primary limitation has been the inability to effectively detect organic peroxy radicals through conversion to OH, because of the time required for conversion under low pressure in the fluorescence cell; again this is limited by the yield of OH from RO_2 in the time from sampling and addition of the reagent NO to the time at which the sampled mixture reaches the excitation laser. The pressure dependence of the yield of OH from RO_2 is compounded since the step to yield HO_2 often requires the presence of oxygen (see Reaction 2.11), though not always (see Reactions 2.23 and 2.24). The conversion of RO_2 though limited has to be considered since it represents a potential interference to the HO_2 measurement (Heard & Pilling, 2003).

ROxLIF - Separate measurement of RO_2 and HO_x

The measurement of organic peroxy radicals through a LIF type of instrument has recently been pioneered (Fuchs, 2006, Fuchs *et al.*, 2008, 2009), and other implementations of this variant of radical instrumentation are under development (D. Heard, private communication). To overcome the limited yield of HO_2 from RO_2 at the reduced pressure of a typical LIF system, a two-stage conversion scheme has been employed. The first stage comprises a flow reactor held at 25 hPa where the addition of reagent NO promotes the efficient conversion of most RO_2 to HO_2 within the mean residence time dictated by the flow (0.6 s (Fuchs *et al.*, 2008)), the reagent NO also converts HO_2 to OH so CO is used as an additional reagent to convert OH back to HO_2 in the flow reactor:

$$RO_2 + NO \rightarrow RO + NO_2 \tag{2.61}$$

$$RO + O_2 \rightarrow R'O + HO_2 \tag{2.62}$$

$$HO_2 + NO \rightarrow OH + NO_2 \tag{2.63}$$

$$OH + CO \rightarrow H + CO_2 \tag{2.64}$$

$$H + O_2 + M \rightarrow HO_2 + M \tag{2.65}$$

The reagent NO and CO concentrations are such that HO_2 and OH quickly reach an equilibrium in the same chain mechanism promoted in traditional PERCA. The partitioning between HO_2 and OH at the conditions within the flow reactor (≈50:1 (Fuchs *et al.*, 2008)) combined with the efficient conversion of RO_2 to HO_2 means that the radical population reaching the exit of the flow reactor is essentially HO_x in the form of HO_2.

Since the ROxLIF technique employs the same reaction mechanism as per the chemical amplification technique it would be expected that it will suffer the same complexities in terms of the quantification of the total RO_2 concentration since the measurement is of course non-specific and will respond with varying sensitivity to individual R_iO_2 (see Section 2.1.1). Recognising this the relative sensitivity of

the ROxLIF instrument has been quantified for a number of organic peroxy radicals (Fuchs, 2006, Fuchs *et al.*, 2008) and validated for CH_3O_2 and $C_2H_5O_2$ by intercomparison with measurements by MIESR (see Section 2.1.3) (Fuchs, 2006, Fuchs *et al.*, 2009) and a modified version of the MCM model (Master Chemical Mechanism) (Fuchs (2006) and references therein). Varying sensitivities were obtained showing this technique also requires careful interpretation of the derived concentration in an ambient air measurement situation where the radical composition may be complex.

Three measurements modes are potentially available though only two are practical (Fuchs, 2006): RO_x mode where reagents NO and CO are added in the flow reactor, HO_x mode I where only the reagent CO is added and HO_x mode II where all reactive reagent gases are replaced by non-reactive N_2. RO_x mode is that described above where the reagents NO and CO promote the conversion of RO_x to HO_2 and maintain all RO_x as HO_2; this mode essentially provides the total RO_x concentration. HO_x mode I converts OH to HO_2 so provides a measurement of total HO_x concentration, the subtraction of this signal from the RO_x measurement therefore also allows determination of the concentration of RO_2. HO_x mode II would offer the potential of further discrimination between HO_2 and OH as per LIF/FAGE, since no conversion of the radical population is employed before the second stage. However, owing to effective OH loss processes within the flow reactor the sampling efficiency for OH is significantly reduced in mode II leading to an significant drop in the instrument sensitivity to OH. HO_x mode II is therefore impractical for measurement of OH alone and the ROxLIF system cannot be used to discriminate OH in the atmosphere. Fuchs (2006) specifies that RO_x mode in combination with HO_x mode I have been used in practice.

The flow reactor is coupled to a LIF system for the detection of HO_x, the second stage of the measurement. At the exit of the flow reactor a transfer nozzle samples the central part of the flow into a detection chamber held at 3.5 hPa (Fuchs, 2006, Fuchs *et al.*, 2008, 2009). The further addition of reagent NO into the gas expansion region lifts the NO concentration within the flow and shifts the

equilibrium between HO_2 and OH from HO_2 to OH which is then detected through LIF at 308 nm as described above (see Section 2.1.2). In application to measurements in the field a second channel has been required to allow the simultaneous measurement of OH through conventional LIF, adding to the complexity of the technique and reducing the ease of use in field measurements.

2.1.3 MIESR (Matrix Isolation Electron Spin Resonance spectroscopy) - Speciated measurement of HO_2, alkyl RO_2, $CH_3C(O)O_2$, NO_3 and NO_2

The MIESR technique was developed by Mihelcic (Mihelcic *et al.*, 1978, 1985, 1990), and provides direct and semi-speciated measurements of peroxy radicals, while it is also capable of detecting a number of other important radical species. The radical species detected are HO_2, the sum of alkyl RO_2, the acetyl peroxy radical ($CH_3C(O)O_2$), the nitrate radical NO_3, and NO_2; all of these are sampled simultaneously. The method of sampling is by drawing ambient air through a critical nozzle into a evacuated chamber, the nozzle critical orifice and the pressure gradient providing a constant flow rate. By doping the sample flow with D_2O vapour and the use a cold finger maintained at -196^{o}C (cooled using liquid nitrogen) the reactive species are isolated on a D_2O-ice matrix preventing any further reactions. Detection follows by transferring the samples to the laboratory for analysis using electron spin resonance (ESR) spectroscopy, the technique is therefore an offline technique. Owing to the similarities of the electronic structure of most organic peroxy radicals only acetyl peroxy can be distinguished by its ESR spectrum, however, in principle all radicals could be identified though this may require improvements in the resolution of the ESR spectra. Sampling times up to 30 minutes are needed to build up sufficient radical concentrations to allow detection, the sampled concentrations are therefore integrated over the sampling period. Clear limitations to the technique exist in terms of complexity and low frequency sampling.

2.1.4 Developmental techniques

Developmental techniques exist which allow speciated measurements of peroxy radicals, however these by their nature have only been employed in laboratory studies and so are only discussed briefly here.

PTR-MS (Proton Transfer Reaction Mass Spectrometry) - Measurement of specific R_iO_2

Proton Transfer Reaction Mass Spectrometry (PTR-MS) is a widely used technique in the detection of the organic compounds in the atmosphere, however its application to the study of organic peroxy radicals is still limited (Hanson *et al.* (2004) and references therein). The principle of the PTR-MS technique is the chemical ionisation of the analyte species by proton transfer from hydronium ions (H_3O^+) if the analyte has a proton affinity greater than that of water. Detection of the ionised product then follows using a mass spectrometry technique. The ionisation reaction is as follows:

$$R + H_3O^+ \cdot (H_2O)_n \rightarrow RH^+ \cdot (H_2O)_m + (n - m + 1)H_2O \tag{2.66}$$

According to Hanson *et al.* (2004) under typical total pressures (less than ∼10 Torr) in the ion drift region, ions with n =0 and 1 can be made to be the most abundant with high electric field strengths, higher drift speeds and higher temperatures resulting in more frequent collisions with neutral gases. At higher pressures (greater than ∼100 Torr) larger clusters ($n = 3 - 5$) dominate with lower drift speeds resulting from lower possible field strengths. Small peroxy radicals are predicted to react efficiently with water proton clusters up to n =3, and a significant drop in sensitivity with increasing water vapour was observed by Hanson *et al.* (2004) which supports this. Currently application of the technique is limited to kinetic studies owing to expected complications in atmospheric measurements because of a water vapour interference. Many species may be identified but in atmospheric measurements these would have to be distinguished over the large number of other atmospheric species that are also efficiently detected, further limiting the technique.

CRDS (Cavity Ringdown Spectroscopy) - Measurement of specific R_iO_2

Cavity ringdown spectroscopy (CRDS) is another technique that offers potential for the speciated detection of organic peroxy radicals, though is yet to be applied except in laboratory studies (Glover & Miller, 2005, Zalyubovsky *et al.*, 2005, Just *et al.*, 2006). CRDS is a long path absorption spectroscopy technique however the sample air is contained within a short resonant cavity terminated by mirrors at each end; multiple reflections between the mirrors effectively create a long path length through the cell integrating the affect of absorption along the path. The group at Ohio State University (Glover & Miller, 2005, Zalyubovsky *et al.*, 2005, Just *et al.*, 2006) have pioneered the technique for monitoring the transient absorption of NIR radiation (1140-1460 nm) by peroxy radicals due to the $\tilde{A} - \tilde{X}$ electronic transition. Owing to the specific structures of absorption spectra it is anticipated a number of organic peroxy radicals can be distinguished with good specificity including even isomers and conformers of a given organic peroxy radical (Glover & Miller, 2005). Despite the indications that this may potentially allow the speciated measurement of mixtures of organic peroxy radicals, there is yet to be a deployment of such an instrument for atmospheric monitoring.

2.1.5 Summary of overview of peroxy radical measurement techniques

Section 2.1 has provided an overview of techniques for the measurement of peroxy radicals and highlighted some of the known limitations. In Table 2.2 each of the established field measurement techniques are specified in terms of typical time resolution, accuracy and detection limits. The table also provides a qualitative summary of the strengths and weaknesses of each approach.

Technique	Time res. (s)	Accuracy (%)	Detection limit (pptV)	Pros	Cons
PERCA ($[RO_x]$)	60	±40	1	Relatively low cost, portable, sensitive to HO_x and RO_2, simple detection method	Non-specific integrated response, varying sensitivity by radical, indirect, interferences, dangerous reagents
PerCIMS/ROxMas ($[HO_x]$, $\Sigma_i[R_iO_2]$)	15	±40	0.4	Highly sensitive CIMS detection, fast response, separated HO_x, RO_2	Indirect, varying efficiency of RO_2 conversion suppression
PERCA-LIF ($[RO_x]$)	60	±10	2.7-3.6[a]	Sensitive to HO_x and RO_2, highly sensitive LIF detection	Non-specific integrated response, varying sensitivity by radical, indirect, interferences, dangerous reagents, more complicated detection method
LIF/FAGE ($[HO_x]$)	30	±35 (OH), ±31 (HO_2)	0.006 (OH), 0.006-0.04 (HO_2)	Direct OH, highly sensitive LIF detection, fast response	Indirect HO_2, more complicated detection method, no RO_2
ROxLIF ($[HO_2]$, $\Sigma_i[R_iO_2]$)	60	±20	0.08 (HO_2), 0.28 ($\Sigma_i[R_iO_2]$)	Sensitive to HO_x and RO_2, highly sensitive LIF detection, fast response, minimised interferences	Non-specific integrated response to RO_2, indirect HO_2 and $\Sigma_iR_iO_2$, varying sensitivity by radical, more complicated detection method
MIESR ($[HO_2]$, $\Sigma_{alkyl}[R_{alkyl}O_2]$, $[CH_3C(O)O_2]$)	1800	±5	20	Specificity, absolute, calibration standard, quantifiable sampling losses	Long sampling time, low sensitivity, practicality in field, offline, cryogenic sample storage

Table 2.2: Summary of established radical measurement techniques. Sampling times are typical of ambient measurements, accuracies are typical values, detection limits have been converted to pptV equivalent at STP. Detection limits often determined from S/N over a period greater than typical time resolution of published data. [a]Detection limits correspond to ambient measurements in the range 50-80% relative humidity, NO_2 + O_3 = 50 ppbV (Sadanaga *et al.*, 2004).

2.2 Previous campaigns involving measurements of radicals

Measurements of free radicals, primarily OH, HO_2 and RO_2 are critical to forming a detailed understanding of the fast photochemistry that is so important in the evolution of the trace composition of the lower atmosphere, hence radical measurements are a key component of many field experiments. Since the development of techniques to measure these key species began in the early 1980's (discussed throughout Section 2.1) they have been employed in many field campaigns, from a variety of platforms from fixed observation sites on the ground to moving platforms such as ships and aircraft. Table 2.3 on page 46 lists a selection of recent campaigns involving the measurement techniques described. Further field campaigns involving such measurements have been listed in both Parker (2007) and Jacob (2006). In terms of the recently developed PERCA-LIF technique, only a single field deployment has been reported (Sadanaga *et al.*, 2004). In this ground measurement campaign (based at the Osaka Prefecture University, Japan, August 2002) midday maximum RO_x concentrations of approximately 150 pptV were observed.

2.3 Chapter 2 Summary

This chapter has introduced the various techniques currently employed and in development for the measurement of peroxy radicals in the lower atmosphere (Section 2.1). The background to the PERCA technique has been discussed in greatest detail being the technique employed for the measurements in this work (Section 2.1, page 18). This information provides context for the measurements and highlights the motivation for the experimental work to characterise the instrumentation (see Chapter 3), to allow better interpretation of the data (see Chapters 5 and 6).

The measurement techniques for peroxy radicals were summarised in terms of typical performance characteristics and advantages and disadvantages in Table 2.2. It is clear that all techniques suffer

Year	Campaign	Location	Technique (s)	Platform	References
2003	TORCH I	Writtle, Essex, UK	PERCA, FAGE	Ground	Emmerson & Carslaw (2009), Emmerson *et al.* (2007), Lee *et al.* (2006b), Jacob (2006)
2004	TORCH II	Weybourne, Norfolk, UK	PERCA, FAGE	Ground	Jacob (2006)
2004	ITOP	Horta Airport, Faial, Azores	PERCA, FAGE	Aircraft	Parker (2007)
2005		Jungfraujoch, Switzerland	PERCA	Ground	Parker (2007), Parker *et al.* (2009)
2005	CHABLIS	Halley, Antarctica	PERCA, FAGE	Ground	Bloss *et al.* (2007)
2005	GABRIEL	Suriname, Guyana	FAGE	Aircraft	Lelieveld *et al.* (2008)
2005		SAPHIR, Juelich, Germany	MIESR, ROxLIF	Ground	Fuchs (2006), Fuchs *et al.* (2009)
2005	HOxCOMP	Juelich, Germany	MIESR, FAGE (×4), ROxLIF, CIMS (OH)	Ground	Fuchs (2006), Fuchs *et al.* (2008)
2006	MIRAGE	Veracruz, Mexico	PerCIMS	Aircraft	Shon *et al.* (2008)
2006	MCMA/MILAGRO	Mexico City, Mexico	FAGE	Ground	Dusanter *et al.* (2009)
2006	TEXAQS	Gulf of Mexico	PERCA	Ship	Sommariva *et al.* (2009)
2006	INTEX-B/MILAGRO	Houston, Texas; Honolulu, Hawaii; Anchorage, Alaska	FAGE	Aircraft	Singh *et al.* (2009), Mao *et al.* (2009)
2006	AMMA	Niamey, Niger	PERCA, FAGE	Aircraft	This work
2006	AMMA	Ouagadougou, Burkina Faso	PERCA	Aircraft	Andres-Hernandez *et al.* (2009)
2007	OOMPH	Southern Ocean-Indian Ocean	PERCA, FAGE	Ship	Not yet published
2007	LAMP	Leicester, UK	PERCA	Ground	Not yet published
2008	OP3 Phase I	Bukit Atur, Borneo, Malyasia	PERCA, FAGE	Ground	Not yet published
2008	OP3 Phase II	Bukit Atur, Borneo, Malyasia	PERCA, FAGE	Ground	Not yet published
2008	OP3 Phase II	Kota Kinabalu, Borneo, Malyasia	PERCA, FAGE	Aircraft	Not yet published
2009	SOLAS	Cape Verde	PERCA	Ground	Not yet published

Table 2.3: Recent field campaigns involving the measurements of peroxy radicals

similar deficiencies in terms of speciating peroxy radicals in application to field measurements. The greatest improvements alternative techniques offer over PERCA are in terms of much greater sensitivity (and therefore lower detection limits) of the underlying detection methodology and reduced susceptibility to interferences. The humidity interference to PERCA (characterised and further discussed in Chapter 3 on page 81) is the greatest limitation, effectively reducing the detection limit and complicating interpretation.

What is clear from the summary of previous field campaigns (Section 2.2) (which is a continuation of those in Parker (2007), Jacob (2006)) and those of Parker (2007), Jacob (2006), is that the PERCA and FAGE techniques are still most widely employed in the field (though this list is only a selection of recent campaigns). This is not surprising, these techniques have been established for almost 30 years so there is greater experience of their application in the field. MIESR, although long established and providing absolute and (selected) speciated measurements does not lend itself to field campaigns owing to the significant technicality of the approach and the limited time resolution compared to other techniques. Those techniques developed more recently have yet to be widely adopted, though they offer various innovations to improve sensitivity, selectivity and reduced interferences compared to PERCA. PERCA still proves a popular methodology due to its relatively low cost, portability, sensitivity to RO_x and the simplicity of the underlying detection method. It is also not surprising that observations are still predominantly ground based since detection of such short lived, reactive and low concentration species is much simpler on a fixed and stable platform.

Chapter 3

Characterisation and calibration of a PERCA instrument

This chapter describes the implementation of the chemical amplification technique for the measurement of peroxy radicals and the experimental work carried out toward the calibration of the instrumentation used during this work. The PERCA technique has been employed to make field measurements of atmospheric peroxy radicals from the marine boundary layer to the lower free troposphere.

3.1 The University of Leicester PERCA instruments

There are two PERCA instruments currently in use at the University of Leicester both of which have been deployed in the field as part of the work for this thesis (AMMA (African Monsoon Multidisciplinary Analysis)) and more recently (AMPEP (Aircraft Measurement of chemical Processing and Export fluxes of Pollutants), OOMPH (Organics over the Ocean Modifying Particles in both Hemispheres), OP3 (Ozone and Particle Photochemical Production above a South-East Asian equatorial rain forest), chamber studies at PSI (the Paul Scherrer Institut) and EUPHORE (the EUropean PHOtoREactor)). These instruments are designated PERCA 3.5 and PERCA 4, initially designed

and built jointly between the University of Leicester and the University of East Anglia. PERCA 3.5 is an instrument constructed from the consolidation of components from older versions of the instrument with the addition of more recent modifications and has been deployed on ground based work (recently LAMP (the Leicester Air quality Measurement Project), OP3, SOLAS (Surface Ocean Lower Atmosphere Study)) and on a ship based platform in TEXAQS (TEXas Air Quality Study) and OOMPH. The instrument designated PERCA 4 has developed and been refined for deployment on an aircraft platform (and is also therefore often referred to as 'the aircraft PERCA') that platform being the NERC/Met Office BAe-146 (described in Chapter 5, Section 5.1) operated from FAAM (the Facility for Airborne Atmospheric Measurement) at Cranfield University. This instrument has been further deployed on the ground in chamber studies (PSI, EUPHORE) and has been the instrument primarily used in the laboratory investigations of instrumental performance (inlet chain length characterisation, humidity/chain length/NO_2 sensitivity dependence).

3.1.1 PERCA 4 – Aircraft PERCA instrument

The aircraft PERCA instrument (PERCA 4) is well described by the Technical Specification of Scientific Equipment version 10 (TSSE v10) (Brookes *et al.*, 2006) and Component Maintenance Manuals (CMM) associated with the instrument; these are the latest and updated versions of these technical documents associated with this instrument required for operation on board the BAe-146. The information presented here is simply to provide context and highlight changes made to the instrument for the AMMA campaign, to illustrate the setup of the instrument as it was used in this work. The TSSE v10 and CMM were produced in early 2006 during the recertification of the instrument, when modifications were made to reduce the instrument onto a single double-width half height 19" rack prior to AMMA (see Chapters 5 and 6). To minimise the weight of the rack components a redesign of the gas cylinder and pump mounting points was made, and some components were removed/upgraded (e.g. uninterruptible power supply (UPS) unit removed and ethernet PC/data PC combination replaced

with a single PC for data acquisition and instrument control). The layout of the inlet systems is shown schematically in Figure 3.1. The current layout of the main rack is shown in Figure 3.2 for

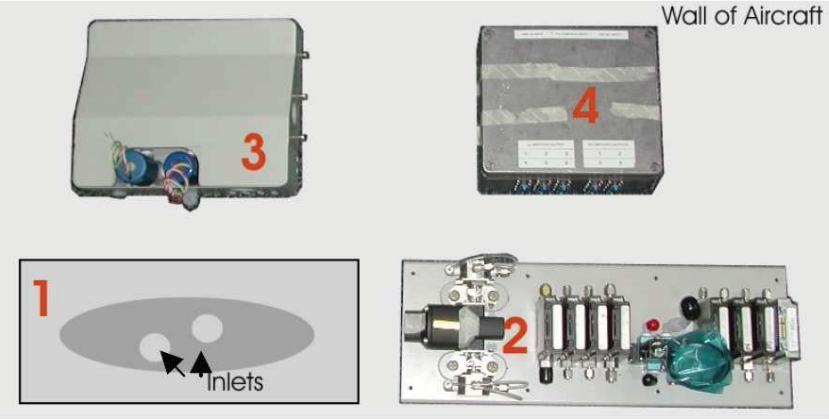

Figure 3.1: PERCA 4 inlet systems layout from (Brookes *et al.*, 2006)

reference. The instrument is divided into two sub-assemblies; the inlet systems and the main rack. The components of each are briefly described in Tables 3.1 and 3.2 respectively, further details can be found in the TSSE (Brookes *et al.*, 2006).

3.1.2 PERCA 3.5 – Ground PERCA instrument

The PERCA 3.5 instrument is very close in design to the aircraft instrument, it differs in the layout of the sub-components described already for PERCA 4 which has been specified for installation onto the BAe-146, but the operating principles are absolutely identical and both are dual channel systems. The main differences are as summarised: the design of the inlets (larger volume); two individual LMA-3 Scintrex NO_2 detectors are employed; a separate radical calibration source unit (see comparison in Figure 3.7, page 60); gases are supplied from cylinders stored separately; linearisation NO_2 flows (see Section 2.1.1, Chapter 2, page 30) are controlled using mass flow controllers; inlet systems are housed within a dedicated weatherproof inlet box; luminol is stored in glass vessel within a conventional refrigerator. The setup of the system is shown in Figure 3.3. Since the inlet box is often mounted on a

Figure 3.2: PERCA 4 instrument layout from (Brookes *et al.*, 2006)

Label	Sub-component name	Description
1	Inlets	Two heated Pyrex inlets for air sampling and reagent addition
2	Mass Flow Controller shelf (MFC Shelf)	Six MFCs (Tylan, FC260) for controlling reagent gas delivery to the inlets, two for controlling delivery of zero air for calibration dilution flows, a pneumatic actuator connected to a pair of ball valves for switching CO/N_2 addition points between front and rear injector ports of inlets, a solenoid valve for triggering the pneumatic actuator
3	Calibration system	Hg lamp and quartz flow tube for photolysis of CH_3I to produce CH_3O_2 radicals for chain length calibration, two valves for switching on/off CH_3I and NO_2 calibration flows for chain length and NO_2 sensitivity calibrations, two valves for directing calibration mixture to either inlet or vent
4	PERCA inlet control module (PICM)	Supplies 230 V AC and 24 V DC to inlets, MFC shelf and Calibration system; takes TTL (Transistor Transistor Logic) input to SSRs (Solid State Relays) to switch supplies on/off as set

Table 3.1: PERCA 4 inlet systems sub-components

sampling mast away from the instrument rack, a dedicated gas loom carries reagent gases to the inlet systems and sample air back to the detectors on the instrument rack; an electrical loom carries voltage supplies to the inlet box and control signals between the instrument rack and the inlet systems.

3.2 Inlet design, implementation and characterisation

As described already in Section 2.1.1 (page 18), the PERCA technique involves the detection of peroxy radicals through chemical conversion of CO to CO_2 and NO to NO_2 in a chain reaction. The concentration of NO_2 produced over the ambient NO_2 background being equal to the chain amplified peroxy radical concentration (i.e. $\Delta[NO_2] = CL \times [RO_2]$). To achieve this the University of Leicester PERCA instruments employ a dual channel system (two inlets and two detectors) to measure both the amplification chemistry produced NO_2 ($NO_{2,amp}$) and the background NO_2 ($NO_{2,back}$) concentrations

Label	Sub-component name	Description
A1	Bottom plate 1	Mounting plate for CO containment box and pump
A2	Bottom plate 2	Mounting plate for gas cylinders
5	Detector systems	Dual LMA-3 Scintrex NO_2 detectors and CO personal alarms
6	Linearisation system	Thermostated oven for calibration/linearisation permeation tubes; needle valves with fixed N_2 backing pressure used to control N_2 carrier flow over permeation tubes
7	PC	Upgraded PC for data acquisition and control
8	Keyboard/Display/Mouse	Input/output devices for PC
9	PSU box	Provides DC voltage supplies to instrument
10	Electrical Distribution Box (EDB)	Distributes 230V AC power to instrument components and house trip switches for these supplies. Also houses exhaust scrubbing system
11	Interconnect Box (ICB)	Routes input/output between instrument and data acquisition cards in PC
12	Isothermal Unit	Houses luminol chiller, luminol waste vessel, sample flow control system and temperature controllers for inlets and luminol chiller
13	NO in N_2 reagent cylinder	Mounting position for 2 litre (Air Liquide, LO2A) cylinder of NO mixture in N_2 (typically 600 ppmV)
14	CO containment system	Airtight box designed to safely contain pure ($\geq$99.99% CO) 2 litre CO reagent cylinder with a permanent vent line to outside, bolted to plate alongside vacuum pump
15	Vacuum pump	Oil filled rotary vacuum pump provides suction to draw sample air flow and luminol waste
16	Compressed gas cylinders	Mounting point for compressed gas cylinders (BOC, AH) of pure synthetic air (BOC, BTCA178) for calibration, zero grade N_2 (BOC, 99.999% N_2), and one other purely used for triggering a pneumatic actuator for switching reagent addition positions at the inlets

Table 3.2: PERCA 4 main rack sub-components

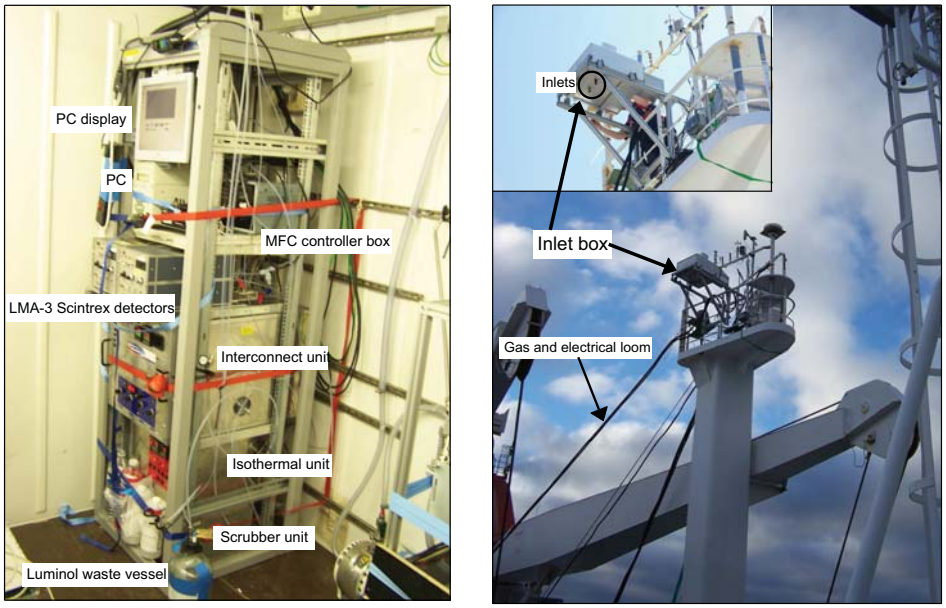

Figure 3.3: Ground PERCA system (PERCA 3.5) – Instrument rack (left) photograph of setup in MPI shipping container during the OOMPH campaign; inlet box (right) photographed mounted to ship mast during the OOMPH campaign

simultaneously; the amplified NO_2 concentration is derived by background subtraction ($\Delta[NO_2] = [NO_2]_{amp} - [NO_2]_{back}$). The dual system employed involves the periodic switching of the measurement mode ("chain amplification mode" to "background measurement mode" and *vice versa*) between the measurement channels, such that the chain chemistry is always active in one channel whilst radical termination in the other channel allows the background measurement. This is shown schematically in Figure 3.4.

The chain reaction sequence promoted in "chain amplification mode":

$$HO_2 + NO \rightarrow OH + NO_2 \tag{3.1}$$

$$OH + CO \rightarrow H + CO_2 \tag{3.2}$$

$$H + O_2 + M \rightarrow HO_2 + M \tag{3.3}$$

In "background measurement mode" the chain reaction is primarily terminated by formation of HONO and heterogeneous wall loss of the radical population without conversion to the less reactive NO_2

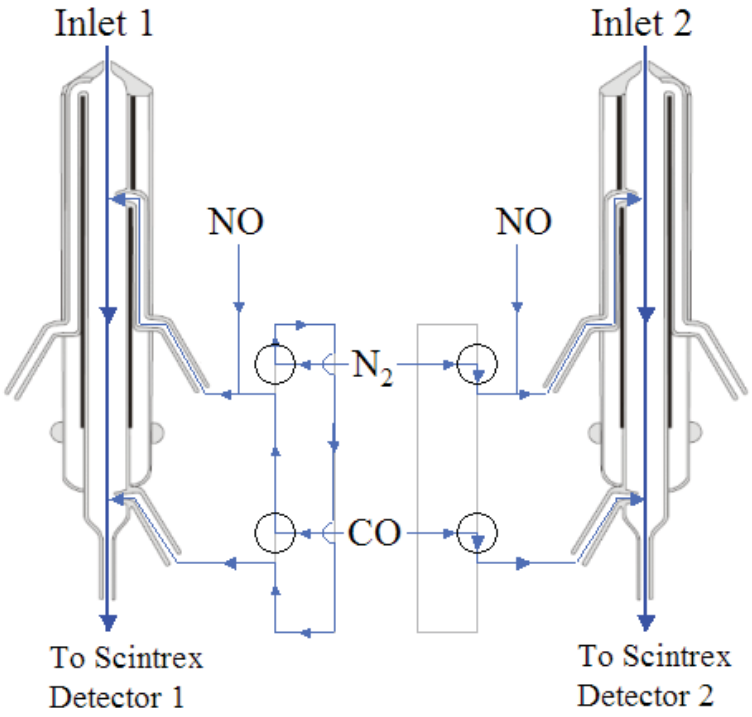

Figure 3.4: University of Leicester Dual Inlet Scheme - Inlet 1 in chain amplification mode (NO and CO addition at front port, N_2 at back), Inlet 2 in background measurement mode (NO and N_2 addition at front port, CO at back), arrows indicate direction of gas flow

product (for further details see Section 2.1.1):

$$HO_2 + NO \rightarrow OH + NO_2 \tag{3.4}$$

$$OH + NO + M \rightarrow HONO + M \tag{3.5}$$

$$HO_2 \rightarrow \text{walls} \tag{3.6}$$

The result is that the signal in each channel modulates out of phase with respect to the other channel, and the signal is apparent from the square wave shape of the raw signal (see for example Figure 3.9). The design of the aircraft inlet is shown to scale in Figure 3.5. A forward injector port delivers a mixture of NO and CO in "chain amplification mode" toward the front of the inlet, while inert N_2 is added downstream in the rear injector port. In "background measurement mode" a mixture of NO and N_2 is delivered to the front *via* the forward injector port, while CO is added downstream through the rear injector port. Mass flow controllers (MFC, Tylan FC260, now manufactured and distributed by Celerity Inc.) typically deliver the NO at 10 sccm, N_2 and CO are delivered at 100 sccm and the total sample flow is maintained at 2 slpm (1.79 slpm ambient air, 0.21 slpm reagent gases) by a combination of mass flow meters (MFM, Tylan FM360, now manufactured and distributed by Celerity Inc.) with stepper motor controlled needle valves - active control of the stepper motors achieved *via* computer software to within ±50 sccm. The switching of the injection points of CO and N_2 (delivered at identical flow rates) between measurement modes serves to reduce pressure pulsing of the sample flow (observed as signal spiking at switching in the raw signals). N_2 is chemically inert and so does not act to promote the chain reaction in the "background measurement mode" and the overall properties of the reagent mixture (NO, CO, N_2) in the sample flow are maintained downstream of the rear injector port independent of the measurement mode. It is important to maintain the reagent mixture in the total sample flow as a varying reagent concentration can affect the sensitivity of the luminol NO_2 chemiluminescence detection technique (as discussed in Section 2.1.1, page 30). The methodology of mass flow control provides stable parts concentrations of the reagents within the sample flow.

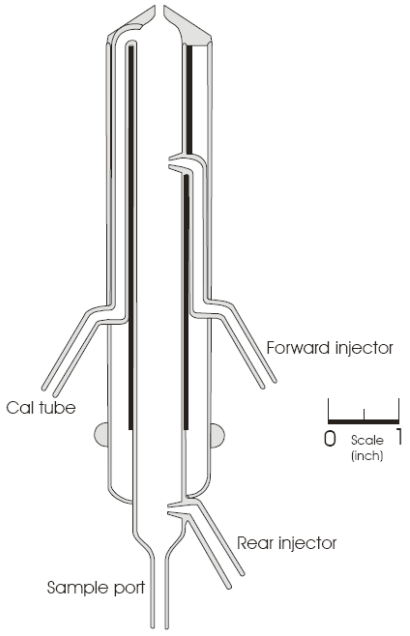

Figure 3.5: Scale diagram of PERCA 4 aircraft inlet from Brookes *et al.* (2006)

The dual channel technique employed in the University of Leicester PERCA instruments was first introduced by Green *et al.* (2006). By modulating between measurement modes in two channels redundancy is maintained since both channels are effectively single channel measurements. Furthermore, any detector drift between channels is easily identified since the background is frequently sampled in both channels, allowing better combination of the two channels of data for a dual measurement. Cantrell *et al.* (1996) was first to employ a dual channel PERCA technique however the methodology was different. One channel was maintained almost continuously in "chain amplification mode" while the other in "background measurement mode" continuously monitored the background, infrequent periodic swapping of the two channels allowed a cross check of the background response. Although data loss is less in principle because fewer switching periods interrupt the measurement, the two channels cannot drift with respect to one another within a measurement period if the data are to be effectively combined. The Cantrell *et al.* (1996) system also made use of large volume inlets meaning that significant differences in travel time between the two measurement channels could be introduced

by slight differences in volume and volume flow rate. This would introduce further noise and bias on combination of the data due to inaccurate synchronisation of the background signal with the chain amplification signal.

Further inlet design features highlighted by Green *et al.* (2006) include the use of relatively low volume inlets. Immediately there is less potential for error introduced by difference in travel time between inlets, as per the Cantrell *et al.* (1996) system. The rate of heterogeneous wall loss has already been highlighted as the main limitation on the chain length in the PERCA technique (see Section 2.1.1), and that which determines the potential instrument sensitivity to various radicals. With a low volume and therefore high surface to volume ratio, a dominant wall loss environment is designed, meaning termination of the radicals in the "background measurement mode" is made efficient. Though this means only lower chain lengths are possible (the termination process also being active in "chain amplification mode"), there is a benefit in the sense that the switch between measurement modes occurs rapidly and the termination process is less variable since it is largely defined by the inlet geometry which does not change. Effective termination of the radicals in the "background measurement mode" is important since chain chemistry could occur downstream of the back injector port during the "background measurement mode" (due to the presence of CO and NO reagents) if residual radicals were left in the sample flow, artificially enhancing the background. Interference through thermal decomposition of NO_2/radical reservoir species such as PAN is also removed in a low volume inlet since the residence time is low.

The plumbing scheme of the PERCA 4 aircraft inlet systems is shown in Figure 3.6, an identical setup is employed for reagent delivery and measurement mode switching within the ground inlet box. As described in Table 3.1 six MFCs (Tylan, FC260) are used for controlling reagent gas delivery to the inlets (NO, CO and N_2 to each channel), and a pneumatic actuator connected to a pair of ball valves is used for switching CO/N_2 addition points between front and rear injector ports of inlets for mode

switching.

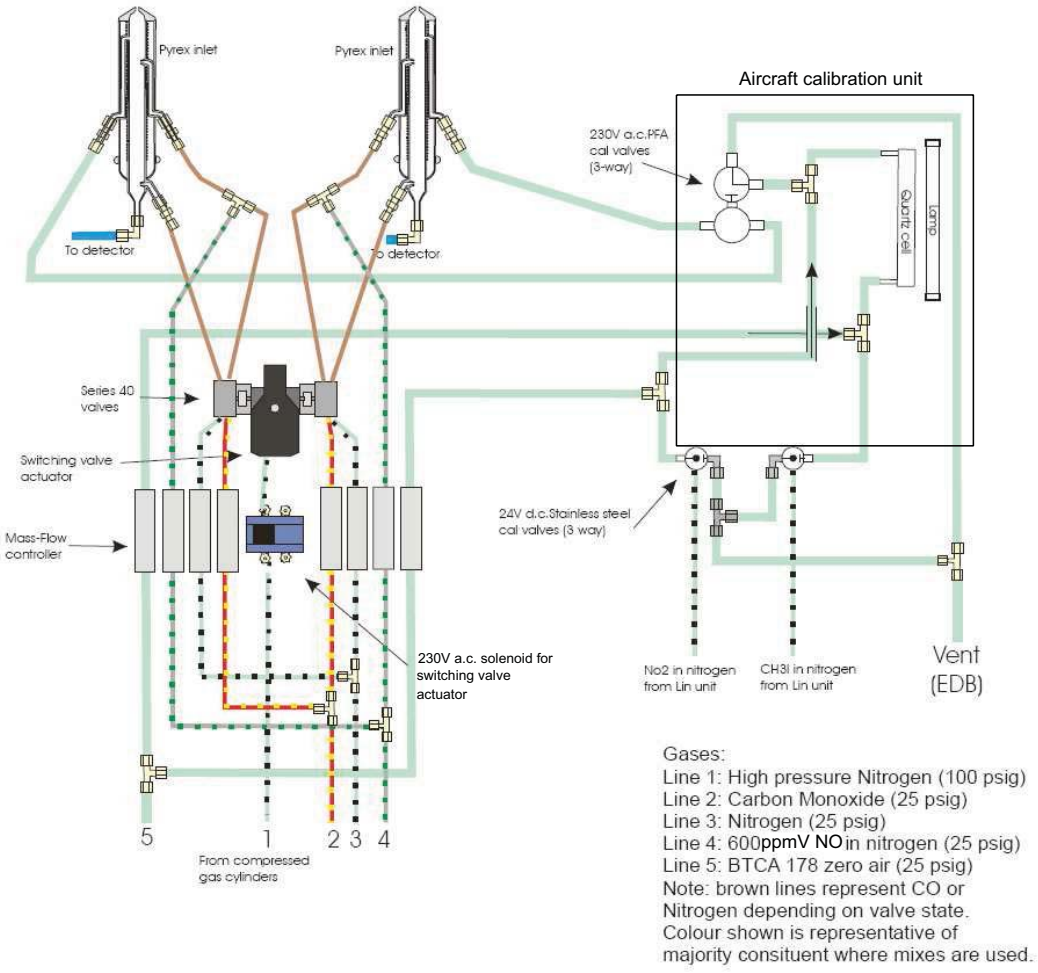

Figure 3.6: Diagram of PERCA 4 aircraft inlet systems plumbing from Brookes *et al.* (2006)

3.2.1 CH_3O_2 chain length calibration

To quantify the PERCA inlets chain length a source of radicals is required that produces known concentrations. A variety of techniques for the production of peroxy radicals have been used for calibration, for example, PAN thermal decomposition to give peroxy acetyl radicals (Hastie *et al.*, 1991), and the widely used photolysis of water vapour to produce equal amounts of OH and HO_2 of Schultz *et al.* (1995). Water vapour photolysis can be used to produce either HO_2 and OH, or

HO_2 alone by reaction of the OH with CO. Furthermore by reaction of OH with suitable VOC's it is possible to produce organic peroxy radicals. The water vapour photolysis technique is therefore a very useful calibration technique due to its potential for producing quantifiable amounts of a variety of radical species, and it has been widely deployed as a field calibration technique by the HO_x measurement community (Heard & Pilling, 2003). A simple field deployable calibration system has been used in this work based on the concept of Clemitshaw *et al.* (1997); that being the production of known concentrations of methyl peroxy radicals (CH_3O_2) by the photolysis of methyl iodide (CH_3I) in synthetic air (BOC BTCA178 zero grade air) using the 253.65 nm line in the Hg spectrum which lies close to the peak in the absorption cross section of methyl iodide at 258 nm. Radical calibration units are shown photographed in Figure 3.7, the plumbing of the calibration system for PERCA 4 is shown in Figure 3.6.

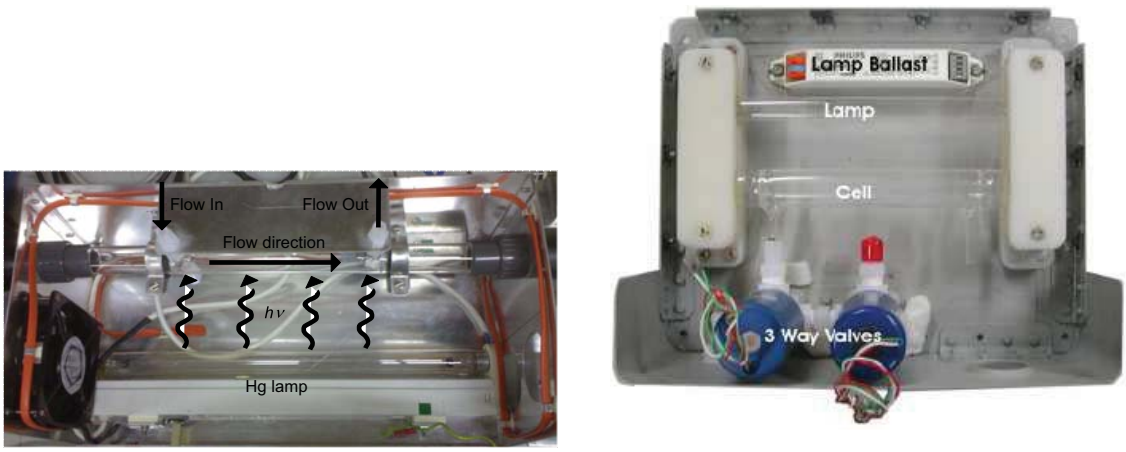

Figure 3.7: CH_3O_2 radical source units - Ground calibration unit (left); Aircraft calibration unit (right)

In application a calibrated permeation tube is used as the source of methyl iodide (p/n 100-007-4600-U40, VICI Metronics Inc.), with the dilution air flow determining the concentration input to the radical source unit (see Section 3.4.1). A quartz "photolysis cell" acts as a flow reactor and a Hg strip lamp (Philips TUV 15W G15T8, in the ground calibration unit; Sylvania Fluorescent Lamp, Osram

Sylvania Products Inc. in the aircraft calibration unit) provides the 253.65 nm UV radiation. The photolysis of CH_3I produces CH_3O_2 radicals through this mechanism:

$$CH_3I + h\nu \rightarrow CH_3 + I \tag{3.7}$$

$$CH_3 + O_2 + M \rightarrow CH_3O_2 + M \tag{3.8}$$

Since the photolysis rate of methyl iodide (j_{CH_3I}) is typically much slower than the combination of the methyl radical with O_2 ($j_{CH_3I} \ll k_{3.8}[O_2]$), the photolysis rate limits the production of methyl peroxy and the concentration produced by the source unit is given by:

$$[CH_3O_2] = j_{CH_3I}[CH_3I]t_{res} \tag{3.9}$$

To calculate the radical concentrations produced it is therefore necessary to know the photolysis rate of methyl iodide, the concentration of methyl iodide in the calibration mixture, and the residence time of the mixture within the photolysis cell, here defined as t_{res}. The total flow (F) through the photolysis cell along with the photolysis cell volume (V) determines the residence time:

$$t_{res} = \frac{V}{F} \tag{3.10}$$

The derivation of the photolysis rate of methyl iodide is discussed in Section 3.4, page 117. Clemitshaw *et al.* (1997) noted that Equation 3.9 neglects potential wall loss of CH_3O_2 within the quartz photolysis cell. Based on this work an average wall loss coefficient of 12.7 ($\pm 2\%$) s^{-1} is included in the calculation of the calibration CH_3O_2 concentration:

$$[CH_3O_2] = j_{CH_3I}[CH_3I]t_{res}\left(1 - \frac{0.127t_{res}}{2}\right) \tag{3.11}$$

An additional injector port designated the "Cal tube" in Figure 3.5 can deliver calibration mixtures (either CH_3O_2 or NO_2) to the front of each inlet in a remote user controlled manner in the aircraft system, when PERCA 4 is fitted to the BAe-146. The methyl iodide on a carrier flow of N_2 is directed to the photolysis cell through a 3-way valve (see Figure 3.6), prior to the cell this mixes into a MFC

controlled dilution flow of synthetic air (BOC BTCA178 zero grade air). The variation of the dilution flow (and residence time) is used to produce varying radical concentrations for calibration, typically flows of 3-5 slpm are used. A further valve directs the calibration mixture to the "Cal tube" on the chosen inlet. A similar remote controlled method is used for NO_2 sensitivity calibration in the aircraft and ground PERCA systems. Radicals can alternatively be supplied externally to the inlets from the ground calibration unit.

If the calibration mixture is delivered through the "Cal tube" injector and the sample flow is 2 slpm, with 3-5 slpm calibration flows a proportion of the calibration mixture then overflows the inlet. Several complications have to be considered in terms of delivering radicals from the aircraft calibration unit and delivery through the "Cal tube" injector: losses of CH_3O_2 between the radical source and the inlet (particularly on the valves of the aircraft calibration unit); the calibration mixture needs to be well mixed prior to sampling such that the proportion of the flow sampled is at the same concentration as that which overflows the inlet. If the calibration mixture is supplied externally from the ground calibration unit, then the system can be arranged such that the inlet samples the calibration mixture perpendicular to the flow and no overflow is needed, meaning mixing of the calibration mixture need not be considered. Furthermore, losses between the radical source unit can be minimised by use of short tubing to deliver the calibration flow to the inlet. For these reasons the ground calibration unit has been used to calibrate the chain lengths of all inlets employed in this work; this arrangement is shown in Figure 3.8. To reliably use the aircraft calibration unit for chain length calibration it needs to be cross calibrated against the ground calibration unit, such that losses are quantified.

There is an unknown contaminant species present in the synthetic air mixture which is also photolysed in the photolysis cell by the UV radiation produced by the Hg lamp. This produces a peroxy radical that is detected by the PERCA during chain length calibration along with CH_3O_2. To determine this "artefact" signal at each synthetic air flow, a period of measurements are performed without CH_3I

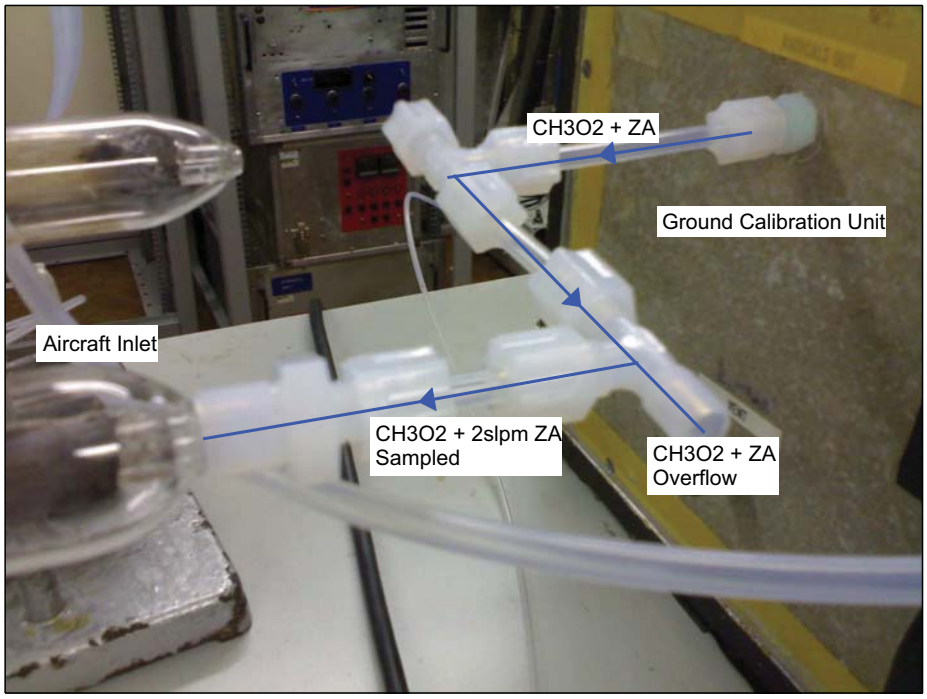

Figure 3.8: Chain length calibration setup: Photograph showing the arrangement of the ground calibration unit and delivery of the calibration flow to an aircraft inlet (ZA = Zero Air)

added to the calibration air flow and the UV lamp switched on. The artefact will add to the signal when CH_3I is present because CH_3O_2 is measured in addition to the artefact peroxy radical, so the chain length is quantified by subtraction of the artefact signal:

$$CL_{CH_3O_2} = \frac{\Delta[\mathrm{NO_2}]_{CH_3O_2+artefact} - \Delta[\mathrm{NO_2}]_{artefact}}{[\mathrm{CH_3O_2}]} \tag{3.12}$$

A typical sequence followed in a chain length calibration is shown in Figure 3.9, whereby concentrations are stepped through by varying the dilution flow and the artefact is measured at each flow. The NO_2 sensitivity is calibrated prior to and after the chain length calibration to allow conversion from raw signals to NO_2 concentration changes. The total NO_2 concentration change with ($\Delta[\mathrm{NO_2}]_{CH_3O_2+artefact}$) and without ($\Delta[\mathrm{NO_2}]_{artefact}$) CH_3I added to the calibration air flow is shown in the top trace of Figure 3.9, and is determined from the difference between the interpolated amplification averages (green trace) and background averages (black trace). The average of a period of artefact measurement is

then subtracted from the average of a period CH_3O_2 measurement at the same flow (and therefore CH_3O_2 concentration) to evaluate Equation 3.12. It is clear from the $\Delta[NO_2]$ trace that the PERCA response to a given concentration of radicals exhibits good precision. Deviations from a flat response in the trace occur where the background signal changes significantly compared to the modulation depth and rapidly (often occurring coincident to changing calibration flows); this happens due to inaccurate background subtraction in a single channel measurement (such as in the chain length calibration) since the background during an amplification cycle is determined from the average of the surrounding background measurement cycles.

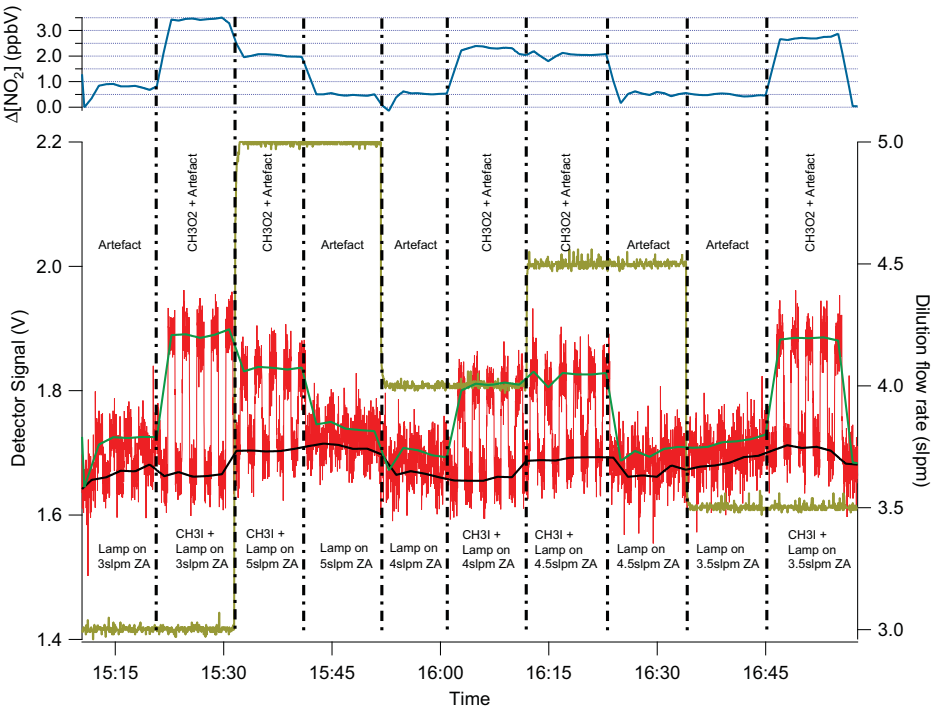

Figure 3.9: Timeseries of signals from the laboratory chain length calibration of the AMMA aircraft inlets using the ground radical source unit (refer to text for description)

3.2.2 Chain length altitude dependence

The kinetics of the chain chemistry employed in PERCA is temperature and pressure dependent owing to the temperature and pressure dependence of the rate constants of the reactions involved. For this

reason the chain lengths of the aircraft PERCA inlets are expected to exhibit an altitude dependence. The altitude dependence of the chain length has not been determined directly for the aircraft PERCA instrument employed in this work (PERCA 4) due to instrumental and operational issues associated with in flight calibrations. However Green *et al.* (2003) measured the altitude dependence for the precursor to the current instrument (PERCA III) and found the chain length varied "as a function of altitude in a reproducible manner, with no sudden degradations after sampling polluted air masses", which is demonstrated in Figure 3.10.

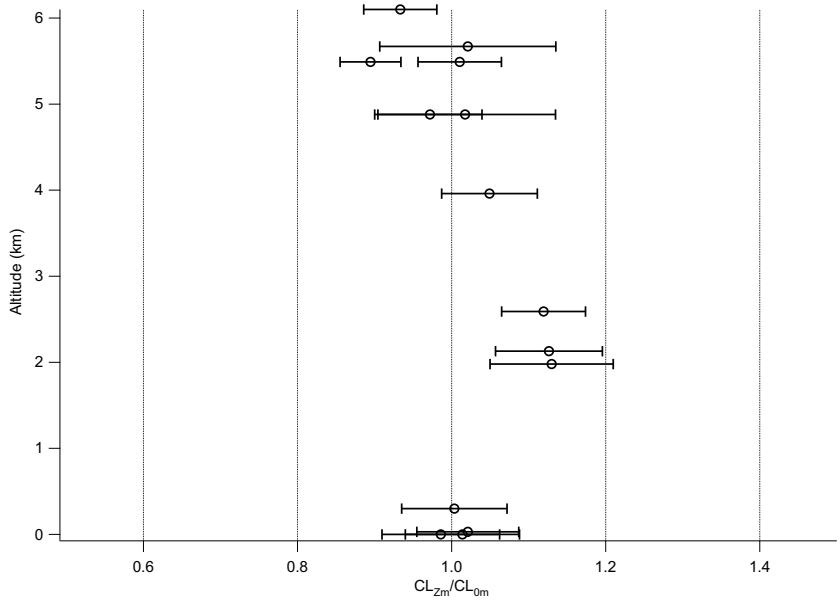

Figure 3.10: Chain length of PERCA III relative to ground level as a function of altitude from MAXOX flight A704 (Green *et al.*, 2003)

The variation of the PERCA III chain length relative to that determined at ground level shown in Figure 3.10 is approximately ±10% from 0-6 km altitude. This is minimal compared to the typical accuracy of the measurement i.e. ±40%, and provides some confidence that the chain length of PERCA 4 (at least with respect to CH_3O_2) is relatively invariant with respect to altitude, though it will likely exhibit some systematic bias. What is also clear is that the chain length of PERCA III was enhanced in flight at low altitudes with respect to the ground, and then degraded steadily with

increasing altitude. This was attributed by Green *et al.* (2003) as owing to improved reagent mixing, and can be seen to compensate effectively for the reduction in chain length predicted from earlier experimental and modelling studies (Jenkin *et al.*, 1999).

PERCA inlet chemistry model

The kinetics of the PERCA chain chemistry as a function of altitude has been further investigated in this work through an updated inlet chemistry reaction mechanism based on that of Hastie *et al.* (1991) and using the FACSIMILE numerical modelling package (Version 4.40.101, MCPA Software Ltd). The reaction mechanism is shown in Tables 3.3 and 3.4, the reaction rates were taken from the latest recommendations of Sander *et al.* (2006) and Atkinson *et al.* (2004, 2006), and temperature and pressure dependencies were calculated based on these recommendations. The mechanism is split between the two tables to highlight the basic steps in the chain reaction in Table 3.3, while additional reactions such as self-reactions, nitrate and nitrite formation, and reaction with ambient species such as ozone are included in Table 3.4.

Reaction	Number	Reference
$CH_3O_2 + NO \rightarrow CH_3O + NO_2$	1	Sander *et al.* (2006)
$CH_3O + O_2 \rightarrow HO_2 + HCHO$	2	Sander *et al.* (2006)
$HO_2 + NO \rightarrow OH + NO_2$	3	Sander *et al.* (2006)
$OH + CO \rightarrow H + CO_2$	4	Sander *et al.* (2006)
$OH + CO \rightarrow HOCO$	5	Sander *et al.* (2006)
$O_2 + HOCO \rightarrow HO_2 + CO_2$	6	Sander *et al.* (2006)
$H + O_2 \rightarrow HO_2$	7	Sander *et al.* (2006)
$OH + NO \rightarrow HONO$	8	Sander *et al.* (2006)
$OH \rightarrow walls$	9	variable
$HO_2 \rightarrow walls$	10	variable
$CH_3O_2 \rightarrow walls$	11	variable

Table 3.3: PERCA inlet chemistry basic chain reaction mechanism using updated reaction rate coefficients including basic conversion steps from CH_3O_2 to HO_2, and losses such as HONO formation and wall loss

Reaction	Number	Reference
$CH_3O_2 + NO \rightarrow CH_3ONO_2$	12	Sander *et al.* (2006)
$CH_3O + NO \rightarrow HCHO + HNO$	13	Sander *et al.* (2006)
$CH_3O + NO \rightarrow CH_3ONO$	14	Sander *et al.* (2006)
$CH_3 + O_2 \rightarrow CH_3O_2$	15	Sander *et al.* (2006)
$OH + HCHO \rightarrow H_2O + HCO$	16	Sander *et al.* (2006)
$HCO + O_2 \rightarrow HO_2 + CO$	17	Sander *et al.* (2006)
$OH + O_3 \rightarrow HO_2 + O_2$	18	Sander *et al.* (2006)
$OH + HNO_3 \rightarrow H_2O + NO_3$	19	Sander *et al.* (2006)
$OH + HONO \rightarrow H_2O + NO_2$	20	Sander *et al.* (2006)
$OH + HO_2NO_2 \rightarrow H_2O + NO_2 + O_2$	21	Sander *et al.* (2006)
$OH + NO_2 \rightarrow HNO_3$	22	Sander *et al.* (2006)
$OH + NO_2 \rightarrow HOONO$	23	Sander *et al.* (2006)
$OH + NO_3 \rightarrow HO_2 + NO_2$	24	Sander *et al.* (2006)
$OH + OH \rightarrow H_2O + O$	25	Sander *et al.* (2006)
$OH + OH \rightarrow H_2O_2$	26	Sander *et al.* (2006)
$OH + HO_2 \rightarrow H_2O + O_2$	27	Sander *et al.* (2006)
$OH + H_2O_2 \rightarrow H_2O + HO_2$	28	Sander *et al.* (2006)
$OH + CH_4 \rightarrow CH_3 + H_2O$	29	Sander *et al.* (2006)
$HO_2 + HO_2 \rightarrow H_2O_2 + O_2$	30	Sander *et al.* (2006)
$HO_2 + HO_2 \rightarrow H_2O_2 + O_2$	31	Sander *et al.* (2006)
$HO_2 + NO_2 \rightarrow HO_2NO_2$	32	Sander *et al.* (2006)
$HO_2 + NO_2 \rightarrow HONO + O_2$	33	Sander *et al.* (2006)
$HO_2 + O_3 \rightarrow OH + O_2 + O_2$	34	Sander *et al.* (2006)
$HO_2NO_2 \rightarrow HO_2 + NO_2$	35	Atkinson *et al.* (2004)
$CH_3O_2 + NO_2 \rightarrow CH_3O_2NO_2$	36	Sander *et al.* (2006)
$CH_3O_2 + CH_3O_2 \rightarrow CH_3O + CH_3O + O_2$	37	Sander *et al.* (2006)
$CH_3O_2 + CH_3O_2 \rightarrow CH_3OH + HCHO + O_2$	38	Sander *et al.* (2006)
$CH_3O_2 + CH_3O_2 \rightarrow CH_3OOCH_3 + O_2$	39	Sander *et al.* (2006)
$CH_3O_2NO_2 \rightarrow CH_3O_2 + NO_2$	40	Atkinson *et al.* (2006)
$NO + O_3 \rightarrow NO_2 + O_2$	41	Sander *et al.* (2006)
$NO_2 + O_3 \rightarrow NO_3 + O_2$	42	Sander *et al.* (2006)
$NO_3 + NO_2 \rightarrow N_2O_5$	43	Sander *et al.* (2006)
$NO_3 + NO_2 \rightarrow NO + NO_2 + O_2$	44	Sander *et al.* (2006)
$N_2O_5 \rightarrow NO_3 + NO_2$	45	Atkinson *et al.* (2004)

Table 3.4: PERCA inlet chemistry reaction mechanism – Additional reactions

The model was written to run for a matrix of initial reagent concentrations that cover the typical range used in PERCA (1-14.05 ppmV NO in 30 steps of 0.45 ppmV and 1-14.05% CO in 30 steps of 0.45%). Essentially this comprised the same model mechanism with 900 different initial conditions solved at each time step. In practice, due to the computational requirements this had to be split into 9 runs with 100 initial conditions. In this way it is possible to simultaneously observe the dependence of the chain length for the whole range in reagent conditions, and to distinguish the reagent concentrations that give the optimum chain length in detail in two dimensions (CO and NO). The model was run for a duration of 5 s and output saved every 0.1 s to allow the observation of the time evolution of the chain length. Initially the model was tested with rate coefficients calculated for T= 298 K and P= 101325 Pa, then to investigate the altitude dependence the temperature and pressure were varied according to the temperature and pressure altitude profile observed during AMMA (see Chapter 5), the various conditions are summarised in Table 3.5. Several model run types were investigated including a baseline model, an "ambient" model, and a sensitivity analysis. In the baseline model the model was started with only reagents (CO and NO) and either 50 pptV HO_2 or 50 pptV CH_3O_2 present; in the "ambient" model the model was started with the reagents, either 50 pptV HO_2 or 50 pptV CH_3O_2, and typical concentrations of ozone, water vapour and methane observed during AMMA; in the sensitivity analysis the model was run with the reagents plus each of the "ambient" species individually with either 50 pptV HO_2 or 50 pptV CH_3O_2 present. An additional sensitivity run included the reagents plus both 50 pptV HO_2 and 50 pptV CH_3O_2. Only the baseline model is considered in this work, though there is scope for further work and analysis of the model output from the other runs. In all model runs the wall loss rates of OH and HO_2 were fixed at 4.75 s^{-1} while the wall loss rate was set to 0 s^{-1} for CH_3O_2. The wall loss rates for OH and HO_2 were set following Hastie *et al.* (1991), Parker (2007) who assessed the sensitivity of the modelled chain length with respect to wall loss rate, and this value provides a reasonable absolute chain length value. The wall loss rates for CH_3O_2 was set to zero since this also provides a reasonable absolute chain length

value. Also the aim is to observe the relative dependence of the CH_3O_2 chain length compared to HO_2 owing to differences in the gas phase chemistry with altitude.

It is recognised that the model only evaluates the kinetics and therefore is not a true representation of the measurement situation since complete and instantaneous mixing of the reagents with the sample flow is assumed. The motivation for this work to is try to understand how the kinetics determines how the chain chemistry behaves under varying temperature and pressure, not to simulate the measurement situation exactly.

Altitude (m)	Temperature (K)	Pressure (Pa)
-	298	101325
0	303.42	101437
500	300.25	95871
1000	297.08	90572
2000	290.74	80725
4000	278.06	63711
8000	252.70	38254

Table 3.5: PERCA inlet chemistry model conditions used to investigate the altitude dependence of the chain length for HO_2 and CH_3O_2

Chain length dependence on the reagent concentration

The processed baseline model output for the T= 298 K, P= 101325 Pa run is shown in Figure 3.11. The top graph illustrates the dependence of the CH_3O_2 chain length on the reagents NO and CO, while the bottom graph illustrates the dependence of the HO_2 chain length on the reagents NO and CO, the colourscale and contours indicating the gradients in the chain length. The line plots beside each graph represent slices through the map of chain length, at right representing chain length as a function of CO at constant NO (3.25 ppmV) and at top representing chain length as a function of NO at constant CO (5.05%). There are clear similarities between the dependence for CH_3O_2 and HO_2, and also some clear differences. In terms of similarities both exhibit gradients in the chain length that

increase with increasing CO concentration, with the rate of change decreasing with increasing CO and NO. Both also exhibit an increase in chain length with increasing NO from low NO concentrations, a peak and then the chain length steadily decreases with further increases in NO. The position of the peak in chain length occurs at an NO concentration that depends on the CO concentration; the higher the CO concentration the higher the NO concentration at which the chain length peaks. The highest chain lengths occur along the peak.

For HO_2 this behaviour can be explained simply by the competition between chain propagating reactions (Reactions 3-7 in Table 3.3) and terminating reactions. At low CO concentrations the chain propagating reactions of CO with OH (Reactions 4 and 5 in Table 3.3) compete with the wall loss of HO_2 and OH (Reactions 9 and 10 in Table 3.3), and dependent on the NO concentration the reaction of OH with NO to form HONO (Reaction 8 in Table 3.3). This explains why at higher NO concentration the rate of increase in chain length with increasing CO is less. Since CO is not involved in any termination steps there is no turnover from positive to negative in the chain length gradient in the CO direction. At low NO concentrations the chain propagating reaction of HO_2 with NO (Reaction 3 in Table 3.3) competes with wall loss (Reaction 10 in Table 3.3) and potentially reaction of HO_2 with NO_2 and O_3 in polluted conditions (Reaction 32-34 in Table 3.3), so increasing the NO concentration increases the chain length initially. Since NO is involved in the loss of OH through HONO formation, further increasing the NO concentration increases the loss route and this explains the turnover from positive to negative in the chain length gradient in the NO direction.

For CH_3O_2 this behaviour is convolved with those reactions yielding HO_2 from CH_3O_2 (Reactions 1 and 2 in Table 3.3) and those competing reactions with CH_3O_2 and the intermediate CH_3O. To investigate this further, the modelled CH_3O_2 chain length relative to the modelled HO_2 chain length was examined by calculating the ratio of the model results in Figure 3.11, the result is shown in Figure 3.12. It is clear that the gradient is much stronger in the NO direction from the colour gradient, the

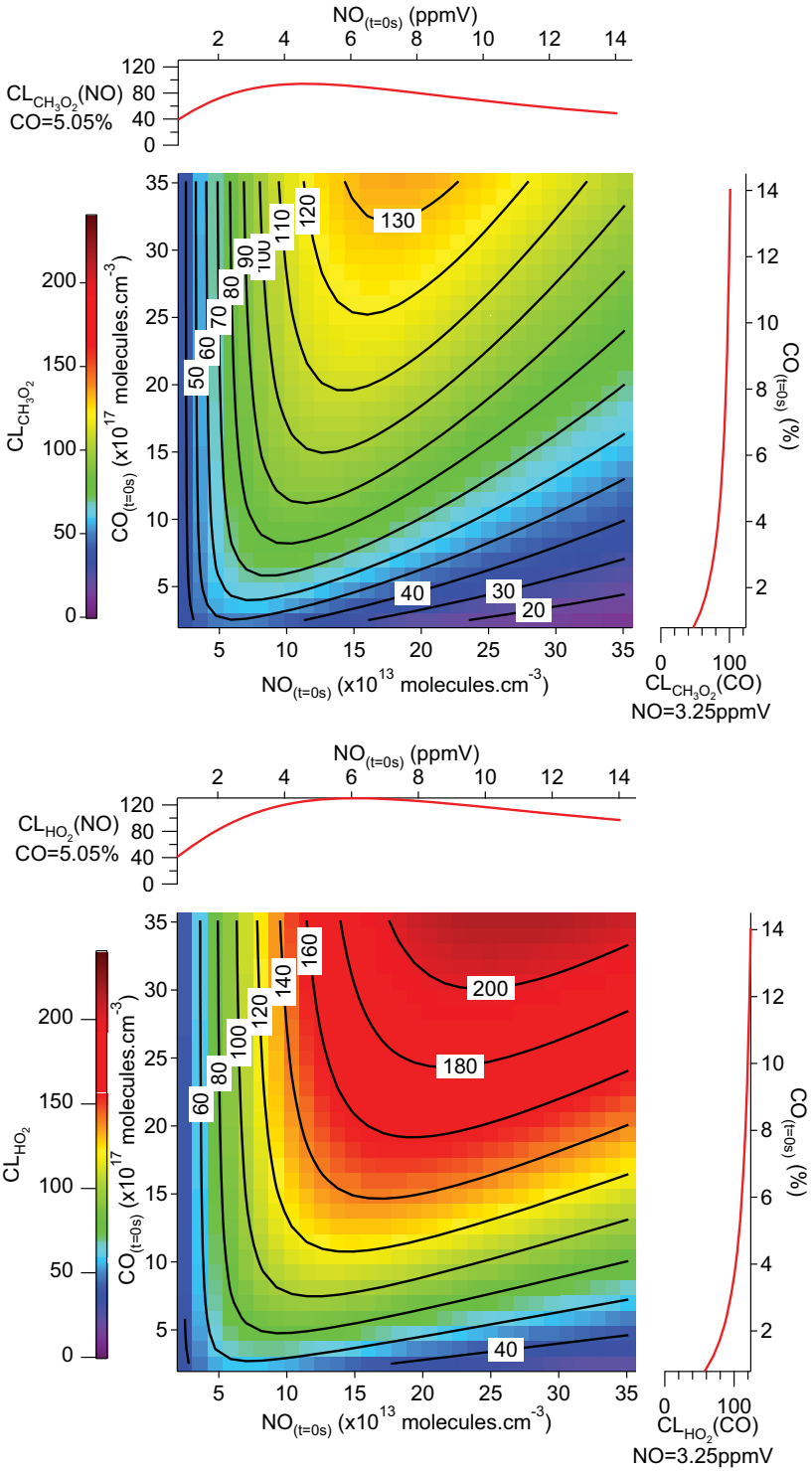

Figure 3.11: Inlet chain length model output for 298 K, 101325 Pa – (Top) Chain length as a function of reagent NO and CO concentration from model run initiated with 50 pptV CH_3O_2; (Bottom) Chain length as a function of reagent NO and CO concentration from model run initiated with 50 pptV HO_2

contours near parallel to the CO gradient, and the much stronger variation in the ratio in the line trace in the NO direction. The initial step in yielding HO_2 from CH_3O_2 (Reaction 1 in Table 3.3) has to compete with loss through methyl nitrate formation (Reaction 12 in Table 3.4). The branching ratio Γ_1 (given by Equation 2.26 on page 23) is independent of the concentration of NO. The second step to yield HO_2 from CH_3O_2 (Reaction 2 in Table 3.3) has to compete with loss through HNO, HCHO and methyl nitrite formation (Reactions 13 and 14 in Table 3.4). The branching ratio Γ_2 (given by Equation 2.27 on page 23) decreases with increasing NO concentration, hence the yield of HO_2 calculated by the model will drop with increasing NO concentration. The branching ratio Γ_2 explains the functional form of the gradient in the ratio of the modelled CH_3O_2 chain length relative to the modelled HO_2 chain length with increasing NO. The upper limit on the yield is dictated by the branching ratio for the initial step, while the dependence on NO is dictated by the branching ratio for the second step. The ratio compares well to the calculated yield of HO_2 from CH_3O_2 (refer to Table 2.1, on page 25) at 3 ppmV NO calculated by Cantrell (1993).

From this analysis it is clear that more optimal chain lengths are potentially achievable than those possible with the reagent concentrations employed in this work (5% CO and 3ppmV NO) which were based on the setup and recommendations of Parker (2007). This model study followed the experimental and field work in this thesis and was motivated to understand the dependence of the chain length on altitude for PERCA 4. It is not sufficient as per previous workers (e.g. Cantrell (1993), Clemitshaw *et al.* (1997), Parker (2007)) to only vary NO or CO at one CO or one NO concentration to determine the peak chain length conditions. The recommendation derived from this work is that concentrations up to the maximum safe concentration of CO should be used (typically 10% - well below the lower explosion limit of 12.5% in air) to maximise the chain length and the NO concentration varied to locate the peak in chain length. The chain length should also be determined as a function of NO at a number of CO concentrations below 10% to map out the form of the chain

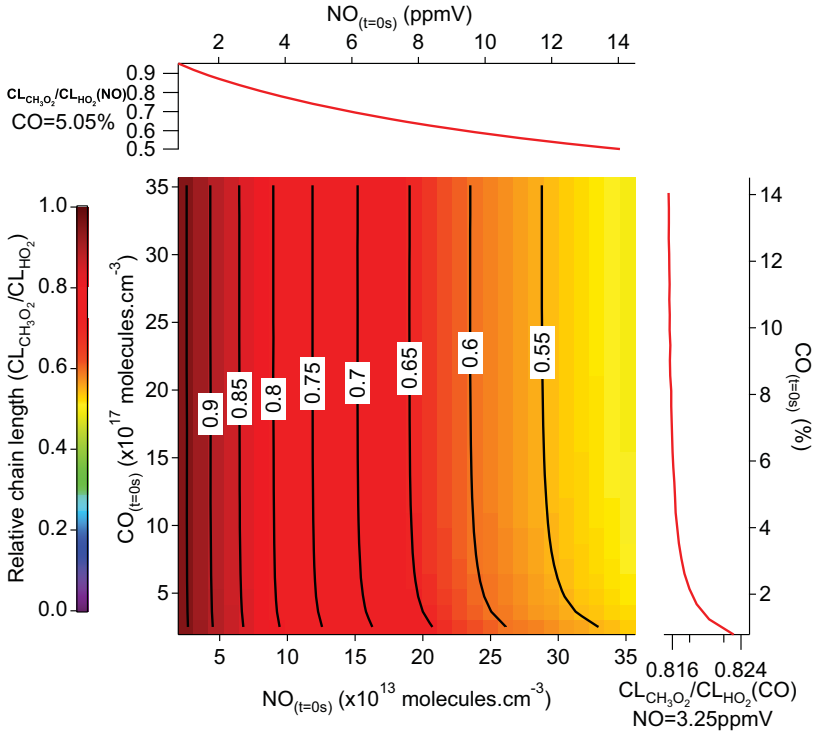

Figure 3.12: Modelled CH_3O_2 chain length relative to modelled HO_2 chain length as a function of reagent NO and CO concentration

length in both dimensions to attempt to reproduce experimentally the relationship derived here from an idealised model. The difference in the position of the peak in chain for HO_2 and CH_3O_2 could be exploited to allow discrimination between HO_x and RO_2 as in the PerCIMS technique (see Section 2.1.1, Chapter 2).

Time scale dependence of the chain reaction on altitude and reagent concentration

One concern in terms of the altitude performance of the PERCA 4 instrument is that sufficient time is available for the chain chemistry to complete within the inlet during "chain amplification mode", and particularly that in the "background measurement mode" the radical population is terminated effectively before reaching the rear injector port (Jenkin *et al.*, 1999). To assess the timescale of the chain chemistry, timeseries of chain length were derived from the matrices of reactants at each model time step as a function of altitude and reagent NO and CO concentrations. A selection of the results are shown for CH_3O_2 and HO_2 in Figures 3.13 and 3.14. The timescale for the chain chemistry is dictated by the efficiency of the chain chemistry which in turn is dictated by the competition between conversion, propagation and termination routes.

For CH_3O_2 and HO_2 the time profiles of the chain length are both relatively insensitive to the altitude for a given NO concentration, while the chain length achievable is reduced with increasing altitude (see Figure 3.13). The timescale (and chain length) varies most strongly by NO concentration; with increasing NO concentrations the timescale is progressively reduced though the chain length rises and falls. This suggests that effectively the timescale is being limited by the gas phase termination routes in the conversion of CH_3O_2 to HO_2 (Reactions 12-14 in Table 3.4), and once converted both gas phase and wall loss of HO_2 and OH (Reactions 4 and 5 in Table 3.3). The timescales for completion of the chain reaction are similar as a function of NO concentration for both CH_3O_2 to HO_2 due to the rapid conversion of CH_3O_2.

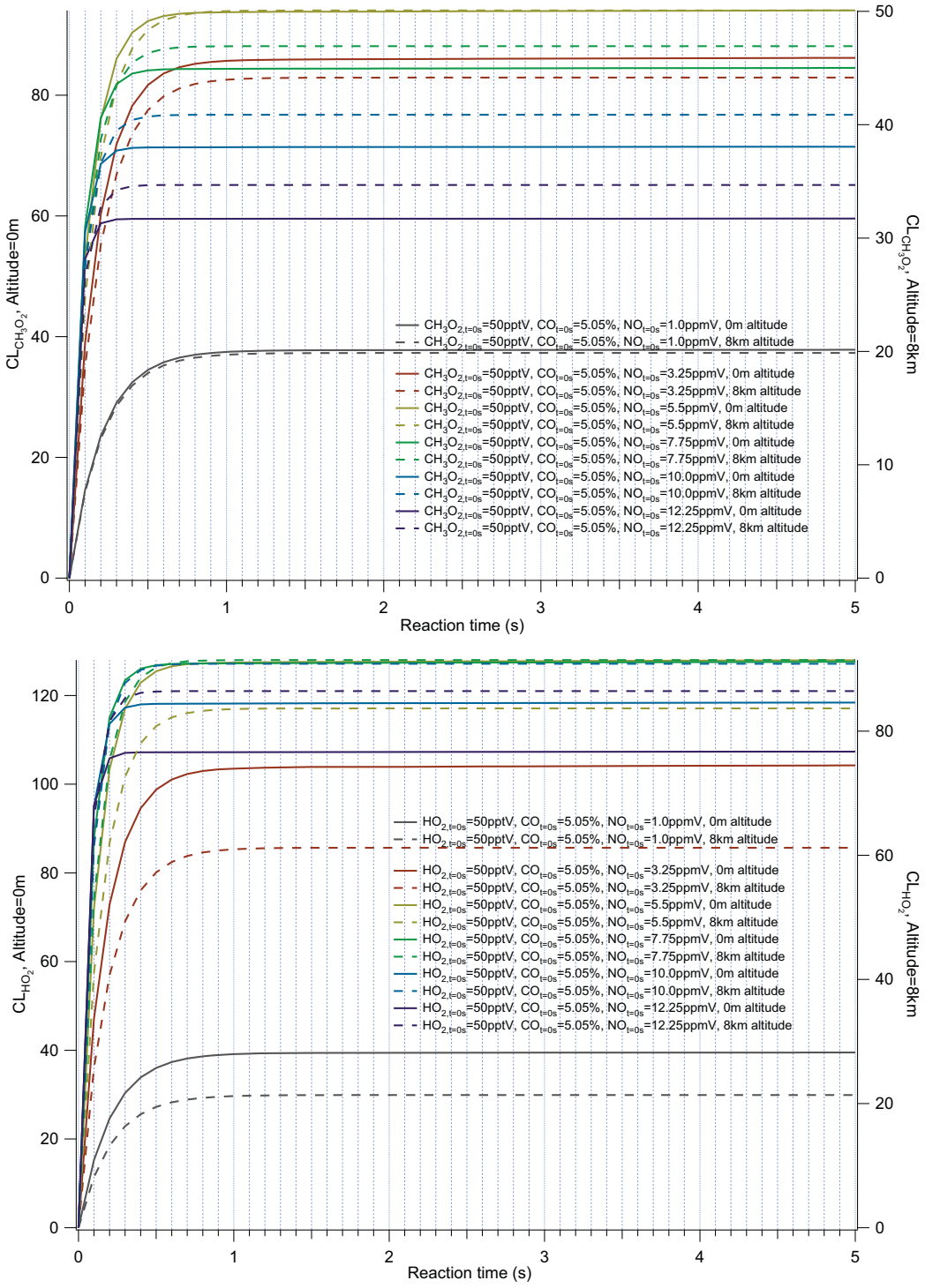

Figure 3.13: Time evolution of chain length at 0 km and 8 km – (Top) Model runs initiated with 50 pptV CH_3O_2, 5.05% CO, varied NO; (Bottom) Model runs initiated with 50 pptV HO_2, 5.05% CO, varied NO

Since there are no termination steps involving CO, the timescale for chain length completion is only dependent on CO concentration through competition of the chain propagating reactions involving CO (Reactions 4 and 5 in Table 3.3) with the wall loss of HO_2 and OH (Reactions 9 and 10 in Table 3.3), and dependent on the NO concentration the reaction of OH with NO to form HONO (Reaction 8 in Table 3.3). The timescale increases for increasing CO concentration but plateaus once the propagation steps dominate (see Figure 3.14). Since this dependence is only impacting the chemistry after conversion of CH_3O_2 to HO_2 the variation in timescale is indistinguishable for CH_3O_2 and HO_2 though the absolute chain lengths are different. As with NO, for CH_3O_2 and HO_2 the time profiles of the chain length are both relatively insensitive to the altitude for a given CO concentration, while the chain length achievable is reduced with increasing altitude.

Given the results of the modelling, the timescale for completion of the chain chemistry (and in "background measurement mode" where only termination reactions act this will be shorter still) is of the order 0.5 s up to 8 km altitude for typical reagent concentrations of 5.05% CO and 3.25 ppmV NO. From a simple consideration of the change in volume flow rate with temperature and pressure at the sample mass flow rate of 2 slpm (see Appendix B, Equation B.10), and knowledge of the inlet volume, the residence time within the inlet only exceeds 0.5 s at an altitude of approximately 5km (based on the AMMA pressure and temperature altitude profile). This is currently beyond the altitude range of the PERCA 4 instrument, which fails to control the sample flow above approximately 4 km altitude.

Comparison of model to measured altitude dependence of the chain length

To assess the change in chain length with altitude the model output at each altitude (500 m, 1 km, 2 km, 4 km, 8 km) is divided by that at ground level (0 m run) such that the chain length relative to that at ground level may be examined. The model output calculated for the whole range in NO and CO is shown in Figures 3.15 (for HO_2) and 3.16 (for CH_3O_2). The general shape of the chain length

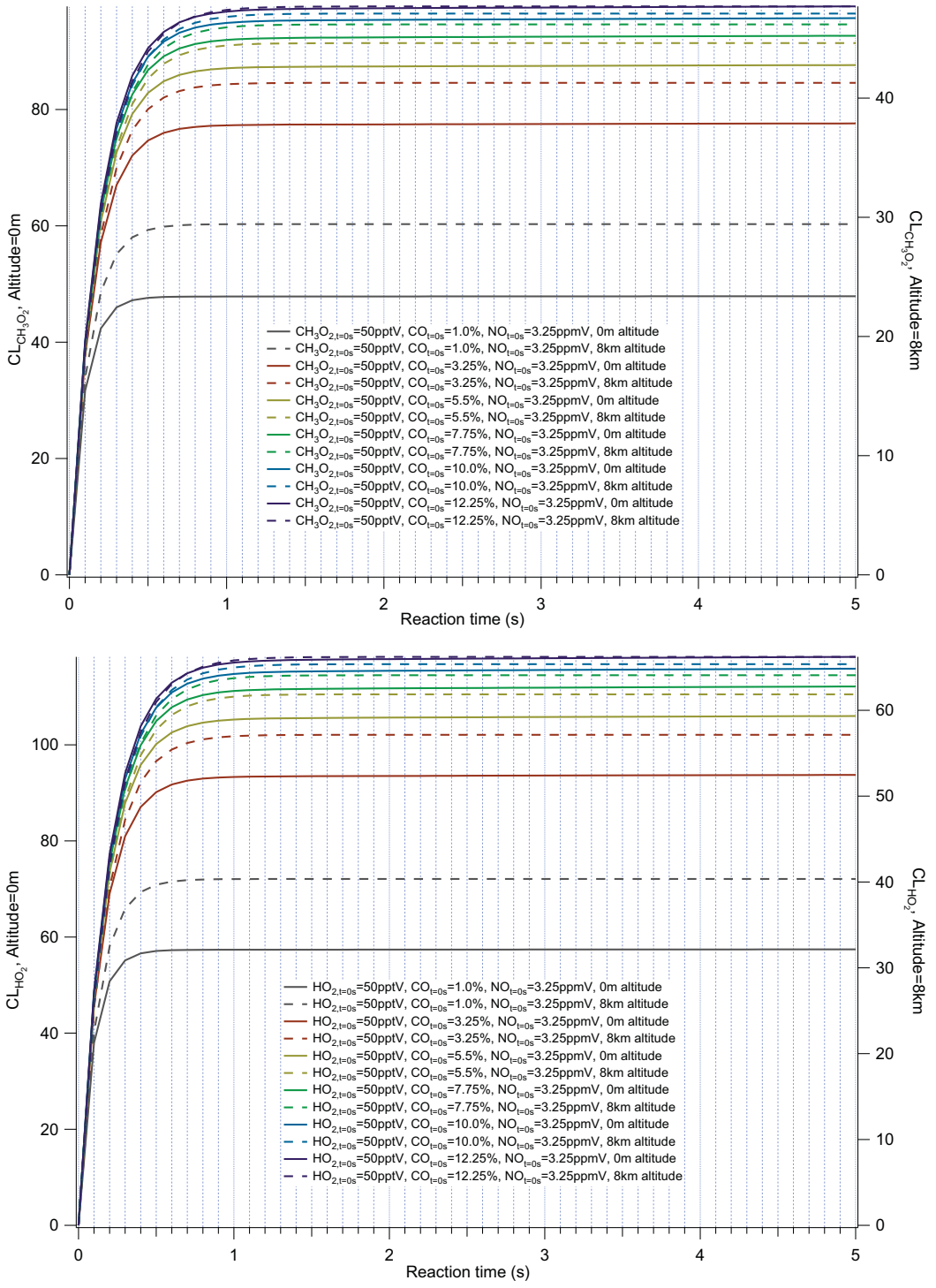

Figure 3.14: Time evolution of chain length at 0 km and 8 km – (Top) Model runs initiated with 50 pptV CH_3O_2, 3.25 ppmV NO, varied CO; (Bottom) Model runs initiated with 50 pptV HO_2, 3.25 ppmV NO, varied CO

relative to that at ground level is similar for all altitudes for both HO_2 and CH_3O_2, though the shape is different for HO_2 and CH_3O_2; this is due to the additional steps in yielding HO_2 from CH_3O_2. At all altitudes the gradient is relatively flat as a function of NO and CO for CH_3O_2 though it becomes steeper from one reagent mixture to the next with altitude; this is also true for HO_2 though it becomes much steeper from one reagent mixture to the next with altitude particularly in the NO direction.

For HO_2 the change in chain length with altitude is much less at high reagent NO concentration (such that the HO_2 chain length may be expected to be relatively invariant with altitude for a high reagent NO concentration) due to the termolecular loss route for HONO formation (Reaction 8 in Table 3.3) which is reduced with increasing altitude (decreasing pressure). The termolecular nature of the propagation reactions between OH and CO (Reactions 4 and 5 in Table 3.3) mean the OH to HO_2 propagation step is reduced with increasing altitude; from Figure 3.15 it is clear that this is significant at low CO and high NO concentrations.

For CH_3O_2 the relationship is a combination of the relationship seen in Figure 3.12 between the CH_3O_2 and HO_2 chain length and the change in HO_2 chain length with altitude seen in Figure 3.15. At low NO concentration the CH_3O_2 chain length is less sensitive to changes in altitude owing to a better yield of HO_2 from the conversion reactions (which are inhibited at higher NO concentrations). At higher NO the chain length is less sensitive to changes in altitude because the HO_2 chain length is maintained, due to the reduction with increasing altitude of the termolecular loss route through HONO formation (Reaction 8 in Table 3.3). A turnover occurs between these regimes.

The model output can now be compared directly to the chain length altitude dependence determined from Green *et al.* (2003) shown in Figure 3.10. The model output has been extracted at 5.05% CO, 3.25 ppmV NO, comparable to typical reagent concentrations employed in this work, and 6.85% CO, 3.25 ppmV NO, comparable to the reagent concentrations quoted in Green *et al.* (2003) (7% CO, 3.0 ppmV NO). The comparison is shown in Figure 3.17. There is very little difference between the

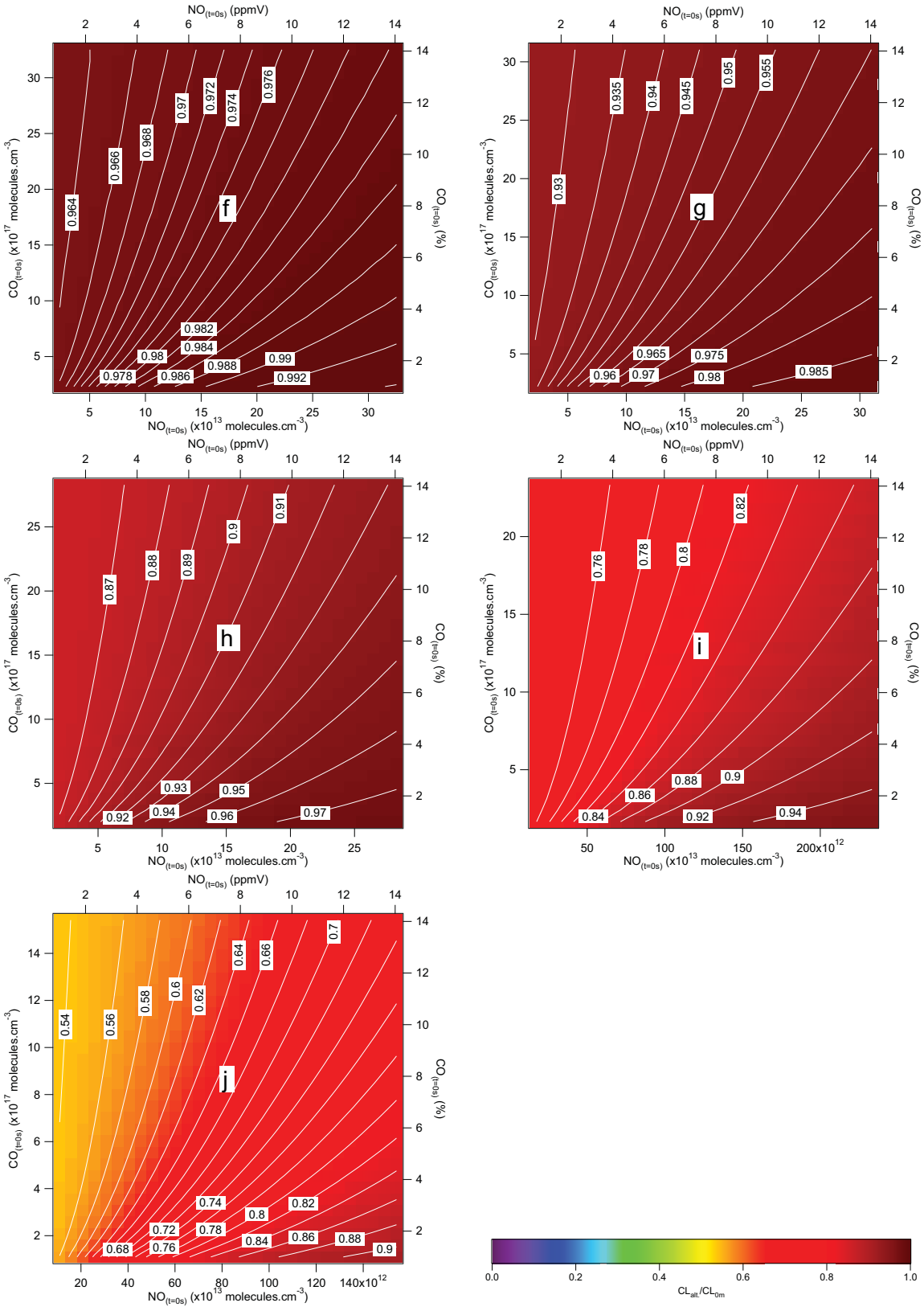

Figure 3.15: HO_2 chain length as a function of reagent NO and CO concentration relative to ground level at (f) 500m, (g) 1km, (h) 2km, (i) 4km, (j) 8km

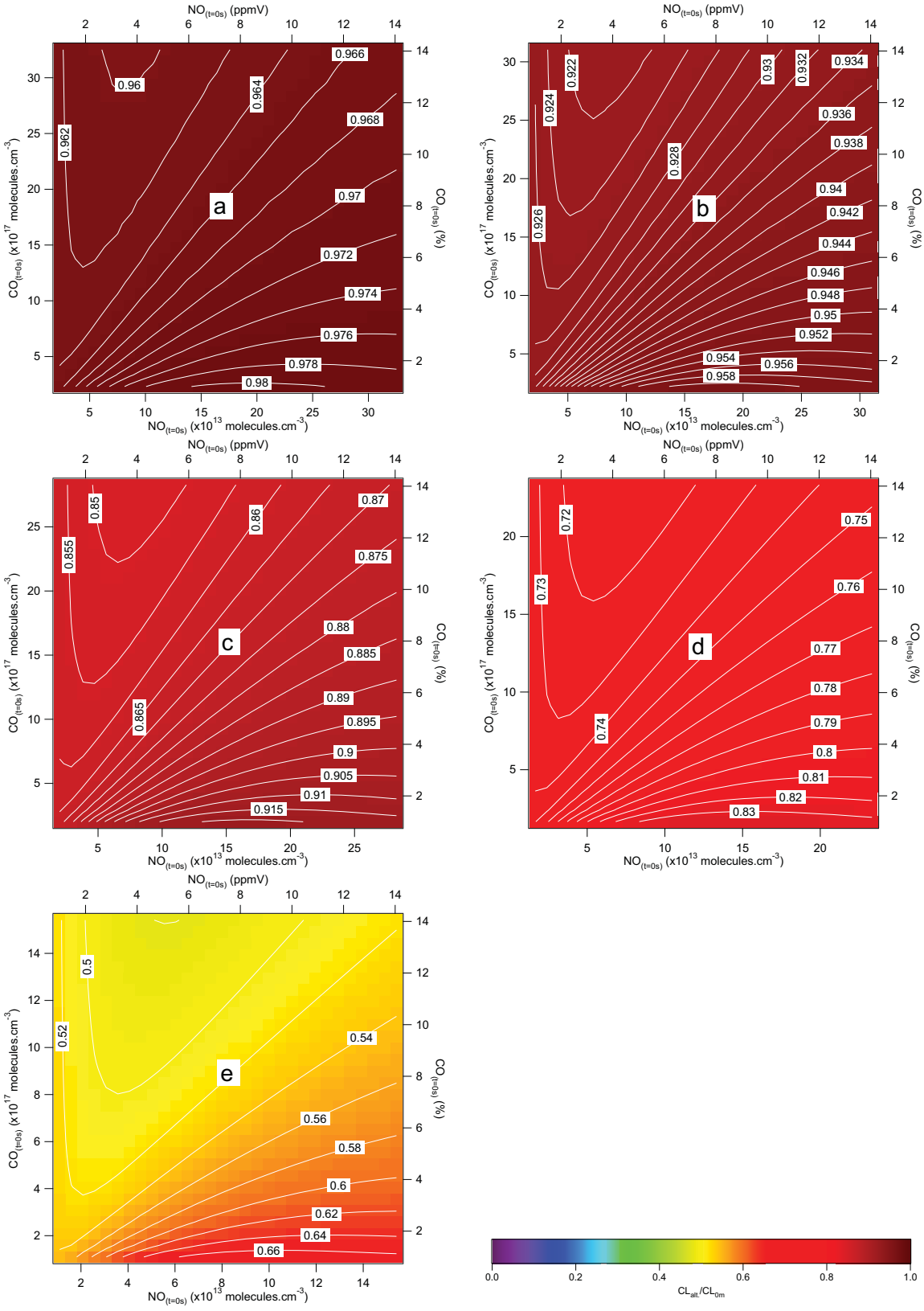

Figure 3.16: CH_3O_2 chain length as a function of reagent NO and CO concentration relative to ground level at (a) 500 m, (b) 1 km, (c) 2 km, (d) 4 km, (e) 8 km

modelled CH_3O_2 chain length altitude profiles at the different reagent mixtures, as expected from the flat gradient in Figure 3.16. Likewise, there is very little difference between the modelled HO_2 chain length altitude profiles at the different reagent mixtures. As already discussed, the measured chain length is enhanced in flight and this is attributed to enhanced mixing of the reagents (Green *et al.*, 2003). To compare the measured altitude trend more directly with the modelled trend for the CH_3O_2 chain length, the measured trend has been offset by 30% in the graph. It is significant that the altitude trend exhibited in the modelled chain length agrees so well with that measured by Green *et al.* (2003) (once offset). It indicates that the model setup (low CH_3O_2 wall loss relative to HO_2, wall loss invariant with altitude) is reasonable for predicting the relative change in chain length with altitude. This suggests a reduction in the chain length for CH_3O_2 of approximately 27% up to 4 km altitude (the ceiling on the aircraft measurements in this work), and for HO_2 of approximately 23% up to 4 km altitude, while this may be positively offset by enhanced reagent mixing in flight. The chain length altitude dependence determined from Green *et al.* (2003) suggests two further conclusions: (1) Chain lengths determined under stable conditions on the ground may lead to underestimation of the inflight chain length, and therefore an over estimation of the radical concentration; (2) Insufficient mixing of the reagents in a ground measurement situation limits the chain lengths achievable.

3.2.3 Chain length humidity interference

The interference of humidity with the PERCA chain length has been introduced in Chapter 2 (see Section 2.1.1, page 29). The interference was first reported in Mihele & Hastie (1998), Mihele *et al.* (1999), and its identification has led to the need for all groups using chain amplification techniques for the measurement of peroxy radicals to consider its influence on their measurements, and if possible correct for it. In chain length calibration, the calibration mixture sampled is completely dry and therefore the chain lengths determined are appropriate for dry conditions. In sampling ambient humid air the real chain length is reduced and therefore it is necessary to know how the chain length changes

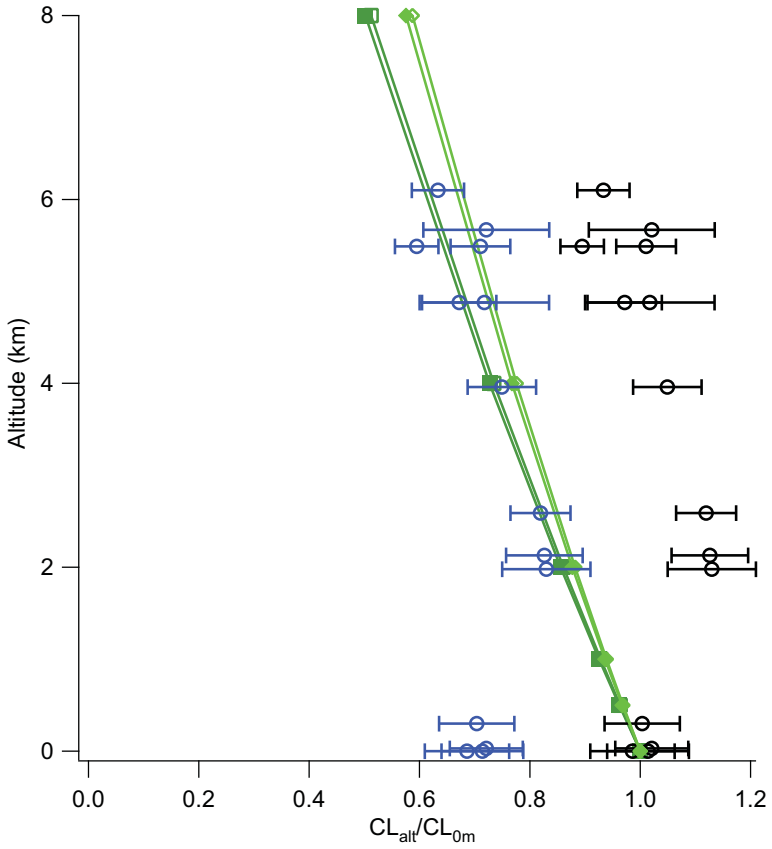

Figure 3.17: Comparison of modelled CL altitude dependence to PERCA III CL altitude dependence – (Black open circles) Chain length of PERCA III relative to ground level as a function of altitude from MAXOX flight A704 (Green *et al.*, 2003); (Blue open circles) Chain length of PERCA III relative to ground level as a function of altitude, offset by 30%; (Dark green open squares) Modelled CH_3O_2 chain length relative to ground level (0 m run) for reagent mixture 3.25 ppmV NO, 6.85% CO; (Dark green filled squares) Modelled CH_3O_2 chain length relative to ground level (0 m run) for reagent mixture 3.25 ppmV NO, 5.05% CO; (Light green open diamonds) Modelled HO_2 chain length relative to ground level (0 m run) for reagent mixture 3.25 ppmV NO, 6.85% CO; (Light green filled diamonds) Modelled HO_2 chain length relative to ground level (0 m run) for reagent mixture 3.25 ppmV NO, 5.05% CO.

relative to the value obtained in dry air to correctly determine radical concentrations. The method of correction is then to scale the radical concentration derived with the dry chain length (CL) by a correction factor (CF_{CL}), which is defined by:

$$CF_{CL} = \frac{CL_{dry}}{CL_{wet}} \tag{3.13}$$

The humidity corrected radical concentration ($[RO_x]_{HC}$) is then given by:

$$[\mathrm{RO}_x]_{HC} = \frac{\Delta\,[\mathrm{NO}_2]}{CL_{dry}} \times CF_{CL} \tag{3.14}$$

$$[\mathrm{RO}_x]_{HC} = [\mathrm{RO}_x] \times CF_{CL} \tag{3.15}$$

Subsequently, the chain length humidity dependence was investigated for the precursor to the current University of Leicester PERCA instruments in the experiments detailed in Salisbury (2001) and the correction later published in Salisbury *et al.* (2002). The correction derived has been applied by co-workers in deployments of the University of Leicester instruments following this (e.g. Fleming *et al.* (2006), Green *et al.* (2006), Parker (2007), Parker *et al.* (2009)); the functional form of the correction factor (CF_{CL}) is given by:

$$CF_{CL} = \frac{100}{(0.17T - 57.08) \times Q + 100} \tag{3.16}$$

The ratio of wet to dry chain lengths (the denominator of Equation 3.16) was expressed as a percentage (hence the factors of 100). Q is the specific humidity (the ratio of the mass of water vapour to the mass of dry air in g kg^{-1}), and T is the inlet temperature in ^{o}C according to Salisbury *et al.* (2002), though in fact this was the measured temperature of the sample airflow within the inlet according to Salisbury (2001). It may be reasonable to assume these are equivalent at ground level, assuming heating the inlet walls effectively heats the sample airflow also. A design feature of the University of Leicester PERCA inlets is highlighted by this – the inlets of both PERCA 3.5 and 4 are typically controlled at a temperature above ambient, with the purpose to reduce the impact of ambient humidity on the chain length.

Salisbury (2001) investigated the dependence of the chain length for a range of Q=0-12 g kg^{-1} in specific humidity and T_{inlet}=10-50 ^{o}C in temperature. In recent field campaigns (AMMA, TEXAQS, OOMPH) involving the University of Leicester PERCA instruments, the high levels of ambient humidity encountered have highlighted issues with the current correction. An example of the levels of humidity encountered is illustrated by the AMMA altitude profiles of specific and relative humidity (RH) in Figure 3.18 – 12 g kg^{-1} is near the minimum humidity encountered at ground level and often exceeded up to an altitude of around 2 km.

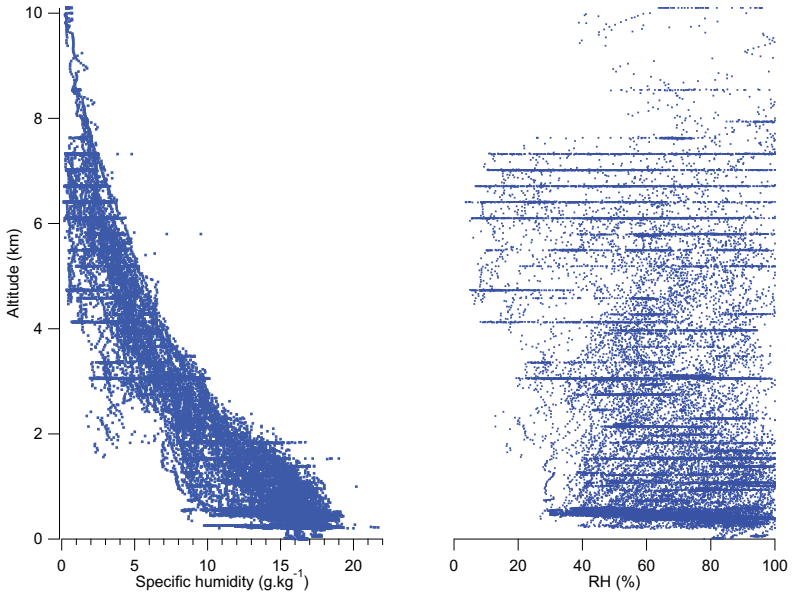

Figure 3.18: AMMA humidity altitude profile – (Left) Specific humidity (g kg^{-1}); (Right) Relative humidity (%)

To apply the Salisbury (2001) correction factor it would be necessary to extrapolate to beyond the limits of the range of specific humidity investigated. Figure 3.19 illustrates the significant non-linearity in extrapolating the correction beyond this range for an example with the inlet (air) temperature at 30^{o}C (typical setup). The correction is discontinuous at a temperature and specific humidity where the denominator of Equation 3.16 tends to zero. All other groups (e.g. Mihele *et al.* (1999), Reichert *et al.* (2003), Sadanaga *et al.* (2004)) have defined humidity corrections in terms of RH and

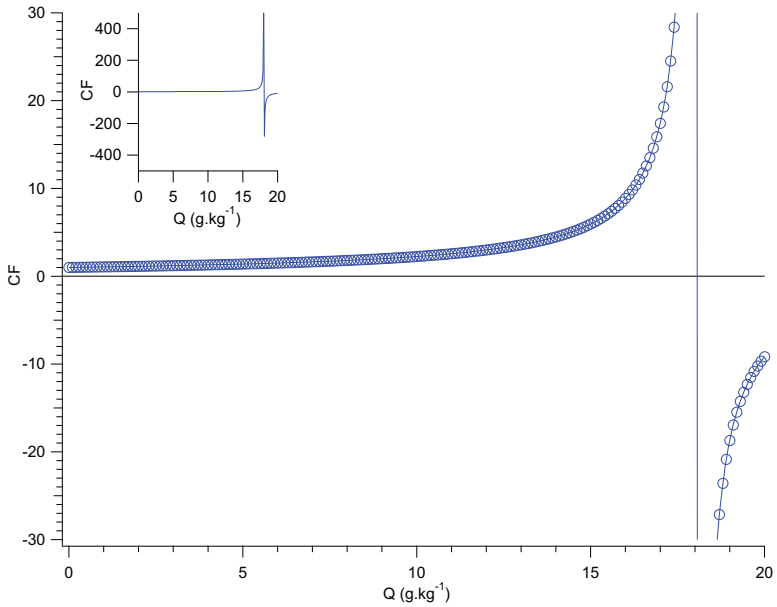

Figure 3.19: Salisbury (2001) chain length humidity correction factor at $T = 30^{o}$C – (Full scale) Graph zoomed in on correction factor between ±30; (Inset) Graph of correction factor over full range calculated

found that the wet chain length dropped non-linearly relative to the dry chain length with increasing *RH*. Reichert *et al.* (2003) confirmed the relationship was constant as a function of *RH* (and therefore independent of air temperature) by comparing the change as a function of *RH* at 20^{o}C and 30^{o}C. In contrast Salisbury (2001), Salisbury *et al.* (2002) could not detect non-linearity in the change in chain length as a function of specific humidity ($CL_{wet}/CL_{dry}(\%) = m \times Q + 100\%$), though the gradient of the relationship was found to decrease with increasing inlet (airflow) temperature ($m = 0.17T - 57.08$).

Mihele & Hastie (1998) suggest three potential components of the chain length humidity dependence: (1) Increased rate of radical loss to the walls; (2) Increased rate of gas phase termination reactions; (3) Decreased rate of gas phase propagation steps. To investigate this (Mihele & Hastie, 1998) ran experiments with HO_2 radicals and different reactor geometries and material compositions (two Teflon, one glass). Enhanced HO_2 wall loss with increased *RH* was stated, but there was no significant difference between the different reactors. Further, on heating the glass reactor walls to 60^{o}C (which

raised the air temperature within the reactor to 37^{o}C, and otherwise experiments were at room temperature of 21^{o}C) a reduction of the chain length dependence with increased absolute humidity was observed. This presentation (versus absolute humidity) is misleading since if the dependence is related to *RH*, the difference for an increased air temperature may only be a result of the reduction of the *RH* within the inlet (compared to the ambient level) as the saturation vapour pressure is increased with increasing temperature (see Equation 3.21). In a first attempt to determine whether the dependence was attributed to enhanced wall loss alone, experiments were run at an enhanced reagent NO concentration (12 ppmV) to push the chain chemistry into a regime dominated by gas phase termination reactions. Although a reduction in the dependence of the chain length with *RH* was observed it was not as strong as expected, suggesting that gas phase chemistry is then also affected.

Mihele *et al.* (1999) measured wall loss rates within a Teflon reactor for HO_2, CH_3O_2 and $C_2H_5O_2$. Identical, low wall loss rates for CH_3O_2 and $C_2H_5O_2$ of 0.8 s^{-1} were observed, with no dependence on humidity. A higher wall loss rate for HO_2 of 2.8 s^{-1} was observed which increased significantly as a function of *RH* confirming a significant wall loss component to the dependence. A model including the known humidity dependence of the self reaction of HO_2, the formation of HO_2 radical water adducts and the measured wall loss dependence did predict most of the decrease in chain length with increased relative humidity but not all, again suggesting some gas phase component to the interference (Mihele *et al.*, 1999). The reduced humidity dependence with increased NO concentration was shown to be underpredicted through the same model, and therefore a possible gas phase component was proposed:

$$HO_2 + NO + H_2O \rightarrow HONO_2 + H_2O \tag{3.17}$$

Or,

$$HO_2 + NO + H_2O \rightarrow HOONO + H_2O \tag{3.18}$$

The confirmed increase in the rate of HO_2 wall loss is significant since the Salisbury (2001), Salis-

bury *et al.* (2002) correction has been applied in this group for a variety of inlet types with varying geometry and therefore wall loss characteristics.

Reichert *et al.* (2003) recognised a wall loss component existed in the chain length humidity dependence and tried through detailed experimental (calibrations with HO_2) and modelling studies to identify a gas phase component. The linearity of chain length calibrations at high humidity as a function of HO_2 in the range 10-200 pptV, ruled out enhanced HO_x self reactions. No significant change in chain length at high humidity was observed with NO_2 concentrations up to 60 ppbV, ruling out reactions involving NO_2. Increasing the length of the reactor (and therefore the residence time) and increasing the temperature after the reactor to 80^oC yielded no change in the chain length in the range 2-90% *RH* at an inlet temperature of 20^oC, ruling out the formation of thermally unstable radical reservoir species. From their analysis two reactions were found to offer a potential explanation for the gas phase component through interference with the chain propagating reactions:

$$HO_2 + NO \overset{nH_2O}{\rightarrow} HNO_3 + nH_2O \tag{3.19}$$

$$HO_2 + CO \overset{nH_2O}{\rightarrow} OH + CO_2 + nH_2O \tag{3.20}$$

The dependence of the chain length on *RH* rather than absolute humidity was proposed to be due to the involvement of water dimers (Reichert *et al.*, 2003). Recent experimental and theoretical work by Butkovskaya *et al.* (2009) has provided clear evidence for the enhancement of the reaction between HO_2 and NO yielding nitric acid. Butkovskaya *et al.* (2009) reports that the enhanced loss of HO_2 is sufficient to account for the additional reduction in chain length observed by Mihele *et al.* (1999) that could not be explained by the increased wall loss rate for HO_2.

Experimental setup

To investigate the chain length dependence for the University of Leicester PERCA instrumentation an experiment was designed to extend the range in humidity (specific humidity). Particularly the aim

was to characterise the aircraft and ground PERCA inlets for levels of humidity comparable to those observed in the tropics. The experimental setup is shown both photographed and schematically in Figure 3.20.

The experimental setup employed a General Eastern Hygro M4 Dew Point Monitor with 1311DR Optical Dewpoint Sensor for the measurement of the humidity (through the dewpoint temperature, T_d) within the calibration air flow. This measurement was logged at 1 Hz with a National Instruments USB-6008 12 bit datalogger connected to a separate laptop computer. This laptop computer was also used to configure the dewpoint sensor connected via a RS-232C connector. The output of the dewpoint sensor is an analogue voltage in the range 0-5 V, which scales linearly to a temperature range configured as -60 to $+40^{o}$C. To allow accurate combination of the humidity data with the PERCA measurements, the laptop time was synchronised to the PERCA 4 computer prior to each experiment. The humid airflow was generated from a supply of synthetic air (BOC BTCA178 zero grade air) by a Kintek 491-M humidifier unit, which can produce varied levels of humidity by mixing a saturated airflow with a dry diluent flow, the flows controlled by mass flow controllers within the humidifier unit. All gas and sample lines were insulated and held at a constant temperature of 35^{o}C using thermostated heating tape to maintain the line temperature above the anticipated dewpoint temperature and therefore prevent condensation. The laboratory temperature was also raised to aid the prevention of condensation, and the body of the dewpoint sensor was held above 35^{o}C to allow the measurement of dewpoints up to this level. CH_3O_2 radicals were generated by the photolysis of methyl iodide (CH_3I) in synthetic air (BOC BTCA178 zero grade air) with the same methodology as described for a conventional chain length calibration (see Section 3.2.1).

Since dewpoint was measured and either specific humidity or relative humidity are required for determination of the chain length dependence, the following conversions were necessary. To calculate both Q and RH, requires the calculation of the partial pressure of water vapour (e_w) from the dewpoint

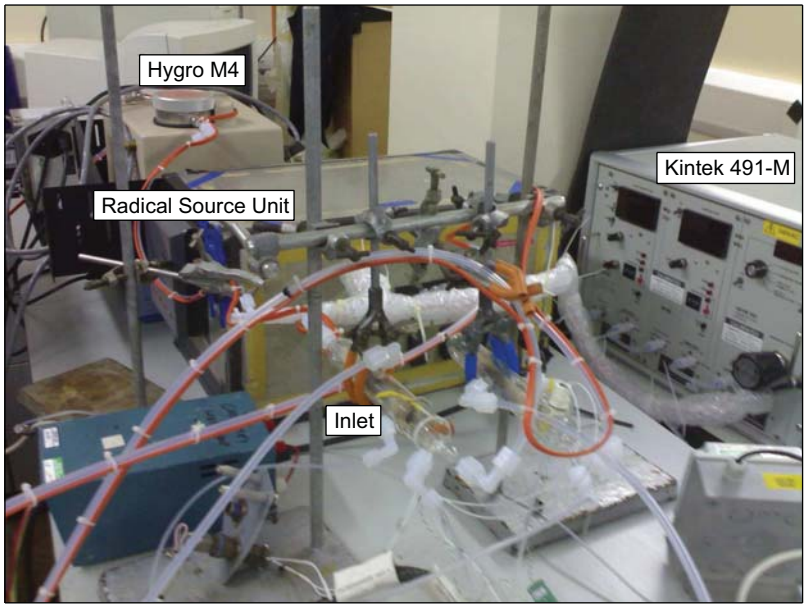

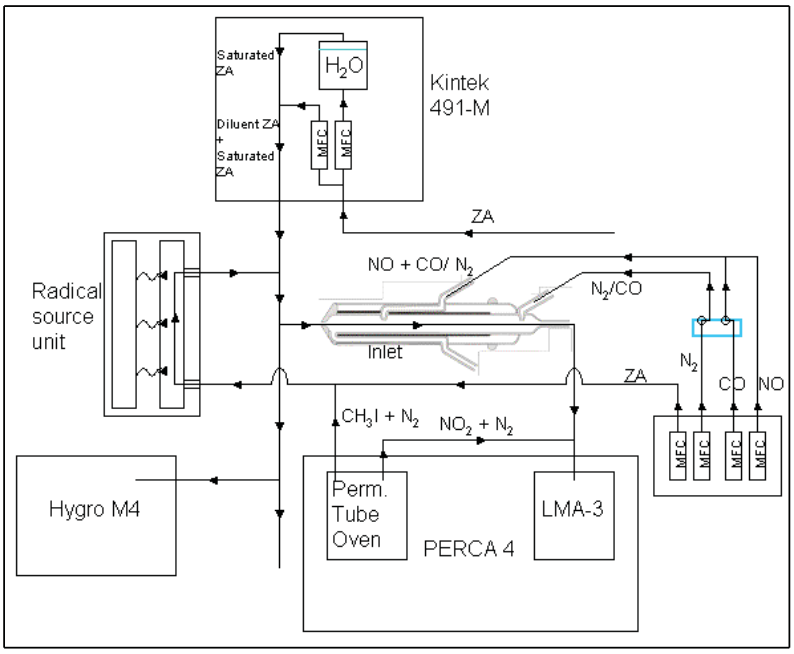

Figure 3.20: Chain length humidity calibration setup – (Top) Photograph of experimental setup; (Bottom) Schematic diagram of experimental setup (ZA = Zero Air)

temperature using the equation (Buck, 1981):

$$e_w = \left[1.0007 + \left(3.46 \times 10^{-6} P\right)\right] \times 6.1121 \times \exp\left\{\frac{17.502 T_d}{240.97 + T_d}\right\} \tag{3.21}$$

The partial pressure of water vapour e_w is in millibar, P is the ambient (total) pressure in millibar and T_d is in ^{o}C. RH is defined as the ratio of the partial pressure of water vapour to the saturation vapour pressure of water, e_{ws}, expressed as a percentage. e_{ws} is the defined as partial pressure at which T_d equals the ambient temperature, T, hence e_{ws} is calculated by substitution of the ambient temperature into Equation 3.21. RH then follows from:

$$RH(\%) = 100 \times \left(\frac{e_w\left(T_d\right)}{e_{ws}\left(T\right)}\right) \tag{3.22}$$

The specific humidity is calculated by using the partial pressure to calculate the mole fraction of water vapour x_w:

$$x_w = \frac{e_w}{P} \tag{3.23}$$

The specific humidity (in kg kg^{-1}) is calculated using the molar mass of water vapour M_w and air M_{air}:

$$Q = \frac{x_w M_w}{x_w M_w + \left(1 - x_w\right) M_{air}} \tag{3.24}$$

$$M_w \simeq 18.01534 \text{ g mol}^{-1} \tag{3.25}$$

$$M_{air} \simeq 28.9644 \text{ g mol}^{-1} \tag{3.26}$$

A specific humidity was targeted by fixing the calibration and humid flows appropriately and adjusting the humidity to achieve a particular dewpoint. Agreement between the measured dewpoint and that calculated given the relative humidity output from the humidifier and the relative flows, provided confidence that there were minimal losses of humidity within the system due to condensation. Minimal losses of CH_3O_2 between the radical source unit and the PERCA inlet are assumed due to the minimal wall loss rate for CH_3O_2, even in the presence of water vapour (Mihele *et al.*, 1999). Since a relative

change in the chain length as a function of humidity is required the absolute concentration of radicals is not significant.

Two further experiments were conducted to complement the determination of the chain length humidity dependence. These related experiments investigated the dependence of the NO_2 sensitivity of the LMA-3 Scintrex in the presence of humidity. There is little in the literature in this regard and no interference currently quantified, though a humidity interference to the luminol chemiluminescence technique would be widely applicable due to the commercial application of this technique in the measurement of NO_x. Reichert *et al.* (2003) hinted at a variation in the NO_2 sensitivity of their luminol NO_2 detector with humidity and state that "a NO_2 calibration under the same (dry-wet) conditions is made for every *CL* determination" to resolve this. Conversely Mihele *et al.* (1999) states that "the ratio of the NO_2 produced in the absence and presence of water for exactly the same air flows is the ratio of the chain lengths and is independent of the absolute concentration of the radicals and the sensitivity of the NO_2 detector, provided the experiments were performed in the linear region of the detector". However this is not true if the sensitivity varies between wet and dry conditions i.e.

$$\frac{CL_{wet}}{CL_{dry}} = \frac{\Delta\left[\mathrm{NO_2}\right]_{wet}}{\Delta\left[\mathrm{NO_2}\right]_{dry}} \tag{3.27}$$

$$\Delta\left[\mathrm{NO_2}\right]_{wet} = \frac{S_{amp} - S_{back}}{Sens_{wet}} \tag{3.28}$$

$$\Delta\left[\mathrm{NO_2}\right]_{dry} = \frac{S_{amp} - S_{back}}{Sens_{dry}} \tag{3.29}$$

S is the signal in Volts, while *Sens* is the NO_2 sensitivity in V ppbV$^{-1}_{NO_2}$. Clearly there is the potential for the chain length humidity dependence to be overstated if the NO_2 sensitivity does vary.

The experimental arrangement for the investigation of the dependence of the NO_2 sensitivity of the LMA-3 Scintrex in the presence of humidity was different to that for the chain length. The setups of the two experiments are shown schematically in Figure 3.21. The first experiment represents an extension to a conventional NO_2 sensitivity calibration with the calibration flow supplied through the

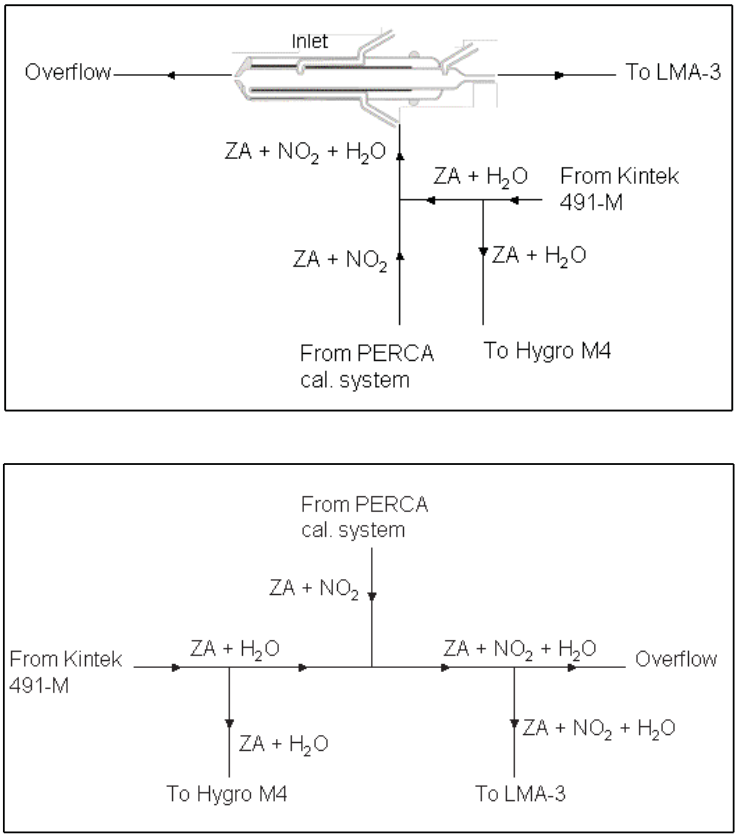

Figure 3.21: NO_2 sensitivity humidity calibration setup – (Top) Schematic of experimental setup for conventional NO_2 sensitivity calibration with addition of water vapour; (Bottom) Schematic of experimental setup for NO_2 sensitivity calibration with addition of water vapour independent of PERCA inlet and reagents NO and CO (ZA = Zero Air).

aircraft inlet via the calibration tube. The generation of the NO_2 calibration mixture (NO_2 diluted into BOC BTCA178 zero grade air) is described in Section 3.3.2. The humid airflow in combination with the NO_2 calibration flow were chosen to obtain a suitable range in both NO_2 concentration (34-124 ppbV) and water vapour (0-20 g kg^{-1}). The humidity was sampled (at a fixed rate) by the dewpoint sensor just prior to the addition point of NO_2, meaning the flow rate of the humid flow was less by the amount sampled. The level of humidity after addition of the NO_2 calibration flow and the concentration of NO_2 was calculated through accurate knowledge of the components of the flow, which were calibrated using a primary flow calibrator (Gillian Gilibrator 2, Sensidyne Inc.). Throughout an experiment the flow rate of the NO_2 calibration flow was fixed. Constant and particular flows from the humidifier were added to target a particular NO_2 concentration. At each particular flow (and therefore NO_2 concentration), a dry flow was first set from the humidifier to determine the dry response, and then the level of humidity varied within the flow to determine the change in response as a function of humidity at constant NO_2. The process was repeated at a number of NO_2 concentrations in the range 34-124 ppbV. Both the step changes in humidity and NO_2 were randomised to make clear any lag in the response from one condition to the next, none was observed.

The response at a given NO_2 concentration was observed to decay as a function of the humidity in the first experiment. The second NO_2 sensitivity humidity experiment followed the same steps to generate varied NO_2 concentrations and humidities at these concentrations, but bypassed the inlet and reagent flows. From this it was possible to assess the affect of humidity on the LMA-3 Scintrex detection independent of the inlet and without the presence of the PERCA reagent gases, to examine if the dependence observed was interfering with the NO_2 response alone.

For the chain length humidity calibration the procedure for a conventional chain length calibration was followed, except that at each radical concentration varying levels of humidity were added. Initially a conventional dry NO_2 sensitivity calibration was performed, the system was then re-plumbed in

line with the setup in Figure 3.20. A low (≃50 sccm) continuous flow of NO_2 in N_2 was added to the calibration flow before it reached the Scintrex detector to maintain the detector response in the linear region (see Section 2.1.1, Chapter 2, page 30). The humid airflow in combination with the CH_3O_2 calibration flow were chosen to obtain a suitable range in both CH_3O_2 concentration (78-124 pptV) and water vapour (0-26 g kg^{-1}). The humidity was sampled (at a fixed rate) by the dewpoint sensor after the addition point of the CH_3O_2 mixture, and therefore the level of humidity measured was that present in the calibration mixture. The inlet sampled the calibration mixture perpendicular to the flow avoiding any complications due to overflowing the inlet. Throughout an experiment the flow rate of the CH_3O_2 calibration flow was fixed. Constant and particular flows from the humidifier were added to target a particular CH_3O_2 concentration. At each particular flow (and therefore CH_3O_2 concentration), a dry flow was first set from the humidifier to determine the dry response (artefact and artefact plus CH_3O_2), and then the level of humidity varied within the flow to determine the change in response as a function of humidity at constant CH_3O_2. At each humidity, a run with and without CH_3I added was performed to allow subtraction of the artefact signal. The process was repeated at a number of CH_3O_2 concentrations in the range 78-124 pptV. Both the step changes in humidity and CH_3O_2 were randomised to make clear any lag in the response from one condition to the next, none was observed.

Humidity calibration results

In both the NO_2 sensitivity humidity experiments the signal at a particular NO_2 concentration was observed to decay with increasing humidity. Furthermore, the background signal (due to the linearisation NO_2 flow) during the chain length humidity calibration experiments exhibited the same trend. The signal and humidity data from each of the NO_2 sensitivity humidity experiments were binned by NO_2 concentration, and the background signal and humidity data of the chain length humidity experiments were binned by the CH_3O_2 concentration to separate out each experimental run. A

global fitting procedure using the IGOR 6.0 package (Wavemetrics, 2007) was used to fit an exponential function to all the experimental runs (raw signal (Volts) versus Q (g kg^{-1})) simultaneously, the function is of the form:

$$y = \alpha \exp\left\{\frac{-Q}{\tau}\right\} \tag{3.30}$$

The dependence is very flat, however an exponential was found to provide a better fit to the data than a linear trend. The scaling variable, α, was determined separately for each run, while the fitting procedure was constrained to determine a common exponent, τ, that best fit all the data. The variable α represents the dry signal response at a given NO_2 concentration (i.e. $\alpha = Sens_{dry}[NO_2]$), y is the signal as a function of NO_2 and humidity, Q is the specific humidity (in g kg^{-1}) and τ is the decay constant. The best fit exponent to the data is given by:

$$\tau_{NO_2} = 61.04 \pm 0.04(1\sigma) \tag{3.31}$$

The raw data for each run normalised by the associated coefficient α (i.e. $\frac{y}{\alpha}$) then represents the ratio of the wet signal to the dry signal and is shown in Figure 3.22 and this is equivalent to the ratio of the wet NO_2 sensitivity to the dry NO_2 sensitivity i.e.

$$y = Sens_{wet}.[NO_2] \tag{3.32}$$

$$\alpha = Sens_{dry}.[NO_2] \tag{3.33}$$

$$\frac{y}{\alpha} = \frac{Sens_{wet}}{Sens_{dry}} \tag{3.34}$$

$$\frac{y}{\alpha} = \exp\left\{\frac{-Q}{\tau}\right\} \tag{3.35}$$

The correction function determined for the NO_2 sensitivity is then the reciprocal of this:

$$CF_{NO_2} = \exp\left\{\frac{Q}{\tau_{NO_2}}\right\} \tag{3.36}$$

The flatness of the dependence of the NO_2 sensitivity with humidity is suggestive of quenching of the chemiluminescence signal under enhanced humidity, since this would produce a linear dependence of the relative change as a function of absolute humidity (as in a Stern-Volmer plot). The curvature in

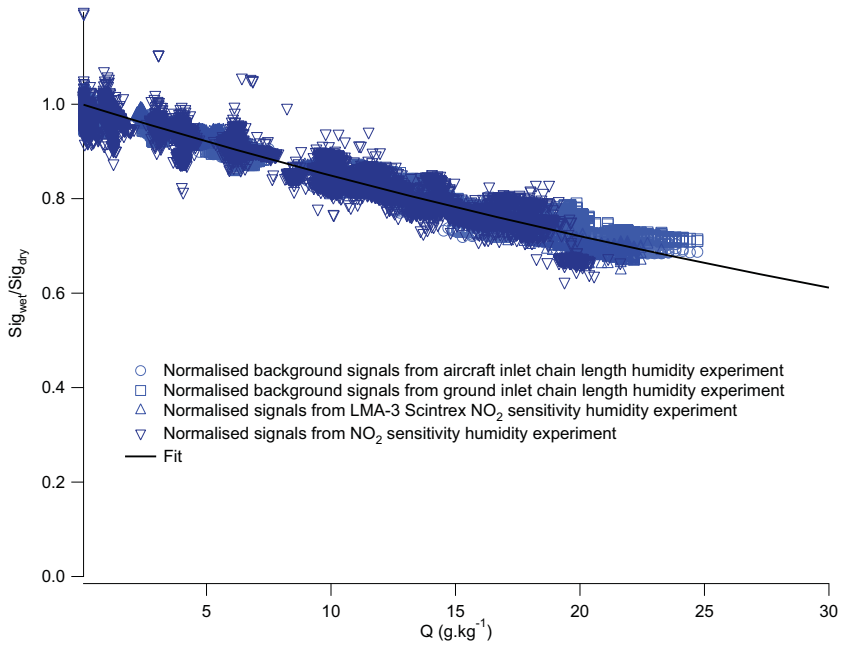

Figure 3.22: PERCA 4 LMA-3 Scintrex NO_2 sensitivity humidity dependence

the dependence is minimal, and an exponential fit is only a slight improvement over a linear fit to the data. Still for the correction of the data in the chain length experiments clearly the best fit is most appropriate for removal of the trend.

In the chain length calibrations a clear drop in the radical signal was observed as a function of humidity, however this was in clear correlation with coincident changes in the background signal. Since the drop in NO_2 detector response as a function of humidity was characterised (Equation 3.30) it was possible to separate the change in radical signal due to a reduction in chain length from that due to the change in detector response. At each radical concentration the NO_2 signal due to CH_3O_2 ($\Delta[NO_2]$) was determined by background and artefact subtraction and application of the dry NO_2 sensitivity. Following this the $\Delta[NO_2]$ data was corrected for the change in detector response:

$$\Delta\left[NO_2\right]_c = \Delta\left[NO_2\right] \times CF_{NO_2} \tag{3.37}$$

The corrected $\Delta[NO_2]$ data, the calculated radical concentrations ($[CH_3O_2]$) and measured humidity were then binned into 36 bins by the humidity in the range 0-26 g kg^{-1}. The binning procedure

also extracted the average and standard deviation of the humidity data for each bin. From this it was possible to determine the chain length for each humidity bin by the gradient of $\Delta[NO_2]_c$ versus $[CH_3O_2]$. Again the IGOR 6.0 package (Wavemetrics, 2007) global fitting procedure allowed the simultaneous fitting of a linear trend to each data bin, the fit was constrained such that the intercept went through the origin. The gradient and its uncertainty represent the average chain length and its uncertainty at the corresponding average humidity in a humidity bin. The chain length as a function of humidity was determined by plotting the chain length for each bin versus the average humidity. An exponential trend was found to best fit the observations, and the fit was weighted according to the errors in humidity (standard deviation of the humidity within a humidity bin) and chain length (standard deviation in the gradient of $\Delta[NO_2]_c$ versus $[CH_3O_2]$). The form of the fitting function is given by:

$$y = \alpha \exp\left\{\frac{-Q}{\tau}\right\} \tag{3.38}$$

In this case the scaling variable, α, represents the dry chain length. To determine the correction function (as per Equation 3.13), the fit to the chain length as a function of humidity was used to extrapolate to the dry chain length value α. The wet chain lengths were divided by α such that the relative change in chain length with humidity could be derived. An identical procedure was adopted for processing the data from both the aircraft inlet and ground inlet experiments. The data for each experiment are compared in Figure 3.23 as a function of specific humidity.

The dependence from a fit to each dataset individually is indistinguishable within their respective errors, so a general dependence was derived by using a global fit to both datasets constrained to find a common decay rate τ. The chain length humidity dependence was initially determined in terms of specific humidity in line with the correction determined by Salisbury (2001), Salisbury *et al.* (2002). Since a non-linear dependence of comparable shape and order of magnitude change to those published by other groups (e.g. Mihele *et al.* (1999), Reichert *et al.* (2003), Sadanaga *et al.* (2004)) was

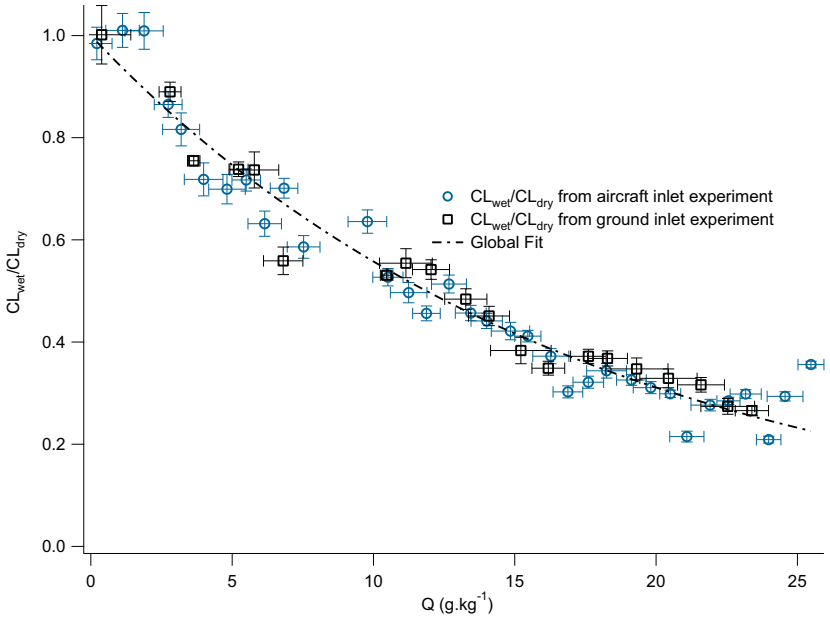

Figure 3.23: University of Leicester PERCA chain length humidity dependence – Comparing dependence observed with ground and aircraft inlets as a function of specific humidity

observed for both aircraft and ground inlets, and the dependence should be temperature independent and constant in terms of relative humidity (Reichert *et al.*, 2003), the humidity data were converted to relative humidity also for the parameterisation of the chain length correction. Fitting a linear trend in the range 0-12 g kg^{-1} to the data gives a gradient of -4.63 ± 0.18. Equating this with the gradient dependence observed by Salisbury (2001), Salisbury *et al.* (2002) the temperature of the air flow can be estimated, allowing the conversion to relative humidity:

$$-4.63 \pm 0.18 = (0.17T - 57.08) \tag{3.39}$$

$$T = 308.5 \pm 1.04K \tag{3.40}$$

$$T = 35.35 \pm 1.04^{o}C \tag{3.41}$$

The calculated temperature of 35.35^{o}C is entirely consistent with the temperature at which the sample lines were maintained i.e. 35^{o}C. Two conclusions are drawn from this: (1) The temperature dependence of the gradient of the chain length dependence as a function of specific humidity observed by

Salisbury (2001), Salisbury *et al.* (2002) is indicative of a constant relationship in relative humidity; (2) Salisbury (2001), Salisbury *et al.* (2002) observed over a temperature range of 10-50^{o}C indicating the relationship is at least constant in relative humidity over that temperature range.

Using an airflow temperature of 35^{o}C, the humidity data were converted to relative humidity and the data from both aircraft inlet and ground inlets fitted using the global fitting procedure to obtain a common function. The data for each experiment as a function of relative humidity are compared along with the fit function in Figure 3.24.

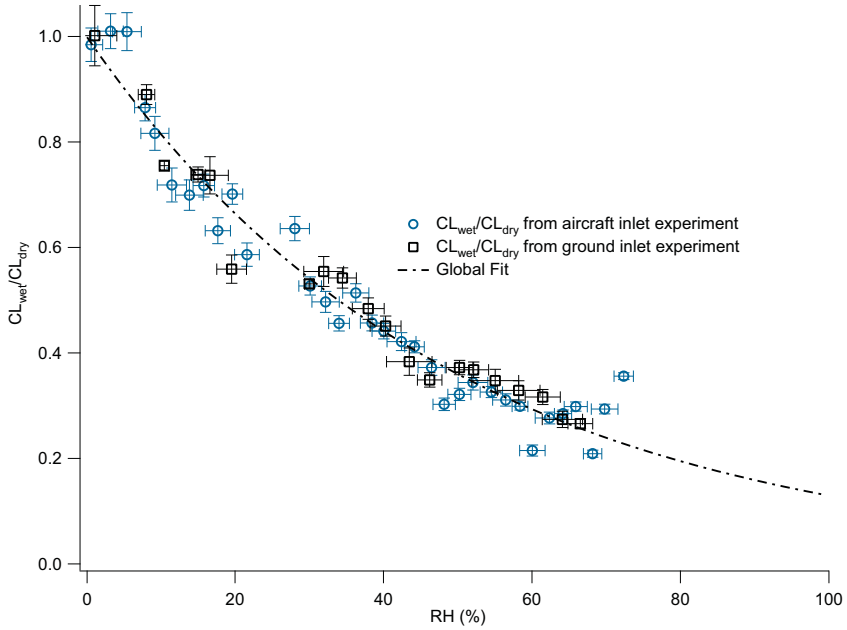

Figure 3.24: University of Leicester PERCA chain length humidity dependence – Comparing dependence observed with ground and aircraft inlets as a function of relative humidity

The best fit exponent to the data is given by:

$$\tau_{CL} = 48.92 \pm 0.96(1\sigma) \tag{3.42}$$

The correction function for the chain length, in terms of relative humidity (RH) and which should be

generally applicable for both the aircraft and ground inlets is then given by:

$$CF_{CL} = \exp\left\{\frac{RH}{\tau_{CL}}\right\} \tag{3.43}$$

To explain the exponential dependence of the chain length with increasing humidity, it is necessary to look for an analytical solution for the chain length. To make this more straightforward a number of simplifications are necessary. Only the simple chain reaction scheme (i.e. Reactions 3.1-3.6) involving HO_x radicals are considered, the differential equations describing the time evolution of HO_2 and OH are then:

$$\frac{d\left[HO_2\right]}{dt} = -k_{3.1}\left[HO_2\right]\left[NO\right] + k_{3.2}\left[OH\right]\left[CO\right] - k_{3.5}\left[HO_2\right] \tag{3.44}$$

$$\frac{d\left[OH\right]}{dt} = k_{3.1}\left[HO_2\right]\left[NO\right] - k_{3.2}\left[OH\right]\left[CO\right] - k_{3.6}\left[OH\right]\left[NO\right] \tag{3.45}$$

The OH radical concentration is small and in equilibrium with HO_2 due to the fast reaction of OH with CO in the inlet (Reaction 3.2). The OH concentration is limited by the relatively slow production rate from the reaction of HO_2 with NO (Reaction 3.1), hence the steady state approximation may be used for estimation of the OH concentration:

$$\frac{d\left[OH\right]}{dt} = 0 \tag{3.46}$$

$$\left[OH\right](t) = \left[HO_2\right](t)\frac{k_{3.1}\left[NO\right]}{k_{3.2}\left[CO\right] + k_{3.6}\left[NO\right]} \tag{3.47}$$

$$\left[OH\right](t) = \alpha\left[HO_2\right](t) \tag{3.48}$$

$$\alpha = \frac{k_{3.1}\left[NO\right]}{k_{3.2}\left[CO\right] + k_{3.6}\left[NO\right]} \tag{3.49}$$

The differential equation describing the HO_2 radical concentration may be solved by substitution of the equilibrium OH concentration:

$$\frac{d\left[HO_2\right]}{dt} = \left[HO_2\right](t)\left\{-k_{3.1}\left[NO\right] + \alpha k_{3.2}\left[CO\right] - k_{3.5}\right\} \tag{3.50}$$

$$\frac{d\left[HO_2\right]}{dt} = \left[HO_2\right](t)\beta \tag{3.51}$$

$$\beta = \left\{-k_{3.1}\left[NO\right] + \alpha k_{3.2}\left[CO\right] - k_{3.5}\right\} \tag{3.52}$$

$$[HO_2](t) = [HO_2](0) \exp\{\beta t\} \tag{3.53}$$

The differential equation describing the time evolution of the chain reaction product NO_2 is given by:

$$\frac{d[NO_2]}{dt} = k_{3.1}[HO_2](t)[NO] \tag{3.54}$$

Substituting in with the solution for the HO_2 radical concentration and solving:

$$\frac{d[NO_2]}{dt} = k_{3.1}[NO][HO_2](0) \exp\{\beta t\} \tag{3.55}$$

$$[NO_2](t) = [HO_2](0) \frac{k_{3.1}[NO]}{\beta} \{\exp\{\beta t\} - 1\} \tag{3.56}$$

The chain length is then derived simply by rearranging:

$$CL_{HO_2} = \frac{[NO_2](t)}{[HO_2](0)} \tag{3.57}$$

$$CL_{HO_2} = \frac{k_{3.1}[NO]}{\beta} \{\exp\{\beta t\} - 1\} \tag{3.58}$$

The variable β describes the time evolution of the HO_2 concentration which is determined by the wall loss rate, and the gas phase termination routes. With increasing wall losses of HO_2 under increasing humidity (Mihele *et al.*, 1999) or a gas phase interference (Mihele *et al.*, 1999, Reichert *et al.*, 2003, Butkovskaya *et al.*, 2009) an exponential decrease in the chain length is predicted and has been observed. This also offers an explanation as to why the chain lengths of both aircraft and ground inlets exhibit the same dependence. Although the inlets are of differing dimensions, the reagent concentrations are identical and the materials of which the inlets are composed are identical. Both would therefore exhibit the same dependence of the wall loss rate for HO_2 with humidity. The gas phase components to the chain length humidity dependence would not be apparent from the experimental work described here. The indications from all studies is that the humidity dependence is dominated by the processes dictating the chain length, i.e. if wall loss is primarily dictating the chain length the humidity dependence will be related primarily to changes in radical wall loss rates; if a high reagent NO concentration is used such that gas phase losses dictate the chain length the humidity dependence will be primarily related to the gas phase losses.

During ambient measurements processes such as aerosol deposition on the inlet walls are known to change the chain length of PERCA inlets determined from field calibrations due to changes in the wall loss rate. This leads to the requirement for regular chain length calibration in the field. If these processes change the way the wall loss rate depends on humidity, they will also change the chain length dependence on humidity beside the change in the dry chain length. This could limit the applicability of a humidity correction derived in the laboratory to field data unless the inlets are somehow maintained in pristine condition (e.g. through regular cleaning). Either field calibration of the chain length under humid conditions is required or regular maintenance of the inlets.

The lack of an observed humidity dependence in the PerCIMS/ROxMAS techniques can also be explained. The reagent NO does not participate in the chain mechanism (it is only present for conversion of HO_2 to OH) and CO is not present, so a gas phase interference cannot interact with the chain chemistry. For these reasons the proposed gas phase interference reactions could not be amplified and interfere as in PERCA. The PerCIMS/ROxMAS instruments described by Edwards *et al.* (2003) and Hanke *et al.* (2002) both employ low pressure flow reactors for the chain chemistry which minimise the impact of wall losses on the chain length, hence removing the interference due to water vapour enhancement of wall losses.

3.3 NO_2 detection and calibration

The method of NO_2 detection through luminol chemiluminescence in the presence of NO_2 and O_2 has been introduced (see Section 2.1.1, page 30). This section describes the practical implementation of this technique in PERCA 3.5 and PERCA 4, and the details of calibration of the NO_2 sensitivity.

3.3.1 LMA-3 Scintrex detector

An improved dual channel LMA-3 Scintrex detector is employed in PERCA 4 as described in Green *et al.* (2006), Brookes *et al.* (2006). This adapted detector incorporates the components of two detectors in a single unit, saving both space and weight which are critical requirements of an aircraft instrument. In PERCA 3.5 two separate Scintrex detectors are employed similarly to monitor two channels independently. Each sample airflow is directed to a detector cell (and measurement channel) where it comes into contact with the luminol flow and the chemiluminescent reaction occurs (in the presence of NO_2 and O_2). The detector cells are made from an acetal block with separate channels for delivery and removal of the air and luminol flows, a wick conducts the liquid luminol flow past the airflow and provides a surface for the reaction. A transparent window opposite the wick allows transmission of the chemiluminescent light signal to a PMT (Photo Multiplier Tube) detector. The cells are dark to prevent spurious signal from stray light reaching the PMT detector. The arrangement is shown schematically in Figure 3.25.

The wick is soaked with a continuous flow of luminol, this is supplied from a dedicated chiller unit (housed in the isothermal unit) in PERCA 4 when the instrument is installed aboard the BAe-146. A conventional refrigerator is used to store and cool the luminol on the ground for PERCA 3.5 and 4. Typically a peristaltic pump and internal luminol reservoirs would be used for luminol flow control and storage in a conventional LMA-3 Scintrex detector. The storage was changed (preceding Green *et al.* (2006)) to save space in the detector unit. The peristaltic pump was removed in both the University of Leicester PERCA systems in preference for what was anticipated to be a simpler and more reliable flow control methodology (Green *et al.*, 2006). The luminol is contained under pressure (20 PSI N_2) in the refrigerated reservoir unit to force it through the tubing and up to the detector box; downstream of the detectors the luminol is pulled to a waste reservoir held under suction by the air sample pump. At the detector box the flow of luminol is controlled by a combination of needle valves (Swagelok

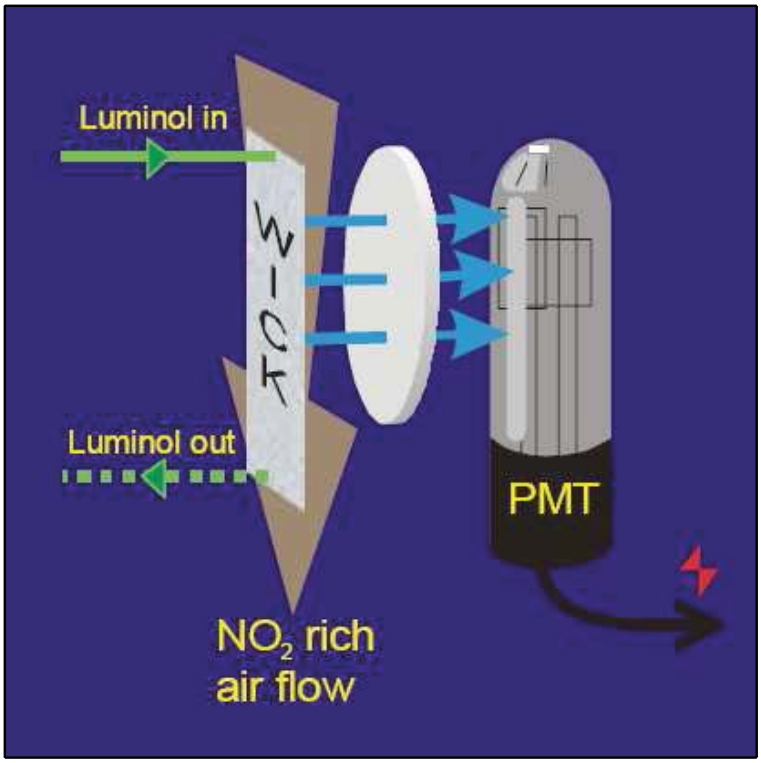

Figure 3.25: Schematic of LMA-3 Scintrex detector illustrating arrangement of detector cell, wick and PMT detector - Adapted from Brookes *et al.* (2006)

SS-SS2-A); one prior to the detector cell controls the supply, another after the detector cell controls the luminol flow to the waste reservoir, a typical flow is of the order 0.5 ml min^{-1}. A baseline NO_2 flow (at a concentration of the order 30 ppbV) may be added to the sample airflow after the inlet and just before the detector box to provide a stable baseline signal, and maintain the detector response in the linear regime (see Section 2.1.1, Chapter 2, page 30). This can be important in a low NO_x environment and is critical during chain length calibrations when there is no background NO_2 due to sampling a synthetic calibration airflow.

3.3.2 NO_2 sensitivity calibration

Quantified concentrations of NO_2 for calibration of the LMA-3 Scintrex detector response are provided by a calibrated NO_2 permeation tube (see Section 3.4.1, page 115) held at 40 ^{o}C in a thermostated oven (the linearisation unit) with a carrier flow of N_2 ($\sim$50 sccm). This concentrated mixture is diluted into a variable flow of synthetic air (BOC BTCA178 zero grade air) typically in the range of 3-5 slpm to produce varied concentrations dependent on the dilution flow. A timeseries plot from an NO_2 sensitivity calibration in Figure 3.26 with a number of features highlighted. Feature A shows a gradual drop in the signal to a stable level after switching from a higher dilution flow to a lower dilution flow, equivalent to switching from a lower to a higher NO_2 concentration. This is indicative of the time it takes for the NO_2 to mix evenly within the calibration flow as sudden switching to a lower dilution flow produces a transient spike in the NO_2 concentration. Feature B shows a transient drop in signal which then returns to the same level after 2 minutes; this is indicative of a short timescale drop in luminol flow which can happen due to bubbles in the line delivering luminol to the detector cell. Feature C is the opposite to feature A - in suddenly switching from a lower dilution flow to a higher dilution flow the NO_2 concentration drops suddenly also, the signal climbs as the NO_2 mixes into the flow and stabilises once the NO_2 is completely mixed. Feature D is due to the same process as feature A i.e. the timescale for the NO_2 calibration mixture to mix on switching from a higher

dilution flow (lower NO_2 concentration) to a lower dilution flow (higher NO_2 concentration). Feature D differs in that initially the signal saturates as the initial spike in NO_2 puts the signal outside the detectable range.

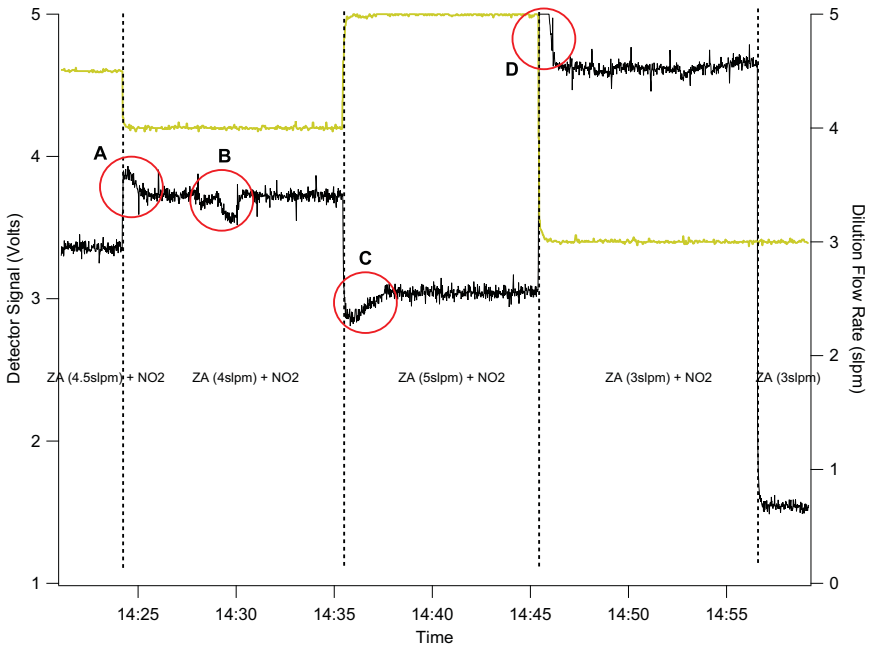

Figure 3.26: Timeseries of signal from NO_2 sensitivity calibration - see text for details

The NO_2 sensitivity calibration plot derived from the calibration shown in Figure 3.26 is shown as an example in Figure 3.27. The signal and error in the signal at a particular NO_2 concentration are derived from the average of the signal at a particular dilution flow; transient features in the signal such as indicated in Figure 3.26 are excluded from the averaging. The NO_2 concentration and related error are derived from the average dilution flow (the average derived for the same points as the signal average), the average carrier flow of N_2 over the NO_2 permeation tube (determined using a primary flow calibrator (Gillian Gilibrator2, Sensidyne Inc.)) and the permeation rate of the NO_2 permeation tube (see Section 3.4).

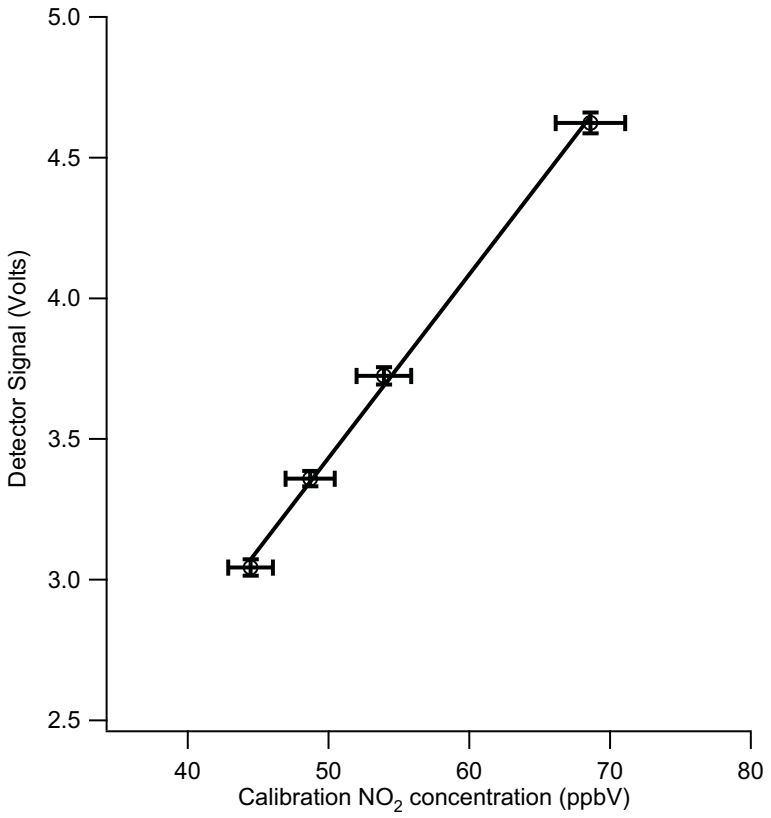

Figure 3.27: NO_2 sensitivity calibration plot, error bars represent 1σ

3.3.3 NO_2 sensitivity altitude dependence

Parker (2007) notes that during the ITOP campaign (the first aircraft deployment of PERCA 4) it was not possible to calibrate in flight using the aircraft calibration unit due to "technical problems". Prior to AMMA (see Chapter 5, page 181) the plumbing of the calibration unit as setup for ITOP was investigated and found to be in error, hence a working scheme was designed (Brookes *et al.*, 2006). To calibrate in flight for NO_2 sensitivity an alternative method was applied for ITOP whereby the PERCA background measurement signal was related to *in-situ* ozone measurements made on board the BAe-146 with a commercial Thermo Environmental Instruments Inc. 49C ozone analyser (Parker, 2007). The basis of this method was that the background signal could be assumed to be due almost entirely to ozone through its oxidation of the reagent NO:

$$O_3 + NO \rightarrow NO_2 + O_2 \tag{3.59}$$

This applies only where the ozone concentration is significantly greater than the ambient NO_2 concentration and other sources of NO_2 that could also be produced once sampled. Accordingly Parker (2007) verified this was the case at all times during ITOP, and derived the detector NO_2 sensitivity (V ppb$V^{-1}_{NO_2}$) by determining the ratio of the background measurement signal to the concentration of O_3.

In practice the inflight calibration of the aircraft PERCA NO_2 sensitivity during AMMA was unreliable due to a number of limitations with the current design of the instrument and aircraft calibration system, and operational issues associated with running on the BAe-146. These limitations are discussed elsewhere (see Section 5.2.1, page 199). It meant an alternative technique needed to be considered, hence the validity of using the *in-situ* ozone measurement as a method of calibrating the NO_2 sensitivity of the LMA-3 Scintrex NO_2 detector response as per Parker (2007) was investigated.

Several compounding issues are recognised with the methodology of Parker (2007) whose assumption

was for 100% conversion of O_3 to NO_2 in the time available from sampling to detection on reaching the PERCA 4 LMA-3 detectors. The sensitivity, $Sens$(V ppbV$^{-1}_{NO_2}$), at a time, t, is then given by the ratio of the background measurement signal, $Signal_{backg'd}$(V), to the concentration of ozone, [O_3](ppbV), being equivalent to the total background NO_2 concentration in this assumption:

$$Sens = \frac{Signal_{backg'd}}{[O_3]} \tag{3.60}$$

One issue is related to the kinetics of reaction 3.59 which has a temperature dependence as given by (Atkinson *et al.*, 2004):

$$k_{O_3+NO,IUPAC}(298\text{K}) = 1.8 \times 10^{-14}\text{cm}^3\text{molecule}^{-1}\text{s}^{-1} \tag{3.61}$$

$$k_{O_3+NO,IUPAC}(T) = 1.4 \times 10^{-12} exp\left(\frac{-1310}{T}\right)\text{cm}^3\text{molecule}^{-1}\text{s}^{-1} \tag{3.62}$$

Over the temperature range 195-308 K, appropriate for conditions found in the troposphere. This is the latest IUPAC recommendation (Atkinson *et al.*, 2004). Alternatively the latest recommendation from NASA JPL (Sander *et al.*, 2006) is given by:

$$k_{O_3+NO,JPL}(298\text{K}) = 1.9 \times 10^{-14}\text{cm}^3\text{molecule}^{-1}\text{s}^{-1} \tag{3.63}$$

$$k_{O_3+NO,JPL}(T) = 3.0 \times 10^{-12} exp\left(\frac{-1500}{T}\right)\text{cm}^3\text{molecule}^{-1}\text{s}^{-1} \tag{3.64}$$

The rate of ozone loss through this reaction is the rate of NO_2 production (assuming this is still the dominant source), the rate equation given by:

$$\frac{d[NO_2]}{dt} = k_{O_3+NO}[O_3][NO] \tag{3.65}$$

The integrated rate law is (Atkins & De Paula, 2006):

$$\ln\left(\frac{[O_3]_t/[O_3]_0}{[NO]_t/[NO]_0}\right) = ([O_3]_0 - [NO]_0)\, k_{O_3+NO}t \tag{3.66}$$

where the subscript 0 denotes the initial concentration of the reactant when the time t=0, and the subscript t the concentration at time t thereafter. The difference between the initial ozone concentration and that after time t is equal to the concentration of NO_2 created. Given the negative temperature

dependence of the rate constant k_{O_3+NO}, the yield of NO_2 after a time t can be expected to drop with increasing altitude. The time evolution of the ozone concentration at temperatures derived from the measured temperature-altitude profile from the AMMA campaign was calculated with the IGOR 6.0 package (Wavemetrics, 2007) ordinary differential equation solver and the BDF method (appropriate for solving stiff problems), shown in Figure 3.28. This demonstrates the drop in rate at which NO_2 is yielded as the altitude increases, 4-5 s being required for 100% conversion even at ground level.

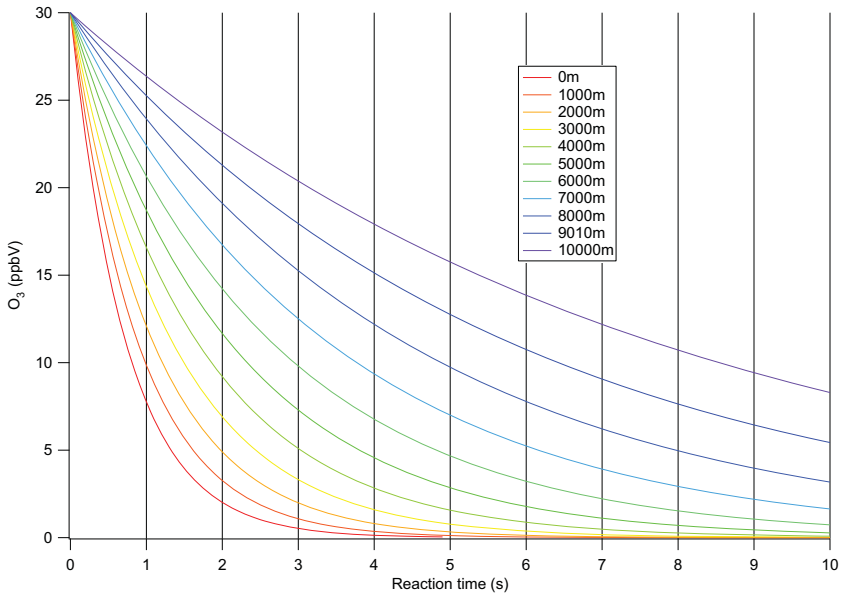

Figure 3.28: Time dependence of ozone NO titration from 0-10 km altitude - Initialised using $[O_3]_0 = 30$ ppbV, $[NO]_0 = 3$ ppmV and calculated using the IUPAC recommended rate constant (see Equation 3.62).

Another issue is related to the methodology of sample and reagent flow control in PERCA 4, i.e. mass flow control (see the Appendix B, page 341). This leads to a exponential increase in the volume flow rate of sample air flow with increasing altitude, which in turn leads to an exponential decrease in the time from sampling at the inlet to detection at the LMA-3 Scintrex detection cell. Combined with the slowing of the reaction rate, the possible yield of NO_2 will be less than 100% for situations where the time to detection is less than the time required for complete conversion and the likelihood of this

increases with increasing altitude.

The volume of the inlets and lines before the LMA-3 Scintrex detector cells in combination with the volume flow rate dictates the reaction time and can be estimated using:

$$t(\mathrm{s}) = \frac{V_{inlets+lines}(\mathrm{m}^3)}{F(\mathrm{m}^3\mathrm{s}^{-1})} \tag{3.67}$$

$V_{inlets+lines}$ represents the effective volume of inlet and tubing between injection of the reagent NO at the inlet and the sample lines before the detectors and F is the true volume flow, calculated from the sample flow rate (slpm) using:

$$F(\mathrm{m}^3\mathrm{s}^{-1}) = F(\mathrm{slpm})\frac{1\times10^{-3}(\mathrm{m}^3)}{60(\mathrm{s})}\frac{SP(\mathrm{Pa})}{ST(\mathrm{K})}\frac{T(\mathrm{K})}{P(\mathrm{Pa})} \tag{3.68}$$

where $ST = 273.15$ K and $SP = 101325$ Pa.

Since $[\mathrm{NO}]_0 \gg [\mathrm{O_3}]_0$, $[\mathrm{NO}]_t/[\mathrm{NO}]_0 \approx 1$, from Equation 3.66 the concentration of ozone as a function of time can then be approximated by:

$$[\mathrm{O_3}]_t = [\mathrm{O_3}]_0 \exp\left\{\left([\mathrm{O_3}]_0 - [\mathrm{NO}]_0\right) k_{O_3+NO} t\right\} \tag{3.69}$$

The NO_2 produced from Reaction 3.59 after a time t is then given by:

$$[\mathrm{NO_2}]_t = [\mathrm{O_3}]_0 - [\mathrm{O_3}]_t \tag{3.70}$$

$$[\mathrm{NO_2}]_t = [\mathrm{O_3}]_0 \left(1 - \exp\left\{\left([\mathrm{O_3}]_0 - [\mathrm{NO}]_0\right) k_{O_3+NO} t\right\}\right) \tag{3.71}$$

Hence Equations 3.64, 3.67, 3.68, 3.71 can then be combined to calculate the NO_2 background concentration produced by Reaction 3.59 along a flight track. The calculation employs the known temperature dependence of the rate constant, k_{O_3+NO}; the calculated true volume flow rate, $F(\mathrm{m}^3\mathrm{s}^{-1})$; the measured ambient ozone concentration, $[\mathrm{O_3}]_0$ (molecules cm^{-3}); the calculated reagent NO concentration, $[\mathrm{NO}]_0$ (molecules cm^{-3}) (based on a 3 ppmV concentration in sample flow); the calculated reaction time (based on estimates of inlet and sample line volume and the true volume flow rate), t(s); and the simplified integrated rate law (which assumes NO is not consumed significantly in

reaction with ozone since $[NO]_0 \gg [O_3]_0$). The temperature and pressure come from *in-situ* measurements made on board the BAe-146, both are core measurements. Temperature is measured by the Rosemount temperature sensors and pressure is provided by a static pressure measurement as part of the RVSM (Reduced Vertical Separation Minimum) equipment the aircraft is required to carry (http://www.faam.ac.uk/).

Equation 3.71 was used to derive along flight track NO_2 sensitivities for the AMMA campaign by determining the scaling between the measured background signal and the calculated NO_2 background concentration derived from Reaction 3.59. The equation for calculation of the NO_2 sensitivity then becomes:

$$Sens = \frac{Signal_{backg'd}}{[NO_2]_t} \tag{3.72}$$

The validity of this approach is confirmed by comparison of the measurements of the ambient ozone and NO_2 concentrations encountered during AMMA as sampled by the BAe-146. Figure 3.29 illustrates this through the ratio of ozone to NO_2 concentrations as a function of altitude. The ratio derived with the TECO 42C instrument is subject to greater noise due to its lower detection limit (50 pptV with 120 s averaging) compared to the NOxy instrument (15 pptV with 15 s averaging) hence the ratio is less reliable. Still, the TECO 42C NO_2 had greater measurement coverage during AMMA due to logistical issues which affected the NOxy running, hence it is shown also. The profiles are broadly similar and illustrate that for all altitudes the ozone concentration is typically 100-1000 times greater than ambient NO_2. Hence, even with only fractional conversion of ambient ozone to NO_2 through reaction with reagent NO this source will dominate the PERCA background signal.

The applicability and validity of the calculated NO_2 background for calibration of the NO_2 sensitivity was further tested through direct comparison to the PERCA background signals measured during AMMA. Figure 3.30 is an example timeseries plot from AMMA flight B217 showing the PERCA raw measured signal alongside the measured ambient ozone concentration (shown in both parts and abso-

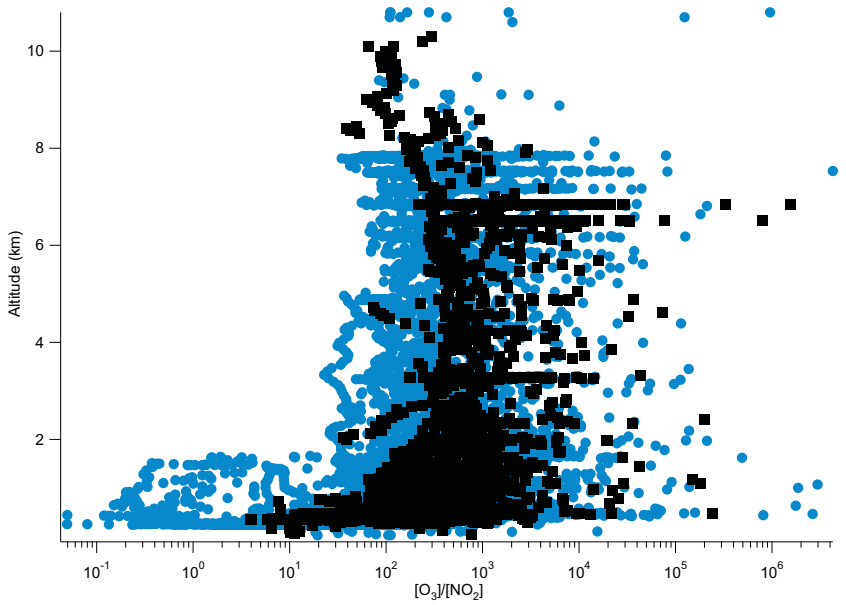

Figure 3.29: Ratio of ambient ozone to NO_2 from 0-10 km altitude - Ozone measurements from the FAAM core instrument (TECO 49C ozone analyser), NO_2 measurements from the FAAM core instrument (TECO 42C chemiluminescence) (blue circles) or UEA NOxy instrument (black squares).

lute number density concentrations), and the calculated NO_2 number density concentration derived from Reaction 3.59. The axes have been scaled to best illustrate the matching of the PERCA raw measured signal to the calculated NO_2.

The calculated NO_2 tracks the PERCA raw signal through changes in altitude since the NO_2 yield from ozone changes with altitude as explained above, even short timescale events in the ambient background are well represented in the PERCA signal. Figure 3.30 represents a best case example, where the sensitivity of the LMA-3 Scintrex detectors were little affected by changes in altitude since no loss of sample flow control occurred (and therefore the luminol flow to the detectors was little perturbed). For periods where the luminol flow remains stable, the signals and NO_2 background track well and the correlation remains high; loss of sample flow at higher altitudes leads to variation of sensitivity but through matching to the known background the sensitivity can be tracked.

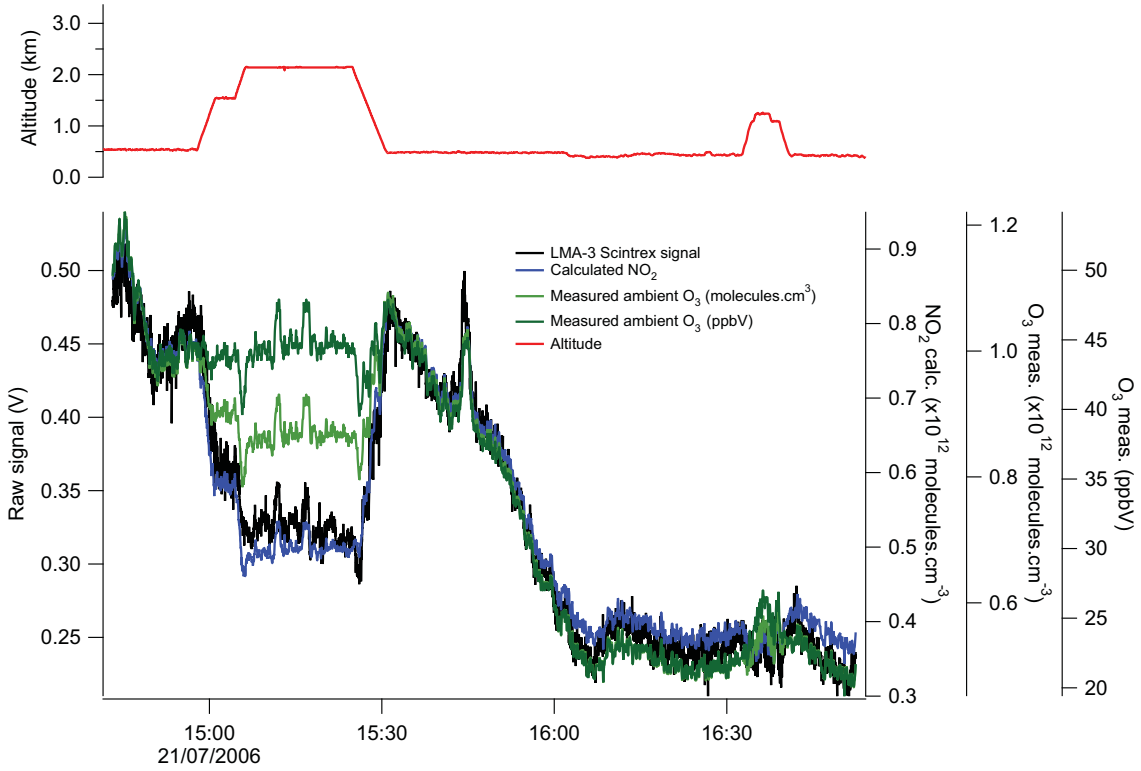

Figure 3.30: Timeseries comparing raw signal to calculated NO_2 background - LMA-3 Scintrex raw signal (black), calculated NO_2 background from Reaction 3.59 (blue), measured ambient ozone concentration (in ppbV (dark green); in molecules cm^{-3} (light green)), altitude (red).

3.3.4 NO_2 sensitivity humidity interference

A significant interference to the NO_2 sensitivity of the LMA-3 Scintrex detectors was observed with the enhanced levels of humidity employed in the chain length humidity dependence calibrations performed for this work. The dependence was partially characterised such that the dependence of the chain length on humidity could be defined independently. It is not clear whether such a correction is generally applicable in ambient measurements so it has not been applied for correction of the signals for the fieldwork in this thesis (see Section 3.2.3, page 81). The influence of humidity on the Scintrex NO_2 sensitivity is irrelevant for aircraft measurements where the NO_2 sensitivity has been determined point by point by linking the PERCA measured background signal to measurements of the background components to NO_2 (primarily O_3). In this situation the sensitivity under ambient conditions is determined so no correction is necessary.

3.4 Calibration and characterisation of radical and NO_2 calibration sources

The accurate calibration and characterisation of the PERCA instrument both in terms of the inlet chain length and NO_2 detection sensitivity depends on well calibrated sources of radicals and NO_2. The experimental work to calibrate the radical source unit and methyl iodide and NO_2 references used in this work are described in this section.

3.4.1 Permeation rate calibrations (NO_2 and CH_3I)

For PERCA chain length calibrations and determination of the LMA-3 Scintrex detector NO_2 sensitivity, calibrated sources of methyl iodide (CH_3I) and NO_2 are required. The chosen methodology

is to employ permeation tubes[1] where the rate of permeation of the calibration gas into a fixed flow of N_2 is known at a given temperature and the addition of a controlled dilution flow determines the concentration of the resulting mixture for calibration purposes. A number of permeation tubes were purchased uncalibrated from VICI Metronics Inc. and used in the field and laboratory work carried out during this project; the permeation rates of uncalibrated permeation tubes are known nominally (within ±25 %) and the particular tube is chosen on the basis that the concentration of calibration mixture covers a relevant range easily achieved by staged dilution. Two types of permeation tube are used; for NO_2 a wafer device is used consisting of a metal resevoir with a permeable window, for CH_3I a tubular device is used where the PTFE tube forms the permeable membrane.

To calibrate the permeation rate the permeation tubes were held under operating conditions for an extended period and weighed periodically. The change in mass of the tube over time is equal to the permeation rate. The usual operating conditions are to hold the permeation tube at 40 ^{o}C with a continuous flow of N_2 (BOC zero grade 99.999% purity) at approximately 50 sccm. The setup for the measurement of the permeation rates was to house the permeation tubes within the PERCA 4 linearisation unit, where the temperature is regulated with an Omega Newport i16D temperature controller and the temperature measurement made using a type-T thermocouple. The nitrogen flow is controlled using a combination of needle valves (Swagelok SS-SS2) and nitrogen pressure regulated at 20 PSI.

Due to the low permeation rates (hundreds of nanograms per minute) precise scales were used (Mettler Toledo, AG245) allowing determination of the mass down to 10^{-5} g, and measurements were made over an extended period in time (approximately every 2 weeks for a 12 week period). Time measurement was through an identical quartz watch for the whole period to maintain consistency in the time measurement. Each mass measurement was determined from the mean of eleven samples and the

[1] A permeation tube consists of a reservoir with a permeable membrane. By regulating the temperature a constant vapour pressure is maintained and the permeation rate through the membrane is held constant.

uncertainty in the mean taken as 3 standard deviations from the mean. The gradient of the average mass versus time (in minutes) weighted by the uncertainty in the average mass[2] was fitted using a weighted least squares fitting approach. The time was recorded when the permeation tubes were removed from the linearisation unit for weighing and the time at which they were replaced. The total time was corrected for the periods that the permeation tubes were not temperature regulated by subtraction of the time it took for a weighing session (typically 20 minutes per permeation tube). An example calibration curve is shown in Figure 3.31, and a summary of the permeation rates derived follows in Table 3.6.

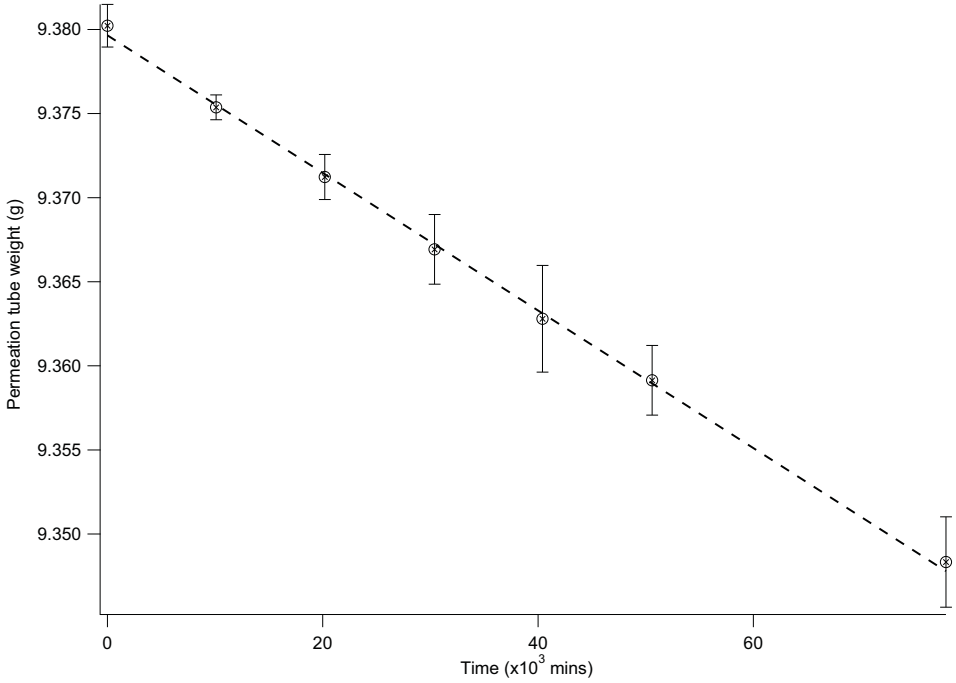

Figure 3.31: CH_3I permeation tube calibration

3.4.2 Determination of j_{CH_3I}

The derivation of photolysis rate of methyl iodide proceeds by a UV absorption spectroscopy technique for monitoring the concentration of a methyl iodide mixture in air over time. The concentration of an

[2]Uncertainty in time on the timescale of minutes was insignificant over the timescale of the calibration period

Compound	Part number	Nominal perm. rate	Calibrated perm. rate ($\pm 3\sigma$)	Application
CH_3I	100-007-4600-U40	350 ng min^{-1}	415.19±2.28 ng min^{-1}	PERCA4
NO_2	140-633-0081-U40	460 ng min^{-1}	584.87±4.35 ng min^{-1}	PERCA4
CH_3I	100-007-4600-U40	350 ng min^{-1}	408.97±29.6 ng min^{-1}	PERCA3.5
NO_2	140-633-0081-U40	460 ng min^{-1}	530.2±9.1 ng min^{-1}	PERCA3.5
NO_2	140-633-0081-U50	230 ng min^{-1}	224.04±16.0 ng min^{-1}	PERCA3.5

Table 3.6: Measured and nominal permeation rates of calibration permeation tubes

absorber can be derived from the Beer-Lambert law:

$$I = I_0 \exp\left(-\sigma[n]x\right) \tag{3.73}$$

where I is the light intensity after passing through a path length x in the presence of an absorber at concentration $[n]$ with absorption coefficient σ. Hence the concentration of the absorber is given by:

$$[n] = \frac{1}{\sigma x} \ln\left(\frac{I_0}{I}\right) \tag{3.74}$$

The photolysis of methyl iodide can be represented as a first order process hence:

$$\frac{d[\mathrm{CH_3I}]}{dt} = -j_{CH_3I}[\mathrm{CH_3I}] \tag{3.75}$$

Integrating:

$$\int_{[CH_3I]_0}^{[CH_3I]_t} \frac{d[\mathrm{CH_3I}]}{[\mathrm{CH_3I}]} = -j_{CH_3I} \int_0^t dt \tag{3.76}$$

$$\ln[\mathrm{CH_3I}]_t - \ln\left[\mathrm{CH_3I}\right]_0 = -j_{CH_3I}(t-0) \tag{3.77}$$

Substituting for $[n]$ =[CH_3I] from Equation 3.74:

$$\ln\left\{\frac{1}{\sigma x}\ln\left[\frac{I_0}{I_{[CH_3I]=[CH_3I]_t}}\right]\right\} = -j_{CH_3I}t + \ln\left\{\frac{1}{\sigma x}\ln\left[\frac{I_0}{I_{[CH_3I]=[CH_3I]_0}}\right]\right\} \tag{3.78}$$

$$\ln\left\{\ln\left[\frac{I_0}{I_{[CH_3I]=[CH_3I]_t}}\right]\right\} = -j_{CH_3I}t + \ln\left\{\ln\left[\frac{I_0}{I_{[CH_3I]=[CH_3I]_0}}\right]\right\} \tag{3.79}$$

The form of this equation is the equation of a straight line i.e. $y = mx + c$, and therefore the photolysis rate can be determined by monitoring the throughput intensity, I, as a function time during photolysis

(and therefore concentration) and by measurement of the intensity without the absorber present, I_0. Then plotting the natural log of the natural log of the ratio of the light intensity without methyl iodide present (I_0) to when it is being photolysed ($I_{[CH_3I]=[CH_3I]_t}$) versus the time over which photolysis occurs yields the photolysis rate from the gradient. Figure 3.32 shows an example of this.

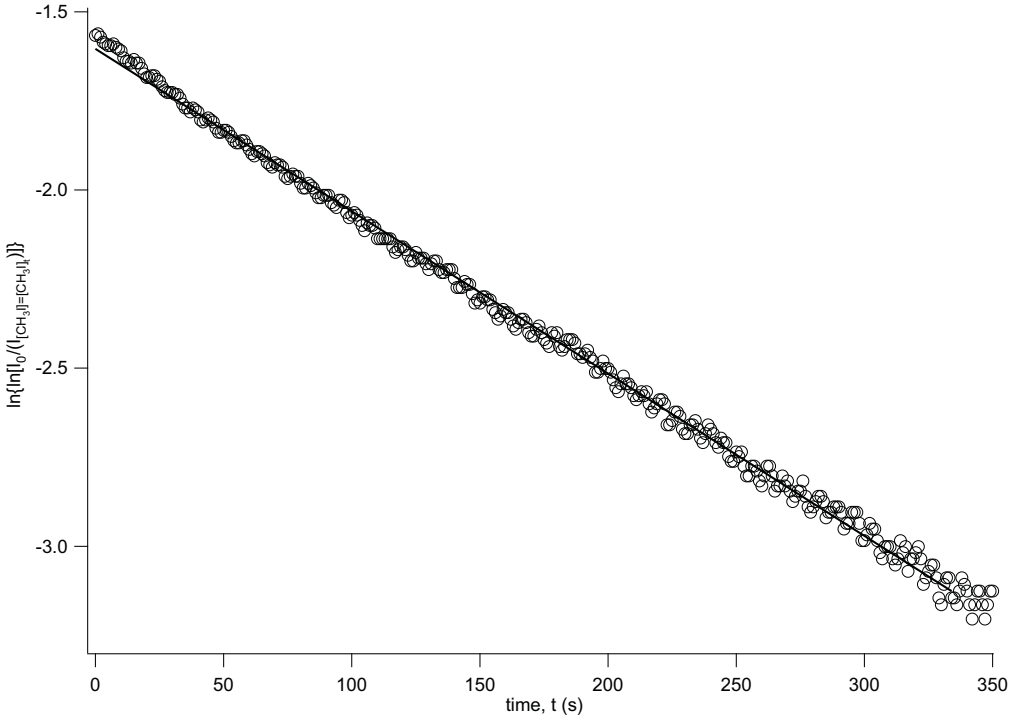

Figure 3.32: j_{CH_3I} calibration fit

The experimental setup for the measurement of j_{CH_3I} is shown schematically in Figure 3.33 and the setup is shown photographed in Figures 3.34 and 3.35.

Within the radical source unit a Hg strip lamp (Philips TUV 15W G15T8) held parallel to the quartz flow tube (custom made by University of Leicester workshops) provides intense 253.7 nm light for photolysis. A stable deuterium reference lamp (Hamamatsu Photonics K.K., L2196) is mounted on the outside of the radical source unit at one end of the flow tube and brought to focus at the opposite window using a fused silica lens (Elliot Scientific, focal length 60 cm, PLCX–25.4-257.5-UV). The quartz windows at each end of the flow tube allow monitoring of the reference lamp output and a

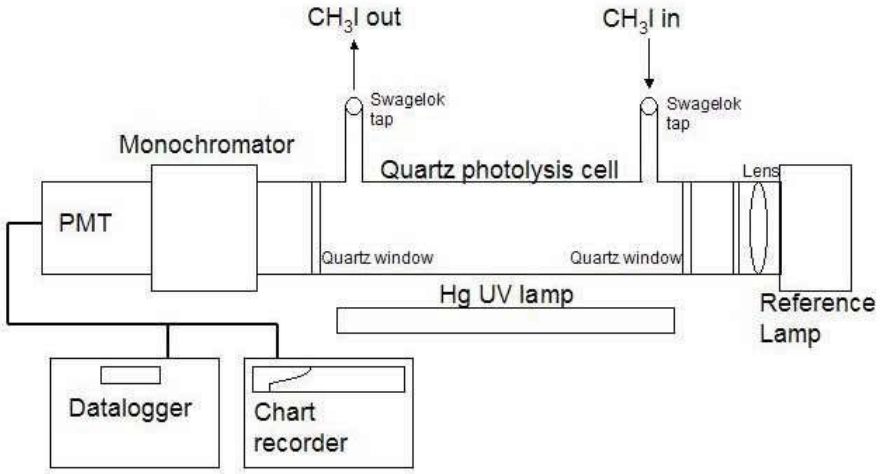

Figure 3.33: Schematic diagram of experimental setup for determination of j_{CH_3I}

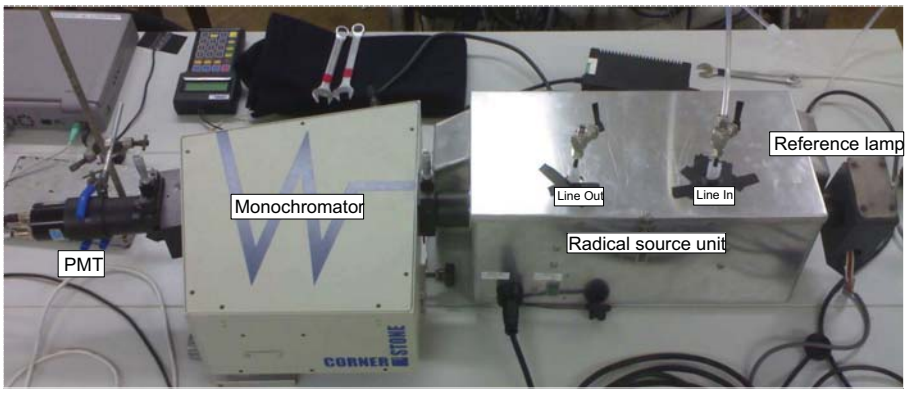

Figure 3.34: Plan photograph of experimental setup for determination of j_{CH_3I}

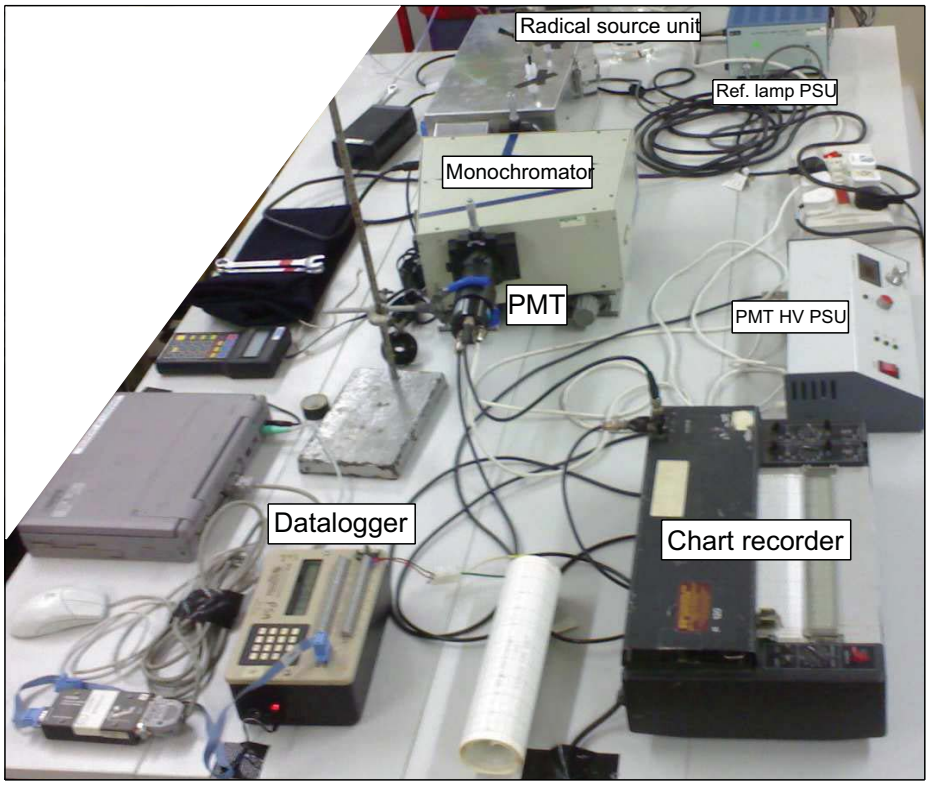

Figure 3.35: Photograph of experimental setup for determination of j_{CH_3I}

monochromator (Oriel, Cornerstone 260 1/4 m) is used to select a monitoring wavelength of 265 nm. The throughput intensity is detected using a photomultiplier tube (PMT) (Hamamatsu Photonics K.K., R4315) mounted at the exit slit of the monochromator and the PMT signal (which corresponds to the measured intensity) is logged using a 16-Bit datalogger (Campbell 21X). A chart recorder connected in parallel to the datalogger provides a visual display of the PMT signal for live monitoring of the progress of photolysis. The wavelength scale of the monochromator is calibrated prior to the measurement of j_{CH_3I} using a Hg pen-ray (UVP) by reference to the Hg spectral lines at 248.2 nm, 253.65 nm, 296.73 nm, 302.15 nm, 312.57 nm and 313.17 nm (UVP Pen-Ray Rare Gas Lamp Spectra datasheet), the results illustrated in Figure 3.36.

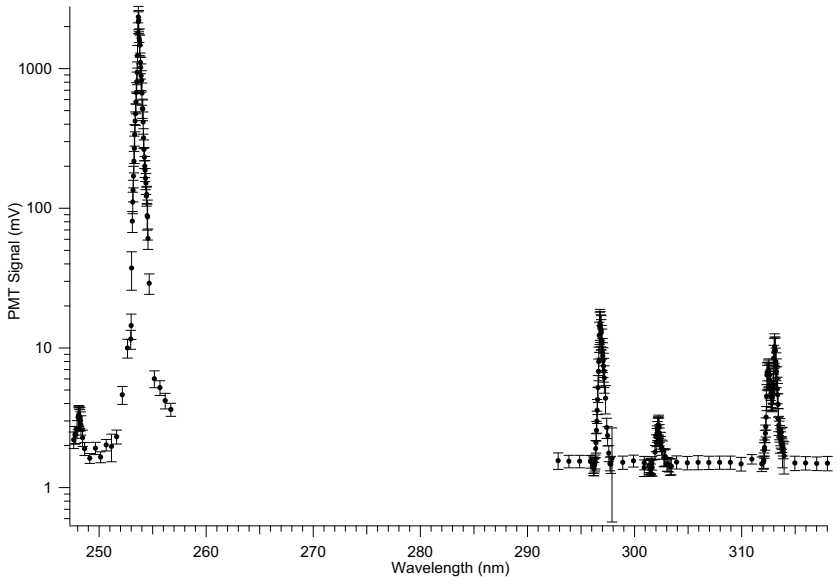

Figure 3.36: Measured spectrum of Hg Pen-ray on calibrated monochromator wavelength scale (monochromator resolution ≤ 0.5 nm)

Initially the monochromator was set to the reference wavelength of 265 nm with the shutter closed and the reference lamp was switched on. Following an extended period of flushing with synthetic air (BOC BTCA178 zero grade air) controlled using a MFC (Tylan FC260, 5 slpm range) opening the shutter allowed measurement of the throughput intensity from the reference lamp without CH_3I

present in the cell (I_0). Switching on the photolysis lamp allowed measurement of the stray light signal, typically 1-5%. Liquid CH_3I was injected into a capillary diffusion tube held at approximately 25°C in a water bath producing CH_3I vapour with sufficient vapour pressure to pass through the capillary. By redirecting the air flow over the capillary tube head space the vapour was picked up and diluted allowing varied CH_3I concentrations to be achieved. The mixture was flowed to exhaust initially to allow mixing and to prevent an initial pulse in CH_3I concentration. With the photolysis lamp switched off the mixture was then directed to the photolysis cell via 1/4" OD PFA tubing, and by observing the steady drop in throughput intensity, the concentration of CH_3I introduced could be chosen. Once the desired level of attenuation was achieved (typically when $I_{[CH_3I]=[CH_3I]_0} \geq 0.8I_0$) the cell was then closed using Swagelok stainless steel taps. The attenuation of the reference lamp was then monitored over time after switching on the photolysis lamp.

Significant photolysis of the CH_3I mixture by the reference lamp was ruled out by observing the change in the throughput signal over time without the photolysis lamp switched on. Stray 265 nm light from the photolysis lamp reaching the PMT was further tested by measuring a dark signal without the reference lamp switched on and switching the photolysis lamp on and off. Even though there is a Hg emission line at 265.2 nm its intensity is much less than the 253.65 nm line, and the deuterium reference lamp offers continuous emission through the UV and its intensity is greater at this wavelength. The PMT spectral response is peaked in the range 200-275 nm and the absorption cross section of CH_3I as mentioned peaks around 258 nm. By monitoring at 265 nm we gain the most out of the detector response and the cross section of CH_3I, while avoiding stray light from the strong 253.65 nm Hg line. The 253.65 nm line dominates the photolysis since while the quantum yield for photolysis, ϕ, is 1 over the range 210-360 nm (Atkinson *et al.*, 2008), no other Hg line matches the peak in the cross section so well.

Non-linearity was observed in the relationship (Equation 3.79) when taken over longer timescales

and particularly after several experiments had been performed; flushing with synthetic air between experiment runs improved the situation. The reason is thought to be related to the buildup of reaction products that absorb in the region of 265 nm during the j_{CH_3I} calibration experiment owing to the high levels of CH_3I used and the mixture being contained within the photolysis cell. For this reason the fitting of the experimental data using Equation 3.79 to determine j_{CH_3I} from the gradient was performed only over the first 100-200 s of each experiment. In practice there is no buildup of reaction products in chain length calibrations since the CH_3I concentrations are very low (pptV) and the CH_3I mixture flows through the photolysis cell. The results of ten repeat experiments with the calibration unit PHOSTO-1 are given in Table 3.7, the value of j_{CH_3I} applied was derived from the average of these repeats.

Experiment run	$j_{CH_3I} \pm 1\sigma$ (s^{-1})
1	$7.2974\times10^{-3}\pm5.27\times10^{-5}$
2	-
3	$5.6578\times10^{-3}\pm3.94\times10^{-5}$
4	$5.1686\times10^{-3}\pm3.36\times10^{-5}$
5	$5.174\times10^{-3}\pm5.13\times10^{-5}$
6	$5.3189\times10^{-3}\pm4.78\times10^{-5}$
7	$5.0978\times10^{-3}\pm5.82\times10^{-5}$
8	$4.9525\times10^{-3}\pm2.57\times10^{-5}$
9	$4.8969\times10^{-3}\pm9.45\times10^{-5}$
10	$4.8449\times10^{-3}\pm5.61\times10^{-5}$
Average $j_{CH_3I} \pm 1\sigma$ (s^{-1})	$5.38\times10^{-3}\pm7.60\times10^{-4}$

Table 3.7: Results of j_{CH_3I} calibration of radical source unit PHOSTO-1

3.5 Data workup and error analysis

As described, the dual channel PERCA technique used by the University of Leicester group is indirect and reliant on two steps; the production of NO_2 through a radical initiated chain reaction and the

detection of this NO_2 from luminol NO_2 chemiluminescence. These steps carry their own uncertainties and contribute to the total uncertainty. Additional uncertainty is introduced by interferences experienced when measuring under ambient conditions and not revealed under standard calibration conditions which may affect the efficiency of either the NO_2 detection or the chain chemistry (e.g. humidity); of course these interferences have to be identified first. A further complication is that the amplified NO_2 is produced on top of an ambient background level including both NO_2 and O_3, so the amplified signal has to be at level sufficient to distinguish detection from background noise and variability. In polluted environments where the background is high and variability enhanced, the process of signal averaging and background subtraction can lead to erroneous results if the averaging period is longer than the timescale of variability, though this is dependent on the background subtraction methodology. Using a single channel technique whereby the background is only measured periodically this is certainly true since the measurement period includes the averaging of two "background measurement mode" cycles and a "chain amplification mode" cycle; the timelength of this duty cycle (1.5-3 minutes) is significant. In a dual channel measurement the background and amplified NO_2 are measured simultaneously on two separate channels which should remove this type of error. The uncertainty in the dual channel technique is therefore determined by the uncertainty in the matching of the two channels i.e. the accuracy and precision of each channel.

The accuracy of the instrument is primarily dependent on the uncertainty in the calibration of the NO_2 detector response to known NO_2 concentrations and the uncertainty in the inlet chain length under typical radical concentrations. Beyond this any calibrations to correct how the measurement efficiency changes under changing ambient conditions then contribute to the accuracy in the determined concentrations. Precision describes the reproducibility of the instrument response at a given concentration under fixed conditions, which is easily quantified from calibrations. To be useful the response should also be reproducible at varying ambient conditions. At the limit it is also neces-

sary to be able to describe the lowest possible concentration measurable with certainty (the detection limit); this is determined by the resolution of the NO_2 detector signal but more so by the point at which the amplified NO_2 signal is indistinguishable from the underlying noise (instrumental and NO_2 background).

3.5.1 Data workup

To understand how the various sources of uncertainty combine, it is necessary to understand how the raw data are processed and combined to derive the radical signal. The raw signals are currently sampled at 1 Hz, though higher frequency sampling is possible and potentially beneficial in improving instrumental signal to noise. The methodology described here for combining the data is that used by the University of Leicester Atmospheric Chemistry group for deriving single and dual channel PERCA data, except the correction functions for humidity and the NO_2 sensitivity for aircraft measurements are from this work.

For both a single channel workup and a dual channel workup the first step involves the averaging and interpolation of the "background measurement mode" and "chain amplification mode" cycles from each channel. For each cycle period this entails determining the mean of the signal from 5 seconds after a switch to 5 seconds before, such that the switching periods are excluded.

$$\overline{V} = \sum_{i=5}^{i=n-5} \frac{V_i}{n-10} \tag{3.80}$$

Linear interpolation is used to fill in between the average values, and the midpoint between the "background measurement mode" and "chain amplification mode" averages is determined from the interpolated averages.

$$\overline{V}_{mid,i} = \frac{\overline{V}_{amp-interp,i} + \overline{V}_{back-interp,i}}{2} \tag{3.81}$$

For a single channel analysis the radical signal is derived by using the interpolated background average to background subtract from the non interpolated amplification average. The resulting data are scaled

to $\Delta[NO_2]$ units and then radical units by dividing by the NO_2 sensitivity ($Sens = \frac{dV}{d[NO_2]}$) and the chain length ($CL$). Further filtering can be applied to remove spikes due to instrumental variability (such as due to luminol flow instability) and averaging can be used to improve the signal to noise. Point by point correction factors (CF_{CL}) for the affect of humidity on the chain length may be derived from concomitant humidity data and applied by multiplying into the derived radical data.

$$[RO_x]_{single-channel,i} = \frac{\overline{V}_{amp,i} - \overline{V}_{back-interp,i}}{Sens \times CL} \times CF_{CL} \tag{3.82}$$

For dual channel data the calculated interpolated midpoint averages for each channel are subtracted from the raw signal to zero the data and remove the overall background trend. The result is a signal that modulates about zero, positive during "chain amplification mode" and negative during "background measurement mode".

$$V_{zero,i} = V_i - V_{mid,i} \tag{3.83}$$

The peak to peak amplitude represents the total signal at all times, essentially the single channel measurement. The data from the two channels is scaled to $\Delta[NO_2]$ units and then radical units by dividing by the NO_2 sensitivity ($Sens$) and the chain length (CL) corresponding to each channel, then combined by taking the difference.

$$[RO_x]_{dual-channel,i} = \left\{ \frac{V_{zero,ch1,i}}{Sens_{ch1} \times CL_{ch1}} - \frac{V_{zero,ch2,i}}{Sens_{ch2} \times CL_{ch2}} \right\} \times CF_{CL} \tag{3.84}$$

Since the detection channels measure out of phase, subtraction results in a $[RO_x]$ signal that modulates about zero depending on which channel was in which mode. When the channel in "background measurement mode" is subtracted from the channel in "chain amplification mode" the result is positive and the amplitude is the measured $[RO_x]$ concentration, when the channel in "chain amplification mode" is subtracted from the channel in "background measurement mode" the result is negative and the amplitude is the measured $[RO_x]$ concentration (though negative). The dual channel signal is then averaged and where the mode has meant the signal subtraction resulted in negative data the result is inverted.

Combining the signals from two channels using the interpolated midpoints and scaling each to radicals prior to subtraction essentially means both channels contribute in the calculation of the background and the amplification signal at all times. The natural alternative is to use one channel to contribute the total amplification signal while the other contributes the total background and *vice versa* when the modes switch. However, by subtracting the midpoint half the amplification signal is contributed by the channel in "chain amplification mode" and the other half is estimated from the average of the preceding and following amplification measurements from the channel in "background measurement mode". Likewise, half the background signal is contributed by the channel in "background measurement mode" and the other half is estimated from the average of the preceding and following background measurements from the channel in "chain amplification mode". The benefit in this approach to combining the data from two channels is that subtraction of the midpoint is effective in removing the background trend and any relative drift in the baseline signal.

The along flight track NO_2 sensitivity has been calculated from the ratio of the interpolated background average signal to the calculated NO_2 background for each channel.

$$Sens_i = \frac{\overline{V}_{back,i}}{[\mathrm{NO_2}]_{calc,i}} \tag{3.85}$$

Where the instrument has been operated on the ground, periodic NO_2 sensitivity calibrations are carried out to determine the NO_2 sensitivity on a regular basis to check for drift.

3.5.2 Components of uncertainty

The components of the uncertainty in the PERCA measurement are broken down in Table 3.8, the components are then quantified in Table 3.9. The error in the background subtraction can be estimated from the precision of the measurement of NO_2 at a fixed concentration which is definable from NO_2 sensitivity calibrations. Further, the error in the amplified signal at a fixed concentration of radicals can be estimated from the precision of the measurement of $[CH_3O_2]$ from chain length

Uncertainty component	Subcomponents
Background subtraction	Precision at fixed $[NO_2]$
	Precision at fixed $[CH_3O_2]$
NO_2 detection	NO_2 sensitivity ($\frac{dV}{dNO_2}$)
	Stability of luminol flow
	Luminol thermal stability
$\frac{dV}{dNO_2}$	Calibration NO_2 concentration ($[NO_2]$)
$[NO_2]$	NO_2 calibration permeation tube output
	Calibration dilution flows
Chain length	NO_2 sensitivity during chain length calibration
	Calibration CH_3O_2 concentration ($[CH_3O_2]$)
$[CH_3O_2]$	CH_3I calibration permeation tube output
	Photolysis rate of CH_3I (j_{CH_3I})
	Residence time in photolysis cell ($t_{res.}$)
($t_{res.}$)	Photolysis cell volume
	Calibration dilution flows
Humidity correction	τ_{CL}
	Relative humidity

Table 3.8: Sources of measurement uncertainty in PERCA

calibrations. The typical precision determined from these calibrations is $\sim 2\%$, and the combined uncertainty is $\sim 3\%$. The uncertainty in the parameters used to calculate the calibration concentrations of NO_2 and CH_3O_2 in NO_2 sensitivity and chain length calibrations dictates the overall accuracy. Further uncertainty in the concentration of peroxy radicals measured is introduced due to the interference of humidity with the chain length. The error in the fit coefficient of the humidity correction function therefore contributes to the accuracy. For the aircraft PERCA measurements where the NO_2 sensitivity has been calibrated through the calculated background NO_2 produced from ozone, the accuracy is dependent on the uncertainty in the calculated NO_2 concentration. The components used in calculation of the NO_2 concentration are the ozone concentration (5%, accuracy of TECO 49C instrument from (Fehsenfeld *et al.*, 2006)), the reagent NO concentration (2%, from precision of reagent flow control), the rate constant k_{O_3+NO} (10% at 298 K, (Sander *et al.*, 2006)) and the reaction time (5%, estimated). All errors are combined using the propagation of errors:

$$\sigma_f^2 = \left(\frac{\partial f}{\partial u_1}\right)^2 \sigma_{u_1}^2 + \left(\frac{\partial f}{\partial u_2}\right)^2 \sigma_{u_2}^2 + \ldots + \left(\frac{\partial f}{\partial u_n}\right)^2 \sigma_{u_n}^2 \tag{3.86}$$

Uncertainty component	Subcomponents	Contribution (2σ)
NO_2 detection	NO_2 sensitivity ($\frac{dV}{dNO_2}$)	2%
	Calculated [NO_2]	21%
Chain length	Photolysis rate of CH_3I (j_{CH_3I})	28%
	CH_3I calibration permeation tube output	4%
	Residence time in photolysis cell ($t_{res.}$)	5%
	Calibration dilution flows	2%
	Nitrogen carrier flow	6%
Humidity correction	Fit coefficient τ	6%
Total uncertainty		37%

Table 3.9: Measurement uncertainty in PERCA 4 during AMMA

The accuracy of ground NO_2 calibrations is dictated by the NO_2 permeation rate ($2\sigma \sim 2\%$), calibration dilution flows ($2\sigma = 2\%$, from precision of mass flow control) and the nitrogen carrier flow ($2\sigma \sim 6\%$) giving a combined total uncertainty of $\sim 7\%$. This is much better than the accuracy of the

calculated NO_2 from background ozone used in calibration of the aircraft measurements due to the high accuracy of the calibrated permeation rate and precision of the dilution flows. However in ground based ambient measurements the sensitivity varies due to variation in the luminol flow and thermal stability (Parker, 2007) which makes the total uncertainty greater ($\sim$ 20%, following Parker (2007)). The along flight track sensitivity method determines the sensitivity at every point so sensitivity drift does not add to the uncertainty.

3.6 Chapter 3 Summary

This chapter has summarised the current setup of the University of Leicester PERCA instruments (see Section 3.1) and presented standard experimental work used in the calibration and characterisation of the University of Leicester PERCA instrumentation, along with a number of significant new experimental and analytical results. The main purpose of the work in this chapter has been to attempt to resolve several outstanding issues in terms of understanding the instrument performance in the field, and further issues that became apparent during the fieldwork undertaken in the past 3 years. These issues include the changing sensitivity of the instrument with altitude (chain length and NO_2 sensitivity) and with operating in humid environments.

The calibration of chain length and NO_2 sensitivity are discussed in Sections 3.2.1 and 3.3.2 respectively. The characterisation of the radical calibration units, NO_2 and CH_3I reference standards is covered in Section 3.4. The processing of raw data to derive the radical signal and measurement uncertainty are discussed in Section 3.5.

Further work includes a modelling study of the chain length dependence on reagent concentration and with variation in the gas phase kinetics due to temperature and pressure such that an altitude dependence may be understood. The variation in the chain length with reagent concentration and

altitude is discussed in terms of the timescale for the chain to terminate, the absolute chain length achieved and the relative change in chain length compared to ground level. The altitude dependence calculated was validated by comparison to previous field work (see Section 3.2.2).

An experimental study to characterise the dependence of the chain length with humidity under enhanced levels as observed in the tropics is discussed in Section 3.2.3. The correction function derived was shown to be consistent with the previous work of Salisbury (2001), Salisbury *et al.* (2002) and explained the temperature dependence of the relationship in terms of specific humidity derived in that work as being consistent with a constant relationship with relative humidity. This result shows that this work and the previous work of Salisbury (2001), Salisbury *et al.* (2002) are entirely consistent with the published results of other groups. An analytical explanation for the functional dependence of the chain length on humidity has been derived and used to offer an explanation for the varied sensitivity to humidity between PERCA instruments and related techniques. A significant change in the NO_2 sensitivity of the LMA-3 Scintrex was observed, leading to a near linear decrease in response with increasing humidity. This is important both in terms of the application of this NO_2 detection technique applied to PERCA but where luminol chemiluminescence is used in commercial applications for measurements of NO_x.

The inflight calibration of the aircraft PERCA instruments NO_2 sensitivity has proven difficult and required an alternative procedure to be adopted. It has been shown that the NO_2 sensitivity is essentially invariant with altitude (beside issues related to disturbances and reduction in luminol flow) by comparing the raw background signal measured to the ambient NO_2 background calculated from the reaction of ambient O_3 with reagent NO. This has required both the temperature dependence of the rate constant and the temperature and pressure dependence of the volume flow rate of the sample flow to be accounted for. The calculation has been derived in Section 3.3.3.

Chapter 4

Airborne Measurement of photolysis frequencies through radiometry

This chapter documents the work carried out to measure photolysis frequencies through the technique of filter radiometry on board the NERC/Met Office BAe-146 (described in Chapter 5, Section 5.1). The background to the technique is described in terms of the theoretical framework and a description of the design and use of the instruments. The technique of filter radiometry is compared to other instrumental techniques used in the measurement of photolysis frequencies. The experimental work carried out to characterise the instruments is described in detail, particularly the errors introduced through non linearities in the calibration of the measurements. A summary of the instruments performance in the field is provided, along with a discussion of the identification of measurement issues and attempts to resolve these.

4.1 Measurements of photolysis frequencies in the atmosphere

The measurement of the photolysis frequencies (otherwise known as photodissociation or photolysis rates) of atmospheric trace species is of clear importance to the interpretation of field measurements of atmospheric chemistry. Many of the chemical cycles which determine the trace composition of the atmosphere are driven through photochemical activity (see Section 1.2.2 of Chapter 1). It is possible to model the solar radiation field (e.g. the Tropospheric Ultraviolet Visible (TUV) model of Madronich & Flocke (1998)) at a given place and time through knowledge of the Earths orbit with respect to the Sun, the intensity of sunlight at the top of the atmosphere and by allowance for the vertical profiles of atmospheric absorbers and scatterers and factors such as surface albedo. However, the characteristics of the atmosphere are temporally and spatially variant (e.g. variability in ozone column density, aerosol loading, surface albedo, the presence and absence of cloud), meaning the solar radiation field is readily perturbed and these parameters cannot be easily defined even in complex atmospheric models. Hence, local measurements of solar radiation are essential to characterise the variability to aid the interpretation of measurements of chemical composition with photolysis rates.

4.1.1 Background theory

The photodissociation of a species AB is a first order process with rate coefficient $j_{(AB)}$.

$$AB + h\nu \rightarrow A + B \tag{4.1}$$

The rate coefficient defined as:

$$j_{(AB)} = \frac{1}{[AB]} \frac{d[AB]}{dt} \tag{4.2}$$

Equation 4.2 leads to a method for derivation of the photolysis frequency, from measurement of the rate of change of the concentration of the parent species or the products, a method commonly referred to as chemical actinometry (see Section 4.1.2).

In the atmosphere the photolysis frequency is determined by the availability of light from all directions of the correct frequency to cause a species to dissociate, the probability of interaction and given that the probability of dissociation. The first term is described by a quantity known as the (spectral) actinic flux, $F(\lambda)$ (photons $\mathrm{nm^{-1}cm^{-2}s^{-1}}$ where the energy per photon is $\frac{hc}{\lambda}$), which is found by integrating the spectral radiance, $L(\lambda, \theta, \phi)$ (photons $\mathrm{nm^{-1}cm^{-2}s^{-1}sr^{-1}}$), over all angles:

$$F(\lambda) = \int_{\phi} \int_{\theta} L(\lambda, \theta, \phi) \sin(\theta) d\theta d\phi \tag{4.3}$$

The spectral radiance describes the "amount" of light incident onto an atmospheric layer, its wavelength and directional dependencies (θ and ϕ being the polar and the azimuthal angles of incidence of the photon interacting with the parent molecule (Hofzumahaus *et al.*, 1999)). The probability of interaction between the molecule AB and a photon is described using the absorption cross section, $\sigma_{(AB)}$. The probability that the molecule will dissociate is described using the quantum yield for dissociation, $\phi_{(AB)}$ (not to be confused with the azimuthal angle ϕ). A "working equation" used for the calculation of $j_{(AB)}$ in terms of these parameters (Madronich, 1987), is given by:

$$j_{(AB)} = \int_{\lambda_{min}}^{\lambda_{max}} \sigma(\lambda, T, P)_{(AB)} \phi(\lambda, T, P)_{(AB)} F(\lambda) d\lambda \tag{4.4}$$

To evaluate Equation 4.4 for a given photolysis process then requires laboratory measurements of the quantum yield and absorption cross section in the appropriate temperature, pressure and wavelength range, and a measurement of the actinic flux. This leads to techniques for derivation of the photolysis frequency from measurement of the actinic flux, through methods commonly referred to as filter and spectral radiometry (see Sections 4.1.3 and 4.1.4 respectively).

Ozone photolysis to form excited $O(^1D)$ followed by reaction of $O(^1D)$ with water vapour is a primary process in the formation of the OH radical (see Section 1.2.2, Chapter 1). The photolysis of NO_2 followed by reaction of the product $O(^3P)$ with O_2, leads to the formation of tropospheric ozone (see Section 1.2.2). As discussed in Section 1.2.1, Chapter 1, the atmospheric cut-off for tropospheric photochemistry is $\lambda \geq 290$ nm, limited owing to absorption at higher altitudes primarily by stratospheric

ozone and O_2. Stratospheric absorption limits NO_2 photolysis to the formation of $O(^3P)$ atoms in the troposphere (Atkinson *et al.*, 2004), however, there are a number of possible fragmentation pathways available in the UV/visible photolysis of ozone. These are given by Reactions 4.5-4.9 (Matsumi *et al.*, 2002):

$$O_3 + h\nu(\lambda < 310 \text{ nm}) \rightarrow O(^1D) + O_2(a^1\Delta_g) \tag{4.5}$$

$$O_3 + h\nu(\lambda < 411 \text{ nm}) \rightarrow O(^1D) + O_2(X^3\Sigma_g^-) \tag{4.6}$$

$$O_3 + h\nu(\lambda < 463 \text{ nm}) \rightarrow O(^3P) + O_2(b^1\Sigma_g^+) \tag{4.7}$$

$$O_3 + h\nu(\lambda < 612 \text{ nm}) \rightarrow O(^3P) + O_2(a^1\Delta_g) \tag{4.8}$$

$$O_3 + h\nu(\lambda < 1180 \text{ nm}) \rightarrow O(^3P) + O_2(X^3\Sigma_g^-) \tag{4.9}$$

The spin-allowed pathways, Reactions 4.5 and 4.9, dominate the quantum yield in the Hartley band at λ <300 nm (Matsumi *et al.*, 2002). For wavelengths greater than 300 nm (the Huggins band) the dominant processes are photolysis of internally excited ozone (Reaction 4.5) and the spin-forbidden process, Reaction 4.6. The absorption cross section for ozone photolysis becomes too small for significant production of $O(^1D)$ at wavelengths greater than 340 nm, although the quantum yield is non-zero (Matsumi *et al.*, 2002).

The convolution of the quantum yield ($\phi_{(O^1D)}$) and cross section ($\sigma_{(O_3)}$) of ozone photolysis to form excited $O(^1D)$ atoms, with a typical spectral actinic flux ($F(\lambda)$) available in the troposphere, shows that the photolysis rate j_{O^1D} peaks for wavelengths in the region 290-320 nm (the wavelength band corresponding to UVB). Likewise, the rate of NO_2 photodissociation, j_{NO_2}, peaks for wavelengths in the region 310-420 nm (corresponding approximately to UVA wavelengths). An example of the wavelength dependence of the photolysis rate is shown in Figure 4.1 adapted from Kraus & Hofzumahaus (1998).

For the photolysis of NO_2 to a good approximation the quantum yield and cross section are insensitive

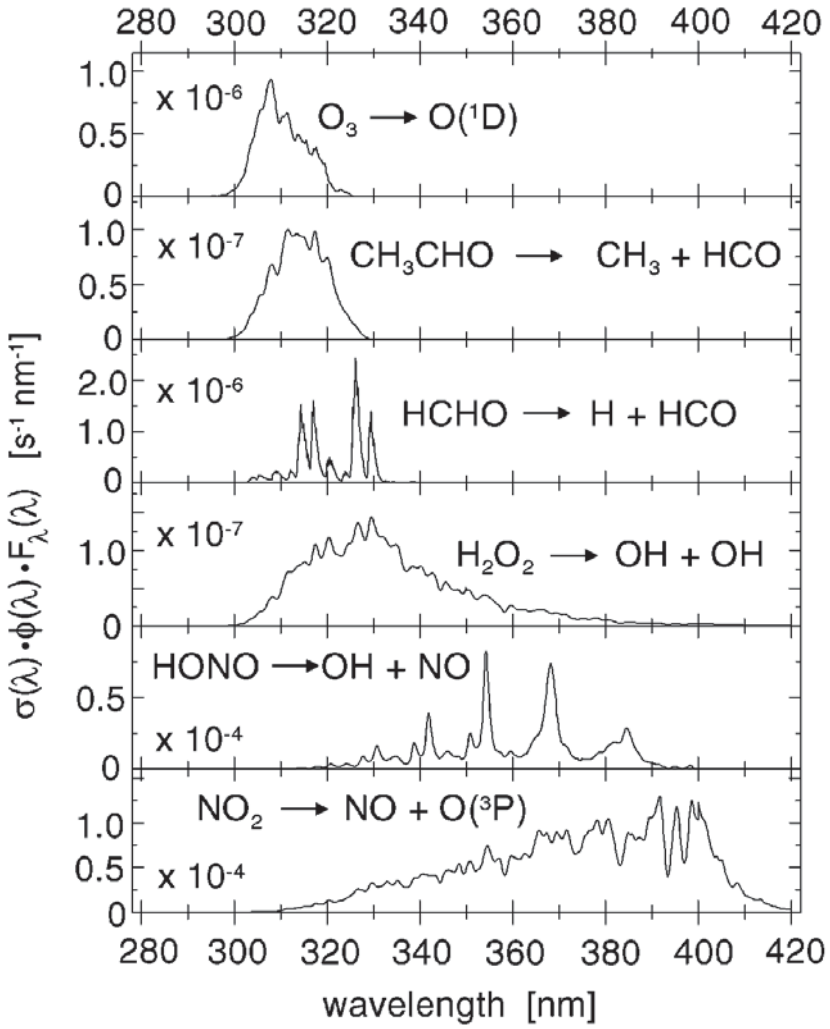

Figure 4.1: Wavelength dependence of selected photolysis rate coefficients for $\chi = 53^o$ measured during POPCORN 1994 (Kraus & Hofzumahaus, 1998).

to temperature (Volz-Thomas *et al.*, 1996), furthermore the spectral form of $F(\lambda)$ in the UVA is largely insensitive to changes in solar zenith angle (SZA) (Volz-Thomas *et al.*, 1996). However, for the photolysis of ozone to O(^{1}D) both the quantum yield and cross sections exhibit significant temperature dependencies. An additional complication occurs in that the spectral form of $F(\lambda)$ in the UVB is strongly dependent on changes in SZA and overhead ozone column density owing to absorption by stratospheric ozone. Therefore the spectral form of j_{O^1D} as shown in Figure 4.1 is variable.

As mentioned the transmission of radiation through the atmosphere is further complicated by the presence of atmospheric absorbers and scatterers and factors such as surface albedo. The actinic flux is often discussed as a sum of direct and diffuse components i.e. the direct solar beam and the diffuse light produced by scattering and albedo. The diffuse component is often split into an upwelling (diffuse radiation coming from all directions in the lower 2π sr of a spherical field of view) and downwelling component (diffuse radiation coming from all directions in the upper 2π sr of a spherical field of view). Hence:

$$F_{tot}(\lambda) = F_0(\lambda) + F_{\downarrow}(\lambda) + F_{\uparrow}(\lambda) \tag{4.10}$$

where $F_0(\lambda)$ represents the direct component of the actinic flux, $F_{\downarrow}(\lambda)$ represents the downwelling diffuse component and $F_{\uparrow}(\lambda)$ the upwelling diffuse component. The diffuse components are given by:

$$F_{\downarrow} = \int_0^{2\pi} \int_0^{\frac{\pi}{2}} L(\lambda, \theta, \phi) \sin(\theta) d\theta d\phi \tag{4.11}$$

$$F_{\uparrow} = \int_0^{2\pi} \int_{-\frac{\pi}{2}}^{0} L(\lambda, \theta, \phi) \sin(\theta) d\theta d\phi \tag{4.12}$$

It is useful to separate the actinic flux in this way since it provides a way to separate the various factors influencing the actinic flux at any one point. For example, the direct component is then represented more simply by only having to consider scattering and absorption along the path of the direct solar beam through the atmosphere. The diffuse components are related to the direct component since they are produced from the scattering of direct sunlight such that diffuse solar radiation reaches a point by a complicated path. By separation of the diffuse components it allows some simplification since,

for example, near to the ground the upwelling component is largely impacted by surface albedo while the downwelling component may be more largely impacted by cloud and Rayleigh scattering. Owing to multiple scattering, the upwelling and downwelling components are still somewhat interrelated.

Clouds can both absorb and scatter incident solar radiation and hence can either decrease the actinic flux through attenuation of direct and diffuse sunlight, or increase the actinic flux by enhancement of diffuse sunlight. The net effect will be dependent on the measurement regime e.g. whether at the surface or at altitude, whether inside, below or above cloud; it will also depend on the characteristics of the cloud environment (clear, broken or overcast) and the relative position of the sun. Madronich (1987) used a simple model to examine the affect on actinic flux for the case of large uniform isolated clouds, of varying optical thickness, which do not absorb but are sufficiently optically thick such that any transmitted light is fully diffuse, and for varying surface albedo. Above cloud the actinic flux was always enhanced as a result of the combination of the incident direct and downwelling diffuse sunlight, the diffuse sunlight from scattering at the cloud top, and the sunlight which has been transmitted to the surface, undergone reflection and then been transmitted back up through the cloud. Below cloud the actinic flux was predicted to be reduced in most cases owing to the reduction in transmitted light as a result of diffuse reflection of incident sunlight at the cloud top (the cloud albedo). Interestingly, for the most optically thin cloud (where complete diffusion of transmitted light was still valid) the actinic flux was calculated to be enhanced below the cloud for a low SZA. In this case the cloud albedo was low enough that sufficient light could be transmitted and owing to the conversion of the direct sunlight to diffuse this lead to a net enhancement of the actinic flux. Madronich (1987) also predicted that for sufficiently optically thick clouds the actinic flux increases from the base of the cloud to the top, and peaks before the cloud top. These predicted relationships were observed in measurements in the recent INSPECTRO field campaign (Kylling *et al.*, 2005), with a maximum in actinic flux observed just below cloud top with the strength of the enhancement greatest for low SZA's.

The wavelength dependence of Rayleigh scattering means that UVB radiation is more easily scattered than UVA by air molecules. This leads to a greater component of diffuse radiation contributing to the j_{O^1D} actinic flux than it does for j_{NO_2}, and the expectation of greater susceptibility of j_{NO_2} to attenuation by cloud (Crawford *et al.*, 1999). Indeed, Crawford *et al.* (1999) did observe marginally greater variability in aircraft measurements of j_{NO_2} than in j_{O^1D} in cloudy conditions, however this behaviour was not consistent since j_{O^1D} was more changeable at times. In the lowest 1 km of their observations, larger magnitude changes in measured photolysis rates were seen but the median change in j_{NO_2} was only 4% greater than in j_{O^1D}. At 10-12 km altitude the median change in j_{NO_2} was 19% greater than in j_{O^1D} but the magnitude of changes were much less. This was seen as indicative of the change by altitude in the relative amounts of direct and diffuse radiation, where diffuse radiation is more significant at low altitudes. Changes in the relative amounts of direct and diffuse actinic flux do therefore follow some reproducible and understandable trends which can help in the interpretation of variability in the j_{O^1D} and j_{NO_2}. Monks *et al.* (2004) also noted enhanced transmission of shortwave radiation from measurements under cloudy conditions, however the impact on j_{O^1D} and j_{NO_2} was variable with attenuation of j_{O^1D} sometimes exceeding j_{NO_2}. Owing to the complexity of the cloud environment, careful consideration is required to explain deviations from these simple trends, and the potential impacts of cloud on photochemistry.

4.1.2 Chemical actinometry

The principle of the technique of chemical actinometry is described in the review of Clemitshaw (2004) and the detailed introduction to Shetter & Muller (1999). A recent application of this technique to the measurement of the photolysis rate of nitrogen dioxide (j_{NO_2}) during the IPMMI (International Photolysis frequency Measurement and Modelling Intercomparison) campaign is described by Shetter *et al.* (2003). The molecule of interest is exposed to the solar radiation field within some form of photolysis cell (e.g. a quartz flow tube, static tube or bulb), the photolysis rate can then be determined

by measurement of the photodissociation products. In this sense the technique is independent of the molecular properties (quantum yield and cross section) of the molecule of interest so is more direct and therefore at an advantage. Its accuracy is largely determined by the technique used to measure the photodissociation products concentration as a function of time. For example, for the measurement of j_{NO_2}, NO_2 flowing in an O_2 rich mixture is photolysed, the product $O(^3P)$ then reacts with O_2 to form ozone while the product NO may be measured by an NO chemiluminescence detector. The NO concentration is then a measure of the amount of NO_2 photolysis (Shetter *et al.*, 2003). The time resolution is limited by the sampling process, typically being from 2s to 60min (Shetter *et al.*, 2003), longer sampling times being a significant disadvantage compared to the radiometric techniques. Further limitations are the need for a separate system to measure each photolysis rate and the size of such an instrument. All these limitations make the technique less suitable for remote field measurements and aircraft deployment. The technique has been largely employed in the measurement of j_{O^1D} and j_{NO_2}, the measurement of the photolysis rates of some alkyl nitrates are also reported e.g. Luke & Dickerson (1988), Luke *et al.* (1989).

4.1.3 Filter radiometry

Filter radiometers have been widely employed in the measurement of the photolysis rates of ozone (j_{O^1D}) and nitrogen dioxide (j_{NO_2}). These processes have been targeted owing to their importance in the formation of the OH radical and tropospheric ozone formation respectively (see Section 1.2.2). Recent application in the measurement of the photolysis rate of the nitrate radical has also been reported e.g. Stark *et al.* (2007). The choice of band pass filters and photoelectric detectors dictates the spectral sensitivity of such instruments and by matching this to the convolution of the quantum yield (ϕ) and cross section (σ) of the photolysis process allows conversion of the measured signal to a photolysis rate. The benefit of such instruments is through their simplicity, portability and fast and sensitive response, which makes them particularly useful for applications such as aircraft

measurements. The drawbacks to the technique are the need for more than one instrument to measure more than one photolysis process, and the requirement for careful matching of the spectral response for the particular photolysis process. This is complicated for the measurement of j_{O^1D} where the product of absorption cross section and quantum yield is variable as described already. A description of the filter radiometers of the University of Leicester Atmospheric Chemistry Group is given here and provides an example of such instrumentation. The calibration and characterisation of these instruments is then described in Section 4.2.

The University of Leicester j_{O^1D} and j_{NO_2} filter radiometers

The design and characteristics of the University of Leicester aircraft j_{O^1D} filter radiometers have been described in particular by Phillips (2002), while the filter radiometers used for the measurement of j_{NO_2} are described in detail by Volz-Thomas *et al.* (1996). To summarise, these instruments are based on the original prescription of Junkermann *et al.* (1989) but with modifications appropriate for operation on board an aircraft following Volz-Thomas *et al.* (1996). A schematic of the design of the j_{O^1D} filter radiometers adapted from Phillips (2002) is shown in Figure 4.2. The instruments receive incident light through a hemispherical, polished quartz dome, and within this a series of sandblasted quartz domes acts to diffuse the incident light. By way of multiple reflections, scattering and refraction, this optical collection system transmits light incident near equally from all angles to provide a full 2π sr field of view. A concentric light shield surrounds the quartz dome to provide an artificial horizon and allows the optimisation of the field of view to 2π sr. The efficiency with which such an optic transmits light incident from different directions dictates the angular response; an ideal entrance optic would exhibit an isotropic response over all angles and Phillips (2002) and Volz-Thomas *et al.* (1996) report close to ideal behaviour for these instruments (the angular response of these instruments has not been determined within this work owing to the lack of an appropriate calibration facility). Hofzumahaus *et al.* (1999) report also that for such an entrance optic there is no

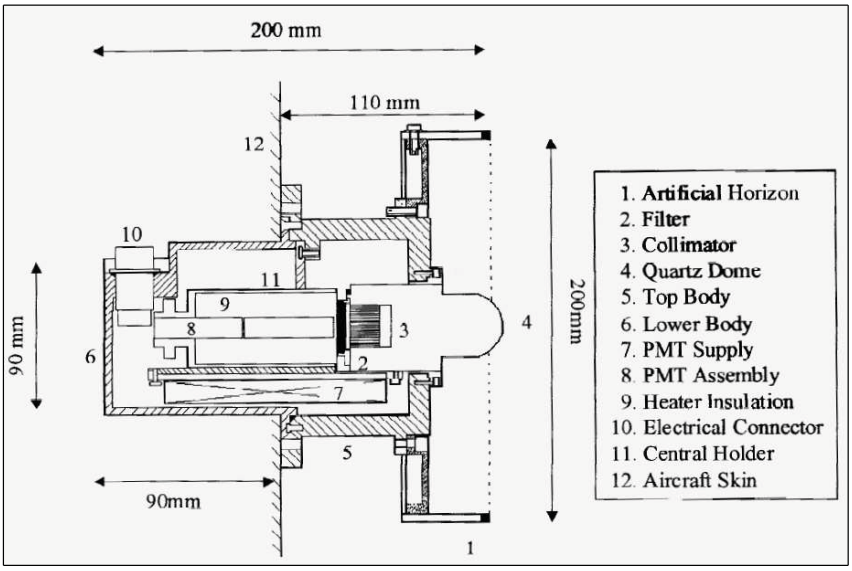

Figure 4.2: Design of the j_{O^1D} aircraft filter radiometer – Adapted from Phillips (2002)

significant wavelength dependence on the angular response, although the light shield can introduce a wavelength dependence unless painted matt black.

The light is guided to an optical filter (j_{O^1D} – bandpass filter BP-35-7921 metal-dielectric-metal filter (Ealing) (Phillips, 2002); j_{NO_2} – a combination of a 2 mm and 1 mm band pass filters with peak transmission/FWHM of 385/110 nm and 320/165 nm respectively (Volz-Thomas *et al.*, 1996)) before the detector (j_{O^1D} – R1893 solar blind PMT (Hamamatsu) (Phillips, 2002); j_{NO_2} – R840 photodiode (Hamamatsu) (Volz-Thomas *et al.*, 1996)) by way of a quartz rod collimator within the innermost dome. The spectral response of each instrument is dictated by the combination of filters and photoelectric detectors (the spectral response of these instruments could not be determined within this work owing to uncertainty with regard to irradiance standards and the spectral sensitivity of the spectral radiometer used in cross calibration of the aircraft filter radiometers (see Section 4.2.3)). An internal heater is incorporated within the j_{O^1D} filter radiometers to stabilise the response of the PMT. A combination of two near identical radiometers (one pair for j_{O^1D} and one pair for j_{NO_2}) mounted above and below the BAe-146 aircraft provide a full 4π sr field of view. The combination

of two radiometers in this way also allows the separate determination of upwelling and downwelling components of the actinic flux contribution to the photolysis rates with knowledge of the aircraft orientation.

4.1.4 Spectral radiometry

As implied by the name, the technique of spectral radiometry measures the spectral actinic flux, allowing calculation of the photolysis rate of any species where the quantum yield and cross section are known through evaluation of Equation 4.4. In principle this makes spectral radiometry the most versatile of all techniques for the measurement of photolysis rates. The original implementation of this technique was described in detail by Hofzumahaus *et al.* (1999), which involved the combination of a 2π sr entrance optic with a scanning spectrometer. The design of entrance optic for this type of instrument is equivalent to that of a filter radiometer, a necessity for the measurement of actinic flux. A quartz diffuser dome accepts incident radiation, the incident light then passes through an entrance slit to either a single or double monochromator system. In double monochromator systems wavelength separation and selection is performed by driving two diffraction gratings in synchrony to scan by wavelength. The selected wavelength passes through a second slit to a single photoelectric detector (e.g. photomultiplier tube) for measurement. The spectral bandpass is determined by the dimensions of entrance and exit slits, the pathlength through the monochromator and the level of diffraction dependent on the gratings employed; Hofzumahaus *et al.* (1999) reports a spectral bandpass of 1 nm for their system and therefore the spectral actinic flux ($F(\lambda)$) is resolved in successive (typically) 1 nm steps. $F(\lambda)$ is acquired over a time interval determined by the rate of scanning, with integration times of up to 90 s typical in the Hofzumahaus *et al.* (1999) system. For this reason Hofzumahaus *et al.* (1999) report that filter radiometer measurements of j_{O^1D} and j_{NO_2} (with 1 s time resolution) were used as auxiliary measurements to account for variation of the actinic flux within a scan interval. A further drawback to such a system is that the precision of motor driven systems used for scanning of

optical components for wavelength selection, can be adversely affected under the unstable conditions which may be encountered in the field. Single monochromator systems offer advantages both in terms of temporal resolution and stability of wavelength precision, requiring no moving parts; the specification of such an instrument is described in detail by e.g. Edwards & Monks (2003). Wavelength selection employs a fixed single grating (hence the description of these as monolithic monochromators) and simultaneous detection of the spectrally resolved actinic flux is achieved by wavelength dispersion onto a detector array (e.g. photodiode array (PDA) or CCD). Drawbacks to this technique are primarily related to suppression and correction for stray light which can lead to significant deviations in response for j_{O^1D} at large SZA's e.g. Bohn *et al.* (2008).

4.2 Calibration of the aircraft filter radiometers

To calibrate a filter radiometer the voltage response of the radiometer has to be determined as a function of the photolysis rate:

$$j_{(AB)} = AU \tag{4.13}$$

where U is the voltage response to a photolysis rate $j_{(AB)}$ and A is the calibration function that relates U and $j_{(AB)}$. The voltage response can be expressed using the following equation (Bohn *et al.*, 2004):

$$U = D_{abs} Z_H \int D_{rel}(\lambda) F(\lambda) d\lambda \tag{4.14}$$

where D_{abs} is a constant that represents the absolute sensitivity, Z_H is a correction function for a non-ideal angular response and $D_{rel}(\lambda)$ is the relative spectral sensitivity of the filter radiometer. The angular response correction Z_H is discussed in detail by Hofzumahaus *et al.* (1999), and is given by the equation:

$$Z_H = \frac{1}{F(\lambda)} \int_\phi \int_\theta Z_p(\theta) L(\lambda, \theta, \phi) \sin(\theta) d\theta d\phi \tag{4.15}$$

$Z_p(\theta)$ is the angular response; already simplified under the assumption that the response is isotropic as a function of azimuth angle ϕ, and so only a function of the zenith angle θ. Equation 4.15 essentially describes the convolution of the angular response with the angular distribution of the spectral radiance $L(\lambda, \theta, \phi)$. Except in an environment where the angular distribution of the spectral radiance is well understood, any significant deviation from an ideal angular response ($Z_p(\theta) = 1$, $0 \leq \theta \geq 90^o$) for a filter radiometer is very difficult to correct. This is especially true for a measurement on a moving platform such as an aircraft, where the angular distribution of the spectral radiance can be highly complex (depending on the angular distributions of contributions such as direct solar radiation, diffuse radiation, ground and cloud albedo) and rapidly varying. Hofzumahaus *et al.* (1999) assessed the potential impact of an imperfect angular response for a ground based measurement case under a variety of situations. The most significant impact occurred for a situation where the surface albedo was high, so by analogy conditions of high surface and cloud albedo will introduce the most significant errors for aircraft filter radiometers with non-ideal angular response. Outside a situation where albedo was enhanced Hofzumahaus *et al.* (1999) found only minimal correction was required, even for an atmosphere where the diffuse radiation was non-isotropic owing to the inclusion of aerosol. Clearly, it is essential that the angular response be optimised for aircraft measurements where the impact of cloud on the albedo is significant.

The calibration function A can be derived by combining Equations 4.4, 4.13 and 4.14:

$$A = \frac{j_{(AB)}}{D_{abs} Z_H \int D_{rel}(\lambda) F(\lambda) d\lambda} \tag{4.16}$$

$$A = \frac{1}{D_{abs} Z_H} \frac{\int \sigma_{(AB)} \phi_{(AB)} F(\lambda) d\lambda}{\int D_{rel}(\lambda) F(\lambda) d\lambda} \tag{4.17}$$

where the potential wavelength, temperature and pressure dependencies of the cross section and quantum yield have been excluded for simplicity. Hence, it can be seen that beside anisotropy in the angular response, the successful design of a filter radiometer depends on close matching of the relative spectral sensitivity (D_{rel}) with the product of the quantum yield and cross section ($\sigma_{(AB)}\phi_{(AB)}$) of

the photolysis process of interest.

Owing to the relative insensitivity of j_{NO_2} to temperature (i.e. $\sigma_{(NO_2)}\phi_{(O^3P)}$ is approximately constant with temperature) and SZA (i.e. $F(\lambda)$ scales approximately linearly with SZA), filter radiometers for the measurement of j_{NO_2} can be calibrated to a good approximation with a single calibration factor, derived by cross calibration against a standard. The spectral sensitivity of a filter radiometer is fixed, however as described already the spectral composition of the actinic flux in the UVB varies dependent on SZA and ozone column density. Further, the spectral forms of the quantum yield and cross section for the photolysis of ozone to form excited O(^{1}D) atoms are temperature dependent. This means it is not possible to match the spectral response of a j_{O^1D} filter radiometer to the spectral shape of the convolved quantum yield and cross section for all conditions. The result is a non-linear relationship between the raw signal measured by a j_{O^1D} filter radiometer and the true photolysis rate, dependent on temperature, SZA and ozone column density. The paper of Bohn *et al.* (2004) discusses in detail a method for the correction of these non-linearities to improve the accuracy of j_{O^1D} derived from filter radiometer measurements. The potential application of such corrections to the aircraft filter radiometer measurements is considered in Section 4.2.4.

The calibration of the aircraft j_{O^1D} and j_{NO_2} filter radiometers was carried out in two stages. Prior to the AMMA field campaign (described in Chapters 5 and 6) the instruments were intercompared with other filter radiometers mounted on the rooftop of the chemistry department at the University of Leicester. Post AMMA these instruments were then compared to a commercially available Met-Con (Meteorologie Consult, GmbH, Germany) spectral radiometer with the purpose of deriving the absolute response of the instruments through cross calibration. For both periods, the measured signals were compared to modelled photolysis rates derived with the Tropospheric Ultraviolet and Visible (TUV) Radiation Model version 4.1 of Madronich (1987), Madronich & Flocke (1998). The model was constrained using the temperature profile of the US Standard Atmosphere (USSA) (NOAA, NASA,

& USAF (1976)). Temperature variations at ground level for all periods do not depart markedly from the USSA profile and therefore will not impact the model derived photolysis rates (j_{O^1D} in particular) significantly (see Section 4.2.4, Figure 4.11). The model was further constrained using the total ozone column density on the day, retrieved from the Ozone Monitoring Instrument (OMI) on the Aura spacecraft. Input to the model to derive photolysis rates consisted of time (seconds since midnight on day of interest), latitude (52.622728^{o}N), longitude (1.124300^{o}W) and altitude (105m above sea level). The model output allowed both a check on drift in the response of individual instruments and a check on the photolysis rates derived from the spectral radiometers.

4.2.1 Intercomparison with ground based filter radiometers prior to AMMA

The intercomparison of the aircraft filter radiometers with other j_{O^1D} and j_{NO_2} filter radiometers was carried out prior to the AMMA SOP2 campaign over a period from 29 January–31 May 2006 (not continuous). The instruments were mounted in parallel on the chemistry department rooftop providing essentially the same field of view allowing direct comparison of the measured outputs. Neither sets of filter radiometers were calibrated at this time so output voltages were compared directly. No useful data were retrieved on the previous deployment of the aircraft filter radiometers during the ITOP campaign (Parker, 2007), owing to a technical problem with the connection to the aircraft data logging system (unknown at the time). This intercomparison also provided an opportunity to assess the working state of the aircraft instruments on the ground. The periods of comparison of each instrument are summarised in Table 4.1. The instruments are here labelled UJO1D, LJO1D, UJNO2 and LJNO2 in reference to whether they are fitted on the upper (U) or lower (L) side of the aircraft and whether they measure j_{O^1D} or j_{NO_2}. Example diurnals for each instrument measured during this intercomparison are shown in Figure 4.3 with the ratio of the reference signal to the aircraft radiometer signal underlying.

Radiometer	Start date (time)	End date (time)
UJO1D	29/01/2006 (08:15)	30/01/2006 (10:51)
UJO1D	16/02/2006 (12:11)	17/02/2006 (15:11)
LJO1D	19/02/2006 (13:04)	20/02/2006 (15:49)
UJNO2	20/02/2006 (15:50)	21/02/2006 (15:42)
LJNO2	21/02/2006 (15:50)	22/02/2006 (15:49)
LJNO2	23/02/2006 (11:40)	24/02/2006 (14:17)
UJO1D	26/02/2006 (14:41)	28/02/2006 (17:02)
LJO1D	23/03/2006 (00:01)	24/03/2006 (15:27)
LJO1D	27/03/2006 (08:07)	28/03/2006 (15:12)
LJO1D	02/05/2006 (13:47)	04/05/2006 (15:15)
LJNO2	04/05/2006 (15:23)	05/05/2006 (12:21)
LJO1D	05/05/2006 (12:30)	05/05/2006 (14:12)
LJO1D	07/05/2006 (06:23)	10/05/2006 (13:11)
UJO1D	10/05/2006 (13:30)	18/05/2006 (15:39)
UJNO2	18/05/2006 (15:40)	22/05/2006 (17:14)
UJNO2	29/05/2006 (07:00)	31/05/2006 (09:51)

Table 4.1: Intercomparison schedule for filter radiometers prior to AMMA

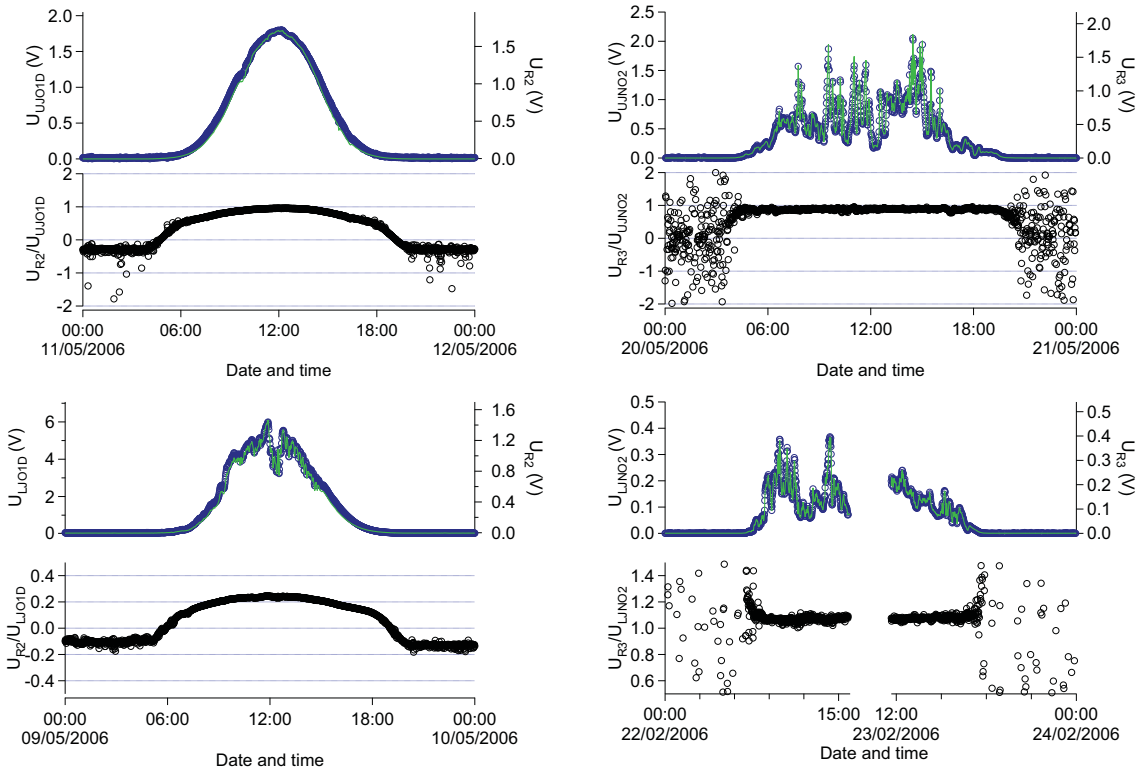

Figure 4.3: Timeseries from intercomparison of filter radiometers prior to AMMA – Aircraft radiometer signals are the blue circles, reference filter radiometer signals are the overlying green traces, underlying (black circles) plots are the ratio of the reference signal to the aircraft radiometer signal: (Top left) Comparison of UJO1D radiometer; (Top right) Comparison of UJNO2 radiometer; (Bottom left) Comparison of LJO1D radiometer; (Bottom right) Comparison of LJNO2 radiometer.

The diurnal signals each show some degree of variability associated with the impact of cloud on the measurements, however, the signal ratios show consistent trends irrespective of the impact of cloud. The raw signals are near indistinguishable for the j_{NO_2} filter radiometers and the signal ratios remain effectively constant throughout a given day. There is some variability in the ratio for the LJNO2 aircraft radiometer, however, this occurs on days when the measured signals were particularly low associated with heavy cloud cover and the variability may be attributed with instrumental noise. The scales are different for each plot dictated by the signal levels on the particular days and the relative sensitivity of the aircraft radiometers in comparison to the references. The ratio of the reference radiometer signals to the aircraft radiometer signal provides a gauge of relative sensitivity; for all but the LJO1D radiometer the ratios are of the order one indicating near equal sensitivities. The ratio for the LJO1D radiometer is nearer 0.2 during daylight indicating the absolute sensitivity of this radiometer is approaching five times the absolute sensitivity of the UJO1D radiometer. The combination of this high sensitivity with the generally enhanced actinic flux associated with measuring at altitude in the tropics, meant the measured signal sometimes exceeded the range of the aircraft data logging system during AMMA when the upwelling component of j_{O^1D} was enhanced above cloud (see Section 4.3). For the j_{O^1D} filter radiometers there is a difference in scaling throughout the day more clearly visible in the signal ratios; this may be attributed to a different spectral sensitivity between the aircraft and reference radiometer owing to a slightly different filter/detector combination. The trend in the ratio is comparable for both aircraft filter radiometers in comparison to the same reference as would be expected since the aircraft filter radiometers are of the same specification. At night the ratios for the j_{O^1D} filter radiometers are negatively biased while the ratios for the j_{NO_2} filter radiometers tend to noise. By applying a voltage bias the signal ratios do not tend to noise where the signal level is low (at the detection limit), but the raw signals must be zeroed properly for calibration. A "dark correction" was not applied for the comparison of these raw signals, but in practice the signal zero was determined by averaging the signal level measured at night, the zero level then subtracted

from all raw signals. An iterative procedure was applied to achieve the optimum zero - the dark signal average was first subtracted and then the average of the dark signal determined again, and this subtracted. The procedure was applied until there was no significant change in the zero level. The high correlation as a function of SZA between different filter radiometers measuring under the same conditions suggests a consistent angular response, and provides some confidence in the ideal angular response assumption. The similar trends in the signal ratios also suggests spectral sensitivities are similar for the respective aircraft radiometers even though the aircraft j_{O^1D} filter radiometers have a different spectral sensitivity to the reference instrument.

4.2.2 Absolute calibration through cross calibration with a spectral radiometer and TUV pre/post AMMA

Following AMMA, the aircraft filter radiometer instruments were compared to a commercially available MetCon (Meteorologie Consult, GmbH, Germany) spectral radiometer (designated 20518) with the purpose of deriving the absolute response of the instruments through cross calibration. The instruments were mounted in parallel on the chemistry department rooftop providing essentially the same field of view, allowing direct comparison of the measured outputs. The intercomparison was carried out over a period from 7-28 August 2007 with the SpecRad running continuously (except for instrument drop outs) and a single filter radiometer running alongside at any one time. The positioning of the filter radiometers with respect to the SpecRad was maintained, meaning relative differences between filter radiometers and the reference SpecRad could be associated with either a common issue with the SpecRad or individual filter radiometer performance. Further to this the filter radiometers and spectral radiometer were compared to TUV. To compare to TUV, days were chosen which exhibited the least interference from cloud from the comparison periods prior to AMMA and post AMMA. The "clear sky" opportunities are listed in Table 4.2, along with the ozone column density in Dobson Units used in constraining the TUV model. The number of "clear sky" opportunities prior to AMMA

were limited, so often only part of a single day is available for comparison. Cloud was intermittent during the post AMMA comparison and therefore periods of cloud have not been excluded. Figure 4.4 shows correlation plots comparing j_{O^1D} and j_{NO_2} derived from TUV with the values measured by the SpecRad (including periods with and without cloud). The raw and calibrated signals derived from the j_{O^1D} and j_{NO_2} filter radiometers from before and after the AMMA campaign are compared to TUV as a function of SZA (χ) in Figures 4.5 and 4.6. No data are available for the LJO1D filter radiometer after the AMMA campaign owing to water damage to that instrument (thought to have occurred during the AMMA field campaign). This was only discovered during the August 2007 experiment.

Radiometer(s)	Date	Ozone column (DU)
LJNO2, LJO1D	05/05/2006	367
LJO1D, UJO1D	10/05/2006	365
UJO1D	11/05/2006	369
UJNO2	31/05/2006	381
UJNO2	08/08/2007	328
UJNO2, UJO1D	09/08/2007	323
UJO1D	11/08/2007	308
LJNO2	23/08/2007	306
LJNO2	24/08/2007	291
LJNO2	26/08/2007	284

Table 4.2: "Clear sky" comparison opportunities for filter radiometers prior/post AMMA

Comparison of the 20518 SpecRad derived j_{O^1D} and j_{NO_2} photolysis rates to TUV (Figure 4.4) immediately shows a scaling difference with some additional strong variability that can be associated with cloud. The scaling is relatively constant for all days irrespective of the level of cloud, also the scaling is near constant for j_{O^1D} irrespective of the ozone column density (which varies from 284-328 DU). The TUV model runs have been constrained by the ozone column density (retrieved from satellite data (OMI)) and therefore a constant scaling indicates that TUV and the SpecRad measurement scale equally with changes in the ozone column density. An additional uncertainty with comparison to the

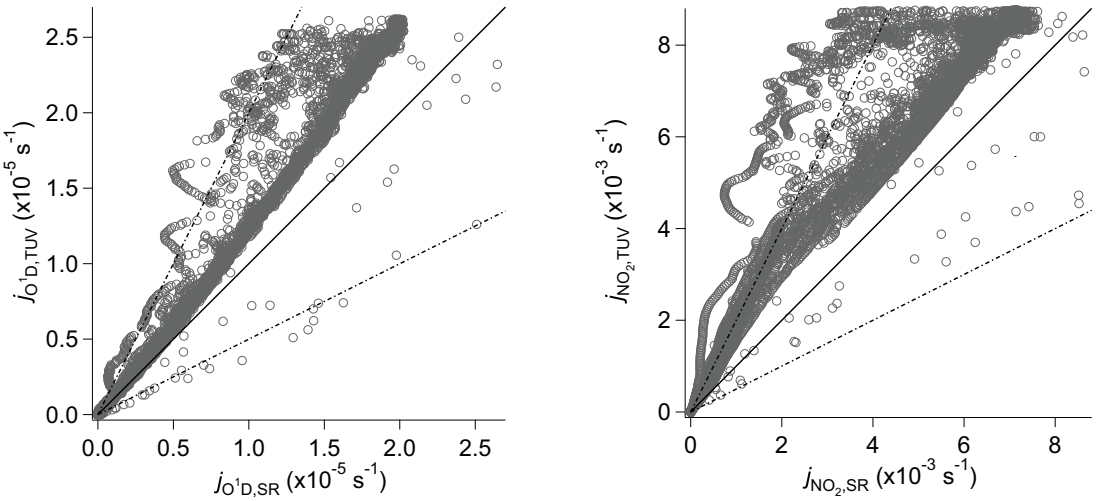

Figure 4.4: Comparison of the 20518 Spectral radiometer to TUV post AMMA – (Left) $j_{O^1D,TUV}$ versus $j_{O^1D,SR}$; (Right) $j_{NO_2,TUV}$ versus $j_{NO_2,SR}$

TUV model output is associated with the atmospheric aerosol load, for which there were no data available to constrain the TUV model output (the model default aerosol profile was assumed) during the comparison periods. To consider whether the scaling difference between TUV and the reference SpecRad instrument was consistent with an unaccounted for aerosol load, the scaling between the aircraft filter radiometer measurements and TUV was investigated using the comparisons prior to and post AMMA. In Figures 4.5 and 4.6 the ratio of TUV model to filter radiometer measurement has been calculated and plotted as a function of SZA. To calculate the ratio the filter radiometer measurements have been calibrated assuming a constant scaling factor, determined from the scaling between TUV and raw signals from "clear sky" periods during the pre AMMA intercomparison exercise. The raw signals are also plotted with the TUV photolysis rates to compare them directly. The j_{NO_2} filter radiometers are used as a guide since their calibrations factors are not significantly complicated by non-linearities. Also Dickerson *et al.* (1997) reports that scattering by aerosols can lead to an enhanced reduction in j_{NO_2} with increasing SZA. A significant aerosol load beyond the TUV baseline level should lead to variation in the scaling between TUV and the filter radiometer j_{NO_2} measurements as a function of SZA.

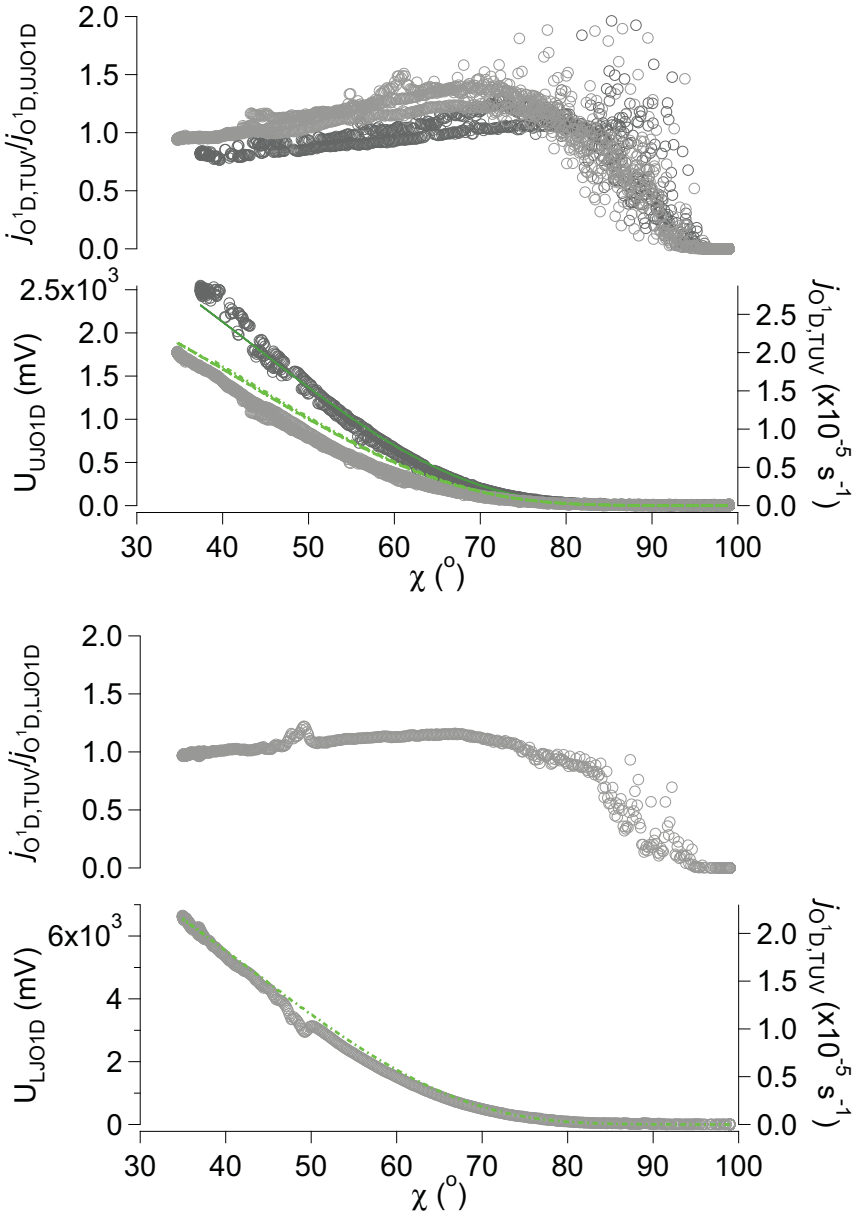

Figure 4.5: Comparison of j_{O^1D} filter radiometers to TUV prior to/post AMMA as a function of SZA – Light grey (green) circles (dashed lines) are measured (TUV modelled) points from the comparison prior to AMMA, dark grey (green) circles (lines) are measured (TUV modelled) points from the comparison after AMMA. (Top graph, top plot) Ratio of $j_{O^1D,TUV}$ to $j_{O^1D,UJO1D}$ with linear calibration factor applied, (Top graph, bottom plot) comparison of UJO1D radiometer raw signal to $j_{O^1D,TUV}$; (Bottom graph, top plot) Ratio of $j_{O^1D,TUV}$ to $j_{O^1D,LJO1D}$ with linear calibration factor applied, (Bottom graph, bottom plot) comparison of LJO1D radiometer raw signal to $j_{O^1D,TUV}$.

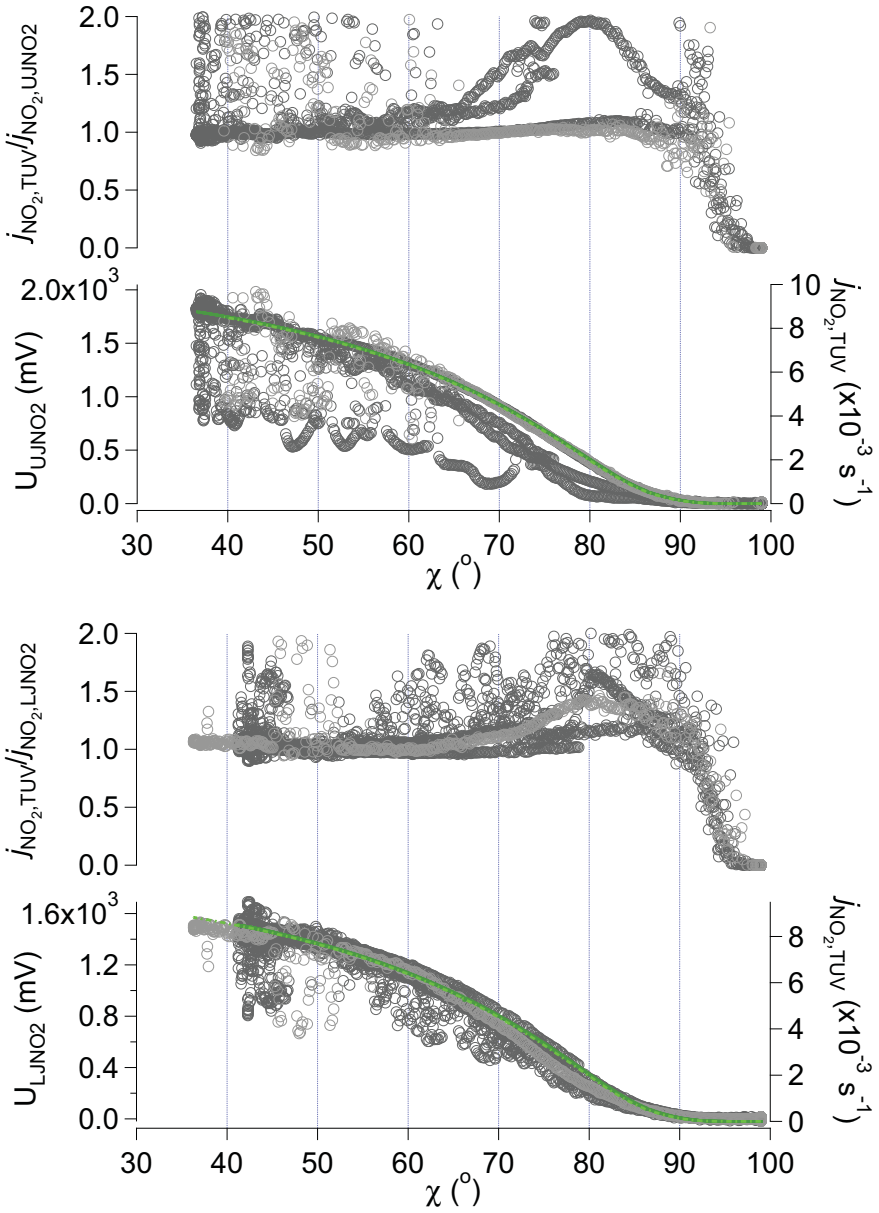

Figure 4.6: Comparison of j_{NO_2} filter radiometers to TUV prior to/post AMMA as a function of SZA – Light grey (green) circles (dashed lines) are measured (TUV modelled) points from the comparison prior to AMMA, dark grey (green) circles (lines) are measured (TUV modelled) points from the comparison after AMMA. (Top graph, top plot) Ratio of $j_{NO_2,TUV}$ to $j_{NO_2,UJNO2}$ with linear calibration factor applied, (Top graph, bottom plot) comparison of UJNO2 radiometer raw signal to $j_{NO_2,TUV}$; (Bottom graph, top plot) Ratio of $j_{NO_2,TUV}$ to $j_{NO_2,LJNO2}$ with linear calibration factor applied, (Bottom graph, bottom plot) comparison of LJNO2 radiometer raw signal to $j_{NO_2,TUV}$.

For the UJNO2 and LJNO2 instruments there is no change in scaling observable from before to after AMMA for periods thought of as "clear sky". During some periods the deviations are $\leq$5% at SZA's up to 80^o. This implies the aerosol influence is not significantly different from that prescribed in the TUV model for both before and after AMMA (during "clear sky" periods), or that aerosol is not making a significant difference to j_{NO_2}; it also provides confidence in the stability of the derived calibration factors over time. Variation from 1:1 scaling happens only during periods where some influence of cloud is seen in the diurnal profiles (not shown) and is most persistent at high SZA's. The intermittent changes at low SZA's are associated with intermittent cloud, but at high SZA's clouds along the horizon and aerosol scattering will both contribute. To explain why the 20518 SpecRad measurement is systematically lower than the TUV model post AMMA would require a constant and significant aerosol influence beyond that prescribed in TUV, which is inconsistent with the j_{NO_2} filter radiometer measurements, and therefore the SpecRad calibration is thought suspicious. Much later, data became available from the same period where the 20518 SpecRad was run alongside a second MetCon SpecRad (designated 45935, same specification), and comparison of these data along with TUV indicates there was an issue with the 20518 SpecRad calibration (see Section 4.2.3). For this reason it was chosen to apply the "clear sky" scaling to TUV to calibrate the AMMA filter radiometer measurements.

The scaling between j_{O^1D} and the raw signal measured by a j_{O^1D} filter radiometer is non-linear as a function of solar zenith angle and ozone column density as discussed in Section 4.2. Therefore the non-linearity in the scaling between TUV and the UJO1D and LJO1D instrument measurements (see Figure 4.5) is not unexpected. The LJO1D comparison is from the 10 May 2006 when the ozone column density (OMI) was 365 DU, which means the absolute sensitivity is weighted to an ozone column density of 365 DU. The scaling to TUV was weighted by the peak $j_{O^1D,TUV}$ values since these are least impacted by interference by cloud, this is also where the SZA is at its minimum,

hence the absolute sensitivity is also weighted to a SZA of $\sim 35^o$. The UJO1D comparison prior to AMMA is from the 10-11 May 2006 where the ozone column density varied from 365-369 DU, while during the comparison after AMMA on the 11 August 2007 the ozone column density was 308 DU. Since the absolute sensitivity has been determined from the scaling between TUV and the UJO1D raw signal from the comparison prior to AMMA, it is weighted to an ozone column density of 365-369 DU and SZA of $\sim 35^o$. This weighting explains the overestimation of j_{O^1D} by the UJO1D instrument during the comparison after AMMA at low SZA since the sensitivity is overweighted at the lower ozone column density and similar SZA's. The SZA weighting means the absolute sensitivity is typically underweighted at SZA's $\geq 35^o$ (j_{O^1D} will be underestimated), and will be overweighted for SZA's $\leq 35^o$ (j_{O^1D} will be overestimated). This is balanced by the weighting according to ozone column density i.e. the absolute sensitivity is underweighted at ozone columns $\geq$365 DU (j_{O^1D} will be underestimated), and will be overweighted for ozone columns $\leq$365 DU (j_{O^1D} will be overestimated). The change in scaling for both the UJO1D and LJO1D instruments as a function of SZA and ozone column is consistent with that described by Bohn *et al.* (2004), however the gradient in scaling as a function of SZA is less for the University of Leicester instruments for a similar ozone column. For low SZA's the change in scaling as a function of SZA is much less anyway (Bohn *et al.*, 2004) suggesting the absolute sensitivity of the University of Leicester instruments is relatively insensitive to SZA for SZA's $\leq 35^o$. The change in scaling between $j_{O^1D,TUV}$ and $j_{O^1D,UJO1D}$ from before AMMA to after AMMA provides an estimate of the change in sensitivity as a function of ozone column for the UJO1D instrument. It is apparent that the sensitivity as a function of ozone column weights the gradient of the sensitivity as a function of SZA (this is consistent with Bohn *et al.* (2004)), and therefore at lower ozone column densities a shallower gradient in the sensitivity scaling as a function of SZA is observed. The average ozone column density over the AMMA region during the SOP2 field campaign (see Chapters 5 and 6) was 287.5 DU (maximum=296 DU, minimum=272 DU) and therefore the aircraft filter radiometers are likely to overestimate j_{O^1D} (of the order 25%) with a weak SZA dependence.

Clearly, it would be more satisfactory to attempt to derive corrections for these non-linearities to improve the accuracy of the j_{O^1D} measurements. However, this correction requires an accurate determination of the instruments spectral sensitivity (see Bohn *et al.* (2004) and Section 4.2.4 of this Chapter). It was not possible to determine the spectral response of these instruments within this work owing to uncertainty with regard to irradiance standards and the spectral sensitivity of the 20518 SpecRad, therefore a linear calibration factor was used for both j_{O^1D} and j_{NO_2} filter radiometers. The errors introduced from an imperfect correction of filter radiometer measurements of j_{O^1D} for solar zenith angle and ozone column can be as large as those from not applying a correction e.g. Bohn *et al.* (2008), so this seemed appropriate. A linear calibration factor is sufficient for the calibration of the j_{NO_2} filter radiometer measurements, and from the above assessment these are believed to be accurate to within the uncertainty of the TUV model. The following Section (4.2.3) which discusses the intercomparison of measurements from the 20518 SpecRad with a second SpecRad and the TUV model provides some additional confidence in the accuracy of the TUV model results for "clear sky" conditions. A recent intercomparison extensively compared a number of radiative transfer models (including versions of the TUV model) along with measurements of photolysis frequencies (that being IPMMI, see e.g. Bais *et al.* (2003)) and found agreement to within a few percent in the UVA at low SZA's, which became worse for shorter wavelengths toward the UVB and at large SZA's. The accuracy of the model output is largely limited by the accuracy of the model inputs e.g. the extraterrestrial solar spectrum, molecular parameters (absorption cross sections and quantum yields), ozone column and aerosol load. A tentative estimate may put the uncertainty for the $j_{NO_2,TUV}$ (and by analogy the accuracy of the filter radiometer measurements) in the range $\geq$10%, while for $j_{O^1D,TUVD}$ the uncertainty may be of the order $\geq$20% and worse at increased SZA's. For the aircraft filter radiometer measurements of j_{O^1D} the accuracy may therefore be at best 20% (for an ozone column of 365DU and a SZA of 35^o) but consideration has to be given to the impact of variation in the measurement sensitivity with changing ozone column and solar zenith as discussed above.

4.2.3 SpecRad-SpecRad-TUV intercomparison

To assess the validity of the choice to calibrate the aircraft filter radiometer absolute response by comparison to TUV in favour of cross calibration with the 20518 SpecRad, the 20518 SpecRad was intercompared with a second MetCon SpecRad (designated 45935, same specification) and both were then compared to TUV. Figure 4.7 shows a diurnal from one of the intercomparison days where cloud cover was least evident. It is immediately apparent from such a plot that there is a significant offset between the photolysis rates derived from each SpecRad, with the 45935 SpecRad very closely matching the TUV model in j_{O^1D} and less so in j_{NO_2}. Also apparent is a marginal asymmetry in the diurnal measurements of j_{O^1D} and j_{NO_2} with respect to the model (more apparent with the 45935 SpecRad which is more closely matched). In the early mornings the measured photolysis rates rise more slowly than TUV, while in the evening TUV falls more rapidly than the measurements. One potential explanation could be a marginal inaccuracy in the time data for the measured photolysis rates, being late with respect to TUV although well synchronised with respect to one another. However, the differences compared to TUV are more in terms of symmetry rather than a general offset. Therefore it is suggested that the orientation of the radiometer false horizons were not completely parallel with respect to the horizon, with the 2π sr field of view tilted marginally toward west, this probably a result of the mounting structure for the instruments for the comparison and therefore common to both instruments. Furthermore, significant step changes are visible in the early morning j_{NO_2} measurements indicative of a shadow restricting the field of view at sunrise. These limitations affect the measured j_{NO_2} more significantly owing to the stronger dependence of j_{NO_2} on direct sunlight, while j_{O^1D} is held up by diffuse sunlight. Cloud also often has a lesser affect on j_{O^1D} for the same reasons (see the discussion in Section 4.1.1).

Figure 4.8 shows the correlation of each measurement with the other for j_{O^1D} and j_{NO_2} (Top left and right respectively), and the correlation of the TUV derived j_{O^1D} and j_{NO_2} (Bottom left and

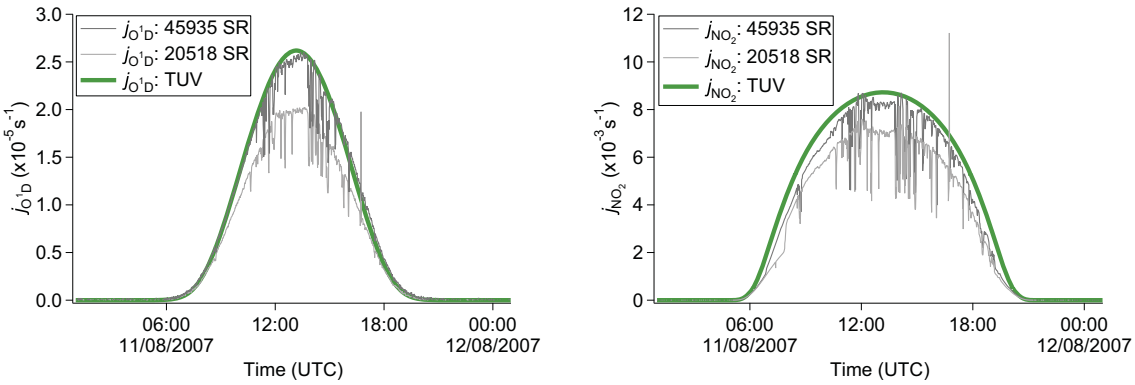

Figure 4.7: Diurnal comparison of SpecRad derived photolysis rates with TUV

right respectively) with both measurements. Overplotted on each are lines indicating 1:2, 1:1 and 2:1 levels of agreement. The asymmetry in the measurements with respect to TUV, owing to the imperfect orientation of the instruments, will carry through into the assessment when the model and measurements are compared directly.

From Figure 4.8 the photolysis rates derived from each SpecRad are clearly highly correlated, however there is a definite systematic bias between the measurements derived from each instrument with the 45935 instrument systematically measuring higher. Noise in the data is most likely associated with an imperfect synchronisation of the measurements with respect to one another, but does not significantly skew the overall trend. The correlation of the measurements was fit using a linear least squares procedure using the IGOR 6.0 package (Wavemetrics, 2007), the fit was constrained such that the line passed through the origin. The fit coefficients derived are as follows:

$$j_{O^1D,(45935)} = 1.239(\pm 0.003) j_{O^1D,(20518)} \tag{4.18}$$

with a correlation coefficient r=0.967;

$$j_{NO_2,(45935)} = 1.128(\pm 0.003) j_{NO_2,(20518)} \tag{4.19}$$

with a correlation coefficient r=0.949. In comparison to the photolysis rates derived from TUV, there is clearly much better agreement between TUV and the 45935 instrument. Deviation from the 1:1

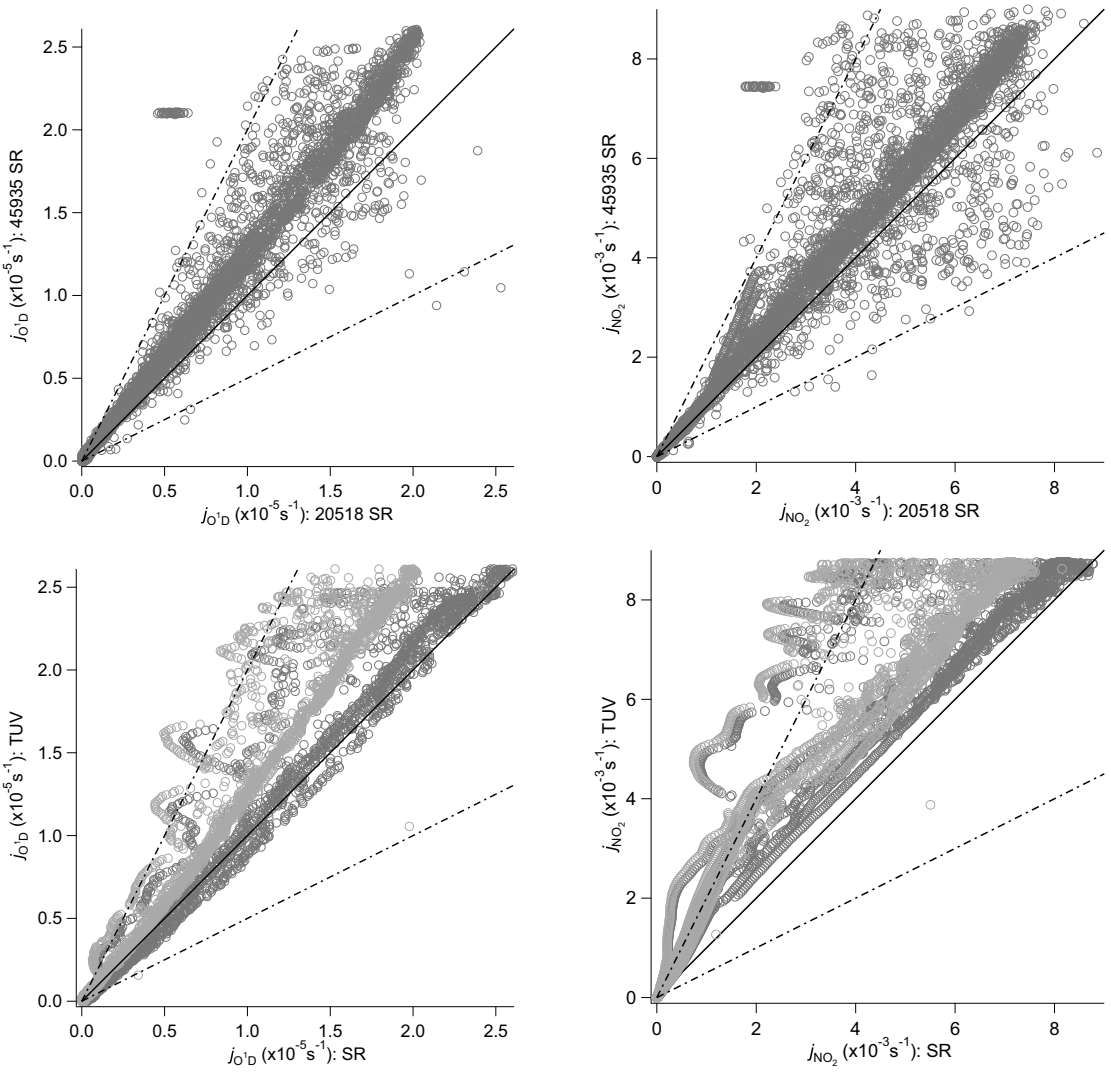

Figure 4.8: Correlation of TUV with SpecRad derived j_{O^1D} and j_{NO_2} photolysis rates – (Top left) j_{O^1D} derived from 45935 SpecRad versus j_{O^1D} derived from 20518 SpecRad; (Top right) j_{NO_2} derived from 45935 SpecRad versus j_{NO_2} derived from 20518 SpecRad; (Bottom left) j_{O^1D} derived from TUV versus j_{O^1D} derived from 20518 (light grey) and 45935 (dark grey) SpecRads; (Bottom right) j_{NO_2} derived from TUV versus j_{NO_2} derived from 20518 (light grey) and 45935 (dark grey) SpecRads.

line is expected since the TUV model output is appropriate for a clear sky situation and does not account for cloud. The deviation is less in j_{O^1D} which results from the reduced impact of cloud on diffuse UVB radiation under certain conditions (see the discussion in Section 4.1.1), in fact the j_{O^1D} measurement from the 45935 SpecRad at times exceeds the modelled photolysis rate. The exceedences are a direct result of the imperfect orientation of the instruments leading to a hysteresis between model and measurement with more significant underestimation in the morning and exceedences in the afternoon. A correlation of modelled and measured photolysis including all measurement points (so skewed somewhat by the influence of cloud) results in the following fits:

$$j_{O^1D,(TUV)} = 1.360(\pm 0.004) j_{O^1D,(20518)} \tag{4.20}$$

$$j_{O^1D,(TUV)} = 1.085(\pm 0.003) j_{O^1D,(45935)} \tag{4.21}$$

with correlation coefficients of r=0.977 and r=0.981 respectively;

$$j_{NO_2,(TUV)} = 1.338(\pm 0.005) j_{NO_2,(20518)} \tag{4.22}$$

$$j_{NO_2,(TUV)} = 1.166(\pm 0.004) j_{NO_2,(45935)} \tag{4.23}$$

with correlation coefficients of r=0.943 and r=0.95 respectively. As expected the fits deviate most from 1:1 and correlate least well for j_{NO_2} owing to the impact of cloud. Although the scaling between model and measurement for the 20518 instrument is similar for j_{O^1D} and j_{NO_2}, the correlation coefficient is improved for j_{O^1D} indicating an issue with scale (and therefore absolute calibration) rather than linearity.

The integrated actinic flux ($\int F(\lambda)d\lambda$ photons.cm^{-2}s^{-1}) from each instrument was also compared, the correlation of which is shown in Figure 4.9. The fit derived from the correlation of these parameters using a linear least squares procedure constrained such that the line passed through the origin is as follows:

$$\int F(\lambda)d\lambda_{(45935)} = 1.123(\pm 0.004) \int F(\lambda)d\lambda_{(20518)} \tag{4.24}$$

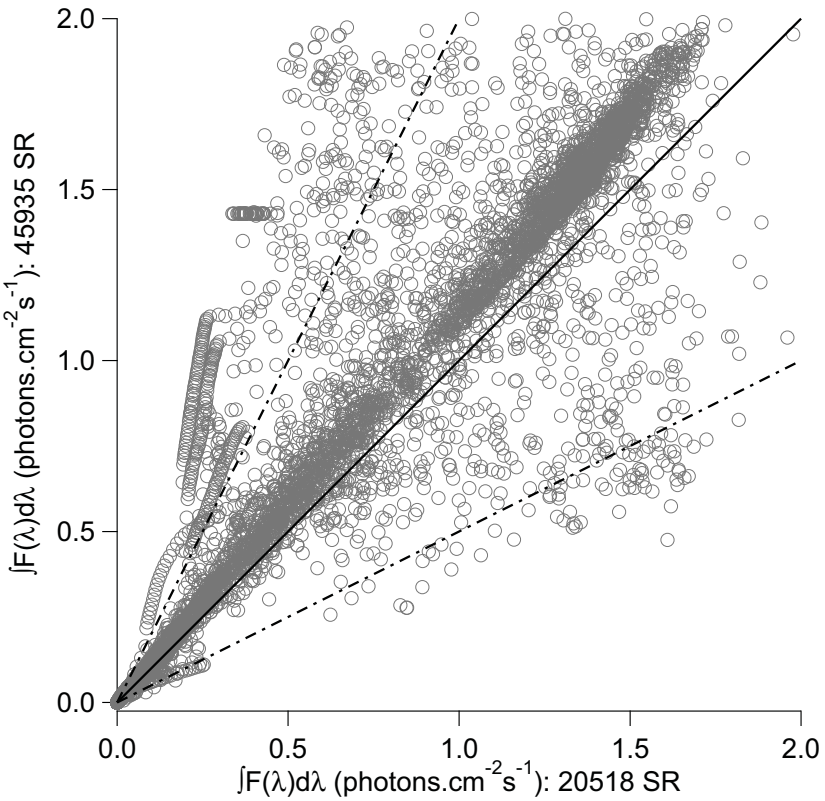

Figure 4.9: Correlation of SpecRad derived integrated actinic flux

with a correlation coefficient r=0.919. The near identical gradient between j_{NO_2} derived from comparison of each instrument and the integrated actinic flux derived from each is understandable in terms of the broad spectral range of the photolysis spectrum ($\sigma(\lambda)\phi(\lambda)$) of NO_2, and is symptomatic of a systematic bias between the instruments spectral sensitivity in the UVA. The even greater scaling between j_{O^1D} derived from each instrument suggests the bias in the spectral sensitivity is worse in the UVB.

The general agreement between TUV and the 45935 SpecRad instruments provides confidence in the validity of TUV for effectively cross calibrating filter radiometer absolute sensitivities, as discussed in Section 4.2.2, under idealised conditions (cloud free). The excellent correlation of the SpecRad measurements with respect to one another offers the potential for revision of photolysis rates derived from the 20518 SpecRad. Furthermore, the 20518 SpecRad data from the cross calibration of the filter

radiometers could be revised allowing the cross calibration to be considered under cloudy conditions, extending the number of comparable points and removing the reliance on clear sky opportunities for cross calibration versus TUV.

4.2.4 Temperature, ozone column and solar zenith angle corrections for j_{O^1D} filter radiometers

The calibration function derived by Bohn *et al.* (2004) separates the various dependencies of j_{O^1D} into several components, the form of the calibration function is given by:

$$A(\chi, t_{O_3}, T) = A(\chi^0, t^0_{O_3}, T^0) f(\chi, t_{O_3}, T^0) b(\chi, t_{O_3}, T) \tag{4.25}$$

The superscript 0 denotes the reference conditions, χ is the solar zenith angle in degrees, t_{O_3} is the ozone column density in Dobson units (DU) and T is the ambient temperature in Kelvin. A^0 ($=A(\chi^0, t^0_{O_3}, T^0)$) is a constant factor to describe the absolute response in comparison to a standard under the reference conditions (essentially that used to calibrate the filter radiometers response in this work). $f(\chi, t_{O_3}, T^0)$ is a dimensionless function which describes the relative dependence of the radiometer response compared to j_{O^1D} with solar zenith angle and ozone column density at the reference temperature T^0 (for Bohn *et al.* (2004) T^0=295 K). $b(\chi, t_{O_3}, T)$ is a function to normalise the measurement response to the temperature dependence of j_{O^1D}, the form of the temperature correction is given by:

$$b(\chi, t_{O_3}, T) = \frac{j_{O^1D}(\chi, t_{O_3}, T)}{j_{O^1D}(\chi, t_{O_3}, T^o)} \tag{4.26}$$

More specifically,

$$b(\chi, t_{O_3}, T) = \frac{\int \sigma(\lambda, T)\phi(\lambda, T)F(\lambda)d\lambda}{\int \sigma(\lambda, T^0)\phi(\lambda, T^0)F(\lambda)d\lambda} \tag{4.27}$$

The temperature dependence of j_{O^1D} is therefore only dependent on the cross section (σ), quantum yield (ϕ) and actinic flux ($F(\lambda)$) and hence as reported by Bohn *et al.* (2004), $b(\chi, t_{O_3}, T)$ should be generally applicable for any radiometric measurement of j_{O^1D} in the sense that it is independent of

any instrumental characteristics. With this in mind Bohn *et al.* (2004) derived a parameterisation for $b(\chi, t_{O_3}, T)$ using simulated $F(\lambda)$ specific to clear sky conditions, a range of solar zenith angles (χ=0-87^o), ozone columns (t_{O_3}=240-460 DU) and temperatures (T=270-320 K). The parameterisation of $b(\chi, t_{O_3}, T)$ and the setup of the model is described in Bohn *et al.* (2004) and references therein. A qualifier on the general applicability of the parameterisation of the temperature correction function is therefore that it was derived using a specific set of simulated spectra appropriate for ground level and for a limited range of conditions. The applicability of the correction beyond the range of temperature considered by Bohn *et al.* (2004) and for altitudes appropriate to airborne measurements of j_{O^1D} such as those obtained during the AMMA SOP2 field campaign (see Chapters 5 and 6) is unknown. Furthermore, there is additional uncertainty in terms of the applicability of the correction to situations where there are significant amounts of cloud or aerosol which may modify $F(\lambda)$ significantly. Bohn *et al.* (2004) assessed the use of the parameterisation by application to a field campaign dataset under cloudy conditions and found it still worked well; the implication is therefore that it may be applicable over a moderate range in altitude and albedo. However, for airborne measurements the potential impact of cloud on measured photolysis rates can be much greater.

Under the assumption that it is valid to extrapolate the parameterisation beyond the range in temperature for which it was defined, the parameterisation of Bohn *et al.* (2004) has been used to calculate the correction over a temperature range of 224-303 K (consistent with the range in temperature observed over the entire altitude profile during the AMMA SOP2 field campaign). The smooth change in the quantum yield as a function of temperature (see Figure 4.10, adapted from the latest IUPAC recommendation) may justify the extrapolation to lower temperatures, and also the fact that the parameterisation was derived using the cross sections of Malicet *et al.* (1995) and the quantum yields of Talukdar *et al.* (1998), which were defined over temperature ranges of 218-295 K and 209-320 K respectively. The calculation provides an assessment of the potential impact of temperature on the

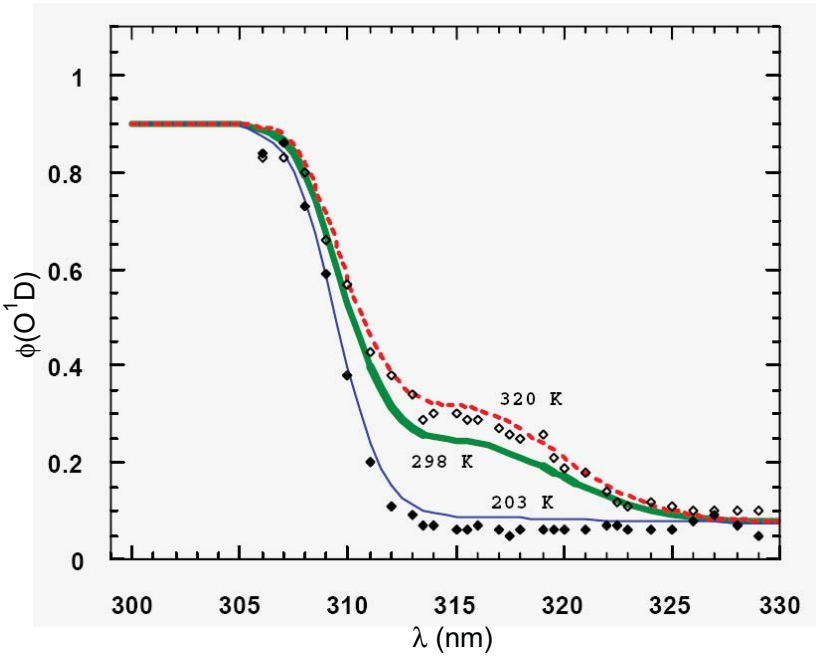

Figure 4.10: Temperature dependence for the quantum yield of $O(^1D)$ from ozone photolysis – Adapted from the latest IUPAC recommendation (Data Sheet POx2 updated 2nd October 2001): Curves show values at 202, 298 and 320 K calculated using the expression derived by Matsumi *et al.* (2002). Selected experimental data from Talukdar *et al.* (1998) at 203 and 320 K are also shown.

j_{O^1D} photolysis rate measurements made during the AMMA SOP2 field campaign. The results of the calculation are shown as a function of temperature (and the associated typical altitude) and solar zenith angle in Figure 4.11. Two profiles are derived appropriate to the lowest (282.25 DU) and highest (293.25 DU) average ozone column densities encountered during the campaign.

From Figure 4.11 it is clear that significant deviations in the measured photolysis rates may occur by not accounting for the temperature dependence of j_{O^1D}. The most significant change occurs for the combination of high ozone column density and at high solar zenith angles ($\sim$35%), hence it is here where inaccuracies will be greatest. For nearly all temperatures (altitudes) the direction of the correction is to reduce j_{O^1D} with decreasing temperature owing to the reduction in quantum yield with temperature seen in Figure 4.10. At the highest temperatures (lowest altitudes) the direction changes such that the correction scales up the measurement. For the range in ozone column densities

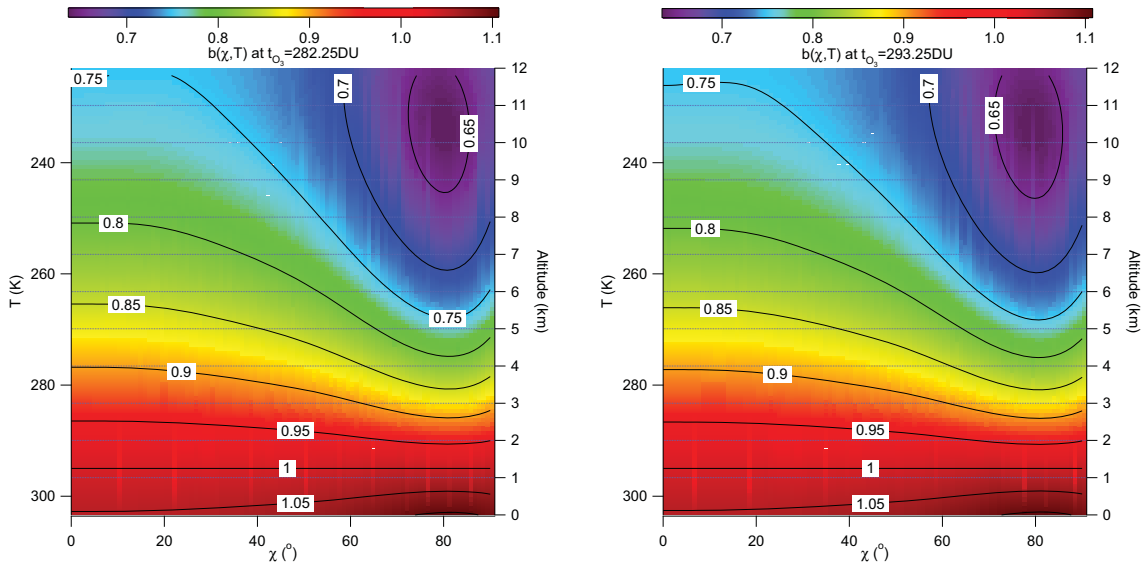

Figure 4.11: Bohn *et al.* (2004) j_{O^1D} temperature correction as a function of temperature and solar zenith angle, calculated for a range of temperatures appropriate to the range observed during AMMA SOP2 – (Left) Calculated for t_{O_3}=282.25 DU, (Right) Calculated for t_{O_3}=293.25 DU.

encountered during AMMA there is only a minimal difference in $b(\chi, T)$. To account properly for the temperature variation appropriate to an airborne campaign such as AMMA SOP2 it would be necessary to derive an along flight track temperature correction rather than using the parameterisation of Bohn *et al.* (2004). Based on Equation 4.27 the relative change in j_{O^1D} as a function of temperature along a flight track may be calculated simply, by using a radiative transfer model (such as TUV) to calculate j_{O^1D} allowing the temperature to vary with the measured temperature profile (i.e. $j_{O^1D}(\chi, t_{O_3}, T)$), and then with the constraint that the temperature is fixed at the reference temperature for calculation of the cross section and quantum yield (i.e. $j_{O^1D}(\chi, t_{O_3}, T^o)$). The ratio of the derived j_{O^1D} without and with the temperature constraint then is equivalent to $b(\chi, t_{O_3}, T)$ along the flight track. A full assessment of the impact of cloud and aerosol modification of the actinic flux would be required to derive $b(\chi, t_{O_3}, T)$ with some certainty.

As mentioned already the relative dependence of a j_{O^1D} filter radiometers response compared to j_{O^1D} as a function of solar zenith angle and ozone column density at a given reference temperature T^0, can

be described as per Bohn *et al.* (2004) using the function $f(\chi, t_{O_3}, T^0)$. The form of this function is given by:

$$f(\chi, t_{O_3}, T^0) = \frac{A(\chi, t_{O_3}, T^0)}{A^0} \tag{4.28}$$

which is the ratio of the absolute response of the radiometer as a function of solar zenith and ozone column density at the reference temperature, to the absolute response at the reference conditions (for Bohn *et al.* (2004) χ^0=30^o, $t^0_{O_3}$=350 DU). More explicitly:

$$f(\chi, t_{O_3}, T^0) = \frac{\frac{1}{D_{abs} Z_H(\chi)} \frac{\int \sigma(\lambda,T^0)\phi(\lambda,T^0)F(\lambda,\chi,t_{O_3})d\lambda}{\int D_{rel}(\lambda)F(\lambda,\chi,t_{O_3})d\lambda}}{\frac{1}{D_{abs} Z_H(\chi^0)} \frac{\int \sigma(\lambda,T^0)\phi(\lambda,T^0)F(\lambda,\chi^0,t^0_{O_3})d\lambda}{\int D_{rel}(\lambda)F(\lambda,\chi^0,t^0_{O_3})d\lambda}} \tag{4.29}$$

where D_{abs} is the absolute sensitivity (V cm^2 s i.e. Volts per unit flux), Z_H is the angular response correction (defined in Equation 4.15) and $D_{rel}(\lambda)$ is the relative spectral sensitivity of the filter radiometer. If to a good approximation the angular response correction is near unity, this simplifies to:

$$f(\chi, t_{O_3}, T^0) = \frac{\int \sigma(\lambda, T^0)\phi(\lambda, T^0)F(\lambda, \chi, t_{O_3})d\lambda}{\int \sigma(\lambda, T^0)\phi(\lambda, T^0)F(\lambda, \chi^0, t^0_{O_3})d\lambda} \frac{\int D_{rel}(\lambda)F(\lambda, \chi^0, t^0_{O_3})d\lambda}{\int D_{rel}(\lambda)F(\lambda, \chi, t_{O_3})d\lambda} \tag{4.30}$$

Both the absolute sensitivity and angular response cancel (under the given assumptions), and therefore the magnitude of the solar zenith angle/ozone column density correction function depends on the matching of the relative spectral sensitivity with the product $\sigma(\lambda, T^0)\phi(\lambda, T^0)$ and how that weights the relative change in actinic flux as a function of solar zenith angle and ozone column density. This implies that to determine a correction for solar zenith angle/ozone column density, the relative spectral sensitivity must be determined experimentally by calibration against a spectral irradiance standard, and this is the procedure recommended by Bohn *et al.* (2004).

A possible alternative to determine the spectral sensitivity of a j_{O^1D} filter radiometer is proposed here which would then make possible the correction of this measurement for SZA and ozone column. The proposed technique does not require the use of irradiance standards or a chemical actinometer, but requires either a well calibrated spectral radiometer or very well constrained radiative transfer model

under clear sky conditions. Equation 4.14 (repeated here as Equation 4.31) relates the measured raw voltage output of a filter radiometer, U, to the spectral actinic flux by the absolute, angular and spectral sensitivity of the radiometer. Given a concurrent measurement of the actinic flux (such as available from a cross comparison with a calibrated spectral radiometer) it is possible to deconvolve the absolute spectral sensitivity.

$$U = D_{abs} Z_H \int D_{rel}(\lambda) F(\lambda) d\lambda \tag{4.31}$$

The measurement or modelling of the spectral actinic flux produces a matrix of values corresponding to the actinic flux per unit wavelength interval; the wavelength interval defined by the spectral resolution of the measurement or model. Making the assumption that the angular response is essentially ideal (which can be achieved by cross comparison at low SZA's), Equation 4.14 can be re-written as follows.

$$\begin{pmatrix} U(t_1) \\ U(t_2) \\ U(t_3) \\ \vdots \\ U(t_n) \end{pmatrix} = \begin{pmatrix} F(t_1,\lambda_1) & F(t_1,\lambda_2) & F(t_1,\lambda_3) & \dots & F(t_1,\lambda_n) \\ F(t_2,\lambda_1) & F(t_2,\lambda_2) & F(t_2,\lambda_3) & \dots & F(t_2,\lambda_n) \\ F(t_3,\lambda_1) & F(t_3,\lambda_2) & F(t_3,\lambda_3) & \dots & F(t_3,\lambda_n) \\ \dots & \dots & \dots & \dots & \dots \\ F(t_n,\lambda_1) & F(t_n,\lambda_2) & F(t_n,\lambda_3) & \dots & F(t_n,\lambda_n) \end{pmatrix} \cdot \begin{pmatrix} D_{abs}D_{rel}(\lambda_1) \\ D_{abs}D_{rel}(\lambda_2) \\ D_{abs}D_{rel}(\lambda_3) \\ \vdots \\ D_{abs}D_{rel}(\lambda_n) \end{pmatrix} \tag{4.32}$$

Here $U(t)$ is the voltage response of the filter radiometer over the time interval $t = 1 \rightarrow n$ to actinic flux $F(t, \lambda)$. The first matrix on the right hand side of Equation 4.32 is a row matrix of dimensions n×n that represents the spectral actinic flux per wavelength interval at each time step, while the second is a column matrix of dimensions 1×n which represents the spectrally resolved instrument spectral response. The spectrally resolved absolute instrument spectral sensitivity ($D_{abs}D_{rel}(\lambda)$) can then be determined by multiplying the inverse of the matrix of spectral actinic flux values by the voltage response of the filter radiometer. To solve for n unknowns requires n linear equations, therefore the required measurement time interval is determined by the bandwidth and the spectral resolution of the reference spectrum. Given a continuous cross comparison of a filter radiometer with a spectral radiometer under varied conditions, the absolute instrument spectral can be determined over several intervals, and in this way good statistics can be built up.

4.3 Instrumental performance during the AMMA campaign

The potential data coverage was 100% at 1 Hz for both the measurement of j_{O^1D} and j_{NO_2} however a number of instrumental and operational issues meant total coverage was reduced. In terms of operational issues a retractable guard shutter used on takeoff and in flight for protection of the radiometer domes during profiling, obscures the field of view of both radiometers in the lower position. The shutter is operated by the FAAM flight manager and its triggering is not logged automatically or as standard through the flight summary log whereby the flight manager notes events during flights. As a result the identification of periods affected by obscuration is achieved by manual flagging of periods where coincident step change drops in the signals from the lower position radiometers are observed, this can lead to errors in flagging. A typical example of the signature of this issue is shown in Figures 4.12 where the flag value 2 indicates shutter obscuration.

In terms of instrumental issues these were associated primarily with the lower position j_{O^1D} radiometer. Owing to the enhanced actinic flux associated with the measurement region of the tropics, the upwelling flux above clouds in combination with the generally enhanced diffuse background and the sensitivity of the lower position j_{O^1D} radiometer, meant the signal above cloud often exceeded the input range of the data recording system (i.e. 10 V). This meant the signal was effectively saturated whenever these factors combined, a typical example of the signature of this issue is shown in Figure 4.12 where the flag value 1 indicates saturation. A major failure of this instrument occurred later in the campaign leading to a complete loss of the upwelling j_{O^1D} measurement, this failure was eventually attributed to water damage of the instrument electronics.

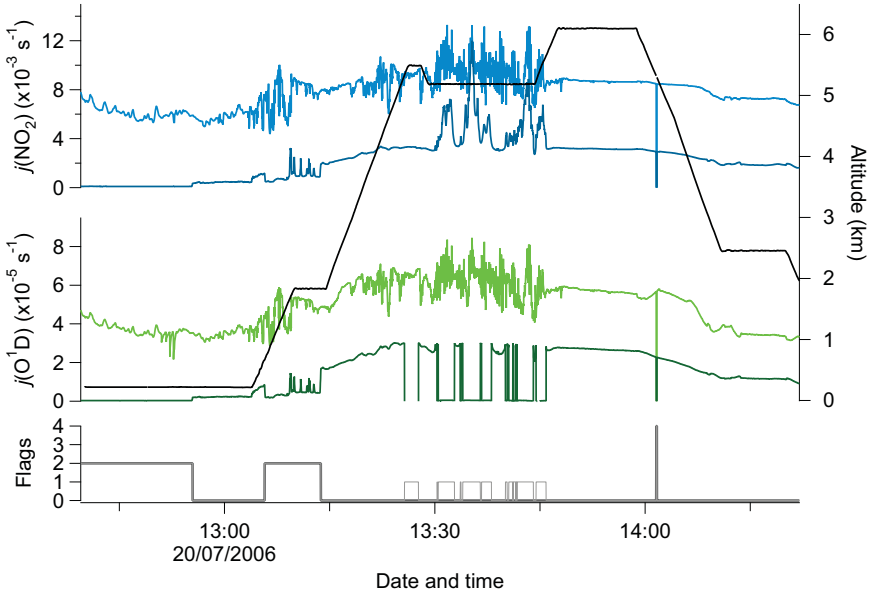

Figure 4.12: Signatures of obscuration and measurement signal saturation in the lower position radiometer signals - (Black trace) Altitude, (Light blue trace) downwelling j_{NO_2}, (Dark blue trace) upwelling j_{NO_2}, (Light green trace) downwelling j_{O^1D}, (Dark green trace) upwelling j_{O^1D}, (Light grey trace) j_{O^1D} flags, (Dark grey trace) j_{NO_2} flags

4.3.1 Assessment of correction for issues with lower position radiometers

The malfunction of the lower position j_{O^1D} radiometer resulted in uncertainty in the total j_{O^1D} due to the loss of the measurement of the upwelling component. From analysis of the fractional contribution of the upwelling signal to the total during the initial part of the campaign where the measurement was available (see Figure 4.13) typically 30% of the signal may be missed and exceptionally up to 60%, due to the lack of this measurement later on. Note however, that the data in this figure misses periods where the signal saturated the data logging system and therefore under represents the contribution of the upwelling j_{O^1D}. Clearly a significant component of the total signal is missed without this measurement and therefore consideration has to be made for a technique to estimate the upwelling component of j_{O^1D}.

The assumption has been made that the lower position aircraft radiometers are predominantly exposed

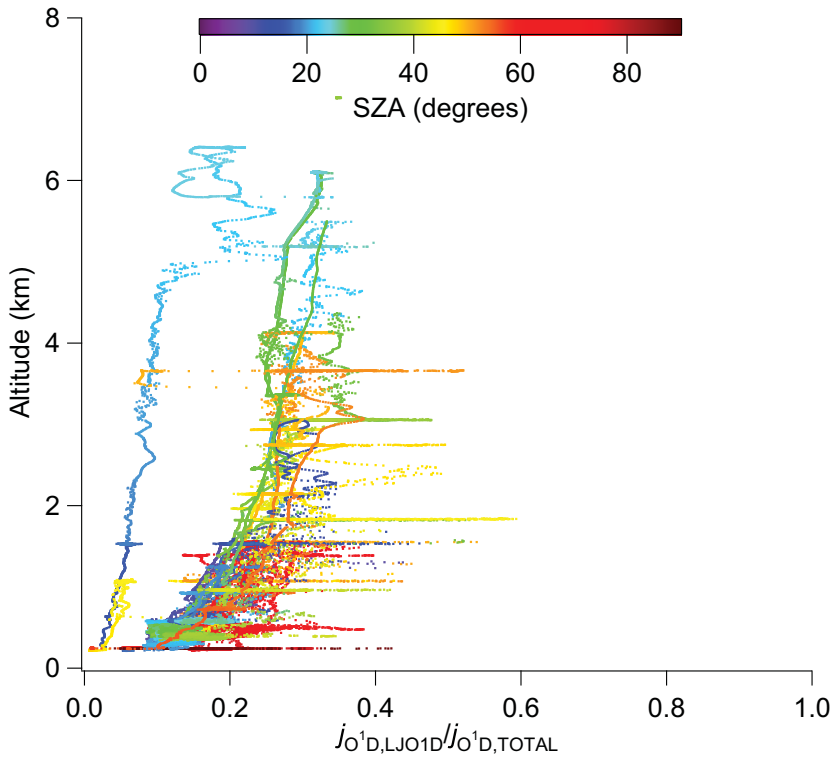

Figure 4.13: Fractional contribution of upwelling j_{O^1D} as a function of altitude

to the upwelling component of the total signal, and the contribution of the pitch and roll of the aircraft in changing the field of view has not been explicitly included in this assessment. The "upwelling component" then refers to the signal measured by the lower position radiometers and the "downwelling component" refers to the signal measured by the upper position radiometers. The separation of the measured signals in this way is equivalent to the separation of the actinic flux into direct, upwelling and downwelling diffuse components as discussed in Section 4.1.1. The direct component of the actinic flux depends on the position of the sun, which can be at zenith angles from 0-90^o. The angle of incidence of direct sunlight with respect to the radiometers can be defined relative to the main vertical axis of the upper position radiometer, while the angle of inclination of the main vertical axis is defined relative to zenith. If the combination of the SZA with the inclination angle of the main axis exceeds 90^o this can put the sun within the field of view of the lower position radiometer. Only for a combination of the high SZA and steep inclination does this become likely, so for the majority of situations the

downwelling component is the sum of direct plus downwelling diffuse actinic flux, while the upwelling component is the upwelling diffuse only. The ratio of downwelling to upwelling signals is therefore a measure of the relative contributions of direct and diffuse radiation.

To assess the possibility of estimating the upwelling j_{O^1D} component, an analysis was carried out to determine if the upwelling j_{O^1D} measurement could be related to the remaining functioning measurements (downwelling j_{O^1D}, downwelling and upwelling j_{NO_2}). A number of possibilities were investigated, including looking at the scaling between upwelling j_{O^1D} and j_{NO_2}, the scaling between downwelling j_{O^1D} and j_{NO_2}, and the correlation of the ratio of upwelling to downwelling j_{NO_2} with the ratio of upwelling to downwelling j_{O^1D} all as a function of SZA. The scaling between downwelling j_{O^1D} and j_{NO_2} as a function of SZA is compared with the scaling between total j_{O^1D} and j_{NO_2} from the TUV model in Figure 4.14. Clear agreement is seen between the measured and calculated scaling with SZA, since the downwelling component is dominated by the direct and downwelling diffuse components of the actinic flux which are less perturbed by scattering and absorption related to clouds. The scaling between upwelling j_{O^1D} and j_{NO_2} as a function of SZA is compared with the scaling between total j_{O^1D} and j_{NO_2} from the TUV model in Figure 4.15. Clear agreement is seen between the measured and calculated scaling with SZA, however the ratio is significantly more perturbed by scattering and absorption related to clouds since the upwelling component is dominated by changes in the diffuse component of the actinic flux and responds directly to changes in surface and cloud albedo. As discussed by Crawford *et al.* (1999), UVB wavelengths are more easily scattered owing to the wavelength dependence of Rayleigh scattering which means j_{O^1D} has a greater diffuse component compared to j_{NO_2}. This may explain the negative bias in the residual, also indicative that the upwelling diffuse j_{O^1D} is more significant a component of the total signal than it is for j_{NO_2}.

Diffuse sunlight is the product of scattered direct sunlight so it is reasonable to expect these quantities to be somewhat correlated, it is also then reasonable to expect the diffuse to direct ratio to be correlated

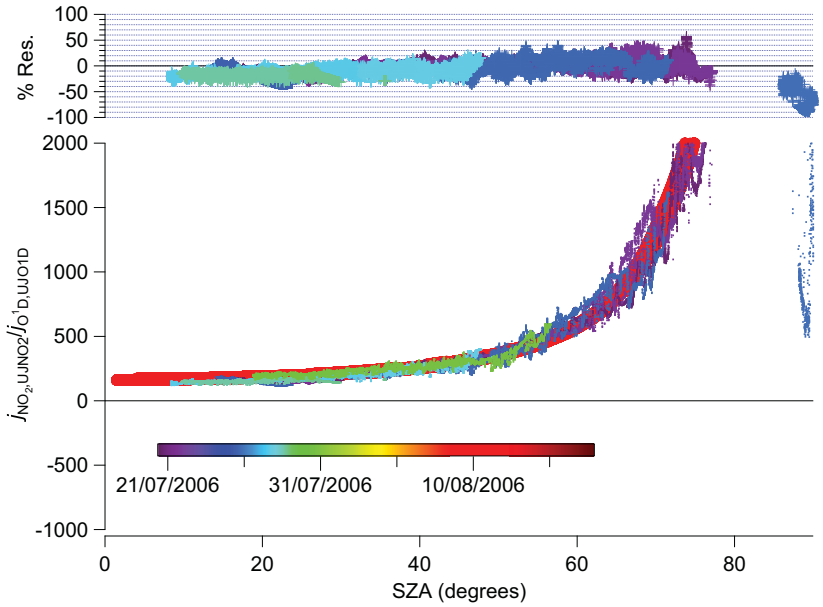

Figure 4.14: Ratio of downwelling j-values colourscaled as a function of SZA – (Dots) Measurement ratio, (Red circles) TUV ratio, (Crosses) Percentage difference between model and measured ratio.

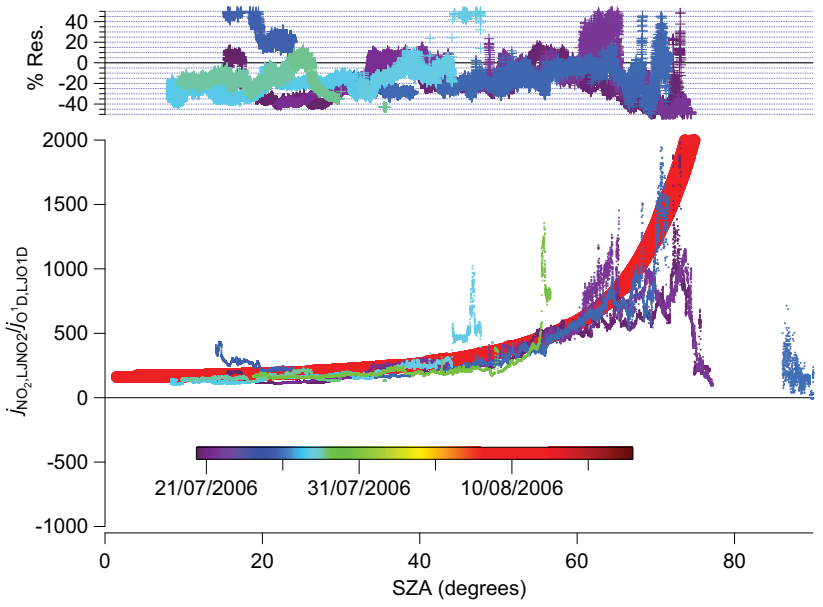

Figure 4.15: Ratio of upwelling j-values colourscaled as a function of SZA – (Dots) Measurement ratio, (Red circles) TUV ratio, (Crosses) Percentage difference between model and measured ratio.

in the UVA and UVB. Figure 4.16 is a correlation of the ratio of upwelling to downwelling j_{NO_2} with upwelling to downwelling j_{O^1D}, where points have been excluded that correspond to SZA's $\geq 70^o$. The diffuse to direct ratio does appear to directly correlate in the UVA and UVB, and the gradient is less than one corresponding to a greater diffuse UVB component as anticipated. The correlation of these parameters offers a way to estimate the upwelling component of j_{O^1D} from the combination of the other measurements and the gradient of the diffuse to direct ratio. The ratio of the diffuse to direct

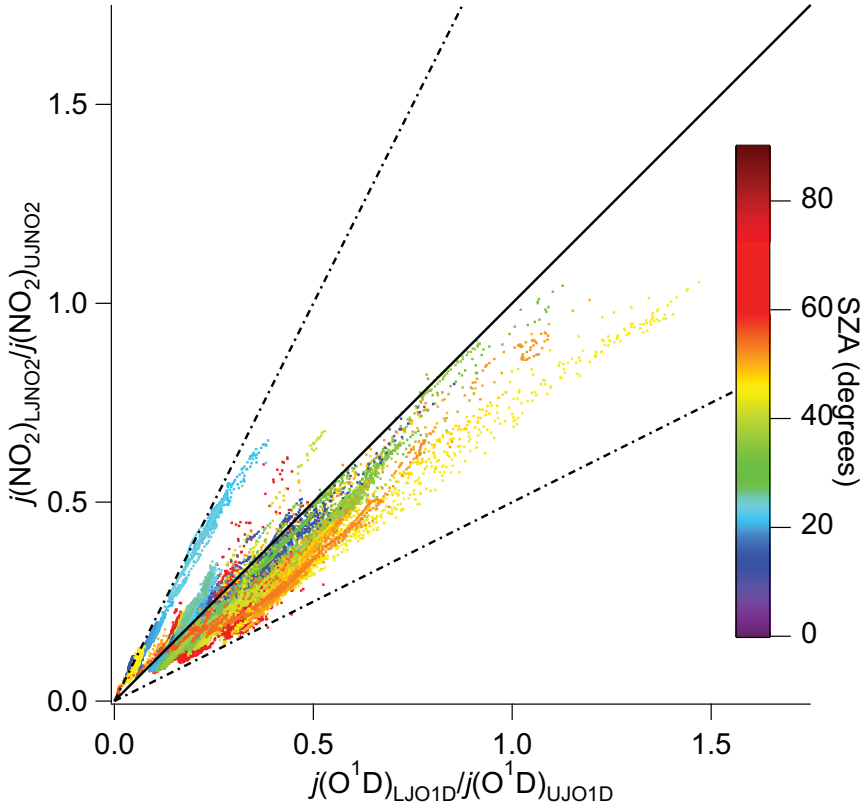

Figure 4.16: Correlation of upwelling to downwelling j-values colourscaled by SZA

ratio in j_{NO_2} with the diffuse to direct ratio in j_{O^1D} is an estimate of the gradient relating these parameters. A histogram of the ratio of diffuse to direct ratio in j_{NO_2} with the diffuse to direct ratio in j_{O^1D} has been calculated and fitted with a gaussian distribution as shown in Figure 4.17. The ratio appears to be normally distributed about a mean value of 0.8661 ± 0.0005, hence this value is taken as the gradient used to estimate the upwelling component of j_{O^1D}. Some deviations from the

average distribution do occur, and this is likely the result of different regimes in terms of how diffuse and direct UVA and UVB radiation are scaling. For example if the average distribution is thought of that under clear sky, below, within and above cloud the diffuse to direct ratio in j_{O^1D} will scale differently to that in j_{NO_2} owing to the wavelengths dependencies of absorption and scattering. The upwelling component of j_{O^1D} has been calculated from:

$$j_{O^1D,Lower} = \frac{j_{O^1D,Upper}}{0.8661} \frac{j_{NO_2,Lower}}{j_{NO_2,Upper}} \tag{4.33}$$

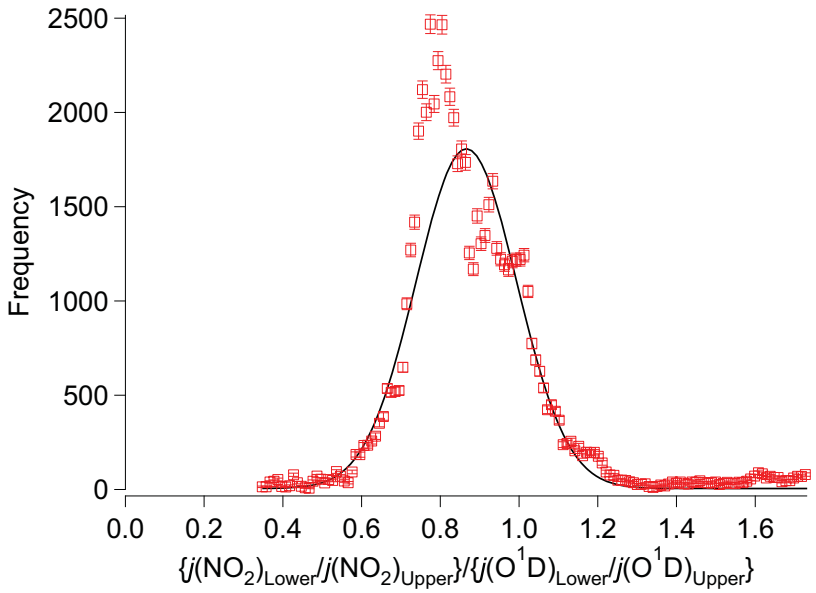

Figure 4.17: Histogram of ratio upwelling to downwelling j-values as a function of SZA, for SZA's $<70^o$

To assess the validity of this approach, Equation 4.33 has been used to calculate an estimate of the upwelling component of j_{O^1D} from the period where the measurement was working, to allow direct comparison of the estimate to the measurement. Figure 4.18 presents a timeseries of the estimated upwelling j_{O^1D}, along with that measured from flight B216 as an example. Figure 4.19 presents a histogram of the difference (residual) between measured and estimated upwelling j_{O^1D}.

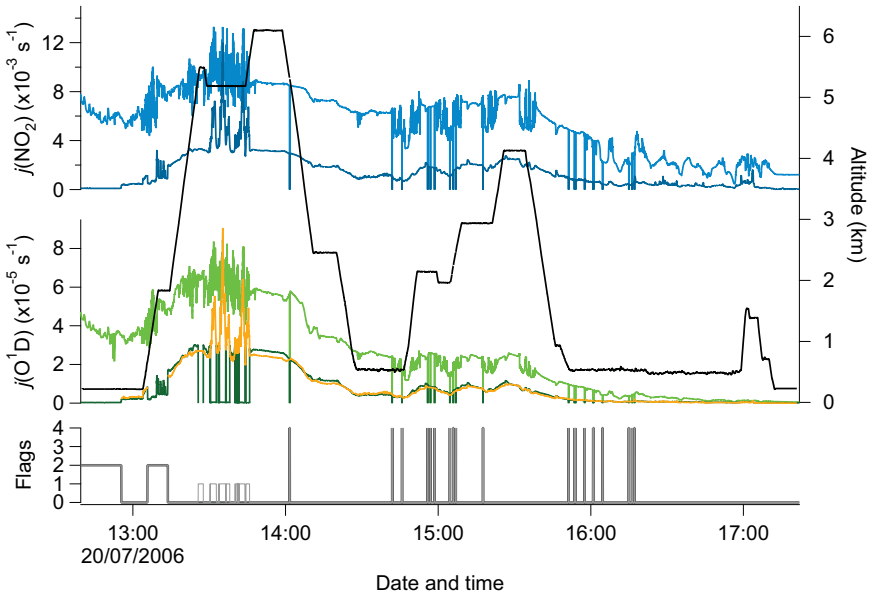

Figure 4.18: Timeseries comparing measured and estimated upwelling j_{O^1D} – (Black trace) Altitude, (Light blue trace) measured downwelling j_{NO_2}, (Dark blue trace) measured upwelling j_{NO_2}, (Light green trace) measured downwelling j_{O^1D}, (Dark green trace) measured upwelling j_{O^1D}, (Yellow trace) estimated upwelling j_{O^1D}, (Light grey trace) j_{O^1D} flags, (Dark grey trace) j_{NO_2} flags

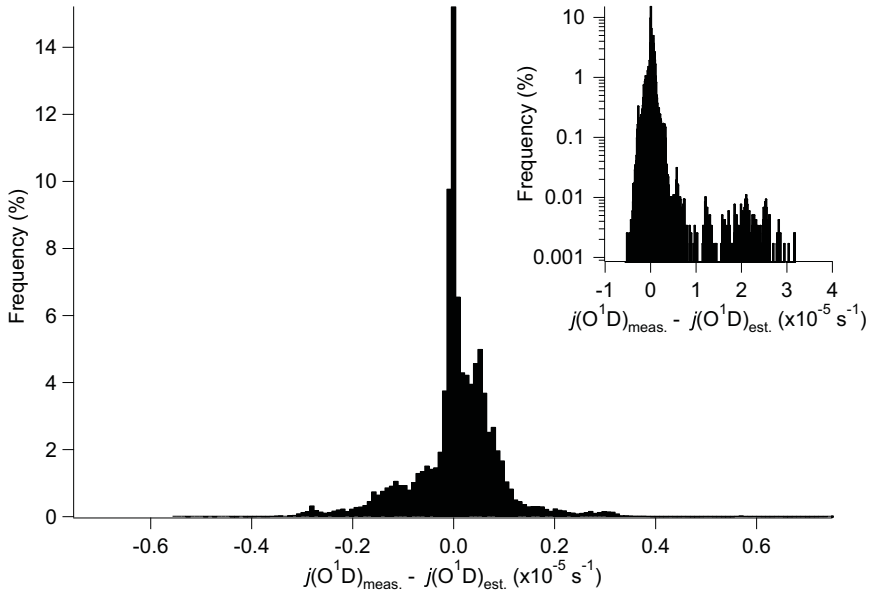

Figure 4.19: Frequency distribution of difference between measured and estimated upwelling j_{O^1D} – (Full scale) Frequency on linear scale, limited range in difference; (Inset) Frequency on log scale, full range in difference

From Figure 4.18 it is apparent that Equation 4.33 provides a reasonable estimate of the upwelling j_{O^1D} component. Minimal differences are visible between the estimate and measurement (except where saturated), and this is made clear from the histogram of the difference between measurement and estimate in Figure 4.19. For the majority of the points of comparison (∼94%) the difference is within $\pm 2\times10^{-6}$ s^{-1}, which only becomes a significant error for large SZA's as total j_{O^1D} tends to zero.

4.4 Chapter 4 Summary

This chapter provides an overview of the measurement of photolysis rates, in particular through the technique of filter radiometry. Filter radiometry was used to measure photolysis rates for the AMMA SOP2 field campaign, the results of which are described in Chapters 5 and 6. Some background to the measurement of photolysis rates is provided in Section 4.1, including the theoretical basis to the derivation of photolysis rates from measurement of actinic flux. The impact of cloud on actinic flux and how this affects photolysis rates in general is discussed, and more specifically how the photolysis of ozone and NO_2 may be modified by changes in the relative amounts of direct and diffuse sunlight. The primary techniques for measurement of photolysis rates are reviewed in Sections 4.1.2-4.1.4, while a more detailed description of the University of Leicester j_{O^1D} and j_{NO_2} aircraft filter radiometers is given in Section 4.1.3.

The calibration of filter radiometer measurements is discussed in Section 4.2, both from a theoretical perspective and also in terms of how it has been performed for the calibration of the measurements in this thesis. The aircraft filter radiometers were intercompared with other filter radiometers before the AMMA campaign and the results of this are detailed in Section 4.2.1. Cross comparison of the aircraft filter radiometers with both a spectral radiometer (20518) and the TUV model were carried out post AMMA in order to derive absolute calibration factors, the results from this are detailed in Section

4.2.2. A scaling difference between the photolysis rates derived from the SpecRad measurements and TUV was discovered and so the validity of both SpecRad measurements and TUV model output were considered. From a comparison of the scaling between the j_{NO_2} filter radiometer signal before and after AMMA to TUV, the TUV model output was found to be consistent under "clear sky" conditions, and therefore the difference between the SpecRad and TUV output could not be explained in terms of unaccounted for cloud or aerosol influences. A subsequent analysis of data from a cross comparison of the 20518 with another equivalent Spectral Radiometer revealed similar scaling differences between the instruments, as observed between the 20518 instrument and TUV (Section 4.2.3). The second instrument agreed much more closely with the TUV output and provided confidence that the decision to calibrate the absolute response of the filter radiometers with the scaling to TUV was valid. The non-linearities in the calibration of j_{O^1D} filter radiometer measurements were considered in Section 4.2.4, and the direction and magnitude of errors introduced by not accounting for these were estimated. A method for the determination of the spectral response of filter radiometers from cross calibration with a spectrally resolved measurement of actinic flux was proposed.

The performance of the aircraft filter radiometers during the AMMA campaign is discussed in Section 4.3, and instrumental and operational issues associated with measurements on board the BAe-146 aircraft are summarised. Owing to the failure of the lower position j_{O^1D} radiometer during the campaign, a significant contribution to the j_{O^1D} signal could be missed. A method for estimation of the missing measurement was derived and this has been assessed by comparison to the periods where the measurement was still operational (Section 4.3.1).

Chapter 5

The African Monsoon Multidisciplinary Analysis (AMMA)

This chapter introduces the AMMA project, the background and motivation behind it and provides an overview of the field work carried out within the project. It also provides an overview of the data coverage and analysis of the dataset in terms of a climatological perspective.

5.1 Overview of the AMMA project

The African Monsoon Multidisciplinary Analysis (AMMA) is an ongoing international programme that has been developing since the year 2000; in 2005 it involved scientists from over 20 countries representing more than 40 national and pan-national agencies (Lebel *et al.*, 2005). The aim has been to improve knowledge and understanding of the West African monsoon (WAM) and its variability over a wide range of scales both spatial (sub-mesoscale (<10 km) to global (10^4 km)) and temporal (sub hourly to interannual). To address the issue of scales AMMA has been structured on three nested

timescales (AMMA-UK, 2004, Lebel *et al.*, 2005):

- Long term Observing Period (LOP): 2002-2010. Using archived data to examine interannual to decadal variability of the WAM, and establishment of sustainable monitoring to document and analyse interannual variability over the AMMA period.
- Enhanced Observing Period (EOP): 2005-2007. Link between the LOP and SOP, documenting the annual cycle in surface and atmospheric conditions and observe surface memory effects at the seasonal scale.
- Special Observing Periods (SOPs): 2006. Detailed observations over the various stages of the wet season i.e. the dry season (SOP0, Jan-Feb); the monsoon onset (SOP1, 15 May-30 June); the peak monsoon (SOP2, 1 July-14 Aug); the late monsoon (SOP3, 15 Aug-15 Sept).

There has been a large UK involvement in the project (AMMA-UK) funded through the Natural Environment Research Council (NERC). Owing to the multidisciplinary nature of the project the scientific strategy of AMMA-UK split the aims into a number of themes entitled work packages (WPs).

- WP1: Land surface and atmosphere interactions.
- WP2: WAM microclimate and applications.
- WP3: Convection and WAM dynamics
- WP4: Tropospheric composition
- WP5: Tropical Tropopause Layer (TTL)

Details of the individual WPs are described in the AMMA-UK summary document (AMMA-UK, 2004).

Under WP4 an intensive period of aircraft observations were undertaken during SOP2, using the Natural Environment Research Council/UK Met Office (NERC/UKMO) BAe 146-300 atmospheric research aircraft, G-LUXE, operated by the Facility for Airborne Atmospheric Measurements (FAAM). The aircraft was based at Niamey airport, Niamey, Niger (13°, 28', 54" N, 2°, 11', 1" E) for the duration of the field campaign (17 July to 17 August 2006). The aircraft is the original BAe-146, first registered in 1981 and originally constructed as a 146-100. It was extended to a 146-300 in 1987 and re-registered as G-LUXE the registration retained since it became a research aircraft. The aircraft has a range of approximately 1,800 nautical miles, a ceiling of 35,000 feet (∼10 km), and a maximum flight duration of over five hours making it suitable for studies of the troposphere. It carries 3 crew and up to 18 scientists along with instruments (http://www.faam.ac.uk/).

5.1.1 Instrumentation fit

During SOP2 the BAe-146 was fitted with instrumentation to allow the measurement of a comprehensive chemical profile, the chemistry fit is summarised in Table 5.1. Further to this aerosol and physical parameters were measured to describe the important aerosol phase and physical variables, a selection of these measurements are summarised in Table 5.2.

5.1.2 Background and motivations

The West African Monsoon (WAM) system has been of great interest for some time due to the strong interannual and interdecadal variability in rainfall which has had a profound impact on the environment and West African societies (Lebel *et al.*, 2005). The pronounced change from wetter (1950-1970) to drier (1970 onwards) monsoon seasons is one of the strongest interdecadal changes in climate in the 20th century (IPCC, 2001, Lebel *et al.*, 2005). Global weather and climate models have been unable to predict or simulate basic characteristics of WAM rainfall on diurnal to annual timescales

Parameter	Technique	Detection limit or uncertainty	Sampling Period or Frequency	Institute
CO	VUV fluorescence	<2ppbV	10s	FAAM
>40 halocarbons	WAS and ground analysis with GC-MS	Sub pptV	90s	UEA
HCHO	Fluorometric	54pptV	30s	UEA
HNO_3	Gold convertor + chemiluminescence	100pptV	1s	UEA
$j(NO_2)$	Photometer	-	1s	Leicester
$j(O^1D)$	Fixed bandwidth radiometry	-	1s	Leicester
NO	Chemiluminescence	3pptV	10s	UEA
NO_2	Photolysis + chemiluminescence	15pptV	10s	UEA
OH	FAGE	$7.2 \times 10^5 mol.cm^{-3}$	30s	Leeds
HO_2	FAGE	$3.1 \times 10^6 mol.cm^{-3}$	1s	Leeds
Oxygenated/aromatic/olefinic hydrocarbons, some sulphur compounds such as DMS, and some nitrogen compounds such as PAN and acetonitrile	PTR-MS	<125pptV	15s	UEA
O_3	UV photometric	1ppbV	60s	FAAM
PAN	Gas chromatography (GC)	<20pptV	90s	FAAM/York
Peroxy radicals (HO_2 + $\Sigma_i R_i O_2$)	PERCA	2pptV	60s	Leicester
Real-time VOCs	ORAC in-flight GC	5pptV	240s	Leeds
Semivolatile VOCs	WAS and ground analysis with 2DGC	0.1-5pptV	90s	York
Speciated peroxides (inorg/organic)	Fluorometric	5pptV	10s	UEA
>100 VOCs inc NMHCs, alcohols, ketones, aldehydes, ethers	Whole air samples (WAS) and ground analysis with dual channel GC	0.1-5pptV	90s	York
Water vapour	Lyman-α fluorescence and dewpoint	$\pm 1^{\circ}C$	1s	UKMO/FAAM

Table 5.1: Chemistry instrumentation fitted aboard G-LUXE during AMMA (AMMA-UK, 2004)

Parameter	Technique	Detection limit or uncertainty	Sampling Period or Frequency	Institute
Aerosol size and composition	AMS	-	1s	UMIST
Broadband radiation	Pyrgeometers and Pyranometers	-	1s	FAAM
Position, winds (u,v,w)	INS, GPS, wind vanes	-	32Hz	FAAM
Scattering	Nephelometer (TSI)	-	1s	FAAM
Temperature	Rosemount PRT	$\pm 0.3^{o}$C	32Hz	FAAM
Vertical profiles of dynamical variables - Pressure, temperature, RH, wind direction, wind speed, dropsonde position	AVAPS dropsondes	-	2Hz	FAAM

Table 5.2: Selected aerosol and physical parameter instrumentation fitted aboard G-LUXE during AMMA (AMMA-UK, 2004)

due to limited understanding of the underlying processes (Parker *et al.*, 2005a). This understanding has been limited by the lack of sufficient and appropriate observations (e.g. Parker *et al.* (2008)) and also due to the complexity of the WAM system determined by the interaction of the atmosphere, biosphere and hydrosphere (Lebel *et al.*, 2005). There is a clear need to be able to better predict the WAM and its local impacts (e.g. land degradation, food and water security) such that the vulnerability of West African societies to climate variability may be reduced. Indeed, characteristic of the variability of the WAM, Janicot *et al.* (2008) states that the Summer 2006 monsoon season was "near normal" except that there was a large scale excess of rainfall north of 15^{o}N, and the onset of the monsoon (after 10 July) was delayed by 10 days compared to the climatology (5-day monsoon index for 2006 compared to 1979-2000 average). The basic structure of the WAM and its annual and diurnal cycles are summarised in Section 5.1.3. Africa is known to influence global weather and climate through the release of latent heat in deep cumulonimbus clouds along the Intertropical Convergence Zone (ITCZ[1]) which represents one of the most significant heat sources on the planet (Lebel *et al.*, 2005). Further

[1]The ITCZ occurs in the region of convergence of low level north easterly trade winds from the northern hemispheric Hadley Cell with the south easterly trades winds from the southern hemispheric Hadley Cell.

evidence for the wider impact of the WAM system is through the correlation between Sahelian[2] rainfall and Atlantic hurricane frequency (Lebel *et al.* (2005) and references therein).

In terms of the importance of the region to atmospheric composition, the seasonal cycle between monsoon and dry season will lead to a variation in the processes affecting emissions, chemistry and transport. Aghedo *et al.* (2007) define four sources of trace emissions in Africa, these being biomass burning, natural (biogenic) emissions from vegetation and soil, lightning NO_x emissions, and other anthropogenic sources (which includes emissions related to the combustion of fossil-fuel for energy, industrial, transport and domestic uses). Of these, Aghedo *et al.* (2007) state that biomass burning, biogenic emissions and lightning NO_x are of global significance, while anthropogenic fossil fuel emissions are regionally significant. Anthropogenic fossil fuel emissions are likely to further increase in association with increasing population density at population centres e.g. Lagos, Cotonou, Niamey. Aerosols are a further significant emission type in terms of their impact on the radiation budget, and they have a number of significant sources both natural and anthropogenic in Africa. The Sahara has been identified as the most significant source of mineral dust aerosol on the planet (Haywood *et al.* (2008) and references therein) and this is a source that is present year round and interacts with the WAM through the Saharan air layer (see Section 5.1.3). Biomass burning in tropical Africa is also a significant source of aerosols, though the location and strength of this source is seasonal, moving with the movement of the dry season. Biomass burning is therefore greatest in the Sahel region during the northern hemisphere winter months peaking in December and January (Lebel *et al.*, 2005), which was the target of the SOP0 observing period and is discussed in the overview of Haywood *et al.* (2008). During the northern hemisphere summer, the period of the WAM and therefore the observing period of SOP2, biomass burning is peaked in Central and Southern Africa so can only impact on the study region of SOP2 through transport. Indeed the global chemical transport model simulations

[2]The Sahel is the semi arid transition region which extends from Senegal in the east to Sudan in the west. It is the region of transition between the Sahara Desert in the north and the more vegetated savanna belt to the south

of Aghedo *et al.* (2007) show the influence of biomass burning in central Africa extending into the Gulf of Guinea. The distribution of African biomass burning emissions during SOP2 is made clear in a composite map of fire locations from the MODIS sensor for a 10 day period (9 August-18 August 2006) shown in Figure 5.1.

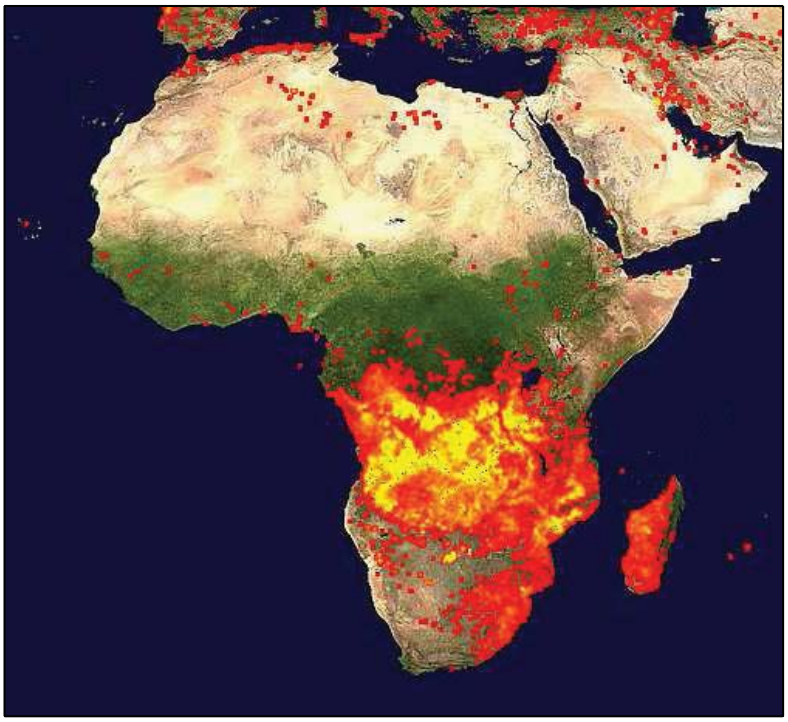

Figure 5.1: MODIS 10-day composite firemap for Africa during SOP2 (9 August-18 August 2006). The colour scale ranges from red where the fire count is low to yellow where number of fires is large. Image courtesy of NASA/GSFC, MODIS Rapid Response (http://rapidfire.sci.gsfc.nasa.gov/firemaps/)

Biomass burning in tropical Africa is a major global source of trace gas emissions contributing 40% of global emissions (Aghedo *et al.* (2007) and references therein). It leads to the production of a large variety of important trace species such as water vapour, CO_2, CO, NO_x, CH_4, non-methane hydrocarbon compounds (NMHC's), NH_3, H_2S and SO_x, so will have a significant impact on the chemistry wherever these emissions are observed. Biomass burning is of relevance to this work in that significant concentrations of volatile organic compounds (VOC's) and NO_x will lead to elevated radical concentrations and ozone production.

Lightning may be a significant source of NO_x leading to ozone production during the WAM where lightning occurs in tropical convective thunderstorms. Lightning activity is known to be maximum in the tropics (Aghedo *et al.*, 2007) though its distribution is presumably seasonal due to the requirement for moist convection. Lightning NO_x production is limited to the middle to upper troposphere (Aghedo *et al.* (2007) and references therein) and hence will primarily influence the chemistry here. Large uncertainty is present in the magnitude and distribution of lightning as a NO_x source (and therefore its impact on ozone production) owing to the fact that tropical storms are least well characterised (Lebel *et al.* (2005), Aghedo *et al.* (2007) and references therein).

VOC emissions are dominated by biogenics both in terms of total mass and also by number of compounds (Guenther *et al.*, 2006). Of these emissions the major components consist of two compounds, methane and isoprene; these species are so widely produced that they each contribute approximately a third of total annual global VOC emissions, biogenic and anthropogenic (Guenther *et al.*, 2006). The main biogenic source of methane has been considered anaerobic decomposition of plant material in wetlands (e.g. IPCC (2001)), although the strength of this source and others are rather uncertain the major sources were thought to have been identified until recently. An additional potentially major biogenic source of methane was discovered by Keppler *et al.* (2006), that being aerobic emissions from living plants and leaf litter. This source has been controversial since the emission mechanism remains unknown and owing to uncertainty with regard to the strength of emissions. Wang *et al.* (2009) suggests that in part this controversy is a result of varying levels of emission across species (even among close relatives) leading to a number of null results, and also owing to strong variation in emission rate dependent on physiological stress caused by environmental variables. The study by Wang *et al.* (2009) looked for a potential effect on emission rate caused by physical injury (in this case simulated by cutting) and under hypoxic conditions (low oxygen levels, but where anaerobic emission due to microbial methanogenesis is ruled out) and found that both stresses can cause and

enhance methane emission, dependent on plant type. Originally Keppler *et al.* (2006) found both sunlight and increased temperatures enhanced methane emission rates. The study of Keppler *et al.* (2006) was motivated in part by satellite observations (from the SCIAMACHY instrument on board ENVISAT) of enhanced methane concentrations within the tropics which could not be explained by emission inventories at the time (i.e. Frankenberg *et al.* (2005)). Recent updates on these satellite observations (i.e. Frankenberg *et al.* (2008), Schneising *et al.* (2009)) have determined that some of the observed enhancement in the retrieved methane column density has been a result of discrepancies in the retrieval algorithms used. Primarily an uncertainty in water vapour spectroscopic line parameters makes the retrieval sensitive to the enhanced levels of water vapour characteristic of the tropics during the wet season. Still, enhanced methane is observed in the tropics (although at reduced strength) and observed by Frankenberg *et al.* (2008) and Schneising *et al.* (2009) using different retrieval techniques. The evidence points toward a significant source of methane emissions by plants in the tropics, with sunlight, temperature and other stresses enhancing these emissions. There is therefore the potential for further enhancements associated with increased stress through climate change, stratospheric ozone depletion, increasing ground-level ozone, spread of plant pests, and land-use changes (Wang *et al.*, 2009). Methane is a long-lived compound with a lifetime of ∼8.4 years (IPCC, 2001) (derived from the ratio of the total atmospheric burden to the estimated global loss rate i.e. 4850 Tg/576 Tg yr^{-1}) meaning emissions become well mixed throughout the atmosphere. Since reaction with methane is a primary route for OH in relatively unpolluted environments (Monks, 2005) (leading to the formation of the methyl peroxy radical (CH_3O_2)), this may have an impact on oxidative capacity and the radical budget in the tropics.

As mentioned, isoprene is thought to contribute a third of total annual global VOC emissions. More than 90% of isoprene emissions are from terrestrial plants (Guenther *et al.*, 2006) illustrating the importance of the terrestrial biosphere. Tropical broadleaf trees are predicted to contribute approx-

imately half of global isoprene emissions, while tropical shrubs and arid land shrubs contribute 28% and 11% respectively (Guenther *et al.*, 2006). Africa is estimated to contribute approximately one fifth of global isoprene emissions (Aghedo *et al.* (2007) and references therein). The emissions of biogenic NMHC's is reviewed in detail by Fuentes *et al.* (2000), and the following information is derived from that review. The predicted importance of tropical emissions is a result of the fact that tropical forest ecosystems are physiologically active throughout the year, and the known environmental factors that control isoprene emission. There is speculation that isoprene emission may be a protective mechanism against frequent and rapid temperature change. Emission is common among trees, in particular those with large leaves suspectible to heating by sunlight, emission is uncommon among herbaceous and crop plants who use large amounts of water to cool their leaves, and emission is not found in cacti who are subject to consistently high temperatures; all these suggest a susceptibility to changes in temperature. A further environmental control is the ambient light level which often shows a similar dependence as that of photosynthesis; shade tolerant plants do not tend to emit isoprene and higher emissions are observed from leaves at the top of a tree canopy to those within it. Leaf development state is another critical factor controlling hydrocarbon emissions, isoprene emission requiring leaves to be fully grown and even then emission requires sufficiently high temperatures. It may therefore be expected that isoprene emissions will be controlled by the progression of the monsoon in the sense that the monsoon rainfall and seasonal growth of vegetation are intimately linked.

Plants emit a large variety of VOC's besides isoprene, the most important group of which are the terpenes ($(C_5H_8)_n$), and the simplest of which is isoprene ($n = 1$), also important are the mono ($n = 2$) and sesquiterpenes ($n = 3$). Oxygenated organic compounds (terpinoids) are also produced, including alcohols, aldehydes and ketones, the most important of these being methanol which has been observed from all plants studied to date, according to Fuentes *et al.* (2000). Monoterpene emissions are dominated by temperature and tropical forests have many monoterpene producing species. The

role of monoterpenes is believed to be a defensive mechanism for plants and therefore younger leaves emit greater amounts due to the greater risk from pests and pathogens. The environmental factors controlling the emissions of biogenic NMHC's are primarily sunlight, temperature and other stresses. There is therefore the potential for the enhancement of biogenic NMHC's emissions associated with increased stress through climate change, stratospheric ozone depletion, increasing ground-level ozone, spread of plant pests, and land-use changes as per methane. In contrast to methane, biogenic NMHC's are typically much more reactive and therefore have a much greater potential to impact on atmospheric composition from local to regional scales as a result of their reduced lifetimes. The typical lifetimes of a number of biogenic NMHC's and their oxidation products have been summarised by Fuentes *et al.* (2000) with respect to OH, NO_3 and O_3 given 12 hour average daytime concentrations of OH, 12 hour average nighttime concentrations of NO_3 and 24 hour average concentrations of ozone. Isoprene has a typical lifetime of the order minutes to hours with respect to OH and NO_3 and little more than a day with respect to ozone. This means it will generally be confined close to its emission source and therefore its spatial distribution should be indicative of the distribution of vegetation. The lifetimes of other terpenes are similarly short due to their highly reactive nature. The lifetimes calculated in this sense are only a guide since the *in-situ* lifetime is dependent on the ambient concentrations of the primary oxidants which vary significantly compared to the average. Increased VOC emissions affect the oxidative capacity of the atmosphere through the consumption of these oxidants. Furthermore, in the presence (absence) of sufficient levels of NO_x, they can lead to photochemical production (destruction) of ozone in the troposphere, affecting the ozone budget. Another impact of significant biogenic VOC emissions is through the production of secondary organic aerosol (SOA), which forms from the oxidation products of certain biogenic VOC's (Finlayson-Pitts & Pitts, 2000). As mentioned, aerosols impact on the radiation budget and their influence is known during the dry season. Potentially significant SOA formation during the monsoon season is a possibility with strong emissions of biogenic VOC's.

Emission from soil is an observed source of NO which results from microbial processes in soils. This emission is enhanced with the onset of rainfall in tropical ecosystems which experience wet and dry seasons. For example Jaegle *et al.* (2004) used satellite NO_2 observations to infer soil emissions of NO from the African Sahel region of comparable levels to dry season emissions related to biomass burning. During the dry season soils accumulate inorganic nitrogen, and then with the onset of rainfall water stressed nitrifying bacteria become active, consume the accumulated nitrogen and produce NO as a by product. Very low soil emissions are observed during the dry season, while spikes of NO emissions are observed from dry savannahs and seasonally dry forest dictated by the frequency of rainfall. With persistent rainfall NO emissions remain high even once excess nitrogen is consumed (Jaegle *et al.*, 2004), without rainfall soils dry out and emissions fall to background levels within 2-3 days (Stewart *et al.* (2008) and references therein).

The presence of significant natural sources of VOC's (primarily biogenic, some potential influence of biomass burning and localised anthropogenic sources) and NO_x (soil emissions into the boundary layer, lightning in the upper troposphere, some potential influence of biomass burning and localised anthropogenic sources) along with the availability of sunlight and water vapour during the monsoon mean the WAM has all the ingredients for active photochemistry. The potential transport of ozone and precursors from the boundary layer to the upper troposphere and beyond through deep convection (see e.g. Prather & Jacob (1997), Jaegle *et al.* (2001)) means the emissions from the WAM region have the potential to influence the ozone budget on a global scale (see e.g. Aghedo *et al.* (2007)). The reported variability in the monsoon system must be expected to impact on the atmospheric composition through changes in emissions, chemistry and transport. Even with the expected importance of the West African region to the chemistry of the atmosphere both locally and globally no systematic observations of chemical composition had been made prior to AMMA (Lebel *et al.*, 2005).

5.1.3 West African Monsoon (WAM) system and dynamics

A schematic view of the West African Monsoon system is shown in Figure 5.2 representing the developed monsoon system and the typical latitudes and pressure levels of the characteristic flows (Lebel *et al.*, 2005, Parker *et al.*, 2005b). The key features of the WAM can be summarised along a north-south transect due to the strong zonal symmetry of the characteristic flows. The zonal symmetry arises due to the meridional gradient in heating from the Gulf of Guinea in the south to the Sahara in the north[3]. The higher air temperature at the surface over land in the north leads to convection and generates an area of low pressure, the Saharan heat low. There is then a pressure gradient between the Saharan heat low and oceanic high pressures of the Santa Helena anticyclone (Janicot *et al.*, 2008). This leads to and controls low level south westerly winds that take humid air from the Atlantic and Gulf of Guinea to the Sahel, and provide most of the moisture to the WAM (Lebel *et al.*, 2005); these are the monsoon winds. A pressure gradient also exists to the north between the Libyan and Azores anticyclones and the Saharan heat low that drives the dry north easterly Harmattan wind (Janicot *et al.*, 2008). The confluence of the monsoon and Harmattan winds at the heat low mark a discontinuity in the zonal winds referred to as the Intertropical discontinuity (ITD).

Parker *et al.* (2005b) describes the regions of the WAM system as made up of a number of coherent layers (refer to Figure 5.2). The humid low level south westerly winds define the monsoon layer, a region of humid air connected to the land surface that extends northward from the Gulf of Guinea, the depth of the layer decreasing toward the north. The monsoon layer varies on a diurnal timescale perturbed by the diurnal variation in the convective mixed layer and the development of shallow cumulus clouds (Parker *et al.*, 2005b). The monsoon layer is bounded above and to the north by the Saharan air layer (SAL); the layer is generated by dry convection over the Sahara and the advection of

[3]The gradient in heating is a result of the greater heat capacity of water compared to land; this means the air over the land warms faster than the air over the water during the northern hemisphere summer in response to radiative heating and causes a temperature gradient in near surface air temperature.

the north easterly Harmattan winds over the monsoon layer, this brings relatively dry Saharan air into the rainy region (Lebel *et al.*, 2005) along with Saharan dust (Janicot *et al.*, 2008). The SAL is deepest in the north where it originates and merges with the Saharan boundary layer and becomes thinner toward the south. The SAL is characterised by its high aerosol dust content (Parker *et al.*, 2005b) but it is not restricted to air of Saharan boundary layer origin, and evidence of mixing has been observed in terms of exchange of air with the monsoon layer through adiabatic motion (Parker *et al.*, 2005b). Further evidence of mixing between the SAL and monsoon layer is perhaps found in the seasonal cycle of aerosol optical thickness (AOT) for 2006 reported in Janicot *et al.* (2008); the AOT is reduced during the Summer monsoon due to wash out of dust particles by precipitation (Janicot *et al.*, 2008).

The African Easterly Jet (AEJ) is a zonal, mid tropospheric (600-700 hPa) jet that is located over North Africa during the northern hemisphere summer in the region of strong low level gradients in potential temperature between the Gulf of Guinea and Sahara (Lebel *et al.*, 2005). It is an important component of the WAM system in that it links the large scale aspects of the WAM to the characteristic weather systems (Parker *et al.*, 2005b). During the summer monsoon the core of the jet is typically located at the northern edge of the area of maximum convection (the ITCZ) e.g. (Redelsperger *et al.*, 2002). This is consistent with the assessment of the AEJ by Parker *et al.* (2005b) based on observations from the JET2000 campaign which characterised the relatively undisturbed AEJ and WAM system. Their analysis confirmed that in the "bulk" sense the presence of the AEJ was driven by thermal wind balance. In the north the temperature profile was close to a dry adiabat indicative of the dominance of dry convection, while in the south the temperature profile was close to pseudoadiabatic consistent with deep moist convection. The position of the core of the AEJ then determined by the pressure level where the meridional temperature contrast between the adiabatic and pseudoadiabatic profiles is zero, in this case approximately 625 hPa (Parker *et al.*, 2005b). The AEJ and the SAL are closed above by an upper tropospheric layer characterised by very low values of humidity, though convection can

penetrate the SAL and bring humid air into the layer. An upper level zonal jet (∼200 hPa) referred to as the Tropical Easterly Jet (TEJ) is also present. The TEJ is enhanced during the peak of the monsoon when it lies to south of the maximum in convection at the ITCZ, and occurs in association with the outflow of convection. Outflow from convection into the region of the TEJ has great potential for the global transport of ozone and precursors highlighted above in Section 5.1.2.

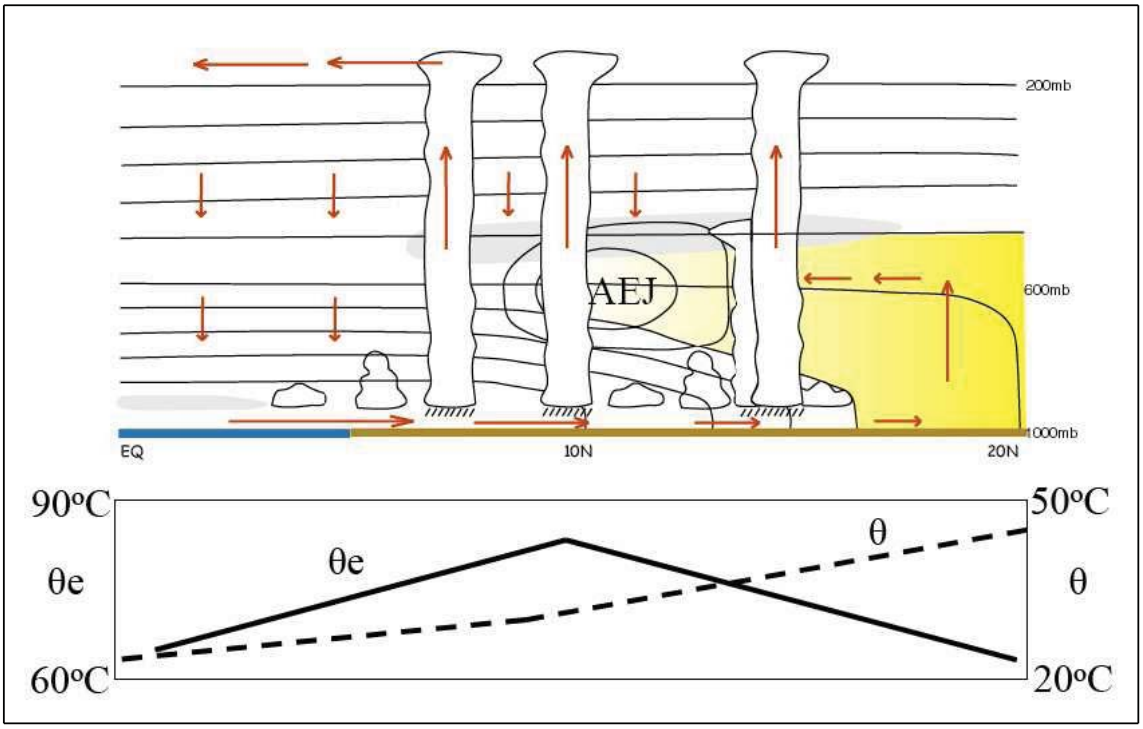

Figure 5.2: Top: Schematic diagram of the West African Monsoon along N-S transect showing the heat-low/AEJ/ITCZ system and SAL (in yellow). Bottom: Schematic representation of meridional gradient in potential temperature (θ) and equivalent potential temperature (θ_e). Diagram from Lebel *et al.* (2005) in turn adapted from Parker *et al.* (2005b)

The annual and diurnal cycles of the WAM

The annual cycle of the WAM is reviewed in Lebel *et al.* (2005) and Janicot *et al.* (2008). Janicot *et al.* (2008) provides an extensive overview of the 2006 rainy season in West Africa relative to the 1968-2005 climatology, and Parker *et al.* (2005a) provides a detailed assessment of the diurnal cycle of the WAM.

The following is a short summary of the typical features of the annual and diurnal cycles of the WAM based on these reviews.

The annual progression of the WAM is characterised by the meridional migration of the ITCZ, progressing northward with the progression of the northern hemisphere summer. Prior to the onset of the WAM there is a transition period when the ITCZ "jumps" northward from the vicinity of the coastal region around 5^oN (where it lies in May-June) to around 10^oN (where it lies in July-August); this transition is also marked by a period of reduced convection across West Africa. The shift in rainfall occurs mostly between 10^oW and 5^oE, where there is a significant north-south gradient in surface heating due to the north-south contrast between land and sea. Convection and associated rainfall then begins over the Sahel following this transition period, which marks the onset of the monsoon. The monsoon peaks, on average, around the beginning of August and following this there is typically a more rapid retreat of the ITCZ marking the end of the wet season (see e.g. the climatology presented in Redelsperger *et al.* (2002)).

Parker *et al.* (2005a) cites the diurnal cycle in monsoon winds as a fundamental mode of atmospheric circulation in the WAM. A model and observational study was used to provide a description of the diurnal cycle, and to explain the origins of this significant mode of variability. By day and into the afternoon the monsoon winds were observed to weaken as a result of strengthening mixing in the daytime convective boundary layer (CBL), with the low level monsoon flow being weakest when the CBL is deepest (and vertical mixing is strongest). In contrast the monsoon winds were most intense at night when convective mixing is suppressed and this leads to vertical stratification of the lowest levels of the monsoon layer. The combined effect is that by day water vapour, trace gases and aerosols may be mixed vertically from the surface to the free troposphere, while meridional advection is favoured at night, with vertical movement restricted to isentropic gliding of air masses. There is a competition between the diurnal cycle in circulation (driven by the diurnal cycle in the Saharan heat low) and the

diurnal cycle of the CBL which through vertical mixing interrupts the meridional circulation. Hence the diurnal contrast is a maximum in the north where the meridional pressure gradient is strong and the diurnal cycle in the CBL is strong due to greater variation in surface temperature between day and night over bare soil. The night time flow is characterised by poleward advection of moist air toward the low pressure region of the Saharan heat low and constitutes the nocturnal jet, with a dry return flow above. While Parker *et al.* (2005a) focuses on the impact of this in terms of water budget, they also allude to the influence that this diurnal circulation will have on the budgets of trace gases. Whether the influence of this circulation and other dynamical features on chemical composition has been observed during SOP2 depends on the sparsity of the observations with respect to the temporal and spatial scales of the processes.

5.2 Overview of data from the aircraft SOP

5.2.1 Data coverage

A total of 25 flights (not including transit flights) were undertaken during SOP2 using the BAe-146. The first flight was on the 20 July and last on the 17 August 2006, totalling approximately 102 flight hours. Details of the individual flights dates, timings and a basic description of the flight aims are given in Table 5.3. According to Janicot *et al.* (2008) the monsoon onset for 2006 was after 10 July and rainfall was in excess north of 15^{o}N. Hence, the sampling period began 10 days post monsoon onset and the excess rainfall to the north indicates a larger extension of the monsoon to the north, and therefore the characteristics of the monsoon described in Section 5.1.3 may be evident in the flight data though shifted northward.

The potential data coverage (spatial and temporal) from the BAe-146 is made clear from composite plots of the flight tracks in altitude, latitude, longitude and time. The spatial distribution of sampling

Flight # (Julian Day)	Date	Take-off (Landing) (UTC)	Description
B216 (201)	20/07/2006	13:03:54 (17:12:16)	Soil moisture flight, NS vegetation gradient and interception of Niamey plume
B217 (202)	21/07/2006	12:57:44 (17:16:00)	Repeat of B216
B218 (203)	22/07/2006	14:37:40 (18:49:08)	Post MCS Repeat of B216
B219A (206)	25/07/2006	12:50:52 (16:50:41)	Daytime sampling over vegetation
B219B (206)	25/07/2006	18:25:15 (22:25:44)	Nocturnal sampling over vegetation
B220 (208)	27/07/2006	10:57:38 (15:10:48)	Sampling over vegetation gradient NS and EW and interception of Niamey plume
B221A (209)	28/07/2006	11:50:45 (16:03:18)	Daytime sampling over soil moisture
B221B (209)	28/07/2006	17:30:33 (20:25:06)	Night time sampling transition over soil moisture
B222 (211)	30/07/2006	11:26:12 (15:48:10)	Sampling NS over vegetation gradient
B223 (212)	31/07/2006	14:59:01 (19:08:33)	Sampling over soil moisture variation ahead of/behind MCS
B224A (213)	01/08/2006	12:46:30 (17:16:16)	Daytime sampling over variation in soil moisture and vegetation NW of Niamey
B224B (213)	01/08/2006	18:33:34 (22:10:39)	Nocturnal repeat of B224A
B225 (215)	03/08/2006	13:26:01 (16:40:03)	Evacuation flight
B226 (217)	05/08/2006	11:33:31 (16:01:44)	Mapping biogenic emissions over Ghana, Togo and Djougou
B227 (218)	06/08/2006	12:56:40 (17:08:02)	Sampling over soil moisture variations due to passage of MCS on previous evening NE of Niamey
B228 (220)	08/08/2006	09:41:01 (13:34:42)	Cotonou flight: SH biomass burning layer near Cotonou
B229 (220)	08/08/2006	15:09:57 (19:10:28)	Lagos flight: Pollution in/outflow from Lagos; convective storm outflow en route to Niamey
B230A (223)	11/08/2006	13:17:33 (17:43:19)	Sampling over soil moisture following heavy rain on a dry surface
B230B (223)	11/08/2006	19:04:04 (22:22:05)	Nocturnal dropsondes
B231 (225)	13/08/2006	07:01:32 (11:32:47)	Cotonou and ocean flight: Monsoon flow; biomass burning layer
B232 (226)	14/08/2006	04:28:39 (08:40:04)	Pre MCS dawn flight: Sampling over vegetation gradient; sampling residual nocturnal boundary layer and developing boundary layer
B233 (227)	15/08/2006	04:30:50 (09:00:08)	Post MCS dawn flight: Similar timings as B232
B234 (228)	16/08/2006	14:18:37 (17:54:56)	Intercomparison flight
B235A (229)	17/08/2006	10:24:27 (14:57:33)	Morning: Congestus flight over Benin
B235B (229)	17/08/2006	16:25:22 (20:52:11)	Day/night transition: Congestus flight over Benin

Table 5.3: Summary of the BAe-146 flights undertaken during AMMA SOP2

is shown in Figure 5.3 with flight tracks by latitude, longitude and altitude with frequency of sampling alongside. The temporal distribution of sampling is shown in Figure 5.4 with position in latitude, longitude and altitude as a function of the time of day with frequency of sampling alongside. The time spent on the ground at Niamey has not been filtered in the frequency histograms and hence the peaks in sampling at the location of Niamey airport (13° 28' 54" N, 2° 11' 1" E) are an anomaly. In terms of the spatial distribution the aircraft observations were most widely spread in latitude though the sampling was predominantly in between 9-16^{o}N; while in longitude the sampling was more focused primarily between 0.5-3^{o}E. This distribution is reasonable considering the reported zonal symmetry of the monsoon system and its northern extent during 2006. By altitude, the majority of sampling was below 1 km altitude, and then fairly even up to approximately 7 km altitude, above which the number of observations is significantly less. In terms of the temporal distribution of sampling the observations were most concentrated in the early afternoon, between 13:00-16:00 UTC. The mornings were significantly less sampled with the least observing time dedicated to the early mornings, which may result in undersampling the diurnality of the atmospheric composition in relation to the diurnality of the monsoon flow discussed in Section 5.1.3.

The data coverage of the University of Leicester measurements of peroxy radicals by PERCA and photolysis rates (j_{O^1D} and j_{NO_2}) through filter radiometry during AMMA SOP2 are summarised in Figures 5.5 and 5.6. A number of operational and instrumental issues limited the data coverage for these measurements, in particular the PERCA measurements and the j_{O^1D} filter radiometer measurements were significantly affected.

In terms of the PERCA measurements overall coverage is limited to ∼25% over the whole campaign (excluding time on the ground at Niamey), still, a significant dataset has been produced. Primarily, a logistical issue with reagent gas provision meant that in early flights (B216-B219B) measurements were performed in a rationed manner (only supplying reagent CO on low altitude runs) until the available

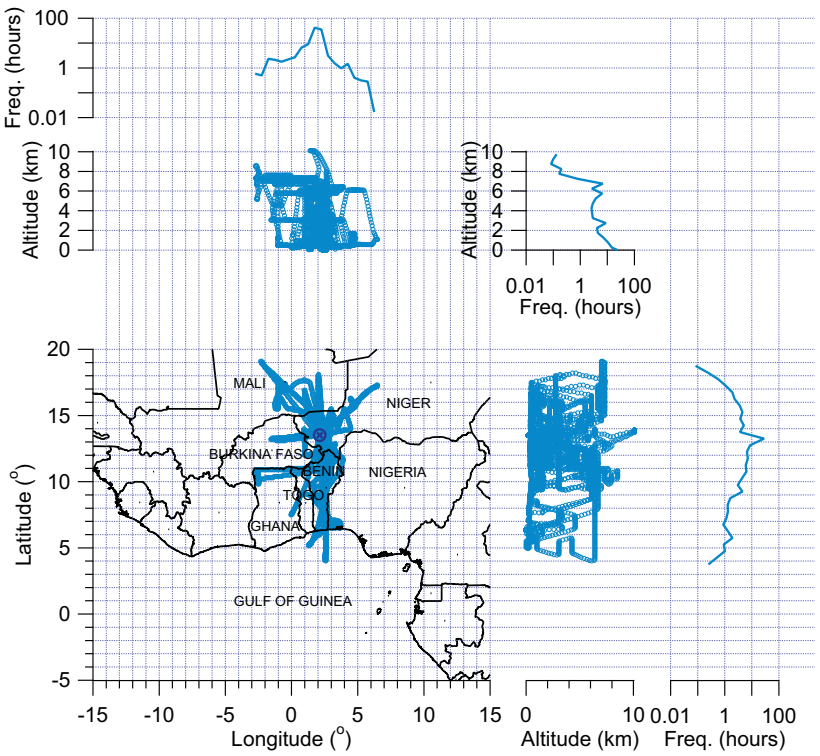

Figure 5.3: Spatial distribution of BAe-146 measurements during AMMA SOP2

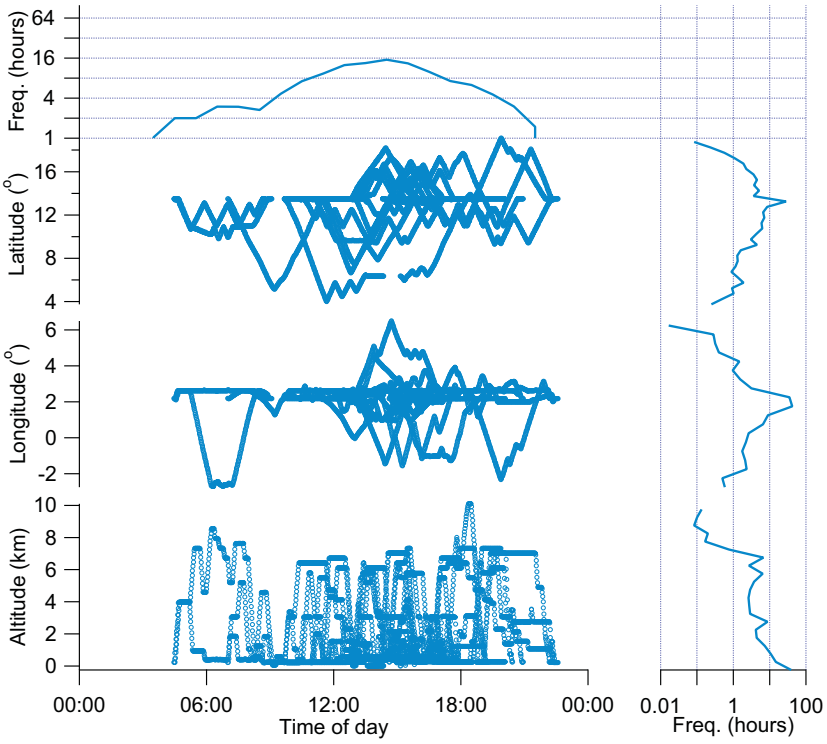

Figure 5.4: Temporal distribution of BAe-146 measurements during AMMA SOP2

gas was consumed. Overall coverage on these early flights (i.e. B216-B219B, including all altitudes and excluding time on ground at Niamey) alone was ∼36%. During flight B220 the reagent gas supply failed and therefore no useful measurements were retrieved; a further 13 flights were missed before gas became available once more. Measurements were then performed on flights B231-B235B, and overall coverage on these flights was ∼39%. The other constraints on data coverage from the PERCA instrument were primarily instrumental; there are a number of significant limitations. Firstly, as observed by Parker (2007) during the ITOP campaign, there remains a problem with maintaining sample flow through the inlets at 2 slpm above an altitude of ∼4.3 km. Above this altitude data is not retrieved since the sample flow and therefore reagent concentrations are not controlled, meaning the chain length will vary in an unknown manner. A further and related issue is associated with the luminol flow to the detectors, which owing to the method of flow control (see Section 3.3.1, page 103) slows or stops where the sample flow cannot be maintained. Although this occurs only where the sample flow also fails, the disturbance of the luminol flow means that on returning to an altitude where sampling at 2 slpm is possible, the luminol flow may not return immediately or alternatively become unstable and require adjusting; in this situation it is not possible to derive a signal. Disturbances to the luminol flow can occur at other times due to the dynamic conditions experienced when running on an aircraft platform. A third issue was related to difficulties with inflight calibration, both instrumental and operational. The time required for mixing of the calibration mixture (essentially the time it took to achieve a stable response to addition of the calibration mixture) was prohibitively long compared to the time available for calibration, meaning there was insufficient opportunity for inflight calibration. An additional uncertainty with the inflight calibration system is through the unreliability of the needle valves used for controlling the flow of nitrogen over the calibration permeation tubes of NO_2 and CH_3I. Inflight calibration of NO_2 sensitivity was instead achieved by an alternative method (described in Section 3.3.3, page 108), however time spent in attempted calibrations reduced the time available for measurement. Examining the data coverage below the altitude ceiling on sample flow control the

sampling is better (i.e. excluding sampling at altitudes ≥4.3 km and excluding time on ground at Niamey), being ∼46% for flights B216-B219B (where measurement opportunities were rationed) and ∼55% for flights B231-B235B.

In terms of the filter radiometer measurements overall coverage over the whole campaign (excluding time on the ground at Niamey) for j_{O^1D} is ∼64% while for j_{NO_2} it is ∼76%. The coverage for j_{O^1D} includes a significant proportion of points (i.e. ∼40% of overall coverage) where the upwelling j_{O^1D} component has been estimated due to one of two instrumental issues (for details of the estimation method see Section 4.3.1, page 172). From flight B221A onwards the lower position j_{O^1D} radiometer failed due to water damage of the instrument electronics, prior to this coverage from the lower position j_{O^1D} radiometer was affected due to saturation of the signal above cloud. An operational issue that affected both j_{O^1D} and j_{NO_2} measurements was shutter obscuration of the lower position radiometers (see Section 4.3, page 171) which resulted in a loss of ∼15% of data coverage for both parameters. No useful measurements could be retrieved in this situation as the contribution of the signal lost is unknown, furthermore it was not possible to estimate the lower position j_{O^1D} radiometer signal where this occurred. These issues and the discussion of correction for them is found in Chapter 4, Sections 4.3 and 4.3.1.

The spatial distribution of sampling achieved with the PERCA is shown in comparison to the spatial distribution of sampling achieved with the j_{O^1D} and j_{NO_2} filter radiometers in Figure 5.5. It is clear that the PERCA measurements are restricted by altitude owing to the flow control issue, though the data coverage below ∼4.3 km is significantly better. By longitude the coverage is restricted owing to missing a large number of flights in the middle of the campaign due to a lack of reagent gases. Owing to the enhanced number of observations by latitude overall, the PERCA measurements sample over nearly the whole latitude band at some time of day. The measurement coverage is therefore reasonable, considering the zonal symmetry of the monsoon as a whole. The temporal distribution of sampling

achieved with the PERCA is shown in comparison to the temporal distribution of sampling achieved with the j_{O^1D} and j_{NO_2} filter radiometers in Figure 5.6. The PERCA dataset has been restricted due to the number of operational flights, still a near diurnal cycle (04:30-22:00 in composite) has been observed over a latitude band of ∼9-14^{o}N, at a single longitude of ∼2.6^{o}E and essentially all below 4 km altitude. Since the PERCA was operated on flights at the beginning and end of the campaign, the monsoon has been sampled close to onset and toward the peak monsoon. In terms of the spatial and temporal coverage of the filter radiometer measurements, due to the good overall coverage these datasets cover essentially the whole range of conditions sampled.

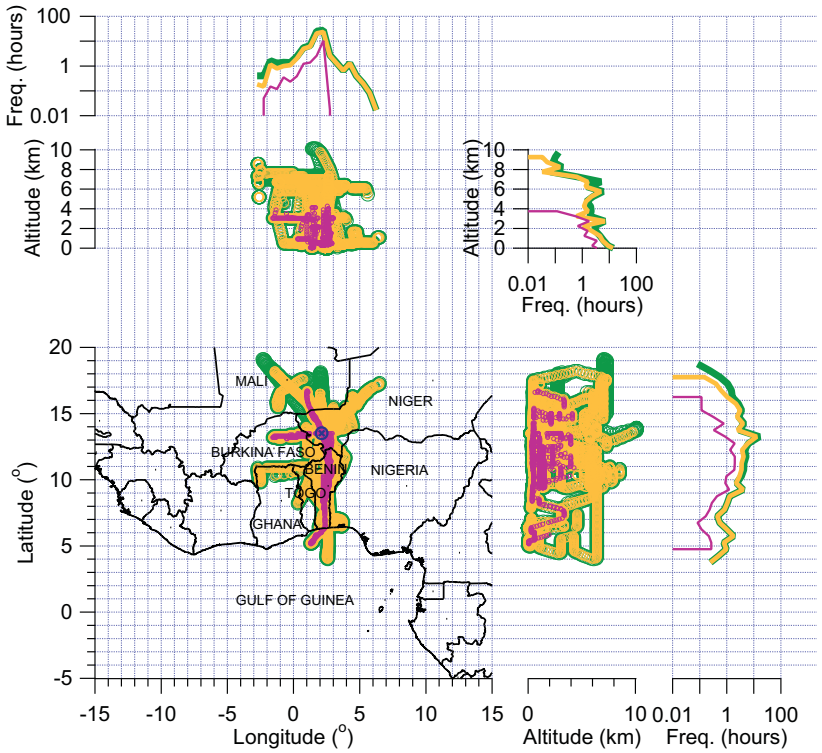

Figure 5.5: Spatial distribution of PERCA and filter radiometer measurements during AMMA SOP2 - PERCA measurements (pink); j_{O^1D} filter radiometer measurements (light yellow); j_{NO_2} filter radiometer measurements (green)

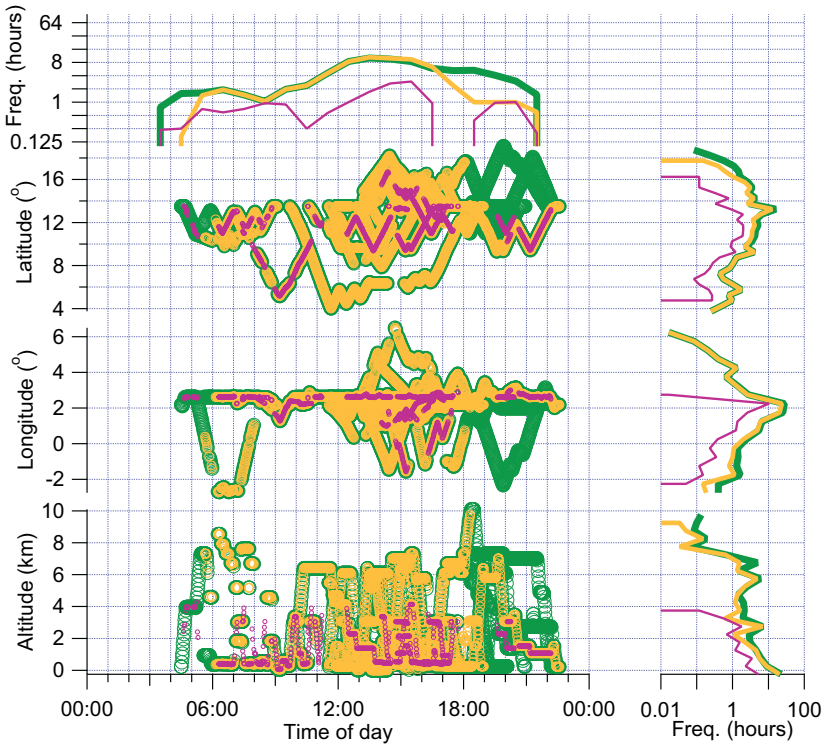

Figure 5.6: Temporal distribution of PERCA and filter radiometer measurements during AMMA SOP2 - PERCA measurements (pink); j_{O^1D} filter radiometer measurements (light yellow); j_{NO_2} filter radiometer measurements (green)

5.2.2 Measurements of radicals and photolysis rates

The total campaign dataset for PERCA measured peroxy radicals (without humidity correction applied), FAGE measured OH and HO_2, and photolysis rates j_{O^1D} and j_{NO_2} are presented for each flight where at least one of these measured parameters was monitored in Figures 5.7-5.17. Also plotted are modelled clear sky photolysis rates (j_{O^1D} and j_{NO_2}) derived using the Tropospheric Ultraviolet and Visible (TUV) Radiation Model version 4.1 of Madronich (1987), Madronich & Flocke (1998) for comparison to the measured photolysis rates. The model was constrained using an altitude temperature profile derived from the ambient air temperature measured by the Rosemount PRT instrument on board the BAe-146 during the campaign. The model was further constrained using the total ozone column density on the day of a particular flight, derived from the average of the overhead total ozone column density at four locations in the region (Niamey, Niger at 13.5^{o}N, 2.1^{o}E; Djougou, Benin at 9.7^{o}N, 1.67^{o}E; Cotonou, Benin at 6.33^{o}N, 2.43^{o}E; Ouagadougou, Burkina Faso at 12.37^{o}N, 1.53^{o}W). The overhead total ozone column density at these locations was retrieved from the Ozone Monitoring Instrument (OMI) on the Aura spacecraft. Input to the model to derive photolysis rates along a flight track consisted of time (seconds since midnight on day of interest), latitude (degrees north), longitude (degrees east), altitude (metres above sea level).

There are a number of preliminary qualitative observations than can be made here with regard to the time series presented in Figures 5.7-5.17. The FAGE measurement of HO_2 has been converted to a mixing ratio and plotted on the same axis as the PERCA measurement for more direct comparison, while the FAGE measurement of OH is left in molecule cm^{-3}. There is considerable variability in the PERCA measured peroxy radical signal, FAGE measured OH and HO_2 and photolysis rate data, though the variability in HO_2 is often reduced. Both the PERCA and FAGE OH measurements suffer more enhanced instrumental noise owing to worse detection limits relative to FAGE HO_2 and the photolysis rate measurements. The PERCA measurement is also a summed response with a

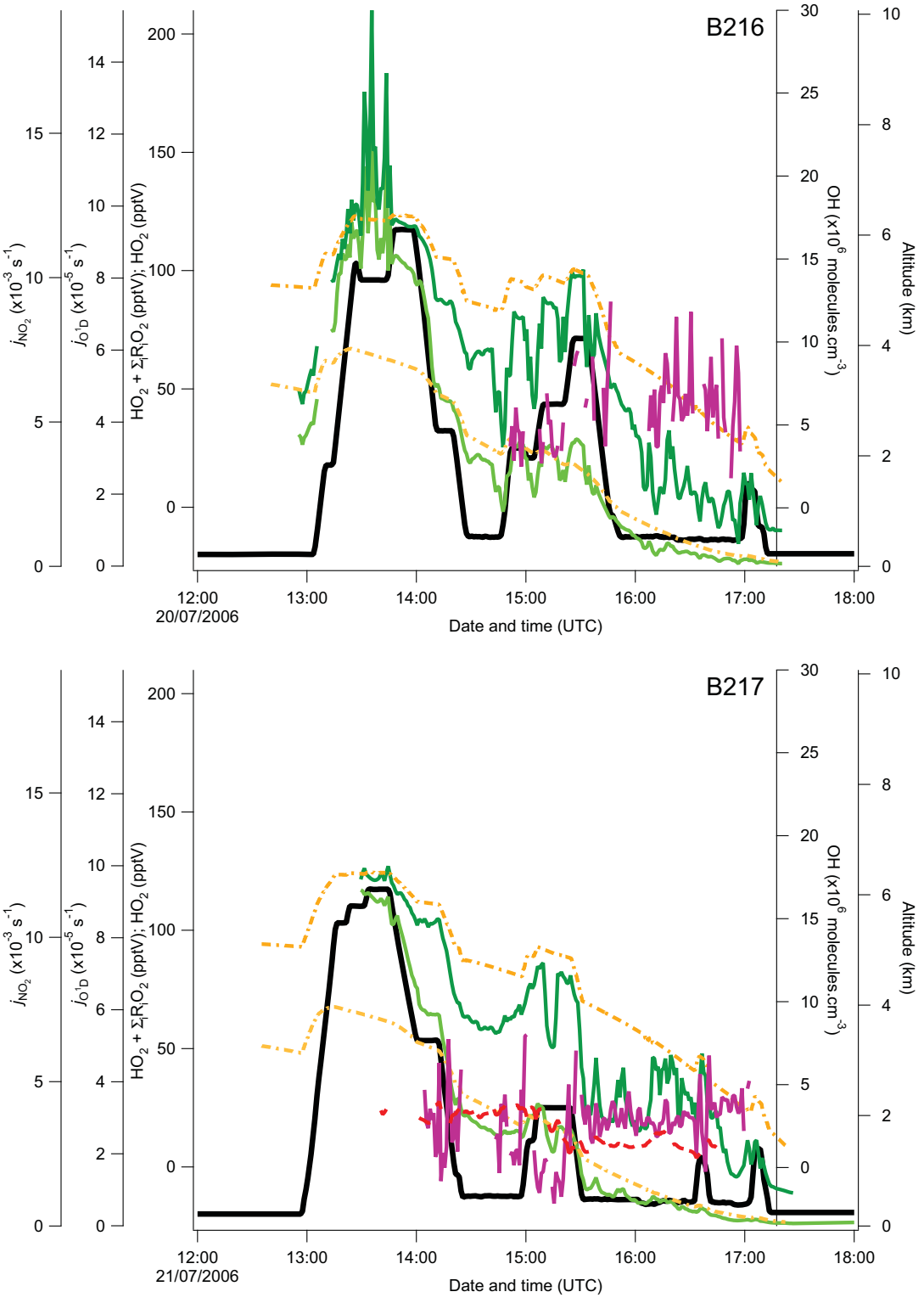

Figure 5.7: Times series of measured peroxy radicals (dark pink), OH (light pink) and HO_2 (red), measured (light green) and modelled (dashed light yellow) j_{O^1D}, measured (dark green) and modelled (dashed dark yellow) j_{NO_2} and altitude (black) for flights B216-B217

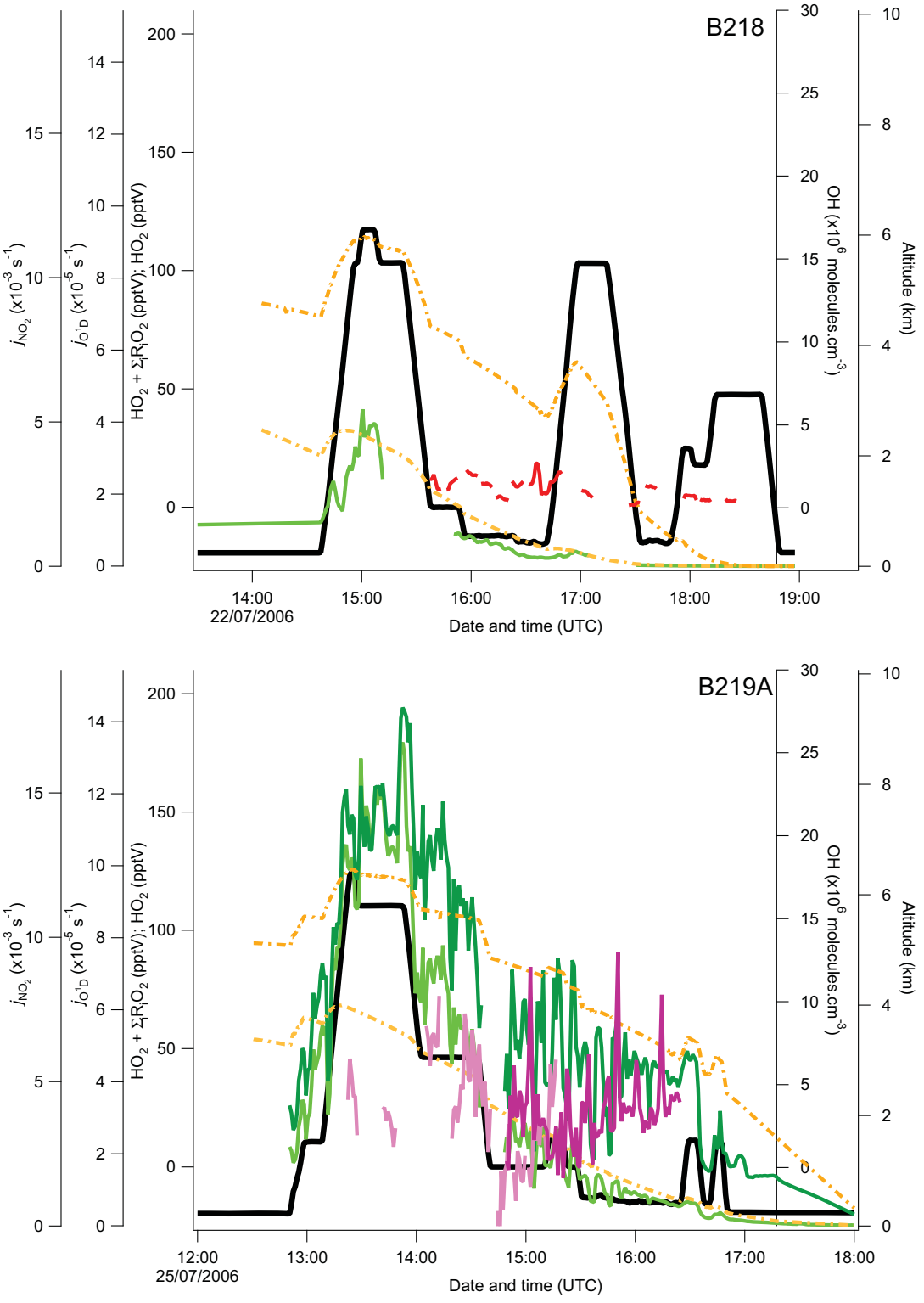

Figure 5.8: Times series of measured peroxy radicals (dark pink), OH (light pink) and HO_2 (red), measured (light green) and modelled (dashed light yellow) j_{O^1D}, measured (dark green) and modelled (dashed dark yellow) j_{NO_2} and altitude (black) for flights B218-B219A

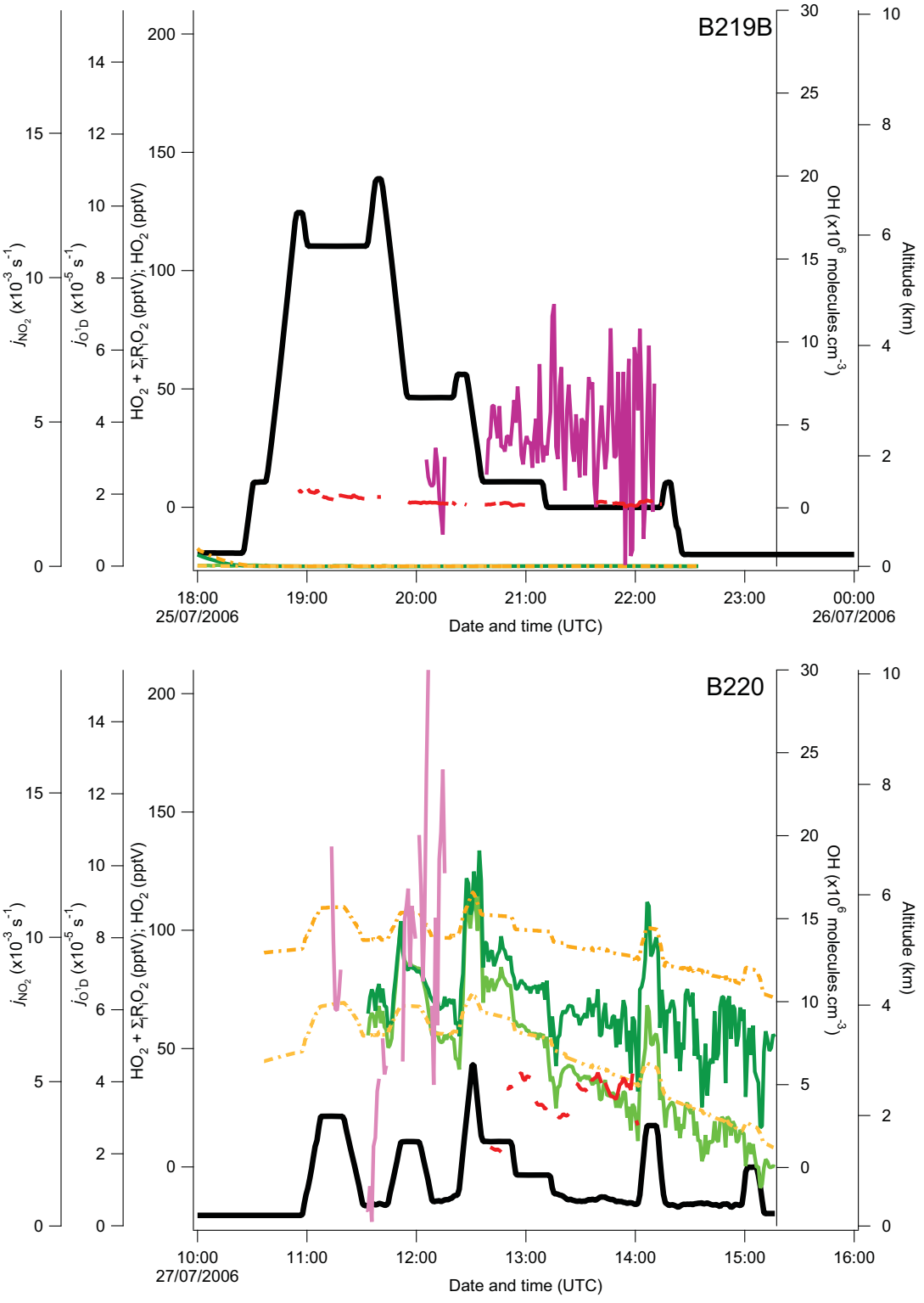

Figure 5.9: Times series of measured peroxy radicals (dark pink), OH (light pink) and HO_2 (red), measured (light green) and modelled (dashed light yellow) j_{O^1D}, measured (dark green) and modelled (dashed dark yellow) j_{NO_2} and altitude (black) for flights B219B-B220

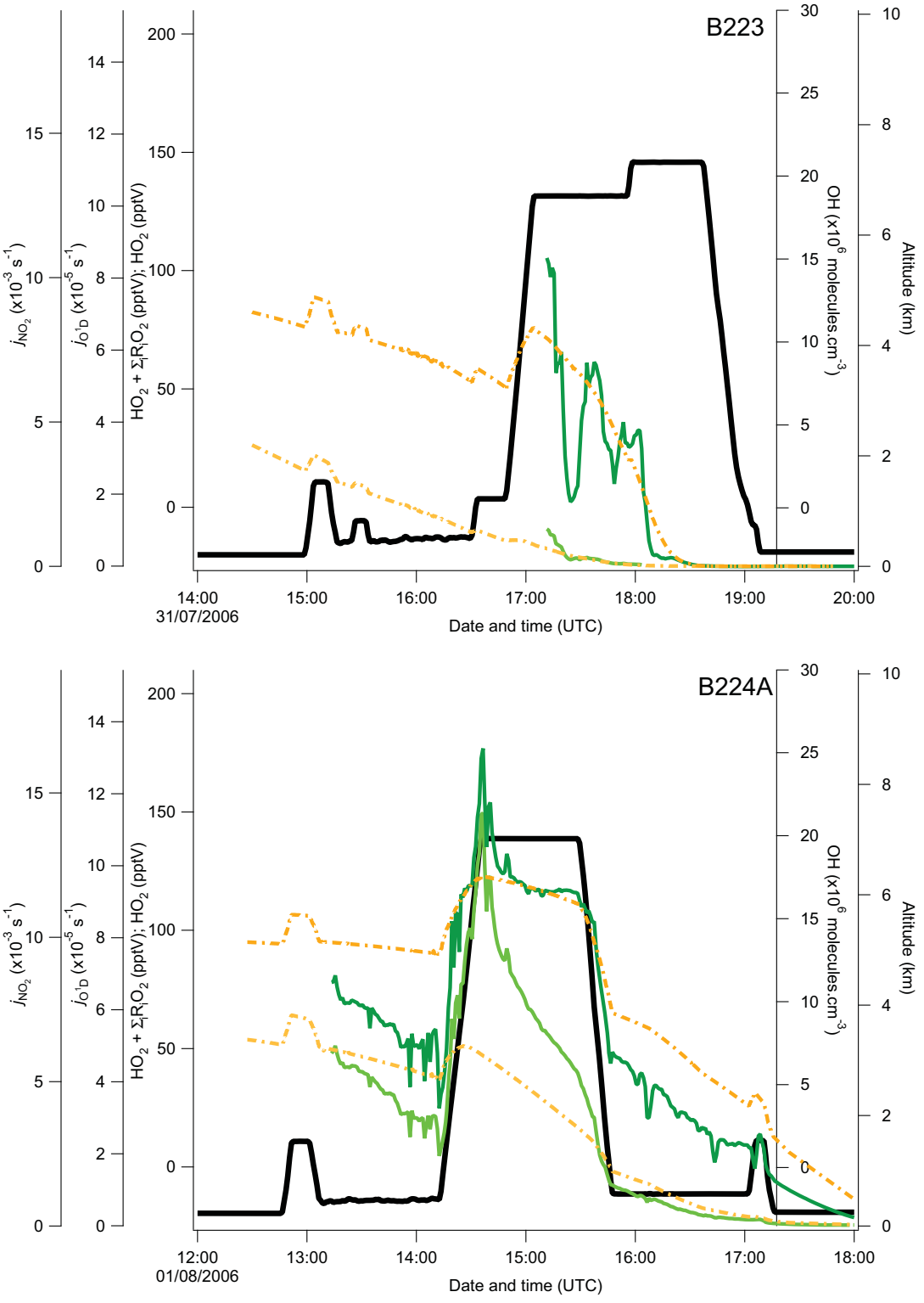

Figure 5.10: Times series of measured peroxy radicals (dark pink), OH (light pink) and HO_2 (red), measured (light green) and modelled (dashed light yellow) j_{O^1D}, measured (dark green) and modelled (dashed dark yellow) j_{NO_2} and altitude (black) for flights B223-B224A

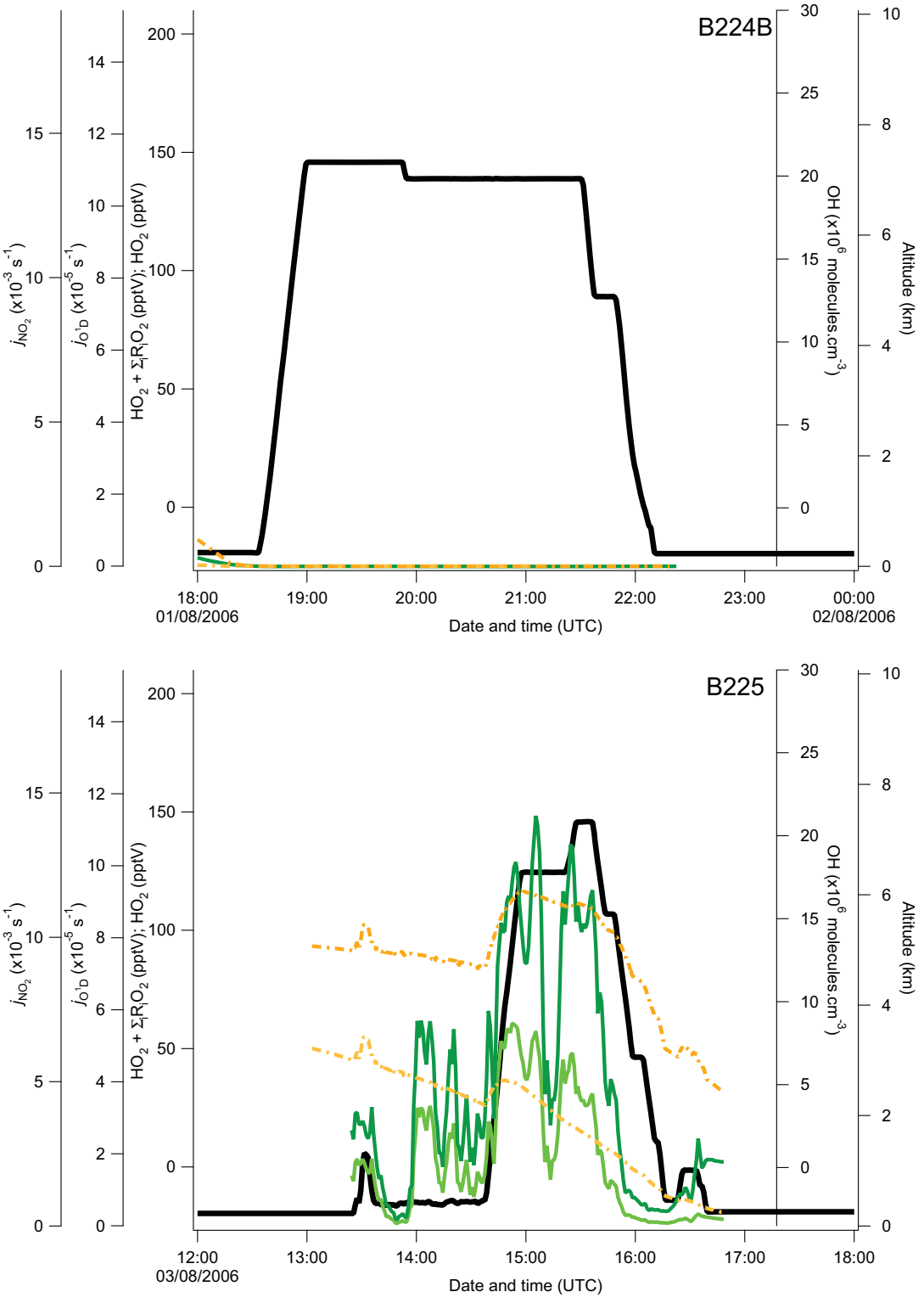

Figure 5.11: Times series of measured peroxy radicals (dark pink), OH (light pink) and HO_2 (red), measured (light green) and modelled (dashed light yellow) j_{O^1D}, measured (dark green) and modelled (dashed dark yellow) j_{NO_2} and altitude (black) for flights B224B-B225

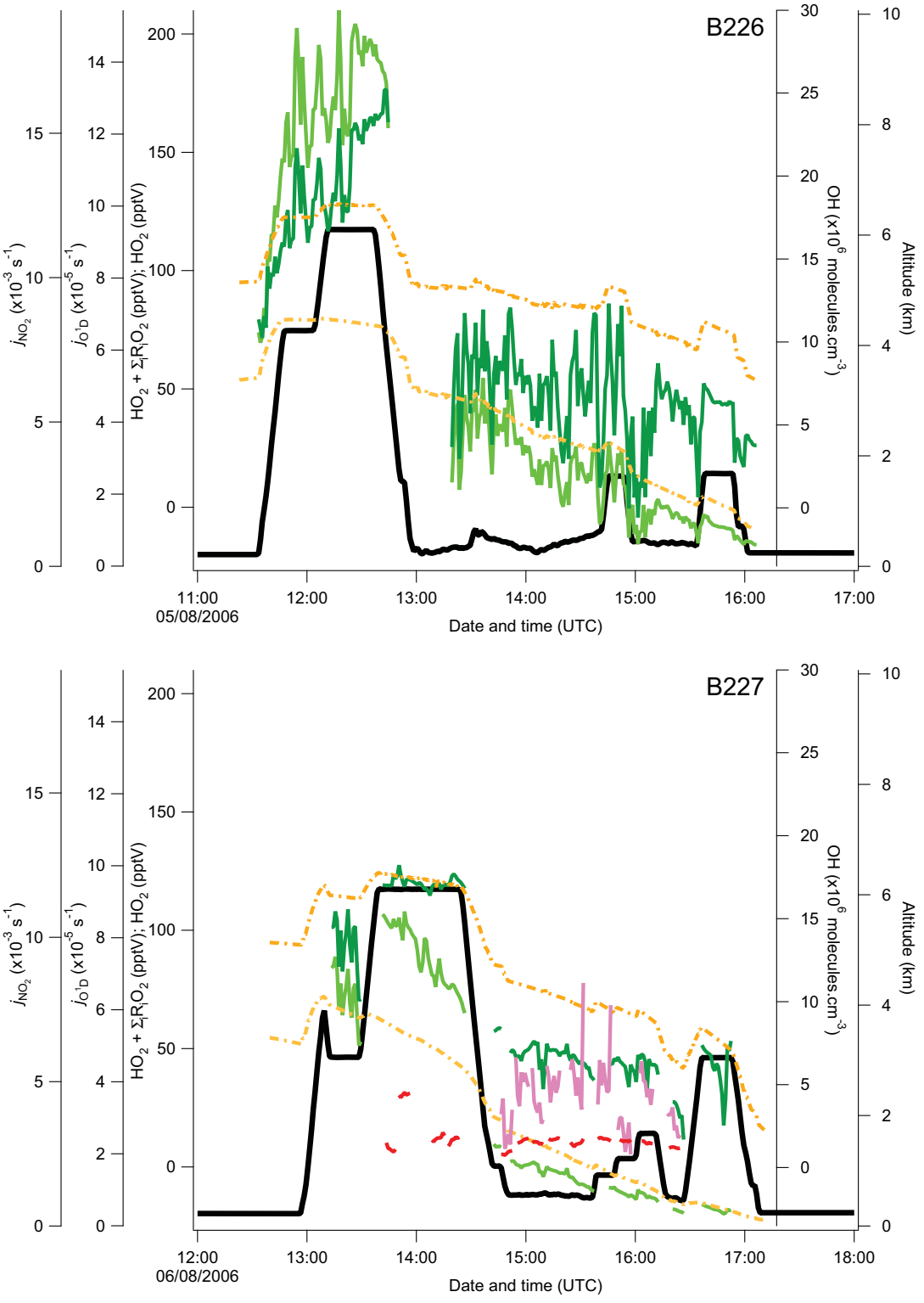

Figure 5.12: Times series of measured peroxy radicals (dark pink), OH (light pink) and HO_2 (red), measured (light green) and modelled (dashed light yellow) j_{O^1D}, measured (dark green) and modelled (dashed dark yellow) j_{NO_2} and altitude (black) for flights B226-B227

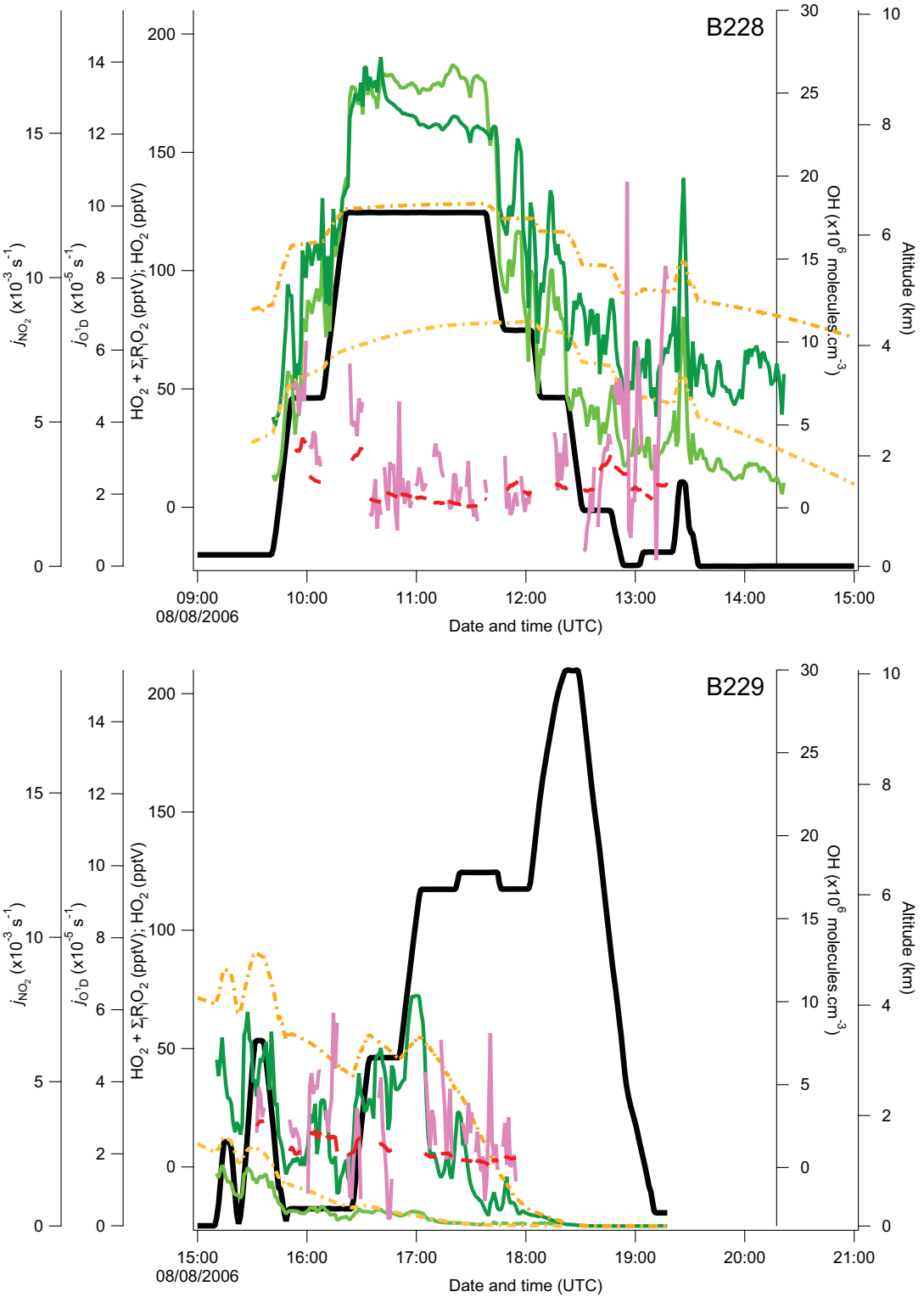

Figure 5.13: Times series of measured peroxy radicals (dark pink), OH (light pink) and HO_2 (red), measured (light green) and modelled (dashed light yellow) j_{O^1D}, measured (dark green) and modelled (dashed dark yellow) j_{NO_2} and altitude (black) for flights B228-B229

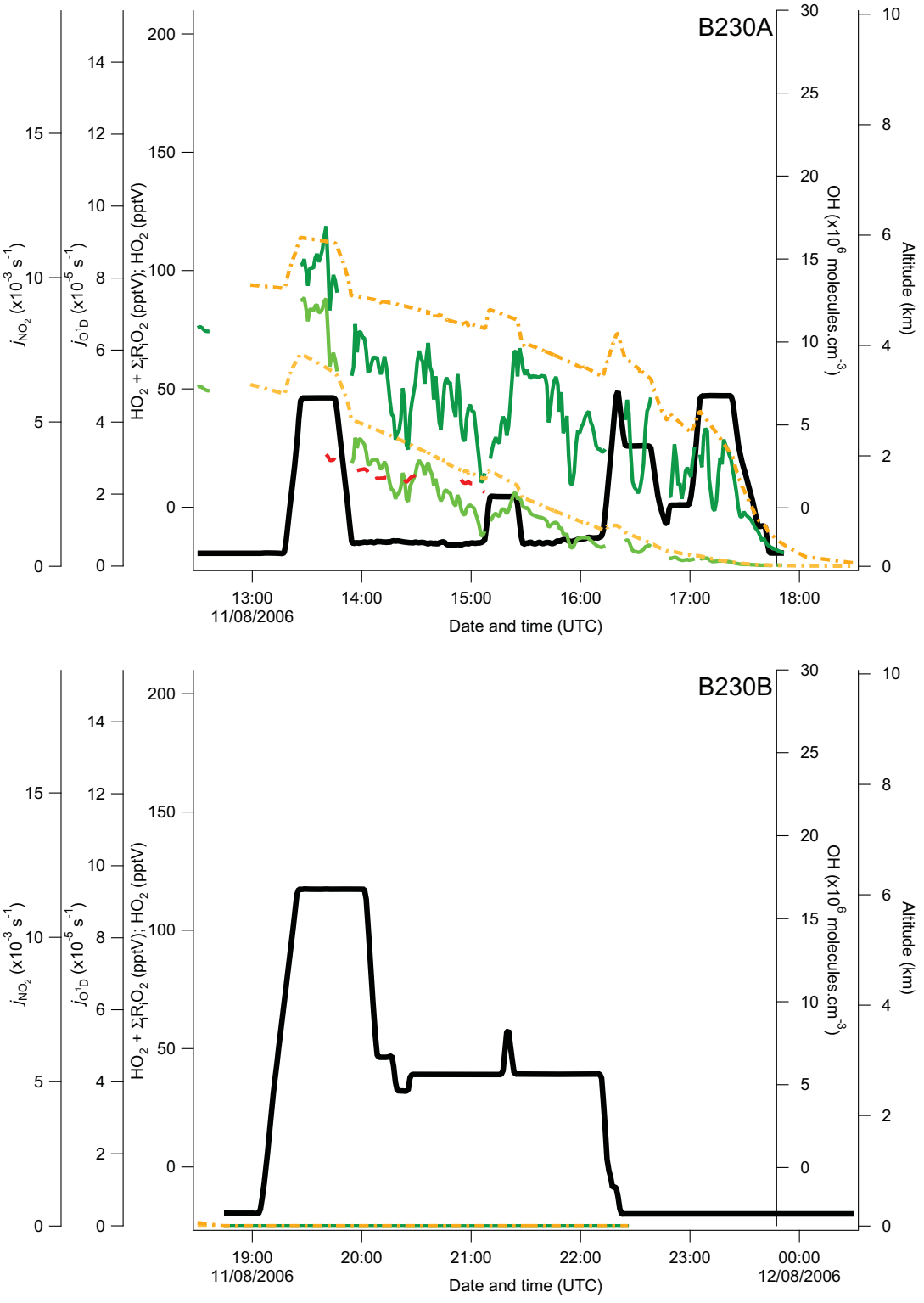

Figure 5.14: Times series of measured peroxy radicals (dark pink), OH (light pink) and HO_2 (red), measured (light green) and modelled (dashed light yellow) j_{O^1D}, measured (dark green) and modelled (dashed dark yellow) j_{NO_2} and altitude (black) for flights B230A-B230B

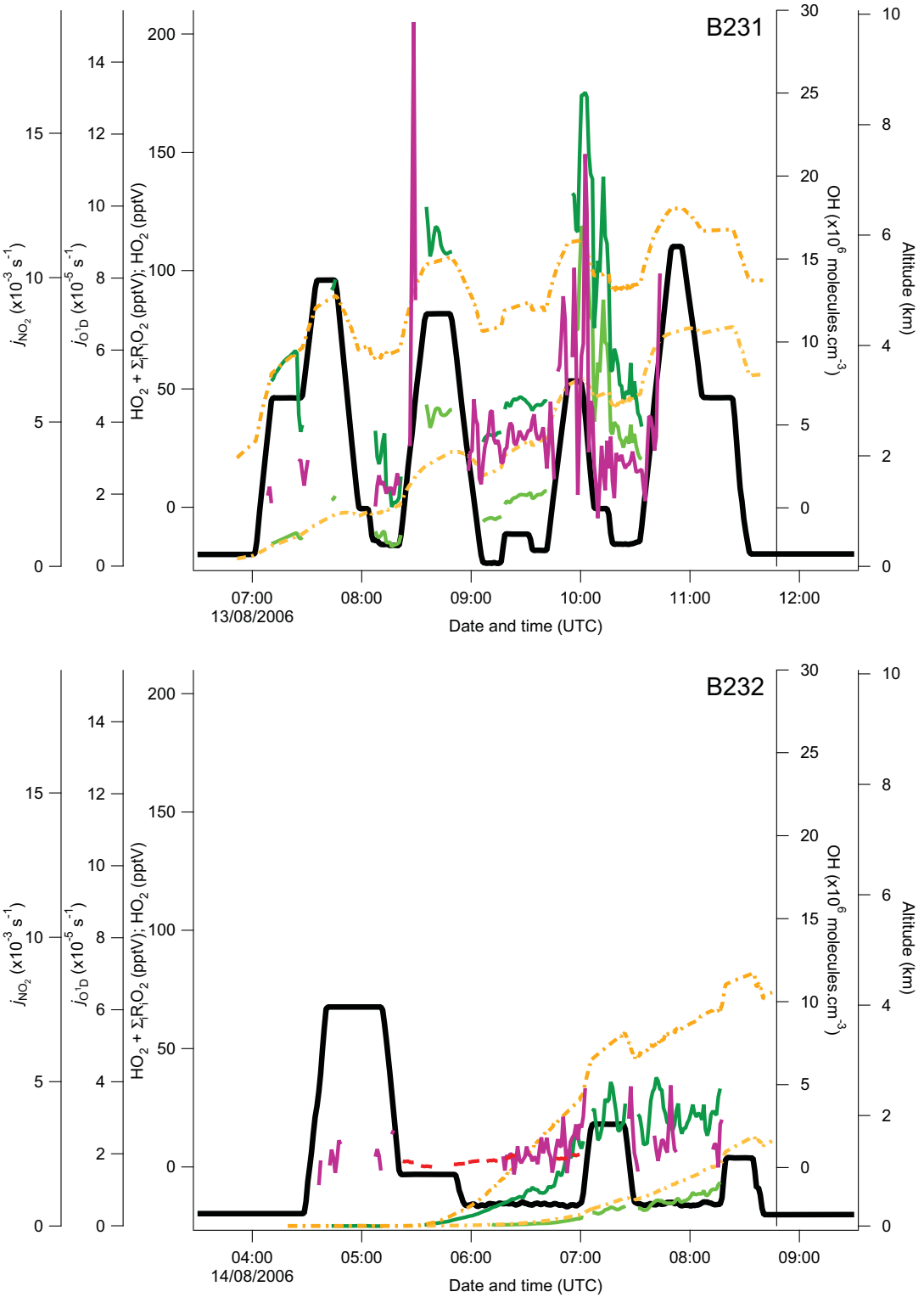

Figure 5.15: Times series of measured peroxy radicals (dark pink), OH (light pink) and HO_2 (red), measured (light green) and modelled (dashed light yellow) j_{O^1D}, measured (dark green) and modelled (dashed dark yellow) j_{NO_2} and altitude (black) for flights B231-B232

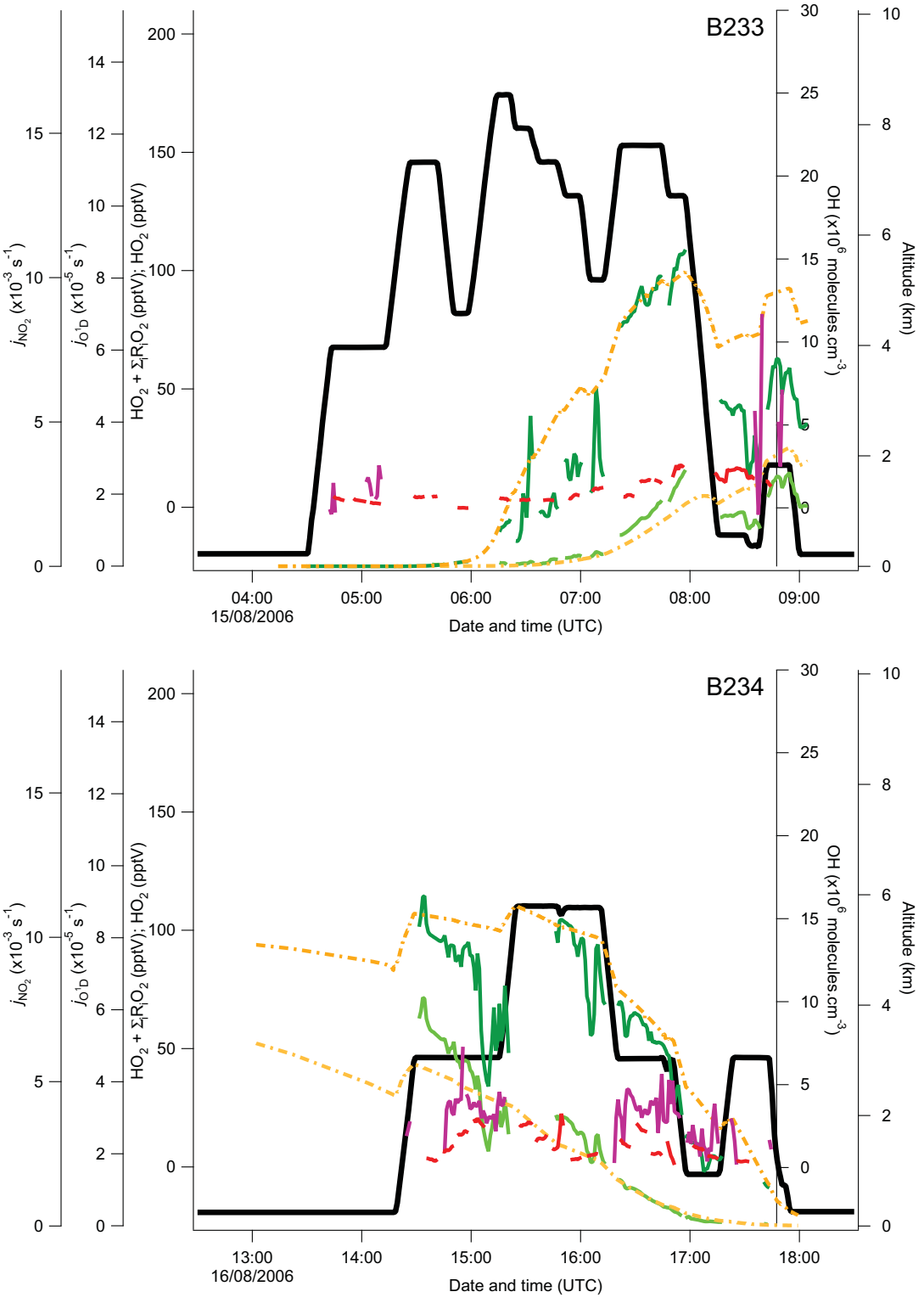

Figure 5.16: Times series of measured peroxy radicals (dark pink), OH (light pink) and HO_2 (red), measured (light green) and modelled (dashed light yellow) j_{O^1D}, measured (dark green) and modelled (dashed dark yellow) j_{NO_2} and altitude (black) for flights B233-B234

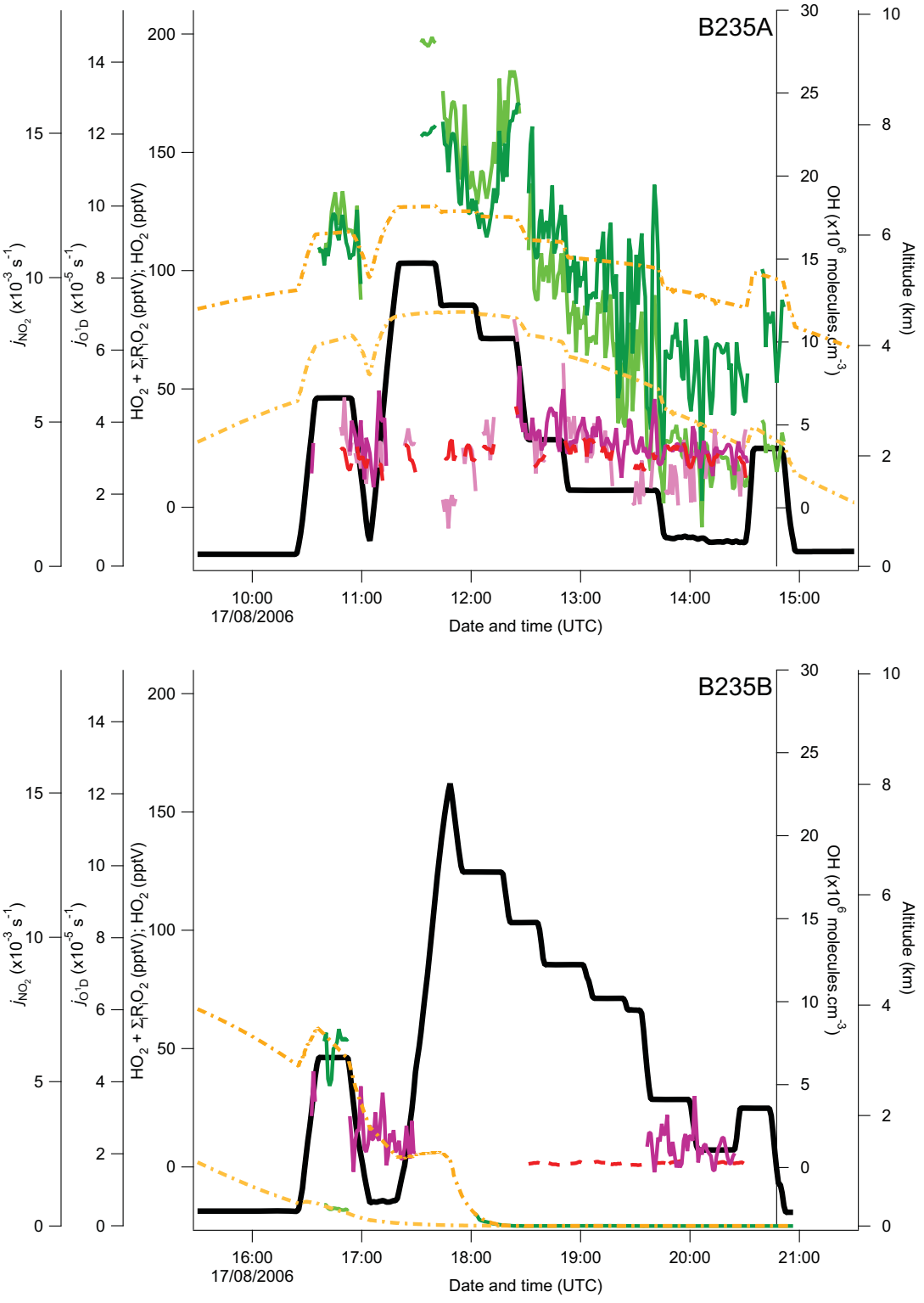

Figure 5.17: Times series of measured peroxy radicals (dark pink), OH (light pink) and HO_2 (red), measured (light green) and modelled (dashed light yellow) j_{O^1D}, measured (dark green) and modelled (dashed dark yellow) j_{NO_2} and altitude (black) for flights B235A-B235B

variable sensitivity dependent on the chain length for the radicals making up the radical population, relative to the reference species (CH_3O_2) (see Equation 2.20, in Chapter 2 and related discussion). The comparability of the PERCA and FAGE measurements is therefore dependent on the relative sensitivity of the PERCA to HO_2, and the proportion of the peroxy radical population present as HO_2. In reference to Table 2.1, the relative difference in sensitivity to HO_2 and CH_3O_2 has previously been calculated and determined experimentally to be of the order $\pm$15% for similar PERCA instruments. The PERCA $[HO_2] + \Sigma_i[R_iO_2]$ signal should therefore never fall significantly (>15%) below the FAGE $[HO_2]$ signal (beside instrumental uncertainty). On one occasion (flight B217 up until ~15:30UTC) the PERCA signal does drop significantly below the FAGE HO_2 signal for a prolonged period, this therefore points to an instrumental issue. Otherwise the PERCA derived RO_x is generally greater than or equal to the FAGE HO_2 concentration. Also the timescale of any variability is generally very similar between all radical and photolysis rate data; indeed the signals generally change in phase and exhibit the same profile (i.e. are well correlated), which suggests that the variation is largely linked to rapid changes in the photochemistry and not instrumental noise. There remains a strong and variable nighttime peroxy radical signal (e.g. during B219B ~20-50 pptV) as measured by the University of Leicester PERCA where the photolysis rates tend to zero and HO_2 concentrations are in the range 0-3 pptV. This is indicative that oxidation chemistry remains active at night, and a dramatic change occurs in the partitioning between inorganic and organic peroxy radicals. To illustrate the trend more clearly, the ratio of the FAGE measured hydroperoxyl radical concentration ($[HO_2]_{FAGE}$) to the PERCA measured summed peroxy radical concentration ($([HO_2] + \Sigma_i[R_iO_2])_{PERCA}$) is plotted as a function of the time of day and coloured by j_{O^1D} in Figure 5.18.

The coverage is limited by the number of opportunities where both the PERCA and FAGE measurements ran simultaneously, however there is still an apparent trend observed over the whole of the SOP2 period. There appears to be a strong diurnal cycle in the ratio $[HO_2]_{FAGE}/([HO_2] + \Sigma_i[R_iO_2])_{PERCA}$,

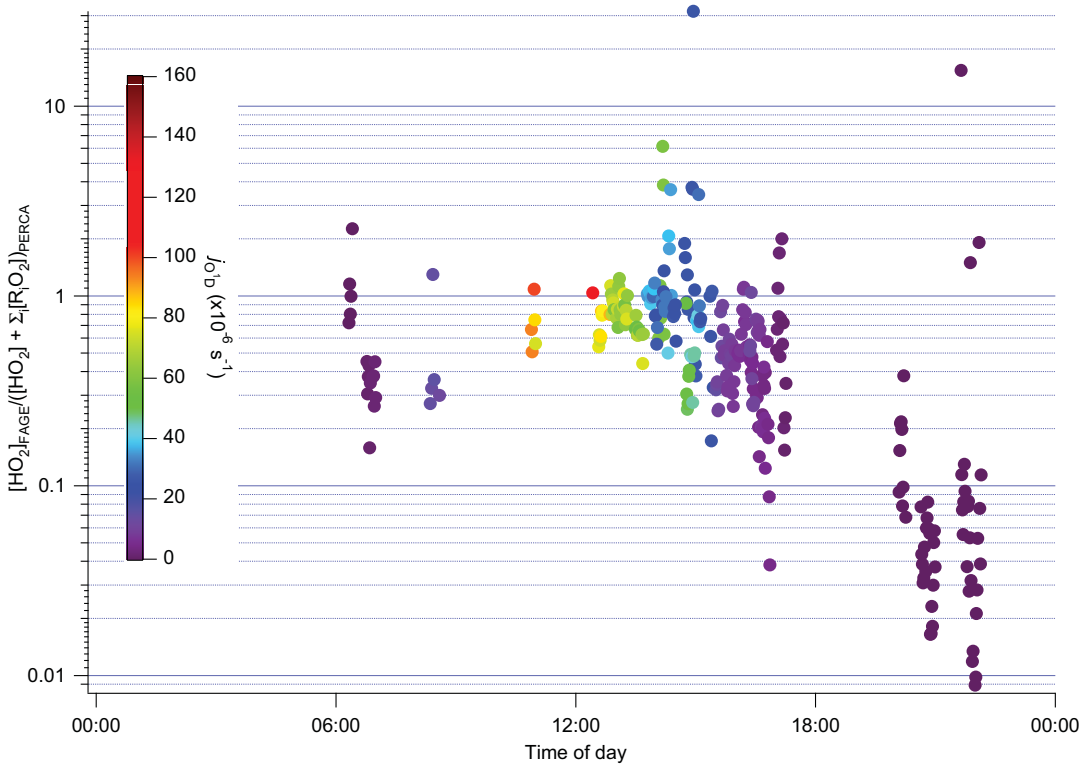

Figure 5.18: Measured $[HO_2]_{FAGE}/([HO_2] + \Sigma_i[R_iO_2])_{PERCA}$ ratio as an indicator for inorganic/organic peroxy radical partitioning

the ratio tends to one during the middle of the day when j_{O^1D} is greatest, while the ratio tends to significantly lower values as j_{O^1D} tends to zero. This suggests that either the University of Leicester PERCA 4 instrument is relatively insensitive to HO_2, that HO_2 is by far the largest proportion of the radical population during the middle of the day, or that the FAGE instrument is systematically too high in terms of the reported HO_2 concentration. On this initial assessment it seems more likely that there may be some systematic difference between the FAGE and PERCA 4 HO_2 sensitivity overall, since it is unlikely that HO_2 would comprise 100% of the radical population. Given there may be some systematic differences in the measurements, the diurnal trend remains indicative of the change in partitioning between inorganic and organic peroxy radicals. A peroxy radical population dominated by HO_2 when HO_x production is greatest in the middle of the day, while at night the concentration of HO_x is suppressed and a significant population of organic peroxy radicals remains. The peroxy radical dataset has been presented without the humidity correction derived earlier (see Section 3.2.3, Chapter 3) applied owing to a discrepancy with the values determined after correction. A quantitative comparison of the measured peroxy radical concentrations (with and without humidity correction) with a detailed box model is given in Section 6.2 of the next chapter in an attempt to reconcile any model to measurement differences. The partitioning of the radical population and processes driving radical production and loss are also discussed.

The measured photolysis rates are of the same order of magnitude as those modelled using TUV but are considerably more variable; this is indicative of rapid changes in the actinic flux associated with cloud and aerosol typical of the monsoon environment but not present in the model. Measured j_{O^1D} often exceeds the TUV modelled photolysis rate at higher altitude, while the measured signal is similar or less at lower altitude; this may be indicative of enhanced upwelling actinic flux at higher altitude when above cloud associated with the convective boundary layer. Measured j_{NO_2} also often exceeds the TUV modelled photolysis rate at higher altitude, while the measured signal is typically

less at lower altitude. Again this is indicative of the enhancement of the upwelling actinic flux at higher altitude when above low lying cloud, and the potentially greater attenuation of j_{NO_2} compared to j_{O^1D} at lower altitude may be associated with the sensitivity of j_{NO_2} to attenuation of the longer wavelength components of the actinic flux in direct sunlight, while j_{O^1D} is held up due to its sensitivity to the diffuse component which is less readily perturbed. A quantitative comparison of modelled to measured photolysis rates is given in Section 6.1 of the next chapter. The method of estimation (see Section 4.3.1, 172) to derive the (primarily) upwelling component of j_{O^1D} when the lower position j_{O^1D} radiometer failed has to be considered in this comparison.

5.2.3 Tracers of dynamics

As discussed in Section 5.1.3 of this chapter, there are some consistent features of the seasonal and diurnal cycles in the monsoon dynamics (e.g. AEJ, SAL, monsoon flow). The impacts of the seasonal and diurnal cycles of the monsoon on trace gas emissions, transport and atmospheric composition have been discussed in Section 5.1.2. Changes in chemistry related to the seasonal cycle of the WAM are best characterised with observations over a number of seasons, which may be achieved by intercomparison of the SOP0 and SOP2 campaigns. The data from the BAe-146 for SOP2 samples the diurnal cycle of the WAM repeatedly (see Section 5.2.1), so it is reasonable to draw some conclusions with regard to changes in chemistry linked to this fundamental mode of WAM dynamics. Figures 5.19 and 5.20 present composite views of the meridional distribution of potential temperature, θ(K), and equivalent potential temperature, θ_e(K), which describe mixing and stability respectively (see Section 1.1.2 of Chapter 1), derived from BAe-146 measurements. Both parameters have been separated by time of day into 6 hour intervals (00:00-06:00, 06:00-12:00, 12:00-18:00, 18:00-24:00) with the colour-scale representing the range in data. Contours have been generated using the IGOR 6.0 package (Wavemetrics, 2007), by averaging the parameters onto a grid of resolution 0.2 km by altitude, 0.5^o by latitude (irrespective of longitude) to overcome some of the sparsity of observations and simplify

computation of the contours. The underlying data are presented in their original form to illustrate the contours are still representative of the original data. Contours are only displayed for the 06:00-12:00, 12:00-18:00 periods since these have the best coverage and the generated contours are more valid.

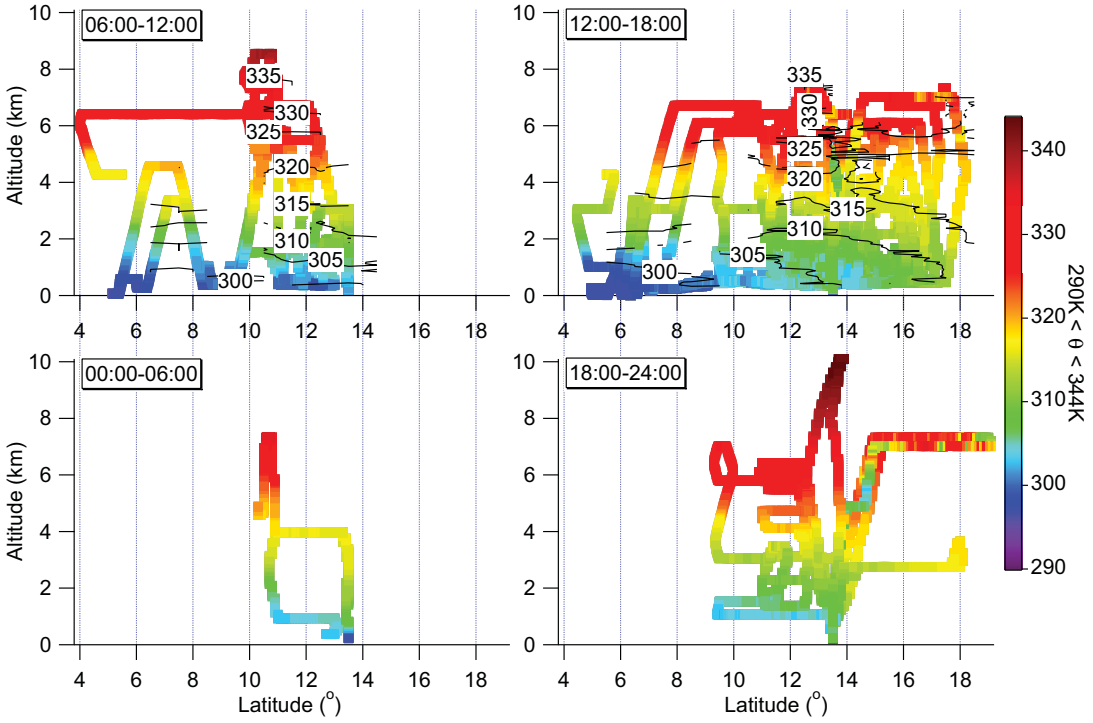

Figure 5.19: Diurnal changes in meridional distribution of potential temperature, θ(K), observed throughout SOP2. Colourscaled in the range 290-344 K representative of the range in potential temperature observed.

Considering the distribution of θ for the 12:00-18:00 period from Figure 5.19, it is consistent with the schematic view of the WAM presented in Figure 5.2. The contours in θ intercept the surface, indicative of a SAL connected by isentropic surfaces (surfaces of constant θ) to the Saharan boundary layer. If approximately 16-18^{o}N is taken as the border of the Sahara (although of course there is in fact a transition i.e. the Sahel), the isentropic surface at θ=310 K can then be used as an indicator for the lower boundary of the SAL. There is therefore a horizontal gradient in θ at low level, with θ increasing toward the north (i.e. the air is horizontally stratified at low level). This gradient is very similar to the gradient in θ observed by Parker *et al.* (2005b), although it has been derived from

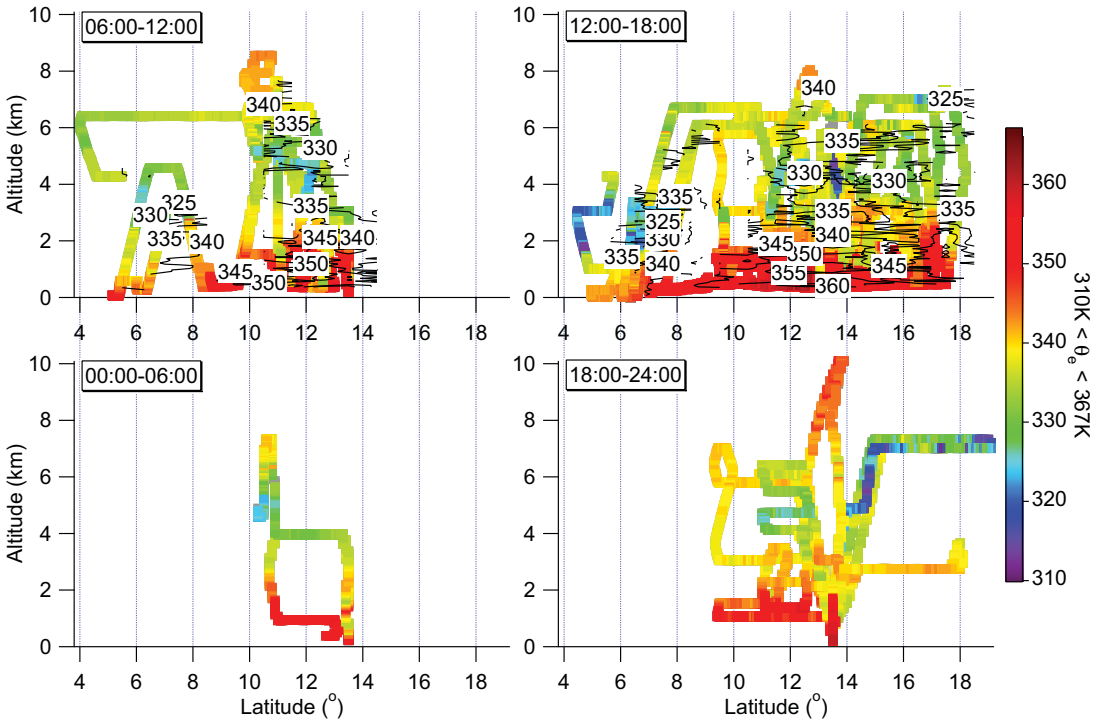

Figure 5.20: Diurnal changes in meridional distribution of equivalent potential temperature, θ_e(K), observed throughout SOP2. Colourscaled in the range 310-367 K representative of the range in equivalent potential temperature observed.

compiled aircraft observations over the period 20 July-17 August 2006 rather than a single flight. The gradient in θ changes from horizontal to vertical around 1 km altitude and increases in depth around 18^{o}N where the low level horizontal gradient in θ is lost. This level indicates the depth of the convective boundary layer as defined by Parker *et al.* (2005b).

Similarly considering the distribution of θ_e for the 12:00-18:00 period from Figure 5.20, there is a horizontal gradient at low level with θ_e increasing from the coast at 6^{o}N to around 12-14^{o}N where there is a turnover with θ_e then decreasing further north until around 18^{o}N. This gradient again is very similar to the gradient in θ_e observed by Parker *et al.* (2005b). In the vertical the gradient in θ_e is negative at all latitudes at low altitudes meaning the air is unstable to convection (see Section 1.1.2 of Chapter 1). Around 12-14^{o}N there is an inversion in θ_e around 4 km altitude which is consistent with the average position of the core of the AEJ in July and August 2006 given in Janicot *et al.* (2008). Toward 18^{o}N the vertical gradient in θ_e is negative and then relatively flat with increasing altitude, meaning the air is unstable to deep convection. The low values of θ_e observed around 4-8^{o}N have been associated with biomass burning plumes of southern hemispheric origin which will be discussed later.

Outside the 12:00-18:00 period the monsoon flow develops with the suppression of convection, and there is no horizontal gradient observable in θ by the 06:00-12:00 period, with the θ=300 K isentrope extended up to at least 14^{o}N. Potentially this situation develops throughout the periods 18:00-24:00 and 00:00-06:00; this is not entirely clear since the dataset at low level is sparse owing to restrictions on low level flying with the BAe-146 at night.

This is a synthetic view of the diurnal cycle since it has been observed incrementally by a number of flights over a number of days and throughout the early stages of the 2006 monsoon season. As such it is representative of an averaged cycle, though the consistent meridional picture in potential temperature provides some confidence that this is reasonable. Some of the flights were planned in pairs such that the same regions were sampled at different times of day within a single day, so provide

opportunities for case studies for individual days.

5.2.4 Distribution of biogenic VOC's

The distribution of biogenic VOC's should be closely related to the surface distribution of vegetation owing to their short lifetime with respect to oxidation, e.g. by OH, O_3, NO_3 as discussed in Section 5.1.2. The distribution of surface vegetation and the physiological activity of plants can be described by vegetation indices derived from satellite measurements in the red/near infrared owing to the sharp absorption contrast in the region 0.65-0.85 μm which results from the chlorophyll absorption maximum at $\sim$0.69 μm (Myneni *et al.*, 1995). For the AMMA SOP2 period the SEVIRI/MSG normalised difference vegetation index (NDVI) product was downloaded from the AMMA-SAT database (http://bddamma.ipsl.polytechnique.fr/available-datasets.html). The product is available at a one day temporal resolution on a 0.05^o resolution grid for the region of West Africa, up until 12 July 2006 and then from 18 August 2006; there is no data available between these dates. The NDVI distribution and its anomaly for 12 July and 18 August 2006 are shown in Figure 5.21; the anomaly has been calculated from the difference between the NDVI distribution on these two days and the average of the two days.

The NDVI distribution for 12 July is representative of the distribution of vegetation at the monsoon onset (onset reported as 10 July 2006 by Janicot *et al.* (2008)), while the distribution on the 18 August is only one day after the last flight so is more representative of the distribution during the latter stages of the observing period. The distributions in NDVI show a similar overall profile with low values in the north over the Sahara, a positive gradient in NDVI toward the equator and the highest values occurring over the tropical forested regions. A northward shift in the highest values of NDVI is apparent but the change in distribution is most clearly seen in the anomaly between the two dates. The anomaly shows a mixed signal of vegetation enhancement relative to the average in southern

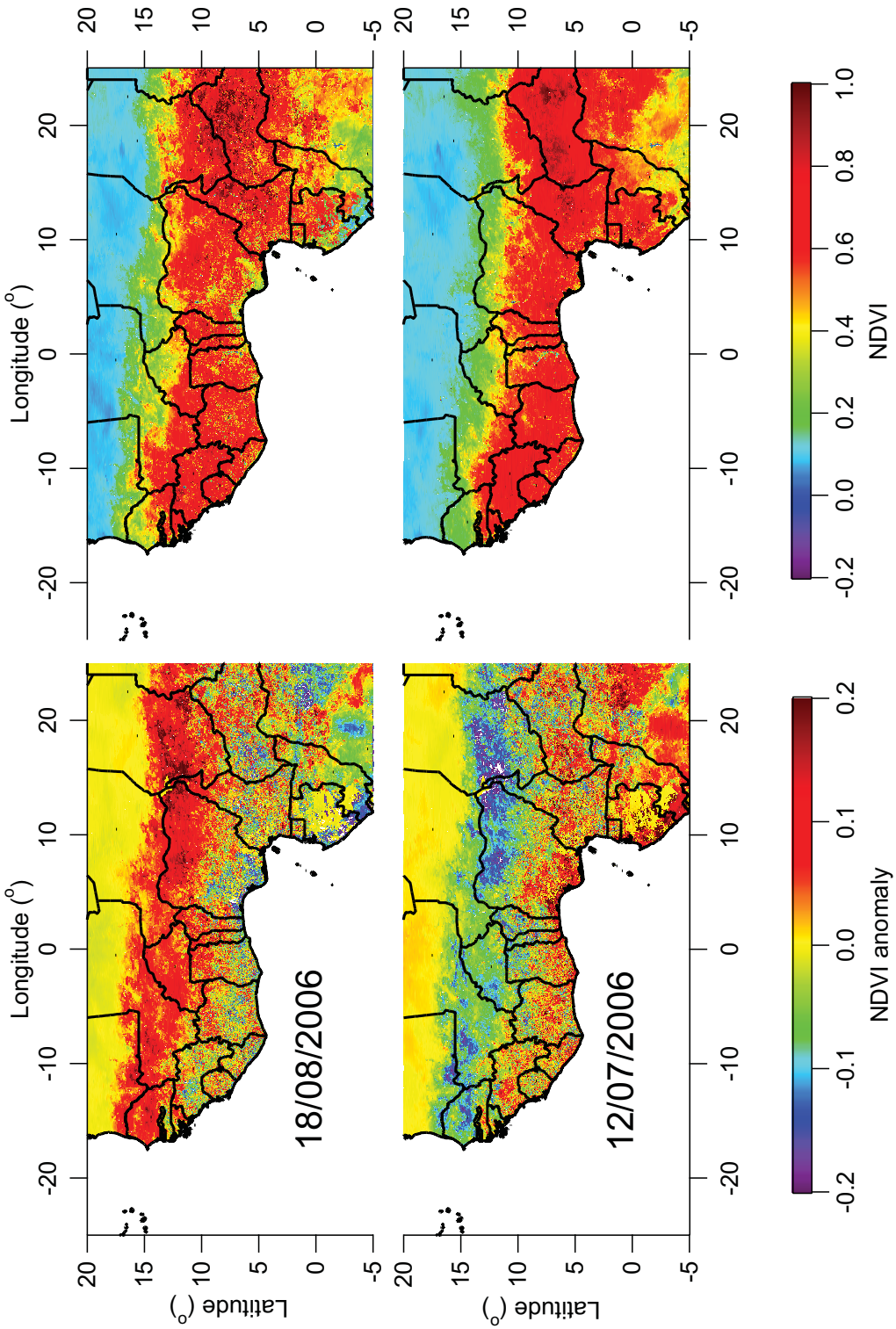

Figure 5.21: SEVIRI/MSG NDVI (Right) and NDVI anomaly (Left) over region of West Africa between 12 July 2006 (Bottom) to 18 August 2006 (Top)

West Africa and central Africa on the 12 July at the onset of the 2006 WAM, with the anomaly net positive or zero; the strongest positive anomaly occurs in central Africa and negative values occur over the Sahel. The location of positive anomaly shifts north into the Sahel over the period up to 18 August 2006, showing the strongest relative enhancement in vegetation activity occurred here. These patterns show the influence of the northward progression of the ITCZ (and with it rainfall) during the monsoon season on vegetation growth and activity. As mentioned in Section 5.1.2, Janicot *et al.* (2008) reported a large scale excess of rainfall north of 15°N during the 2006 WAM season, and the anomaly in NDVI here shows reasonable agreement with the rainfall anomaly reported in that paper.

Figure 5.22 presents all data for isoprene and MVK+MACR from the BAe-146 compiled as an altitude by latitude profile, which is broadly representative of the meridional distribution of biogenic VOC's since isoprene is the dominant primary biogenic VOC emitted by terrestrial plants (as discussed in Section 5.1.2); methyl vinyl ketone and methacrolein (MVK+MACR) are primary products of isoprene oxidation so are representative of secondary biogenics. The data presented here for MVK+MACR are from the PTR-MS measurements on board the BAe-146 during SOP2. Since both MVK and MACR occur at the same mass to charge (m/z) ratio they are indistinguishable using the PTR-MS technique (see e.g. Lee *et al.* (2006a)) and hence the concentrations are given as a sum. Overplotted are the contours of constant potential temperature (from the 12:00-18:00 period, see Section 5.2.3, Figure 5.19) indicating the daytime monsoon structure. The concentration profiles are also shown by altitude.

The concentration of isoprene is elevated over a very limited range of altitude (up to 1.25-1.75 km altitude) confirming its short atmospheric lifetime compared to the timescale of transport outside of the boundary layer. Elevated isoprene levels are also confined to latitudes associated with the peak in vegetation cover. Further, the region of elevated isoprene lies directly between the θ=300 K, θ=305 K contours of potential temperature (refer to Figure 5.19) linking the extent of isoprene to these

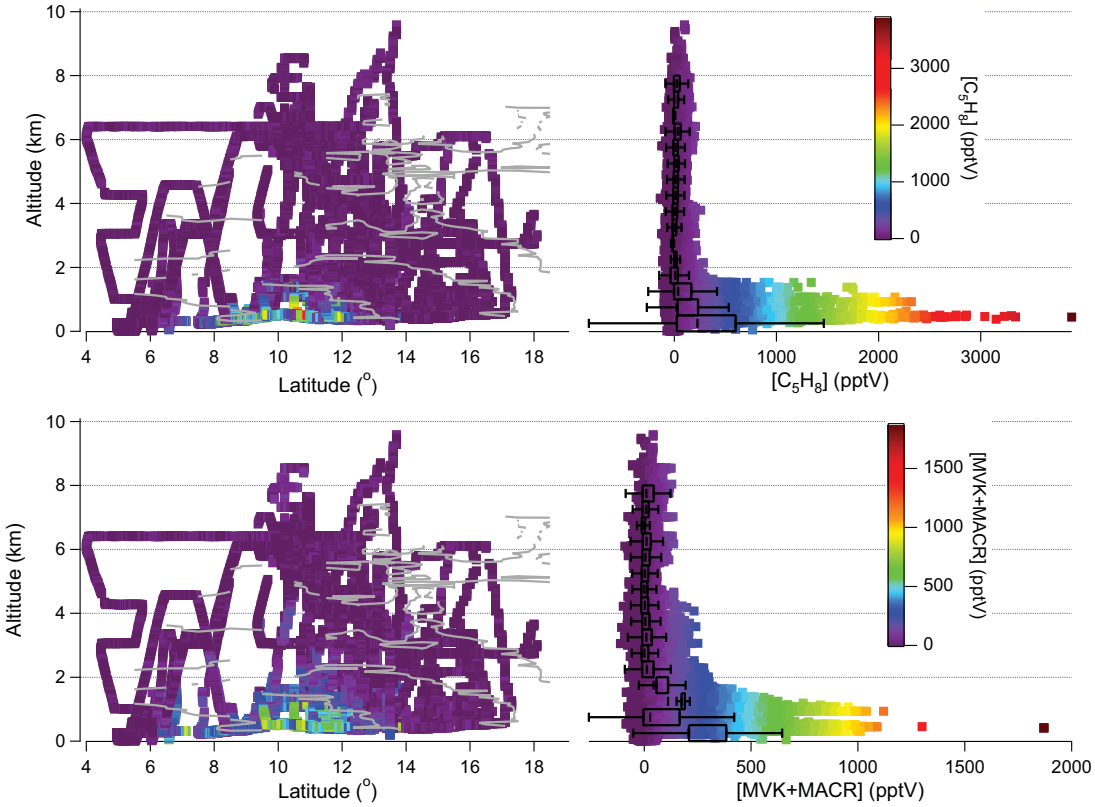

Figure 5.22: Meridional (Left) and vertical (Right) distributions of isoprene (Top) and MVK+MACR (Bottom); in the vertical profile box centres represent median values, box edges Q25 and Q75 and whiskers lower and upper inner fences. Contours of constant potential temperature are plotted in grey.

isentropes. To illustrate the link between the surface vegetation cover and isoprene concentration in the boundary layer, the NDVI has been extracted along the flight tracks by latitude and longitude where the aircraft was at or below 1 km altitude (an altitude chosen according to the altitude profile in isoprene concentration and consistent with the convective boundary layer height during the daytime). These data are presented by latitude and longitude in comparison to the measured concentrations of isoprene and MVK+MACR in Figure 5.23, the regions defined by the surface type are also categorised as ocean (<6.4^{o}N), forest (7.2-13.25^{o}N) and Sahel (>13.25^{o}N), and the bands where emissions associated with Lagos (6.4-7.1^{o}N) and Niamey (∼13.5^{o}N) may be located.

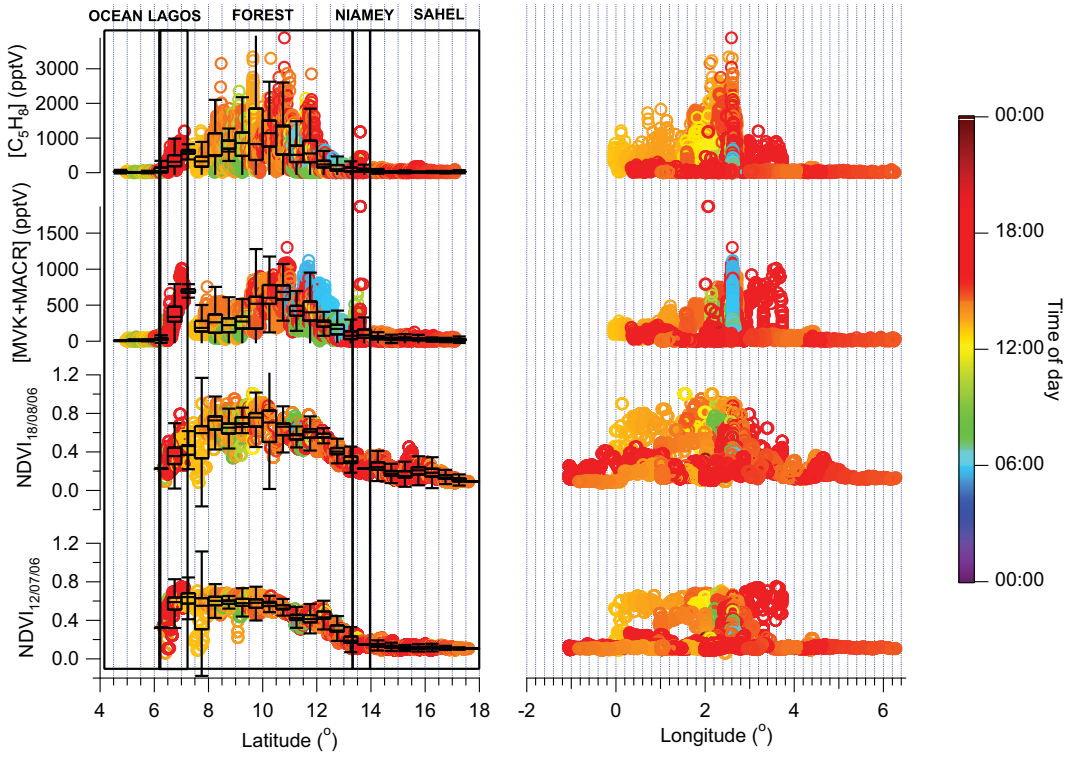

Figure 5.23: Matching of biogenics distribution with NDVI by latitude (Left) and longitude (Right): (Top) Isoprene; (Second from top) MVK+MACR; (Third from top) NDVI (18/08/06); (Bottom) NDVI (12/07/06); In the latitude profiles box centres represent median values, box edges Q25 and Q75 and whiskers lower and upper inner fences

The distribution in NDVI from the 12 July 2006 shows a smooth increase from north to south,

beginning at the northern edge of the forested region at ∼13.25^{o}N, flattening in the south and ending with a sharp transition, indicating the location of the coast at 6.4^{o}N. The zonal distribution is relatively unstructured showing considerable symmetry by longitude at this time over the region covered by the flight tracks. The distribution in NDVI from the 18 August 2006 in comparison shows the same sharp transition at 6.4^{o}N indicating the location of the ocean but with the NDVI much lower going north from the coast with values more comparable to the Sahel until around ∼7.2^{o}N. There is a more peaked meridional profile, the peak at a similar latitude (∼10^{o}N) to that of the matched isoprene profile, though the profile in isoprene is relatively northward shifted. Some increase in NDVI between 12 July and 18 August north of ∼13.25^{o}N is not reflected by the isoprene profile and is likely the result of the re-growth of grassland and cultivated areas over the Sahel region with the supply of rainfall from the monsoon as reported by Janicot *et al.* (2008) – grasses and crops have not been observed to be significant isoprene emitters (Klinger *et al.*, 1998, Fuentes *et al.*, 2000, Guenther *et al.*, 2006). Klinger *et al.* (1998) defined a successional gradient in vegetation along a transect from grassland Savanna to primary rainforest in central Africa by using the Leaf Area Index (LAI) derived from satellite data (AVHRR). The vegetation gradient was related to isoprene emission potentials[4] for a large number of representative vegetation species across the transect. The authors found the gradient in vegetation led to a gradient in isoprene emission potential, and found the lowest isoprene emission potentials for areas of grassland Savanna and those affected by intensive agriculture; these conclusions seem consistent with the trends between isoprene and NDVI observed here.

The significant isoprene and MVK+MACR peaks around ∼6.4-7.1^{o}N and ∼13.5^{o}N in the vicinity of Lagos and Niamey respectively are likely related to anthropogenic sources (the Lagos and Niamey plumes). The points around Niamey represent only a few data points, however on the flight which observed the Lagos plume (B229), the BAe-146 flew a continuous circuit around the city to characterise

[4]Klinger *et al.* (1998) defines emission potential as the emission at optimum or near optimum light and temperature conditions for a given VOC.

the in/outflow of air and made a missed landing to produce an altitude profile. The peaks in isoprene and MVK+MACR are coincident and correlated with peaks in anthropogenic tracers such as benzene, suggesting a related source. Emissions of MVK, MACR and isoprene have been found to correlate with vehicle exhaust emissions previously, e.g. Biesenthal & Shepson (1997), Reimann *et al.* (2000). The levels of isoprene are lower than the peak levels observed over the forested region, but the level of MVK+MACR is much closer to that observed related to biogenic isoprene emissions. A significant source of isoprene, MVK and MACR which is related to the anthropogenic emissions observed around Lagos should therefore be considered and taken into account in terms of the biogenic VOC budget.

The NDVI distribution of 18 August shows much greater zonal structure again in contrast to that of 12 July, with the peak in NDVI coincident with that in isoprene concentration ($\sim$2-2.8^{o}E). Small scale features in the isoprene profile are also similarly located with those in the 18 August NDVI profile by latitude and longitude, though the structure is less easily discernible in NDVI. All data in Figure 5.23 has been colour-scaled by time of day to illustrate some of the diurnal variability in isoprene and MVK+MACR concentration which is not present in the one day resolution NDVI. The distribution of MVK+MACR is more widely spread in altitude (elevated concentrations up to 2 km altitude) and the concentration peaks appear shifted further north in comparison to the isoprene peak and NDVI in both Figures 5.22 and 5.23. A very distinct feature in Figure 5.23 is the northward shifted peak in MVK+MACR that appears in the early morning (blue points in the profile) indicative that these isoprene oxidation products remain elevated in concentration through the night.

The relative shift north of isoprene compared to NDVI, and MVK+MACR compared to isoprene indicates the influence of low level transport in the monsoon flow as described by Parker *et al.* (2005a) and traced through potential temperature in Figure 5.19. These trends are illustrated more clearly in Figures 5.24 and 5.25, where the ratio of MVK+MACR to isoprene concentration has been calculated. The ratio has only been calculated for points where both the MVK+MACR and isoprene

concentration were greater than 200 pptV; below 200 pptV there is much greater variability in both species concentrations (the detection limit reported for the PTR-MS being <125 pptV) and therefore the ratio becomes spuriously large as a result of underlying noise. The dataset has been separated by time of day into 6 hour intervals (00:00-06:00, 06:00-12:00, 12:00-18:00, 18:00-24:00) with the colour-scale representing the magnitude of the ratio. Figure 5.24 indicates the trends in 3 dimensions with a meridional profile separated into the 4 time intervals. It also puts the data in context with the positions sampled during the time intervals, with the overall data coverage in each time interval given by the grey points. Overplotted are the contours of constant potential temperature (for the 06:00-12:00 and 12:00-18:00 periods, see Section 5.2.3, Figure 5.19) indicating the diurnal cycle in monsoon structure.

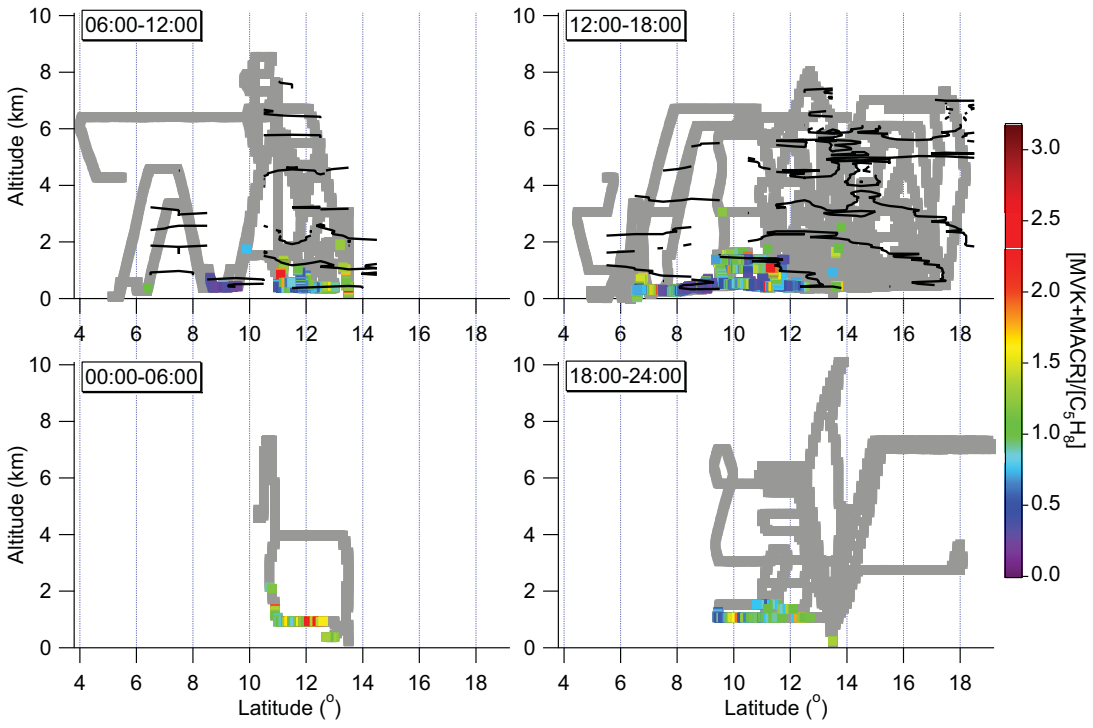

Figure 5.24: Meridional profile of the ratio of [MVK+MACR] to [isoprene] throughout the diurnal where [MVK+MACR]>200 pptV AND [isoprene]>200 pptV. Contours of constant potential temperature are plotted in black.

The ratio [MVK+MACR]/[C_5H_8] is enhanced at the northern edges of the locations where NDVI

and isoprene are peaked in the early morning to dawn (00:00-06:00), dawn to midday (06:00-12:00) and dusk to late night (18:00-24:00) periods, while the enhancement is located at higher altitude in the midday to dusk (12:00-18:00) period. The enhancements are also confined within the θ=300 K, θ=305 K contours of potential temperature (refer to Figure 5.19) in both time periods confirming the link between the extent of biogenic emissions with these isentropes. Incursion of the monsoon flow below the θ=300 K level at night drives the daytime emissions of biogenics north (with the flow) and marginally vertically above the surface in an elevated residual layer between the θ=300 K, θ=305 K levels. Even though the data at low altitudes are sparse during the night, the enhancements in [MVK+MACR]/[C_5H_8] in the 18:00-24:00 and 00:00-06:00 periods are consistent with this description.

The increase in the ratio away from the peak in isoprene concentration means that the isoprene concentration falls more rapidly away from its source region than the reaction products. Though MVK and MACR are typically dominant products observed from reaction of isoprene with OH, NO_3 and ozone (Fuentes *et al.*, 2000), the total yield of MVK plus MACR is not 100% (yields of 33% and 23% are reported for MVK and MACR respectively from reaction of isoprene with OH in the presence of NO (Atkinson *et al.*, 2006)). [MVK+MACR]/[C_5H_8] ratios greater than one therefore indicate a significant drop in isoprene concentration relative to the products concentration. Fuentes *et al.* (2000) reports that ratios greater than 0.8 have been observed in forested areas impacted by photooxidant plumes during the daytime and ratios as high as 10 are observed at night; these ratios are consistent with those derived here (the range being from 0.113-3.175, a mean of 0.821 and a median value of 0.751). The ratios that have been observed in field studies during daytime are typically attributed to reaction with OH (in the presence of NO) and dispersion and transport in the atmosphere, with differences between locations dependent on variation in these factors (Fuentes *et al.*, 2000). The lifetimes of MVK and MACR with respect to reaction with OH, NO_3 and ozone are greater than isoprene and hence the enhanced ratio is consistent with transport and dispersion. The diurnal

changes in the location of enhanced [MVK+MACR]/[C_5H_8] ratio, presented in Figure 5.25, are also consistent with the diurnal cycle in WAM circulation described by Parker *et al.* (2005a) and illustrated by the gradients in potential temperature described here.

Daytime convection (strongest from midday through afternoon) mixes surface emissions of trace gases vertically throughout the CBL on short timescales. Examining Figure 5.25, the [MVK+MACR]/[C_5H_8] ratio in this interval (12:00-18:00) is observed to increase with increasing altitude; the scale of the ratio and its gradient within the CBL observed over West Africa are consistent with that observed for the CBL at midday and into the afternoon over the central Amazonian rainforest reported by Kuhn *et al.* (2007). Mixing of fresh air masses containing recent emissions of isoprene with those that have undergone chemical processing, mean the gradient of the ratio with increasing altitude is reduced within the CBL. Kuhn *et al.* (2007) observed a considerable increase in the gradient above the CBL owing to the longer timescale of transport in the lower free troposphere and the preferential removal of isoprene relative to the longer lived MVK+MACR. The dataset for the ratio by altitude is of limited vertical extent within all time intervals and particularly those outside the 12:00-18:00 period. This can be explained using the altitude profile in the concentration of isoprene and MVK+MACR – both rapidly fall around 1.5-2 km altitude and the ratio becomes noisy above this. Further, an asymmetrical diurnal profile in isoprene emissions peaking around 15:00 UTC has been observed both on the ground e.g. (Saxton *et al.*, 2007), and is observable in the aircraft data over a given location (not plotted) consistent with the environmental factors that control isoprene emission from plants (temperature and the availability of sunlight). This leads to low isoprene emissions outside the 12:00-18:00 period and hence less data are likely to meet the 200 pptV criteria used in determining the [MVK+MACR]/[C_5H_8] ratio. Hence a substantial increase in the gradient of the [MVK+MACR]/[C_5H_8] ratio with altitude beyond the CBL is not observable in this dataset. No significant gradient by altitude is observable within time intervals outside 12:00-18:00 for the same reasons, however the range of values observed

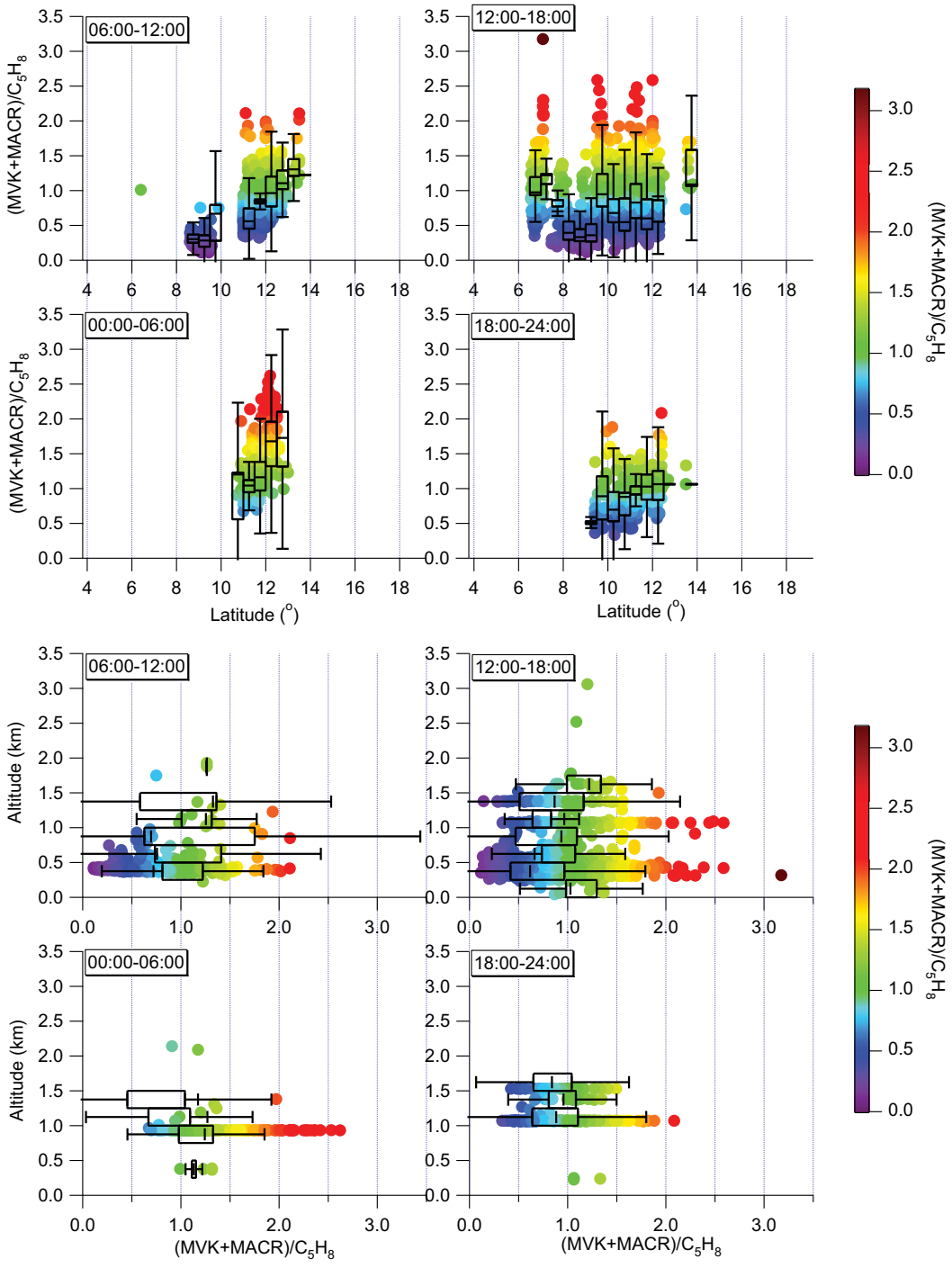

Figure 5.25: Latitude (Top) and altitude (Bottom) profiles of the ratio of [MVK+MACR] to [isoprene] throughout the diurnal where [MVK+MACR]>200 pptV AND [isoprene]>200 pptV; in each profile box centres represent median values, box edges Q25 and Q75 and whiskers lower and upper inner fences

are of the same magnitude as the daytime values.

Still considering Figure 5.25, the gradient of the [MVK+MACR]/[C_5H_8] ratio by latitude follows the diurnal cycle of the monsoon flow. Within the 12:00-18:00 period there is no significant gradient in the ratio with increasing latitude as horizontal transport is suppressed by convection. When the low level meridional wind as reported by Parker *et al.* (2005a) is meant to be most strong (in the early morning before dawn) the gradient by latitude of the ratio is greatest (i.e. in the 00:00-06:00 interval). In the intermediary time intervals, lesser but still significant gradients in the [MVK+MACR]/[C_5H_8] ratio by latitude are observed. Air masses transported horizontally in the day when meridional winds are suppressed come into contact and mix with fresh biogenic emissions across the latitude gradient in vegetation so the [MVK+MACR]/[C_5H_8] ratio is suppressed by latitude and altitude. In turn, convection is suppressed at night so isoprene emitted earlier and mixed to higher altitude is left in the residual layer, and when transported the concentration only changes relative to that of MVK+MACR as a result of chemistry not mixing, so strong [MVK+MACR]/[C_5H_8] gradients arise in the direction of transport.

5.2.5 Chemical tracers

The meridional distributions of selected chemical tracers determined from measurements on board the BAe-146 during SOP2 are shown compiled in Figures 5.26-5.30. Overplotted on each meridional distribution (black traces) are the contours of constant potential temperature (from the 12:00-18:00 period, see Section 5.2.3, Figure 5.19) indicating the daytime monsoon structure. Also plotted with each are the latitudinal concentration profiles below 1 km altitude (bottom) and the total concentration profiles by altitude (right) indicating the gradients within the boundary layer and by altitude respectively. Overplotted on these concentration profiles the box and whiskers give an overview of the spread in concentrations by latitude (0.5^o bins) and altitude (0.5 km bins), box centres represent

median values, box edges Q25 and Q75 and whiskers lower and upper inner fences. Inset (bottom right) with each meridional concentration distribution, a frequency histogram shows the typical distribution of concentrations sampled throughout the campaign, with the number of points observed at each concentration converted into the number of hours observed.

Since relatively few strongly polluted air masses were observed, the concentration scale of the axes and the range in the colourscale in Figures 5.26-5.30 should not be taken as the complete range in concentration observed. A compromise has been made between choosing a scale appropriate to the total range in concentrations observed and a scale appropriate to the range in concentration across gradients by altitude and latitude. This difference is most clear in the box and whisker plots by altitude and latitude, where polluted plumes are often far outside the upper quartile. The trends observed by latitude and altitude are also influenced by the data coverage, whereby the median is representative of the background level if greater coverage is available, while individual plumes skew the trend where the data coverage is less. To clarify the range of concentrations observed, a summary for the tracers presented is given in Tables 5.4 and 5.5; where the concentration has reached the detection limit this is indicated by DL.

Tracer (Unit)	Max	Min	Median	Mean	SD
Ozone (ppbV)	128.0	DL	38.8	39.3	14.7
CO (ppbV)	1930	DL	98.2	112.9	80.6
NO_{NOxy} (ppbV)	1.26	DL	0.044	0.059	0.058
$NO_{2,NOxy}$ (ppbV)	5.83	DL	0.157	0.245	0.419
$NO_{2,TECO}$ (ppbV)	50	DL	0.28	0.76	2.88
$NO_{y,NOxy}$ (ppbV)	2.243	DL	0.389	0.469	0.325
Benzene (pptV)	1670	DL	24	38	64
Acetonitrile (pptV)	912	23	135	145	65

Table 5.4: Overall statistics for selected tracers

A number of observations may be made with regard to the distributions presented in Figures 5.26-5.30. From a visual inspection the background level of ozone may be thought to exhibit a distinct

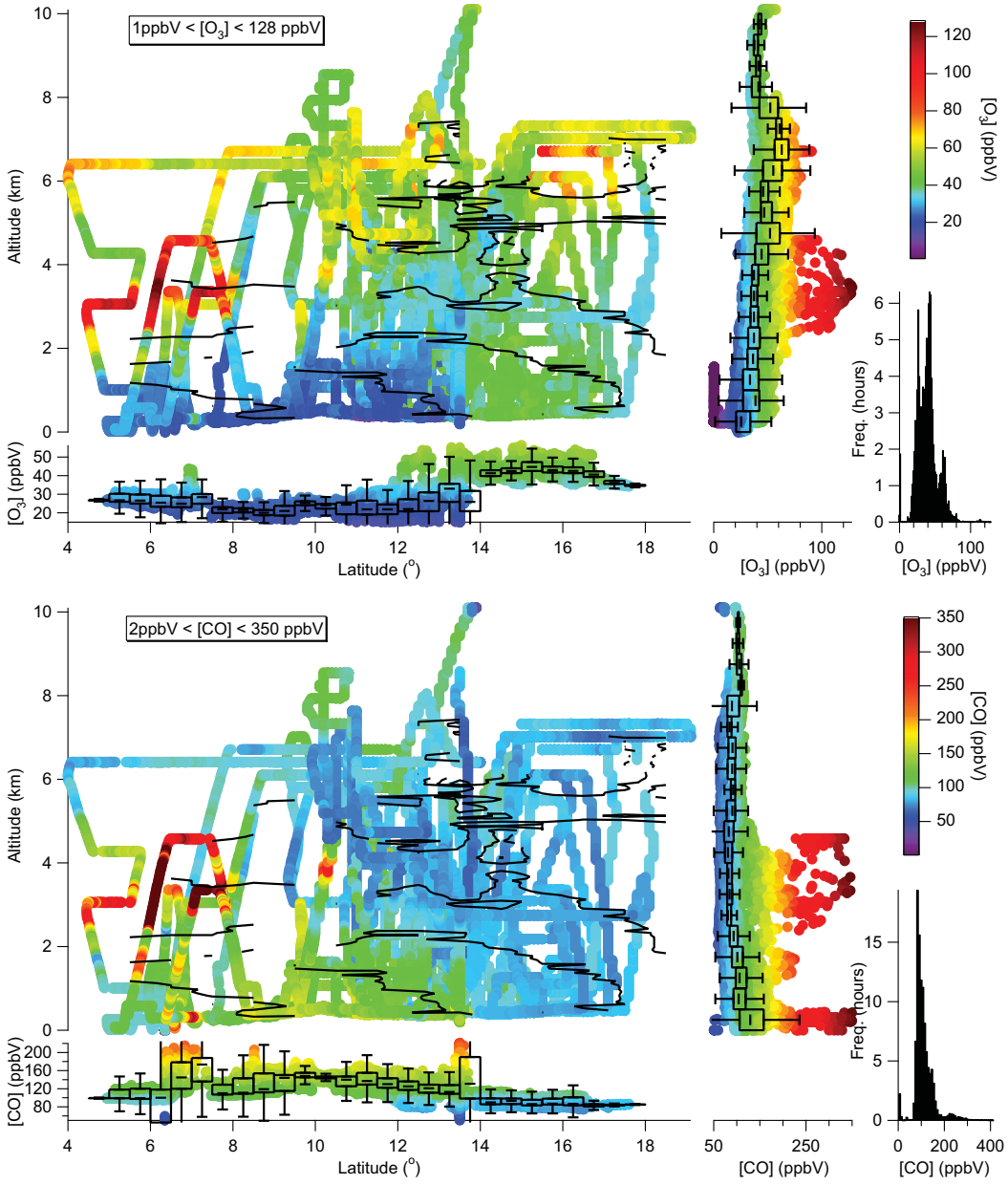

Figure 5.26: Meridional distributions of ozone (Top) and CO (Bottom) concentration observed throughout SOP2, colourscaled in the range 1-128 ppbV, 2-350 ppbV for the ozone, CO measurements respectively – Insets to each: (Bottom) Concentration profile by latitude for all data below 1 km altitude; (Right) Concentration profile by altitude for all data; (Bottom right) Frequency distribution of concentrations sampled during SOP2.

Tracer (Unit)	Max	Min	Median	Mean	SD
Ozone (ppbV)	56.4	DL	26.7	28.9	11.2
CO (ppbV)	1930	DL	118.0	127.0	98.2
NO_{NOxy} (ppbV)	1.26	DL	0.052	0.069	0.066
$NO_{2,NOxy}$ (ppbV)	5.83	DL	0.212	0.360	0.509
$NO_{2,TECO}$ (ppbV)	49.9	DL	0.37	1.16	3.06
$NO_{y,NOxy}$ (ppbV)	1.145	DL	0.389	0.393	0.214
Benzene (pptV)	1670	DL	60	75	85
Acetonitrile (pptV)	614	28	139	142	41

Table 5.5: Statistics for selected tracers below 1 km altitude

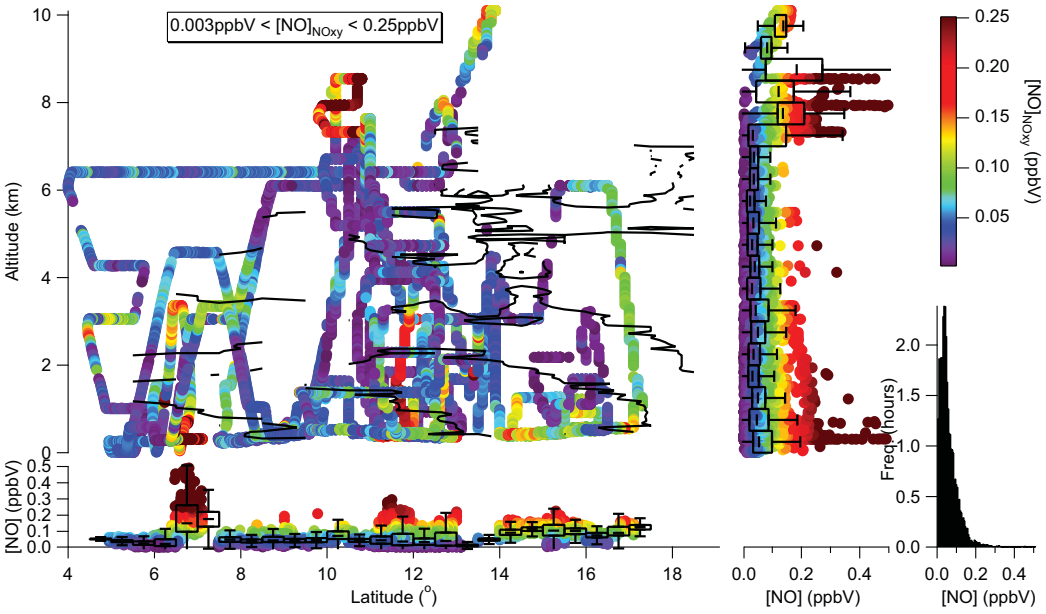

Figure 5.27: Meridional distribution of NO concentration observed throughout SOP2 derived from the UEA NOxy instrument, colourscaled in the range 0.015-1 ppbV – Insets: (Bottom) Concentration profile by latitude for all data below 1 km altitude; (Right) Concentration profile by altitude for all data; (Bottom right) Frequency distribution of concentrations sampled during SOP2.

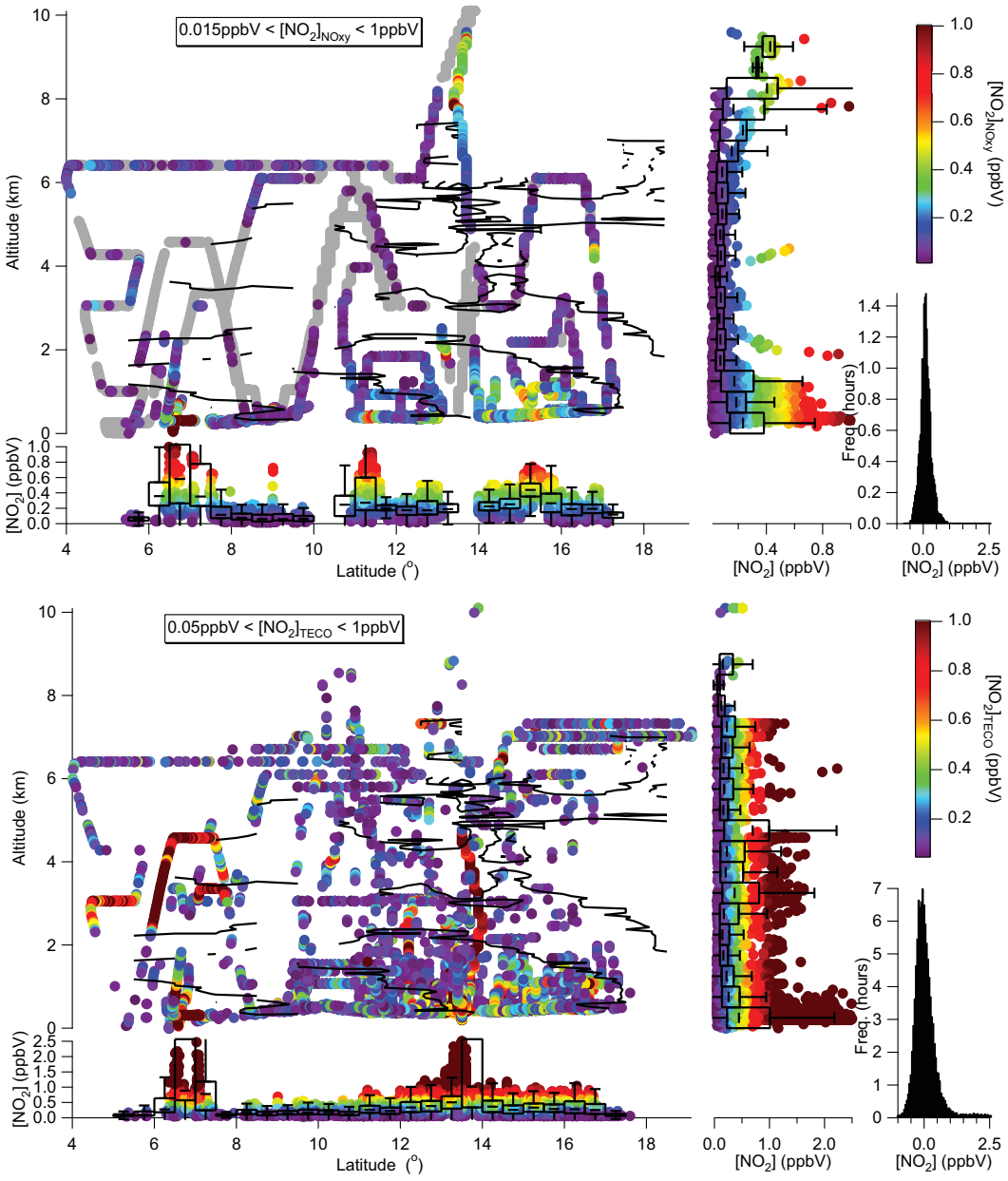

Figure 5.28: Meridional distribution of NO_2 concentration observed throughout SOP2 derived from the UEA NOxy (Top) and FAAM TECO (Bottom) instruments, colourscaled in the range 0.015-1 ppbV, 0.05-1 ppbV for the NOxy, TECO instruments respectively – Where the concentration has been at or below the detection limit for the UEA NOxy these points are highlighted in grey. Insets to each: (Bottom) Concentration profile by latitude for all data below 1 km altitude; (Right) Concentration profile by altitude for all data; (Bottom right) Frequency distribution of concentrations sampled during SOP2.

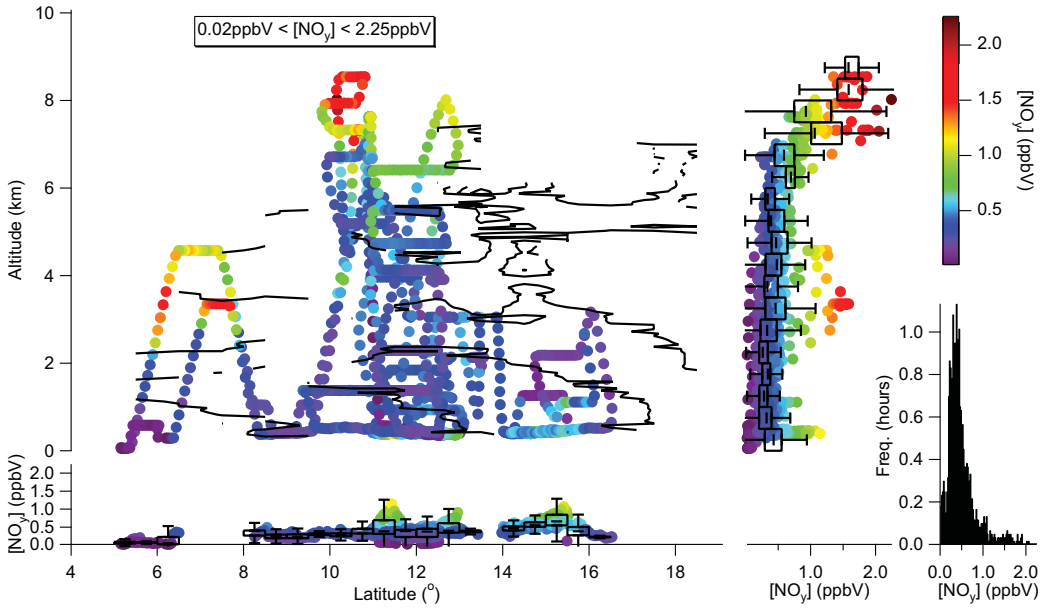

Figure 5.29: Meridional distribution of NO_y concentration observed throughout SOP2 derived from the UEA NOxy instrument, colourscaled in the range 0.02-2.25 ppbV – Insets: (Bottom) Concentration profile by latitude for all data below 1 km altitude; (Right) Concentration profile by altitude for all data; (Bottom right) Frequency distribution of concentrations sampled during SOP2.

overall anticorrelation with the background level of CO. The gradients in ozone and CO are also reflected by the gradients in potential temperature indicating the influence of transport within the WAM system on chemical composition. Indeed, it is apparent that the extent of the low levels of ozone (and correspondingly high levels of CO) in the boundary layer are similar in extent to the region influenced by the low level monsoon flow. The distinct transition in concentration of both ozone (from ∼20 ppbV background level to ∼50 ppbV) and CO (from ∼120 ppbV background level to ∼90 ppbV) that occurs north of approximately 12-14°N (this occurring over a range in latitude as a result of variations by longitude) and above approximately 1.5-2 km altitude is indicative of a change in air mass. Again this is consistent with the dynamical picture of Figure 5.2 where the monsoon layer is capped above and to the north by the Saharan Air Layer (SAL).

Figure 5.31 plots the observed ozone concentrations versus that of CO and uses a first order air mass classification of "monsoon layer" defined as having $[O_3] \leq 30$ ppbV, "SAL" defined as having $[CO] \leq 90$

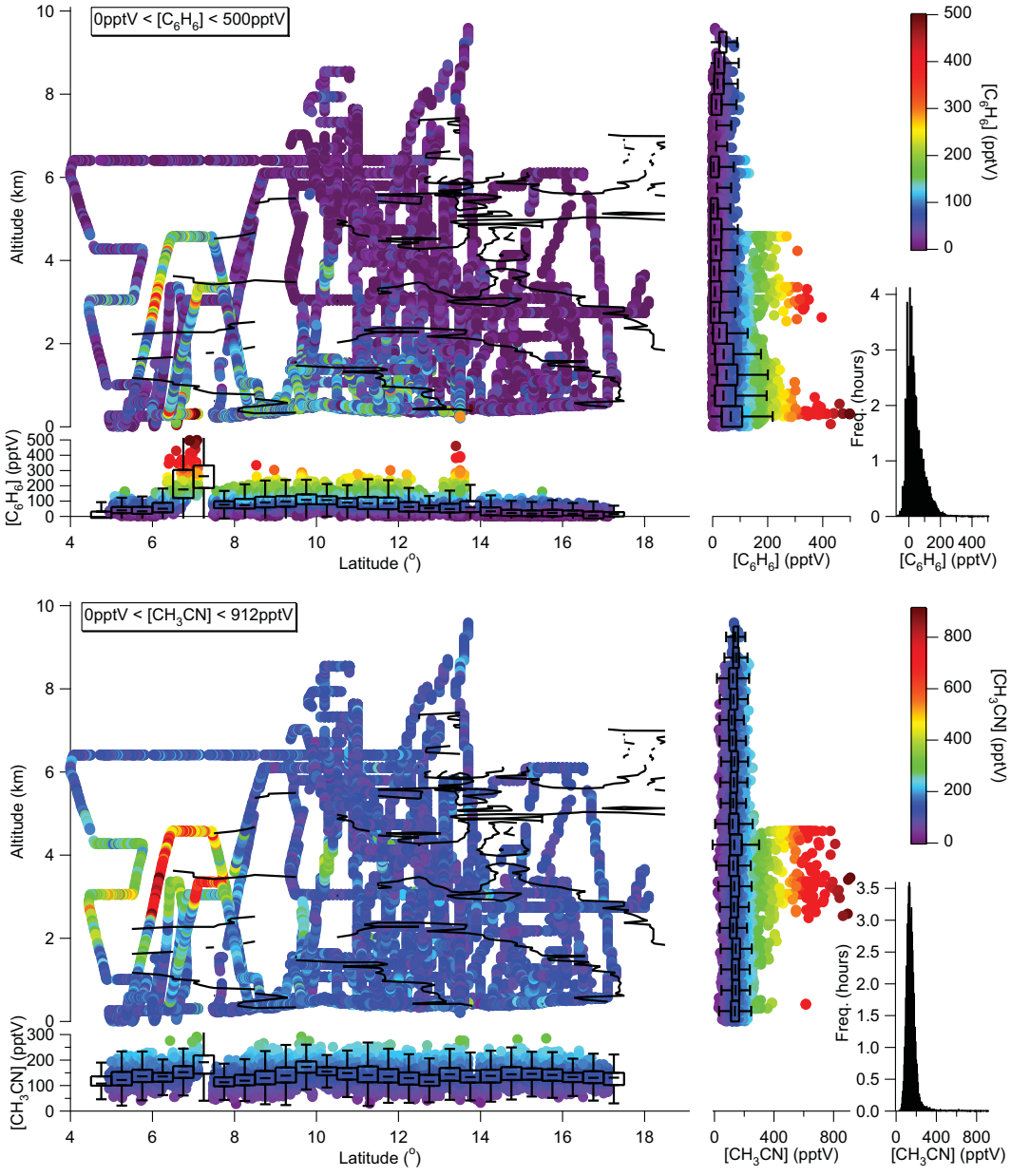

Figure 5.30: Meridional distribution of benzene (Top) and acetonitrile (Bottom) concentrations observed throughout SOP2 derived from the UEA PTR-MS instrument, colourscaled in the range 0-500 pptV, 0.05-1 ppbV for benzene, acetonitrile respectively – Insets to each: (Bottom) Concentration profile by latitude for all data below 1 km altitude; (Right) Concentration profile by altitude for all data; (Bottom right) Frequency distribution of concentrations sampled during SOP2.

ppbV, and "anthropogenic influenced" defined as [CO]≥150 ppbV. Assuming 90 ppbV as the upper limit on CO concentration in the "SAL" air mass and using this as a filter on ozone and CO data, there is no obvious correlation (correlation coefficient of -0.12) between ozone and CO within the SAL in Figure 5.31. Similarly taking 30 ppbV as the upper limit on ozone concentration in the "monsoon layer" air mass and using this as a filter on ozone and CO data, there again is no obvious correlation (correlation coefficient of -0.17) between ozone and CO within the monsoon layer in Figure 5.31. It is clear therefore that the apparent anticorrelation between background ozone and CO concentrations observed by latitude simply reflects the spatial distribution of air masses within the WAM system. The "anthropogenic influenced" air masses are colourscaled by acetonitrile (a primary tracer of biomass burning) concentration where available and otherwise coloured black with a slightly different symbol to distinguish these points. It is clear that in the "anthropogenic influenced" air masses there is often a significant positive correlation between ozone and CO, indicative of ozone production. Those points highlighted by coincident enhanced levels of acetonitrile identify air influenced by biomass burning. Anthropogenic plumes associated with cities such as Lagos (∼6.4-7.1^{o}N) and Niamey (∼13.5^{o}N) are apparent where acetonitile concentrations become low, while there is still a positive correlation between ozone and CO. In these plumes benzene is enhanced rather than acetonitrile; this distinction is clear by comparison of the distributions in Figure 5.30. The gradients in ozone versus CO in the "anthropogenic influenced" plumes are indicative of the relative level of ozone production from these sources, although processes occurring during transport (e.g. ozone deposition, production of CO on oxidation of VOC's) will impact the trend. The thick black trace overplotted on Figure 5.31 represents a linear fit to the data for a particular biomass burning plume, intercepted on flight B231 on the 13 August 2006; the fit is derived using data from a level run within the plume at ∼4.5 km altitude. In this case the fit derived gives $[O_3]$(ppbV)=0.232(±0.005)[CO](ppbV) + 17.59(±1.44), with a correlation coefficient of r=0.985. Similar gradients are derived from the data associated with other biomass burning plume interceptions on this flight, and on flights B228 and B229 on the 8 August 2006, although this is a particularly

strong example. The thick red trace represents a linear fit to the data from flight B229 on the 8 August 2006 where the the BAe-146 flew a continuous circuit around Lagos at ∼0.3 km altitude sampling the in/outflow of air from the city. In this case the fit derived gives $[O_3]$(ppbV)=0.091(±0.003)[CO](ppbV) + 12.40(±0.53), with a correlation coefficient of r=0.913, indicating lower levels of ozone production relative to the biomass burning plumes.

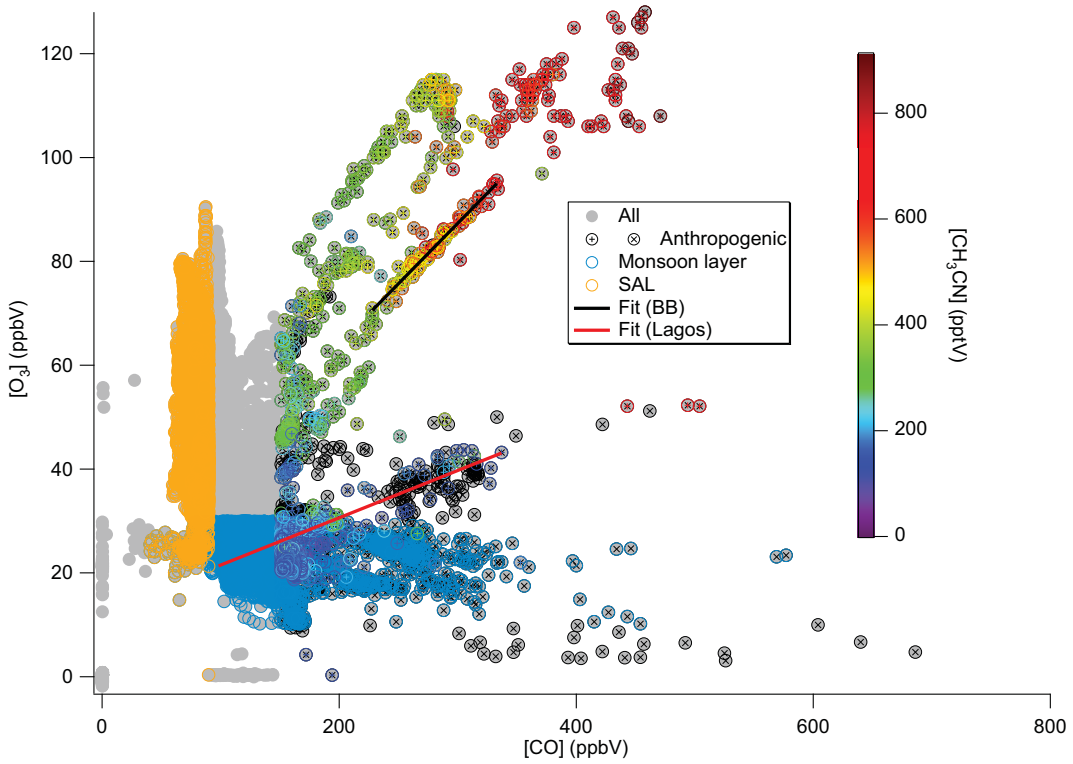

Figure 5.31: Correlation of ozone with CO by air mass – (Grey) All points; (Light blue open circles) Monsoon layer defined as having $[O_3]$≤30 ppbV; (Dark yellow open circles) SAL defined as having [CO]≤90 ppbV; (Crossed circles, colourscaled by [acetonitrile] or black where [acetonitrile] unavailable) Anthropogenic influenced defined as [CO]≥150 ppbV, (Black trace) Linear fit to ozone versus CO for one particular biomass burning plume.

Comparison of the distributions in NO_x and NO_y reveals some interesting features and instrumental differences. The distributions of NO_2 in Figure 5.28 as measured by the UEA NOxy (Top) and FAAM TECO (Bottom) instruments show some similarities and some differences. The data coverage of the UEA NOxy was limited within AMMA due logistical issues with the supply of consumables, which meant the instrument was only operated on later flights (B226-B235). However, the differences

between the distribution of NO_2 cannot be explained by the data coverage. Where the NOxy NO_2 signal was at or below the detection limit (grey points) the TECO instrument intermittently picked up significant signals, this is most clear in the biomass burning plumes observed at lower latitudes. Stewart *et al.* (2008) report that the TECO instrument is susceptible to interference from NO_y species, and for the AMMA SOP2 campaign that the TECO NO_x data was systematically 16% higher in the boundary layer. Comparing all data, the measurements were assessed to be most comparable (though still with some systematic offset) if restricted to concentrations below 1 ppbV, which excludes the biomass burning plumes. From Figure 5.29 NO_y is seen to be enhanced within the biomass burning plumes and supports the idea of an NO_y interference to the TECO measurement. The distribution of NO derived from the UEA NOxy instrument is given in Figure 5.27; the NO data from the FAAM TECO instrument (not shown) was unreliable, because the range of NO concentrations observed within the whole campaign was of the order the detection limit for this instrument. There are definite enhancements in NO, NO_2 and NO_y in the boundary layer north of $\sim 11^o$N, indicative of a widely distributed source, while there also strong point sources located at Lagos and Niamey (although the Niamey plume appears excluded from the NOxy dataset). Stewart *et al.* (2008) and Delon *et al.* (2008) have positively associated the spatial distribution of NO_x enhancements over the Sahel ($>13.5^o$N) with biogenic emissions from soils promoted by the onset of monsoon rainfall (as discussed briefly in Section 5.1.2). The investigation of Stewart *et al.* (2008) was limited to a number of case study flights which took place north of 14^oN. The low level transport associated with the monsoon flow brings biogenic VOC emissions as far north as 14^oN as demonstrated above in Section 5.2.4. The combination of enhanced NO_x and VOC's provides the potential for significant ozone production, which will be investigated in the next Chapter; ozone is observed to be enhanced in the boundary layer coincident with the enhancements related to soil NO_x. Enhancements occur in NO_x and NO_y above $\sim$7 km altitude while CO is marginally enhanced and ozone is marginally suppressed. This is indicative of the convective uplift of air from the surface; coincident enhancements occur in other tracers such as

acetone and formaldehyde (not shown) which support this.

The distributions of benzene and acetonitrile as measured by the UEA PTR-MS instrument are presented in Figure 5.30 as primary tracers of anthropogenic and biomass burning emissions respectively. As illustrated by Figure 5.31 acetonitrile may be used to positively identify those plumes associated with biomass burning. The gradient by latitude of benzene in the boundary layer is strongly correlated with that of CO, and from Figure 5.31 it is also clear the there is some overlap between the air defined as "anthropogenic influenced" and that associated with the "monsoon layer". This is demonstrated in Figure 5.32, where the benzene concentration is plotted as a function of CO concentration for all points below 1 km altitude ($[C_6H_6]$(pptV)=2.014($\pm$0.0273)[CO](ppbV) - 162.47($\pm$3.33), correlation coefficient r=0.705). From this fit the background level of CO within the boundary layer ($[CO]_{bg}$) can be calculated more precisely from the point where $[C_6H_6]$=0 pptV, i.e. $[CO]_{bg}$=80.67$\pm$1.98 ppbV, consistent with the overall background level of $\sim$90 ppbV estimated from the distribution in Figure 5.26. There is a therefore clear evidence to point to the monsoon flow transporting CO (along with other longer lived anthropogenic emissions) from coastal cities over the vegetated regions up to 13.5^{o}N. The correlation is not perfect so there may be evidence to support an additional biogenic source of CO through the ozonolysis of alkenes (e.g. Rockmann *et al.* (1998)) or OH initiated oxidation of terpenes (e.g. Miyoshi *et al.* (1994)). The level of ozone in the boundary layer over the same region is systematically lower than that over the Gulf of Guinea, which may be a combination of ozone deposition to trees at the surface, or ozonolysis of biogenic and anthropogenic alkenes. The lack of NO_x (beside some individual point sources) up to $\sim$11^{o}N likely contributes to the depletion of ozone in the boundary layer, owing to photochemical ozone destruction.

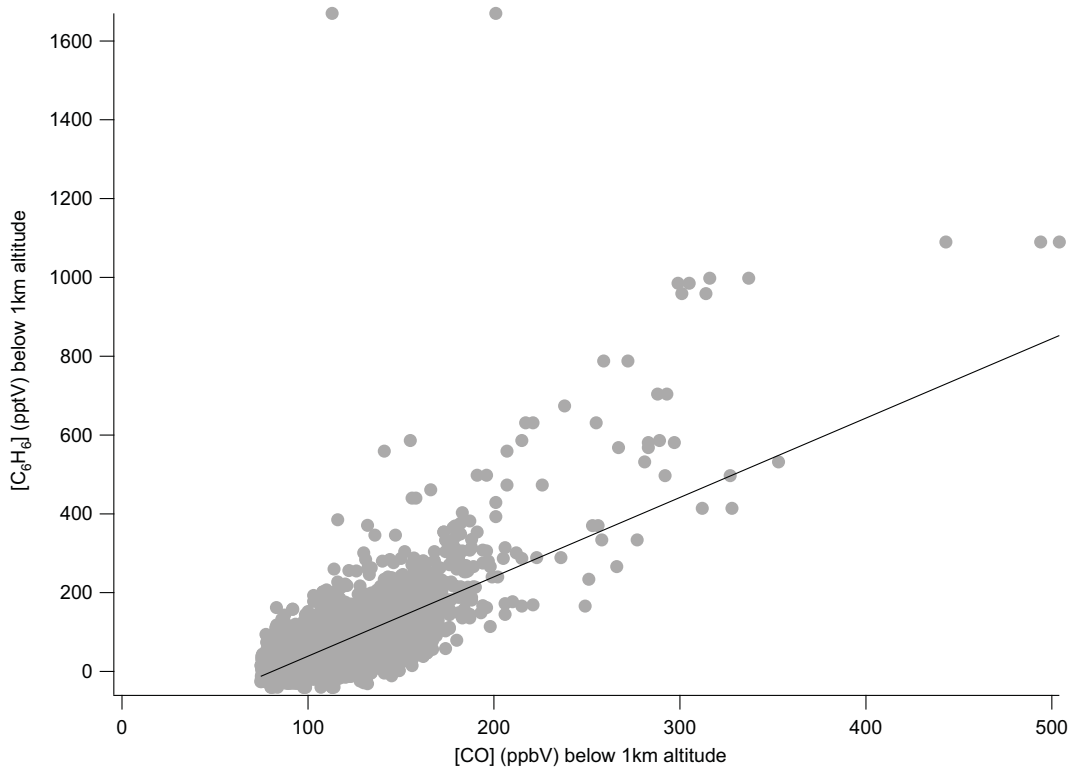

Figure 5.32: Correlation of benzene with CO within the boundary layer – Data restricted to points where the aircraft altitude was <1 km.

5.3 Chapter 5 Summary

This chapter has provided an overview of the background to the AMMA project, in particular the aircraft field campaign carried out during the Special Observing Period 2 (see Section 5.1). The motivations to the project have been discussed in Section 5.1.2, and a brief summary of the WAM system has been given in Section 5.1.3. The details of the organisation of the aircraft campaign have been summarised and data coverage resulting from the campaign are provided in Sections 5.1.1 and 5.2.1. In particular the spatial and temporal coverage of the measurements of peroxy radicals and photolysis rates for this thesis have been put into context with the overall data coverage, and potential biases due to undersampling in time and space have been discussed. The results of the radical and photolysis rate measurements have been presented as flight by flight time series in Section 5.2.2, with an initial discussion of the observations, in particular focusing on the comparison of the PERCA measured peroxy radical concentrations with the FAGE measured HO_x concentrations, and measured and modelled photolysis rates.

The diurnal cycle of the WAM has been identified in changes in the gradients in potential and equivalent potential temperature in Section 5.2.3. The distribution of vegetation across West Africa has been inferred from the normalised difference vegetation index (NDVI), with changes in the distribution related to the progression of the monsoon rainfall (see Figure 5.21); in turn the distribution of vegetation has been related to the distribution of biogenic VOC's in Section 5.2.4. The diurnal cycle in monsoon dynamics identified in Section 5.2.3 has then been used to explain diurnal variation in the distribution of isoprene and its oxidation products (MVK and MACR) by latitude and altitude, also in Section 5.2.4.

The meridional distribution of a selection of chemical tracers measured during SOP2 have been presented in Section 5.2.5. The distribution of ozone and CO have been largely explained in terms of the

structure of the WAM, using the contours in potential temperature derived in Section 5.2.3. No correlation is observed in the background levels of ozone and CO when defined in terms of the "Saharan Air Layer" and "monsoon layer" using a first order air mass classification. The persistent observation of the anticorrelation of ozone and CO by latitude within SOP2 may be explained through the difference in chemical composition of these air masses related to the large scale structure of the WAM. The air mass classification has also been used to identify air masses influenced by anthropogenic emissions, while acetonitrile has been used as a tracer to separate biomass burning plumes from other anthropogenic sources. Correlation of ozone and CO within the anthropogenically influenced air masses is seen as an indicator for strong photochemical ozone production. Strong positive correlation is observed between ozone and CO in the biomass burning plumes and the Lagos plume; the gradient is greater for the biomass burning plumes indicating enhanced ozone production relative to the Lagos plume. The strong correlation of benzene with CO in the boundary layer has been used to provide evidence for an anthropogenic source of the enhanced CO within the monsoon layer over the vegetated regions. The correlation is not perfect and along with the strong emissions of biogenic VOC's and the depletion of ozone, there is likely an additional biogenic source of CO. The relationship derived between boundary level benzene and CO has allowed the calculation of the background concentration of CO, calculated to be $[CO]_{bg}$=80.67±1.98 ppbV. There is clearly a strong coupling between the dynamics of the monsoon, the surface landcover and related emissions, and atmospheric composition over West Africa.

Chapter 6

Analysis of results from AMMA

The African Monsoon Multidisciplinary Analysis (AMMA) project and the Special Observing Period 2 (SOP2) field campaign in particular have been described in Chapter 5. The emphasis of Chapter 5 was to provide the context to the measurements and an overview of the data. This chapter makes use of the measurements of peroxy radicals and photolysis rates undertaken during SOP2. In particular, the measurements are interpreted using modelling of these parameters and put into context with the results from Chapter 5. Radical composition is assessed through a consideration of VOC reactivity and measured trends and compared to the output of a photochemical box model. The processes controlling ozone production and loss are considered though a calculation of the net ozone tendency.

6.1 Comparison of photolysis rate measurements to the TUV model

The photolysis rates of ozone (j_{O^1D}) and NO_2 (j_{NO_2}) were measured during the AMMA SOP2 field campaign using filter radiometers. A description of the instruments and their calibration is given in Chapter 4. The photolysis rates of ozone and NO_2 have also been modelled using the Tropospheric Ultraviolet and Visible (TUV) Radiation Model version 4.1 of Madronich (1987), Madronich & Flocke

(1998); the setup of the model for the AMMA campaign has been described in Section 5.2.2 of Chapter 5. Flight by flight time series of measured and TUV modelled j_{O^1D} and j_{NO_2} were presented for comparison in Figures 5.7-5.17 of Chapter 5. The observations from the initial comparison were:

- Measured and TUV modelled photolysis rates are mostly of the same order of magnitude.
- Measured photolysis rates are often considerably more variable.
- Variability is on timescales down to a minute or less.
- Variability is often well correlated with radical measurements suggesting these rapid changes are linked.
- Measured j_{O^1D} often exceeds TUV modelled at higher altitude.
- Measured j_{O^1D} is similar or less than TUV at lower altitude.
- Measured j_{NO_2} often exceeds TUV modelled at higher altitude.
- Measured j_{NO_2} is typically less than TUV at lower altitude.

The initial conclusions drawn from this assessment are that the variability is likely to be associated with rapid changes in the actinic flux, perturbed by cloud and aerosol typical of the monsoon environment but not present in the model. Enhancements with respect to the model are then likely to result from the enhancement of upwelling actinic flux at higher altitude when above cloud associated with the convective boundary layer. The opposite is true at lower altitudes where cloud and aerosol aloft will attenuate the actinic flux and reduce the measured photolysis rates with respect to the model. The marginally greater attenuation of j_{NO_2} compared to j_{O^1D} at lower altitude may be associated with the sensitivity of j_{NO_2} to attenuation of the longer wavelength components (UVA) of the actinic flux in direct sunlight, while j_{O^1D} is held up owing to its sensitivity to the shorter wavelength (UVB) diffuse component which is less readily perturbed, e.g. Monks *et al.* (2004). The lower position j_{O^1D}

radiometer failed during the campaign and a first order method of estimation of the missing signal component was derived to compensate for this (see Section 4.3.1, Chapter 4, page 172). The impact of the method of estimation is considered in the following comparison.

The compiled measurement data have been quantitatively compared with the TUV modelled photolysis rates by calculating the ratio $j_{X,TUV}/j_{X,Meas.}$ (where X represents the photolysis process). In Figure 6.1 the ratio is plotted as a function of altitude and colourscaled either by j_{O^1D} or j_{NO_2}. The ratio has been plotted on both a log scale including all data (left of plot, Figure 6.1), and a more narrow scale (right of plot, Figure 6.1) which therefore excludes outliers in the data but shows the trend more clearly. From this quantitative assessment a clear altitude trend is observed in the model to measurement ratio for both j_{O^1D} and j_{NO_2}, with significant dispersion in the trend occurring as a function of the magnitude of the photolysis rates and therefore as a function of solar zenith angle (more significant for j_{O^1D}). The trends are consistent with the initial findings, in that both measurements are lower with respect to the model below an altitude of ∼2-3 km, while both equal or exceed the modelled photolysis rates above this and the difference is greater for j_{O^1D} – median values of $j_{O^1D,TUV}/j_{O^1D,Meas.}$ reach ∼0.7 above 4 km altitude, while median values of $j_{NO_2,TUV}/j_{NO_2,Meas.}$ reach ∼1.0. The median values are reasonably constant above 4 km altitude which suggests that further changes in the measured photolysis rates scale consistently with the clear sky TUV model output. Above 6 km there are fewer data points and therefore the variability observed is not characteristic of the average situation rather the few cases sampled at these altitudes.

The j_{O^1D} filter radiometer measurements have not been corrected to account for the temperature dependence of the quantum yield and cross section of j_{O^1D}, or the ozone column density and SZA dependencies of the actinic flux in the UVB (see Section 4.2.4 of Chapter 4). The relative change in j_{O^1D} by altitude within the troposphere is related to its variation by temperature also (owing to the strong positive lapse rate in the troposphere), and therefore the altitude trend will be most

significantly modified by the temperature dependencies of j_{O^1D} not accounted for in calibration of the measurement. There is no strong temperature dependence in the quantum yield and cross section for j_{NO_2} and therefore the lack of an altitude (and therefore temperature) dependence in both the ratios $j_{O^1D,TUV}/j_{O^1D,Meas.}$ and $j_{NO_2,TUV}/j_{NO_2,Meas.}$, suggests that in any case the temperature dependence in j_{O^1D} is much weaker above an altitude of 4 km where temperatures were $\leq$275 K during the field campaign. This is consistent with the parameterisation for the temperature dependence of j_{O^1D} developed by Bohn *et al.* (2004) which has been discussed (in Section 4.2.4 of Chapter 4) and evaluated for a range in temperatures characteristic to the range in ambient temperature encountered during the campaign – the correction factor does indeed exhibit a gradient that decreases by altitude (see Figure 4.11). So, although the trend in $j_{O^1D,TUV}/j_{O^1D,Meas.}$ is likely accentuated by not accounting for the temperature dependence in j_{O^1D}, the similar trends by altitude suggests that the photolysis rates are truly modified in such a manner in the environment of the WAM.

To illustrate the difference in applying the Bohn *et al.* (2004) temperature correction parameterisation to the aircraft j_{O^1D} data, Figure 6.2 compares the altitude dependence of the median data with and without such a correction applied, using a campaign average ozone column density of 287.5 DU. There is some decrease in the gradient by altitude as expected, however the overall trend is still apparent, and it is not certain that this correction is valid under the conditions of the aircraft measurements (refer again to Section 4.2.4 of Chapter 4). In particular the altitude trend and variability in the measured photolysis rates suggests a significant impact of cloud and aerosol during the WAM, which modify j_{O^1D} by changing the spectral composition of the actinic flux, although not changing the temperature dependencies of the quantum yield and cross section for ozone photolysis.

The ozone column density dependence of the actinic flux in the UVB was predicted to lead to an overestimation of j_{O^1D} of the order 25% at SZA's $\leq 35^o$. This results from the weighting of the j_{O^1D} filter radiometer calibration factors to an ozone column density of $\sim$365 DU, while the average ozone

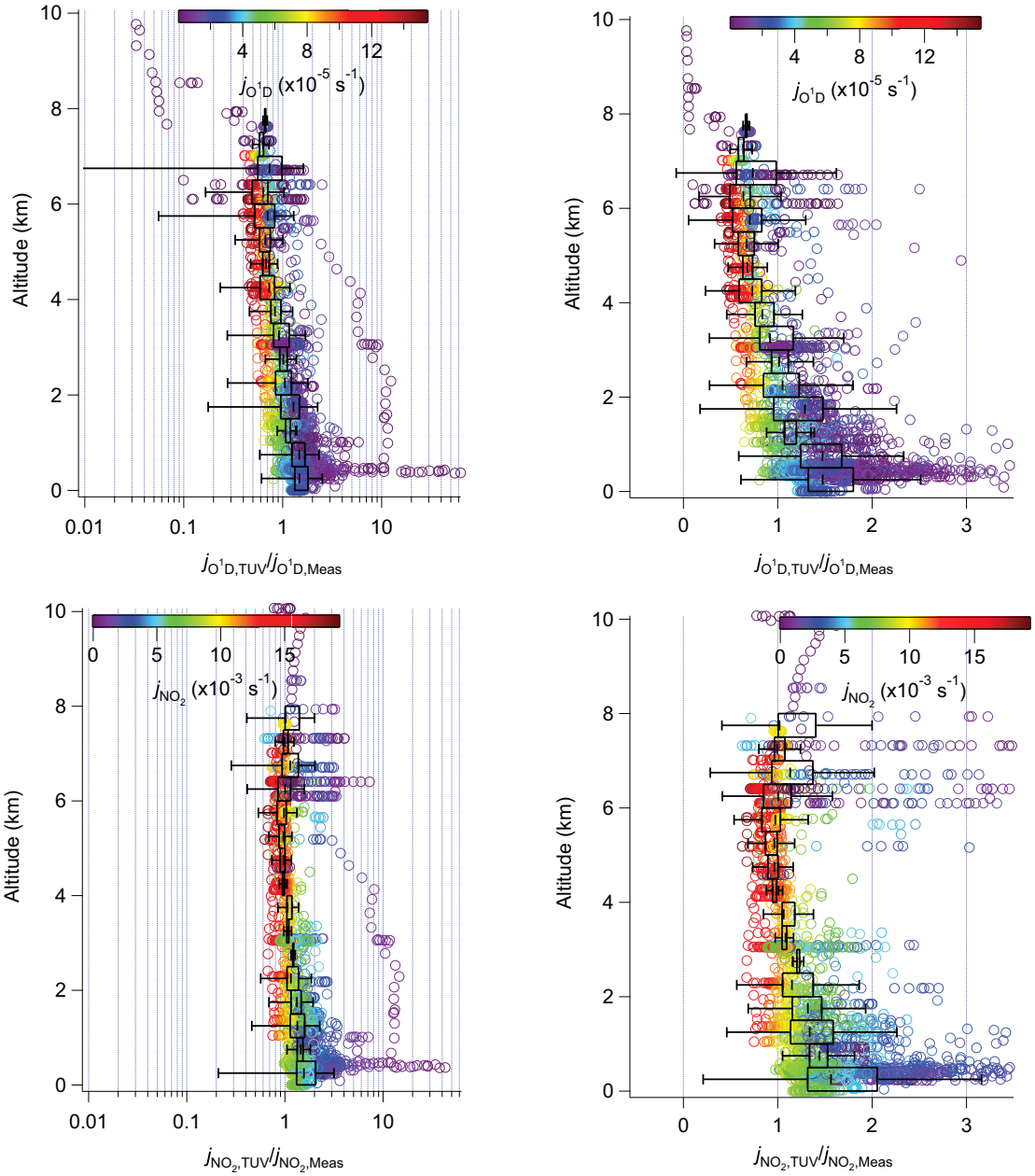

Figure 6.1: Ratio of TUV modelled to measured photolysis rates as a function of altitude – (Top left) All j_{O^1D} data including outliers; (Top right) j_{O^1D} data excluding outliers; (Bottom left) All j_{NO_2} data including outliers; (Bottom right) j_{NO_2} data excluding outliers. Box centre represents median, box edges Q25 and Q75 and whiskers lower and upper inner fences

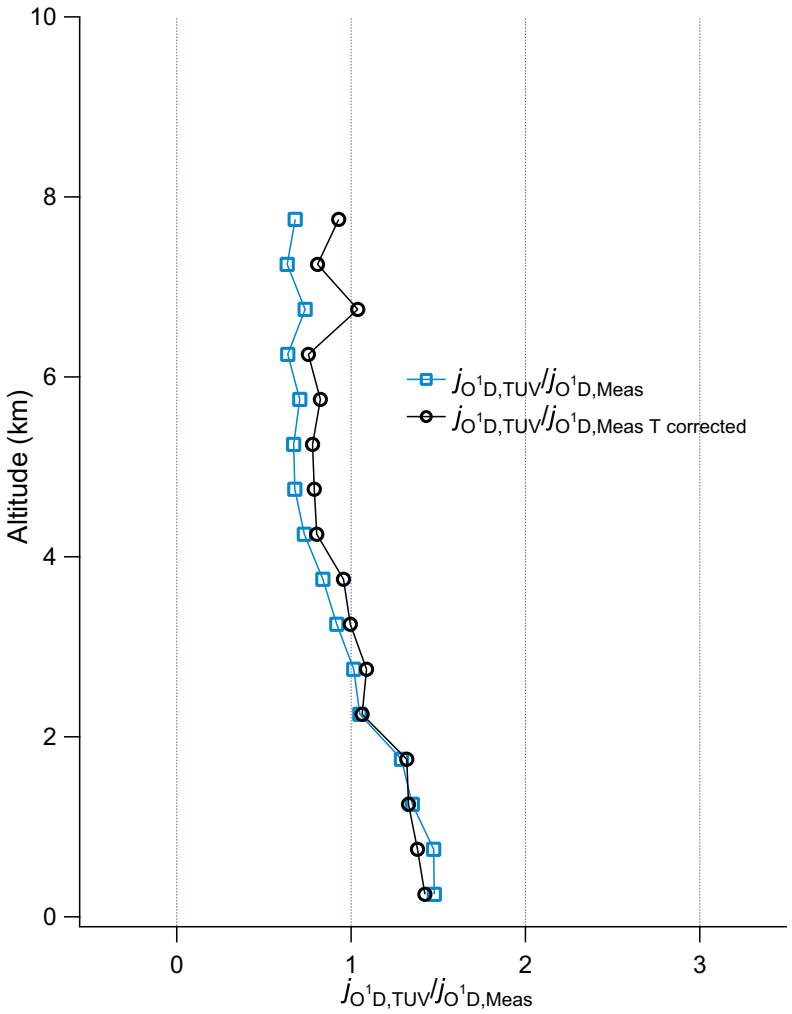

Figure 6.2: Comparison of median modelled to measured j_{O^1D} by altitude with (black open circles) and without (blues open squares) temperature correction

column density observed over the AMMA region during SOP2 was 287.5 DU (refer again to Section 4.2.4 of Chapter 4). The solar zenith angle dependence of the actinic flux in the UVB in combination with the weighting of the j_{O^1D} filter radiometer calibration factors to a SZA of $\sim 35^o$, means the measured j_{O^1D} will be underweighted at SZA's $\geq 35^o$, and will be marginally overweighted for SZA's $\leq 35^o$. Figure 6.3 compares both the absolute values and the ratio of TUV modelled to filter radiometer measured j_{O^1D} and j_{NO_2} as a function of time of day (equivalent to SZA). The ratio points have been colourscaled by altitude to distinguish the trend by altitude.

There is again a consistent trend in both the ratio for j_{O^1D} and j_{NO_2}, which suggests that the photolysis rates are enhanced with respect to "clear sky" at low solar zenith angles and attenuated with respect to "clear sky" at high solar zenith angles. The common trend is believed to be real, since there is no strong solar zenith angle dependence in j_{NO_2} except owing to cloud and aerosol e.g. Dickerson *et al.* (1997). However, the enhancement of measured j_{O^1D} above 4 km will be accentuated by the weighting of the calibration factor by ozone column density, while below 4 km the trend of attenuation of measured j_{O^1D} will be reduced (for low SZA's) compared to reality. For an ozone column density of $\sim$290 DU, an altitude range of 4-6 km and SZA$\leq 35^o$ the correction for temperature is of the order 0.85, while the correction for ozone column and SZA is estimated as $\sim$0.75, combining these gives a scaling of $\sim$0.64 which is very close to the median values of $j_{O^1D,TUV}/j_{O^1D,Meas.}$ above 4 km altitude which are $\sim$0.7. Considering the dispersion in the ratio $j_{O^1D,TUV}/j_{O^1D,Meas.}$ by SZA, the discussed weighting of the calibration factors for j_{O^1D} would reduce the level of dispersion by scaling up the measured j_{O^1D} at SZA's $\geq 35^o$, and marginally scaling down the measured j_{O^1D} at SZA's $\leq 35^o$. The attenuation of both j_{O^1D} and j_{NO_2} at low altitude and high SZA's has a common source, i.e. boundary layer cloud and enhanced aerosol load, and therefore this feature is believed to be a real signature of the impact of the monsoon on photolysis rates, and is likely to modify photochemistry within the boundary layer and free troposphere above. The weighting of the calibration factors for

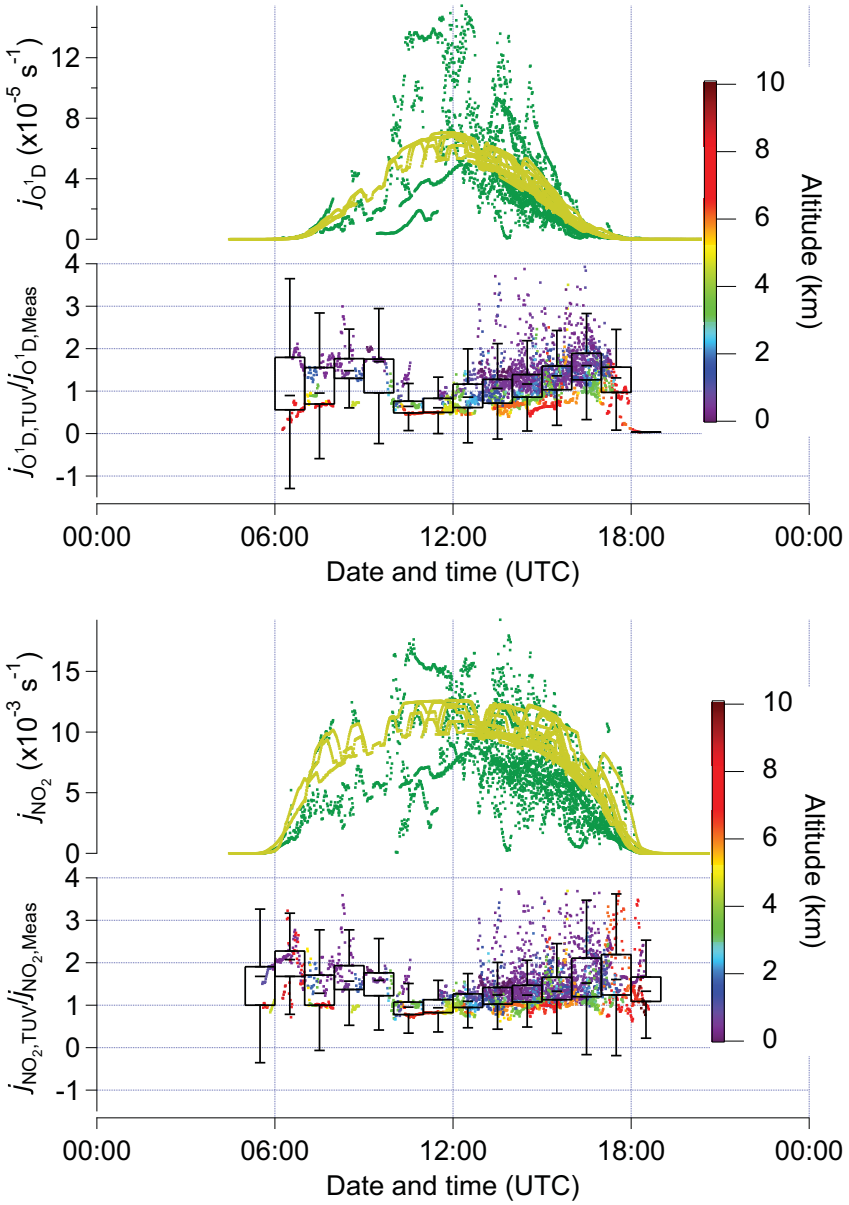

Figure 6.3: Comparison of modelled and measured photolysis rates as a function of time – (Top graph, top plot) Measured (Green dots) and modelled (Yellow dots) j_{O^1D} data by time of day; (Top graph, bottom plot) Ratio of modelled to measured j_{O^1D} by time of day, colourscaled by altitude; (Bottom graph, top plot) Measured (Green dots) and modelled (Yellow dots) j_{NO_2} data by time of day; (Bottom graph, bottom plot) Ratio of modelled to measured j_{NO_2} by time of day, colourscaled by altitude. Box centre represents median, box edges Q25 and Q75 and whiskers lower and upper inner fences

the filter radiometer measurements of j_{O^1D} would bring the ratio $j_{O^1D,TUV}/j_{O^1D,Meas.}$ much closer to 1:1 outside the boundary layer.

Figure 6.4 presents meridional profiles of flight tracks where (Top left and right) the colourscale represent the magnitude of the ratio $j_{X,TUV}/j_{X,Meas.}$ ($j_{O^1D,Meas.}$ without weighting for temperature, ozone column or SZA). Also plotted (Bottom left) is a meridional profile identifying those locations where the lower position j_{O^1D} radiometer signal has been estimated, and (Bottom right) a meridional profile with the colourscale indicating the SZA. The SZA plot identifies those points where the measurement may be expected to vary significantly compared to the clear sky model as a result of attenuation of the actinic flux at large SZA's, associated with increased cloud and aerosol along the line of sight as the sun approaches the horizon. Further differences may be expected for j_{O^1D} owing to the SZA dependence of the calibration function, discussed above. Overplotted on each meridional distribution of $j_{X,TUV}/j_{X,Meas.}$ are the contours (black traces) of constant potential temperature (from the 12:00-18:00 period, see Chapter 5, Section 5.2.3, Figure 5.19) indicating the daytime monsoon structure.

The meridional distributions $j_{X,TUV}/j_{X,Meas.}$ are similar for j_{O^1D} and j_{NO_2} as may be expected from the similar altitude trend. It is evident that the ratio is high (i.e. TUV enhanced with respect to the measurements) within the region associated with the daytime convective boundary layer (CBL) with the depth of the region of enhancement of the ratio increasing to the north, consistent with the depth of the CBL (see Section 5.2.3, Chapter 5). This supports the conclusion that at lower altitudes cloud and aerosol aloft are attenuating the actinic flux compared to the clear sky model and therefore reducing the measured photolysis rates. Decreases in the ratio common to both j_{O^1D} and j_{NO_2} occur in the south in air masses that have been associated with biomass burning, while common increases occur in the coastal city plumes (see Section 5.2.5, Chapter 5). These changes suggest that in these air masses the actinic flux may be enhanced or attenuated relative to the clear sky model, possibly

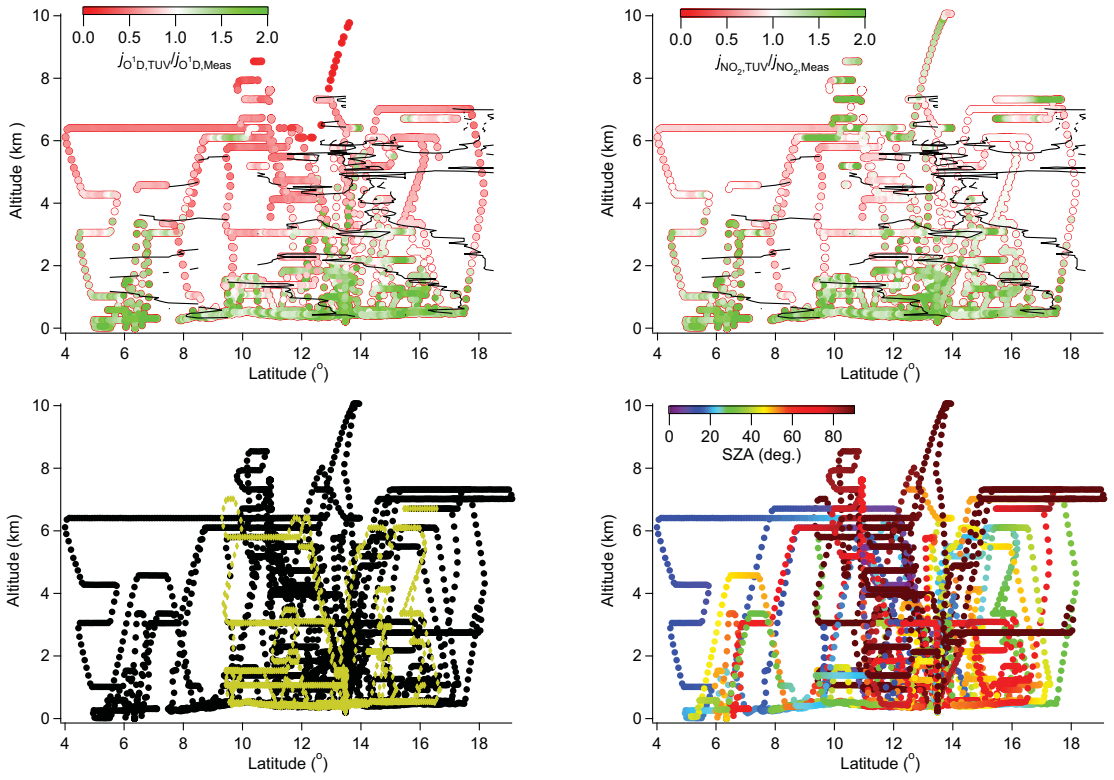

Figure 6.4: Meridional profile of the ratio of TUV modelled to filter radiometer measured photolysis rates – (Top left) Meridional profile for $j_{O^1D,TUV}/j_{O^1D,Meas.}$; (Top right) Meridional profile for $j_{NO_2,TUV}/j_{NO_2,Meas.}$; (Bottom left) Meridional profile indicating points with (black circles) and without (yellow diamonds) estimated upwelling j_{O^1D}; (Bottom right) Meridional profile colourscaled by solar zenith angle

related to an enhanced aerosol load which is reasonable within heavily polluted air masses. On some occasions, distinguished by a combination of high altitudes and large solar zenith angles, while the ratio $j_{X,TUV}/j_{X,Meas.}$ is significantly reduced for j_{O^1D} (i.e. the measurements enhanced with respect to TUV) it is significantly enhanced for j_{NO_2} (i.e. TUV enhanced with respect to the measurements). This may be a result of the opposing relationship of j_{O^1D} and j_{NO_2} to the relative amounts of direct and diffuse radiation, whereby a reduction in direct sunlight reduces j_{NO_2} more significantly than j_{O^1D} owing to the greater component of diffuse sunlight contributing to j_{O^1D}. The measured data at high SZA's is less certain particularly for j_{O^1D} where the upwelling component is estimated (as it is in these cases). No significant differences in the overall trend is distinguishable for those points where j_{O^1D} is estimated otherwise, and since these points represent those where the photolysis rates are significantly diminished, any large relative error is likely insignificant on an absolute basis in terms of the impact on photochemistry.

6.2 Comparison of peroxy radical measurements to a photochemical box model

The concentration of the sum of peroxy radicals [RO_x] (=[OH]+[HO_2]+Σ_i[R_iO_2]) was measured through the PERCA technique using the University of Leicester PERCA 4 instrument during the AMMA SOP2 field campaign. The background to the technique and the characterisation and calibration of the instrument have been described in Chapters 2 and 3 respectively. Measurements of peroxy radicals using the PERCA technique are known to have varying sensitivity owing to variation in the chain length, dependent on the radical composition and conditions within the sample inlet. Owing to their typically short lifetime with respect to transport, the concentration of peroxy radicals is controlled by *in-situ* chemistry and depends largely on the concentrations of precursors and the rates of production and loss. A detailed, observationally constrained box model is therefore an ideal

comparator for measurements of peroxy radicals because it can take into account the known dependencies of the radical concentration and composition while not requiring knowledge of the transport of precursors. Understanding the primary causes for variation in the sensitivity of the PERCA technique it is possible to attempt to reconcile any differences between modelled and measured concentrations. Further, by identifying any remaining differences and the conditions under which they occur, an explanation can be sought either in terms of a deficiency in understanding of the measurement technique or missing chemistry in the model. Of course, the differences between model and measurement that can be rationalised through an understanding of the measurement technique, measurement platform, and measurement environment point to further experimental work required to validate these conclusions and develop the technique. With this aim the University of Leicester PERCA measurements from the AMMA SOP2 field campaign are compared to box model results derived from the Dynamically Simple Model of Atmospheric Chemical Complexity (DSMACC), a model developed and run at the University of Leeds. The model has been run and the output data supplied by D. Stone at the School of Chemistry and Earth and Environment, University of Leeds. DSMACC is a zero-dimensional box model written in FORTRAN, with the chemistry scheme written using the Kinetics PreProcessor (KPP) (Sandu & Sander, 2006). The chemistry scheme used in this study is the Master Chemical Mechanism (MCM) model (v3.1), which has recently been described in Emmerson & Evans (2009), where it was applied as the benchmark for comparison to a number of "small and "reduced" gas-phase schemes currently employed in composition transport models. The MCM specification is summarised here in Table 6.1 based on the description in Emmerson & Evans (2009) and that of (D. Stone, private communication); the constraints on individual models runs used in this comparison are described in Table 6.2.

The model is initialised by the observed concentrations from measurements (the constraints in Table 6.2), these constraining concentrations (except NO_x) are held constant while the model is run

No. of reactions	No. of species	Model chemistry included
13500	5600	135 VOCs including 22 alkanes $\leq C_{12}$, 16 alkenes $\leq C_6$, 6 aldehydes, 18 aromatics, isoprene, α and β-pinene

Table 6.1: Specification of the Master Chemical Mechanism (MCM)

Model run	Constraints
090620-a	VOCs from PTR-MS where available, GC-FID where not and parameterised from linear relationship with CO where neither measurement is available; measured O_3, CO, H_2O; TUV modelled j_{O^1D}, j_{NO_2}; NO_x^{tot} conserved, constrained by measured NO from NOxy instrument
090706-a	VOCs from PTR-MS where available, GC-FID where not and parameterised from linear relationship with CO where neither measurement is available; measured O_3, CO, H_2O, j_{O^1D}, j_{NO_2} where available; NO_x^{tot} conserved, constrained by measured NO from NOxy instrument

Table 6.2: Description of constraints on DSMACC model runs used for comparison to the University of Leicester PERCA AMMA SOP2 dataset

forward until a diurnal steady state is reached. The output from the model is extracted using the values determined once the model is in diurnal steady state, with the output for a given simulation being taken at the equivalent time of day as the observations were made. In this way, to run the box model along a flight track involves many individual and independent model runs, as each measurement point corresponds to an individual constraining point. NO_x is constrained differently; NO or NO_2 are allowed to vary within a diurnal, while total short lived NO_x, i.e. NO_x^{tot} (NO_x^{tot}=[NO]+[NO_2]+[NO_3]+2[N_2O_5]+[HONO]+ [HO_2NO_2]), is conserved for each diurnal cycle. NO_x^{tot} is calculated such that the modelled NO or NO_2 equal the measured value at the time of day the observations were made.

The spatial and temporal coverage of the model output is restricted by the crossover in coverage of the measurement data used to constrain the model. The number of points available for comparison to the PERCA measurements are then dictated by the crossover between the constraining data and the

PERCA measurements. The primary limitations associated with the constraining data are associated with the availability of reliable NO_x and photolysis rate measurements. NO_x measurements from the FAAM TECO instrument provided excellent coverage but proved unreliable (discussed in Section 5.2.5 of Chapter 5) meaning the model has been constrained by the NO data from the UEA NOxy instrument. This measurement only became available on the last 10 flights of the campaign (B226-B235). For the 090706-a model run, the box model has been constrained using the filter radiometer measurements of j_{O^1D} and j_{NO_2}. These measurements provided good coverage (see Chapter 5, Section 5.2.1), however the failure of the lower position j_{O^1D} filter radiometer from flight B221A onwards means this component of the total j_{O^1D} signal has been estimated (see Chapter 4, Sections 4.3 and 4.3.1). The estimate was not applied where any of the measurements reached the detection limit, meaning a total j_{O^1D} measurement cannot be derived for low signal levels and for this reason there are no nighttime model output from the 090706-a model run. The box model can be constrained with photolysis rates provided by the TUV model, so rather than arbitrarily assigning the photolysis rate measurements a zero value to overcome the lack of a measurement, an additional model run (090620-a) was constrained using TUV. The 090620-a run is therefore used for comparison to periods where the solar zenith angle has exceeded 90°. The DSMACC model has been compared to the established NASA model (described by e.g. Crawford *et al.* (1999), Olson *et al.* (2004, 2006), Ren *et al.* (2008)) for a large HO_x dataset from the INTEX-A campaign (D. Stone, private communication). The models were in good agreement with respect to one another, which provides confidence in their relative skill, however, both failed to capture the observed concentrations of OH although agreement with observed HO_2 was significantly better. The conclusions were that both models may be missing sources and sinks of HO_x, and owing to the relatively high reactivity of OH, both measurements and modelling of OH are subject to greater uncertainty.

The two model runs produced two separate datasets, that were combined into a single model dataset

for comparison to the PERCA measurements. A SZA criterion has been used to combine the data, so if data from the fully constrained model run (090706-a) were available and the SZA was <90° these data were selected. Otherwise, if the SZA was ≥90° and data from the TUV constrained model run (090620-a) were available, these data were selected. In advance of attempting to interpret the comparison of modelled and measured peroxy radicals, it is worth summarising the potential biases that may impact the comparison. There are a number of known potential biases affecting PERCA measurements that have been considered in this thesis:

- Humidity dependence of the chain length – See Section 3.2.3 of Chapter 3.
- Altitude dependence of the chain length – See Section 3.2.2 of Chapter 3.
- HO_2 yield from reaction of R_iO_2 with NO – See Section 2.1.1 of Chapter 2.
- Sampling losses – See Section 2.1.1 of Chapter 2.

The humidity dependence of the chain length of the PERCA 4 aircraft and ground inlets have been investigated through an experimental and analytical study presented in this thesis (see Section 3.2.3 of Chapter 3). The chain length was found to vary exponentially with relative humidity in the experiments, consistent with the analytical solution for the time dependence of the chain length (Equation 3.58). Mihele *et al.* (1999) reported the humidity dependence of the chain length to be largely dependent on wall losses which are increased for HO_2 as a function of humidity, though not for the organic peroxy radicals CH_3O_2 and $C_2H_5O_2$. Recent evidence has been found (Butkovskaya *et al.*, 2009) for the gas phase interference to the chain chemistry proposed by Mihele *et al.* (1999), Reichert *et al.* (2003).

The altitude dependence of the chain length has been considered in terms of the temperature and pressure dependencies of the gas phase reactions, using a numerical model and an inlet chemistry reaction mechanism (see Section 3.2.2 of Chapter 3). The results of the chain length modelling by

altitude (temperature and pressure) were consistent with previous inflight determinations of the chain length (Green *et al.*, 2003) in terms of the trend by altitude. Direct comparison of the model results to the results of Green *et al.* (2003) suggests the decrease in the chain length by altitude may be positively offset by improved reagent mixing within the inlets when in flight.

To detect organic peroxy radicals through PERCA, they need to be efficiently converted to HO_2 to undergo chain amplification and therefore produce a measurable response. The structural dependence of the yield of HO_2 from organic peroxy radicals was considered qualitatively in Section 2.1.1 of Chapter 2 in terms of the gas phase chemistry and heterogeneous wall loss. Similar yields by species have been predicted (Cantrell, 1993, Ashbourn *et al.*, 1998), however the gas phase losses have been found to be overstated in simple calculations of the HO_2 yield, thought owing to inefficient mixing of reagent NO (Ashbourn *et al.*, 1998). Wall loss was reportedly the largest factor determining the HO_2 yield and therefore chain length in the experimental study of Ashbourn *et al.* (1998). Further, the wall loss rate for HO_2 was found to reduce the chain length for HO_2 to such an extent that the organic peroxy radicals were measured with greater sensitivity.

Considering the DSMACC model, a number of factors can be proposed that would lead to uncertainty in the output:

- Underlying chemistry scheme.
- Accuracy of rate coefficients.
- Missing sources/sinks.
- Biases in constraining data.
- Parameterisation of missing constraining data.
- Steady state assumption.

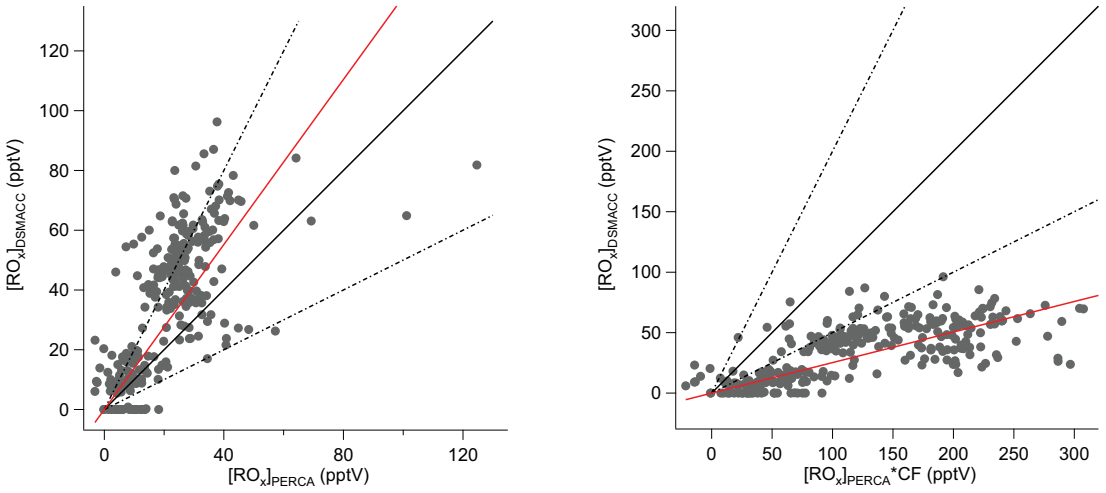

Figure 6.5: Modelled versus measured RO_x – (Red) Line of best fit, (Black dashed lines) 2:1 and 1:2 level of agreement, (Black full line) 1:1 level of agreement: (Left graph) Model versus PERCA measured RO_x without humidity correction applied; (Right graph) Model versus PERCA measured RO_x with humidity correction applied.

As discussed, a potential bias of the order 30% is thought to be present in the daytime measured j_{O^1D} data owing to the non-linearity of the calibration factors for j_{O^1D} measured by filter radiometry (see Section 6.1), which is likely to have a significant affect on modelled daytime photochemistry and the radical budget through its impact on the primary production of OH. Having identified this potential bias in the measured j_{O^1D} used to constrain the model, it is suggested that a sensitivity study should be performed, where a reduction of the measured j_{O^1D} photolysis rates could be assessed in terms of whether it improves model to measurement agreement. Other model biases are largely beyond the scope of this discussion.

Figure 6.5 presents correlation plots of the DSMACC modelled total RO_x (=[OH]+[HO_2]+Σ_i[R_iO_2]) versus the PERCA measured RO_x signal, both without and with the chain length humidity correction applied. Without humidity correction a linear regression to model versus PERCA measurement, constrained such the fit passes through the origin gives [$RO_{x,DSMACC}$] = 1.38(±0.04)[$RO_{x,PERCA}$], with a correlation coefficient of r=0.64. With the humidity correction factor (CF) applied to the PERCA measurement a linear fit gives [$RO_{x,DSMACC}$] = 0.25(±0.01)[$RO_{x,PERCA}$]*CF, with a corre-

lation coefficient of r=0.66. Considering these first comparisons, the level of correlation as indicated by the fit coefficients is reasonable which suggests variability between model and measurement is in reasonable agreement. The model concentrations are greater when compared to the PERCA measurements without humidity correction, however with the correction applied the measured values become significantly greater than the model. Also noted are a significant number of points where the model predicts essentially zero total RO_x, while a range of the order 0–20 pptV (values without humidity correction) was measured - these represent nighttime measurements, some from flight B233 (pre-dawn on the 15 August 2006) but primarily from flight B235B (on the evening of 17 August 2006) which was the final flight.

The concentration levels supposedly measured with the humidity correction applied do not seem realistic (a RO_x concentration of 300 pptV is not something observed before for the atmosphere), while those without are more realistic but the scaling suggests some bias which may be related to either model or measurement as described above. If there were a significant humidity dependence contributing to the model to measurement bias (where the humidity correction has not been applied to the measurement), the model to measurement ratio would be expected to relate to the level of relative humidity, owing to the strong dependence of the PERCA chain length on relative humidity, and the high level of humidity encountered throughout the campaign. As derived in Chapter 3 the ratio of wet to dry PERCA chain length is equal to the ratio of the uncorrected PERCA measurement to the humidity corrected measurement. Similarly, the ratio of the uncorrected measurement to the model could be used as an indication of the ratio of the wet to dry PERCA chain length, if the model is assumed to be an unbiased representation of the true concentration measured.

Figure 6.6 presents the ratio of PERCA measured RO_x (without humidity correction applied) to modelled total RO_x as a function of RH; also plotted is the ratio of the wet to dry PERCA chain length as a function of RH for comparison. The ratio of wet to dry chain lengths is in the range 0–1

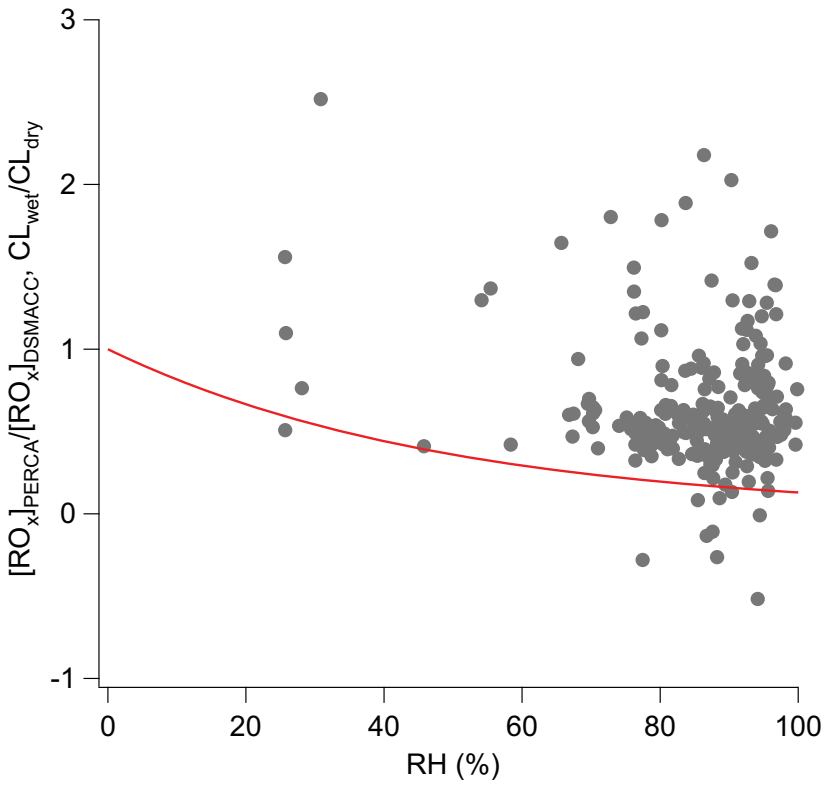

Figure 6.6: Measured to modelled total RO_x ratio as a function of RH compared to the ratio of wet to dry chain length (the reciprocal of Equation 3.43) – (Red) Ratio of wet to dry chain length as a function of RH, (Dark grey) Ratio of PERCA measured RO_x (without humidity correction applied) to modelled total RO_x as a function of RH.

(1 being the maximum by definition, at RH = 0%, CL_{wet}=CL_{dry}), however the ratio of measurement to modelled total RO_x varies over a much greater scale. The y-scale in Figure 6.6 has been restricted to the range -1–3 to show the majority of points on a scale whereby the dominant trends are visible. The negative values represent measured data at the detection limit; those points where the ratio becomes many orders of magnitude greater than 3 (and therefore are outside the displayed range) are the nighttime measurements where the model predicts very low concentrations, while concentrations similar to daytime levels were observed so the ratio can tend to infinity.

The range in relative humidity is restricted (i.e. persistently high) so it is not possible to completely rule out a trend in the ratio of measured to modelled RO_x with relative humidity, since the humidity dependence becomes relatively flat as a function of RH near saturation. Still, a fit restricted to those

points within the graphed range (which avoids skewing the fit by the nighttime points) exhibits very little correlation (correlation coefficient of r=-0.01). Also, the magnitude of the measured to modelled RO_x ratio (comparing the daytime values) is typically 4-5 times greater than the CL_{wet}/CL_{dry} ratio at humidities $\geq$60%. All evidence points to little if any bias in the measurements related to humidity, which is highly significant considering the widely reported dependence of the PERCA chain length on relative humidity which has been confirmed in the laboratory for this instrument, in this work (see Section 3.2.3 of Chapter 3). The disparity suggests several possibilities:

- An altitude (pressure or temperature) dependence to the humidity dependence mechanism which makes it less important at altitude.
- The levels of relative humidity reported are potentially in error.
- A fundamental difference between the laboratory calibration situation where the humidity dependence was characterised and the conditions in the field.

It may be that there is a pressure dependence to the humidity dependence mechanism, however the lack of a clear trend whatsoever between the measured to modelled RO_x ratio and RH does not support this as an explanation. The humidity dependence of the PERCA chain chemistry has been determined to be constant as a function of RH in a number of studies e.g. Reichert *et al.* (2003) and the corroboration of the work of Salisbury (2001), Salisbury *et al.* (2002) by the work presented in this thesis (see Section 3.2.3 of Chapter 3), meaning that no temperature dependence is expected over a limited range ($\sim$10-50 ^{o}C, this work and Salisbury (2001), Salisbury *et al.* (2002)).

The most significant differences between the laboratory calibration situation and the conditions in the field are related to the sampling situation, and potentially an invalid assumption that the relative humidity in the sampled airflow is the same as ambient. The observed values of relative humidity follow consistent trends throughout the campaign; high relative humidities at the surface and instability to

convection mixes humid air upwards, and owing to the decrease in temperature by altitude the air is persistently near saturation. Examining timeseries of altitude, temperature, dewpoint temperature and relative humidity, the relationships between these parameters are consistent; the temperature falls with altitude and where the temperature reaches dewpoint, the relative humidity saturates, so the ambient humidity data are not thought to be in error. However, on many occasions relative humidities of greater than 100% are reported, i.e. the air is supersaturated, occurring at temperatures both above and below freezing; these conditions are outside the range of conditions explored in the laboratory. Supersaturation occurs because the equilibrium vapour pressure for a curved surface (such as a cloud water drop) at any temperature is greater than the saturation vapour pressure over a plane surface, while spherical drop formation is energetically favoured on condensation since it represents the shape of minimum surface energy (Wayne, 2000). The difference in vapour pressure is greater the smaller the water drop, so by definition the atmosphere must then be supersaturated with respect to the saturation vapour pressure over a plane surface for spontaneous condensation to occur. However, for a water drop to condense spontaneously (i.e. not onto a surface) and not immediately evaporate requires a sufficient number of water molecules to aggregate that a critical droplet radius is exceeded, the probability for spontaneous condensation is therefore low. Supersaturation then represents a balance between thermodynamic instability with respect to the liquid phase, and stability with respect to spontaneous condensation. Surfaces (such as cloud condensation nuclei) allow condensation to form without supersaturation, so in a highly saturated environment such as that encountered during AMMA, condensation onto the aircraft skin and sampling inlets to all instruments is expected.

To reduce the susceptibility of the University of Leicester PERCA instruments to humidity, the inlets are designed to be thermostated above ambient temperature; in effect to reduce the relative humidity by increasing the sample airflow temperature. However, the inlet temperature control currently fails inflight when operating the PERCA 4 on board the BAe-146, and therefore the sampled airflow has

been assumed to be at ambient temperature and relative humidity (in calculation of the humidity correction). Owing to the design of the inlets (low thermal mass) they are likely to be in thermal equilibrium with the surroundings (ambient air, aircraft hull and aircraft cabin) with a temperature gradient set up from the nose of the inlets (in contact with the ambient air) to the rear (in contact with the cabin). Having recognised the issue with inlet heating following the AMMA campaign, a supplementary measurement of inlet temperature was taken during test flying for the last aircraft deployment of the PERCA 4 instrument in the OP3 field campaign. A thermocouple attached directly to the sample port of one of the inlets (refer to Figure 3.5, on page 57) provided a measurement of the inlet temperature at the rear of the inlet, through a handheld digital thermometer readout. The indications from this limited assessment are that the temperature at the rear of the inlet does indeed respond to the outside air temperature and the cabin temperature within the aircraft. The inlet temperatures measured were intermediate between the cabin and outside air temperature and fell in response to falling temperature with altitude, consistent with a temperature gradient between the nose and rear of the inlet.

The PERCA 4 inlets are mounted sampling perpendicular to the direction of flight and sample at a constant mass flow rate of 2 slpm. From consideration of the inlet dimensions and typical flow speed, Reynolds numbers of the order 200 are calculated at all altitudes sampled, for the conventional sample flow rate of 2 slpm, indicating laminar flow within the inlet. At a given volume flow rate (which depends on the temperature and pressure), and under the assumption of plug flow, the flow speed through the inlet (of the order 0.2 ms^{-1}) is many times less than the air speed (of the order hundreds of ms^{-1}) past the inlet, and therefore the trajectory of air sampled (sampling speed diverts the air sampled by less than an arc minute from the direction of travel) intercepts the rear edge of the very tip of the inlet. The inlet tip and the surrounding housing then represent the coldest point in direct contact with the ambient air, the most turbulent region of the sample flow, and the

region where the most strong interactions between the sample air and inlet surface. It could be that condensation/sublimation occurs at this cold point meaning the humidity sampled is reduced, so within the inlet where chain chemistry is promoted the reduced humidity has minimal impact on the chain length. HO_2 wall loss is known to be enhanced with humidity (Mihele *et al.*, 1999) and therefore condensed water at the nose of the inlet will potentially lead to significant sampling losses of HO_2. Considerable sampling losses of HO_2 have been observed (though for different inlets) with the precursor to the current University of Leicester instrument, with 100% loss of HO_2 under condensing conditions, while losses of CH_3O_2 were minimal (Green *et al.*, 2003). The loss of HO_2 would also offer some explanation of the trend observed in comparison of the FAGE HO_2 measurement to the PERCA RO_x measurement, as discussed in Section 5.2.2 of the previous chapter. The near parity of the FAGE measured HO_2 with the PERCA RO_x in the middle of the day suggesting near equal partitioning of HO_x and RO_2, while at night where the PERCA RO_x measurement is significantly greater indicates a significant concentration of organic peroxy radicals develops/remains at night. Considering the ambient temperature measurements made from the BAe-146 during AMMA, freezing point was reached at an altitude in the region of 4-4.5 km, if frost or ice built up in the inlet tip this may also provide an explanation for the reduction in sample flow above this altitude (see Section 5.2.1, page 199, of the last Chapter). This reasoning is mirrored in the discussion of Ryerson *et al.* (1999), Neuman *et al.* (1999) regarding the characterisation of an aircraft inlet for the measurement of NO_y. That system also employed an unheated inlet which sampled perpendicular to the direction of flight and consideration was given to the efficiency of transmission of NO_y components for various inlet materials and temperature and humidity levels.

Considering the potential sampling losses of HO_2 anticipated, and the lack of an observed dependence of the measurement on ambient humidity, it is reasonable to predict the PERCA 4 measurement of RO_x on the BAe-146 to be predominantly sensitive to the organic peroxy radical composition, and

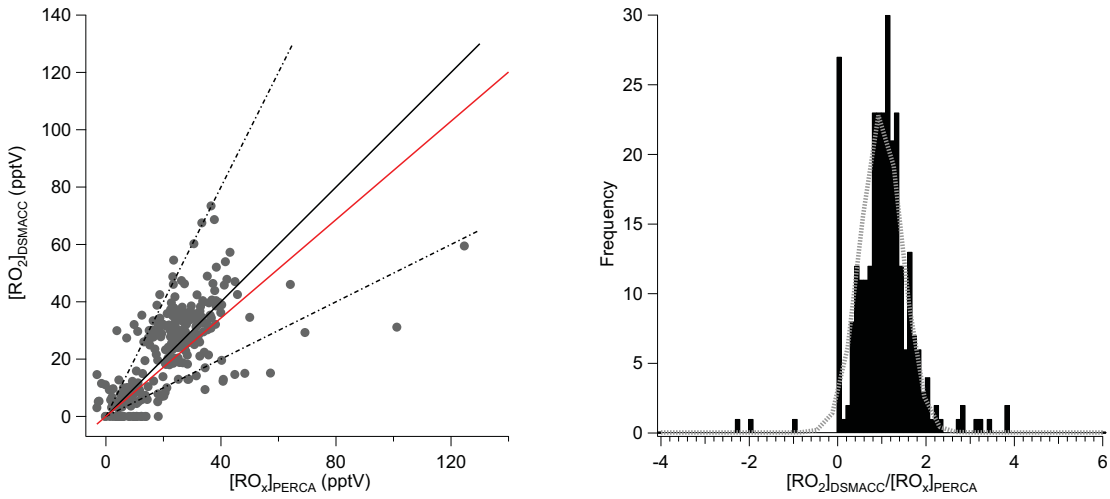

Figure 6.7: (Left graph) – (Grey circles) Modelled $\sum_i \mathrm{R}_i\mathrm{O}_2$ versus PERCA measured RO_x without humidity correction applied, (Red) Line of best fit, (Black dashed lines) 2:1 and 1:2 level of agreement, (Black full line) 1:1 level of agreement. (Right graph) – (Black bars) Histogram of the ratio $[\mathrm{RO}_2]_{DSMACC}/[\mathrm{RO}_x]_{PERCA}$ and overplotted (Dashed grey line) gaussian fit

therefore to correlate with the modelled sum of organic peroxy radicals (define $[\mathrm{RO}_2] = \sum_i [\mathrm{R}_i\mathrm{O}_2]$). A correlation plot of modelled RO_2 versus measured RO_x without humidity correction is given in Figure 6.7. A linear regression to the data, constrained such that the fit passes through the origin gives $[\mathrm{RO}_{2,DSMACC}] = 0.86(\pm 0.03)[\mathrm{RO}_{x,PERCA}]$, with a correlation coefficient of r=0.60. Although the correlation coefficient and gradient of the fit is not one, the fit is clearly skewed owing to the outliers in the data where differences remain between the model and measurement. The majority of data lies close to the 1:1 level of agreement, and this is demonstrated through a histogram of the ratio $[\mathrm{RO}_2]_{DSMACC}/[\mathrm{RO}_x]_{PERCA}$ shown also in Figure 6.7. Clearly a significant number of points also lie at or close to zero, where the model predicts very low concentrations at night while significant concentrations were measured. Also there is some marginal asymmetry to the distribution representing the remaining biases between the model and measurement; a gaussian fit to the ratio puts the mean at 0.99±0.01.

Considering Equation 2.20 (reproduced here as Equation 6.1) and the discussion of Section 2.1.1, Chapter 2 regarding the PERCA technique, the implication of the results thus far is that the effective

chain length for HO_2 is limited owing to heterogeneous losses on sampling. Further, the transmission and relative sensitivity to organic peroxy radicals must be relatively well approximated by the chain length for methyl peroxy ($CL_{ref.} = CL_{CH_3O_2}$) which weights the response, or methyl peroxy dominates the organic peroxy radical composition to such an extent that differences in sensitivity to other organic peroxy radicals are masked.

$$[RO_x]_{calc.} = \frac{CL_{OH}}{CL_{ref.}}[OH] + \frac{CL_{HO_2}}{CL_{ref.}}[HO_2] + \sum_i \frac{CL_{R_iO_2}}{CL_{ref.}}[R_iO_2] \tag{6.1}$$

Hence:

$$[RO_x]_{calc.} \sim \sum_i [R_iO_2] \tag{6.2}$$

Having accounted for the potential measurement bias related to humidity and heterogeneous loss of HO_2, consideration must be given to the expected altitude dependence of the chain length (assessed in Section 3.2.2 of Chapter 3). A working assumption is that the transmission and relative sensitivity to organic peroxy radicals is well approximated by the chain length for methyl peroxy, or methyl peroxy dominates the organic peroxy radical composition to such an extent that differences in sensitivity to other organic peroxy radicals are masked. The ratio $\frac{[RO_{2,DSMACC}]}{[RO_{x,PERCA}]}$ should then exhibit an equivalent altitude dependence as the chain length for methyl peroxy ($\frac{CL_{CH_3O_2,0m}}{CL_{CH_3O_2,Zm}}$), assuming the measurement is biased by altitude owing to the change in chain length, while the model is an unbiased estimate. $CL_{CH_3O_2,0m}$ represents the chain length at 0 m altitude (ground level, STP), and $CL_{CH_3O_2,Zm}$ represents the chain length at Z m altitude. As seen in Chapter 3, the chain length is expected to decrease with altitude, although this can be positively offset by improved reagent mixing. Figure 6.8 compares the ratio $\frac{[RO_{2,DSMACC}]}{[RO_{x,PERCA}]}$ to the altitude dependence of the chain length for methyl peroxy. If the measurement is biased as a function of altitude in the same way that the modelled CH_3O_2 chain length varies with temperature and pressure, while the DSMACC box model RO_2 is unbiased, the ratio $\frac{[RO_{2,DSMACC}]}{[RO_{x,PERCA}]} / \frac{CL_{CH_3O_2,0m}}{CL_{CH_3O_2,Zm}}$ should equal one. Figure 6.8 also presents a histogram determined from this ratio as a representation of the altitude bias "corrected" distribution, with the

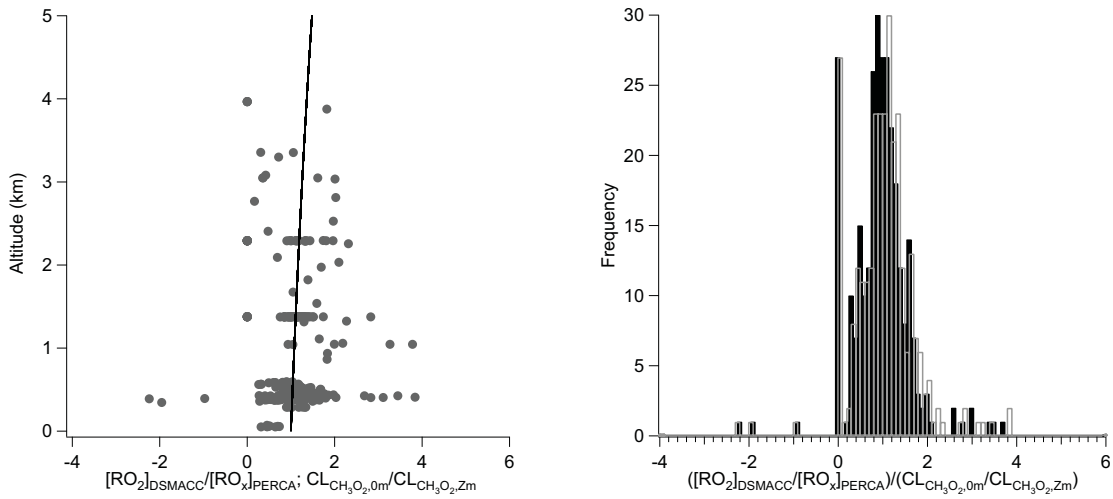

Figure 6.8: (Left graph) – (Grey circles) Ratio $\frac{[RO_{2,DSMACC}]}{[RO_{x,PERCA}]}$ compared to (Black line) relative change in CH_3O_2 chain length as a function of altitude. (Right graph) – (Black filled bars) Histogram of the ratio $(\frac{[RO_{2,DSMACC}]}{[RO_{x,PERCA}]}/\frac{CL_{CH_3O_2,0m}}{CL_{CH_3O_2,Zm}})$ and overplotted (Grey open bars) Histogram of the ratio $\frac{[RO_{2,DSMACC}]}{[RO_{x,PERCA}]}$

original distribution overplotted for comparison.

The ratio $\frac{[RO_{2,DSMACC}]}{[RO_{x,PERCA}]}$ does appear to exhibit a similar altitude dependence as the chain length for methyl peroxy, although a number of outliers exist. Also, there is no evidence for an offset in the response between measurement and model by altitude, indicating that the chain length determined under laboratory conditions subsequent to AMMA is applicable and reagent mixing is comparatively efficient on the ground with inflight. The histogram appears to be marginally more symmetrical, although owing to the limited dataset and the wide ranging conditions covered a fit to the distribution is skewed by the outliers. The altitude dependence of the chain length is of course appropriate to methyl peroxy so it is only strictly relevant where methyl peroxy dominates the composition, unless the chain lengths for other organic peroxy radicals exhibit similar altitude dependencies. That is:

$$[\mathrm{RO}_{2,DSMACC}] \simeq [\mathrm{RO}_{x,PERCA}]\frac{CL_{CH_3O_2,0m}}{CL_{CH_3O_2,Zm}} \tag{6.3}$$

when $[\mathrm{RO}_2]\sim[\mathrm{CH}_3\mathrm{O}_2]$, or if $CL_{R_iO_2}(Z)\sim CL_{CH_3O_2}(Z)$. Of course, this condition will not be completely fulfilled so further differences may be investigated related to changes in the radical composition.

Indeed, the variability in the altitude trend is greatest at the lowest altitudes where the influence of biogenic emissions is strongest (refer to Section 5.2.4 of the last chapter), and the radical composition will be more complex.

6.3 Radicals and composition

The comparison of the PERCA measurements of peroxy radicals to the DSMACC box model correlates best under the assumptions of a negligible humidity dependence to the chain length, complete losses of HO_2 on sampling, and either that organic peroxy radicals are measured with near equal efficiency, or methyl peroxy dominates the organic peroxy radical composition to such an extent that differences in sensitivity to other organic peroxy radicals are masked. The level of agreement between model and measurement is therefore likely to depend on the validity of $[RO_2] \sim [CH_3O_2]$, or if $CL_{R_iO_2}(Z) \sim CL_{CH_3O_2}(Z)$. That is, the level of model to measurement agreement should also be tested in line with an assessment of the radical composition. In turn the rate of loss of peroxy radicals determines their lifetime with respect to transport and whether their concentration can be accurately represented by steady state, which will dictate the validity of the box model approach. The processes dictating the production and loss of radicals is also key to understanding the processes controlling the oxidative capacity within the WAM region, and the potential for ozone production and loss.

In steady state, the rates of radical production and loss are assumed to be in balance:

$$\frac{d[\mathrm{RO}_x]}{dt} = P_{RO_x} - L_{SR} - L_{NO_2} \tag{6.4}$$

$$\frac{d[\mathrm{RO}_x]}{dt} = 0 \tag{6.5}$$

L_{SR} represents the rate of radical loss through self- and cross-reaction, L_{NO_2} is the rate of loss through reaction with NO_x, and P_{RO_x} is the rate of radical production. Mihele & Hastie (2003) extended the analytical approach of Penkett *et al.* (1997) (which describes the steady state peroxy

radical concentration under clean marine background and background free tropospheric conditions), to allow an assessment of the dominant production and loss routes controlling the concentration of peroxy radicals at a remote forested site. An expression was derived for the steady state:

$$\frac{d[\mathrm{RO}_x]}{dt} = 2fj_{O^1D}[\mathrm{O_3}](1+\gamma) - 2k_{SR}\alpha(1+\beta)[\mathrm{RO}_x]^2 \tag{6.6}$$

This approach explicitly includes radical production through ozone photolysis in the presence of water vapour as a major source of radicals (as per Penkett *et al.* (1997)), whereby:

$$\mathrm{O_3} + h\nu \rightarrow \mathrm{O(^1D)} + \mathrm{O_2} \tag{6.7}$$

$$\mathrm{O(^1D)} + \mathrm{M} \rightarrow \mathrm{O(^3P)} + \mathrm{M} \tag{6.8}$$

$$\mathrm{O(^1D)} + \mathrm{H_2O} \rightarrow 2\mathrm{OH} \tag{6.9}$$

f represents the fraction of $\mathrm{O(^1D)}$ atoms to react with water vapour yielding two OH radicals (hence the factor 2):

$$f = \frac{k_{6.9}[\mathrm{H_2O}]}{k_{6.9}[\mathrm{H_2O}] + k_{6.8}[\mathrm{M}]} \tag{6.10}$$

γ was introduced by Mihele & Hastie (2003) to represent the fraction of additional radical production from routes besides ozone photolysis e.g. photolysis of aldehydes, PAN decomposition, alkene ozonolysis. Hence:

$$P_{RO_x} = 2fj_{O^1D}[\mathrm{O_3}](1+\gamma) \tag{6.11}$$

Gas phase losses of radicals in the troposphere occur primarily through self- and cross-reactions to form peroxides under low NO_x conditions, while reaction with NO_x dominates where the NO_x concentration exceeds a certain threshold e.g. Monks (2005), so the second term in Equation 6.6 represents the combination of these. Losses through self- and cross-reaction occur by:

$$\mathrm{HO_2} + \mathrm{HO_2} \rightarrow \mathrm{H_2O_2} + \mathrm{O_2} \tag{6.12}$$

$$\mathrm{HO_2} + \mathrm{RO_2} \rightarrow \mathrm{ROOH} + \mathrm{O_2} \tag{6.13}$$

$$\mathrm{RO_2} + \mathrm{RO_2} \rightarrow \mathrm{ROOR} + \mathrm{O_2} \tag{6.14}$$

Hence:

$$L_{SR} = 2k_{6.12}[\mathrm{HO_2}][\mathrm{HO_2}] + k_{6.13}[\mathrm{HO_2}][\mathrm{RO_2}] + 2k_{6.14}[\mathrm{RO_2}][\mathrm{RO_2}] \tag{6.15}$$

Several assumptions can be made to simplify as per Mihele & Hastie (2003), i.e. $\mathrm{k_{6.12}} \approx \mathrm{k_{6.13}} \gg \mathrm{k_{6.14}}$. The parameter $\beta = \frac{L_{NO_2}}{L_{SR}}$ is also introduced to describe the dominant loss regime, and the parameter $\alpha = \frac{[HO_2]}{[RO_x]}$ is introduced to describe the partitioning between inorganic and organic peroxy radicals. The loss of radicals through self reaction is then approximated by:

$$L_{SR} = 2k_{SR}\alpha[\mathrm{RO}_x]^2 \tag{6.16}$$

The combined loss rate is then:

$$L_{SR} + L_{NO_2} = 2k_{SR}\alpha(1+\beta)[\mathrm{RO}_x]^2 \tag{6.17}$$

As noted by Parker (2007), Parker *et al.* (2009), the assumption that $\mathrm{k_{6.12}} \approx \mathrm{k_{6.13}}$ is only valid where organic peroxy radicals are predominantly in the form of CH_3O_2. Where the radical composition is more complex, the loss rate for the cross-reaction of HO_2 with organic peroxy radicals can exceed that for HO_2 self-reaction, in particular Parker (2007), Parker *et al.* (2009) notes the cross-reaction with the acetylperoxy radical ($CH_3C(O)OO$). Also of importance is the reported enhancement of the self reaction of HO_2 with increased humidity e.g. Atkinson *et al.* (2004). Recently it has been suggested that the enhancement with humidity could be greater still and exhibit a strong negative temperature dependence such that loss of HO_2 through self-reaction increases with altitude (Stone & Rowley, 2005). An additional complication is through the recently proposed recycling of OH from isoprene oxidation, as reported by Lelieveld *et al.* (2008) and references therein. The mechanism proposed occurs through cross-reaction of HO_2 with the organic peroxy radicals that are products of OH isoprene oxidation. Theoretical efforts (Peeters *et al.*, 2009, Silva *et al.*, 2010) have identified potential recycling mechanisms for OH through the rapid unimolecular decomposition of organic peroxy radical intermediates formed in the oxidation of isoprene by OH. The implication of this recycling is that both OH and as a result peroxy radicals, may be sustained under low NO_x conditions.

Assuming steady state, Equation 6.6 can be rearranged to provide an estimate of the instantaneous total peroxy radical concentration:

$$[\mathrm{RO}_x] = \sqrt{\frac{2fj_{O^1D}[\mathrm{O_3}](1+\gamma)}{2k_{SR}\alpha(1+\beta)}} \tag{6.18}$$

$$[\mathrm{RO}_x] = \sqrt{\frac{fj_{O^1D}[\mathrm{O_3}]}{k_{SR}}}\sqrt{\frac{1}{\alpha}}\sqrt{\frac{1}{1+\beta}}\sqrt{1+\gamma} \tag{6.19}$$

The parameters α, β, γ demonstrate qualitatively how variation in the dominant production and loss routes modifies the radical concentration. On first appearances it may seem that Equation 6.19 dictates that the radical concentration must be zero in the absence of primary production ($2fj_{O^1D}[O_3] = 0$), however if the equation is expanded through $\gamma = \frac{P_{Sec.}}{P_{Pri.}}$ (where $\mathrm{P}_{Pri.}$ denotes the rate of radical production through the primary route of ozone photolysis in the presence of water vapour, and $\mathrm{P}_{Sec.}$ denotes the rate of radical production through the secondary or additional routes), then even in the absence of this route steady state may still be reached if the additional production is sufficiently fast.

6.3.1 VOC reactivity

The VOC's measured on board the BAe-146 during AMMA SOP2 have been used to calculate reactivity with respect to OH where measurements are available. The VOC's measured and references to the rate constants used in the calculation of reactivity are given in Tables 6.3 and 6.4. Those VOC's listed in Table 6.3 were sampled using the WAS (Whole Air Sampling) system on the BAe-146 followed by measurement on the ground by the York University dual channel GC-FID instrument. As such these compounds are not measured continuously and the data coverage is less comprehensive. The compounds measured by techniques beside this are listed in Table 6.4, along with the measurement technique and institution responsible for the measurement. The reactivity of a VOC to an oxidant, X, is given by Equation 6.22.

$$\mathrm{VOC} + \mathrm{X} \rightarrow products \tag{6.20}$$

$$\frac{d[\mathrm{X}]}{dt} = k_{VOC+X}[\mathrm{VOC}][\mathrm{X}] \tag{6.21}$$

$$\frac{d[\mathrm{X}]/dt}{[\mathrm{X}]} = k_{VOC+X}[\mathrm{VOC}] \tag{6.22}$$

Reactivity is therefore the rate of reaction of the VOC with respect to the oxidant X, per unit concentration of oxidant, and has units s^{-1}. Given the concentration of the VOC, oxidant and rate constant, this equation may be rearranged and inverted to also calculate the chemical lifetime of either VOC or oxidant. The total reactivity is estimated by summation of the individual reactivities. As discussed by Sinha *et al.* (2008) the total reactivity to OH calculated in this way can miss some reactive species owing to limitations on the number of species that can be measured in a given field campaign, and therefore may be underestimated. Direct measurements of total reactivity to OH do not suffer this limitation and have been made at ground level e.g. Sinha *et al.* (2008), and recently an aircraft instrument has been deployed for the first time (Mao *et al.*, 2009). However, accepting this limitation the reactivity calculated here provides a best estimate of the species that dominate the total. The oxidation of VOC's by OH is a source of organic peroxy radicals, while ozone + alkene reactions can be a significant source of HO_x and RO_2 at night when the concentration of OH tends to zero (Monks, 2005). Hence, the dominant reactive compounds can also provide an indication of the additional sources of peroxy radicals.

Methane was not measured on board the BAe-146 and therefore its concentration has been assumed to be constant at 1800 ppbV (based on Bergamaschi *et al.* (2007)) for every point; it therefore makes a constant contribution to OH reactivity except for variation as a result of the temperature dependence of the rate coefficient. As mentioned the VOC's derived from WAS samples have less data coverage, which potentially may lead to some bias in the total reactivity derived. To illustrate the variation in data coverage, the number of VOC's used to calculate reactivity for each measurement point over the campaign are displayed in Figure 6.9. The total OH reactivity as a function of latitude and altitude is given in Figure 6.10, it has been restricted to daylight hours (i.e. 06:00-18:00 UTC) since outside

Compound	Rate coefficient reference
Methanol	Atkinson *et al.* (2006)
Acetylene	Atkinson *et al.* (2006)
Ethene	Atkinson *et al.* (2006)
Acetaldehyde	Atkinson *et al.* (2006)
Ethane	Atkinson *et al.* (2006)
Ethanol	Atkinson *et al.* (2006)
Propadiene	Atkinson & Arey (2003)
Propene	Atkinson *et al.* (2006)
Acetic acid methyl ester	Andersen *et al.* (2009)
Propane	Atkinson *et al.* (2006)
Iso-butane	Atkinson & Arey (2003)
n-butane	Atkinson *et al.* (2006)
1,2-butadiene	Atkinson & Arey (2003)
1,3-butadiene	Atkinson & Arey (2003)
Trans-2-butene	Atkinson & Arey (2003)
1-butene	Atkinson & Arey (2003)
Iso-butene	Atkinson & Arey (2003)
Cis-2-butene	Atkinson & Arey (2003)
MEK	Atkinson *et al.* (2006)
Cyclopentane	Atkinson & Arey (2003)
Iso-pentane	Atkinson & Arey (2003)
n-pentane	Atkinson & Arey (2003)
Cyclohexane	Atkinson & Arey (2003)
n-hexane	Atkinson & Arey (2003)
Toluene	Atkinson & Arey (2003)
Ethylbenzene	Atkinson & Arey (2003)
m+p-xylene*	Atkinson & Arey (2003)
o-xylene	Atkinson & Arey (2003)
Octane	Atkinson & Arey (2003)

Table 6.3: WAS VOC measurements used for calculation of reactivity. *Average of individual rate coefficients for reaction of OH with m-xylene and p-xylene was applied.

Compound	Technique	Institution	Rate coefficient reference
CO	VUV fluorescence	FAAM	Atkinson *et al.* (2006)
Formaldehyde	Fluorometric	UEA	Atkinson *et al.* (2006)
Methane	Not measured	-	Atkinson *et al.* (2006)
Acetonitrile	PTR-MS	UEA	Atkinson *et al.* (2006)
Acetone	PTR-MS	UEA	Atkinson *et al.* (2006)
MVK+MACR*	PTR-MS	UEA	Atkinson *et al.* (2006)
Isoprene	PTR-MS	UEA	Atkinson *et al.* (2006)
Benzene	PTR-MS	UEA	Atkinson & Arey (2003)

Table 6.4: Other VOC measurements used for calculation of reactivity. *PTR-MS cannot separate MVK from MACR so WAS MACR measurement was used to determine the relative proportion of MVK and MACR by comparison to PTR-MS total i.e. [MVK]= 1.301 ± 0.053[MACR]; the rate coefficient applied was scaled to reflect the proportions of MVK and MACR.

daylight the concentration of OH should be negligible. The relative contributions of the VOC's that dominate OH reactivity across the region are then given in Figures 6.11-6.15, again these have been restricted to daylight hours. Also note that the colourscale used for the distribution of the total reactivity (Figure 6.10) has been restricted to the range 0-5 s^{-1} to cover the dynamic range of most of the variability, however it does not represent the total range in reactivity (maximum observed 25.25 s^{-1}).

There is some variation in the degree of data coverage for the measured VOC's (Figure 6.9), however a smooth variation in total reactivity still results suggesting the overall trends are real. The trends are linked to the dynamical picture of the monsoon system through the overlayed contours of constant potential temperature from the 12:00-18:00 period (refer to Section 5.2.3, Chapter 5), as may be expected from the distributions of VOC's discussed previously (refer to Sections 5.2.4 and 5.2.5, Chapter 5). In terms of the absolute daytime reactivity to OH, Figure 6.10 shows this to be highest over the forest regions coincident with the biogenic emissions of isoprene. Also the VOC reactivity to OH is enhanced in the regions influenced by emissions from the coastal cities of Lagos and Cotonou, and to a lesser extent within the aged biomass burning plumes. In terms of relative reactivity, CO

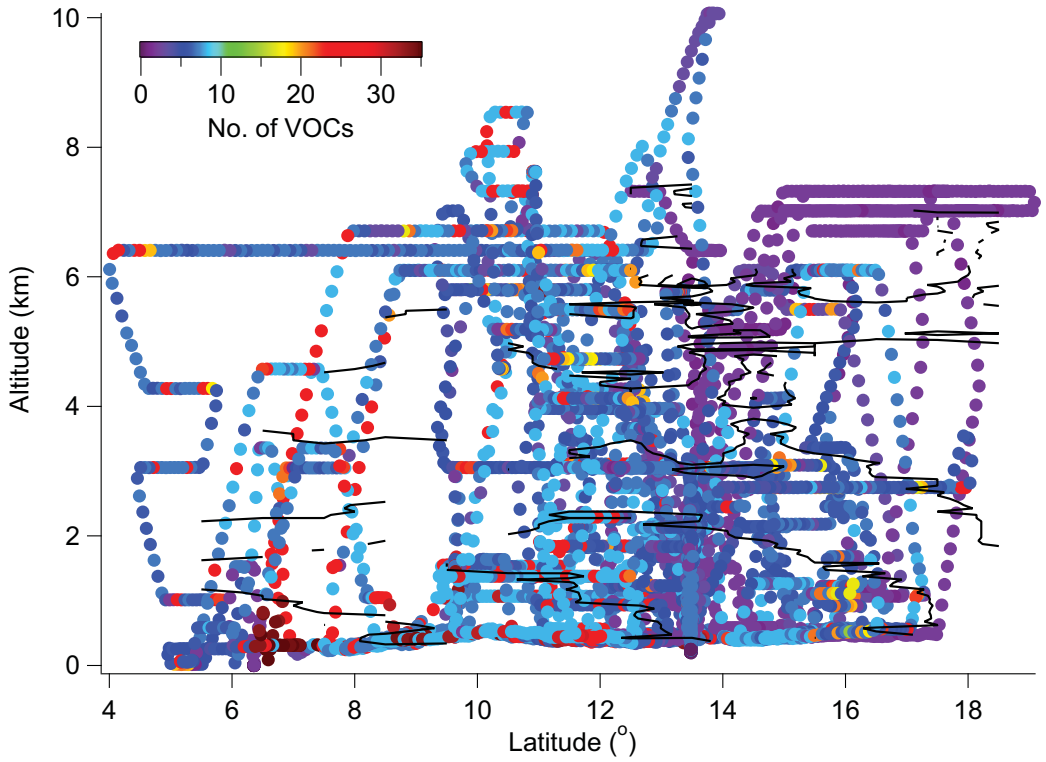

Figure 6.9: Meridional distribution of number of VOCs used to calculate OH reactivity

and methane are observed to dominate overall outside the boundary layer and in regions not influenced by biogenic and anthropogenic emissions, consistent with background air. Isoprene dominates the reactivity in the boundary layer over the forested regions both in a relative sense and also dominates the region as a whole in terms of the absolute reactivity to OH. Since isoprene is the dominant primary biogenic VOC emitted by terrestrial plants (as discussed in Section 5.1.2, Chapter 5) the total absolute reactivity calculated provides a lower limit to the total owing to biogenic emissions. Sinha *et al.* (2008) lists reactivities determined at a number of urban and forested sites, with median values in the range 10-40 s^{-1}. The calculated total reactivity observed for AMMA has *most* values in the range 0-5 s^{-1} suggesting the reactivity is underestimated. Indeed, the highest total reactivities are calculated where more VOC measurements are available (though there is no overall correlation) suggesting an undersampling of the total OH sink. Of course the region is undersampled in time and space, meaning diurnal variation in VOC emissions are missed, while measurements away from the

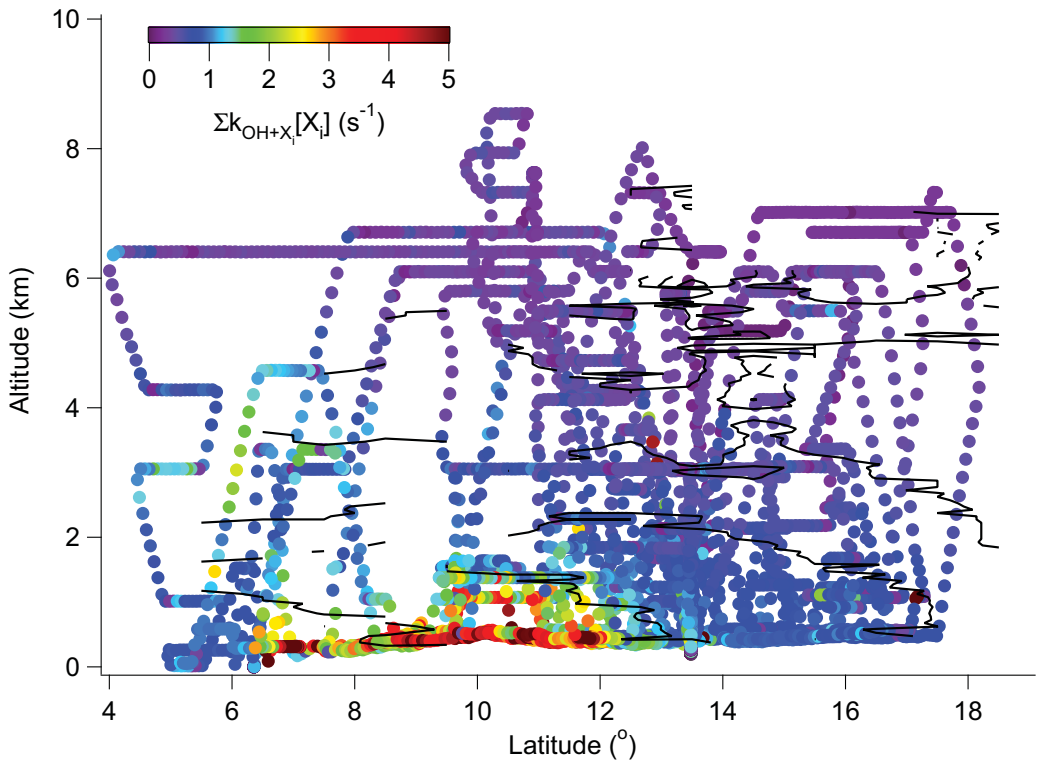

Figure 6.10: Meridional distribution of VOC OH reactivity – Colourscale limited to range 0-5 s^{-1} does not represent total range.

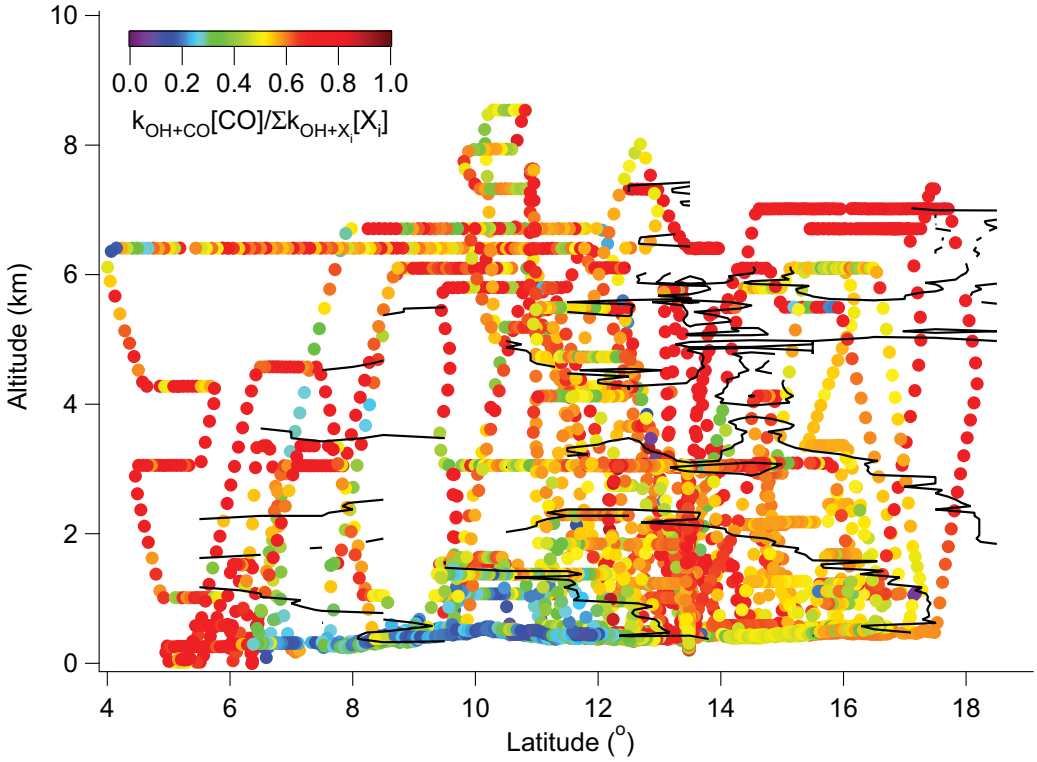

Figure 6.11: Meridional distribution of relative contribution of CO to OH reactivity

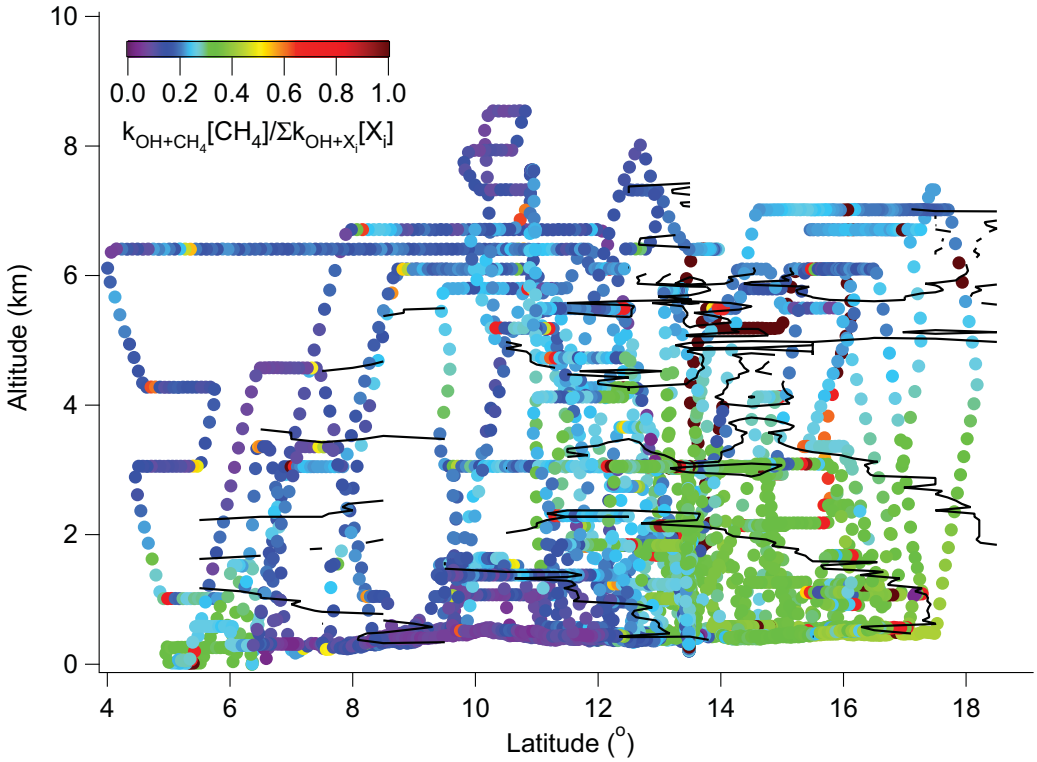

Figure 6.12: Meridional distribution of relative contribution of methane to OH reactivity

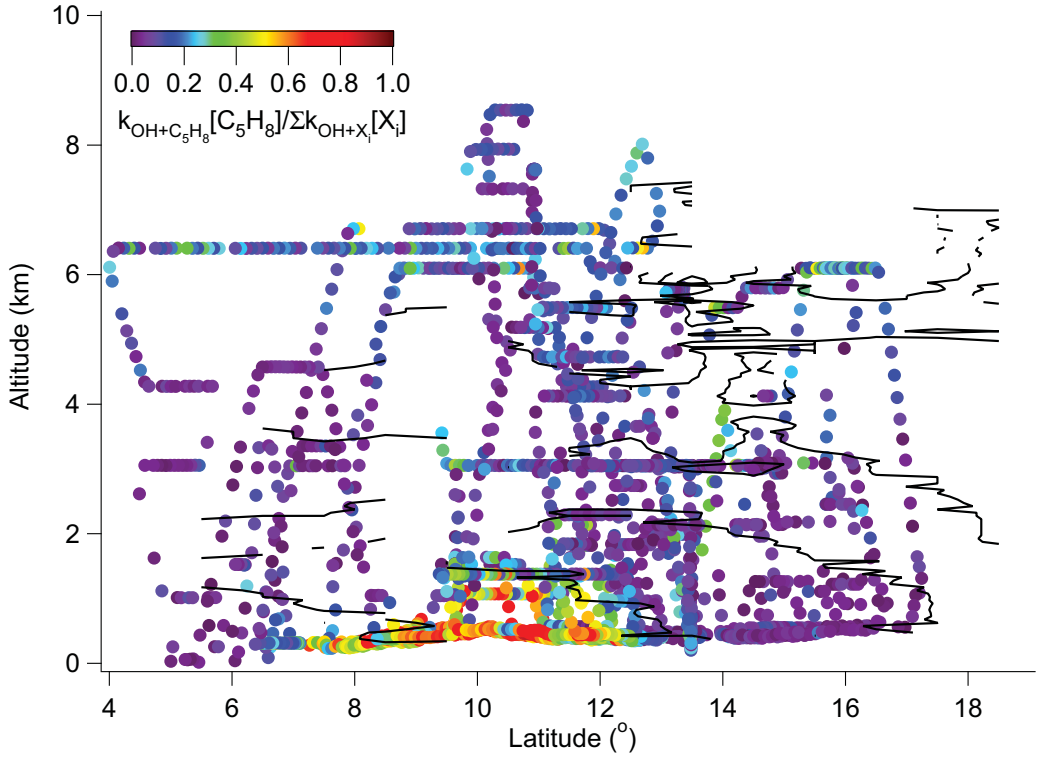

Figure 6.13: Meridional distribution of relative contribution of isoprene to OH reactivity

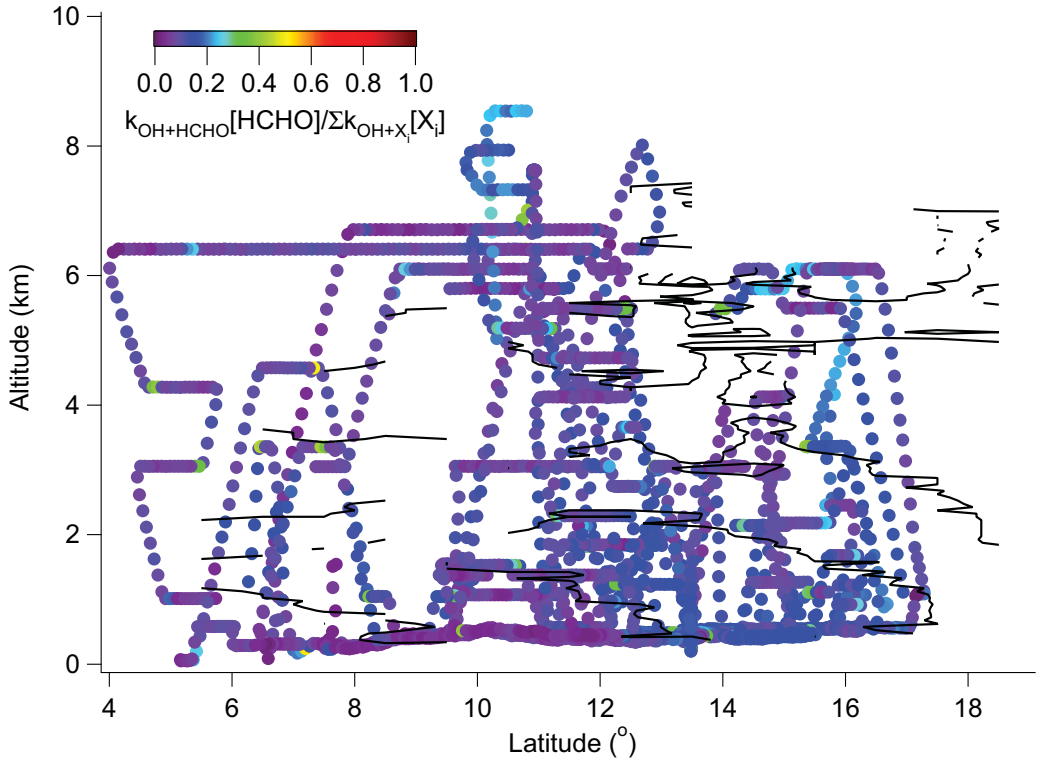

Figure 6.14: Meridional distribution of relative contribution of formaldehyde to OH reactivity

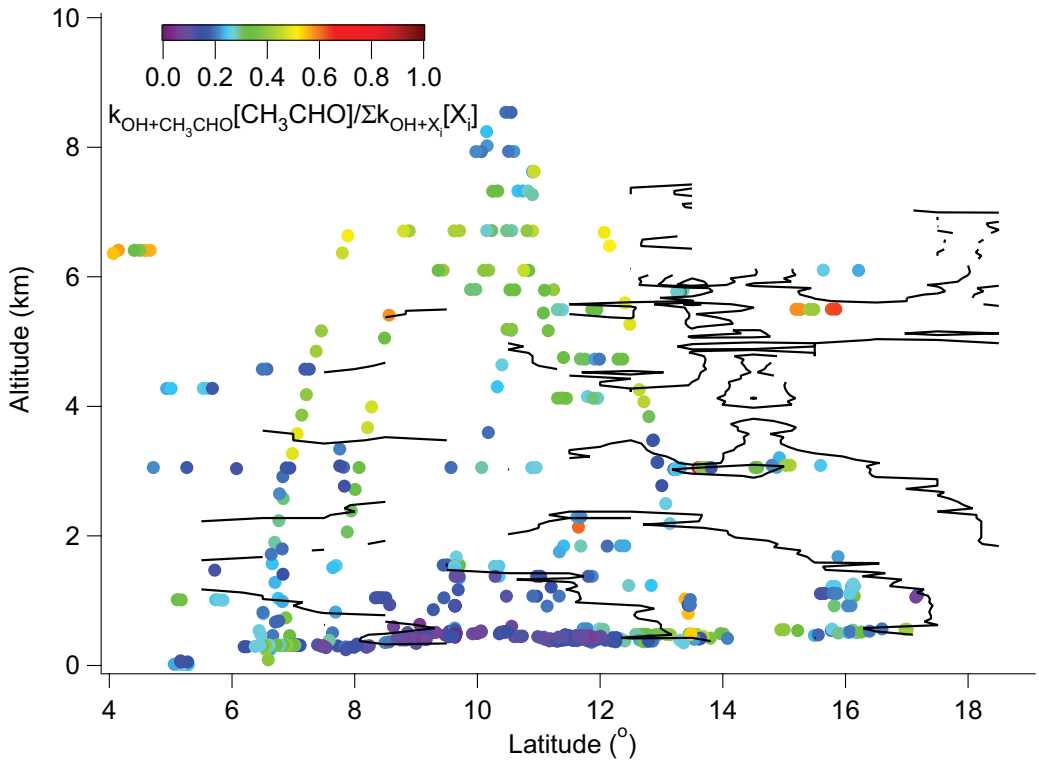

Figure 6.15: Meridional distribution of relative contribution of acetaldehyde to OH reactivity

surface emissions will dominate the low reactivities observed. Of the calculated total reactivity, on average ∼87% is accounted for by methane, CO and isoprene. Oxgenated VOC's make a significant but lesser contribution to the total OH reactivity overall, however within the anthropogenically influenced plumes they contribute more significantly to the reactivity along with CO. In particular formaldehyde and acetaldehyde appear significant, with acetaldehyde often contributing ∼40-50% of the total. Exceptionally acetaldehyde dominates the reactivity within the Lagos plume. Including formaldehyde and acetaldehyde accounts for on average ∼96% of the calculated total reactivity. Although the total reactivity to OH is likely underestimated the trends are thought representative. It is expected that outside the monsoon layer and the influence of anthropogenic plumes, a relatively simple radical composition will exist, dominated by HO_2 and CH_3O_2 and the acetylperoxy radical ($CH_3C(O)OO$) generated from the oxidation of acetaldehyde. Where isoprene dominates in the boundary layer the radical composition will therefore be more complex, with OH oxidation and ozonolysis of alkenes gen-

erating many radical intermediates. The presence of oxygenated VOC's will generate radicals through photolysis of carbonyls, or their reaction with OH.

6.3.2 Measured radicals

The observed distributions of measured radicals (OH and HO_2 measured by the University of Leeds FAGE instrument, and RO_x measured by the University of Leicester PERCA 4 instrument) are presented here, and interpreted by considering the dominant sources and sinks as incorporated into the steady state production and loss of radicals (Equation 6.19), and the distributions in precursors and OH reactivity. Measurements of RO_x were also made from the German DLR-Falcon aircraft during AMMA (Andres-Hernandez *et al.*, 2009) and an inflight intercomparison of the BAe-146 and DLR-Falcon measurements was made on flight B234. The results of the intercomparison are the subject of a paper submitted to the journal Atmospheric Chemistry and Physics Discussions (ACPD), see reference in Appendix A.8, and are not discussed here.

The observed distributions illustrate the variability in the measurements of these highly reactive species owing to the many variables controlling their concentration. The photochemical production of radicals during the day (e.g. primary production from ozone photolysis) can give rise to a characteristic diurnal cycle which is presented in Figures 6.16-6.18. The diurnal profiles have been colourscaled by the rate of primary production to demonstrate the degree of correlation, calculated using $P_{Pri.} = 2fj_{O^1D}[O_3]$ (where f is calculated from Equation 6.10). Data are not available for the calculation of $P_{Pri.}$ for all points where there is a radical measurement so the radical data are plotted additionally in grey behind the colourscaled points. The nature of an aircraft campaign is that many locations are sampled at various times (and not always repeatedly), hence the diurnals in Figures 6.16-6.18 can be thought of as composites of diurnal cycles sampled across the region. For any spatial distribution of radicals the diurnal variability of the driving variables will add a diurnality to a composite view. Further, although

the lifetimes of radicals are typically short enough (at least during the day) that transport does not affect radical concentrations directly, transport does dictate the composition of radical precursors. The meridional distributions of the measured radicals are presented in Figures 6.19-6.21 where the colourscale represents the radical concentration observed; for HO_2 and RO_x where there is greater data coverage, and more obvious diurnal changes are present, the dataset has been separated by time of day into 6 hour intervals (00:00-06:00, 06:00-12:00, 12:00-18:00, 18:00-24:00). Overplotted (black traces) are contours of constant potential temperature for the 06:00-12:00 and 12:00-18:00 periods (see Section 5.2.3, Figure 5.19, Chapter 5) indicating the diurnal cycle in monsoon structure. It should be noted that the range in colourscale in Figure 6.19 is not representative of the total range in concentrations observed for the PERCA RO_x measurement; the highest concentrations (observed concentrations were in the range 0-205pptV) were far above the average and therefore the normal range in variability would not be clear if the colourscale extended this far. A histogram of RO_x and HO_x concentrations presents the frequency distribution of observed concentration during AMMA SOP2 in Figure 6.22.

Considering the diurnal profiles, there is a clear diurnal cycle in the composite views of $[HO_2]$ and $[RO_x]$ with high concentrations observed coincident with high radical production rates through ozone photolysis. Still, for HO_2 and RO_x in particular, the measured concentrations are non-zero where $P_{Pri.}$ tends to zero at night. A diurnal cycle is not clear in OH, possibly related to the more limited data coverage and the variability of driving variables but also a result of the difficulty of this measurement. The data have not been filtered for points less than the detection limit as this represents a significant proportion of the OH dataset, these values have then been incorporated into the hourly binned data and it is notable that non-zero median values are present even in OH toward night ($\sim 7\times10^5$ molecule cm^{-3}). The $[HO_2]$ profile is marginally asymmetrical with higher $[HO_2]$ persisting in the afternoon indicative of secondary production maintaining the concentration at this time. The concentrations of

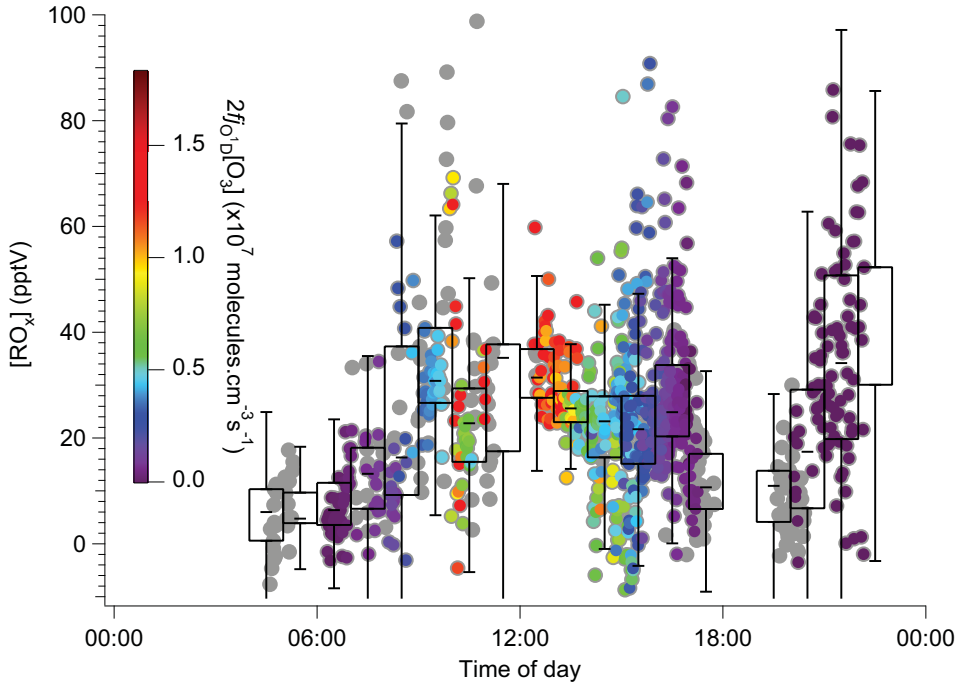

Figure 6.16: Diurnal cycle in RO_x measured by the University of Leicester PERCA 4 instrument during AMMA SOP2 – Box centres represent median values, box edges Q25 and Q75 and whiskers lower and upper inner fences

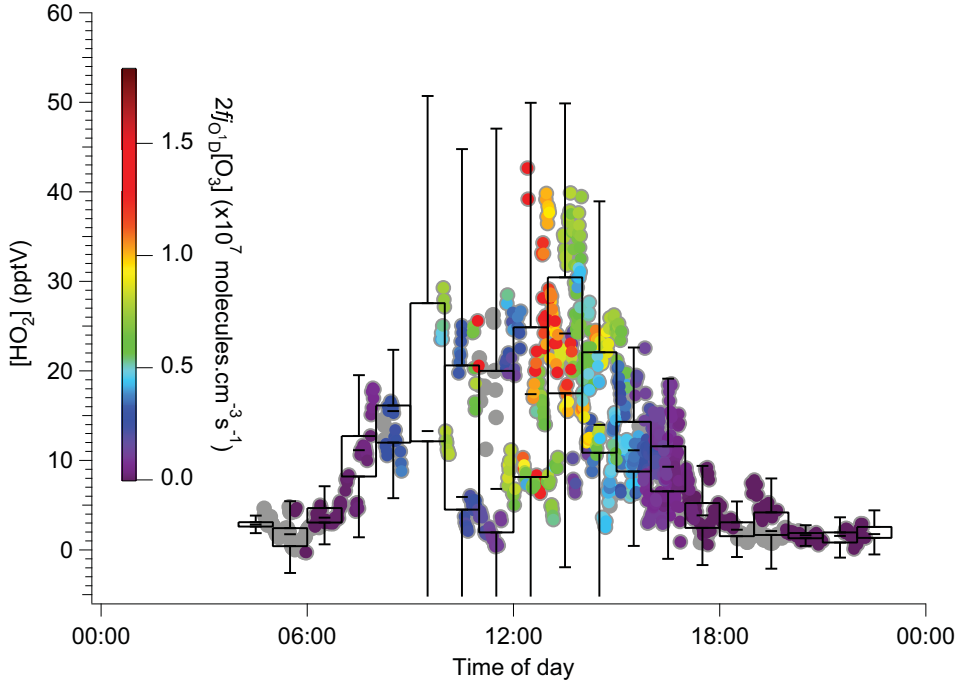

Figure 6.17: Diurnal cycle in HO_2 measured by the University of Leeds FAGE instrument during AMMA SOP2 – Box centres represent median values, box edges Q25 and Q75 and whiskers lower and upper inner fences

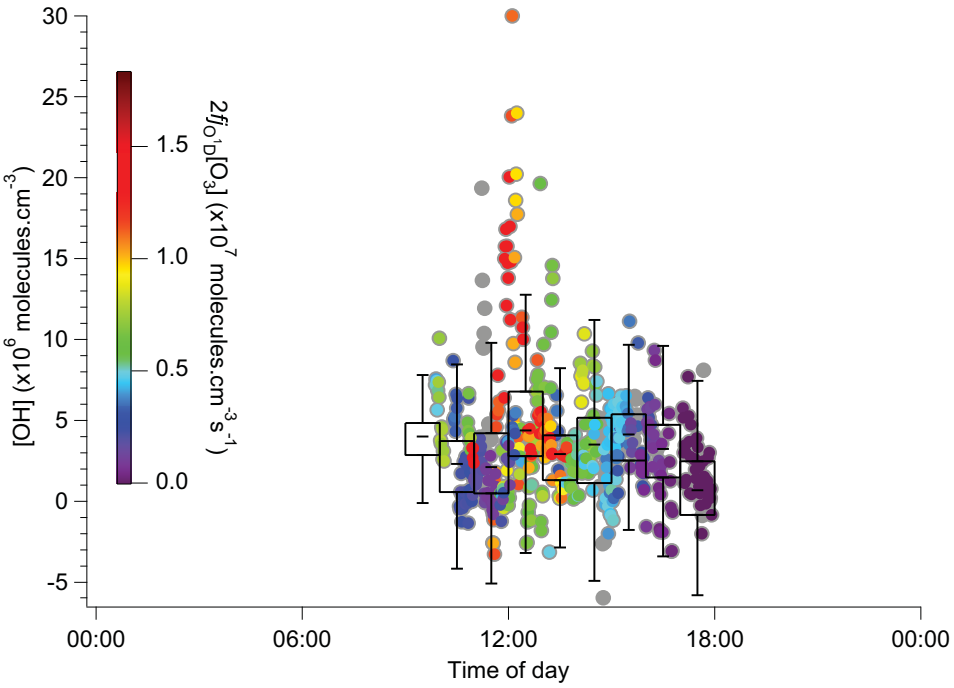

Figure 6.18: Diurnal cycle in OH measured by the University of Leeds FAGE instrument during AMMA SOP2 – Box centres represent median values, box edges Q25 and Q75 and whiskers lower and upper inner fences

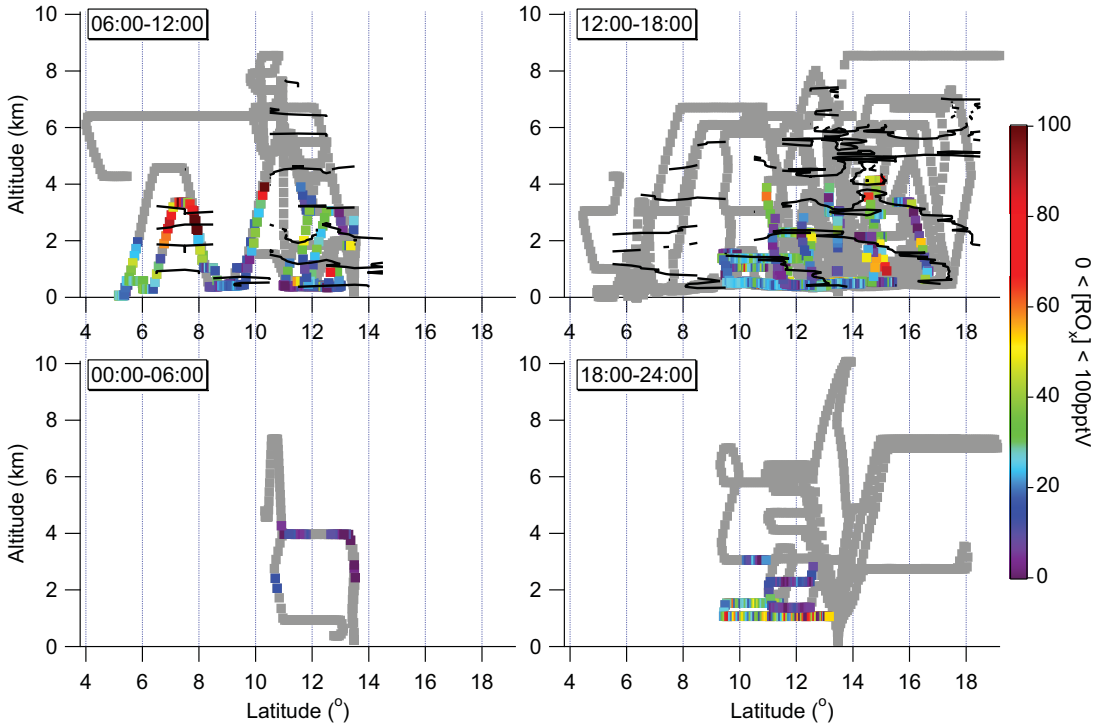

Figure 6.19: Meridional distribution of RO_x throughout the diurnal measured by the University of Leicester PERCA 4 instrument during AMMA SOP2

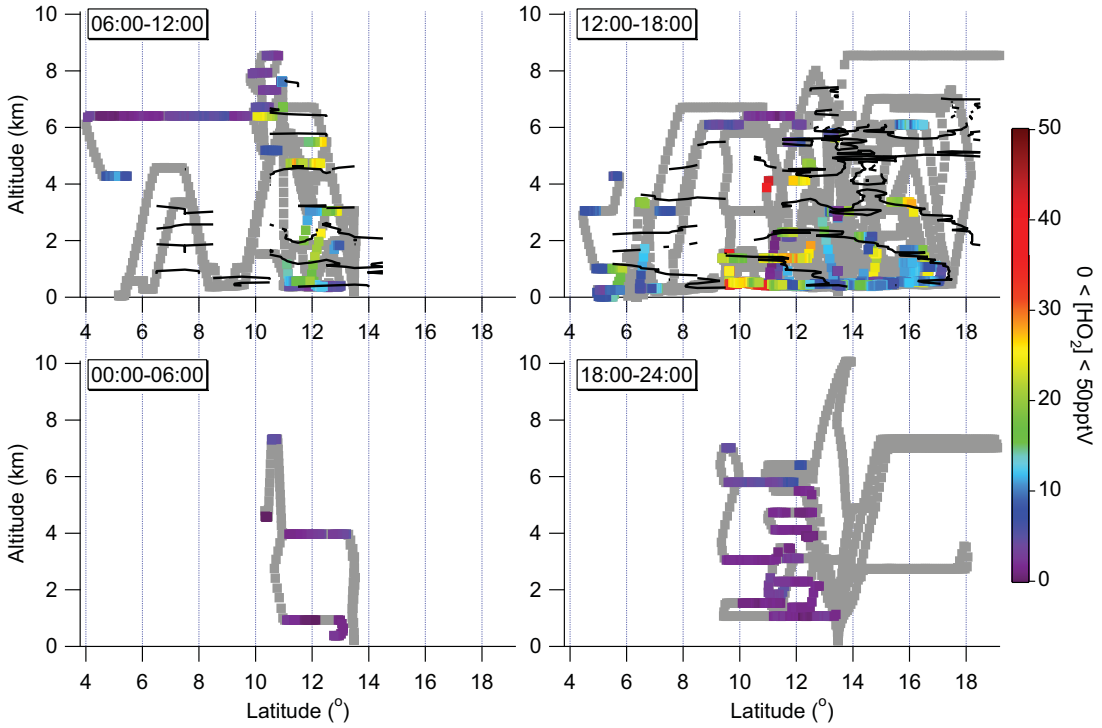

Figure 6.20: Meridional distribution of HO_2 throughout the diurnal measured by the University of Leeds FAGE instrument during AMMA SOP2

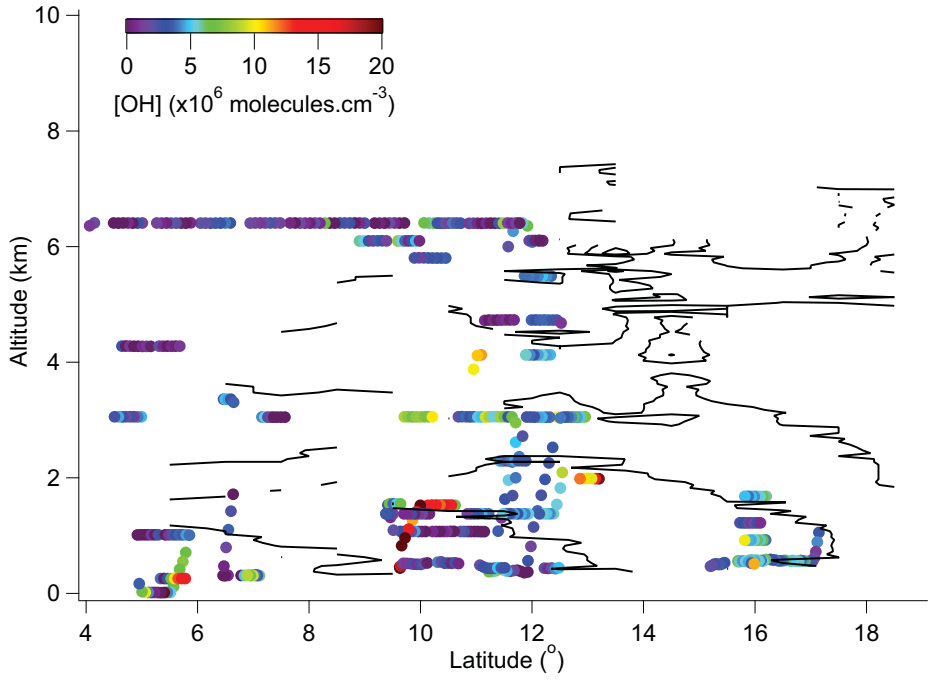

Figure 6.21: Meridional distribution of OH measured by the University of Leeds FAGE instrument during AMMA SOP2

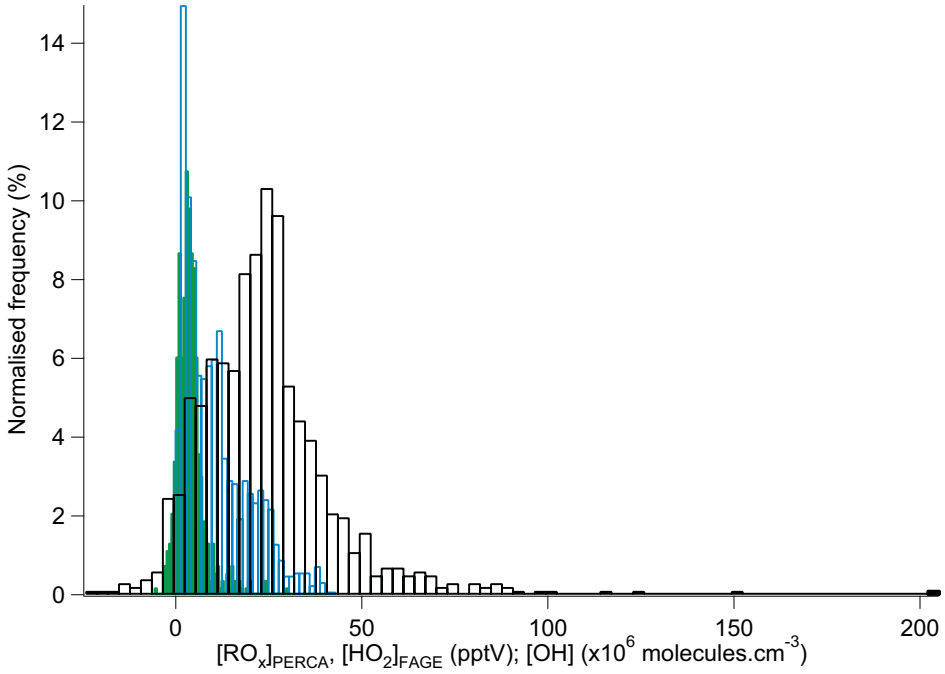

Figure 6.22: Normalised frequency distribution of observed [RO_x] and [HO_x] measured during AMMA SOP2 – (Black bars) Distribution of observed [RO_x]; (Blue bars) and (Green bars) Distributions of observed [HO_2] and [OH] respectively

HO_2 tend to be much lower (though non-zero) at night, with median values of the order 2 pptV. The composite [RO_x] diurnal cycle is distinctly asymmetrical with higher concentrations in the afternoon that persist at night. Some low values in the evening and at night are indicative that the concentrations are not elevated everywhere; median values of the order 30 pptV represent significant nighttime concentrations.

A number of processes could be expected to lead to enhanced radical concentrations that peak later into the day. The emission of biogenic VOC's e.g. isoprene and monoterpenes, are linked to temperature (as discussed in Section 5.1.2 of the last chapter) and therefore the concentrations of these species tend to peak in the afternoon. This can be seen in the isoprene data from the BAe-146 when restricted to the boundary layer, it has also been observed on the ground during SOP2 at a rural field site in Benin (Saxton *et al.*, 2007). The decomposition of radical reservoir species such as PAN is temperature dependent and therefore the lifetimes of such species will be least close to the surface, and also less

in the afternoon when surface temperatures are highest. For example the lifetime of PAN (calculated using the temperature and pressure dependent rate constant for the thermal decomposition of PAN from Atkinson *et al.* (2006)) varies from ∼10 minutes close to the surface to over 2 days at 4 km altitude, and from ∼10 minutes in the mid afternoon to ∼2 hours in the early morning. Nighttime oxidation chemistry is thought to be initiated either by nitrate radicals, NO_3, or through ozone + alkene reactions which are active throughout the day (Wayne, 2000). The peroxy radicals that are products of this oxidation chemistry then react with NO_3, O_3 and each other (self- and cross-reactions), and owing to the much slower rate of self-reactions among organic peroxy radicals, RO_2 will tend to persist at higher concentration (considering in particular the enhancement of the self-reaction of HO_2 with humidity). If the lifetimes of peroxy radicals are extended sufficiently then transport becomes important in their concentration; significant transport does occur at night with the monsoon flow, which may explain the model measurement deviations observed (see Section 6.2, e.g. Figure 6.7). At night NO is rapidly converted to NO_2 in the absence of NO_2 photolysis to maintain the photostationary state. For RO_2 to convert to HO_2 typically requires reaction with NO, and in combination with the absence of the primary production of HO_x through ozone photolysis, the balance of the radical population will shift toward organic peroxy radicals. Still, with NO_3 present this can act instead of NO in reaction with organic peroxy radicals to form HO_2 and potentially OH. The distinctly higher organic peroxy radical concentrations measured by the PERCA relative to the coincident HO_2 concentrations measured by FAGE, suggests that nitrate radical chemistry may be limited.

A dominant mode of transport in the WAM is the diurnal cycle of the monsoon flow (Parker *et al.*, 2005a), which was seen to lead to gradients in the distribution of biogenics and their oxidation products (see Section 5.2.4, Chapter 5). The meridional profiles locate the regions of enhanced peroxy radical concentrations within the monsoon system, and the diurnal cycle of the monsoon flow. It should be

noted that in Figures 6.19 and 6.20 the range of the colourscales are different (owing to the larger range in observed [RO_x]); with this in mind the distributions show similar trends. [RO_x] and [HO_2] show similar concentrations in the daytime (06:00-12:00, 12:00-18:00 periods) over the biogenics source regions between 7.2-13.25^{o}N, and in the north where enhanced ozone production has been observed in association with soil NO_x emissions (Stewart *et al.*, 2008, Delon *et al.*, 2008). Enhancements in the south are coincident with interceptions of biomass burning plumes and pollution from coastal cities (Lagos, Cotonou); these appear in different time bands for RO_x and HO_2 since they represent occasions when either the PERCA or FAGE instruments were operating but not both. At night the concentration of HO_2 is low and shows no observable trends on this scale, while RO_x (essentially RO_2) is distinctly enhanced in the 18:00-24:00 period over a band extending from ∼9-13.5^{o}N. Notably enhancements were seen at the same time in the ratio [MVK+MACR]/[C_5H_8] with a gradient where the ratio increased toward the north (see Figure 5.25, Section 5.2.4, Chapter 5); similarly RO_x shows an increase toward the north. This gradient has been attributed to the northward transport of isoprene in the nocturnal jet and its oxidation on transport (see Section 5.2.4 and Figure 5.25 in particular); organic peroxy radicals are intermediates in this oxidation and therefore the RO_x measurements are consistent with this conclusion, which also provides an explanation of the model to measurement differences at night.

6.3.3 Modelled radical composition

The results of the DSMACC box model were used to determine the dominant radical species as a whole and under various conditions, to assess whether the model predicted trends validate the expected trends. Based on the derived composition, the PERCA measurements of RO_x are compared to the modelled RO_x and total organic peroxy radicals (RO_2) in order to interpret any model to measurement bias based on composition.

The first order air mass classification defined in Section 5.2.5 of the Chapter 5 identified a number of features. The distinct asymmetries in the overall distributions of ozone and CO appear to trace the dynamical picture of the monsoon and reflect the presence or absence of sources and sinks for these species: CO enhanced within the low level monsoon flow owing to both natural and anthropogenic sources, while ozone is suppressed either as a result of net photochemical ozone destruction or stronger losses through deposition and alkene ozonolysis; within the SAL the natural and anthropogenic sources of CO are much reduced, while soil NO_x emissions enhance the photochemical source of ozone. In terms of radical composition differences over and above the underlying diurnal trend are expected dependent on the influence of biogenic and anthropogenic emissions that characterise the WAM environment (this is clear in the distribution of OH reactivity in Section 6.3.1, Figure 6.10). To investigate air masses under the direct influence of biogenic emissions and not directly influenced by anthropogenics a classification of "direct biogenics" has been defined where isoprene and the combined concentration of the oxidation products methyl vinyl ketone (MVK) and methacrolein (MACR) are $\geq$200 pptV, and [CO] is <180 ppbV. To investigate air masses directly influenced by anthropogenic emissions the classification of "direct anthrop." is defined where [CO] is $\geq$180 ppbV. This limit was chosen because it restricted the classification to the regions close to the point sources of CO at the surface, and the strongest pollution plumes aloft, and therefore is sufficiently above the background level (see Figure 5.26, in Section 5.2.5, Chapter 5). Air masses outside the direct influence of anthropogenic and biogenic VOC emissions (classified as "Other") were then defined where [MVK+MACR] and [C_5H_8] are <200 pptV and [CO] is <180 ppbV. To investigate whether there was a distinction between the radical composition throughout the day the model output was also filtered by time of day into 06:00-12:00 and 12:00-18:00 periods. Pie charts presenting the modelled radical composition within these air mass classifications and time periods are given in Figure 6.23. Owing to the large number of radicals represented within the model, the composition for each classification was determined by sorting the species by concentration and extracting those that represented the top 10 by concentration; typically

$\geq$80% of the total concentration is represented by these species and those that remain represent $\leq$1% each by concentration.

A common feature reflected by the overall composition chart is the dominance by concentration of HO_2 and CH_3O_2 as may be expected; this is essentially representative of the composition outside the direct influence of biogenic or anthropogenic emissions and is reflected by the composition of the "Other" class. Still, peroxy radicals derived from isoprene oxidation by OH (ISOPBO2), and the acetylperoxy radical derived primarily from the reaction of acetaldehyde with OH and PAN thermolysis, also dominate the radical population, illustrating the influence of biogenic emissions across the WAM region as a whole. The "direct biogenics" class is characterised by a more complex mix of radicals, which is as expected, dominated by derivatives of isoprene (besides HO_2 and CH_3O_2), with proportionally less CH_3O_2 and a similar proportion of HO_2. Since this air mass classification prescribes that the concentrations of isoprene and its first oxidation products MVK and MACR are elevated, the composition will be dominated by the intermediaries of the initial oxidation steps. The "direct anthrop." class is the simplest mix with the HO_2 radical representing almost half the concentration; this is likely the result of the catalytic recycling of HO_x radicals in the presence of the high levels of ozone, CO and NO_x that characterise these air masses. Further, the increased proportion of acetylperoxy within the "direct anthrop." class is not unexpected owing to the derived contribution of acetaldehyde to the VOC reactivity within these air masses. The variation of the composition within the day also validates the expected trend, whereby the proportion of organic peroxy radicals is increased in the latter part of the day, with a more complex mix resulting from the higher emissions of biogenic VOC's with higher temperature in the afternoon.

In terms of the comparison of the modelled RO_x and total RO_2 to the PERCA measurement it is difficult to assess any degree of bias related to composition from Figure 6.24, owing to the low number of comparable points (reduced when the dataset is split). This is most significant for the

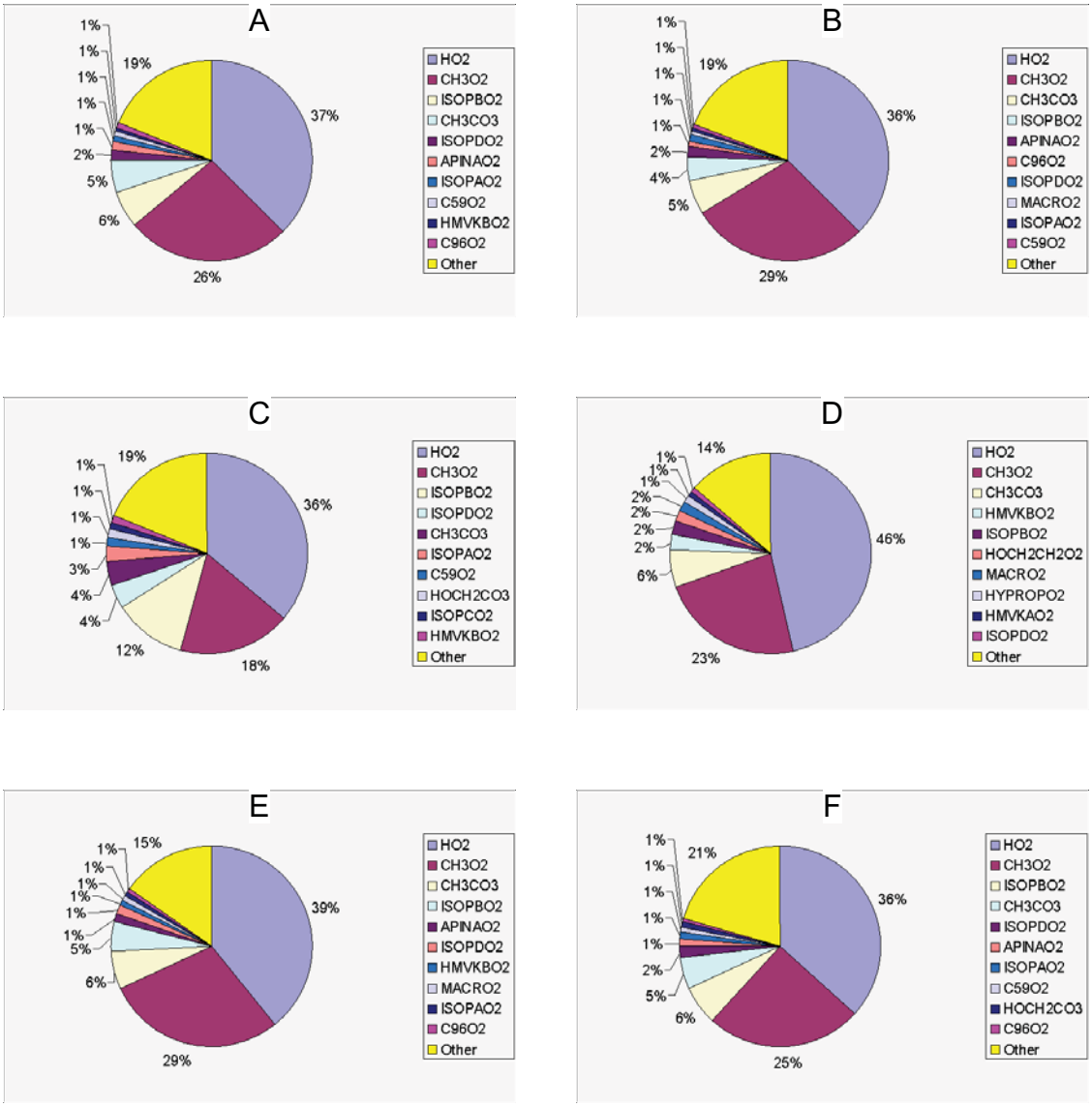

Figure 6.23: Radical composition by air mass – (A) Overall composition; (B) Other composition; (C) Direct biogenics composition; (D) Direct anthrop. composition; (E) 06:00-12:00 period composition; (F) 12:00-18:00 period composition

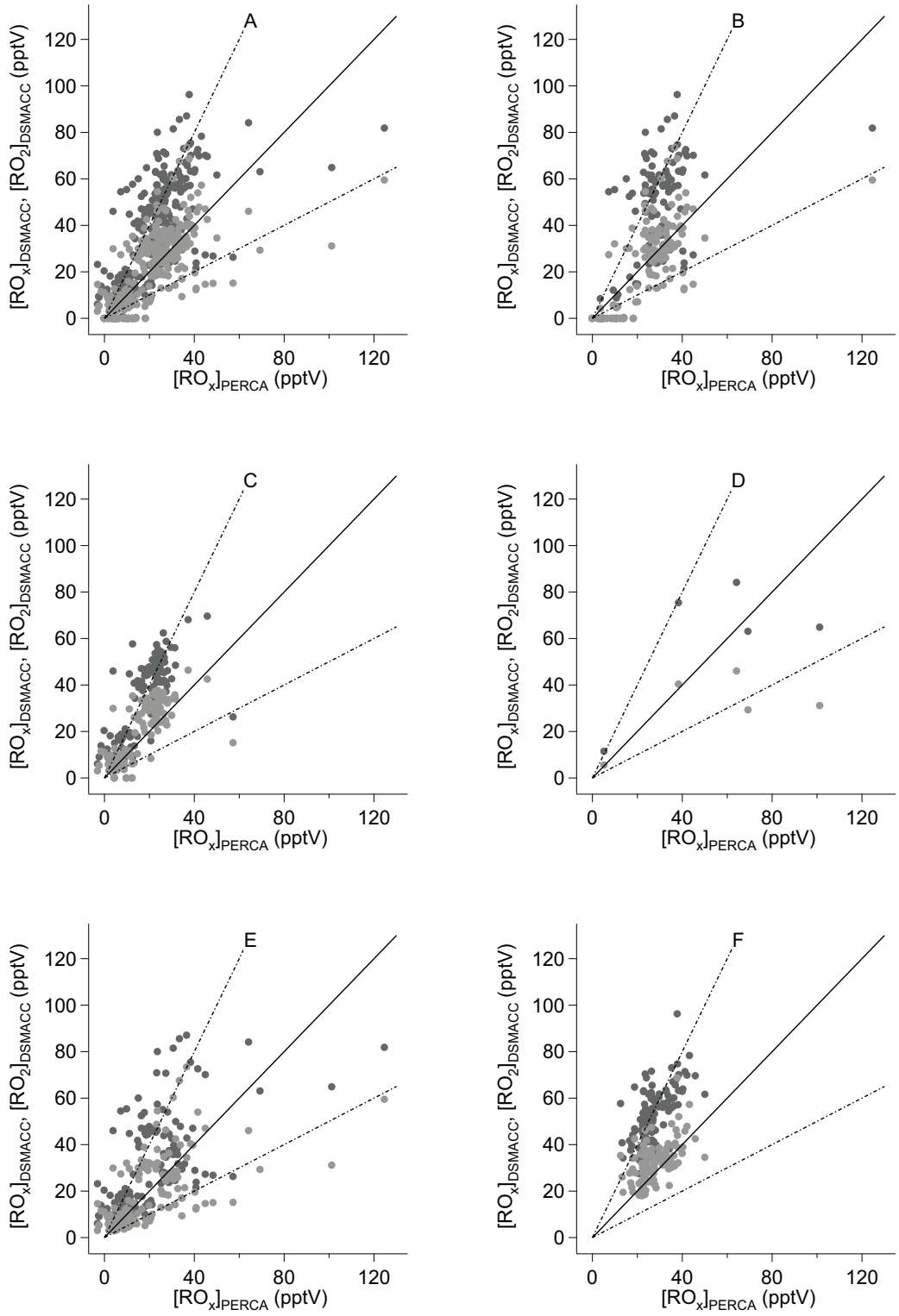

Figure 6.24: Modelled [RO_x] (dark grey), [RO_2] (light grey) versus measured [RO_x] by air mass, (Black dashed lines) 2:1 and 1:2 level of agreement, (Black full line) 1:1 level of agreement – (A) Overall composition; (B) Other composition; (C) Direct biogenics composition; (D) Direct anthrop. composition; (E) 06:00-12:00 period composition; (F) 12:00-18:00 period composition

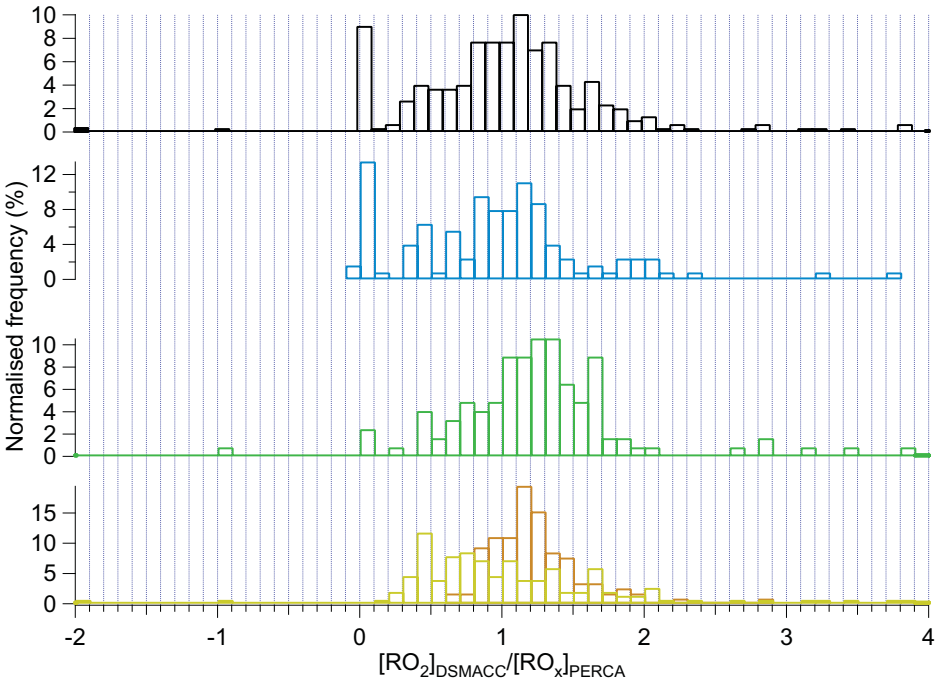

Figure 6.25: Histogram of the ratio $[\mathrm{RO_2}]_{DSMACC}/[\mathrm{RO}_x]_{PERCA}$ by air mass – (Black bars) Overall composition; (Blue bars) Other composition; (Green bars) Direct biogenics composition; (Yellow bars) 06:00-12:00 period composition; (Orange bars) 12:00-18:00 period composition

"direct anthrop." class where only 5 points of comparison are available, so outliers skew any fit. Also, the dynamic range in concentration in some of these classes is of the order the variability in the data and therefore the level of correlation in a linear fit is low even if the modelled and measured concentrations are similar. To provide some quantitative assessment of the agreement, the ratio $[\mathrm{RO_2}]_{DSMACC}/[\mathrm{RO}_x]_{PERCA}$ has been calculated for each class except "direct anthrop." where there is insufficient data, the frequency histograms of each are shown in Figure 6.25.

Comparing the level of agreement between the modelled $[\mathrm{RO}_x]$, total $[\mathrm{RO_2}]$ and the PERCA measurement of $[\mathrm{RO}_x]$, using the correlation plots in Figure 6.24 and the model to measurement ratios in Figure 6.25, the measurement is always better represented by modelled total $[\mathrm{RO_2}]$ irrespective of the conditions. Considering the whole dataset, the "Overall" composition model to measurement ratio distribution shows near 1:1 agreement between modelled total $[\mathrm{RO_2}]$ and measured $[\mathrm{RO}_x]$ for the majority of points, which is also reflected in the "Other" class. As discussed the composition in this

class is more simple, with CH_3O_2 representing the major component by concentration of RO_2. Points where the model to measurement ratio is <1 or zero, represent points where the model has predicted a lower concentration than measured (as it does at night) or potentially the reference chain length is too low (not likely). The earlier assessment seems reasonable in that methyl peroxy does dominate the organic peroxy radical composition overall, so this may mask differences in sensitivity to other organic peroxy radicals when the dataset is taken in bulk. It may also be true that measurement bias related to composition is evenly distributed (with this radical population mix) and acts to mask any measurement bias overall. For the "direct biogenics" class the tendency is for the modelled concentration to be higher with respect to measured; this could be interpreted as a result of the weighting of the PERCA chain length to CH_3O_2. In this air mass class [CH_3O_2] represents only ∼28% of the [RO_2] according to the model, a reduced chain length with respect to the other components would then mean the reference chain length is too high, and therefore the measurement response will be overweighted and the true concentration underestimated; alternatively the model would have to be over predicting the concentration. Between the 06:00-12:00 and 12:00-18:00 periods, the measurement goes from being high with respect to the model to being low. This could potentially be explained similarly, through the differences in composition and the weighting of the measurement response to CH_3O_2. In the 06:00-12:00 period although CH_3O_2 and $CH_3C(O)OO$ dominate the organic peroxy radical composition (∼57% of [RO_2]), the distribution of the model to measurement ratio is actually rather wide and flat, though with more points where the measurement exceeds the model. A measurement overestimate would require that the reference chain length is too low (not likely), or that the model is underpredicting the concentration. In part this may simply result from these values representing the lowest concentrations measured, and therefore being subject to greater relative uncertainty. These particular points also correspond to times when the primary production of radicals through ozone photolysis is low, which may suggest the model is missing an additional source of radical production in the early morning. The monsoon flow remains active within this period (see Figure 5.25, Section

5.2.4, Chapter 5) and is likely to be strongest during the earliest hours (Parker *et al.*, 2005a), NO concentrations are relatively low, and without primary production active the lowest HO_x concentrations are observed. Altogether this results in an extended lifetime for organic peroxy radicals (calculated with respect to NO, the lifetime of CH_3O_2 being typically ∼1-10 minutes) and if transport occurs the extended lifetime will make a steady state box model approach to the calculation of the concentration inaccurate. In the 12:00-18:00 period, the model concentration is typically high with respect to that measured. Again, this may be interpreted through a lower chain length with respect to organic peroxy radicals derived from isoprene oxidation, which are a larger component of the composition as in the "direct biogenics" class. A lower chain length with respect to the majority components would mean the reference chain length is too high; therefore the measurement response will be overweighted and the true concentration underestimated, but not to the extent that it was biased for the "direct biogenics" class, since the composition is not as strongly dominated by these species. Alternatively the model would have to be over predicting the concentration. To illustrate the diurnality of the partitioning between HO_2 and RO_2 measured (assuming the PERCA measures [RO_2]) and modelled, the total RO_x concentration was determined as the sum of the FAGE measured [HO_2] and the PERCA measured [RO_2], along with the fractional contribution of each to the total. Figure 6.26 presents the comparison; there is a clear diurnality measured in the fractional contributions of HO_2 and RO_2 which is not reflected by the model results. Indeed the model predicts a smaller change in partitioning throughout the day though the component of RO_2 is greater in the afternoon and particularly much greater than observed just after midday. The model predicts very low radical concentrations at night while significant concentrations were measured and therefore the modelled partitioning at high solar zenith angles and outside daylight hours is not thought reliable.

This assessment has shown that it is possible to explain a large proportion of the differences between the PERCA RO_x measurement and a detailed photochemical box model through an understanding

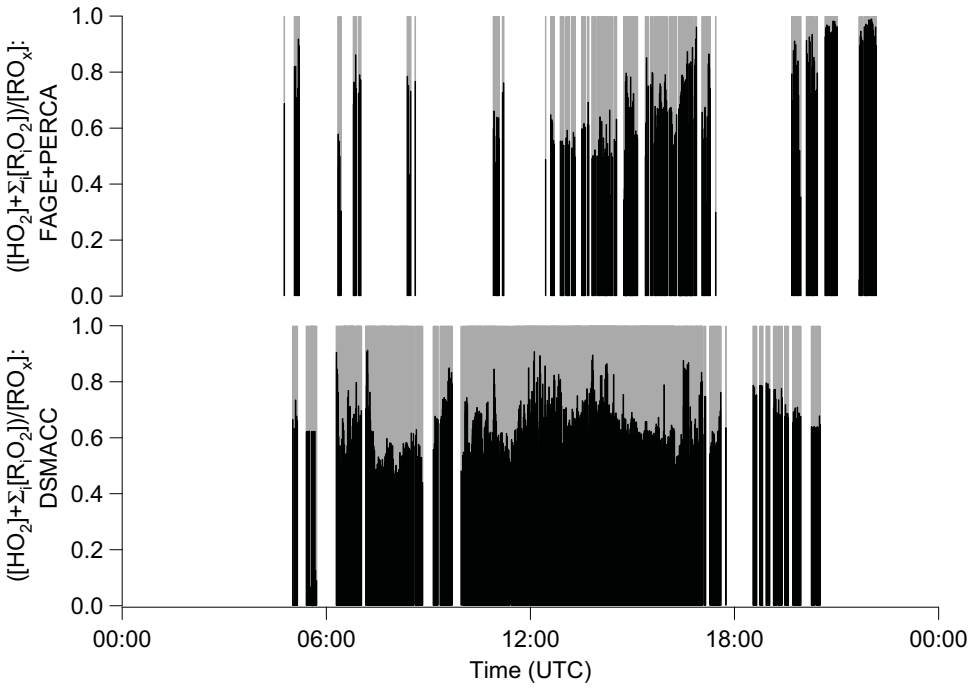

Figure 6.26: Diurnal partitioning of HO_2 and RO_2 measured and modelled during AMMA SOP2, where grey bars represent the fraction of HO_2 and black bars the fraction of RO_2 – (Top) Measurement fractions; (Bottom) Model fractions

of potential measurement biases. Ideally the measurement biases should be constrained by further experimental work. In particular the source of the discrepancy between the chain length humidity dependence observed in the laboratory and not observed in these field measurements could be verified by an *in-situ* measurement of the humidity within the inlets in-flight. If water vapour is condensing or freezing out of the gas phase this may provide an explanation for the lack of a humidity dependence to the PERCA aircraft measurements, the loss of flow at altitudes above the freezing point, and the suspected sampling losses of HO_2. Verification of the pressure and temperature related changes in the chain length is required with respect to those radicals that typically dominate the composition. Also the relative chain length for the dominant radicals is needed to improve interpretation and reduce the biases within this measurement. Although the box model has been used as an aid to interpretation of the measurement, it is not expected to be without some bias, and therefore further experimental characterisation of the measurement performance is essential to reduce the uncertainty within both. In

particular the measured diurnal trend in the partitioning between HO_2 and RO_2 is not well represented by the model, although the absolute values correlate well.

6.4 Ozone production and loss

The photochemical production of ozone can be investigated by calculation of the net ozone tendency, $N(O_3)$:

$$N(O_3) = P(O_3) - L(O_3) \tag{6.23}$$

Here $P(O_3)$ represents the rate of production of ozone, while $L(O_3)$ represents the rate of ozone loss. In the troposphere the only known route to ozone formation is through the photolysis of NO_2. The reaction of NO with ozone produces NO_2 as part of the photostationary state between ozone and NO_x but this represents a null cycle. Additional conversion of NO to NO_2 occurs through reaction with peroxy radicals:

$$HO_2 + NO \rightarrow OH + NO_2 \tag{6.24}$$

$$RO_2 + NO \rightarrow RO + NO_2 \tag{6.25}$$

$$NO_2 + h\nu \rightarrow NO + O(^3P) \tag{6.26}$$

$$O(^3P) + O_2 + M \rightarrow O_3 + M \tag{6.27}$$

The photolysis of NO_2 and the reaction of the photoproduct $O(^3P)$ are part of the photostationary state so have no net effect, and therefore the rate of ozone production is given by:

$$P(O_3) = [NO](k_{6.24}[HO_2] + \sum_i (k_{6.25}[R_iO_2])) \tag{6.28}$$

Beyond the reaction of ozone with NO (part of the photostationary state null cycle), additional ozone loss occurs through reaction with HO_x and photolysis in the presence of water vapour:

$$OH + O_3 \rightarrow HO_2 + O_2 \tag{6.29}$$

$$HO_2 + O_3 \rightarrow OH + 2O_2 \tag{6.30}$$

$$O_3 + h\nu \rightarrow O(^1D) + O_2 \tag{6.31}$$

$$O(^1D) + H_2O \rightarrow 2OH \tag{6.32}$$

The excited $O(^1D)$ atom may be collisionally quenched back to the ground state, and reform ozone through Reaction 6.27. Hence the loss of ozone through photolysis depends on the fraction that yields OH, f:

$$O(^1D) + H_2O \rightarrow 2OH \tag{6.33}$$

$$O(^1D) + M \rightarrow O(^3P) + M \tag{6.34}$$

$$f = \frac{k_{6.9}[H_2O]}{(k_{6.33}[H_2O] + k_{6.34}[M])} \tag{6.35}$$

The rate of ozone loss is given by:

$$L(O_3) = [O_3](f.j(O^1D) + k_{6.29}[HO_2] + k_{6.30}[OH]) \tag{6.36}$$

This treatment neglects other potential loss processes e.g. reaction with alkenes, halogens, NO_3 chemistry, cloud chemistry and dry deposition (Monks, 2005). These processes may represent a minor component of the loss in the free troposphere, but will be particularly significant within the boundary layer. As noted in Chapter 1, Read *et al.* (2008) observed that up to 50% of ozone loss in the tropical Atlantic marine boundary layer can be associated with halogen chemistry. It is possible that halogens may play a significant role in the ozone budget over the Gulf of Guinea. At most this makes $L(O_3)$ a lower limit to the total loss rate, and more representative of the gas phase loss. The net ozone tendency calculated in this way will therefore be biased toward net ozone production; essentially this is the gas phase ozone tendency. The additional loss of ozone through alkene ozonolysis has been calculated using the same VOC dataset (restricted to alkenes) earlier used to calculate OH reactivity (see Section 6.3.1, Tables 6.3 and 6.4), and is shown as a meridional profile in Figure 6.27. The rate coefficients for this calculation were taken preferentially from the latest evaluation of Atkinson *et al.*

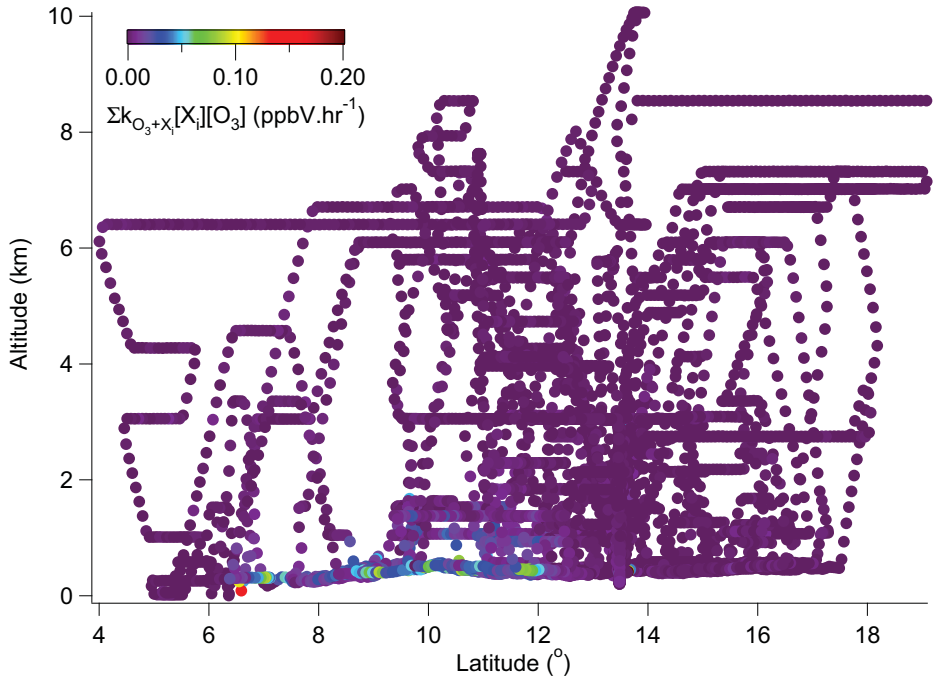

Figure 6.27: Meridional distribution of ozone loss through alkene ozonolysis during AMMA SOP2

(2006), and otherwise from Atkinson & Arey (2003). Of course, as with the calculation of OH reactivity the loss rate through alkene ozonolysis is a lower limit owing to the limitations on the number of VOC's measured.

The ozone production rate has been calculated here from the PERCA RO_x measurements under the assumption that these represent the organic peroxy radical concentration ($[RO_x]_{PERCA} = \sum_i [R_i O_2]$), based on the assessment of Section 6.3. Owing to the unreliability of the NO_x measurements from the FAAM TECO instrument (discussed in Section 5.2.5, Chapter 5) the calculation is restricted to the NO data from the UEA NOxy instrument. This measurement only became available on the last 10 flights of the campaign (B226-B235), while the PERCA could not be run during the middle of the campaign owing to a logistical issue with reagent gas provision. The two instruments then ran concurrently on flights B231-B235B at the end of the campaign which means the dataset available for the calculation of $N(O_3)$ is severely restricted. Where the FAGE HO_2 measurement is also available concurrently this is used to calculate the ozone production rate through Equation 6.28. Otherwise, the

concentration of HO_2 is estimated as being equal to $\frac{0.37}{0.63}[RO_x]_{PERCA}$ in the calculation of the ozone production rate; this is based on the overall composition determined from the results of the DSMACC box model, see Figure 6.25. This estimate (i.e. 37% HO_2 and 63% RO_2) is thought reasonable since in direct comparison of FAGE measured $[HO_2]$ and PERCA measured $[RO_x]$ the $[HO_2]/[RO_2]$ ratio is found to be in the range 1:1 (i.e. 50% HO_2 and 50% RO_2) to 1:9 (i.e. 10% HO_2 and 90% RO_2) typically during daytime, dependent on the level of primary production though ozone photolysis (see Figure 5.18, Chapter 5). The rate coefficient for Reaction 6.25 is taken as that for methyl peroxy, since this represents the majority component of the organic peroxy radical concentration (see Figure 6.25). Since the net ozone tendency requires concurrent values of the ozone production and loss rates, this can only be calculated where there are PERCA measurements. For the calculation of the ozone loss rate, the FAGE HO_2 measurement is used preferentially to represent the HO_2 concentration, however if the FAGE measurement is not available then a fraction of $\frac{0.37}{0.63}[RO_x]_{PERCA}$ is again used to estimate the concentration of HO_2. Owing to the sparsity of the measurements of OH, the sensitivity of ozone loss owing to reaction with OH is estimated by using the upper and lower limits of its concentration derived from the FAGE measurements, i.e. 3.0×10^7 molecule cm^{-3} and 6.9×10^5 molecule cm^{-3} (the lower limit estimated from the minimum median value determined from hourly averages) respectively. Rate coefficients for the gas phase reactions involving O_x, HO_x and NO_x only have been taken from the latest evaluation of Atkinson *et al.* (2004). Rate coefficients for the gas phase reactions involving organic species have been taken from the latest evaluation of Atkinson *et al.* (2006). The additional loss through alkene ozonolysis is considered separately using the values calculated and presented in Figure 6.27. The ozone tendency (calculated for [OH]=6.9×10^5 molecule cm^{-3}, 1.0×10^7 molecule cm^{-3} and 3.0×10^7 molecule cm^{-3}), rate of ozone production and rate of ozone loss are presented as a diurnal (restricted to the period 06:00-15:00 UTC owing to the crossover in data coverage), with the concurrent NO concentration for comparison in Figure 6.28. The net ozone tendency (calculated for [OH]=1.0×10^7 molecule cm^{-3}), rate of ozone production, rate of ozone loss, and distribution of NO

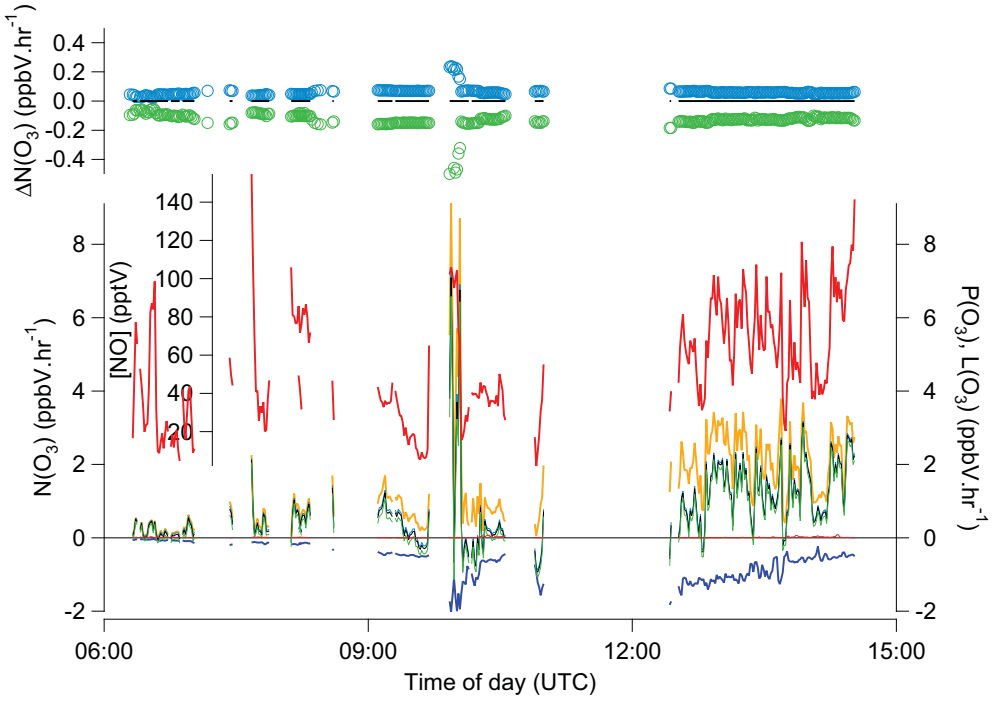

Figure 6.28: Diurnal variation of net ozone tendency during AMMA SOP2 – (Top plot) Difference in $N(O_3)$ dependent on [OH] relative to [OH]=1.0×10^7 molecule cm^{-3}: (Light blue circles) $N(O_3)$([OH]=6.9×10^5 molecule cm^{-3})–$N(O_3)$([OH]=1.0×10^7 molecule cm^{-3}), (Green circles) $N(O_3)$([OH]=3.0×10^7 molecule cm^{-3})–$N(O_3)$([OH]=1.0×10^7 molecule cm^{-3}). (Central plot): (Red) [NO] (pptV). (Bottom plot): (Light blue) $N(O_3)$([OH]=6.9×10^5 molecule cm^{-3}), (Black) $N(O_3)$([OH]=1.0×10^7 molecule cm^{-3}), (Green) $N(O_3)$([OH]=3.0×10^7 molecule cm^{-3}), (Yellow) $P(O_3)$([OH]=1.0×10^7 molecule cm^{-3}), (Blue) $L(O_3)$([OH]=1.0×10^7 molecule cm^{-3}).

concentration are presented as a meridional profile in Figure 6.29.

Inspection of the diurnal trend in Figure 6.28 shows the net ozone tendency calculated with either the lower or upper estimate of [OH] are near indistinguishable. An intermediate concentration of 1.0×10^7 molecule cm^{-3} was chosen for comparison, and differences in the net ozone tendency calculated are shown to be of the order 0.1 ppbV hr^{-1} except in cases where $N(O_3)$ significantly enhanced. The relative error introduced dependent on the concentration of OH is not significant and therefore the intermediate value is used in the following assessment. Comparing the observed diurnal and meridional variations in the calculated ozone tendency with the additional loss through alkene ozonolysis, the maximum observed loss through alkene ozonolysis is 0.2 ppbV hr^{-1}, though on average it is con-

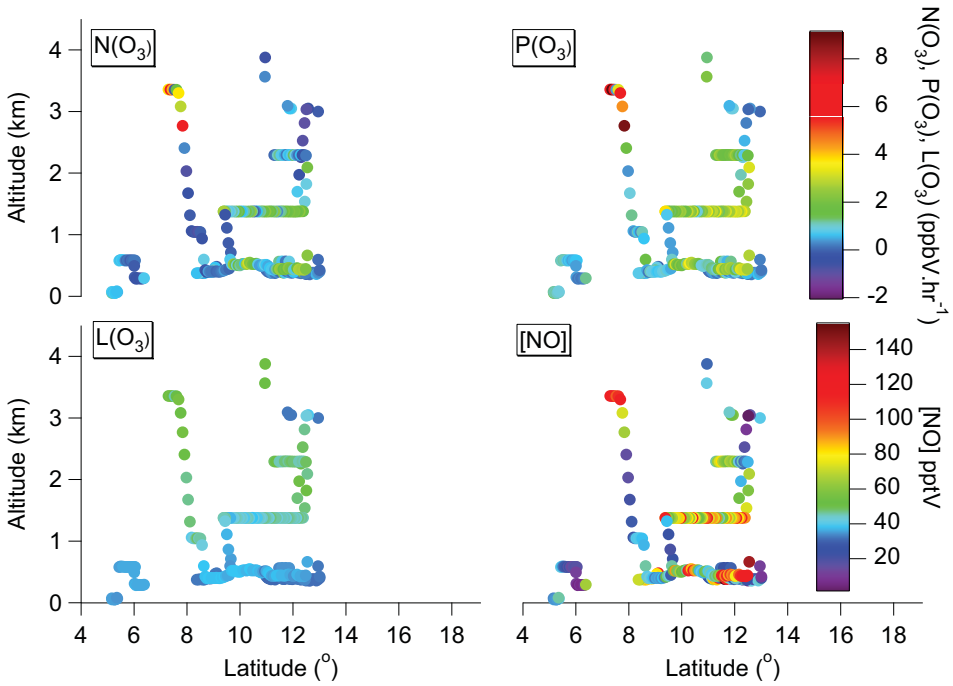

Figure 6.29: Meridional variation of ozone tendency during AMMA SOP2 – (Top left) $N(O_3)$, (Top right) $P(O_3)$, (Bottom left) $L(O_3)$, (Bottom right) [NO].

siderably lower at 3.7 pptV hr^{-1}. From the meridional profile of the ozone alkene loss rate it is clear that the impact is limited to points close to surface sources of alkenes (anthropogenic and biogenic), with the highest value occurring in the downwind plume of Niamey, while other enhancements are associated with coastal city plumes (Lagos, Cotonou) and the forested regions where biogenic emissions of isoprene dominate. Of the points where the net ozone tendency has been calculated, the maximum loss associated with alkene ozonolysis is 0.09 ppbV hr^{-1} and on average 0.01 ppbV hr^{-1}, while that calculated through Equation 6.36 is at most 2.02 ppbV hr^{-1} and on average 0.63 ppbV hr^{-1}. Considering the level of uncertainty introduced by estimation of [OH] is of the order the maximum additional ozone loss from alkene ozonolysis, the impact of alkene ozonolysis is clearly of low significance.

The highest level of net ozone production calculated (7.1 ppbV hr^{-1}) is associated with a biomass burning plume of Central African origin intercepted around 7^oN at 2.7-3.3 km altitude on flight B231 on the 13 August 2006. These plumes are a recurrent feature observed during the period of the WAM

in 2006, and their transport is thought to be controlled by the strength and position of the southern hemispheric component of the African Easterly Jet (AEJ-S) (Mari *et al.*, 2008). The 13 August lies within an "active phase" of the AEJ-S, during which advection of biomass burning plumes out over the Atlantic ocean was efficient in the mid-troposphere (Mari *et al.*, 2008). Acetonitrile has been used as a tracer to associate air masses with biomass burning (see Figure 5.30, in Section 5.2.5, Chapter 5) and the origin of this air mass has been confirmed through back trajectories calculated using the HYSPLIT trajectory model (Draxler & Rolph, 2003) presented here in Figure 6.30, and linked to the biomass burning region of Central Africa through MODIS firemaps (see Figure 5.1, in Section 5.1.2, Chapter 5) and the OMI aerosol index product for the 13 August 2006 (see Figure 6.30). A timeseries of the PERCA RO_x measurements, measured and modelled photolysis rates from flight B231 is shown along with ozone in Figure 6.31.

This particular plume is notable in that it represents the most photochemically active air mass observed during the campaign, as indicated by the highest persistent concentrations of many tracers. It is also important in that it provides an example of the long range transport of biomass burning influenced air masses into the WAM during the monsoon season. The plume was intercepted on two occasions; peak ozone concentrations of 125.5 ppbV were observed in the first interception of the plume, and mean concentrations of 75.6 ppbV and 85.7 ppbV in the first and second interceptions respectively; this compared to a campaign average of 39.3 ppbV. CO peaked at 449.4 ppbV in the first interception and mean concentrations of 255.1 ppbV and 258.9 ppbV were observed in the first and second interceptions respectively, compared to a campaign average of 112.9 ppbV. The highest levels of peroxy radicals measured by the PERCA during SOP2 were also associated with this plume where RO_x concentrations spiked at 205 pptV. This concentration is well outside the norm, and although the radical concentrations are believed to be high and variable, the rapidly changing ozone background may have induced some of the measured variability through inaccuracy in the PERCA background

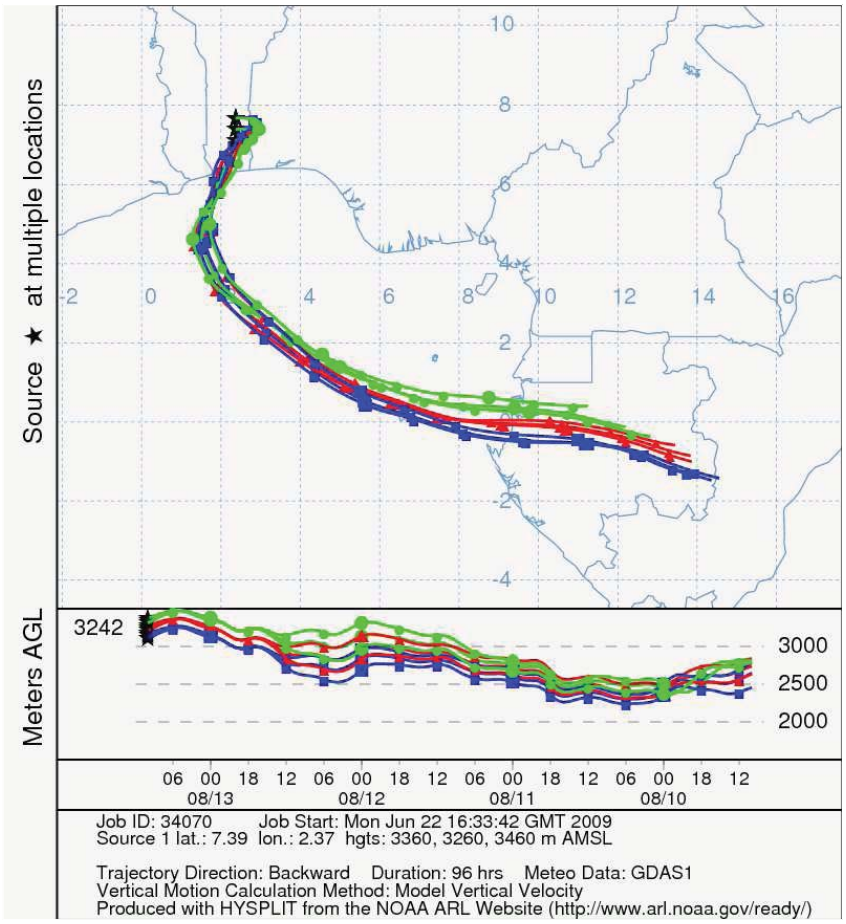

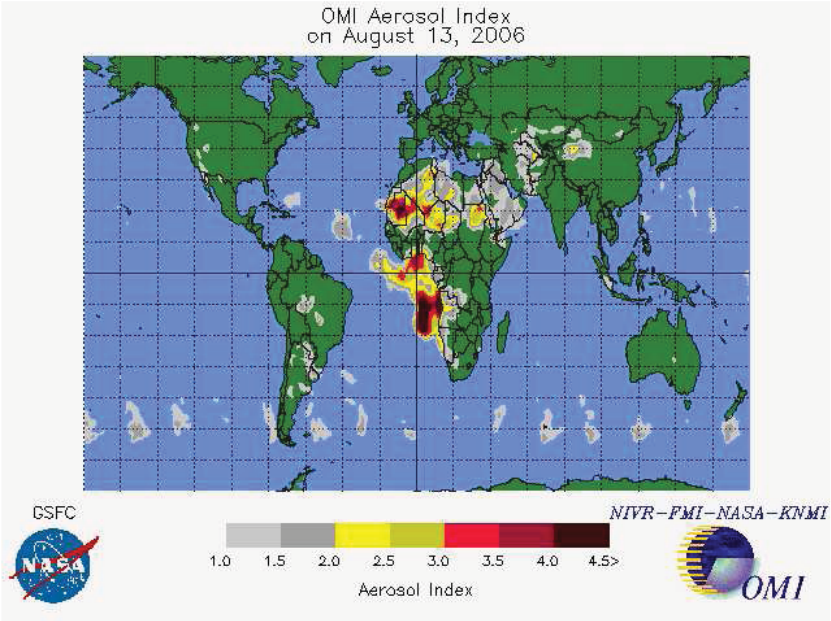

Figure 6.30: (Top) HYSPLIT back trajectories for biomass burning plume observed during flight B231, (Bottom) OMI aerosol index for 13 August 2006

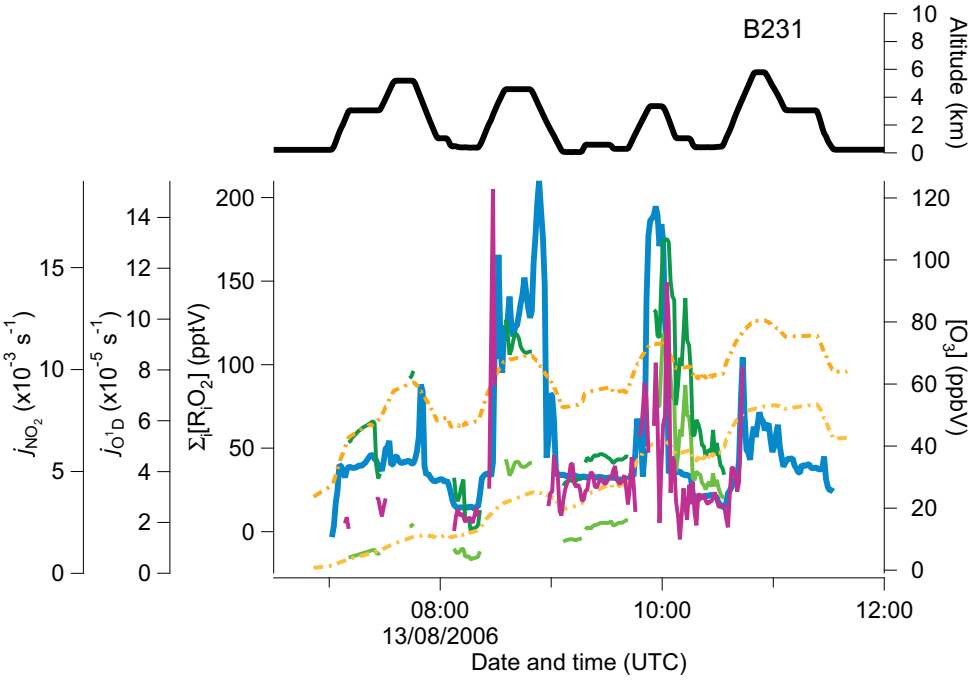

Figure 6.31: Timeseries from flight B231 showing biomass burning plume interception – Measured peroxy radicals without humidity correction (dark pink), measured (light green) and modelled (dashed light yellow) j_{O^1D}, measured (dark green) and modelled (dashed dark yellow) j_{NO_2} and altitude (black), ozone (blue)

subtraction (see discussion of Section 3.5, Chapter 3), hence the absolute RO_x concentration may be in question. Still, the variability in the PERCA measurement correlates very well with the variability in the ozone and the measured photolysis rates (which were both strongly enhanced and attenuated inside the plume, and attenuated below the plume). Also the dynamic range of these driving variables is similar to the change in RO_x observed which may provide confidence in the values.

On the first interception the aircraft profiled upward through the plume beyond the altitude where the PERCA was operational, producing the initial spike in $[RO_x]$ on passing. The instrument recovered on descent where the aircraft then flew out over the Gulf of Guinea before profiling up and through the plume on the return leg. On the second interception the aircraft flew within the plume for approximately 10 minutes; therefore the concentrations measured here are more representative (though still variable), averaging approximately 70 pptV. $N(O_3)$ could only be calculated on the last interception and so should be subject to less uncertainty (at least in the mean). The German DLR-Falcon aircraft also intercepted a related biomass burning plume at the coast of Ghana on the 13 August 2006 and RO_x concentrations of up to 60-70 pptV were reported by Andres-Hernandez *et al.* (2009), consistent with the observations here. The high net ozone production rates calculated (average of $\sim$3.7 ppbV hr^{-1}) are distinct from all others observed, reflecting both the high radical concentrations but also concurrent high NO; notably these air masses were also very dry which will reduce the loss of ozone through photolysis. The highest persistent levels of PAN observed throughout the campaign were also associated with this plume, peaking at 1386 pptV on the first interception, with mean levels of 1062 pptV and 576 pptV associated with the two interceptions of the plume. Compared to the campaign average level of 7.1 pptV, this suggests considerable levels of peroxyacetyl radical production on transport and oxidation of the plume, with much being sequestered as PAN at the temperatures characteristic of the plume altitude (lifetimes of the order 10 hours to more than 2 days). The strong temperature dependence of the lifetime also explains the gradient in PAN concentration increasing

with altitude within the plume. The thermal decomposition of PAN is effectively determined by the availability of NO through which the peroxyacetyl radical yielded on decomposition may react to yield $CH_3C(O)O$ rather than reacting with NO_2 to reform PAN. $CH_3C(O)O$ rapidly decomposes leading to further radical production (Finlayson-Pitts & Pitts, 2000):

$$CH_3C(O)OO + NO_2 + M \leftrightarrow CH_3C(O)OONO_2 + M \quad (6.37)$$

$$CH_3C(O)OO + NO \rightarrow CH_3C(O)O + NO_2 \quad (6.38)$$

$$CH_3C(O)O \rightarrow CH_3 + CO_2 \quad (6.39)$$

The reformation of PAN versus the formation of further peroxy radicals is determined by the relative rates of reactions 6.37 and 6.38 and the relative concentrations of NO_2 and NO. Using the temperature dependencies of the rate constants from Atkinson *et al.* (2006), the ratio of the rate constants $k_{6.37}/k_{6.38}$ is in the range 0.45-0.48 for all altitudes, and therefore the radical yield depends largely on the relative concentrations of NO_2 and NO. There are limited NO_2 data from the NOxy instrument for this flight and the TECO NO_2 data are contaminated by NO_y, which is particularly apparent for this flight owing to the high levels of PAN (as discussed in Section 5.2.5, Chapter 5); hence, it is not possible to quantify the yield of radicals from this channel. Still the high concentration of PAN suggests that it is acting as a reservoir for both radicals and NO_x in this plume, and provides an indication of an aged air mass. The correlation of the measured RO_x concentration with the variability in photolysis rates suggests that primary production is driving the radical concentration. Further inspection of the OH reactivity profiles and in particular that of the relative contribution of CO to the total reactivity in Figure 6.11 shows that CO dominates in these biomass burning plumes, such that the reaction of OH with CO to yield HO_2 will dominate radical production. In turn, the calculated net ozone tendency is here driven by the variations in the RO_x concentration.

Examining the meridional trend in Figure 6.29 it is apparent that in the absence of [NO] above a particular level the tendency is for net ozone destruction, indicative of a NO_x limited regime. By

latitude and at lower altitudes there exists a gradient with the tendency for net ozone production increased in the north, where enhanced concentrations of NO are observed near the surface. These concentrations are increased in the afternoon and therefore the ozone tendency is also greater at this time of day in Figure 6.28. Referring also to the diurnal trend in measured RO_x and HO_2 (see Figures 6.16 and 6.17) there is an asymmetry in the concentrations of peroxy radicals with higher radical production through secondary sources occurring later in the day. In particular, the ratio of organic to inorganic peroxy radicals increases. The combination of enhancements in NO, with the asymmetry in radical concentrations later in the day owing to secondary production drives the increase in $N(O_3)$. Furthermore, while organic peroxy radicals are maintained later in the day, ozone photolysis and linked to this $[HO_2]$ fall more rapidly, so while the rate of ozone loss falls the rate of ozone production increases, and enhances the net ozone production tendency. Except on the interception of the biomass burning plume on flight B231, no correlation is observed between NO and the anthropogenic tracers CO, benzene and acetonitrile (correlation coefficients of 0.19, 0.31 and 0.20 respectively) for the dataset used to calculate the net ozone tendency. This suggests the enhancements in NO concentration near the surface may be related to biogenic soil emissions; a similar justification was used in the assessment of soil NO_x emissions during AMMA SOP2 reported by Stewart *et al.* (2008). The trends apparent by latitude, if associated with biogenic soil emissions are likely to be transient and spatially variable since as proven by Stewart *et al.* (2008), they are modulated by the spatial distribution of rainfall. In general, the expectation may then be for net ozone production given sufficient NO, and enhancements in the tendency for ozone production in the afternoon owing to the observed diurnal cycle in the ratio of organic to inorganic peroxy radicals.

As discussed, the diurnal and meridional variations in the calculated net ozone tendency are well correlated with NO, suggesting a NO_x limited regime. A plot of net ozone tendency (including additional loss from alkene ozonolysis) versus NO demonstrates that these quantities are near linearly

related, proving that at least in terms of this sparse dataset, NO_x is typically driving the ozone photochemistry (Figure 6.32). The outliers represented by the high net ozone production are those associated with the biomass burning plume and therefore represent a different regime, however the observations are too few to draw any significant conclusions. A linear fit to the net ozone tendency versus NO plot allows an estimate of the balance point between net ozone production and loss. The net ozone tendency is related to the NO concentration by: $N(O_3) = 0.024(\pm0.001)[NO](pptV) - 0.546(\pm0.086)$, with a correlation coefficient $r = 0.72$ indicating a good degree of correlation. From this the balance point is derived to be 22.3($\pm$3.75) pptV, such that only low concentrations of NO are required for gas phase ozone production to occur. The model assessment of Saunois *et al.* (2009) derives a threshold of 60 pptV of NO_x and 15 pptV of NO over vegetation and 100 pptV of NO_x and 30 pptV of NO north of 12^oN, and therefore is consistent with the value derived here. The gradient by latitude observed in the ozone concentration at the surface is attributed by Saunois *et al.* (2009) to surface deposition to trees over the forested regions in the south in combination with the NO_x limited ozone production regime. Increased surface emissions of NO in the north then dictate the enhanced levels of ozone observed in the north over the Sahel. The assessment here is consistent with the modelled trends of Saunois *et al.* (2009), however the levels of ozone production calculated here are greater owing to these values being instantaneous *in-situ* rates while those reported by Saunois *et al.* (2009) are averaged over a whole day and the coarse spatial resolution of the model.

6.5 Chapter 6 Summary

This chapter has presented an analysis of the measurements made during the AMMA SOP2 campaign for this thesis. The measurements of photolysis rates were discussed in reference to the known non-linearities in the calibration factors (refer to Section 4.2, of Chapter 4), in Section 6.1. With these potential biases in mind trends identified on initial inspection (see Figures 5.7-5.17 of Chapter 5) have

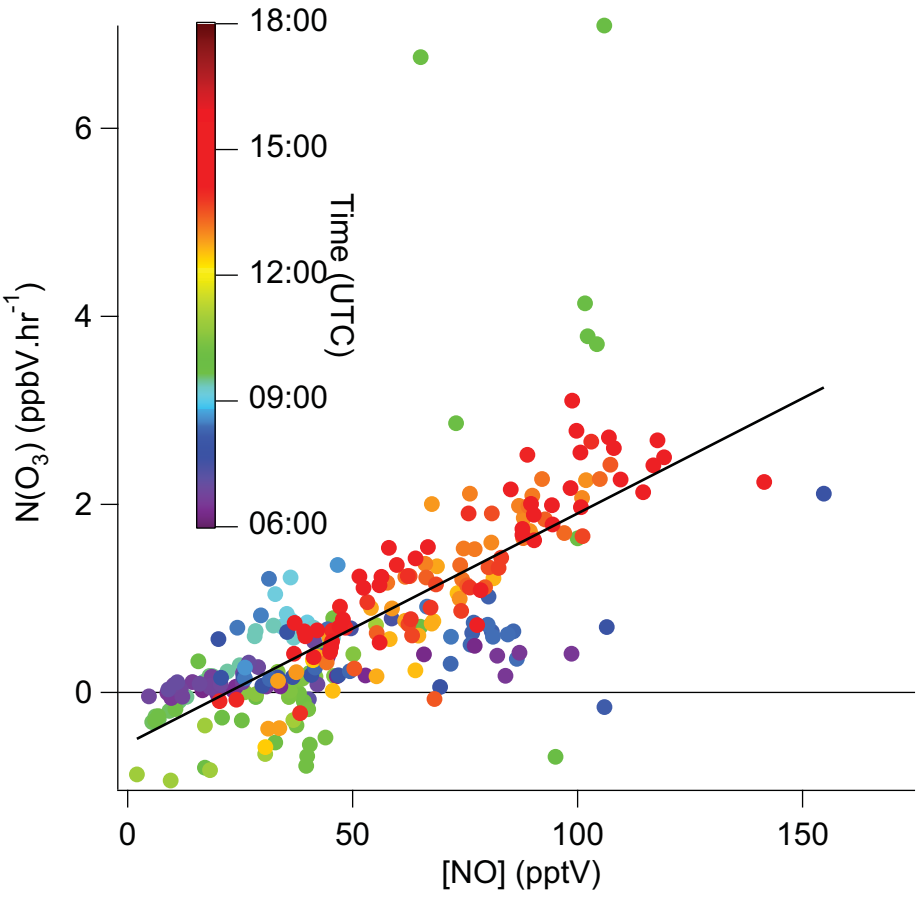

Figure 6.32: Net ozone tendency versus NO

been explained by altitude, ozone column and SZA in comparison to results from the TUV model appropriate to "clear sky" conditions. By consideration of the weighting of the calibration factors for the j_{O^1D} filter radiometers it has been shown that better agreement between modelled and measured photolysis rates is likely above 4 km altitude. The structure of the monsoon has also been used to explain the observed trends (attenuation of the actinic flux at low altitude and high SZA), and was identified as a driver for differences in photochemistry within the monsoon environment. No significant bias has been observed to be introduced by the estimation of the upwelling component of the j_{O^1D} signal (for details see Section 4.3.1, of Chapter 4), except in cases where the SZA becomes large, where the absolute error introduced is unlikely to be significant photochemically.

In Section 6.2 the measurements of radicals performed during SOP2 using the University of Leicester PERCA 4 instrument are compared to the results of a detailed photochemical box model (DSMACC). The aim of the comparison has been to attempt to explain differences between model and measurement in terms of the understood biases in the PERCA measurement, and in turn identify any failings in the model. The major known potential biases in the PERCA measurement technique have been considered in detail in Chapters 2 and 3 of this thesis. Equation 2.20 (reproduced in this chapter as Equation 6.1) is key to the interpretation of the measured RO_x concentration by the PERCA technique. The measurement biases are summarised and a number of potential causes for bias in the box model are proposed. The key findings of the assessment can be summarised here: The observed humidity dependence of the measurement sensitivity is not found in the SOP2 results; The measurements correlate considerably better with the modelled [RO_2]; The dominance of CH_3O_2 as a component of [RO_2] masks much of any further bias related to varying sensitivity to individual R_iO_2; Altitude bias in the measurement can be largely explained through the pressure and temperature dependence of the chain length for CH_3O_2 which weights the measurement response. An explanation for the lack of a humidity dependence has been derived based on the weight of evidence which could

also explain the loss in sampling flow at altitude, and the apparent insensitivity to HO_2. Near parity in the FAGE measurements of HO_2 and PERCA measurements of RO_x (without humidity correction) during the midday, while the PERCA measured significant nighttime signals in RO_x in the absence of HO_2 is seen as the first indication of a reduced sensitivity to HO_2 (see e.g. Figure 5.18 of Chapter 5); and also a diurnal trend in the partitioning between inorganic and organic peroxy radicals. The preferential loss of HO_2 in the presence of condensed water, the lack of a trend in the PERCA measurement with relative humidity, and the loss of sample flow at altitudes corresponding to the freezing point, all suggest the effective removal of water from the gas phase on or prior to sampling by condensation/sublimation leading to removal of HO_2 before the reaction zone. This interpretation requires experimental verification and further experimental work is suggested (see p301).

In section 6.3 the radical composition is discussed both qualitatively and quantitatively in terms of the steady state production and loss of RO_x, VOC reactivity with respect to OH (Section 6.3.1), the trends in measured radical concentrations (Section 6.3.2) and the modelled composition (Section 6.3.3). VOC reactivity is found to be dominated by isoprene in an absolute sense, though its direct influence is restricted to the forested regions by day. Enhancements related to anthropogenic emissions are related to the plumes from Niamey and the coastal cities of Lagos and Cotonou, and also long range transport into the monsoon region of biomass burning plumes. The derived contribution of acetaldehyde to the VOC reactivity within anthropogenic influenced air masses is reflected by an increased proportion of the acetylperoxy radical within the modelled composition of these air masses. The background CO and methane are found to dominate the reactivity to OH outside the direct influence of biogenic and anthropogenic emissions. Related changes in radical composition are inferred from this. Section 6.3.2 discusses the measured trends. A strong diurnal is present in both HO_2 and RO_x even though the measurements represent composites over the whole region sampled, and persistent signals are observed at night, particularly significant in RO_x (RO_2). These trends are explained through the secondary

production of radicals which have an afternoon peak; particular highlights are the enhanced radical concentrations associated with biomass burning plume interceptions and the observed enhancement of measured RO_x at night collocated with the nocturnal transport and oxidation of isoprene within the monsoon flow. Self- and cross- reaction of peroxy radicals control their concentration and partitioning under low NO_x conditions, and where primary production is limited; this is offered as an explanation of the diurnal trend in $[HO_2]/[RO_2]$. The proposed recycling of OH from isoprene oxidation, as reported by Lelieveld *et al.* (2008), Peeters *et al.* (2009), Silva *et al.* (2010) and references therein, also offers a potential explanation of the persistence of RO_2, HO_2 and potentially OH at night. Nitrate radical chemistry would modify the $[HO_2]/[RO_2]$ partitioning in favour of HO_2, so the relative enhancement of RO_2 is seen as evidence that nitrate radical chemistry is limited. The modelled composition discussed in Section 6.3.3 follows the expected trends, and variation in modelled $[RO_2]$ versus the PERCA measurement can be explained in terms of composition by air mass and time of day. In particular, the model does not predict the strong diurnality in $[HO_2]/[RO_2]$ partitioning that has been observed.

The ozone balance has been discussed in Section 6.4, and investigated through the calculation of the net ozone tendency. The additional impact of alkene ozonolysis has been found to be insignificant to the net ozone tendency under most conditions, and the net ozone tendency was found to be relatively insensitive to the concentration of OH which was set to a constant value owing to the sparsity of the data coverage. The particular case of the biomass burning plume interception of the 13 August 2006 on flight B231 has been discussed in some detail, representing the most photochemically active air mass sampled throughout SOP2 and an example of this type of long range transport into the WAM. With the exception of this plume, this limited assessment suggests that the WAM is predominantly NO_x limited in terms of the ozone tendency. In particular the diurnal changes in the partitioning of $[HO_2]/[RO_2]$ enhance the tendency for net ozone production in the presence of NO. No correlation was observed between NO and anthropogenic tracers (excepting the biomass burning plume) and therefore

the observed NO increase in the afternoon is thought to have a biogenic source. The balance point for net ozone production is found to be 22.3($\pm$3.75) pptV similar to the model assessment of Saunois *et al.* (2009). The low level meridional gradient in ozone by latitude has been attributed to the loss of ozone by deposition over the forested regions where the surface source of NO is also reduced, while in the north over the Sahel surface deposition is less while NO emission is enhanced. The diurnal changes in $[HO_2]/[RO_2]$ observed in this work will likely modulate the ozone balance, while soil emissions of NO limit the tendency for ozone production. The nighttime transport of ozone precursors at low level in the monsoon flow will also contribute to the north south gradient.

Chapter 7

Summary and Conclusions

This chapter summarises the contents of this thesis, and brings together the results and conclusions drawn from it. The aim is to provide the link between the various threads of work, propose more general conclusions and identify areas requiring further research and development.

7.1 Summary of chapters

Chapter 1 (pp1-16) provides context to the measurements and fieldwork described in later chapters in terms of relevant aspects of the chemistry, structure, composition and dynamics of the atmosphere. Chapter 2 (pp17-47) presents an overview of techniques used for the measurements of peroxy radicals in the atmosphere. Particular attention is given to the technique of chemical amplification by which peroxy radicals were measured during the AMMA SOP2 field campaign (chapters 5 and 6), highlighting the known sources of potential bias with the technique, to aid the understanding of these measurements. Chapter 3 (pp48-132) then describes the experimental and analytical work carried out for the calibration and characterisation of the University of Leicester PERCA 4 instrument. Beyond standard calibration work (chain length and NO_2 sensitivity) significant results include: characterisation and analytical interpretation of the chain length dependency on humidity; identification of a

humidity dependence to the luminol chemiluminescence method for NO_2 detection; derivation of the HO_2 and CH_3O_2 chain length dependency on reagent gas concentration, temperature and pressure by means of an inlet chemistry model; derivation of a method for online calibration of the NO_2 sensitivity of the LMA-3 Scintrex under ambient measurement conditions.

Chapter 4 (pp133-180) provides an overview of the theory and application of measurements of photolysis rates. The focus of this chapter is the technique of filter radiometry by which the photolysis rates of ozone (j_{O^1D}) and NO_2 (j_{NO_2}) were measured during the AMMA SOP2 field campaign (Chapters 5 and 6), to aid quantification of the measurements made in the field. The calibration of these instruments is then described and particular attention is given to understanding bias introduced owing to the non-linearity of the calibration function of the j_{O^1D} filter radiometers as a function of temperature, ozone column density and solar zenith angle (SZA). An alternative cross calibration technique to determine the spectral sensitivity of a j_{O^1D} filter radiometer is proposed which would make possible the correction of this measurement for SZA and ozone column. Further work includes the description of instrumental and operational factors affecting the aircraft measurements made during AMMA SOP2, and the derivation and assessment of a procedure to estimate upwelling j_{O^1D} where the lower position j_{O^1D} filter radiometer failed.

Chapter 5 (pp181-248) provides an overview of the background to the African Monsoon Multidisciplinary Analysis (AMMA) project, in particular its motivation and organisation into nested periods and scales of observation. The field work in this thesis concerns the Special Observing Period 2 (SOP2) during the peak of the West African Monsoon (WAM), and therefore this chapter presents information relevant to this season (e.g. emissions, dynamics) and data collected from instrumentation on board the Natural Environment Research Council/UK Met Office (NERC/UKMO) BAe 146-300 atmospheric research aircraft. Particular highlights include the significant dataset of measurements of radicals (HO_x, RO_x), the first of their kind over Africa where a diurnal trend in the partitioning

between organic and inorganic peroxy radicals is observed. Satellite vegetation indices were found to well represent the distribution of biogenic VOC concentrations, these indices also tracked the growth of vegetation with the progression of the monsoon; differences between the distributions of biogenics and vegetation indices are interpreted as relating to the successional gradient in surface vegetation cover by latitude and the diurnality of biogenic emissions. Tracers of dynamics were found to relate the spatial distributions of longer lived chemical tracers to the monsoon structure; a significant highlight was the identification of gradients by altitude and latitude in the ratio of isoprene concentration to that of its oxidation products methyl vinyl ketone and methacrolein which can be understood through the characteristic diurnal cycle of the monsoon flow. Selected chemical tracers measured on board the BAe-146 were used to identify particular air masses and emission sources within a meridional view of the monsoon. Particularly the non-correlation of ozone with CO within air masses outside the influence of anthropogenic emissions was observed. The persistent observation of the "anticorrelation" of ozone and CO by latitude within SOP2 is rather a reflection of the asymmetry of the spatial distribution of their concentrations and not a direct relationship owing to chemistry. This is caused by the meeting of distinct air masses (the monsoon layer and Saharan Air Layer) related to the large scale structure of the WAM, with characteristically different chemical composition. Anthropogenic influenced air masses were distinct by a positive correlation between ozone and CO, and strong positive correlation is observed between ozone and CO in the biomass burning plumes and the Lagos plume; the gradient is greater for the biomass burning plumes indicating enhanced ozone production relative to the Lagos plume. Acetonitrile clearly identified those plumes influenced by biomass burning, and benzene those with an anthropogenic influence other than biomass burning. Broadly distributed boundary layer enhancements of NO_x are thought to be related to soil emissions, coincident enhancements of ozone and the demonstrated transport of VOC's within the monsoon flow is proposed to provide the potential for significant ozone production. A strong correlation of CO and benzene in the monsoon layer is found, evidence for the low level transport of longer lived anthropogenic emissions

from coastal cities (particularly Lagos) onto the continent with the monsoon flow. The correlation does not explain all of the variance and therefore along with the strong emissions of biogenic VOC's and the depletion of ozone, there is likely an additional biogenic source of CO, through the ozonolysis of alkenes (e.g. Rockmann *et al.* (1998)) or OH initiated oxidation of terpenes (e.g. Miyoshi *et al.* (1994)). The relationship derived between boundary level benzene and CO allowed the calculation of the background concentration of CO, calculated to be $[CO]_{bg}$=80.67±1.98 ppbV. Ozone deposition, alkene ozonolysis and the reduced emissions of NO_x are suggested as contributory to the depletion of ozone in the biogenic source regions.

Chapter 6 (pp249-320) is focused on the analysis and interpretation of the observations of photolysis rates and peroxy radicals from SOP2. The interpretation of the trends in measured photolysis rates is discussed through comparison to "clear sky" photolysis rates derived from the Tropospheric Ultraviolet and Visible (TUV) Radiation Model (Madronich, 1987, Madronich & Flocke, 1998), and from understanding the potential biases associated with the non-linearity of the calibration function of the j_{O^1D} filter radiometers evaluated in Chapter 4. Highlights from this include the distinction of a clear spatial trend in both the photolysis rates of ozone and NO_2 when compared to the "clear sky" model results, whereby the actinic flux is attenuated at lower altitudes (≤4 km) and high SZA's, which is thought related to the influence of cloud and aerosol characteristic of the monsoon. This was identified as a potential driver for differences in photochemistry within the monsoon environment. Consideration of the weighting of the calibration factors for the j_{O^1D} filter radiometers has shown that better agreement between modelled and measured photolysis rates is likely above 4 km altitude. The estimation of the upwelling component of the j_{O^1D} signal where the measurement was unavailable was not seen to introduce significant bias except in the cases where the SZA becomes large, and where the absolute error introduced is unlikely to be significant photochemically.

A comparison of the concentrations of peroxy radicals measured during AMMA SOP2 to those calcu-

lated from an observationally constrained photochemical box model (DSMACC), is used to understand the influence (or lack) of potential biases in the PERCA measurements while also considering the potential for failings in the model. Key findings include: No humidity bias is found in contrast to that observed in the laboratory (Chapter 3); The PERCA measurements correlate and scale best with the model when considered only to be measuring the sum of organic peroxy radicals (RO_2); Dominance of methyl peroxy in [RO_2] masks most bias (excepting humidity which is not observed) related to varying sensitivity to individual R_iO_2; Altitude bias is largely explained through the pressure and temperature dependence of the chain length for CH_3O_2 which weights the measurement response; Near parity in the FAGE measurements of HO_2 and PERCA measurements of RO_x (without humidity correction) during the midday, while the PERCA measured significant nighttime signals in RO_x in the absence of HO_2, also indicates a reduced sensitivity of the PERCA to HO_2 and a diurnal trend in the partitioning between inorganic and organic peroxy radicals; Loss of sample flow occurs at altitudes corresponding to the freezing point. A proposal is made to interpret the PERCA measurements based on this combined evidence: The preferential loss of HO_2 in the presence of condensed water e.g. Mihele *et al.* (1999), Green *et al.* (2003), the lack of a trend in the PERCA measurement with relative humidity, and the loss of sample flow at altitudes corresponding to the freezing point, all suggest the effective removal of water from the gas phase on or prior to sampling by condensation/sublimation further leading to removal of HO_2 before the reaction zone.

The VOC reactivity with respect to OH, observed trends in measured radicals, and modelled radical composition have been used to discuss radical production and loss and composition for the West African Monsoon during the SOP2 period. Isoprene is found to dominate VOC reactivity to OH in an absolute sense but owing to its short lifetime, its *direct* influence is observed to be largely restricted to the forested regions *by day* where its emissions are strongest. VOC reactivity was also enhanced within anthropogenic related plumes associated with the urban plume of Niamey and coastal

cities of Lagos and Cotonou. Oxygenated VOC's (primarily acetaldehyde and formaldehyde) make a significant but low contribution to the total OH reactivity overall, but contribute most significantly to the reactivity of anthropogenically influenced plumes along with CO. Exceptionally acetaldehyde dominates the reactivity within the Lagos plume. Long range transport of biomass burning plumes into the monsoon region is observed, and the reactivity to OH within these plumes is dominated by CO. The background CO and methane are found to dominate the reactivity to OH outside the direct influence of biogenic and anthropogenic emissions. Related changes in radical composition are inferred from the distribution of VOC reactivity which are corroborated by the box model output. A strong diurnal is observed in the measured peroxy radical concentrations despite them being composite views from over the whole region sampled, which suggests a reasonably coherent picture. Persistent nighttime radical concentrations have been observed, particularly in RO_2, suggesting oxidation chemistry remains active at night. These temporal trends may be explained through the secondary production of radicals which has an afternoon peak. Particular highlights of the meridional distributions are the enhanced radical concentrations associated with biomass burning plume interceptions, and the observed enhancement of measured RO_x at night collocated with the nocturnal transport and oxidation of isoprene within the monsoon flow. Self- and cross-reaction of peroxy radicals control their concentration and partitioning under low NO_x conditions, and where primary production is limited; this is offered as an explanation of the diurnal trend in $[HO_2]/[RO_2]$. The proposed recycling of OH from isoprene oxidation, as reported by Lelieveld *et al.* (2008), Peeters *et al.* (2009), Silva *et al.* (2010) and references therein, also offers a potential explanation of the persistence of RO_2, HO_2 and potentially OH at night. Nitrate radical chemistry would modify the $[HO_2]/[RO_2]$ partitioning in favour of HO_2, so the relative enhancement of RO_2 is seen as evidence that nitrate radical chemistry is limited. The DSMACC box model does not predict the strong diurnality in $[HO_2]/[RO_2]$ partitioning that has been observed, and most significantly does not predict the absolute concentrations of either RO_2 or HO_2 at night as illustrated here in Figure 7.1. The combination of the active monsoon flow at night, low concentrations

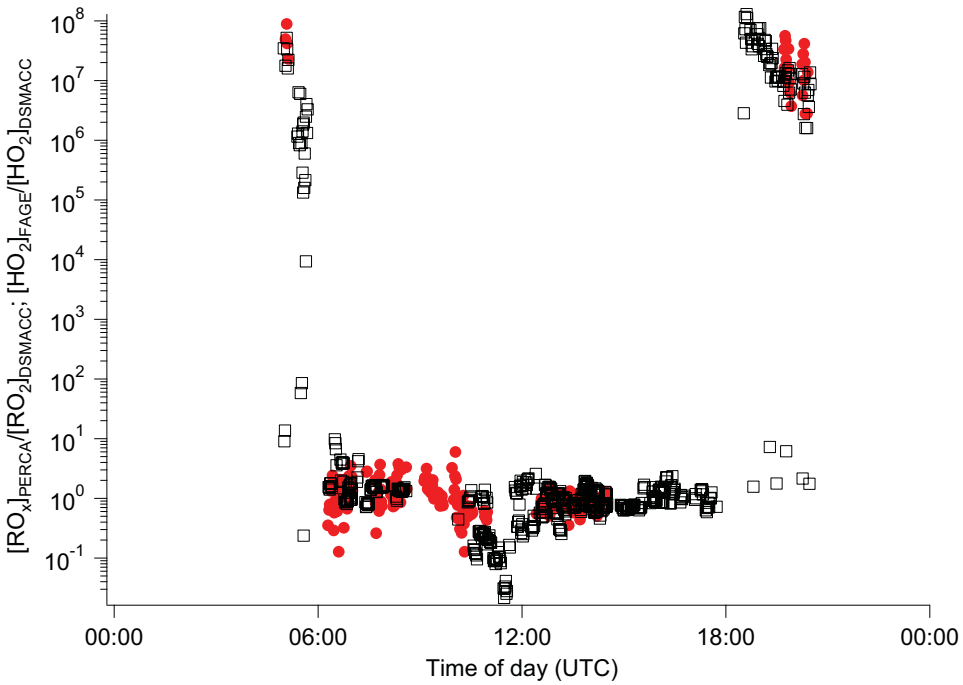

Figure 7.1: Diurnal composite of the ratio of measured to modelled peroxy radicals – (Red filled circles) PERCA measured [RO_x] relative to DSMACC model [RO_2]; (Black open squares) FAGE measured [HO_2] relative to DSMACC model [HO_2]

of NO and low concentrations of HO_x results in an extended lifetime for peroxy radicals (in particular organic peroxy radicals) and makes the steady state box model approach to the calculation of the concentration inaccurate. The (daytime) modelled composition follows the expected trends, and variation in modelled [RO_2] versus the PERCA measurement was explained in terms of measurement bias by composition, air mass and time of day.

The ozone balance for the West African Monsoon during the SOP2 period was evaluated by calculation of the net ozone tendency. Alkene ozonolysis was found to be insignificant compared to the net ozone tendency under most conditions, and therefore is unlikely to explain the depletion of ozone within the boundary layer over the biogenics source region. The net ozone tendency was also found to be relatively insensitive to the concentration of OH. The interception of a biomass burning plume on the 13 August 2006 was investigated in some detail, representing the most photochemically active air mass observed throughout the campaign. With the exception of this plume the results of the

limited assessment suggest that the WAM is predominantly NO_x limited. Of the dataset used for the calculation of the net ozone tendency (limited by crossover in data) a biogenic source of NO is suggested for enhancements in NO concentration owing to the near complete lack of correlation between NO and anthropogenic tracers. A balance point of [NO]=22.3($\pm$3.8) pptV is found for net ozone production similar to other assessments in the literature. The observed diurnal changes in partitioning of $[HO_2]/[RO_2]$ are suggested to modulate the balance between ozone production and loss within the day while soil emissions of NO limit the tendency. The observed nighttime transport of ozone precursors is suggested to contribute to the latitudinal gradient in ozone.

7.2 General conclusions and recommendations for further research

The work in this thesis has developed from an evaluation of the techniques of chemical amplification and filter radiometry, through to the application of these techniques in a complex aircraft field campaign for the measurement of peroxy radicals and photolysis rates respectively. Finally, the analysis and interpretation of the measurements has been achieved based on the understanding gained from the experimental and analytical work used to characterise the measurements.

Peroxy radicals are key tracers of the degradation of VOC's through their intermediary role in the catalytic oxidation cycles initiated by the OH radical, and hence their measurement is an essential element to understanding the processes dictating the composition of the atmosphere. Their central role in the transformation of NO to NO_2 beyond the photostationary state between ozone, NO and NO_2, is essential to the balance of ozone as NO_2 photolysis is the only known route to ozone production within the troposphere. The short lifetime of peroxy radicals owing to their inherent high reactivity makes them diagnostics of *in-situ* chemistry, making them ideal targets for the validation of models of atmospheric chemistry. The photolysis of ozone is a significant loss process, while also providing

the primary route to the formation of the hydroxyl radical given the presence of water vapour. The photolysis of NO_2 is essentially the final step in the formation of ozone in the troposphere, and therefore a critical process in the photostationary state. Without well defined measurements it is not possible to quantify these processes directly or test models that may hope to fill in the gaps where measurements are not defined now, or extrapolate into the past or future to predict the effects of the changing composition of the atmosphere.

Measurements all suffer some deficiencies in terms of absolute limitations dictated by underlying precision, and accuracy related to the underlying uncertainty in calibration. Considering the measurement of peroxy radicals the most significant limitations are in terms of specificity and the ability to speciate, and while partial speciation can be achieved no one measurement technique developed thus far measures anywhere near to the degree of chemical complexity represented by the most explicit schemes of atmospheric chemistry. Measurements such as the PERCA technique and those derived from it are purported to respond to the sum of peroxy radicals, but do this with varying efficiency depending on the composition of radicals and the measurement conditions. The publication of a single number $[RO_x]$ being supposedly equal to $[HO_2] + \sum_i [R_iO_2]$ is really an approximation to this and may lead to misinterpretation if the details of the measurement are not understood. The accuracy of the approximation and the true definition of $[RO_x]$ as measured through the PERCA technique is given by Equation 2.20 derived in Chapter 2, which has formed the basis of the interpretation of the measurements in Chapters 5 and 6. The importance of this is dramatically demonstrated by the assessment that the PERCA 4 measurements during AMMA could be best interpreted as responding primarily to organic peroxy radicals, and deviations in this response were likely the result of the weighting of the measurements response to the sensitivity to CH_3O_2. Immediately a number of experiments are identified that are needed to validate the interpretation of the measured response: The source of the discrepancy between the chain length humidity dependence observed in the laboratory and not ob-

served in the field measurements could be verified by an *in-situ* measurement of the humidity within the inlets in-flight; Verification of the pressure and temperature related changes in the chain length is required with respect to those radicals that typically dominate the composition; The relative chain length for the dominant radicals is needed to improve interpretation and reduce the biases within this measurement. Ideally this requires the development of a calibration setup that can simulate the ambient measurement situation where known quantities of key peroxy radicals may be introduced. In the meantime, the inlet chemistry model described in Chapter 3 that has been found to represent the altitude dependency of the chain length for methyl peroxy, could be extended to examine the potential pressure and temperature dependencies for further important radical species. The conclusion from this is that it is important to interpret the measured RO_x concentration by the PERCA technique (and similarly related techniques) through understanding of the relative response along with careful consideration of the known chemistry of free radicals in a coupled way.

In a similar manner the calibration of filter radiometer measurements, in particular those for the measurement of j_{O^1D} is complicated since these measurements have a fixed spectral sensitivity while the wavelength dependence of j_{O^1D} is a function of temperature, solar zenith angle and ozone column density. Satisfactory calibration requires the definition of the spectral sensitivity of filter radiometer and convolution of this with the spectral variation of j_{O^1D} to determine how the measured response varies under different conditions. Definition of the spectral response of the aircraft filter radiometers was not possible prior to AMMA and subsequent problems were identified with the spectral radiometer meant to be used as an absolute reference for calibration. The potential bias introduced from the calibration adopted has been assessed in Chapter 4, and by consideration of the direction and magnitude of this bias, the potential difference to the photolysis rate measurements during AMMA has been considered in Chapter 6. The recommendation is then that where these measurements have been applied, sensitivity studies should be used to assess the potential impact of the derived bias.

An alternative technique to determine the spectral sensitivity of a j_{O^1D} filter radiometer proposed in Chapter 4 which would make possible the correction of this measurement for SZA and ozone column, should be tested. The ability of spectral radiometers to measure the spectral actinic flux is a considerable advancement over the fixed bandwidth filter radiometer approach for j_{O^1D}, though similar considerations are still necessary in its calibration as required for a filter radiometer. The current implementation of the TUV model should be adapted to allow the derivation of temperature, ozone column and solar zenith angle corrections to the aircraft j_{O^1D} filter radiometer measurements, following the definition of the instrument spectral response.

The model versus measurement assessment of the PERCA RO_x measurements in Chapter 6, demonstrated that it is possible to explain a large proportion of the differences between the PERCA RO_x measurement and a detailed photochemical box model through an understanding of potential measurement biases. Although the box model has been used as an aid to interpretation of the measurement, it is not expected to be without some bias, and therefore further experimental characterisation of the measurement performance is essential to reduce the uncertainty within both. In particular the measured diurnal trend in the partitioning between HO_2 and RO_2 is not well represented by the model, although the absolute values correlate well during the daytime. All results and the conclusions that can be drawn are limited by the crossover between temporal and spatial coverage of observations with the times and scales over which the processes being studied vary. Owing to the broadly zonal symmetry of the WAM and the coherence of the processes dictating the chemical composition across the region, a coherent view has been observed from a significant but still sparse dataset. A NO_x limited regime is determined from the derivation of the net ozone tendency in Chapter 6 using a limited dataset, the overall non-correlation between ozone and CO broadly across the WAM suggests the photochemical regime is NO_x limited on the whole, within the lower troposphere. The distributions of the key compounds ozone and CO are thought to be explained by the surface distribution of their respective

sources and sinks, modified by transport within the monsoon flows. The budget of CO should be quantitatively considered in terms of the additional sources of CO (beyond anthropogenic) within the monsoon layer, the relative yield of CO from alkene ozonolysis versus OH initiated oxidation may be compared. The VOC reactivity calculated in Chapter 6 with respect to OH is considerably greater than with respect to ozone, so this suggests oxidation by OH may represent a more likely source dependent on yield.

Saxton *et al.* (2007) reports that terpene emissions observed at a rural field site near Djougou, Benin, during the period prior to monsoon onset in 2006, were dominated by non-native introduced species. Lebel *et al.* (2005) reports that significant landcover changes occurred over the Sahel since the 1950's driven by reduced rainfall, changing land use and demographic pressure. For example, reduced rainfall led to reduced crop productivity, while a high birth rate increased pressure on food resources; which led farmers to clear natural bush land in order to extend cultivated areas. The difference observed between the change in NDVI with the progression of the monsoon, compared to the profile of biogenic isoprene emission illustrates how variations in landcover can result in significant variations in atmospheric composition. There is significant uncertainty in changes in landcover on a regional scale over West Africa (Lebel *et al.*, 2005), and with that significant uncertainty in predicting isoprene emissions (e.g. Guenther *et al.* (2006)). Lebel *et al.* (2005) also reports significant deforestation occurred in countries along the coast of the Gulf of Guinea; since the isoprene profile is seen to be linked more closely to the forested region it suggests that related changes in isoprene emissions and therefore atmospheric composition are likely to have occurred. A changing landscape such as this will change VOC emissions and budgets and may influence the ozone balance and oxidative capacity overall, through changing the amount and composition of reactive VOC's supplied by the monsoon flow north to soil NO_x emission regions over the Sahel where the potential for ozone production is greatly enhanced.

In overall summary, measurements of radicals and photolysis rates, and their interpretation in the

context of the WAM have provided insight into the complex couplings between surface landcover, natural biogenic and anthropogenic emissions, atmospheric dynamics and composition. There is much that is still required in the development of measurements of radicals, particularly concerning their application to airborne platforms where the complexities of the measurement environment complicate interpretation. In general terms, the accurate partitioning and speciation of the radical population remains a goal.

Appendix A

Research Training Record

A.1 Induction Sessions

- Departmental induction
- Graduate School Induction and registration
- Cross Faculty Induction
- Introduction to techniques
- Fire Safety

A.2 Training Sessions

- Information skills for chemists
- Writing skills course

A.3 Level 3 and 4 Courses

- CH4108 Photochemistry
- CH3035 Advanced Molecular Spectroscopy

A.4 Departmental Seminars

17/10/05 - "Aspects of Chiral Surface Chemistry: An Electrochemical Perspective" - Professor Gary Attard, University of Cardiff.

26/10/05 - "Structural and Functional Analogues of Molybdenum and Tungsten Oxotranferases/Hydroxylases: What can be learned" - Joseph Chatt Lecture by Professor R. Holm, Harvard University, US.

07/11/05 - "New Physics and Chemistry of Drug Transport" - Professor Richard Templer, Imperial College, London.

29/11/05 - "From highly excited to ultracold molecules: Chemical dynamics in the extreme" - Professor Tim Softley, University of Oxford.

20/02/06 - "Ion Mobility Spectrometry: Shaping up for structural and trace analysis" - Professor Colin Creaser, Nottingham Trent University.

08/04/06 - "Soft Ionisation MS for quantitative studies of non-covalent interactions" - Professor R. Zenobi, ETHZ.

08/05/06 - "Origin and evolution of the atmosphere" - Professor Richard Wayne, Oxford University.

07/02/07 - "Molecular Spectroscopy and Space" - Professor Peter Bernath, University of York.

16/05/07 - "Meteors and their impact on the atmosphere" - RSC Theophilus/Redwood Lecture,

Professor J. M. C. Plane, University of Leeds.

13/06/07 - "Applications of Chemometrics: Biology, forensics and materials" - RSC Theophilus/Redwood Lecture by Professor R. G. Brereton, University of Bristol.

06/11/07 - "Directed self-assembly within systems of subcomponents" - Griess Lecture by Dr Jonathon Nitschke, University of Cambridge.

12/11/07 - "Exploring the dynamics of single aerosol particles" - Dr Jonathon Reid, University of Bristol.

12/02/08 - "Fingerprinting Air: Decoding the Atmosphere" - Inaugural lecture, Professor Paul Monks, University of Leicester.

18/02/08 - "On-line sensor systems to capture the chemical signature of brain injury" - Dr Martyn Boutelle, Imperial College London.

12/05/08 - "Correlated Quantum Dots" - RSC Tilden Lecture by Professor David Logan, University of Oxford.

23/02/09 - "From the Poles to the Tropics: Measurements of free radicals in the atmosphere using Laser Induced Fluorescence Spectroscopy" - Professor Dwayne Heard, University of Leeds.

A.5 Conferences/Meetings attended

26/10/05 - Tri-Universities Gas-Phase Chemical Physics Meeting; Leicester, Birmingham, Warwick - Hosted at the University of Leicester.

09/01/06-11/02/06 - European Research Course on Atmospheres 2006 - University Joseph Fourier, Grenoble, France and Observatoire Haute Provence.

03/05/06 - Meeting of the Atmospheric Chemistry Special Interest Group of the Royal Meteorological Society (ACSG) - Hosted at the University of Leicester.

04/10/06 - Informal meeting of the Birmingham, Leicester, Nottingham and Warwick Gas-Phase Research Groups - Hosted at the University of Warwick.

06/11/06-10/11/06 - AMMA Workshop "SOP debriefing and preparation of process studies" - Toulouse, France.

04/04/07 - Meeting of the Atmospheric Chemistry Special Interest Group of the Royal Meteorological Society - Hosted at the University of Leicester.

26/11/07-30/11/07 - Second International AMMA Conference - Hosted at Forschungzentrum Karlsruhe, Karlsruhe, Germany.

25/01/08 - AMMA-UK Chemical Modelling Meeting - Hosted at the Unversity of Leeds.

03/03/08-03/04/08 - AMMA-UK meeting - Hosted at the University of East Anglia, Norwich.

18/03/08 - Meeting of the Atmospheric Chemistry Special Interest Group of the Royal Meteorological Society - Hosted at the University of Leicester.

11/02/09-13/02/09 - AMMA Joint Meeting of WP's 2.4, 2.1.2 & 4.1.3 - Toulouse, France.

23/09/2009 - AMMA UK Meeting - Hosted at the Unversity of Leeds.

A.6 Conference Presentations

10/01/06 - European Research Course on Atmospheres 2006 - Talk entitled: "Control of atmospheric composition in the West African Monsoon".

10/01/06 - European Research Course on Atmospheres 2006 - Poster entitled: "Control of atmospheric composition in the West African Monsoon".

14/12/06 - NCAS Conference - Aircraft Instrumentation and Observations - Talk entitled: "Airborne measurements of peroxy radicals ($HO_2 + \Sigma_i R_i O_2$) and the photolysis rates of O_3 and NO_2 during AMMA: Initial results".

26/11/07-30/11/07 - Second International AMMA Conference, Forschungzentrum Karlsruhe, Karlsruhe, Germany - Poster entitled: "Airborne measurements of peroxy radicals ($HO_2 + \Sigma_i R_i O_2$) and the photolysis rates of O_3 and NO_2 during AMMA: Initial results".

12/02/2009 - AMMA Joint Meeting of WP's 2.4, 2.1.2 & 4.1.3, Toulouse, France - Talk entitled: "Airborne measurements of peroxy radicals during the AMMA IOP".

23/09/2009 - AMMA UK Meeting, Unversity of Leeds, UK - Talk entitled: "Peroxy radical measurements and modelling from AMMA SOP2".

A.7 Departmental Presentations

16/12/05 - Departmental talk: "Short-term variations of the oxidising power of the atmosphere".

01/06/06 - First year postgraduate talk: "Control of Atmospheric Composition in the West African Monsoon".

31/03/06 - Departmental talk: "Ozone, water vapour, and temperature in the upper tropical troposphere: Variations over a decade of MOZAIC measurements".

24/11/06 - Departmental talk: "Strong correlation between levels of tropospheric hydroxyl radicals and solar ultraviolet radiation".

11/05/07 - Departmental talk: “The interaction of the Ocean with the atmosphere and its importance”.

04/06/07 - Second year postgraduate talk: “Peroxy radical photochemistry and the composition of the atmosphere”.

14/03/08 - Departmental talk: “Utilising shade to optimise UV exposure for vitamin D”.

A.8 Papers

M. D. Andres-Hernandez, D. Stone, D. M. Brookes, R. Commane, C. E. Reeves, H. Huntrieser, D. E. Heard, P. S. Monks, J. P. Burrows, H. Schlager, D. Kartal, M. J. Evans, C. F. A. Floquet, T. Ingham, J. Methven, and A. E. Parker, Peroxy radical partitioning during the AMMA radical intercomparison exercise (submitted ACPD).

R. Sommariva, S.S. Brown, J.M. Roberts, D.M. Brookes, P.S. Monks, A.E. Parker, J.B. Gilman, B.M. Lerner, H.D. Osthoff, S.C. Tucker et al., Peroxy radicals in the Houston industrial area and the Gulf of Mexico during TexAQS 2006 (paper in preparation).

A.9 Other

Z. H. Beygi, H. Fischer, M. Martinez, H. Harder, U. Parchatka, P. Joeckel, C. Gurk, R. Koenigstedt, D. Brookes, P. Monks and J. Lelieveld. Oxidation photochemistry in the Southern Atlantic boundary layer: Unexpected deviations of photochemical steady state, American Geophysical Union 2009 Fall Meeting, San Francisco, USA (14-18 December 2009).

R. Sommariva, S.S. Brown, J.M. Roberts, A.E. Parker, D.M. Brookes, P.S. Monks, H.D. Osthoff, J.B. Gilman, P.D. Goldan, W.C. Kuster, B.M. Lerner, D. Welsh-Bon, E.J. Williams, F.C. Fehsenfeld, A.R.

Ravishankara, M. Trainer, J.A. de Gouw, G. Frost, S.C. Herndon, C. Warneke, M.S. Zahniser. Radical Chemistry and Ozone Production in the Houston Industrial Area, American Geophysical Union 2007 Fall Meeting, San Francisco, USA (10-14 December 2007).

R. Sommariva, S.S. Brown, J.M. Roberts, A.E. Parker, P.S. Monks, D.M. Brookes, S.C. Herndon, H.D. Osthoff, B.M. Lerner, E.J. Williams, M.S. Zahniser, F.C. Fehsenfeld, A.R. Ravishankara, M. Trainer. Peroxy Radicals Abundances and Ozone Production during TexAQS-GoMACCS 2006, Royal Meteorological Society Conference, Edinburgh, UK (3-6 September 2007).

R. Sommariva, S. S. Brown, J. M. Roberts, A. E. Parker, P. S. Monks, D. M. Brookes, H. D. Osthoff, B. M. Lerner, E. J. Williams, F. C. Fehsenfeld, A. R. Ravishankara and M. Trainer. Peroxy Radical Measurements from R/V Brown during TEXAQS 2006 TEXAQS Campaign Data Workshop.

Appendix B

Flow Control Methodology

The method of flow control employed in the University of Leicester PERCA instruments 3.5 and 4 is through mass flow control. It is important to understand the implications of this flow control methodology as the PERCA technique is indirect, and the conversion chemistry has a finite timescale that can be significant in terms of determining both the yield from conversion due to the timescale of the chain chemistry and the background signal due to the reaction between ozone and reagent NO. This appendix discusses the principles of mass flow control and derives a method for calculation of the true volume flow rate given the ambient temperature and pressure relative to the standard flow rate at standard temperature and pressure.

B.1 Mass Flow Control

The current methodology for sample air and reagent gas flow control is by a combination of mass flow meters (MFM, Tylan FM360, now manufactured and distributed by Celerity Inc.) with stepper motor controlled needle valves for sample flow control and mass flow controllers (MFC, Tylan FC260) for the control of reagents added to the sample flow at the inlets. The principle of operation of these type of flow meters and controllers is that they are calibrated to measure the mass flow rate of a designated

gas by a technique described as thermal mass flow control (Celerity, 2002).

The principle of thermal mass flow control as described by Celerity (2002), is through the determination of mass flow rate by measurement of heat flux. To do this in a flow controller or meter a small proportion of the gas flow is directed through a heated capillary tube. The temperature before and after the capillary tube are measured using 2 resistance temperature detectors (RTDs), the mass flow rate is then calculated from:

$$q = \dot{M} C_p \Delta T \tag{B.1}$$

Where q is the heat loss to the gas flow, $\dot{M}$ is the mass flow rate, C_p is the specific heat capacity for a constant pressure and ΔT the temperature difference between upstream and downstream sensors.

In terms of the chain length it is important to maintain the concentrations of the reactants (the reagent gases), the time for radical termination in background measurement mode, and the time over which radical to NO_2 conversions can occur in chain amplification. In terms of both chain amplication and background measurement this reaction time needs to be maintained within a limit determined by the time between front and rear inlet injection points of the reagents. At the reduced temperatures and pressures associated with making measurements at altitude, although the mass flow rates of the sample flow and reagents can be expected to be controlled (so long as the flow control copes) can we expect the reagent concentrations and the time available for chain chemistry to be maintained and is any change significant on the timescale required for chain completion?

The total mass of gas flowing M, is given by:

$$M = N m_i \tag{B.2}$$

Where N is the number of molecules and m_i the molecular mass of the given gas being controlled. Hence, if the mass flow rate is controlled, the number of molecules sampled per unit time is also

conserved in the flow:

$$\dot{M} = \dot{N} m_i = constant \tag{B.3}$$

$$\dot{N} = constant \tag{B.4}$$

The time available for chain chemistry can be related to the mass flow rate by relating the number of molecules, N, to temperature, T, pressure, P, and volume, V, through the ideal gas law,

$$N = \frac{PV}{k_B T} \tag{B.5}$$

This can then be used to determine the volume flow rate, $\dot{V}$,

$$\dot{N} = \frac{P}{k_B T} \dot{V} \tag{B.6}$$

From this it is possible to then relate volume flow rates at a constant mass flow rate but at different temperatures and pressures,

$$\frac{P_1}{k_B T_1} \dot{V_1} = \frac{P_2}{k_B T_2} \dot{V_2} \tag{B.7}$$

$$\dot{V_2} = \frac{P_1}{T_1} \dot{V_1} \frac{T_2}{P_2} \tag{B.8}$$

MFCs and MFMs are referenced to Standard Temperature and Pressure (101325 Pa and 0 °C following the Celerity User guide for Tylan TN260 mass flow controllers and meters (Celerity, 2008)) i.e. though the mass flow rate is maintained, the volume flow rate varies in proportion to the standard volume flow rate ($P_1 = 101325$ Pa and $T_1 = 273.15$ K (0 °C)). With temperature decreasing with altitude and pressure decreasing exponentially the ratio of pressure to temperature also decreases exponentially with increasing altitude. The result is that the sample volume flow rate has to increase exponentially with altitude relative to that at standard temperature and pressure to maintain the same mass flow rate. The pressure to temperature ratio as a function of altitude, Z, determined from the AMMA dataset (see Figure B.1) was fitted using a relationship of the form:

$$\frac{P_2}{T_2} = y0 + A \exp\left[\frac{x0}{\tau}\right] \exp\left[\frac{-Z}{\tau}\right] \tag{B.9}$$

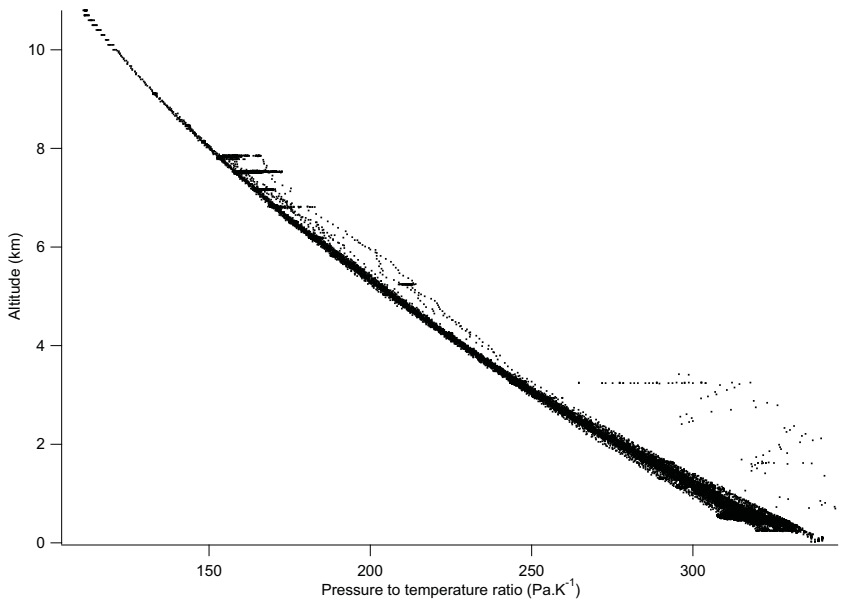

Figure B.1: Ratio of pressure to temperature as a function of altitude measured during the AMMA field campaign

Where $y0$ and $x0$ are fitting constants that determine the y and x offsets of the fit and τ describes the rate of fall of the exponential. The volume flow rate at a given altitude (applicable to the AMMA dataset) can then be determined, relative to the standard volume flow rate $\dot{V}_1$:

$$\dot{V}_2 = \frac{101325}{273.15}\dot{V}_1\left\{y0 + A\exp\left[\frac{x0}{\tau}\right]\exp\left[\frac{-Z}{\tau}\right]\right\}^{-1} \tag{B.10}$$

Since the sample inlet volume (V_{inlet}) is fixed, an exponential increase in the sample volume flow rate with altitude reduces the time available for chain chemistry exponentially ($t \propto V_{inlet}/\dot{V}_2$). The question then remains whether the reduction in the time available is at a level significant on the timescale required for completion of the chain cycle and termination of radicals during background measurement.

As proven, the volume flow rate of the sample flow increases exponentially with altitude to maintain a constant mass flow. The reagent mass flows are only dependent on the backing pressure which is essentially constant whilst the cylinder supplying the gas is not empty. The number of molecules passing through a cross section of the inlet per unit time is constant so the relative number of reagents

molecules to sample air molcules is maintained i.e. the mixing ratio of reagents is constant. However, the volume in which that number of molecules is contained increases as temperature and pressure decrease, meaning the number of molecules per unit volume (the absolute concentration) decreases.

Bibliography

Aghedo, A. M., Schultz3, M. G. & Rast, S. *Atmospheric Chemistry and Physics*, **7**, pp1193–1212, 2007.

AMMA-UK. Summary of the research programme, 2004.

Andersen, V. F., Nilsson, E. J. K., Jrgensen, S., Nielsen, O. J. & Johnson, M. S. *Chemical Physics Letters*, **472**(1-3), 23–29, 2009. 0009-2614 doi: DOI: 10.1016/j.cplett.2009.02.066.

Andres-Hernandez, M. D., Kartal, D., Reichert, L., Burrows, J. P., Meyer Arnek, J., Lichtenstern, M., Stock, P. & Schlager, H. *Atmos. Chem. Phys.*, **9**(11), 3681–3695, 2009. ACP 1680-7316.

Ashbourn, S. F. M., Jenkin, M. E. & Clemitshaw, K. C. *Journal of Atmospheric Chemistry*, **29**(3), 233–266, 1998. Times Cited: 17.

Atkins, P. & De Paula, J. *Physical Chemistry*. Oxford University Press, 8 edition, 2006.

Atkinson, R., Baulch, D. L., Cox, R. A., Crowley, J. N., Hampson, R. F., Hynes, R. G., Jenkin, M. E., Rossi, M. J. & Troe, J. *Atmos. Chem. Phys.*, **4**(6), 1461–1738, 2004. ACP 1680-7316.

Atkinson, R., Baulch, D. L., Cox, R. A., Crowley, J. N., Hampson, R. F., Hynes, R. G., Jenkin, M. E., Rossi, M. J., Troe, J. & Subcommittee, I. *Atmos. Chem. Phys.*, **6**(11), 3625–4055, 2006. ACP 1680-7316.

Atkinson, R., Baulch, D. L., Cox, R. A., Crowley, J. N., Hampson, R. F., Hynes, R. G., Jenkin, M. E.,

Rossi, M. J., Troe, J. & Wallington, T. J. *Atmos. Chem. Phys.*, **8**(15), 4141–4496, 2008. ACP 1680-7316.

Atkinson, R. & Arey, J. *Chemical Reviews*, **103**(12), 4605–4638, 2003. doi: 10.1021/cr0206420 0009-2665 doi: 10.1021/cr0206420.

Bais, A. F., Madronich, S., Crawford, J., Hall, S. R., Mayer, B., van Weele, M., Lenoble, J., Calvert, J. G., Cantrell, C. A., Shetter, R. E., Hofzumahaus, A., Koepke, P., Monks, P. S., Frost, G., McKenzie, R., Krotkov, N., Kylling, A., Swartz, W. H., Lloyd, S., Pfister, G., Martin, T. J., Roeth, E.-P., Griffioen, E., Ruggaber, A., Krol, M., Kraus, A., Edwards, G. D., Mueller, M., Lefer, B. L., Johnston, P., Schwander, H., Flittner, D., Gardiner, B. G., Barrick, J. & Schmitt, R. *Journal of Geophysical Research*, **108**(D16), 2003.

Bergamaschi, P., Frankenberg, C., Meirink, J. F., Krol, M., Dentener, F., Wagner, T., Platt, U., Kaplan, J. O., Korner, S., Heimann, M., Dlugokencky, E. J. & Goede, A. *Journal of Geophysical Research*, **112**(D02304), 2007.

Biesenthal, T. A. & Shepson, P. B. *Geophysical Research Letters*, **24**(11), 1375–1378, 1997.

Bloss, W. J., Lee, J. D., Heard, D. E., Salmon, R. A., Bauguitte, S. J. B., Roscoe, H. K. & Jones, A. E. *Atmos. Chem. Phys.*, **7**(16), 4171–4185, 2007. ACP 1680-7316.

Bohn, B., Corlett, G. K., Gillmann, M., Sanghavi, S., Stange, G., Tensing, E., Vrekoussis, M., Bloss, W. J., Clapp, L. J., Kortner, M., Dorn, H. P., Monks, P. S., Platt, U., Plass-Dulmer, C., Mihalopoulos, N., Heard, D. E., Clemitshaw, K. C., Meixner, F. X., Prevot, A. S. H. & Schmitt, R. *Atmos. Chem. Phys.*, **8**(17), 5373–5391, 2008. ACP 1680-7316.

Bohn, B., Kraus, A., Muller, M. & Hofzumahaus, A. *Journal of Geophysical Research-Atmospheres*, **109**(D10), 2004. D10S90.

Brookes, D., Parker, A. E., Green, T. J. & Monks, D. P. S. Perca iv technical specification of scientific equipment. Technical Report Issue 10, University of Leicester, 2006.

Buck, A. L. *Journal of Applied Meteorology*, **20**(12), 1527–1532, 1981. ISI Document Delivery No.: NF513 Times Cited: 152 Cited Reference Count: 20.

Butkovskaya, N., Rayez, M.-T., Rayez, J.-C., Kukui, A. & Le Bras, G. *The Journal of Physical Chemistry A*, **113**(42), 11327–11342, 2009. doi: 10.1021/jp811428p 1089-5639 doi: 10.1021/jp811428p.

Cantrell, C. A. *Journal of Geophysical Research*, **98**(D2), 2897–2909, 1993. Cited By (since 1996): 40 Export Date: 17 March 2008 Source: Scopus.

Cantrell, C. A., Edwards, G. D., Stephens, S., Mauldin, L., Kosciuch, E., Zondlo, M. & Eisele, F. *Journal of Geophysical Research-Atmospheres*, **108**(D6), 2003. Times Cited: 11.

Cantrell, C. A., Shetter, R. E. & Calvert, J. G. *Analytical Chemistry*, **68**(23), 4194–4199, 1996. ISI Document Delivery No.: VV333 Times Cited: 11 Cited Reference Count: 14.

Cantrell, C. A. & Stedman, D. H. *Geophysical Research Letters*, **9**(8), 846–849, 1982. ISI Document Delivery No.: PC665 Times Cited: 52 Cited Reference Count: 15.

Cantrell, C. A., Stedman, D. H. & Wendel, G. J. *Analytical Chemistry*, **56**(8), 1496–1502, 1984.

Celerity. Basics of thermal mass flow control - technology update. Technical Report TKS-002-0001 REVC 4/02, 2002.

Celerity. Tn260/tn360 series mass flow controllers and meters user guide. Technical Report 900457001 REV.002 01/08, 2008.

Clemitshaw, K. C. *Critical Reviews in Environmental Science and Technology*, **34**(1), 1 – 108, 2004.

Clemitshaw, K. C., Carpenter, L. J., Penkett, S. A. & Jenkin, M. E. *Journal of Geophysical Research*, **102**(D21), pp25,405–25,416, 1997.

Crawford, J., Davis, D., Chen, G., Shetter, R., Muller, M., Barrick, J. & Olson, J. *Journal of Geophysical Research-Atmospheres*, **104**(D5), 5725–5734, 1999. ISI Document Delivery No.: 177WV Times Cited: 24 Cited Reference Count: 21.

Crutzen, P. J. *Quarterly Journal of the Royal Meteorological Society*, **96**(408), 320–325, 1970. 10.1002/qj.49709640815.

Delon, C., Reeves, C. E., Stewart, D. J., Serca, D., Dupont, R., Mari, C., Chaboureau, J. P. & Tulet, P. *Atmos. Chem. Phys.*, **8**(9), 2351–2363, 2008. ACP 1680-7316.

Dickerson, R. R., Kondragunta, S., Stenchikov, G., Civerolo, K. L., Doddridge, B. G. & Holben, B. N. *Science*, **278**, 827–830, 1997.

Draxler, R. & Rolph, G. Hysplit (hybrid single-particle lagrangian integrated trajectory), 2003.

Drummond, J. W., Topham, L. A., Mackay, G. I. & Schiff, H. I. Use of chemiluminescence techniques in portable, lightweight, highly sensitive instruments for measuring no2, no(x), and o3. In *Measurement of atmospheric gases*, volume 1433 of *Society of Photo-Optical Instrumentation Engineers (SPIE Proceedings)*, pages 224–231, Los Angeles, CA, 1991.

Dusanter, S., Vimal, D. & Stevens, P. S. *Atmos. Chem. Phys.*, **8**(2), 321–340, 2008. ACP 1680-7316.

Dusanter, S., Vimal, D., Stevens, P. S., Volkamer, R. & Molina, L. T. *Atmos. Chem. Phys.*, **9**(5), 1665–1685, 2009. ACP 1680-7316.

Edwards, G. D., Cantrell, C. A., Stephens, S., Hill, B., Goyea, O., Shetter, R. E., Mauldin, R. L., Kosciuch, E., Tanner, D. J. & Eisele, F. L. *Analytical Chemistry*, **75**(20), 5317–5327, 2003. Times Cited: 8.

Edwards, G. D. & Monks, P. S. *Journal of Geophysical Research*, **108**(D16), 2003.

Emmerson, K. M. & Carslaw, N. *Atmospheric Environment*, **43**(20), 3220–3226, 2009. 1352-2310 doi: DOI: 10.1016/j.atmosenv.2009.03.042.

Emmerson, K. M., Carslaw, N., Carslaw, D. C., Lee, J. D., McFiggans, G., Bloss, W. J., Gravestock, T., Heard, D. E., Hopkins, J., Ingham, T., Pilling, M. J., Smith, S. C., Jacob, M. & Monks, P. S. *Atmos. Chem. Phys.*, **7**(1), 167–181, 2007. ACP 1680-7316.

Emmerson, K. M. & Evans, M. J. *Atmospheric Chemistry and Physics*, **9**(5), 1831–1845, 2009. ISI Document Delivery No.: 418FA Times Cited: 0 Cited Reference Count: 42.

Farman, J. C., Gardiner, B. G. & Shanklin, J. D. *Nature*, **315**(6016), 207–210, 1985. 10.1038/315207a0 10.1038/315207a0.

Fehsenfeld, F. C., Ancellet, G., Bates, T. S., Goldstein, A. H., Hardesty, R. M., Honrath, R., Law, K. S., Lewis, A. C., Leaitch, R., McKeen, S., Meagher, J., Parrish, D. D., Pszenny, A. A. P., Russell, P. B., Schlager, H., Seinfeld, J., Talbot, R. & Zbinden, R. *J. Geophys. Res.*, **111**, 2006.

Finlayson-Pitts, B. J. & Pitts, J. N. *Chemistry of the upper and lower atmosphere : theory, experiments, and applications*. Academic Press, 2000.

Fleming, Z. L., Monks, P. S., Rickard, A. R., Bandy, B. J., Brough, N., Green, T. J., Reeves, C. E. & Penkett, S. A. *Atmos. Chem. Phys.*, **6**(12), 5415–5433, 2006. ACP 1680-7316.

Frankenberg, C., Bergamaschi, P., Butz, A., Houweling, S., Meirink, J. F., Notholt, J., Petersen, A. K., Schrijver, H., Warneke, T. & Aben, I. *Geophysical Research Letters*, **35**(15), 2008. ISI Document Delivery No.: 338LL Times Cited: 6 Cited Reference Count: 23 L15811.

Frankenberg, C., Meirink, J. F., van Weele, M., Platt, U. & Wagner, T. *Science*, **308**(5724), 1010–1014, 2005. ISI Document Delivery No.: 927JR Times Cited: 72 Cited Reference Count: 25.

Fuchs, H., Brauers, T., Hseler, R., Holland, F., Mihelcic, D., Msgen, P., Rohrer, F., Wegener, R. & Hofzumahaus, A. *Atmos. Meas. Tech.*, **2**(1), 55–64, 2009. AMT 1867-1381.

Fuchs, H. *Measurement of Peroxy Radicals using Laser-Induced Fluorescence Technique*. PhD thesis, Forschungszentrum Julich, 2006.

Fuchs, H., Holland, F. & Hofzumahaus, A. *Review of Scientific Instruments*, **79**(8), 084104–12, 2008.

Fuentes, J. D., Lerdau, M., Atkinson, R., Baldocchi, D., Bottenheim, J. W., Ciccioli, P., Lamb, B., Geron, C., Gu, L., Guenther, A., Sharkey, T. D. & Stockwell, W. *Bulletin of the American Meteorological Society*, **81**(7), 1537–1575, 2000. ISI Document Delivery No.: 329BY Times Cited: 179 Cited Reference Count: 236.

Glover, B. G. & Miller, T. A. *The Journal of Physical Chemistry A*, **109**(49), 11191–11197, 2005.

Green, T. J., Reeves, C. E., Brough, N., Edwards, G. D., Monks, P. S. & Penkett, S. A. *Journal of Environmental Monitoring*, **5**, 75–83, 2003.

Green, T. J., Reeves, C. E., Fleming, Z. L., Brough, N., Rickard, A. R., Bandy, B. J., Monks, P. S. & Penkett, S. A. *Journal of Environmental Monitoring*, 2006.

Guenther, A., Karl, T., Harley, P., Wiedinmyer, C., Palmer, P. I. & Geron, C. *Atmos. Chem. Phys.*, **6**(11), 3181–3210, 2006. ACP 1680-7316.

Hanke, M., Uecker, J., Reiner, T. & Arnold, F. *International Journal of Mass Spectrometry*, **213** (2-3), 91–99, 2002. Times Cited: 19.

Hanson, D., Orlando, J., Noziere, B. & Kosciuch, E. *International Journal of Mass Spectrometry*, **239** (2-3), 147–159, 2004. 1387-3806 doi: DOI: 10.1016/j.ijms.2004.07.021.

Hard, T. M., O'Brien, R. J., Chan, C. Y. & Mehrabzadeh, A. A. *Environ. Sci. Technol.*, **18**(10), 768–777, 1984.

Hastie, D. R., Weissenmayer, M., Burrows, J. P. & Harris, G. W. *Analytical Chemistry*, **63**(18), 2048–2057, 1991. ISI Document Delivery No.: GE858 Times Cited: 55 Cited Reference Count: 42.

Haywood, J. M., Pelon, J., Formenti, P., Bharmal, N., Brooks, M., Capes, G., Chazette, P., Chou, C., Christopher, S., Coe, H., Cuesta, J., Derimian, Y., Desboeufs, K., Greed, G., Harrison, M., Heese,

B., Highwood, E. J., Johnson, B., Mallet, M., Marticorena, B., Marsham, J., Milton, S., Myhre, G., Osborne, S. R., Parker, D. J., Rajot, J. L., Schulz, M., Slingo, A., Tanre, D. & Tulet, P. *Journal of Geophysical Research-Atmospheres*, **113**, 2008. ISI Document Delivery No.: 383JK Times Cited: 12 Cited Reference Count: 60 D00C17.

Heard, D. E. & Pilling, M. J. *Chemical Reviews*, **103**(12), 5163–5198, 2003.

Hofzumahaus, A., Kraus, A. & Muller, M. *Applied Optics*, **38**(21), 4443–4460, 1999.

http://www.faam.ac.uk/. Faam webpage.

IPCC. Climate change 2001: The scientific basis. Technical report, 2001.

Jacob, M. *Measurement of Peroxy Radicals in the Regional Boundary Layer using the PERCA Technique*. PhD thesis, University of Leicester, 2006.

Jaegle, L., Jacob, D. J., Brune, W. H. & Wennberg, P. O. *Atmospheric Environment*, **35**(3), 469–489, 2001. ISI Document Delivery No.: 395TK Times Cited: 89 Cited Reference Count: 63.

Jaegle, L., Martin, R. V., Chance, K., Steinberger, L., Kurosu, T. P., Jacob, D. J., Modi, A. I., Yoboue, V., Sigha-Nkamdjou, L. & Galy-Lacaux, C. *Journal of Geophysical Research-Atmospheres*, **109**(D21), 2004. ISI Document Delivery No.: 872EM Times Cited: 28 Cited Reference Count: 63 D21310.

Janicot, S., Thorncroft, C. D., Ali, A., Asencio, N., Berry, G., Bock, O., Bourles, B., Caniaux, G., Chauvin, F., Deme, A., Kergoat, L., Lafore, J. P., Lavaysse, C., Lebel, T., Marticorena, B., Mounier, F., Nedelec, P., Redelsperger, J. L., Ravegnani, F., Reeves, C. E., Roca, R., de Rosnay, P., Schlager, H., Sultan, B., Tomasini, M., Ulanovsky, A. & team, A. f. *Ann. Geophys.*, **26**(9), 2569–2595, 2008. ANGEO 0992-7689.

Jenkin, M. E., Ashbourn, S. F. M. & Clemitshaw, K. C. Laboratory and modelling studies of the per-

oxy radical chemical amplification (perca) technique. Technical Report AEAT-4861/20147001/003 Issue 1, 1999.

Jenkin, M. E., Derwent, R. G. & S.M., S. The calculated fractional response of the chemical amplification technique to peroxy radical populations on a boundary layer trajectory over europe. In Larsen, B., Versino, B. & Angeletti, G., editors, *Proceedings of the 7th European Symposium on Physico-Chemical Behaviour of Atmospheric Pollutants, the Oxidising Capacity of the Troposphere*, pages 144–148, European Commission, Luxembourg, 1997.

Johnston, H. *Science*, **173**(3996), 517–522, 1971.

Jones, A. E. & Shanklin, J. D. *Nature*, **376**(6539), 409–411, 1995. 10.1038/376409a0 10.1038/376409a0.

Junkermann, W., Platt, U. & Volzthomas, A. *Journal of Atmospheric Chemistry*, **8**(3), 203–227, 1989.

Just, G. M. P., Sharp, E. N., Zalyubovsky, S. J. & Miller, T. A. *Chemical Physics Letters*, **417**(4-6), 378–382, 2006. 0009-2614 doi: DOI: 10.1016/j.cplett.2005.10.036.

Kelly, T. J., Spicer, C. W. & Ward, G. F. *Atmospheric Environment. Part A. General Topics*, **24**(9), 2397–2403, 1990.

Keppler, F., Hamilton, J. T. G., Bra, M. & Rockmann, T. *Nature*, **439**(7073), pp187–191, 2006.

Klinger, L. F., Guenther, G., Tyndall, G., Zimmerman, P., Bangui, M. M., Moutsambote, J. M. & Kenfack, D. *J. Geophys. Res.*, **103**, 1998.

Kraus, A. & Hofzumahaus, A. *Journal of Atmospheric Chemistry*, **31**(1-2), 161–180, 1998. ISI Document Delivery No.: 156FP Times Cited: 46 Cited Reference Count: 52.

Kuhn, U., Andreae, M. O., Ammann, C., Araujo, A. C., Brancaleoni, E., Ciccioli, P., Dindorf, T., Frattoni, M., Gatti, L. V., Ganzeveld, L., Kruijt, B., Lelieveld, J., Lloyd, J., Meixner, F. X., Nobre,

A. D., Poschl, U., Spirig, C., Stefani, P., Thielmann, A., Valentini, R. & Kesselmeier, J. *Atmos. Chem. Phys.*, **7**(11), 2855–2879, 2007. ACP 1680-7316.

Kylling, A., Webb, A. R., Kift, R., Gobbi, G. P., Ammannato, L., Barnaba, F., Bais, A., Kazadzis, S., Wendisch, M., Jakel, E., Schmidt, S., Kniffka, A., Thiel, S., Junkermann, W., Blumthaler, M., Silbernagl, R., Schallhart, B., Schmitt, R., Kjeldstad, B., Thorseth, T. M., Scheirer, R. & Mayer, B. *Atmos. Chem. Phys.*, **5**(7), 1975–1997, 2005. ACP 1680-7316.

Lebel, T., Redelsperger, J.-L. & Thorncroft, C. The international science plan for amma. Technical report, 2005.

Lee, A., Goldstein, A. H., Kroll, J. H., Ng, N. L., Varutbangkul, V., Flagan, R. C. & Seinfeld, J. H. *Journal of Geophysical Research*, **111**(D17305), 2006a.

Lee, J. D., Lewis, A. C., Monks, P. S., Jacob, M., Hamilton, J. F., Hopkins, J. R., Watson, N. M., Saxton, J. E., Ennis, C., Carpenter, L. J., Carslaw, N., Fleming, Z., Bandy, B. J., Oram, D. E., Penkett, S. A., Slemr, J., Norton, E., Rickard, A. R., K Whalley, L., Heard, D. E., Bloss, W. J., Gravestock, T., Smith, S. C., Stanton, J., Pilling, M. J. & Jenkin, M. E. *Atmospheric Environment*, **40**(39), 7598–7613, 2006b. 1352-2310 doi: DOI: 10.1016/j.atmosenv.2006.06.057.

Lelieveld, J., Butler, T. M., Crowley, J. N., Dillon, T. J., Fischer, H., Ganzeveld, L., Harder, H., Lawrence, M. G., Martinez, M., Taraborrelli, D. & Williams, J. *Nature*, **452**(7188), 737–740, 2008. 0028-0836 10.1038/nature06870 10.1038/nature06870.

Luke, W. T. & Dickerson, R. R. *Geophys. Res. Lett.*, **15**(11), 1181–1184, 1988.

Luke, W. T., Dickerson, R. R. & Nunnermacker, L. J. *J. Geophys. Res.*, **94**(D12), 14905–14921, 1989.

Madronich, S. *Journal of Geophysical Research-Atmospheres*, **92**(D8), 9740–9752, 1987. ISI Document Delivery No.: J7727 Times Cited: 349 Cited Reference Count: 68.

Madronich, S. & Flocke, S. The role of solar radiation in atmospheric chemistry. In Boule, P., editor, *Handbook of Environmental Chemistry*, pages pp1–26. Springer-Verlag, New York, 1998.

Maeda, Y., Aoki, K. & Munemori, M. *Analytical Chemistry*, **52**, 307–311, 1980.

Malicet, J., Daumont, D., Charbonnier, J., Parisse, C., Chakir, A. & Brion, J. *Journal of Atmospheric Chemistry*, **21**, 263–273, 1995.

Mao, J., Ren, X., Brune, W. H., Olson, J. R., Crawford, J. H., Fried, A., Huey, L. G., Cohen, R. C., Heikes, B., Singh, H. B., Blake, D. R., Sachse, G. W., Diskin, G. S., Hall, S. R. & Shetter, R. E. *Atmos. Chem. Phys.*, **9**(1), 163–173, 2009. ACP 1680-7316.

Mari, C. H., Cailley, G., Corre, L., Saunois, M., Atti, J. L., Thouret, V. & Stohl, A. *Atmos. Chem. Phys.*, **8**(14), 3951–3961, 2008. ACP 1680-7316.

Matsumi, Y., Comes, F. J., Hancock, G., Hofzumahaus, A., Hynes, A. J., Kawasaki, M. & Ravishankara, A. R. *Journal of Geophysical Research*, **107**(D3), 2002.

Matsumoto, J., Hirokawa, J., Akimoto, H. & Kajii, Y. *Atmospheric Environment*, **35**(16), 2803–2814, 2001.

Matsumoto, J. & Kajii, Y. *Atmospheric Environment*, **37**(34), 4847–4851, 2003.

Mihelcic, D., Ehhalt, D. H., Kulessa, G. F., Klomfass, J., Trainer, M., Schmidt, U. & Rohrs, H. *Pure and Applied Geophysics*, **116**(2-3), 530–536, 1978. ISI Document Delivery No.: EW064 Times Cited: 34 Cited Reference Count: 13.

Mihelcic, D., Musgen, P. & Ehhalt, D. H. *Journal of Atmospheric Chemistry*, **3**(3), 341–361, 1985. ISI Document Delivery No.: A0292 Times Cited: 56 Cited Reference Count: 19.

Mihelcic, D., Volz-Thomas, A., Ptz, H. W., Kley, D. & Mihelcic, M. *Journal of Atmospheric Chemistry*, **11**(3), 271–297, 1990. 10.1007/BF00118353.

Mihele, C. M. & Hastie, D. R. *Geophysical Research Letters*, **25**(No. 11), 1911–1913, 1998.

Mihele, C. M. & Hastie, D. R. *Journal of Geophysical Research-Atmospheres*, **108**(D15), 2003. ISI Document Delivery No.: 712PH Times Cited: 0 Cited Reference Count: 36 4450.

Mihele, C. M., Mozurkewich, M. & Hastie, D. R. *International Journal of Chemical Kinetics*, **31**(2), 1999.

Miyoshi, A., Hatakeyama, S. & Washida, N. *J. Geophys. Res.*, **99**, 1994.

Molina, M. J. & Rowland, F. S. *Nature*, **249**(5460), 810–812, 1974. 10.1038/249810a0 10.1038/249810a0.

Monks, P. S. *Chemical Society Reviews*, **34**, pp376395, 2005.

Monks, P. S., Rickard, A. R., Hall, S. L. & Richards, N. A. D. *Journal of Geophysical Research*, **109** (D17206), 2004.

Myneni, R. B., Hall, F. G., Sellers, P. J. & Marshak, A. L. *IEEE Transactions on Geoscience and Remote Sensing*, **33**(2), 481–486, 1995. ISI Document Delivery No.: QN940 Times Cited: 179 Cited Reference Count: 30.

Neuman, J. A., Huey, L. G., Ryerson, T. B. & Fahey, D. W. *Environmental Science and Technology*, **33**(7), 1133–1136, 1999. doi: 10.1021/es980767f 0013-936X doi: 10.1021/es980767f.

NOAA, NASA & USAF. Us standard atmosphere, 1976, 1976.

Olson, J. R., Crawford, J. H., Chen, G., Fried, A., Evans, M. J., Jordan, C. E., Sandholm, S. T., Davis, D. D., Anderson, B. E., Avery, M. A., Barrick, J. D., Blake, D. R., Brune, W. H., Eisele, F. L., Flocke, F., Harder, H., Jacob, D. J., Kondo, Y., Lefer, B. L., Martinez, M., Mauldin, R. L., Sachse, G. W., Shetter, R. E., Singh, H. B., Talbot, R. W. & Tan, D. *J. Geophys. Res.*, **109**, 2004. 10.1029/2003JD004278.

Olson, J. R., Crawford, J. H., Chen, G., Brune, W. H., Faloona, I. C., Tan, D., Harder, H. & Martinez, M. *J. Geophys. Res.*, **111**, 2006. 10.1029/2005JD006617.

Parker, A. E. *Measurement of Peroxy Radicals, Chemistry and Transport in the Atmosphere*. PhD thesis, University of Leicester, 2007.

Parker, A. E., Monks, P. S., Wyche, K. P., Balzani-Loov, J. M., Staehelin, J., Reimann, S., Legreid, G., Vollmer, M. K. & Steinbacher, M. *Atmos. Chem. Phys.*, **9**(6), 1989–2006, 2009. ACP 1680-7316.

Parker, D. J., Burton, R. R., Diongue-Niang, A., Ellis, R. J., Felton, M., Taylor, C. M., Thorncroft, C. D., Bessemoulin, P. & Tompkins, A. M. *Quarterly Journal of the Royal Meteorological Society*, **131**(611), 2839–2860, 2005a. 10.1256/qj.04.52.

Parker, D. J., Fink, A., Janicot, S., Ngamini, J. B., Douglas, M., Afiesimama, E., Agusti-Panareda, A., Beljaars, A., Dide, F., Diedhiou, A., Lebel, T., Polcher, J., Redelsperger, J. L., Thorncroft, C. & Wilson, G. A. *Bulletin of the American Meteorological Society*, **89**(7), 1015–1027, 2008. ISI Document Delivery No.: 439GD Times Cited: 6 Cited Reference Count: 17.

Parker, Douglas, J., Thorncroft, Chris, D., Burton, Ralph, R. & Diongue-Niang, A. *Quarterly Journal of the Royal Meteorological Society*, **131**(608), 1461–1482, 2005b. 10.1256/qj.03.189.

Peeters, J., Nguyen, T. L. & Vereecken, L. *Physical Chemistry Chemical Physics*, **11**(28), 5935–5939, 2009. ISI Document Delivery No.: 471DJ Times Cited: 8 Cited Reference Count: 22.

Penkett, S. A., Monks, P. S., Carpenter, L. J., Clemitshaw, K. C., Ayers, G. P., Gillet, R. W., Galbally, I. & Meyer, C. P. *Journal of Geophysical Research*, **102**(D11), 12805–12817, 1997.

Perner, D., Arnold, T., Crowley, J., Klpfel, T., Martinez, M. & Seuwen, R. *Journal of Atmospheric Chemistry*, **34**(1), 9–20, 1999. 10.1023/A:1006208828324.

Phillips, G. J. *Studies of Atmospheric Photochemistry in the European Troposphere*. Doctor of philosophy, University of Leicester, 2002.

Prather, M. J. & Jacob, D. J. *Geophysical Research Letters*, **24**(24), 3189–3192, 1997. ISI Document Delivery No.: YN927 Times Cited: 102 Cited Reference Count: 27.

Read, K. A., Mahajan, A. S., Carpenter, L. J., Evans, M. J., Faria, B. V. E., Heard, D. E., Hopkins, J. R., Lee, J. D., Moller, S. J., Lewis, A. C., Mendes, L., McQuaid, J. B., Oetjen, H., Saiz-Lopez, A., Pilling, M. J. & Plane, J. M. C. *Nature*, **453**(7199), 1232–1235, 2008. 0028-0836 10.1038/nature07035 10.1038/nature07035.

Redelsperger, J. L., Diongue, A., Diedhiou, A., Ceron, J. P., Diop, M., Gueremy, J. F. & Lafore, J. P. *Quarterly Journal of the Royal Meteorological Society*, **128**(582), 1229–1257, 2002. ISI Document Delivery No.: 564XR Times Cited: 35 Cited Reference Count: 44 Part B.

Reichert, L., Hernandez, M. D. A., Stobener, D., Burkert, J. & Burrows, J. P. *Journal of Geophysical Research-Atmospheres*, **108**(D1), 2003. 4017.

Reimann, S., Calanca, P. & Hofer, P. *Atmospheric Environment*, **34**(1), 109–115, 2000. 1352-2310 doi: DOI: 10.1016/S1352-2310(99)00285-X.

Reiner, T., Hanke, M. & Arnold, F. *Journal of Geophysical Research-Atmospheres*, **102**(D1), 1311–1326, 1997. Times Cited: 18.

Ren, X., Olson, J. R., Crawford, J. H., Brune, W. H., Mao, J., Long, R. B., Chen, Z., Chen, G., Avery, M. A., Sachse, G. W., Barrick, J. D., Diskin, G. S., Huey, L. G., Fried, A., Cohen, R. C., Heikes, B., Wennberg, P. O., Singh, H. B., Blake, D. R. & Shetter, R. E. *J. Geophys. Res.*, **113**, 2008. 10.1029/2007JD009166.

Rickard, A. R., Johnson, D., McGill, C. D. & Marston, G. *The Journal of Physical Chemistry A*, **103** (38), 7656–7664, 1999. doi: 10.1021/jp9916992 1089-5639 doi: 10.1021/jp9916992.

Rockmann, T., Brenninkmeijer, C. A. M., Neeb, P. & Crutzen, P. J. *J. Geophys. Res.*, **103**, 1998.

Ryerson, T. B., Huey, L. G., Knapp, K., Neuman, J. A., Parrish, D. D., Sueper, D. T. & Fehsenfeld, F. C. *Journal of Geophysical Research-Atmospheres*, **104**(D5), 5483–5492, 1999. ISI Document Delivery No.: 177WV Times Cited: 48 Cited Reference Count: 21.

Sadanaga, Y., Matsumoto, J., Sakurai, K., Isozaki, R., Kato, S., Nomaguchi, T., Bandow, H. & Kajii, Y. *Review of Scientific Instruments*, **75**(4), 864–872, 2004. ISI Document Delivery No.: 805CI Times Cited: 3 Cited Reference Count: 26.

Salisbury, G. *Measurements of peroxy radicals in the marine boundary layer*. PhD thesis, University of Leicester, 2001.

Salisbury, G., Monks, P. S., Bauguitte, S., Bandy, B. J. & Penkett, S. A. *Journal of Atmospheric Chemistry*, **41**, 163–187, 2002.

Sander, S. P., Finlayson-Pitts, B. J., Friedl, R. R., Golden, D. M., Huie, R. E., Keller-Rudek, H., Kolb, C. E., Kurylo, M. J., Molina, M. J., Moortgat, G. K., Orkin, V. L., Ravishankara, A. R. & Wine, P. H. *JPL Publication*, **06-2**, 2006.

Sandu, A. & Sander, R. *Atmos. Chem. Phys.*, **6**(1), 187–195, 2006. ACP 1680-7316.

Saunois, M., Reeves, C. E., Mari, C. H., Murphy, J. G., Stewart, D. J., Mills, G. P., Oram, D. E. & Purvis, R. M. *Atmos. Chem. Phys.*, **9**(16), 6135–6155, 2009. ACP 1680-7316.

Saxton, J. E., Lewis, A. C., Kettlewell, J. H., Ozel, M. Z., Gogus, F., Boni, Y., Korogone, S. O. U. & Serca, D. *Atmos. Chem. Phys.*, **7**(15), 4095–4106, 2007. ACP 1680-7316.

Schneising, O., Buchwitz, M., Burrows, J. P., Bovensmann, H., Bergamaschi, P. & Peters, W. *Atmospheric Chemistry and Physics*, **9**(2), 443–465, 2009. ISI Document Delivery No.: 406WN Times Cited: 0 Cited Reference Count: 52.

Schultz, M., Heitlinger, M., Mihelcic, D. & Volzthomas, A. *Journal of Geophysical Research-*

Atmospheres, **100**(D9), 18811–18816, 1995. ISI Document Delivery No.: RV887 Times Cited: 57 Cited Reference Count: 28.

Shetter, R. E., Junkermann, W., Swartz, W. H., Frost, G. J., Crawford, J. H., Lefer, B. L., Barrick, J. D., Hall, S. R., Hofzumahaus, A., Bais, A., Calvert, G., Cantrell, C. A., Madronich, S., Mueller, M., Kraus, A., Monks, P. S., Edwards, G. D., McKenzie, R., Johnston, P., Schmitt, R., Griffioen, E., Krol, M., Kylling, A., Dickerson, R. R., Lloyd, S. A., Martin, T., Gardiner, B., Mayer, B., Pfister, G., Roeth, E. P., Koepke, P., Ruggaber, A., Schwander, H. & Weele, M. v. *Journal of Geophysical Research*, **108**(D16), 2003.

Shetter, R. E. & Muller, M. *Journal of Geophysical Research-Atmospheres*, **104**(D5), 5647–5661, 1999. ISI Document Delivery No.: 177WV Times Cited: 76 Cited Reference Count: 37.

Shon, Z. H., Madronich, S., Song, S. K., Flocke, F. M., Knapp, D. J., Anderson, R. S., Shetter, R. E., Cantrell, C. A., Hall, S. R. & Tie, X. *Atmos. Chem. Phys.*, **8**(23), 7153–7164, 2008. ACP 1680-7316.

Silva, G. d., Graham, C. & Wang, Z.-F. *Environmental Science and Technology*, **44**(1), 250–256, 2010. doi: 10.1021/es900924d 0013-936X doi: 10.1021/es900924d.

Singh, H. B., Brune, W. H., Crawford, J. H., Flocke, F. & Jacob, D. J. *Atmos. Chem. Phys.*, **9**(7), 2301–2318, 2009. ACP 1680-7316.

Sinha, V., Williams, J., Crowley, J. N. & Lelieveld, J. *Atmos. Chem. Phys.*, **8**(8), 2213–2227, 2008. ACP 1680-7316.

Sommariva, R., Brown, S. S., Roberts, J. M., Brookes, D., Monks, P. S., Parker, A. E., Frost, G., Gilman, J. B., Lerner, B. M., Osthoff, H. D. & Tucker, S. C. *In preparation*, 2009.

Stark, H., Lerner, B. M., Schmitt, R., Jakoubek, R., Williams, E. J., Ryerson, T. B., Sueper, D. T., Parrish, D. D. & Fehsenfeld, F. C. *Journal of Geophysical Research*, **112**(D10S04), 2007.

Stevens, P. S., Mather, J. H., Brune, W. H., Eisele, F., Tanner, D., Jefferson, A., Cantrell, C., Shetter, R., Sewall, S., Fried, A., Henry, B., Williams, E., Baumann, K., Goldan, P. & Kuster, W. *Journal of Geophysical Research-Atmospheres*, **102**(D5), 6379–6391, 1997. ISI Document Delivery No.: WQ021 Times Cited: 55 Cited Reference Count: 38.

Stewart, D. J., Taylor, C. M., Reeves, C. E. & McQuaid, J. B. *Atmos. Chem. Phys.*, **8**(8), 2285–2297, 2008. ACP 1680-7316.

Stolarski, R. S. & Cicerone, R. J. *Canadian Journal of Chemistry-Revue Canadienne De Chimie*, **52** (8), 1610–1615, 1974. ISI Document Delivery No.: S9575 Times Cited: 335 Cited Reference Count: 26.

Stone, D. & Rowley, D. M. *Physical Chemistry Chemical Physics*, **7**(10), 2156–2163, 2005. ISI Document Delivery No.: 924OI Times Cited: 10 Cited Reference Count: 34.

Stull, R. B. *An Introduction to Boundary Layer Meteorology*, volume 13 of *Atmospheric and Oceanographic Sciences Library*. Kluwer Academic Publishers, 1988.

Talukdar, R. K., Longfellow, C. A., Gilles, M. K. & Ravishankara, A. R. *Geophysical Research Letters*, **25**(2), 143–146, 1998.

Volz-Thomas, A., Lerner, A., Patz, H.-W., Schultz, M., McKenna, D. S., Schmitt, R., Madronich, S. & Roth, E. P. *Journal of Geophysical Research*, **101**(D13), pp18,613–18,627, 1996.

Wang, Z. P., Gulledge, J., Zheng, J. Q., Liu, W., Li, L. H. & Han, X. G. *Biogeosciences*, **6**(4), 615–621, 2009. ISI Document Delivery No.: 441BB Times Cited: 0 Cited Reference Count: 40.

Wavemetrics. Igor pro manual version 6.0, 2007.

Wayne, R. P. *Chemistry of Atmospheres*. Oxford University Press, 3rd edition, 2000.

Zalyubovsky, S. J., Glover, B. G., Miller, T. A., Hayes, C., Merle, J. K. & Hadad, C. M. *The Journal of Physical Chemistry A*, **109**(7), 1308–1315, 2005.